Imperial College London

Numerical Modelling of the Continental Break-up of the southern South Atlantic

Author:

Chandra Sajjini Amber Taposeea

A doctoral thesis submitted in fulfilment of the requirements for the degree of

Doctor of Philosophy

of

Imperial College London

Department of Earth Science and Engineering

Imperial College London

January 2017

Copyright Declaration

The copyright of this thesis rests with the author and is made available under a Creative Commons Attribution Non-Commercial No Derivatives license. Researchers are free to copy, distribute or transmit the thesis on the condition that they attribute it, that they do not use it for commercial purposes and that they do not alter, transform or build upon it. For any reuse or redistribution, researchers must make clear to others the license terms of this work.



Chandra Sajjini Amber Taposeea
Department of Earth Science and Engineering
Imperial College London
January 2017

Declaration of Originality

I declare that this thesis titled, ***Numerical Modelling of the Continental Break-up of the southern South Atlantic***, and the work presented in it are my own, performed under the supervision of Jenny S. Collier at the Department of Earth Science and Engineering, Imperial College London and John J. Armitage at the Dynamique des Fluides Geologiques, Institut de Phyisque du Globe de Paris. All published and unpublished material used in the thesis has been given full acknowledgement. This thesis has not been previously submitted in whole or in part for a degree or any other qualification at this University or any other institution.



Chandra Sajjini Amber Taposeea
Department of Earth Science and Engineering
Imperial College London
January 2017

Abstract

The southern South Atlantic has often been considered a classic example of continental break-up in the presence of a starting mantle plume, evidenced from the Paraná-Etendeka continental flood basalts, the Rio Grande Rise & Walvis Ridge, and wide-spread presence of seaward dipping reflectors & high-velocity lower-crustal bodies along the conjugate margins. However, inconsistencies remain, including a stark contrast of non-volcanic and volcanic passive margins north and south of the aseismic ridges, and evidence from seaward dipping reflector distributions suggesting segmentation influenced magmatism. Within this project, different methods for the formation of the volcanic passive margins in the southern South Atlantic have been explored.

To test the main influence on magmatism during break-up, observational constraints of post and syn-rift magmatism originate from 38 wide-angle and multichannel seismic profiles. These measurements show that at 450 km south of the Walvis Ridge, oceanic crust has a thickness of 11.7 km, thinning to 6.1 km at a distance of 2300 km along-strike. Overall, oceanic crustal thickness decreases linearly along-strike with little indication of segmentation. Active mantle upwelling was also tested using the relationship between melt volumes and seismic velocity from syn-rift magmatism, with little evidence for this process. Using a numerical model of continental rifting capable of producing melt thickness and major element oxide compositions through time, the observational constraints from post and syn-rift magmatism required a hot layer present decreasing in temperature relative to the asthenosphere from 250 °C in the north to 50 °C at a distance of 2300 km south along-strike. By reconstructing the lithosphere thickness at break-up, it was suggested that the sublithospheric topography had a strong influence on magmatism throughout the region, including on the asymmetry in magmatism along the margins. Overall however, modelling results suggest that temperature, and in turn possibly a plume, was the primary control of magmatism during the opening of the southern South Atlantic.

Acknowledgements

Firstly, I would like to thank my supervisors Jenny Collier and John Armitage for their advice and guidance during my PhD. I would also like to thank members of our research group, Carl McDermott the SDR resident expert and Noemi Gyori our amazing UROP student. I am also grateful to several members of the science community for providing me with their data, including Klaus Bauer, Stewart Fishwick, Maryline Moulin, Katarina Becker and Robert Trumbull. My gratitude goes to ION Geophysics for allowing me to use their data. I would like to thank the John Archer Endowment Fund and the American Geophysical Union for their grants to me. And finally thank you to Ian Bastow, for helping me with all things Linux, GMT, and LaTeX at the start, and for always having his door open for generally good advice over the years.

On a personal note, I am grateful for the many tables in various places upon which I have done much work - the dining room in the Fisher household in Salisbury, Rikke's table in Brussels, several AirBnBs around Europe and countless coffee shop, train and plane tables. Alexis, thank you for always having a place for me to crash in Paris when visiting IPGP, or when the Eurostar messed up. I would like to thank the people in my corner of Level 2 (I've lost count of how many crosswords we have done!). Thanks to Angus for help with my start in MATLAB and many other things, Conor with random LaTeX and Linux requests answered online, to Izzy for being my figures critique in the past year. Thanks to Dom for making sure my hands worked in the final few months despite the RSI. Thanks to Christopher Dean for all the much needed hugs over the years from two pods away. I would also like to thank The Fishers, The Salmons and The Scotts for their constant support and understanding. To Heddi and Mette, thank you for being my first Norwegian friends and welcoming me with open arms during my internship at Statoil. To the whole 'Back to the Smoke' group, thank you for always making me smile. Bekki and Charlotte, thank you for your friendship and our chats, my life would be a lot duller without you!

To Ellie, for always being interested in what I'm doing, and for your help with random alternative word requests during the times I am reminded that English isn't technically my first language. To Steph, thank you for always always always being there for me no matter where you are in the world, letting me go on PhD-related tangents that you may not really follow but always give good advice on, and for always being a voice of reason when I'm anxious. To Catriona, for the countless coffee breaks, and for always giving me sound advice on whatever qualm I may have had. To Rebecca, I still remember we sat down together for lunch on the first day of our PhDs, and just continuing for pretty much the next 4 years - thank you everything and for always having my back.

To Mamy for inspiring my love of all things cooking, which proved to be a great release from work. To Papy for inspiring my desire to understand things. To Steven, my godfather, for all the space-related items over the years! Also, had he not gone to Imperial first, I would have probably never ended up being the wide-eye 17 year old in 2007.

Finally and most importantly, to my family and Ed. Kal, thank you for always having a place for me. To Mum and Dad. I can't even thank you enough for all the love and support you continuously give me every single day. I wouldn't even be close to where I am today without you. Words cannot express my gratitude. Thank you for always being there even if you guys are far. Love you so much! Ed, you have always believed in me with all of my endeavours. I don't think I would still have my sanity if you weren't there when I came home at night from college or finally left the dining room table. Thank you for all the love and support over the years. I couldn't have done it without you or my parents, I can't thank you all ever enough.

To my parents.

For always being behind me and being my biggest supporters.

List of Publications, Conferences and Awards

Journal Publication

Taposeea et al. (2016): Asthenosphere and lithosphere structure controls on early onset oceanic crust production in the southern South Atlantic, Tectonophysics, http://dx.doi.org/10.1016/j.tecto.2016.06.026

Conference Proceedings

Dec 15	American Geophysical Union Fall Meeting, San Francisco, USA (poster)
Sep 15	British Geophysical Association Postgraduate Meeting, Southampton, UK (oral)
Sep 13	British Geophysical Association Postgraduate Meeting, Southampton, UK (poster)

Awards

Student Travel Grant	American Geophysical Union (2015)
John S. Archer Endowment Fund	Imperial College London (2013)

Contents

Title Page **1**

Copyright Declaration **3**

Declaration of Originality **4**

Abstract **5**

Acknowledgements **6**

List of Publications, Conferences and Awards **8**

Table of Contents **9**

List of Figures **17**

List of Tables **24**

List of Acronyms **26**

1 Introduction **27**

1.1 Passive Margins 27

1.2 Non-Volcanic Passive Margins 28

1.3 Volcanic Passive Margins . . . 29

1.4 Flood Basalts . . . 31

1.5 The *Mantle Plume - VPM Theory* . . . 32

1.5.1 Mantle plumes . . . 32

1.5.2 Identification of mantle plumes through associated volcanic passive margins . . . 34

1.6 Departures from the *Mantle Plume - VPM Theory* . . . 35

1.6.1 Inconsistencies with a classic "mushroom head" plume . . . 36

1.6.2 Volcanic passive margins with no associated continental flood basalts . . . 38

1.7 Modifications to the *Mantle Plume - VPM Theory*: Rift History . . . 39

1.8 Alternative mechanisms for the formation of Volcanic Passive Margins . . . 41

1.8.1 Small-scale convection . . . 41

1.8.2 Active mantle upwelling . . . 42

1.8.3 Segmentation . . . 43

1.9 Thesis Outline . . . 44

2 Geological and Geophysical Setting 46

2.1 Introduction . . . 46

2.2 Pre-Rift Geology . . . 48

2.3 Reconstruction . . . 50

2.4 Onshore Volcanism: Paranà-Etendeka Traps and Dyke Swarms . . . 53

2.5 Volcanic Passive Margins . . . 54

2.5.1 Evidence from seismic data . . . 54

2.5.2 Evidence from gravity data . . . 55

2.6 Production of Ocean Crust: evidence from seafloor spreading magnetic anomalies . . . 56

2.7 Segmentation . . . 59

2.8 Rio Grande Rise and Walvis Ridge . . . 61

2.9 DSDP expeditions . . . 61

2.10 Departures from *Mantle Plume - VPM Theory* within the South Atlantic . . . 62

3 Observational Constraints **64**

3.1 Introduction . . . 64

3.2 Identification of Magmatism . . . 65

3.2.1 Landward Limit of Oceanic Crust . . . 66

3.2.2 Syn-rift magmatism . . . 67

3.3 Wide-Angle Profiles: African Margin . . . 68

3.3.1 Profile from Fromm et al., 2015: Profile AF0 . . . 69

3.3.1.1 Original data . . . 69

3.3.1.2 Identification of syn-rift magmatism . . . 69

3.3.2 Profiles from Bauer et al., 2000: Profiles AF1 & AF2 . . . 70

3.3.2.1 Original data . . . 70

3.3.2.2 Identification of LaLOC and syn-rift magmatism . . . 72

3.3.3 Profiles from Schinkel, 2006 and Hirsch et al., 2009: Profiles AF3 & AF4 . . . 77

3.3.3.1 Original data . . . 77

3.3.3.2 Identification of LaLOC and syn-rift magmatism . . . 80

3.4 Wide-Angle Profiles: South American Margin . . . 84
3.4.1 Profiles from Becker et al., 2014: Profiles SA1 & SA3 . . . 85
3.4.1.1 Original data . . . 85
3.4.1.2 Identification of LaLOC and syn-rift magmatism . . . 88
3.4.2 Profile from Schnabel et al., 2008: Profile SA2 . . . 94
3.4.2.1 Original data . . . 94
3.4.2.2 Identification of LaLOC and syn-rift magmatism . . . 94
3.5 Summary of Wide-Angle Profiles . . . 98
3.6 Multi-Channel Seismic Data . . . 99
3.6.1 Original data . . . 99
3.6.2 Identification of LaLOC . . . 99
3.7 Age Constraints . . . 107
3.8 Summary . . . 108

4 Numerical modelling of Continental Rifting 110

4.1 Introduction . . . 110
4.2 Equations of Conservation . . . 114
4.3 Decompression Melting . . . 115
4.4 Calculation of Major Element Oxide Composition . . . 118
4.4.1 Calculation of seismic velocity from major element oxides . . . 120
4.5 Model Set-Up . . . 121
4.5.1 Dimensions . . . 121

4.5.2 Model space . . . 121

4.6 Model Sensitivities: the Choice of Parameters . . . 125

4.6.1 Resolution . . . 125

4.6.2 Temperature, spreading rate and lithosphere thickness . . . 125

4.6.3 Composition parametrisation and major element oxides . . . 128

4.7 Summary . . . 130

5 Asthenosphere and lithosphere structure controls on early onset oceanic crust production in the southern South Atlantic 132

5.1 Introduction . . . 132

5.2 Methodology . . . 134

5.2.1 Tectonic framework: along-strike variability . . . 134

5.2.2 Initial oceanic crustal thickness . . . 134

5.2.3 Numerical modelling . . . 137

5.2.3.1 Understanding model sensitivity . . . 137

5.2.3.2 Initial lithosphere thickness and rate of extension . . . 139

5.2.3.3 Model asthenosphere temperature structure . . . 142

5.3 Results . . . 143

5.3.1 Observed variation in ocean crustal thicknesses . . . 143

5.3.2 Results from numerical model . . . 146

5.3.2.1 Establishing model asthenosphere temperature . . . 146

5.3.2.2 Establishing hot layer temperatures . . . 147

5.3.2.3 Results for segment-age trends . . . 149

5.4 Discussion . . . 151

5.5 Summary . . . 152

6 Testing models of syn-rift melt generation in the southern South Atlantic 154

6.1 Introduction . . . 154

6.1.1 Active Mantle Upwelling . . . 155

6.1.2 Numerical model of continental rifting and the *Mantle Plume - VPM Theory* . . . 155

6.2 Testing for the presence of Active Mantle Upwelling: H_c-V_p method . . . 156

6.2.1 Holbrook et al. (2001) approach . . . 156

6.2.2 Parkin and White (2008) approach . . . 158

6.2.3 H_c - V_p curves for Profiles AF0–AF4 . . . 159

6.3 Assessing the *Mantle Plume - VPM Theory* for Syn-Rift Magmatism: Numerical Modelling of Continental Rifting . . . 163

6.3.1 Composition parametrisation for the calculation of major element oxides . . . 164

6.3.2 Model asthenosphere temperature structure . . . 166

6.3.3 Results from numerical model of continental rifting . . . 167

6.3.3.1 Matching of model melt areas to observed melt areas . . . 167

6.3.3.2 Matching of model seismic velocity trends to observed seismic velocity trends . . . 169

6.4 Summary . . . 171

7 Discussion: the evidence for a plume in the South Atlantic 174

7.1 Introduction . . . 174

7.2 Critical evaluation of Alternative Models . . . 174

7.2.1 Evidence for segmentation . . . 175

7.2.2 Active mantle upwelling . . . 176

7.3 Critical evaluation of the *Mantle Plume - VPM Theory* . . . 177

7.3.1 Duration of rifting . . . 177

7.3.2 Extent of volcanic passive margins in the Southern Segment . . . 178

7.3.3 Reduction in magmatism along-strike from observational constraints . . . 180

7.3.4 Evidence from results of the numerical model of continental rifting . . . 181

7.3.5 Comparison to the North Atlantic and Indian Ocean . . . 183

7.4 Departures from the *Mantle Plume - VPM Theory* . . . 185

7.4.1 Asymmetry in magmatism between the conjugate margins . . . 185

7.4.2 Magmatism in the Central Segment . . . 187

7.5 Tristan Plume: a configuration . . . 188

7.5.1 Additional observational constraints for the Tristan Plume . . . 189

8 Conclusions **191**

Bibliography **196**

A Appendix A: Additional wide-angle seismic data information **218**

A.1 Wide-Angle Seismic Surveys . . . 218

A.2 Wide-Angle Data Location . . . 219

B Appendix B: Geochemistry Data **223**

B.1 DSDP Drill Holes . . . 224

B.1.1 Drill holes reaching pre/syn-rift sediment 224

B.1.2 Drill holes reaching basement 224

B.2 Mid-Atlantic Ridge Geochemistry 226

C Appendix C: Permissions **228**

D Appendix D: Taposeea et al. (2016): *Asthenosphere and lithosphere structure controls on early onset oceanic crust production in the southern South Atlantic*, Tectonophysics **235**

List of Figures

1.1 Global distribution of passive margins, demonstrating locations for volcanic, non-volcanic, transform and intermediate/uncertain margins. 28

1.2 Schematic cross section of a non-volcanic passive margin, adapted from Franke (2013). 29

1.3 Locations of SDRs identified by Hinz (1981). 30

1.4 Schematic cross section of a volcanic passive margin, adapted from Geoffroy (2005). 30

1.5 Schematic of a rising plume head through the asthenosphere and the impact of a plume in the North Atlantic, adapted from Coffin and Eldholm (1994) and White and McKenzie (1989). . . . 33

1.6 Igneous thickness of SIGMA lines from the North Atlantic versus distance from hotspot track, adapted from Holbrook et al. (2001). 34

1.7 Present day North Atlantic margins with break-up volcanism and measurement points of initial oceanic crustal thickness plotted along-strike. 35

1.8 Wide-angle Profile P3 crossing the Walvis Ridge along strike, adapted from Fromm et al. (2015). 36

1.9 Present day Indian Ocean with break-up volcanism 37

1.10 Location of East Coast Magnetic Anomaly and seismic transects found along the margin, adapted from Kelemen and Holbrook (1995). 38

1.11 Location of Cuvier and Gascoyne volcanic margins offshore Western Australia. 39

1.12 Example of small-scale convection resulting from the insulation of the mantle below a supercontinent, adapted from King and Anderson (1995) and King and Anderson (1998). 41

1.13 Predicted relationship for crustal thickness and mean seismic velocity, used to demonstrate melting due to a thermal anomaly or active mantle upwelling, adapted from Holbrook et al. (2001). . 42

1.14 SDRs and segment boundaries from Franke et al. (2007) and Koopmann et al. (2014b) 43

1.15 Model of increased magmatism at segment boundaries shown in the model space, adapted from Koopmann et al. (2014a). 44

2.1 Main tectonic features of the South Atlantic with age progressive LIPs 47

2.2 Schematic map showing locations of cratons and Neoproterozoic fold belts, adapted from Frimmel et al. (2011). 48

2.3 Reconstruction of West Gondwana with lithosphere thickness in the Permian, adapted from McKenzie et al. (2015). 49

2.4 Simplified versions of reconstructions model, adapted from Pérez-Díaz and Eagles (2014). 50

2.5 Differences between the Moulin et al. (2010) and Heine et al. (2013) reconstruction models . . . 51

2.6 Reconstruction of the South Atlantic at 121 Ma using the rotation poles from Moulin et al. (2010) 52

2.7 Schematic of the South Atlantic at ∼130 Myr, showing location of Mesozoic dike swarms. Adapted from Trumbull et al. (2007). 53

2.8 Map showing coverage of published seismic tracklines in the South Atlantic 54

2.9 Free-air gravity anomaly (v21) from Sandwell et al. (2013) 56

2.10 Magnetic anomaly (EMAG2) grid from Maus et al. (2009) and Moulin et al. (2010) magnetic isochrons location 57

2.11 Location of Cretaceous Magnetic Quiet Zone 58

2.12 Spreading rates for the South Atlantic, adapted from Heine et al. (2013). 59

2.13 Map of the gravity gradient from Sandwell et al. (2013) for the study area, showing the location of Segments 1–4 60

2.14 Map of DSDP drill hole locations 62

3.1 Location of African wide-angle seismic profiles 68

3.2 Profile AF0 (P100) originating from Fromm et al. (2015). 69

3.3 Syn-rift magmatism for Profile AF0 70

3.4 Profile AF1 (Transect 1) from Bauer et al. (2000) 71

3.5 Profile AF2 (Transect 2) from Bauer et al. (2000) 72

3.6 Syn-rift magmatism and possible locations of the LaLOC for Profile AF1 74

3.7 Syn-rift magmatism and possible locations of the LaLOC for Profile AF2 75

3.8 Depth-V_p profiles for the three potential LaLOC locations for Profiles AF1 and AF2. 76

3.9 Map of possible LaLOC locations for Profiles AF1 and AF2. 76

3.10 Proximal MCS profile to Profiles AF1 and AF2 from Koopmann et al. (2014b) 77

3.11 Profile AF3 (Orange line), from Schulze et al. (2007) and originating from Schinkel (2006). . . . 78

3.12 Profile AF4 (Springbok line) from Hirsch et al. (2009) 79

3.13 Syn-rift magmatism and possible locations of the LaLOC for Profile AF3 81

3.14 Syn-rift magmatism and possible locations of the LaLOC for Profile AF4 82

3.15 Depth-V_p profiles for the three potential LaLOC locations for Profiles AF3 and AF4. 83

3.16 Map of possible LaLOC locations for Profiles AF3 and AF4. 83

3.17 Location of South American wide-angle seismic profiles 84

3.18 Profile SA1 (BGR04-01) from Becker et al. (2014) 86

3.19 Profile SA3 (BGR04-02) from Becker et al. (2014) 87

3.20 Syn-rift magmatism and possible locations of the LaLOC for Profile SA1 89

3.21 Coincidental MCS line with Profile SA1 90

3.22 Syn-rift magmatism and possible locations of the LaLOC for Profile SA3 91

3.23 Depth-V_p profiles for the two potential LaLOC locations for Profiles SA1 and SA3. 92

3.24 Map of possible LaLOC locations for Profile SA1. 92

3.25 Map of possible LaLOC locations for Profiles SA2 and SA3. 93

3.26 Profile SA2 (BGR98-REFR2) from Schnabel et al. (2008) 95

3.27 Syn-rift magmatism and possible locations of the LaLOC for Profile SA2 96

3.28 Depth-V_p profiles for the three potential LaLOC locations for Profile SA2. 97

3.29 Coincidental MCS line with Profile SA2 97

3.30 Map of Location of BGR MCS lines 100

3.31 Seismic profiles BGR98-01 and 41. 101

3.32 Seismic profiles BGR98-05 and 15. 102

3.33 Seismic profiles BGR98-18 and 07. 103

3.34 Seismic profiles BGR98-20 and 22. 104

3.35 Seismic profile BGR04-08/13. 105

3.36 Seismic profile BGR87-01B 106

3.37 Crustal thickness measurement at the LaLOC locations for Winterbourne et al. (2014) data. . . . 106

3.38 Moulin-Gee age grid for South America and Africa 107

3.39 Reconstructions using GPlates shown at 121 Ma with oceanic crustal thickness at LaLOC locations for conjugate margins 109

4.1 Examples of different types of numerical models of rifting, with different lithospheric stretching and depth dependent viscosities. 111

4.2 Schematic demonstrating the difference between wet and dry solidus melting regimes. 116

4.3 Model Space . . . 122

4.4 Model progression for Temperature and Viscosity, a zoomed perspective . . . 122

4.5 Model progression for Temperature and Viscosity . . . 123

4.6 Model flowchart . . . 124

4.7 Base Model Runs: differing resolutions of 256 x 256 and 512 x 512. . . . 125

4.8 Base Model Runs: Varying model asthenosphere temperatures . . . 126

4.9 Base Model Runs: Varying hot layer temperatures . . . 126

4.10 Base Model Runs: Differing spreading rates . . . 127

4.11 Base Model Runs: Differing initial lithosphere thickness . . . 127

4.12 Melt production vs Melt depletion for WM91 . . . 128

4.13 Melt production vs Melt depletion for N97 . . . 129

4.14 Different major element oxides compositions results for different composition parametrisations . . 130

5.1 Wide-angles crustal thickness measurement at the LaLOC . . . 135

5.2 Varying hot layer temperatures with pre, syn and post-rift phases . . . 138

5.3 Evolution plots for different initial lithosphere thickness and excess hot layer temperature . . . 139

5.4 Comparison of two seismic tomography models . . . 140

5.5 Reconstruction at 121 Ma with lithosphere thickness . . . 141

5.6 Initial oceanic crustal thickness plotted against distance along-strike . . . 143

5.7 Ocean crustal thickness from the ION Geophysical long-offset data . . . 144

5.8 Ocean crustal thickness from two ION Geophysical lines transgressing segments . . . 145

5.9 Determining the model asthenosphere temperature using ocean crust thicknesses from the long-offset ION Geophysical lines. . . . 146

5.10 Matching models with observational constraint from Profiles AF1–AF4 and SA1–SA3 147

5.11 Error margins for models matched with observational constraint from Profiles AF1–AF4. 148

5.12 Model results per segment on the South American margin using ION Geophysical data. 149

5.13 Hot layer temperature vs. distance along-strike for post-rift magmatism 150

6.1 Profile AF0: velocity model and line drawing with $6.5\,\mathrm{km\,s^{-1}}$ and $6.7\,\mathrm{km\,s^{-1}}$ contours. 157

6.2 H_c-V_p reference models, adapted from Holbrook et al. (2001) 158

6.3 H_c-V_p reference models, adapted from Parkin and White (2008) 159

6.4 H_c-V_p for African profiles, using the Holbrook et al. (2001) approach 161

6.5 H_c-V_p for African profiles, using the Parkin and White (2008) approach 162

6.6 H_c-V_p for African profiles using information solely from the HVLC bodies. 163

6.7 Comparison of model composition at steady-state to normalised DSDP values. 165

6.8 Comparison of model composition at steady-state to normalised MAR values. 166

6.9 Comparison of model melt areas to areas from Profile AF2 167

6.10 Results from matching model results to melt areas from Profiles AF0-AF4, presented as hot layer temperature against lithosphere thickness. 169

6.11 Model results for Profile AF0 for seismic velocity trends 170

6.12 Model results for Profiles AF1 & AF2 for seismic velocity trends 170

6.13 Model results for Profiles AF3 & AF4 for seismic velocity trends 171

6.14 Hot layer temperature vs. distance along-strike for syn-rift magmatism 172

7.1 Summary of the H_c-V_p curves for Profiles AF0–AF4 using the Holbrook et al. (2001) correction. 176

7.2 Reconstructions using GPlates shown at 121 Ma with LaLOC locations for conjugate margins, including mantle temperatures from numerical modelling results and onshore temperatures derived from MgO values. 179

7.3 Igneous Crustal Thickness for Profiles AF0–AF4 as a function of distance along-strike and age. . 181

7.4 Overall trend for hot layer temperature vs. distance along-strike using model results matched to observational constraints from post and syn-rift magmatism. 182

7.5 Numerical model results for hot layer temperature for this project in the southern South Atlantic compared to results from the North Atlantic and Indian Ocean. 184

7.6 Line drawings of Profiles SA1 and SA3 and the closest conjugates Profiles AF3 and AF4. 186

7.7 Map of the Central Segment with locations of possible magmatism. 187

7.8 Schematic of a possible explanation for the magma-rich and magma-poor passive margins in the South Atlantic, using a transect of reconstructed lithosphere thickness. 189

7.9 Evidence of plumes within the mantle using a global, radially anisotropic, whole-mantle shear-wave velocity model. 190

A.1 Profile AF1 & AF2 trackline and OBH locations, with bathymetry 219

A.2 Profile AF3 location from Schulze et al. (2007) and Becker et al. (2014) 220

A.3 Profile AF4 trackline and OBH locations, with bathymetry 221

A.4 Profile SA2 trackline and OBH locations, with bathymetry 222

B.1 Location of geochemistry data in the study area. 223

B.2 Map of Location of DSDP drill holes reaching syn-rift sediment 225

B.3 Map of Location of DSDP drill holes reaching basement. 226

List of Tables

2.1 Isochron ages from Gee and Kent (2007) 58

3.1 Summary of seismic data results for syn-rift magmatism. 98

3.2 Crustal thickness measurement at the LaLOC 108

4.1 Variables used for 2D-modelling, as used in previous iterations of the model (Nielsen and Hopper, 2004; Armitage, 2008; Armitage et al., 2008, 2009, 2010, 2011). 114

5.1 Crustal thickness measurements, with maximum and minimum ranges at the LaLOC for all seismic sections used in this study. 136

5.2 Assigned model parameters of lithosphere thickness and spreading rates per segment on conjugate margins 141

6.1 Assigned model parameters of lithosphere thickness and spreading rates per segment for the African margin 164

6.2 Model results in comparison to crustal areas without additional SDR areas. 168

6.3 Model results in comparison to crustal areas with additional SDR areas. 168

6.4 Summary of model matches to observational constraints from seismic velocity trends 171

A.1 Details of the wide-angle seismic surveys (locations in Fig. 3.1 & 3.17). 218

A.2 Profile AF1 & AF2 OBH coordinates 219

A.3 Profile AF3 OBH coordinates 220

A.4 Profile AF4 OBH coordinates 221

A.5 Profiles SA1 and SA3 OBH coordinates 222

A.6 Profile SA2 OBH coordinates 222

B.1 Major element oxides compositions from DSDP samples 225

B.2 Major element oxides compositions from Mid-Atlantic Ridge samples 227

List of Acronyms

All acronyms used within thesis, in order of appearance:

Acronym	**Definition**
MCS	Multichannel Seismic
SDRs	Seaward Dipping Reflectors
ODP	Ocean Drilling Programme
HVLC	High-Velocity Lower-Crust
LIPs	Large Igneous Provinces
Mantle Plume-VPM Theory	Mantle Plume - Volcanic Passive Margin Theory
H_c-V_p	Crustal Thickness - Seismic Velocity
LMA	Large Magnetic Anomaly
CMQZ	Cretaceous Magnetic Quiet Zone
BGR	Bundesanstalt fr Geowissenschaften und Rohstoffe
LaLOC	Landward Limit of Oceanic Crust
OBH	Ocean Bottom Hydrophone
COB	Continent-Ocean Boundary
DSDP	Deep Sea Drilling Programme
WM91	Watson and McKenzie, 1991
N97	Niu, 1997
N97-FG87	N97 with pyrolite bulk earth composition from Falloon and Green, 1987
N97-HK93	N97 with peridotite bulk earth composition from Hirose and Kushiro, 1993
NRMSE	Normalised Root Mean Square Error

Chapter 1

Introduction

1.1 Passive Margins

A passive margin is formed through the rifting of continental crust and lithosphere to give way to seafloor spreading, representing the transition from continental to oceanic lithosphere. Synonymous to the term rifted margin, these zones cover an aggregate length of 105,000 km worldwide (Bradley, 2008). The sedimentary successions located on the continental shelf within the passive margins are recognised to be some of the most economically valuable zones found in the ocean. For example, they contain a sizeable amount of the Earth's phosphorite deposits (Cook and McElhinny, 1979), carbonate-hosted lead-zinc deposits (Leach et al., 2001), and an important part of the world's hydrocarbon reservoirs (Mann et al., 2003; Bradley, 2008). Passive margins are often considered an ideal environment to host a petroleum play, as they commonly have both source and reservoir rocks and seals present. A key aspect of comprehending a petroleum play system is to understand the temperature and pressure history of a source rock, including the heat-flow structure. As a result, it is important to study the evolution of passive margins and how the conditions of break-up (i.e. thermal settings) may change along them. A rudimentary first step to understanding their conditions of formation is through the classification of passive margins into types, largely defined by the amount of magmatism present (types and distribution in Fig. 1.1). Studying the characteristics of magmatism and how it may change over a distance will bring us closer to understanding the mechanism through which passive margins are formed.

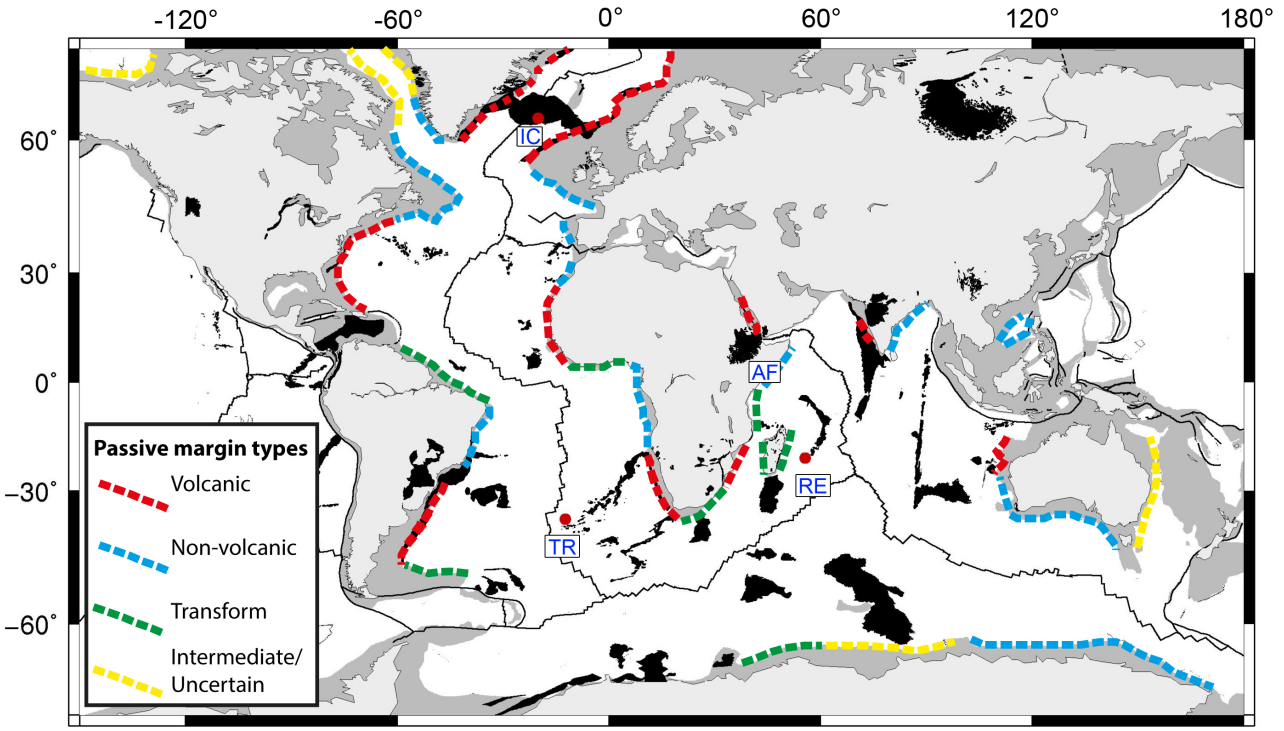


Figure 1.1: Global distribution of passive margins. Four types of passive margins are demonstrated: volcanic (red lines), non-volcanic (blue), transform (green), and intermediate/uncertain (yellow). Large igneous provinces are in black, from Coffin and Eldholm (1994). Mantle plumes that are often associated to volcanic passive margins are the Iceland Plume (IC), the Tristan Plume (TR), the Réunion Plume (RE) and the Afar Plume (AF). Figure originates from a pers. comm., J. Collier, 31 Oct, 2016.

1.2 Non-Volcanic Passive Margins

Non-volcanic passive margins are the result of continental break-up with little or no volcanic activity found in the transitional crust (Fig. 1.2). They are formed from stretched continental crust, creating a series of listric faults, and often have exhumed upper mantle in the form of serpentinized peridotite (Lavier and Manatschal, 2006; Reston, 2010; Geoffroy et al., 2015). Although they are termed non-volcanic, they are not devoid of magmatism. This is evidenced from the passive margins of Iberia and the exhumed margins in the Swiss Alps, where limited amounts of melt have been observed (Müntener et al., 1993).

Non-volcanic passive margins can be further classified into Type I and Type II margins (Huismans and Beaumont, 2011). Type I margins tend to have a very narrow region between thick and thin continental crust (less than 100 km), with the presence of exhumed serpentinized mantle in the continent-ocean transition zone (Huismans and Beaumont, 2011). Locations include the Iberia and the Newfoundland margins (e.g., Reston, 2007; Whitmarsh et al., 2001). In contrast, Type II margins have a larger region of thinned continental crust, with no clear serpentinized mantle but some syn-rift magmatism (Huismans and Beaumont, 2011). Locations include the Central South Atlantic (e.g., Aslanian et al., 2009; Contrucci et al., 2004; Mohriak et al., 1990) and the South China Sea (e.g., Zhou et al., 1995; Zhou and Yao, 2009). Both Type I and Type II margins have

thinner than average oceanic crustal thickness, and can be as thin as 2.5–3 km, as evidenced by the Galicia Bank on the Iberian margin (Whitmarsh et al., 1996)).

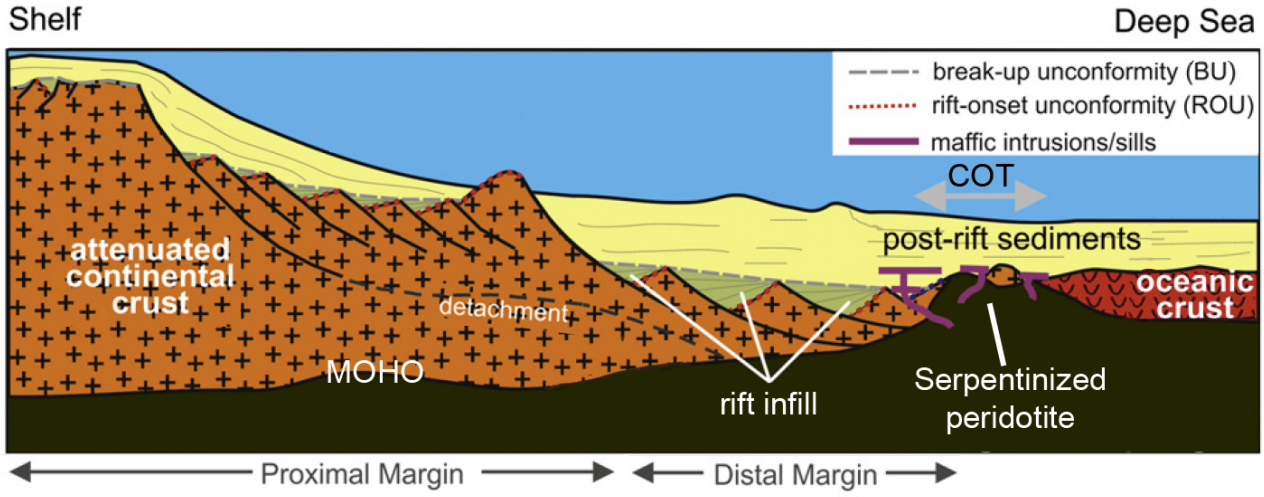


Figure 1.2: Schematic cross section of a non-volcanic passive margin, adapted from Franke (2013). Present are stretched continental crust (orange with crosses), syn-rift sediments (green within continental fault blocks), newly formed oceanic crust (red with chevrons) and post-rift sediments (yellow). Also present is serpentinized peridotite.

1.3 Volcanic Passive Margins

In contrast with non-volcanic passive margins, volcanic passive margins are primarily identified through the presence of syn-rift magmatism (Fig. 1.4; Roberts et al., 1984; White, 1987; White and McKenzie, 1989). The syn-rift magmatism, occurring during the final stages of continental break-up through to oceanic crustal production (Gladczenko et al., 1997), is manifested predominantly in the form of (1) seaward dipping reflections, (2) mafic to ultra-mafic magma 'underplated' bodies, and (3) a thicker than average initial oceanic crustal thickness (Fig. 1.4). Locations of volcanic passive margins include the southern South Atlantic conjugate margins, Southeast Greenland, the Norwegian margins and the East Coast of the U.S. (see the global distribution in Fig. 1.1).

Seaward dipping reflectors, or SDRs, are long basaltic flows interlayered with sediments. Seen on the Outer Vøring Plateau and in the Lofoten Basin in 1974 using multichannel seismic (MCS) data (Hinz and Weber, 1976), the SDRs were eventually found to cover a 1000 km distance parallel to the Norwegian coast (Eldholm et al., 1979; Hinz, 1981; Mutter et al., 1982). In addition to the Norwegian coast, Hinz (1981) identified SDRs off South Greenland and the Rockall Plateau, the Wedell Sea in Antarctica, Southwest Africa, Western Australia, the East Coast of the U.S. and West India (more locations are plotted in Fig. 1.3).

SDRs have become ubiquitous with volcanic passive margins. It is suggested SDRs form from differential loading and subsidence resulting from a build-up of lavas (Mutter, 1985). SDRs are generally mapped

as one seismic facies, as the large amount of scatter and interference from seismic waves due to the high intra-basalt impedence contrasts renders it difficult to pick out individual flows. As a result, magnetic data sets are often used to constrain their locations (e.g., Mutter, 1985; Talwani et al., 1995; Gladczenko et al., 1997). SDR seismic velocities are typically between 4.8 - 5.5 $\mathrm{km\,s^{-1}}$ (Whitmarsh and Miles, 1987; Bauer et al., 2000), ranging in thickness from less than a kilometre to over 15 km (e.g., Stica et al., 2014), with flows reaching up to 100 km in length (e.g., Franke et al., 2010). Two main types of SDRs exist; sub-aerial inner SDRs and sub-aqueous outer SDRs (Planke et al., 2000; Fig. 1.4). The sub-aerial inner SDRs, usually found closer to the continental crust, tend to be smooth long lying layers and are interpreted to represent the start of break-up prior to the existence of a proto-ocean. The sub-aqueous outer SDRs, found closer to and possibly overlapping the ocean crust, have shorter layers and are interpreted to represent the later stages of syn-rift magmatism. A limited number of SDRs have been drilled, and ODP drilling sites (Sites 642, 917 and 918) indicated SDRs could be up to 80% basalt (Planke, 1994). However, previous authors have estimated a 50 - 50 basalt to sediment ratio, as shown by magnetic susceptibility values used in magnetic modelling (e.g., Bauer et al., 2000; Collier et al., 2008; Koopmann et al., 2014b).

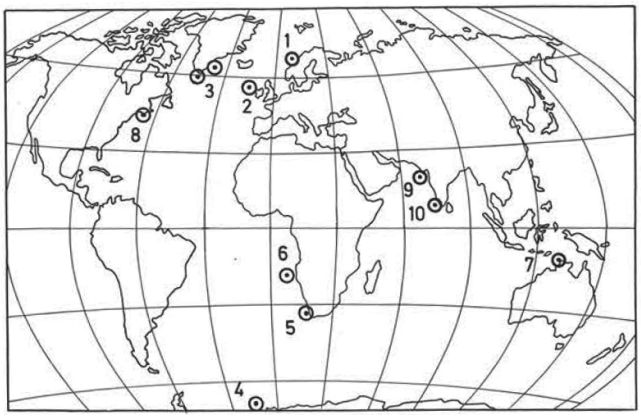


Figure 1.3: Locations of SDRs identified by Hinz (1981). 1 = Norwegian continental margin (Lofoten Basin, Vøring Plateau, Møre Basin), 2 = Rockall Bank, 3 = East and West Greenland, 4 = Weddell Sea, East Antarctica, 5 = Cape Basin, 6 = Abutment plateau, Walvis Ridge, 7 = Scott Plateau and Argo Abysall Plain, 8 = Baltimore Canyon Trough and Georges Bank, 9 = North West India, 10 = South West India. Figure adapted from Hinz (1981).

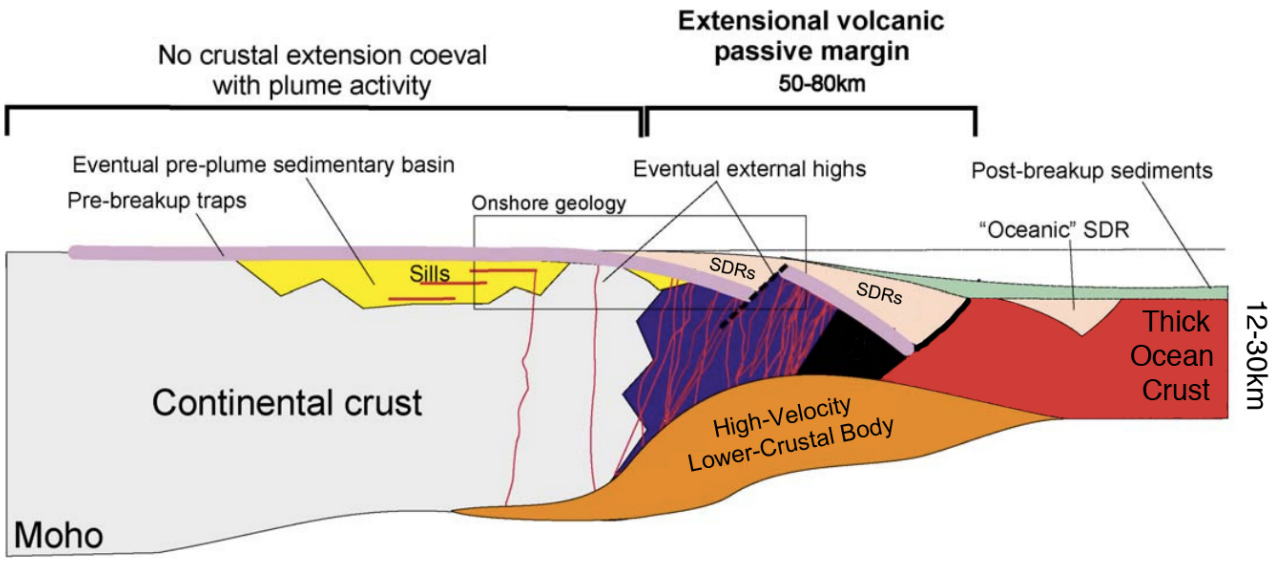


Figure 1.4: Schematic cross section of a volcanic passive margin, adapted from Geoffroy (2005). Orange shape represents the high-velocity lower-crustal body, concurrent with extrusive SDRs.

Often located coincidental to the SDRs, the existence of high seismic velocity bodies found in the lower

crust of passive margins, sometimes named 'underplating', has been noted since the 1980s (e.g., Herzberg et al., 1983; Furlong and Fountain, 1986; White et al., 1987; Mutter et al., 1988). White et al. (1987) imaged a lower crustal body, with velocities of 7.3 - 7.4 $\mathrm{km\,s^{-1}}$ and a thickness of up to 15 km at the Hatton Bank margin in the North Atlantic. There is a well defined top boundary to the body, indicated by an abrupt change in velocity gradient, and a prominent disconformity between the high-velocity lower-crustal (HVLC) body and the Moho. These HVLC bodies are suggested to represent mafic to ultra mafic basaltic intrusions into stretched and thinned continental crust (Furlong and Fountain, 1986; Kelemen and Holbrook, 1995; White and McKenzie, 1989). However, no HVLC body as such has been drilled, and there is no known exhumed example, hence its exact composition and method of emplacement is unknown. HVLC bodies were initially suggested to be created by magma pools, hence the term 'underplating'. Their thicknesses can reach over 30 km, and they have depth ranges between ∼10–40 km (Holbrook et al., 2001). Their seismic velocities range from $\geq$ 7.0 - 7.6 $\mathrm{km\,s^{-1}}$ (e.g., Kelemen and Holbrook, 1995; White, 1992), and these are attributed to high concentrations of magnesium oxide found within the melt (Sobolev and Babeyko, 1994; Behn and Kelemen, 2003).

The final main characteristic found along volcanic margins is the presence of thickened oceanic crust. From global seismic and geochemical data, average oceanic crustal thickness is ∼7 km (White et al., 1992; Bown and White, 1994), but oceanic crust found within volcanic passive margins can be up to four times thicker. A thickened initial oceanic crust of 28 km can be observed on seismic profile SIGMA-2 (Holbrook et al., 2001), found offshore Southeast Greenland (location in Fig. 1.6). Areas with thickened initial oceanic crust were also identified on the conjugate margins within the North Atlantic, including the Vøring margin (17.4 km thick; Mjelde et al., 1992), the Møre margin (18.1 km thick; Olafsson et al., 1992), and the Northeast Greenland margin (12.9 km thick; Mutter et al., 1988). Other volcanic passive margins that have thickened oceanic crust include the Western Australian margin (10 km thick; Hopper et al., 1992) and the East Coast of the U.S. (8 km thick; Holbrook et al., 1994b).

1.4 Flood Basalts

A spatial and temporal association between volcanic passive margins and continental flood basalts was made by White and McKenzie (1989). Flood basalts and oceanic plateaus, collectively known as Large Igneous Provinces (LIPs), are predominantly mafic in origin and erupt with enormous volumes of basalt (locations in Fig. 1.1; Campbell, 2007). Examples include the Deccan Traps on the Indian Subcontinent with a volume of $\sim 1.3 \times 10^6\,\mathrm{km^3}$ (Jay and Widdowson, 2008; Chalapathi Rao and Lehmann, 2011; Chalapathi Rao et al., 2011) and the Paraná-Etendeka Traps found on either side of the South Atlantic with a total area of $\sim 1.5 \times 10^6\,\mathrm{km^2}$ (Erlank et al., 1984; Peate, 1997; Courtillot et al., 1999).

Flood basalts eruption times have all been found as relatively short on a geological timescale, with generally a duration of a few million years (e.g., Bryan and Ferrari, 2013; Coffin and Eldholm, 1994; Courtillot, 1994). For example, recent magnetostratigraphy studies for the Etendeka traps from Dodd et al. (2015) found that the

eruption was already underway by at least magnetic isochron M15n, lasting until isochron M11n, dated 135.96 Ma and 130.84 Ma respectively (using Gee and Kent, 2007 timescale), suggesting an eruption time scale of ∼5 Myr. Similarly, the Siberian Traps, using $^{39}Ar/^{40}Ar$ dating, were found to have erupted on an even shorter time scale of ∼2 Myr around 250 Ma (Reichow et al., 2009).

Flood basalts are argued to represent the first eruptive product of new mantle plumes (Saunders et al., 1992) signalling the start of continental break-up. The flood basalts can, although not always exclusively, be linked to the current location of the mantle plume through a volcanic island and/or seamount chain (Saunders et al., 1992; Campbell, 2007) flanked by volcanic passive margins. Examples include the volcanic margin offshore west India and the Chagos-Laccadive-Mascarene trail that links the Réunion Hotspot to the Deccan Traps, and the Walvis Ridge and Rio Grande Rise that links the Tristan de Cunha Hotspot to the Paraná-Etendeka Traps, with the volcanic passive margin to the south of the aseismic ridges (Fig. 1.1).

1.5 The *Mantle Plume - VPM Theory*

1.5.1 Mantle plumes

White and McKenzie (1989) were among the first to observe a variability in the volume of magmatism during continental break-up world-wide. They created a simple 1-D model aimed at providing a method for the generation of rapid and intense magmatism, such as flood basalts, from simple rifting above a hot mantle. The degree of magmatism at a margin was suggested to be determined by mantle temperature, where the formation conditions of volcanic passive margins had an elevated mantle temperature compared to non-volcanic passive margins. The elevated mantle temperature was attributed to the presence of a mantle plume (White and McKenzie, 1989; White and McKenzie, 1995; Storey, 1995; Kelemen and Holbrook, 1995).

Wilson (1963) first suggested Hawaii was formed by the movement of oceanic lithosphere over a stationary 'hotspot' in the mantle, but did not offer an explanation of its mechanism. Morgan (1971) further suggested that hotspots were probably the result of plumes of hot mantle, originating from the core-mantle boundary, hence the term 'mantle plume'. Since then, the Wilson-Morgan hypothesis has become well-established, tested by both analogue experiments and numerical models. In this project, a differentiation between 'hotspot' and 'mantle plume' is made, with the understanding that the former is the result of the latter. The presence of a mantle plume on the Earth's surface is identified by several main characteristics, including linked flood basalts erupting prior to break-up, associated volcanic passive margins and an age-progressive volcanic island and/or seamount chain. Courtillot et al. (2003) also proposes a large buoyancy flux, a high $^{4}He/^{3}He$ ratio and, due to a plume's elevated temperature, a significant low shear wave velocity zone in the mantle should be used to verify the existence of a mantle plume.

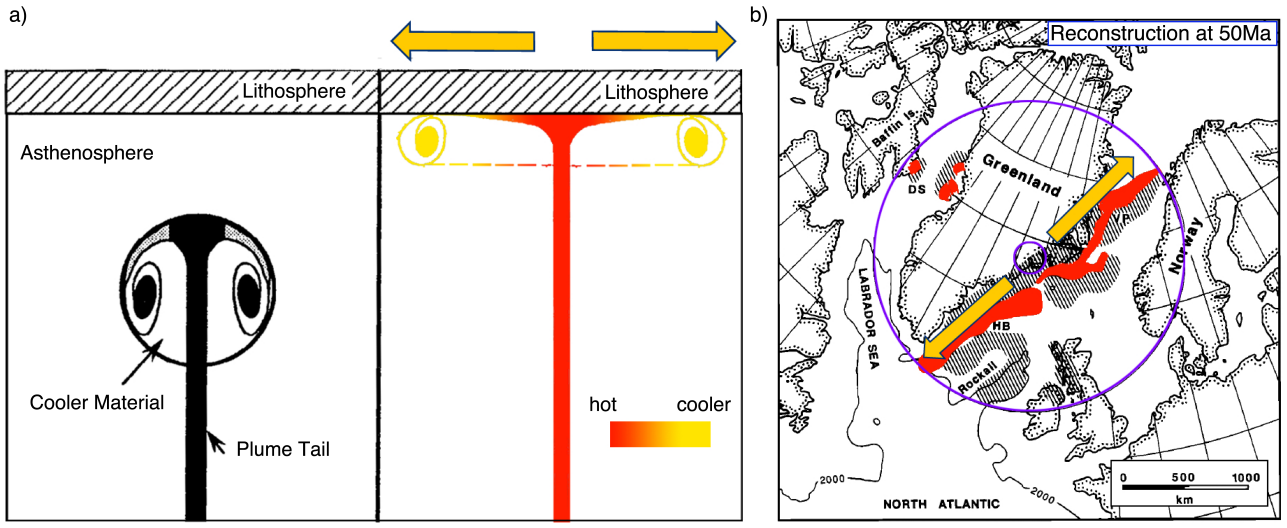


Figure 1.5: Schematic of a rising plume head through the asthenosphere and the impact of a plume in the North Atlantic. Part (a) is adapted from Coffin and Eldholm (1994), and demonstrates a schematic of a mantle plume rising through the asthenosphere. Part (b) is adapted from White and McKenzie (1989), showing a reconstruction of the North Atlantic at ∼50 Ma. The red shapes show the locations of volcanic passive margins, with the purple circles representing the centre of the plume and the area affected by the flattened plume head. The yellow arrows in parts (a) and (b) show the direction of diminishing mantle temperature, from hottest to coolest.

The classical view of a mantle plume is one of a large head of hot material driven by buoyancy, followed by a thin tail connecting it to the core (Fig. 1.5a; Griffiths and Campbell, 1990; Campbell, 2007). Following the White and McKenzie (1989) model, a starting mantle plume impinges the rheological barrier of the lithosphere-asthenosphere boundary (Fig. 1.5a), causing its head to flatten and spread into a disk with a diameter of 2000-2500 km (Griffiths and Campbell, 1990, 1991). With the impact of the plume at the base of the lithosphere, domal uplift occurs due to the buoyancy of the anomaly, placing the lithosphere under tension leading to eventual eruption of flood basalts and consequent break-up (White, 1992; Campbell, 2007).

Although there is a wide belief that eruption flood basalts precede continental rifting, a recent review by Buiter and Torsvik (2014) found that the eruption of flood basalts was often coeval to break-up. In a majority of cases, rifting had already been ongoing for varying amounts of time, and Buiter and Torsvik (2014) suggested that full break-up was triggered by the reduction in lithosphere strength due to excess temperature from the plume. Additionally, the existence of a pure thermal plume has been debated, and some have argued that they are instead closer to a 'thermochemical' plume, considering density variations as a result of both thermal and chemical differences (e.g., Dobretsov et al., 2003; Dobretsov, 2008; Dannberg and Sobolev, 2015). Plumes however, whether purely thermal or thermochemical, should still be represented by a continuous, vertical, thin low seismic velocity zone due to their excess temperature, and have successfully been imaged underneath several recognised hotspots (French and Romanowicz, 2015).

Despite clear geological and geophysical evidence for the existence of mantle plumes, some scepticism remains arising from inconsistencies in what is expected of an arriving plume head and what is observed. These include, among others, inconsistencies in the near surface geological record, lack of low-shear zones in the upper mantle

(e.g., Montelli et al., 2004), differences in expected heat-flow measurements (e.g., Foulger and Natland, 2003), unexplained changes in hotspot track directions (i.e. Hawaii), and lack of age-progressive tracks in some instances (e.g., Lawver and Müller, 1994). Departures noted from near surface geology are looked at in more detail in Section 1.6.

1.5.2 Identification of mantle plumes through associated volcanic passive margins

The thermal structure of the plume can also aid in its identification. It is assumed that the highest temperatures are found at the plume axis (Fig. 1.5a), with the hot conduit of material supplying this central area. Putirka (2005) found the plume centre to be 250 ± 50 °C and 165 ± 50 °C hotter than normal mantle potential temperature for the Hawaii and Iceland magma sources respectively. This was similar to Herzberg and Ohara (2002), who found the mantle potential temperature to be elevated for Hawaii, Baffin Island and West Greenland, with a range of 1520 - 1570 °C. There is a reduction in temperature towards the fringes of the plume head (Campbell, 2007), and this is suggested to be represented by a systematic reduction in magmatism along-strike relative to the proximity of the plume axis (Kelemen and Holbrook, 1995; Holbrook et al., 2001; Collier et al., 2009). The reduction in magmatism observed on volcanic passive margins along-strike can be tested by initial oceanic crustal thicknesses, distribution of SDRs and volumes of HVLC bodies. The association between the presence of a mantle plume and the formation of volcanic passive margins (VPM) will be continuously tested throughout this thesis, and this theory will henceforth be referred to as the *Mantle Plume - VPM Theory*.

Holbrook et al. (2001) tested the *Mantle Plume - VPM Theory* in the North Atlantic for the Southeast Greenland coast using the SIGMA profiles (Fig. 1.6). They observed igneous crust >30 km thick on the Greenland-Iceland-Ridge, reducing to ∼17 km thickness at an along-strike distance of 1100 km (Fig. 1.6). This translated

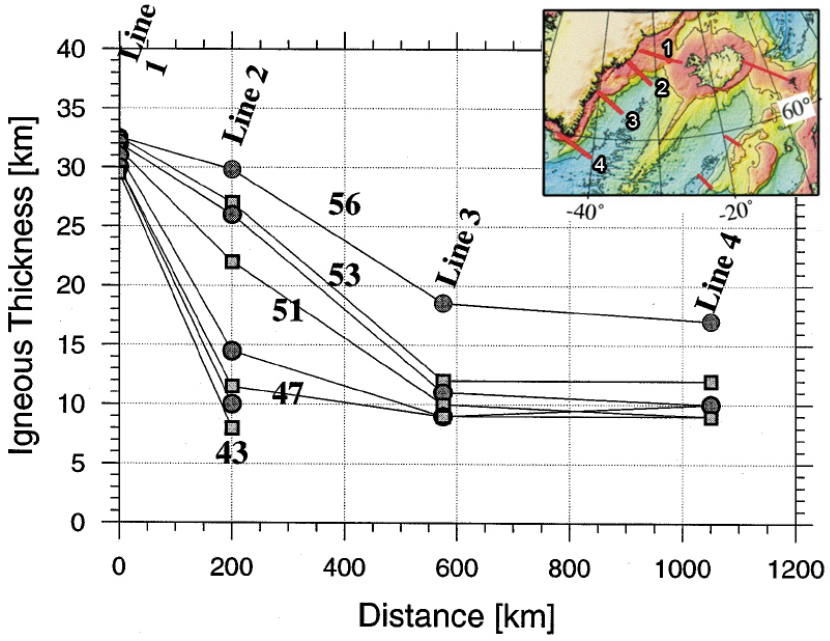


Figure 1.6: Igneous thickness of SIGMA lines from the North Atlantic versus distance from hotspot track, with locations found in the inset map, adapted from Holbrook et al. (2001). Also shown are the igneous thickness at different ages (56 Ma, 53 Ma, 51 Ma, 47 Ma and 43 Ma).

to observed magmatic productivity rates of $\sim 1800 \pm 300\,km^3/km/Ma$ at the Greenland-Iceland-Ridge to only $700 \pm 200\,km^3/km/Ma$ in the distal zone. In addition to initial thicknesses and rates, Holbrook et al. (2001) also showed a reduction in igneous productivity through time (Fig. 1.6), with magmatic productivity rates halving over a 13 Myr year period to $600 \pm 50\,km^3/km/Ma$ and $300 \pm 50\,km^3/km/Ma$ in the proximal and distal zones respectively. This reduction trend was further tested by Collier et al. (2009) using initial oceanic crustal thickness. Using a total of 17 profiles from a compilation of published seismic lines found north and south of the Greenland-Iceland-Faroe Ridges, Collier et al. (2009) identified the initial oceanic crustal thickness and plotted them versus distance from hotspot. A clear reduction in oceanic crustal thickness of $\sim$11 km per 500 km is observed (Fig. 1.7). Similarly to the SIGMA profiles, Becker et al. (2014) found there was a clear reduction in size from north to south for the HVLC bodies found in the southern South Atlantic. The variation in magmatism found north and south of the Greenland-Iceland and Iceland-Faroe Ridges and south of the Rio Grande Rise and Walvis Ridge show a clear reduction along-strike from the proximal to distal regions of the plume axis, agreeing with a reduction in magmatism away from the plume axis.

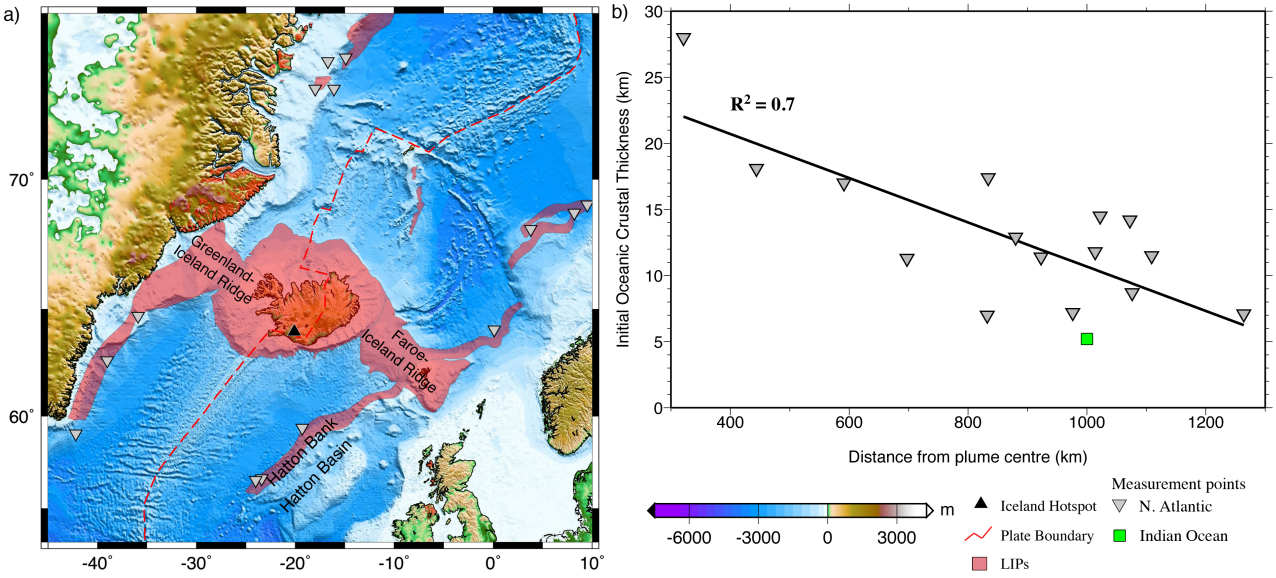


Figure 1.7: Present day North Atlantic margins with break-up volcanism, with measurement points of initial oceanic crustal thickness. Part (a) represents present day North Atlantic, with the location of the Iceland Hotspot (black triangle), plate boundary (dashed red line), volcanism (opaque red shapes) and measurement points for the North Atlantic (inverted grey triangles) found along the continental margins. Part (b) shows the relationship between initial oceanic crustal thickness vs distance from plume centre, with a best-fitting straight line. The measurements for the North Atlantic (inverted grey triangles) were synthesised by Collier et al. (2009), originating from Goldschmidt-Rokita et al. (1994); Mjelde et al. (1992); Olafsson et al. (1992); Fowler et al. (1989); Vogt et al. (1998); Barton and White (1997); Mutter et al. (1988); Voss and Jokat (2007); Holbrook et al. (2001); Chian and Louden (1994); Chian et al. (1995). In addition, there is the measurement point found in the Indian Ocean (green square) from Collier et al., 2009 (location in Fig. 1.9).

1.6 Departures from the *Mantle Plume - VPM Theory*

There are several localities where the *Mantle Plume - VPM Theory* tends to break down. Some volcanic passive margins do not have 'linked' flood basalts (e.g. East Coast of the U.S.), and, likewise, some flood basalts do not

have any associated volcanic passive margins (e.g. the Siberia Traps). A very rapid transition between volcanic and non-volcanic passive margins has been observed at several localities (e.g. South Greenland and the South Atlantic), which is not in line with the arrival of a mantle plume. This has led to some workers proposing different shapes than the classic axisymmetric "mushroom head" (Fig. 1.5a) geometry as an explanation (e.g., Houseman, 1990). Due to inconsistencies within the *Mantle Plume - VPM Theory*, the existence and role of mantle plumes has been questioned, and alternative methods for the production of volcanic passive margins have been suggested. These include small scale-convection (e.g., Anderson, 1994) and active mantle upwelling (e.g., Holbrook et al., 2001), which may enhance magmatism over a large area during the rifting of continental margins. A differentiation in this project is made between active mantle upwelling caused by a mantle plume and active mantle upwelling initiated rifting with the absence of a hot layer. Additionally, segmentation, originating from pre-rift structural weaknesses within the continents, may help focus magmatism towards fracture zones (e.g., Franke et al., 2007; Koopmann et al., 2014b).

1.6.1 Inconsistencies with a classic "mushroom head" plume

Areas where a classic "mushroom head" shape would not be compliant include the Labrador Sea for the Iceland Plume (Nielsen et al., 2002), the South Atlantic for the Tristan plume (Fromm et al., 2015) and the Indian Ocean for the Réunion plume (Collier et al., 2009). The Labrador Sea and the South Atlantic both have sharp contrasts between volcanic and non-volcanic passive margins. In the North Atlantic, the Southwest Greenland

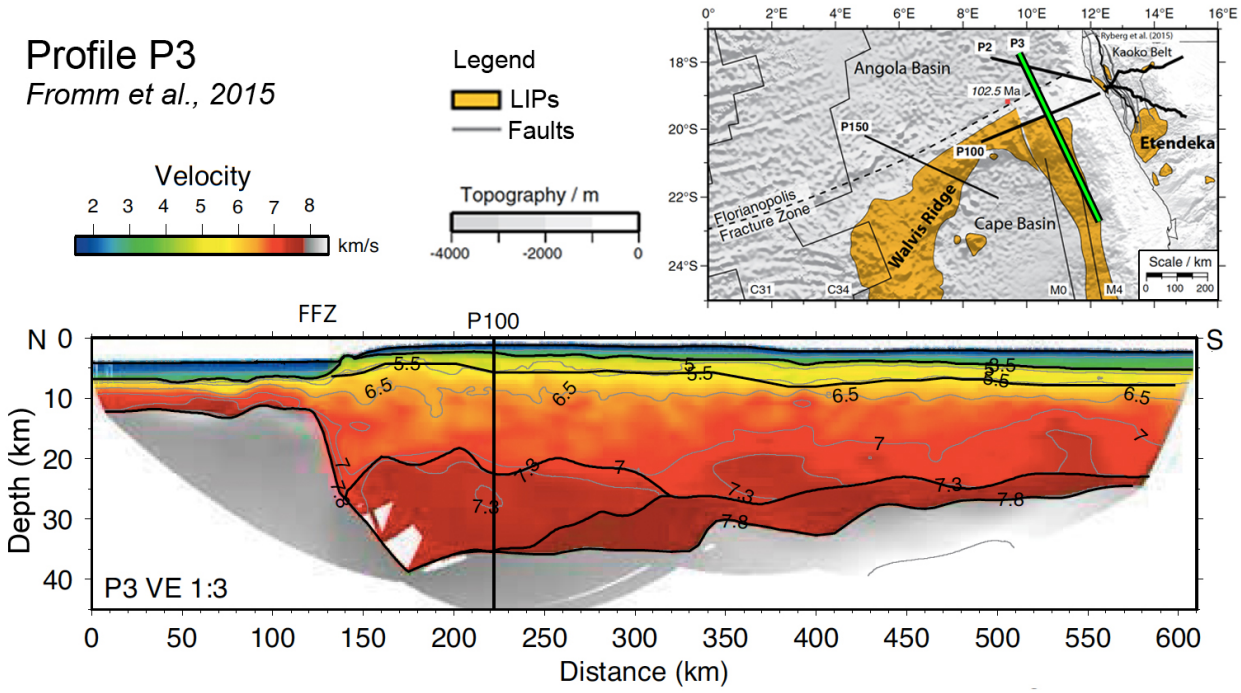


Figure 1.8: Wide-angle Profile P3 (green line found on inset map), crossing the Walvis Ridge along-strike, adapted from Fromm et al. (2015). LIPs from Coffin et al. (2006), faults from Foster et al. (2009). There is a stark contrast in igneous crustal thickness from a 30 km thick crust on the Walvis Ridge to only ~5–6 km in thickness north of the Walvis Ridge.

margin in the Labrador Sea was formed at approximately the same time as the volcanic passive margins of Southeast Greenland (approx. Chrons 27N and 25N respectively; Chalmers and Laursen, 1995; Tegner et al., 1998). It is assumed to fall within the area of Iceland's plume influence (Fig. 1.5b), and hence expected to be volcanic. However, Nielsen et al. (2002) observed contrasting non-volcanic and volcanic passive margins in this region, with the change being relatively abrupt over a 100–200 km distance. Nielsen et al. (2002) concluded the sub-lithospheric topography influenced areas of magmatism, with the Greenland Craton impeding the lateral spread of the plume head in the Labrador Sea, creating the stark contrast observed in magmatism. Additionally, numerical models demonstrated that sublithospheric bathymetry, forming an upside-down drainage pattern, can have a profound effect on the lateral flow of plume material (Sleep, 1996, 2006).

Similar to the Southwest Greenland margin, a sharp contrast between volcanic and non-volcanic margins is observed in the South Atlantic. Fromm et al. (2015) imaged a sharp change in regime from a 30 km thick crust on the Walvis Ridge to a 5–6 km thick ocean crust to the north in the Angolan Basin over a distance of ∼50 km (Fig. 1.8). There is a polarising difference between the non-volcanic margins seen north of the Walvis Ridge (e.g., Contrucci et al., 2004) and those to the south of the Walvis Ridge (e.g., Bauer et al., 2000; Hirsch et al., 2009). Similar to the Labrador Sea in southwest Greenland, this asymmetry in magmatism does not fit with the classic mushroom head shape.

Finally, the Seychelles Margin (location Fig. 1.9) was expected to be predominantly volcanic due to the proximity of the Deccan Traps, with SDRs also being identified by Hinz (1981) offshore of India (localities 9 & 10 in Fig. 1.3). However, Collier et al. (2009) found evidence of poorly developed SDRs and relatively thin oceanic crust at a thickness of 5.2 km on the Seychelles Margin (Fig. 1.7b; location 1.9). Collier et al. (2009) suggested that the classic plume head shape was not compliant with observations from the north Seychelles margin and proposed a more complicated shape for the arriving plume head. Additionally, it is possible the Réunion plume lacked an incubation period to thermally equilibrate beneath the lithosphere prior to rifting (Collier et al., 2009).

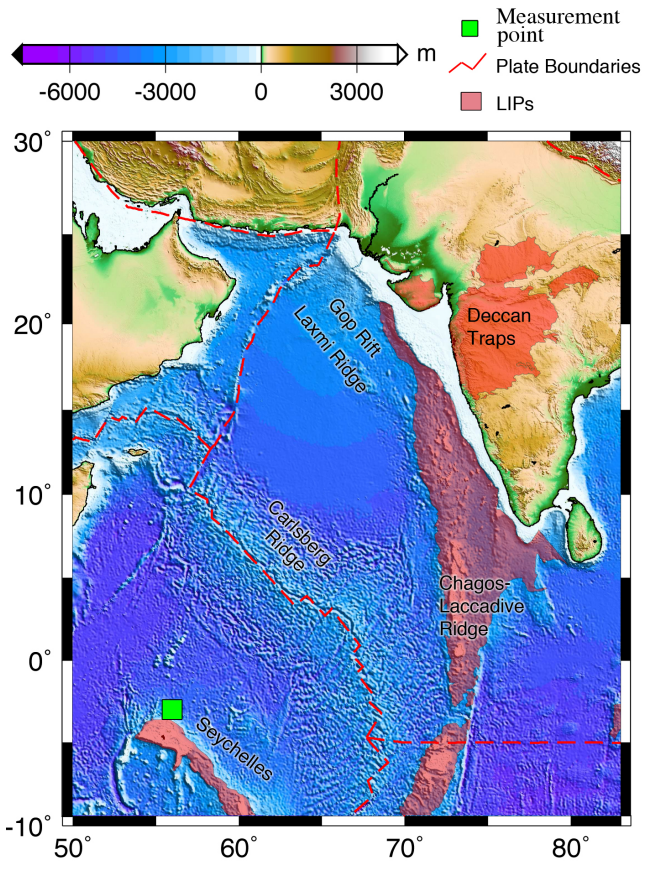


Figure 1.9: Present day Indian Ocean, with the plate boundary (dashed red line), volcanism (opaque red shapes), and measurement point (green square). The measurement point can be seen on Fig. 1.7b, at a 1000 km distance from the plume centre and a thickness of 5.2 km.

1.6.2 Volcanic passive margins with no associated continental flood basalts

The conjugate margins of the East Coast of the U.S. and offshore Morocco are an example of volcanic passive margins with no associated flood basalts. Seismic profiles offshore Morocco showed evidence of SDRs and high-velocity lower-crustal bodies (Klingelhoefer et al., 2009). On the conjugate margin, the LASE project (LASE Study Group et al., 1986; Diebold et al., 1988) and EDGE transects (Lizarralde et al., 1994; Holbrook et al., 1994a,b) both found evidence for the East Coast of the U.S. being strongly volcanic. The transects (location in Fig. 1.10a), presented by Holbrook et al. (1994a) in the Carolina Trough and Holbrook et al. (1994b) offshore Virginia, found igneous thicknesses of 20–25 km (Fig. 1.10b & c), thicker than the Hatton Bank and Vøring Margin in the North Atlantic (20 km and 17.4 km respectively; Barton and White, 1997; Mjelde et al., 1992).

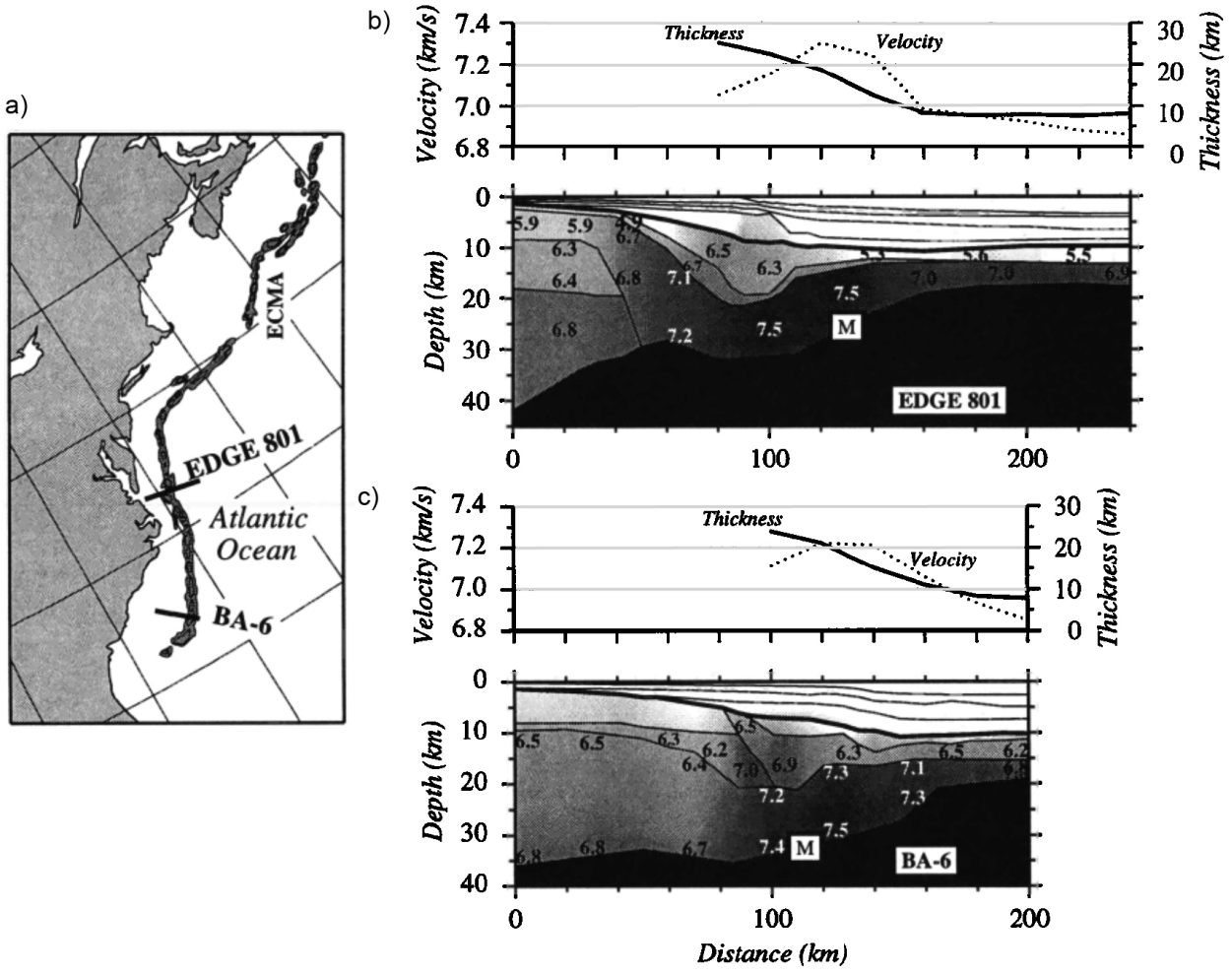


Figure 1.10: Location of East Coast Magnetic Anomaly and seismic transects found along the margin, adapted from Kelemen and Holbrook (1995). Part (a) shows the location of the East Coast Magnetic Anomaly, along with the location of seismic transects EDGE 801 and BA-6 from Holbrook et al. (1994a) and Holbrook et al. (1994b) respectively. Parts (b) and (c) show profiles EDGE 801 and BA-6 respectively. Upper plots for each transect represent igneous crustal thickness (solid line) and average seismic velocity (dotted line). Lower plots for each transect show crustal velocity structure.

Kelemen and Holbrook (1995) found the distribution of igneous material was constant for more than 1000 km along the margin. An abrupt change was observed from a 25 km thick crust to an 8 km thick crust over a distance

of 40–60 km towards the south (Holbrook and Kelemen, 1993). This observation directly counters the *Mantle Plume - VPM Theory*, where igneous crustal thickness should decrease towards the distal margins and not remain constant. In addition to this, no hotspot track with a corresponding age and geographic position is present (Morgan, 1983), and the magmatism spans over at least a 38 Myr period (De Boer et al., 1988; Klitgord et al., 1988; Manspeizer and Cousminer, 1988), contrary to the short-lived volcanic eruptions seen with plume related magmatism.

Another region where volcanic passive margins have no associated flood basalts or hotspot track is the Western Australian margin (e.g., Mutter and Larson, 1989). Anomalously thick oceanic crust was found in the Cuvier and Gascoyne margins (10 km and 14 km thick respectively; Hopper et al., 1992; Rey et al., 2008). Previously thought non-volcanic, thick SDR sequences were found on the Gascoyne margin. The along-strike variation in magmatism and dimension for the Gascoyne Margin, Cape Range Fracture Zone and Cuvier Margin was likened by Rey et al. (2008) to the variation seen in the Vøring Margin, Jan Mayen Fracture Zone and Møre Margin in the North Atlantic (Berndt et al., 2001; Planke et al., 2005), where the respective fracture zones represent a less magmatic transform segment. It was suggested that the shear-rift setting promotes magmatism and would affect the along-strike variation in magmatism (Rey et al., 2008; Borissova et al., 2015).

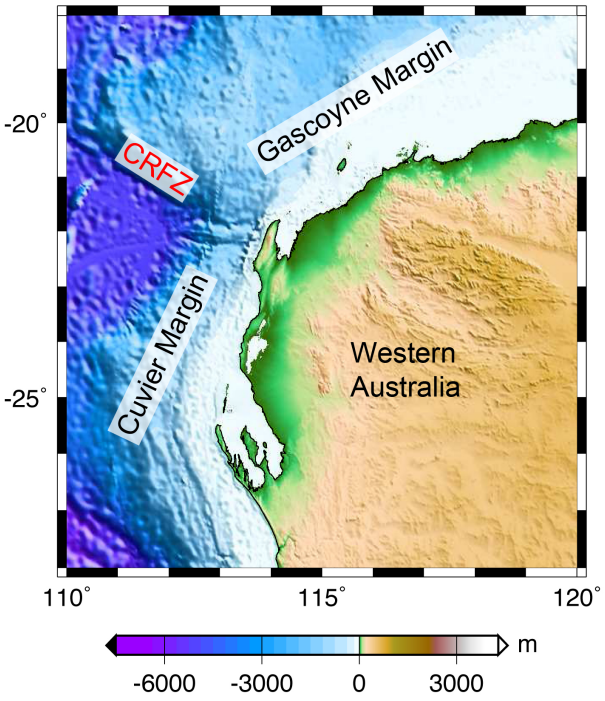


Figure 1.11: Location of Cuvier (Hopper et al., 1992; Mihut and Müller, 1998) and Gascoyne (Rey et al., 2008) volcanic passive margins offshore Western Australia, separated by the Cape Range Fracture Zone (CRFZ).

1.7 Modifications to the *Mantle Plume - VPM Theory*: Rift History

The cause of the variation in magmatism in the North Atlantic has long been assumed to primarily be mantle temperature, with White and McKenzie (1989) concluding that initial lithosphere thickness had little influence

on this variability. However, relatively recent work found that lithosphere thickness and previous rift history had an important influence. The Hatton Basin (location Fig. 1.7a) was formed in the late Cretaceous, ∼20 Myr prior to the earliest flood basalts on the Southeast Greenland margin (Armitage et al., 2010). The continental crust and lithosphere was also considered thinned by a β factor of 2 during this initial phase of rifting (Smith et al., 2005). Using a 2D fluid dynamic model of lithospheric extension, Armitage et al. (2010) found that if the previous rifting event at the Hatton Basin was ignored, an igneous crust 17 km thick could not have been produced as the hot material would have been held beneath a 125 km thick lithosphere. If extension prior to break-up did occur, this would have allowed the thermal anomaly to spread into the thinner zone of lithosphere. Coupled with a high enough extension rate, enough melt could be generated to match the observations of igneous crustal thickness.

Another case where the previous rift history had an influence on magmatism is within the Indian Ocean. There is an undisputed association of the continental flood basalts in conjunction with continental rifting (Courtillot et al., 1999; Collier et al., 2009), where the Deccan Traps are estimated to have erupted 65.5 ± 1 Ma (Courtillot and Renne, 2003). The flood basalts can be linked through the Chagos-Laccadive-Mascarene Ridge to the still active volcano of Piton de la Fournaise on the island of Réunion. However, a seismic survey on the Laxmi Ridge (location Fig. 1.9) found a modest initial oceanic crustal thickness of 5.2 km, and a relatively low amount of syn-rift magmatism (Minshull et al., 2008; Collier et al., 2009). The lack of magmatism observed here was not expected following the *Mantle Plume - VPM Theory*. In addition, rare-earth element inversions suggested the presence of a 200 °C thermal anomaly during the eruption of the Deccan Traps (White and McKenzie, 1995), inconsistent with the thin ocean crust observed. However, the thick ocean crust and syn-rift magmatism expected was observed to some extent on the Gop Rift (location Fig. 1.9; Collier et al., 2008).

Similar to the Hatton Basin, the Gop Rift opened prior to break-up. Whilst the rifting during the formation of the Hatton Basin focused magmatism, it was suggested the opening of the Gop Rift approximately 6 Myr prior to the Deccan Traps eruption partially exhausted the thermal anomaly before extension had migrated to the Seychelles/Laxmi ridge margin (Armitage et al., 2010). The consequent pause in rifting allowed the thermal anomaly to cool by heat conduction, resulting in the melting of a mildly depleted mantle at the Laxmi Ridge (Armitage et al., 2010). As a result of the findings for the North Atlantic and Indian Ocean, rift history, including extension rates and the interaction of mantle conditions with an extended lithosphere, has an important influence on magmatism during rifting. Although some generalisations can be applied, continental passive margins are unique and must be studied individually.

1.8 Alternative mechanisms for the formation of Volcanic Passive Margins

1.8.1 Small-scale convection

The East Coast of the U.S. demonstrates very little variation in magmatism along-strike (Holbrook et al., 1994a,b; Kelemen and Holbrook, 1995), and therefore does not comply with the *Mantle Plume - VPM Theory*. An alternate model was proposed, where small-scale convection is responsible for increased magmatic activity in the absence of a mantle plume (e.g., Mutter et al., 1988). A build-up of heat is suggested to occur under supercontinents, due to the insulation they provide (Gurnis, 1988; Anderson, 1994; Lowman and Jarvis, 1995, 1996). In this case, the base of the cratonic root found in the supercontinents is hotter than that of the ocean lithosphere, resulting with an upper mantle convection cell capable of producing a 200 °C anomaly (Fig. 1.12; King and Anderson, 1995, 1998). The resulting hotter upper mantle could mimic the characteristics of a mantle plume during rifting. A weaker force, known as edge-driven convection, is suggested to arise from changes in sub-lithospheric bathymetry, between thicker, older, stable lithosphere (e.g. a craton root) and thinner, younger lithosphere (e.g., King and Anderson, 1998; King and Ritsema, 2000). With the cratonic root and the ocean lithosphere both considered stable, their respective bases will be at a similar temperature. The cratonic root represents an "edge" boundary along which a vertical temperature variation is driven, resulting in small-scale flow.

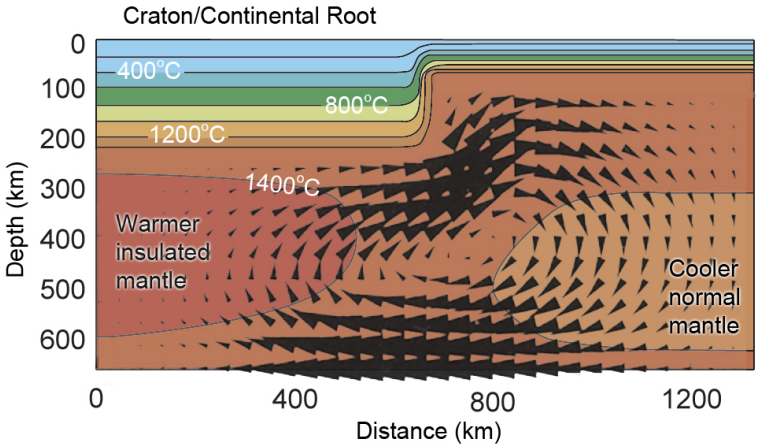


Figure 1.12: Example of small-scale convection resulting from the insulation of the mantle below a supercontinent, adapted from King and Anderson (1995) and King and Anderson (1998). This model has a 150 °C mantle temperature perturbation, with direction of flow seen as the black arrows.

Several numerical models have attempted to recreate small-scale and edge-driven convection. Nielsen et al. (2002) and Nielsen and Hopper (2004) found that edge-driven convection did not tend to the production of a steady state oceanic crustal thickness, with hot material necessary to recreate magmatism volumes seen on volcanic passive margins. Similarly, Sleep (2007) was unable to recreate a melt thickness comparable to those seen on volcanic passive margins, and found the asthenosphere below thin lithosphere not favourable for large amounts of melting. More recently, Simon et al. (2009) was able to produce a moderately 11–15 km thick crust. Whilst the thickness range from Simon et al. (2009) was unable to match the igneous crustal thickness seen on

the East Coast of the U.S., they managed to have a reasonable fit with the overall distribution of igneous crust. Sleep (2007) had previously noted that whilst current numerical models cannot recreate these conditions, the parameter space may not be detailed enough. Three-dimensional models over a long geological time scale may be needed to recreate the necessary conditions (Sleep, 2007).

1.8.2 Active mantle upwelling

It has also been suggested that active mantle upwelling is sufficient to initiate rifting with the absence of a hot layer (e.g., Keen and Boutilier, 2000). Active upwelling is defined by Holbrook et al. (2001) as when the half-spreading rate of the rift exceeds the upwelling rate of the mantle found in the melting zone. Active upwelling produces different melt compared to melt resulting from higher temperatures. Due to their differing conditions, the two types of melt produce different major element compositions, as MgO and SiO_2 compositions are affected by the depth of melting (Parkin and White, 2008). Melt produced from high temperatures has higher average pressure and melt fraction conditions, due to a deepened solidus and an increased melt column height (Holbrook et al., 2001). It is therefore expected to have a higher MgO content and a lower SiO_2 content, and thus, using the empirical function defined by Kelemen and Holbrook, 1995 & Behn and Kelemen, 2003, a higher mean seismic crustal velocity. In contrast, melt produced from active upwelling has on average lower pressure and melt fraction conditions, producing melt with a lower MgO content and a higher SiO_2 content and thus a lower mean seismic crustal velocity. By using the H_c-V_p method (Fig. 1.13, Kelemen and Holbrook, 1995; Holbrook et al., 2001; Parkin and White, 2008), the relationship between crustal thickness and mean seismic velocity can be utilised to test for the presence of active upwelling or the presence of a thermal anomaly (to be looked at in more detail in **Chapter 6**). Kelemen and Holbrook (1995) did not rule out that the formation of the volcanic passive margin on the East Coast of the U.S. was due to active mantle upwelling. Additionally, Holbrook et al. (2001) found evidence for active mantle upwelling during the break-up of the North Atlantic, but this was in conjunction with the presence of the Iceland Plume.

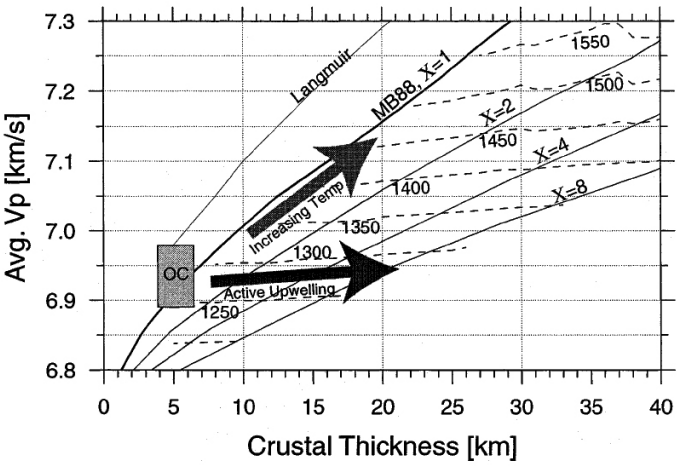


Figure 1.13: Predicted relationship for crustal thickness and mean seismic velocity, used to demonstrate melting due to a thermal anomaly or active mantle upwelling, adapted from Holbrook et al. (2001). Two melting models are compared here, the Langmuir et al. (1992) and McKenzie and Bickle (1988). When $X = 1$ there is passive upwelling, and $X = 2$, 4 & 8 represents different active upwelling ratios. Average ocean crust (grey box) is mean ocean crust velocity from the East Pacific Rise (Canales et al., 1998). Arrows represent the different effects on trends for active mantle upwelling (flat, with no significant change in seismic velocity) and a thermal anomaly (upwards, with changes in seismic velocity). OC represents average oceanic crust thickness and seismic velocity.

1.8.3 Segmentation

During continental break-up, the propagation of the rift system will form segmented continental margins originating from pre-existing structural weaknesses in the continents (Clemson et al., 1997). Like most continental margins, the southern South Atlantic has clear segmentation present along-strike. The continents of South America and Africa contain areas of structural weakness, which are inferred to have influenced continental break-up and initial sea floor spreading (Rosendahl, 1987; Clemson et al., 1997, 1999; Jungslager, 1999; Franke et al., 2007). Franke et al. (2007) and Koopmann et al. (2014b) presented four major transfer zones in the South American and African margins respectively, linked to the Proterozoic mobile fold belts found on adjacent continents (Fig. 1.14). Seen from observations of increasing areas of SDRs towards segment boundaries (Fig. 1.14), Franke et al. (2007) and Koopmann et al. (2014b) proposed that increased magmatism observed

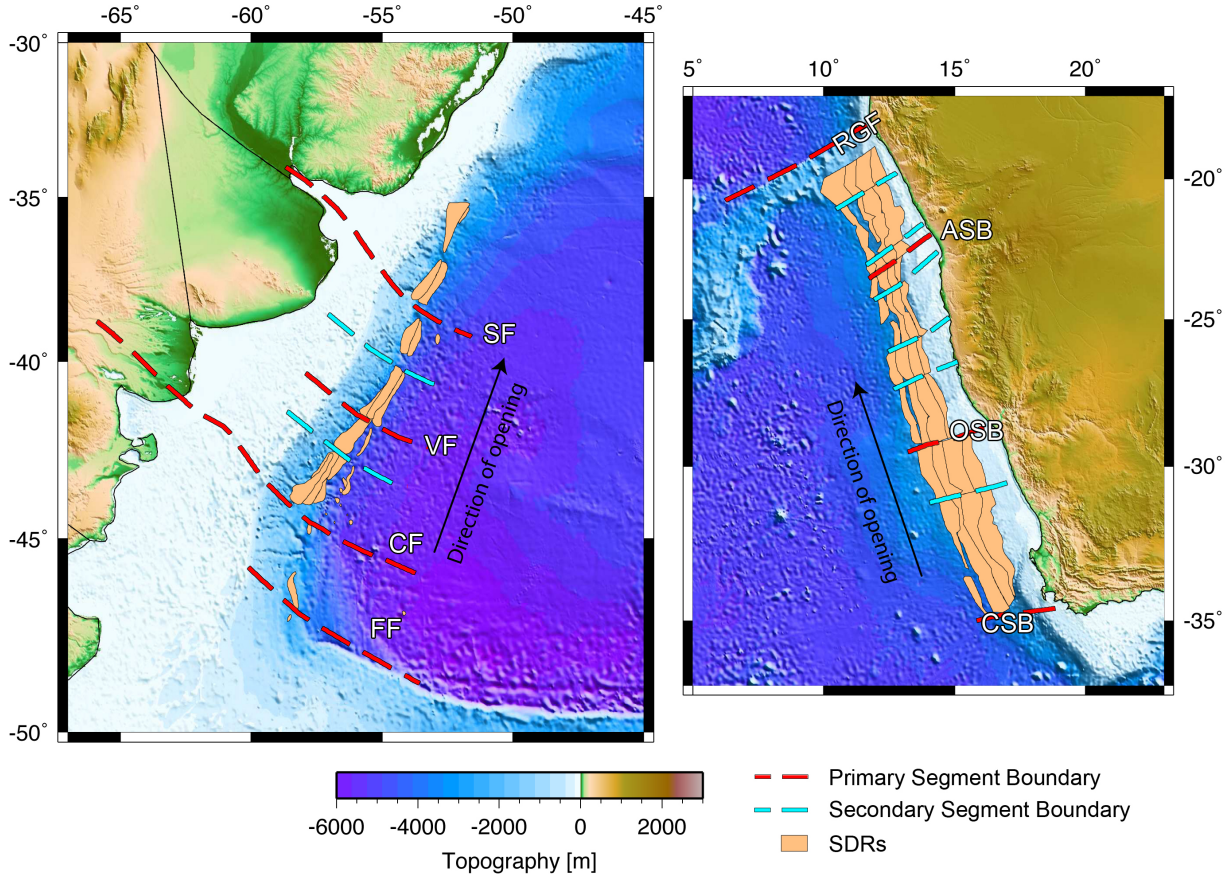


Figure 1.14: SDRs and segment boundaries from Franke et al. (2007) and Koopmann et al. (2014b). There is a general widening of SDRs approaching the segment boundaries, attributed to increased decompression melting. South American primary segment boundaries are the Falkland Fracture Zone (FF), Colorado Fracture Zone (CF), Ventana Fracture Zone (VF) and the Salado Fracture Zone (SF). African primary segment boundaries are the Cape Segment Boundary (CSB), Orange Segment Boundary (OSB), Austeib Segment Boundary (ASB) and the Rio Grande Fracture Zone (RGF).

towards these zones is due to increased decompression melting. It was suggested that the lithospheric segment boundaries act as rift-propagation barriers to convecting asthenospheric mantle material, resulting in enhancing and focusing volcanic activity south of these zones (Koopmann et al., 2014a). The increased melting resulted in increased SDR thicknesses and areas (Fig. 1.15, Franke et al., 2007; Koopmann et al., 2014a,b). Rey et al.

(2008) similarly proposed that the along-strike variation seen in the Gascoyne Margin from the Cape Range Fracture Zone in Western Australia (Fig. 1.11) could be the result of the shear-rift setting.

Segmentation was tested by Koopmann et al. (2014a) using a numerical model, where a lateral pressure gradient between sequentially opening segments causes a rift parallel flow with consequent elevation in temperature at segment boundaries (Fig. 1.15). The modelling results show increased decompression melting relative to the interior of the segments. Thus, segmentation is suggested to be a viable influential control of magmatism

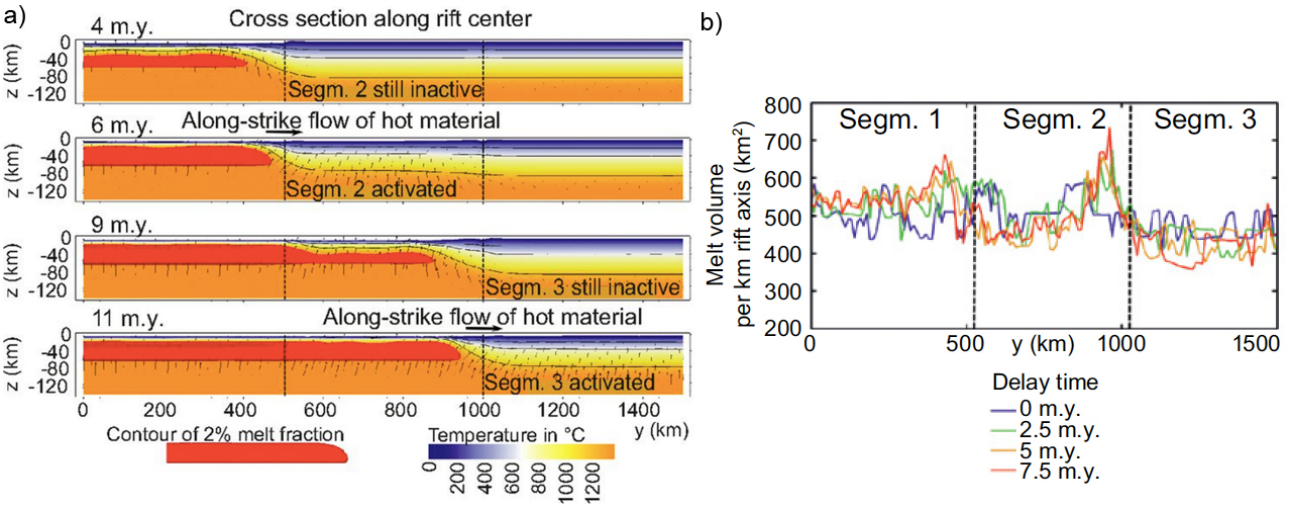


Figure 1.15: Model of increased magmatism at segment boundaries (locations Fig. 1.14), adapted from Koopmann et al. (2014a). Part (a) shows the temperature and melt fraction through the segments at different stages. Part (b) show the melt production (y-axis) as a response to rift-delay duration, plotted against along-strike distance (x-axis).

for volcanic passive margins. Franke et al. (2007) and Koopmann et al. (2014b) both suggested that segmentation has a high influence on magmatism in the South Atlantic region, seeing no systematic increase in SDR volumes towards the Rio Grande Rise and Walvis Ridge.

1.9 Thesis Outline

Chapter 1 has provided an overview of our current state of knowledge on the formation of volcanic passive margins, including possible causes of variation (or lack) of magmatism observed along-strike. It introduces the *Mantle Plume - VPM Theory*, including localities where it can be applied and localities where it tends to break down. Additionally, alternatives to the theory were explored, including small-scale convection, active mantle upwelling and segmentation.

Chapter 2 introduces the study area, the southern South Atlantic, and discusses the geological and geophysical setting of its margins.

Chapter 3 is the presentation of observational constraints from 24 published and 14 unpublished seismic data

lines along the continental margins of Namibia, South Africa, Uruguay and Argentina, used as observational constraints to test the *Mantle Plume - VPM Theory*. Different types of seismic data available are discussed, along with observations that can be extracted from the seismic lines.

Chapter 4 is dedicated to understanding the fluid dynamic model of continental rifting used in this project, previously developed by Nielsen and Hopper (2004) and Armitage (2008). The model results can be used to match observations from observational constraints from seismic data in the southern South Atlantic (**Chapter 3**) to understand the conditions of break-up. The different parameters are explored, including the initial lithosphere thickness, spreading rates and mantle asthenosphere temperature, which need to be determined prior to the matching of model results to observational constraints. Additionally, within this project, the module for calculating major element compositions is modified with respect to relatively recent research on the method of melt production.

Chapter 5 is based on an article published in *Tectonophysics* (Taposeea et al., 2016). It focuses on the initial oceanic crustal thickness and tests the influence of temperature and segmentation along-strike. To test the primary cause of along-strike variation, the thickness of early onset oceanic crust is first mapped using seismic data found along the margins. Following this, the calculated crustal thickness (h_c) from the fluid dynamic model will be used to match thickness observed at the landward limits of ocean crust and beyond for the wide-angle and high quality MCS data set to explore the controls on magmatism within this region.

Chapter 6 focuses on syn-rift magmatism, consisting of SDRs and high-velocity lower-crustal intrusions (HVLC). The syn-rift magmatism areas and seismic velocity trends show the evolution of the continental margin from continental to oceanic crust, and their relationship can be used to categorise the relationship between the mantle temperature, degree of active upwelling and melt generation through the H_c–V_p method (Kelemen and Holbrook, 1995; Holbrook et al., 2001; Parkin and White, 2008). The numerical model is then used to match areas of syn-rift magmatism from seismic data on the African margin. Once the choice of composition parametrisation using the geochemical data is finalised, seismic velocity can be calculated using an empirical formula derived from laboratory experiments. As a result, the model also has the capability of matching seismic velocity trends observed from wide-angle data.

Chapter 7 discusses the main results from previous chapters, critically evaluating the different mechanisms for the control of magmatism within the study area. With a wide spread of observations derived from seismic data (up to ∼2300 km south of the Rio Grande Rise and Walvis Ridge), the numerical modelling results can aid in understanding the distribution and cause of along-strike variation of magmatism in the southern South Atlantic. A comparison is made to numerical models of continental rifting from the North Atlantic and the Indian Ocean. A suggestion is made for the configuration of the Tristan Plume, a possible explanation to the asymmetries observed between the Central and Southern Segments.

Lastly, **Chapter 8** presents a final overview for the results formulated within this project and looks at possible further work.

Chapter 2

Geological and Geophysical Setting

2.1 Introduction

Western Gondwana broke up to form the South Atlantic Ocean in the Early Cretaceous (White and McKenzie, 1989). The South Atlantic break-up shows numerous signs pointing to the presence of a plume and aligning with the *Mantle Plume - VPM Theory*. There are (1) flood basalts in the form of the Paraná-Etendeka Large Igneous Provinces on the South American and African continents respectively, (2) the presence of volcanic passive margins evidenced by the wide-spread presence of SDRs and HVLC bodies on the conjugate margins, (3) an age progressive chain of volcanic islands and/or seamounts, recognized as the Rio Grande Rise and Walvis Ridge and (4) a volcanic island still active today, in the form of the Tristan da Cunha Island (Fig. 2.1, O'Connor and Duncan, 1990; Courtillot et al., 1999; Hirsch et al., 2009; Koopmann et al., 2014b; Becker et al., 2014; O'Connor and Jokat, 2015). The formation of Paraná-Etendeka Traps, Rio Grande Rise and Walvis Ridge and volcanic passive margins has historically been attributed to the arrival of the Tristan Plume and its influence on subsequent continental rifting (White and McKenzie, 1989; O'Connor and Duncan, 1990; Renne et al., 1992; Campbell, 2007).

There are however several important inconsistencies with respect to the *Mantle Plume - VPM Theory*. Although the volcanic passive margins in the South Atlantic can be 'linked' to the Paraná-Etendeka traps, the flood basalts themselves present a large asymmetry inconsistent with a mushroom head plume, with areas of 1.5 million km^2 (Courtillot et al., 1999; Peate, 1997) and 80,000 km^2 (Erlank et al., 1984) respectively. There is also a sharp transition from volcanic to non-volcanic passive margins to the north of the Rio Grande Rise and Walvis Ridge (Fig. 1.8). Additionally, it has been suggested from SDR area variations observed along-strike that segmentation may have been a major influence on magmatism (Franke et al., 2007; Koopmann et al., 2014a,b).

The South Atlantic rift system is postulated to host large amounts of hydrocarbon reservoirs, in both syn-

rift and post-rift sedimentary sequences. As a result, whilst seismic surveys in the region are biased towards hydrocarbon exploration focus areas, the margins are generally well covered by a range of seismic data (Brune et al., 2016). However, these data sets vary in quality and depth imaged. They include refraction surveys from the early 70s (e.g., Leyden et al., 1971), relatively shallow time sections (e.g., Light et al., 1992), wide-angle refraction surveys showing the full margin crustal structure (e.g., Bauer et al., 2000), and high-resolution deep penetrating multichannel seismic data sets (e.g., Stica et al., 2014). The South Atlantic has recently garnered lots of renewed attention from the petroleum industry, with up to five exploration wells scheduled to be drilled

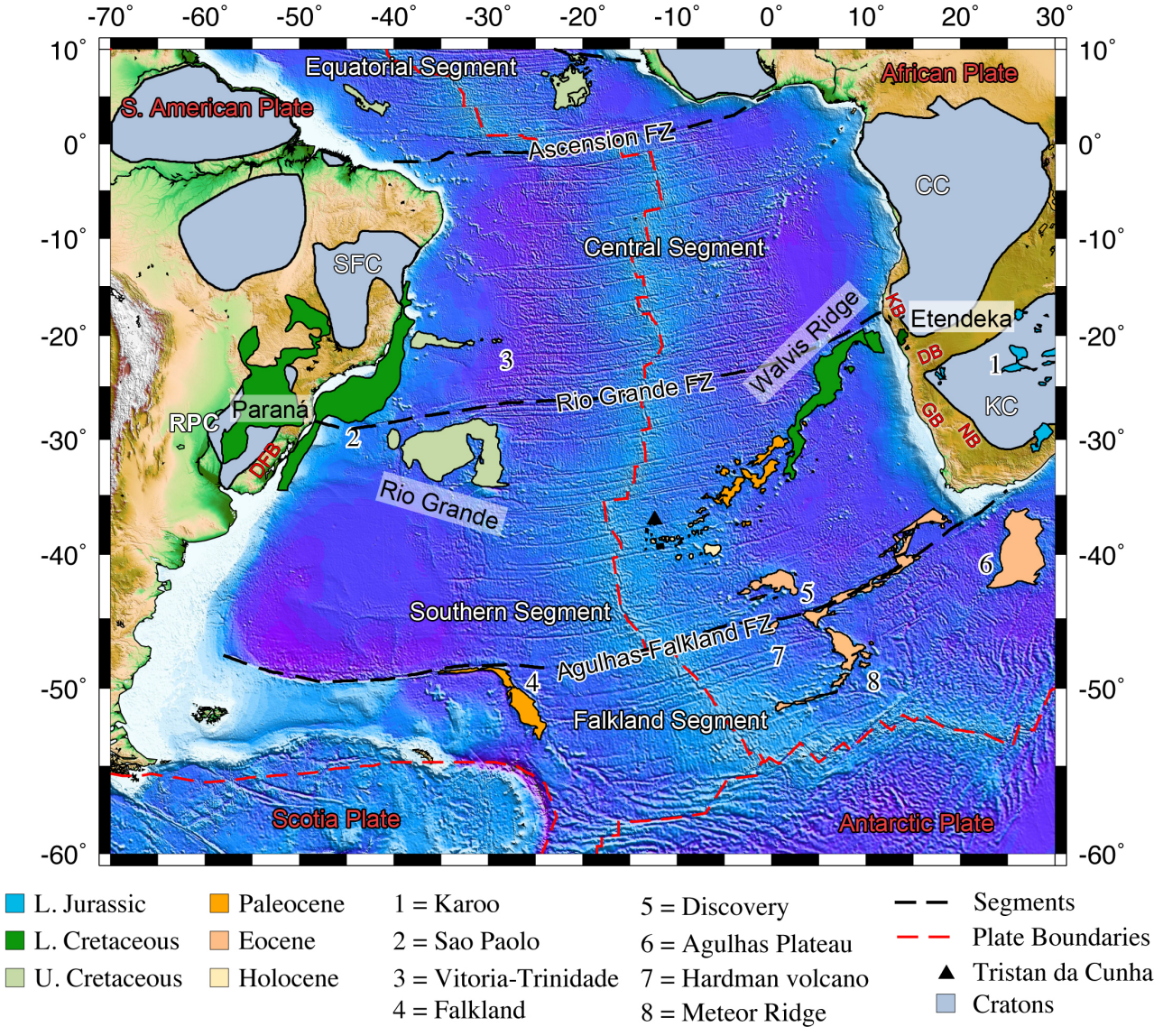


Figure 2.1: Main tectonic features with age progressive LIPs, dated from the Late Jurassic to the Holocene (colour boxes in key) (Coffin and Eldholm, 1994). Craton locations from Gubanov and Mooney (2009), where CC = Congo Craton, KC = Kalahari Craton, RPC = Rio de la Plata Craton and SFC = São Francisco Craton. Mobile belts include DFB = Dom Feliciano Belt, KB = Koako Belt, DB = Damara Belt, GB = Gariep Belt and NB = Namaqua-Natal Mobile Belt. Equatorial, Central, Southern and Falkland Segments are separated by different fracture zones.

off the coast of Namibia in 2016 alone (Njini, 2014). Previous exploration wells have had mixed results, with some indications of petroleum but not at commercial level (Ratcliffe, 2014; Green, 2014).

In order to understand the conditions of formation of the volcanic passive margins, in turn an important contribution to the continued efforts of hydrocarbon exploration, this project will study the variation of magmatism and test the *Mantle Plume - VPM Theory* compared to other mechanism of formation for the volcanic passive margins of the southern South Atlantic. The southern South Atlantic as defined in this project forms the Southern Segment, the latter part of the four main segments commonly defined within the South Atlantic. These are the Equatorial Segment, the Central Segment, the Southern Segment (also known as the Austral Segment) and the Falkland Segment (Fig. 2.1). First noted by Popoff (1988), the different sections in the South Atlantic are based on significant fracture zones. The Southern Segment is bounded by the Rio Grande Fracture Zone in the north and Falkland-Agulhas Fracture Zone in the south (Fig. 2.1). Using observational constraints from seismic profiles, the presence and magnitude of a thermal anomaly in the mantle will be tested according to the *Mantle Plume - VPM Theory* and other alternative models. The project will be aided by the use of a 2D numerical model of rifting, previously used in the North Atlantic and Indian Ocean (Armitage et al., 2009, 2010, 2011).

2.2 Pre-Rift Geology

The South American and African continents were formerly part of the supercontinent Gondwana. From the Mesoproterozoic to around 500 Myr ago, Western Gondwana was affected by the Pan-African and Brasiliano Orogenies, including tectonic, magmatic and metamorphic activities (Kröner and Stern, 2004). Rifting in the

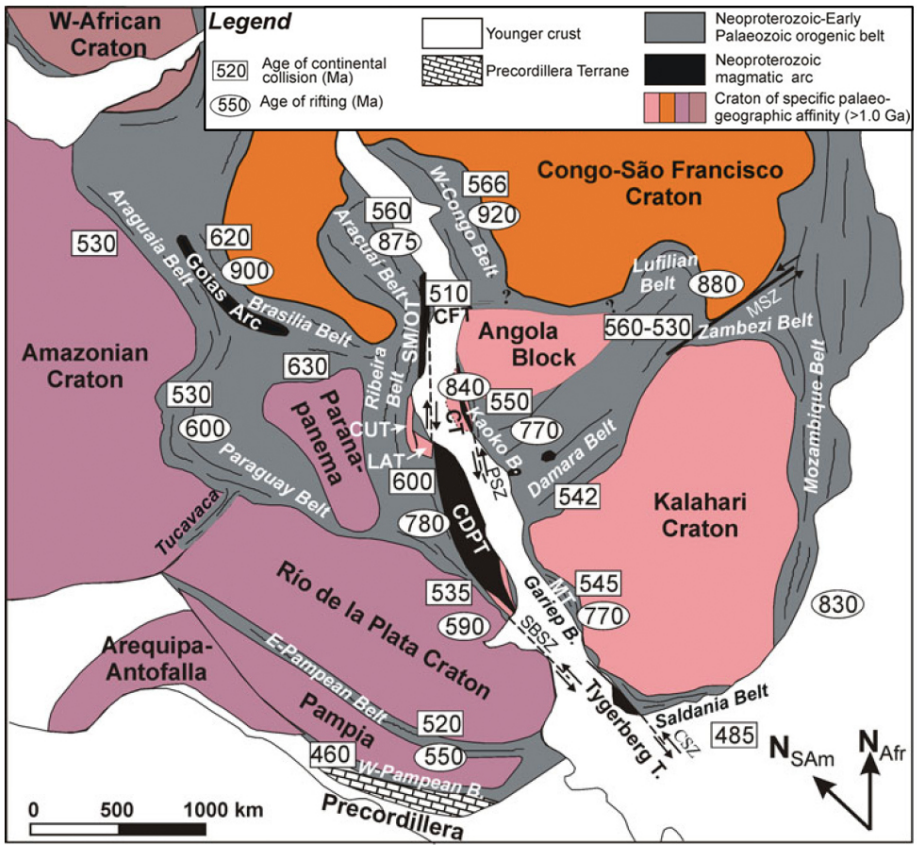


Figure 2.2: Schematic map showing locations of cratons and Neoproterozoic fold belts, adapted from Frimmel et al. (2011)

Neoproterozoic led to the formation of mobile belts and failed ocean basins between the cratons (Fig. 2.2, Frimmel et al., 2011), such as the Koako, Gariep and Damara belts on the African side and the Dom Feliciano Belt on the South American side (Fig. 2.1; Porada, 1979; Miller, 1983). The location of cratons and mobile belts are indicated by lithosphere thickness, represented by thick and thin regions respectively. This correlation was demonstrated in a reconstruction of the lithosphere thickness during the Permian (Fig. 2.3), published by McKenzie et al. (2015). The mobile belts influence on present day geology is evidenced by their correlation to fracture zones within the oceanic lithosphere.

There is evidence some rifting events occurred following the Pan-African and Brasiliano Orogenic event prior to full break-up. Light et al. (1993) suggested the existence of a proto-Atlantic rift with a shallow sea in the Late Carboniferous to Early Permian, but subsequent studies have found little evidence for this. There were also a series of north-south extensional faults coinciding with the South Atlantic opening location in the Early Permian, resulting in controlled basin development (Grill, 1996; Stollhofen et al., 1998). A regional magmatic event also occurred in the mid-Jurassic (Duncan et al., 1997), which produced the Karoo Large Igneous Province (Fig. 2.1) in southern Africa.

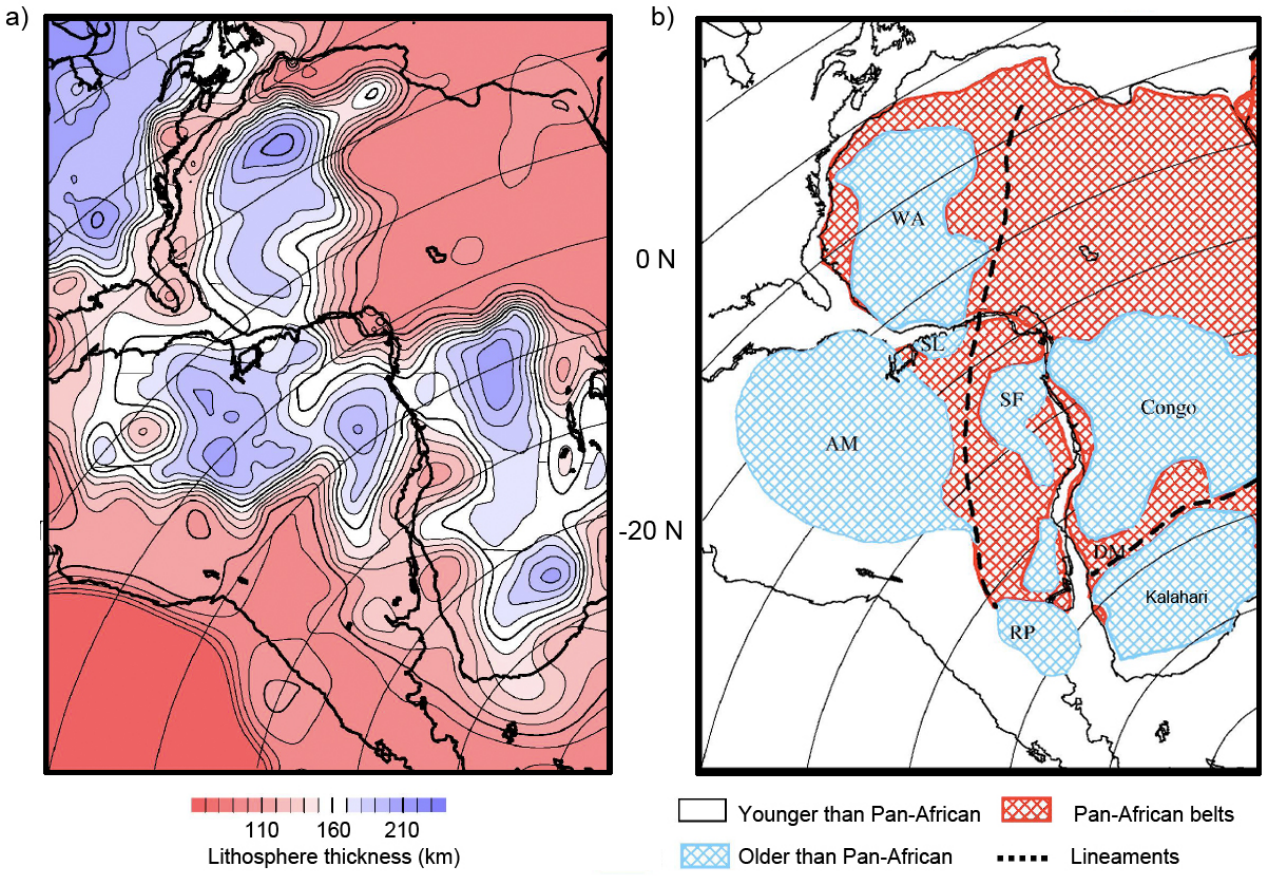


Figure 2.3: Reconstruction of West Gondwana with lithosphere thickness in the Permian (part a), adapted from McKenzie et al. (2015). Part (b) shows the major Pan-African orogenic belts (red), cratons within the region (blue), and continental-scale structural lineaments (black dashed lines). Cratons: West African (WA), Congo, Kalahari, Amazonian (AM), São Francisco (SF), Rio de la Plata (RP). The Damara Belt is denoted by DM.

2.3 Reconstruction

Attempts of reconstruction for the South Atlantic have occurred since the beginnings of the continental drift theory (Rupke, 1970). In order to compare the data from conjugate margins, the reconstruction models of

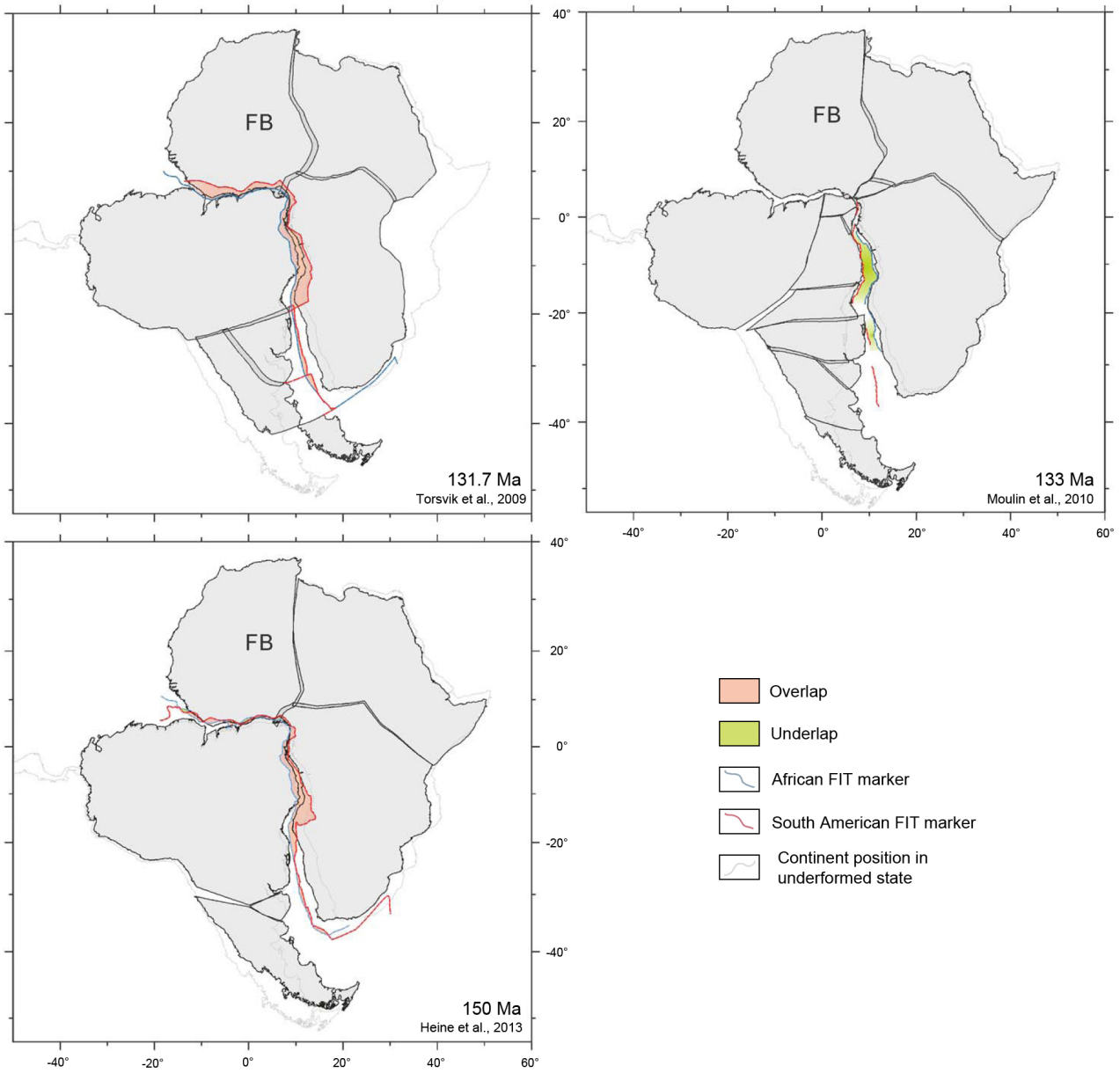


Figure 2.4: Simplified versions of reconstructions model, adapted from Pérez-Díaz and Eagles (2014). Different models shown here are Torsvik et al. (2009), Moulin et al. (2010) and Heine et al. (2013). FB = Fixed block.

Torsvik et al. (2009), Moulin et al. (2010) and Heine et al. (2013) were investigated (Fig. 2.4). Using the GPlates software package, these reconstructions were combined with the most-recent satellite gravity and magnetic data sets (Sandwell et al., 2013; Maus et al., 2009). The model from Torsvik et al. (2009) relied heavily on the Aptian Salt present in the Central Segment for the reconstruction model, with less emphasis on magnetic data. Heine et al. (2013) used on-shore evidence to support plate deformations and orientations, whilst Moulin et al. (2010) focused on fitting magnetic data, fracture zones and conjugate systems. Whilst the flowlines had a good overlap

with the Mid-Atlantic Ridge fracture zones for the Heine et al. (2013) model, they did not match the fracture zones towards the continental margins and curved away (Fig. 2.5a). The Moulin et al. (2010) model however had flowlines that were overall more parallel to the fracture zones (Fig. 2.5a). Additionally, the magnetic anomalies correlated best with the Moulin et al. (2010) reconstruction, with fewer magnetic isochrons matching anomalies in the Heine et al. (2013) model (Fig. 2.5b). Therefore the Moulin et al. (2010) model is used henceforth. The commencement points of the Rio Grande Rise and Walvis Ridge (shown by the two '+' symbols in Fig. 2.6) were also determined using the Moulin et al. (2010) reconstruction model, taking care they matched at time of break-up.

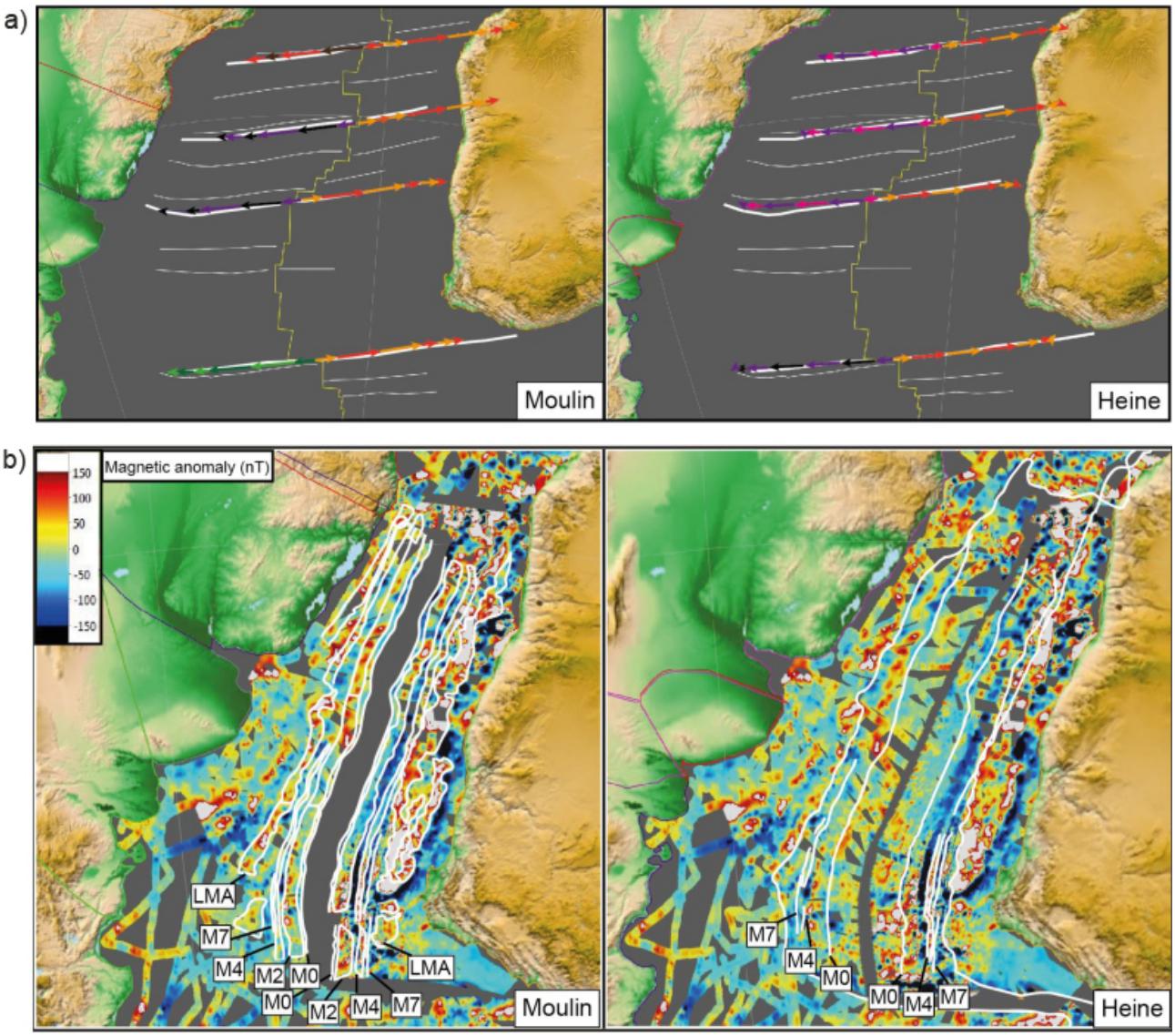


Figure 2.5: Differences between the Moulin et al. (2010) (left panels) and Heine et al. (2013) (right panels) reconstruction models, with this work and figure produced from UROP student Noemi Gyori. Part (a) represents the comparison between the flowlines (coloured lines and arrows) generated in GPlates and fracture zones (white lines) at 85 Ma, indicating the model's compatibility with data. Part (b) represents new magnetic data from ION Geophysical fitted with the magnetic anomalies from both Moulin et al. (2010) and Heine et al. (2013), outlined in white, at 115 Ma.

From the progressive younging of magnetic isochrons to the north (Fig. 2.11), it is known the South Atlantic opened in a south to north unzipping fashion, with break-up happening in stages. In addition to a new magnetic

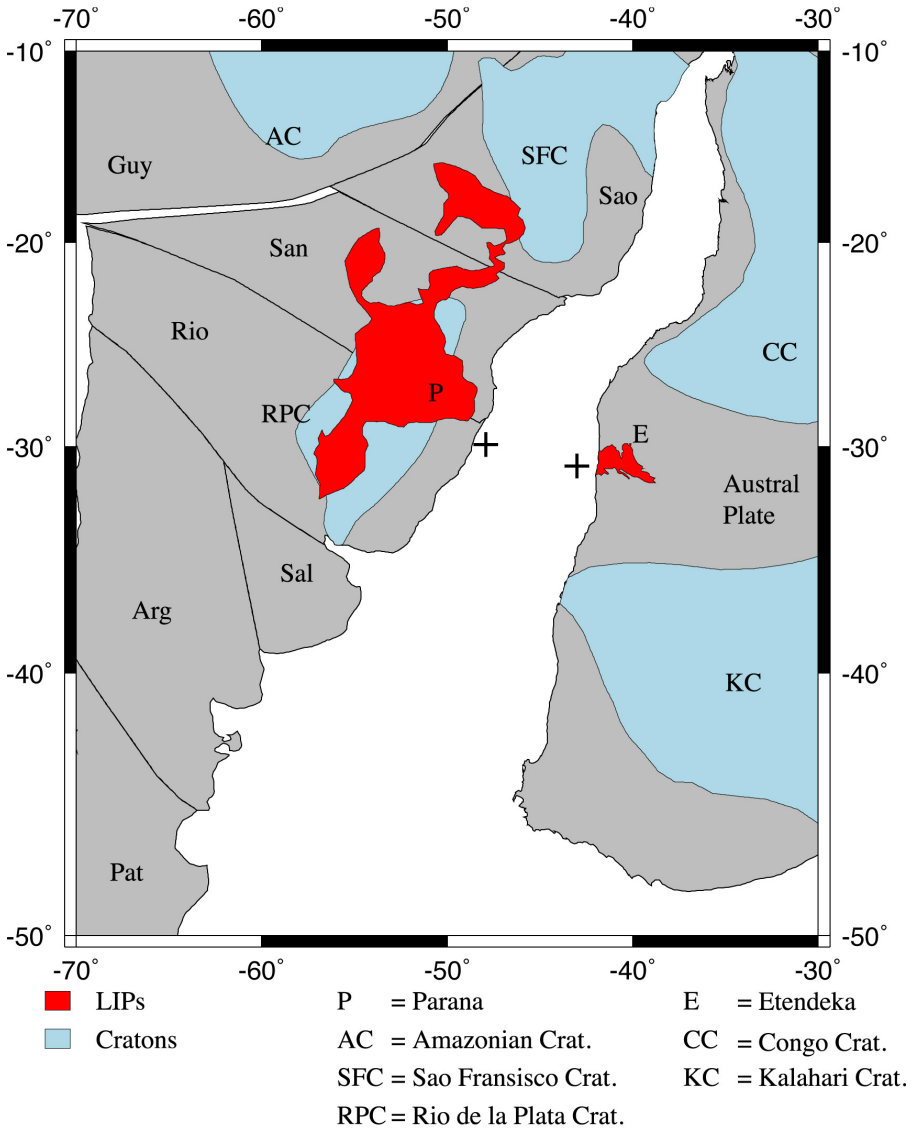


Figure 2.6: Reconstructions from GPlates shown at 121 Ma, using rotation poles of Moulin et al. (2010) with the sub-plates of South America (thin black lines) and showing the major geological features. The positions of cratons are from Gubanov and Mooney (2009), the location of the Etendeka-Paraná flood basalts is from Coffin and Eldholm (1994). The '+' marks the reconstructed landfall of the Rio Grande Rise and Walvis Ridge. Sub-plates are Patagonia (Pat), Argentina (Arg), Salado (Sal), Rio de la Plata (Rio), Santos (San), São Francisco (Sao), Guyana and (Guy).

isochron model, Moulin et al. (2010) also summarised the break-up by sub-plate. For the Moulin et al. (2010) model, the portion of the South American continent covering the study area is divided into the São Francisco, Santos, Rio de la Plata, Argentina, and Salado blocks. The sub-plates movements are timed according to sea floor magnetic isochrons M7, M4, M2 and M0 (locations in Fig. 2.13). In the south of present-day South America, the strike-slip movement between the Punta del Este and Salado Basins (Zambrano and Urien, 1970; Urien and Zambrano, 1973; Jac; Franke et al., 2006) suggests the Salado and Argentina sub-plates (Fig. 2.13) had started to move westward relative to the African plate prior to magnetic isochron M7. Between M7 and M4, the Rio de la Plata sub-plate moved westward, allowing the opening of the northern part of the South Atlantic. Following M2, the Rio de la Plata, Salado and Argentina sub-plates moved as one, and movement of the Santos plate also commenced. North of the Rio Grande Fracture Zone, the timing of the Atlantic initiation is less well constrained as it occurred within the Cretaceous Magnetic Quiet Zone from ~121-83Ma (Gee and Kent, 2007). Complete break-up is assumed to have occurred ~104 Ma for the whole region (Heine et al., 2013).

2.4 Onshore Volcanism: Paranà-Etendeka Traps and Dyke Swarms

The most apparent onshore volcanism around the time of break-up are the Paranà-Etendeka Traps. The Paranà-Etendeka Traps are found on the South American and African continents, with areas of 1.5 million km ^{2} (Courtillot et al., 1999; Peate, 1997) and 80,000 km ^{2} (Erlank et al., 1984) respectively (Fig. 2.1). The duration of

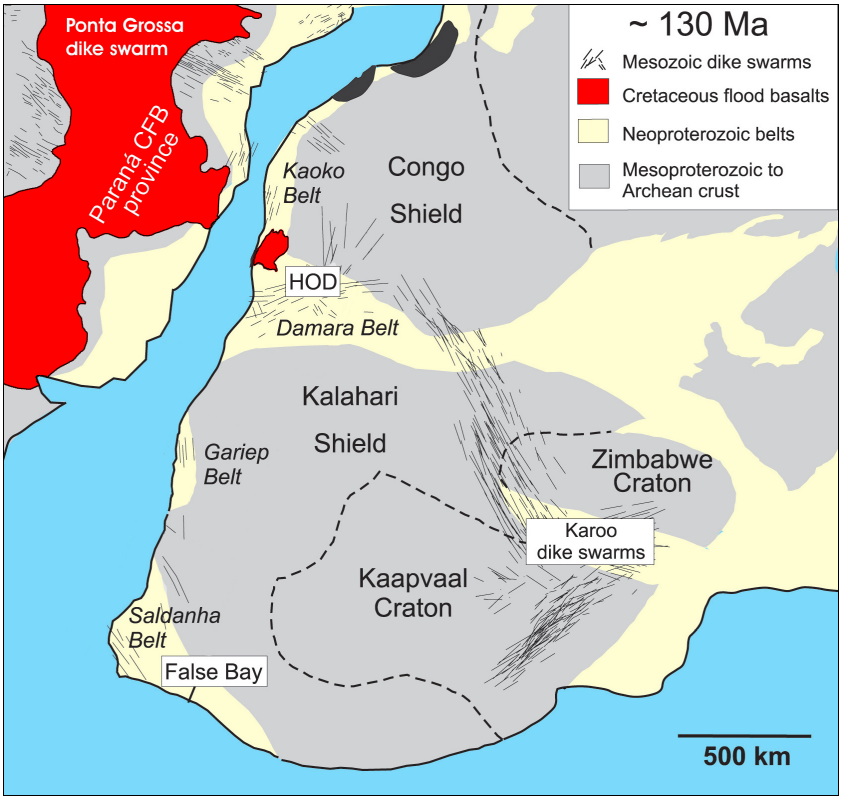


Figure 2.7: Schematic of the South Atlantic at ∼130 Myr, showing location of Mesozoic dike swarms. Adapted from Trumbull et al. (2007). HOD = Henties Bay-Outjo dikes. The dike swarms along the west African coast are dated in the Early Cretaceous, and the Karoo dike swarms are dated in the Jurassic.

the continental flood basalts eruption is debated. From ^{39}Ar/^{40}Ar dating and paleomagnetic results, Renne et al. (1992) concluded that the eruption of the Paranà occurred at 133±1 Ma in a time frame of less than a million years, in agreement with Bellieni et al. (1983) and Hawkesworth et al. (1992). Also using ^{39}Ar/^{40}Ar dating, Turner et al. (1994) showed evidence of the eruption lasting for ∼10Myr, between 137Ma and 127Ma, which is considered on a geological time scale relatively long for flood basalts. However, from recent magnetostratigraphy studies for the Etendeka portion of the large igneous province, it was found the eruption was already underway by at least magnetic isochron M15n lasting to isochron M11n (Dodd et al., 2015), dated 135.96 Ma and 130.84 Ma by Gee and Kent (2007) respectively. This shortened time scale still suggests the eruption began shortly prior to continental rifting, with the first recognised seafloor spreading anomaly being magnetic isochron M7, dated at 127.23 Ma (Fig. 2.10).

Additionally to the flood basalts, several dyke swarms dated in the Early Cretaceous formulate some of the earliest onshore evidence of magmatism during continental rifting. They are present on both the African and South American continents (Fig. 2.7), reaching as far south as the Cape Peninsula (Trumbull et al., 2007). From geochemical data, MgO content suggests dykes that erupted in the north near the Etendeka traps have a higher melt temperature and degree of melting, at 1560 °C and 20% respectively, compared to those in the

south near the Cape Peninsula (Trumbull et al., 2002, 2007).

2.5 Volcanic Passive Margins

2.5.1 Evidence from seismic data

Despite a relatively good coverage of seismic data in the South Atlantic due to the hydrocarbon exploration focus (Fig. 2.8), there is a relative lack in coverage of published high quality profiles showing the full margin structure from continental to oceanic crust inclusive of the Moho. Through the use of the seismic surveys, researchers have studied the voluminous SDRs and high-velocity lower-continental crustal bodies, considered by many to be complimentary to onshore Early Cretaceous dyke swarms and the Paranà-Etendeka Traps.

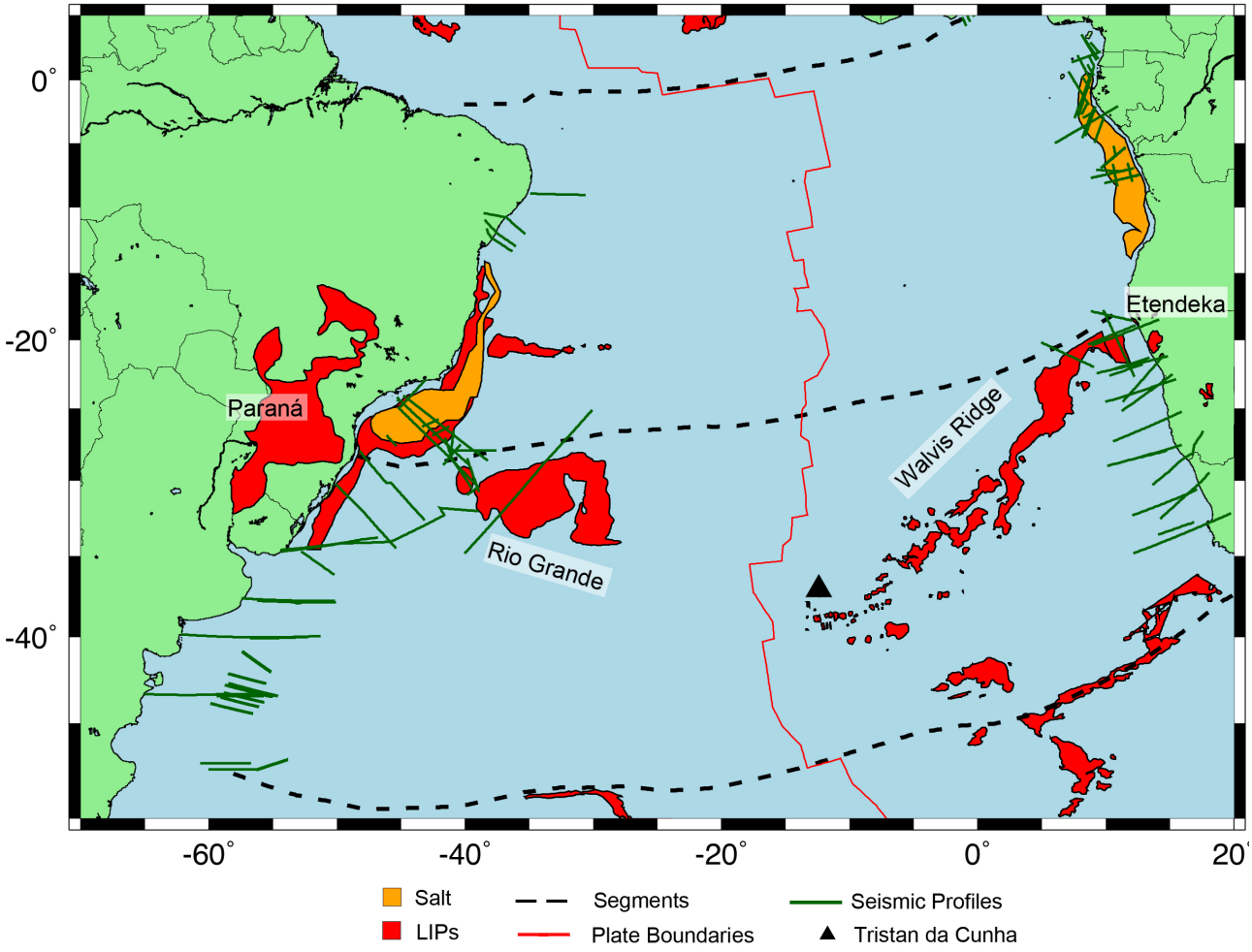


Figure 2.8: Map showing coverage of published seismic tracklines. South American seismic data include Leyden et al. (1971); Mohriak et al. (1998); Franke et al. (2007); Blaich et al. (2008); Schnabel et al. (2008); Dragoi-Stavar and Hall (2009); Mohriak et al. (2010); Franke et al. (2010); Becker et al. (2014); Evain et al. (2015). African seismic data include Gladczenko et al. (1998); Bauer et al. (2000); Stewart et al. (2000); Turner et al. (2003); Wilson et al. (2003); Attoh et al. (2004); Contrucci et al. (2004); Moulin et al. (2005); Schinkel (2006); Hirsch et al. (2009); Dupre et al. (2011); Fromm et al. (2015).

Leyden et al. (1971) had two refraction lines offshore Uruguay and South Brazil, and were possibly the first to image portions of HVLC in the region. They identified velocities reaching up to 7.51 $\mathrm{km\,s^{-1}}$, and noted that these values were lower than those typically seen in the upper mantle. Following this, Hinz (1981) identified the presence of SDRs on the African margin (locations Fig. 1.3), equally observed by Austin and Uchupi (1982) and Gerrard and Smith (1982). SDRs on the conjugate margin were also seen (Hinz, 1990), establishing volcanic passive margins south of the Rio Grande Rise and Walvis Ridge. Gladczenko et al. (1997, 1998) suggested the presence of HVLC bodies offshore Namibia using gravity modelling on depth converted transects from MCS lines. This was confirmed by Bauer et al. (2000), using two wide-angle refraction lines to image thick HVLC bodies. Since then, there has been several more published wide-angle surveys confirming the existence of HVLC bodies on the conjugate margins found south of the Rio Grande Rise and Walvis Ridge (Schinkel, 2006; Schnabel et al., 2008; Hirsch et al., 2009; more details in **Chapter 3**).

Away from the study and north of the Rio Grande Rise and Walvis Ridge, deep-penetration seismic surveys in the Central Segment have somewhat been hampered by the presence of Aptian Salt (location Fig. 2.8). However, the growing number of seismic surveys revealed starkly different magmatism volumes north of the Walvis Ridge. Contrucci et al. (2004) found the presence of non-volcanic passive margins off the Angolan margin, and the fast transition from volcanic to non-volcanic was imaged by Fromm et al. (2015) along the Walvis Ridge (Fig. 1.8). Whilst the passive margins of the Central Segment are classified as predominantly non-volcanic, there is still some evidence of localised magmatism (e.g., Fraser and Clark, 2016; Marzoli et al., 1999; Quirk et al., 2013).

There are currently several high-resolution deep-penetrating unpublished seismic data sets within industry covering the parts of the Central and Southern Segments on the South American margin and African margin (ION Geophysical, 2013a,b,c,d). As these lines start to be published (e.g., Stica et al., 2014), our understanding of the margin structures will continue to improve. This includes HVLC and SDR distributions, or lack thereof, and any resulting trends observed.

2.5.2 Evidence from gravity data

Free-air gravity anomaly grids can be complimentary to seismic data as evidence of offshore volcanism and the extent of the volcanic passive margins. On the South American side, the free-air gravity anomaly shows a continuous, prominent and elongated gravity anomaly high (Fig. 2.9; Blaich et al., 2009). East of this gravity high, there is a prominent free-air gravity low, running sub-parallel to the coastline (Fig. 2.9). The contrast between the high and low gravity areas, or the "edge effect" (marked in Fig. 2.9), was initially considered to be the juxtaposition of continental and oceanic crust (Rabinowitz and LaBrecque, 1979; Watts and Fairhead, 1999). Later, the edge effect anomaly was found to be coinciding with the HVLC and SDRs in this region, running from ∼30°S to ∼43.5°S (Hinz et al., 1999; Fig. 2.9).

On the African side of the study area (Fig. 2.9), similar to the South American margin, there is also a

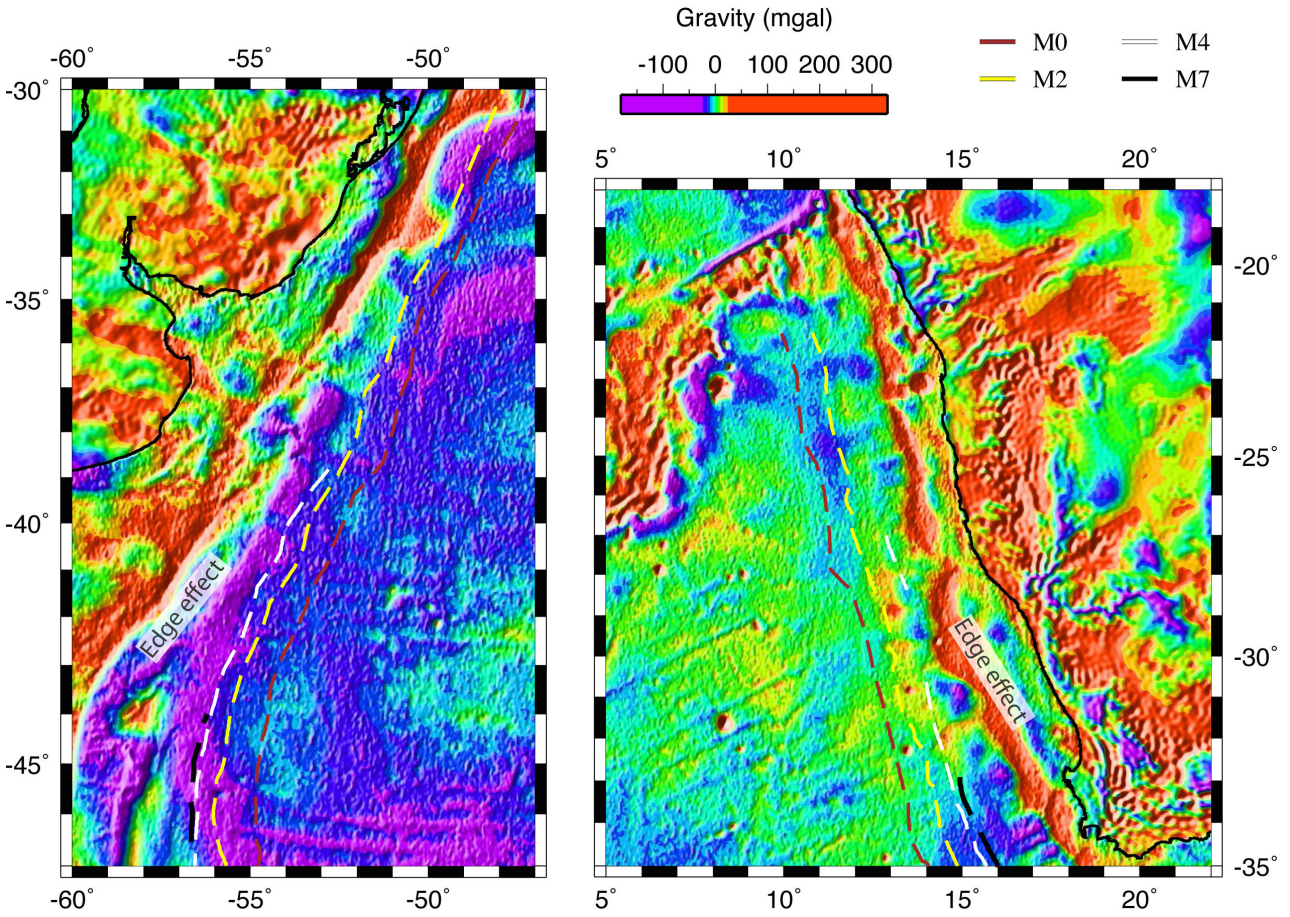


Figure 2.9: The free-air gravity anomaly grid (v21) is from Sandwell et al. (2013) (Fig. 2.9), originating from satellite altimetry data (e.g. Jason 1, Cryosat). Gravity high marked as "edge effect" can be seen all along the margin. There is also a second "outer gravity high" positive anomaly first seen by Bauer et al. (2000), most prominent between 27 °S and 33 °S (Hirsch et al., 2009). Seafloor spreading magnetic reversals M7, M4, M2 and M0 are from Moulin et al. (2010).

gravity high zone parallel to the coast (marked in Fig. 2.9). In addition, there is a gravity high present further offshore, described by Bauer et al. (2000) as an "outer gravity high". It is more prominent between 27°S and 33°S Hirsch et al. (2009), and the "outer gravity high" is considered to be the termination of SDR packages (seen in Fig. 2.9, Hirsch et al., 2009). Whilst the gravity data sets are not as informative as seismic profiles, they are still a useful guide to fill in information between transects.

2.6 Production of Ocean Crust: evidence from seafloor spreading magnetic anomalies

Rabinowitz and LaBrecque (1979) were the first to identify magnetic isochron reversals in this region, identifying chrons M11 to M0. Initially, M11 was described as the continent-ocean boundary, but was later discovered to fall within the SDR packages. As SDRs are basalt flows, they can record magnetic reversals, but they are not representative of a true ocean crust magnetic reversal (Moulin et al., 2010). M11 and M9, the inner two

magnetic anomalies described by Rabinowitz and LaBrecque (1979), were also considered as over-interpreted, and renamed the 'Large Magnetic Anomaly' or LMA (Moulin et al., 2010; location in Fig. 2.10).

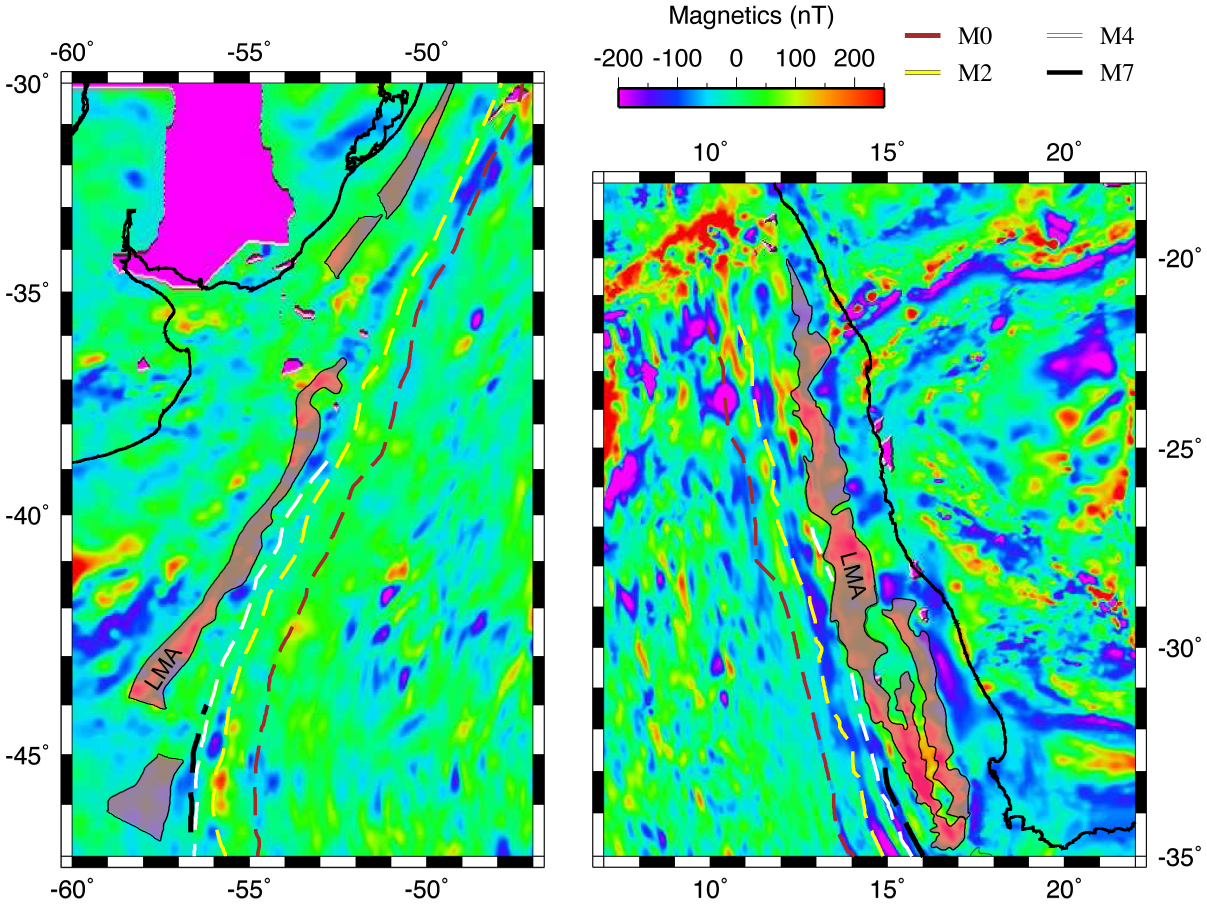


Figure 2.10: Magnetic anomaly (EMAG2) grid from Maus et al. (2009). The magnetic maps show the magnetic sequence interpretation from Moulin et al. (2010). Seafloor spreading magnetic reversals shown are M7, M4, M2 and M0. Additionally there is the interpretation of the LMA location by Moulin et al. (2010).

One of the more recent studies of magnetic isochrons in the study area is from Moulin et al. (2010). Moulin et al. (2010) interpreted magnetic isochrons M7, M4, M2 and M0 (Fig. 2.10), using a compilation of data from various sources. In order to comprehend the evolution of the passive margins through time, a time scale has to be assigned. There are several versions of time scales for the magnetic isochrons (Gradstein et al., 2004; Gee and Kent, 2007; Gradstein et al., 2012), but the main difference surrounds the age of M0r, with vastly different ages between time scales. Gee and Kent (2007) suggested this age to be 121 Ma, whilst Gradstein et al. (2012) suggested an older age of 125 - 126 Ma. This particular chron represents the Barremian-Aptian boundary, and would subsequently affect absolute ages of the pre-Aptian stratigraphic stages, as the biostratigraphic events are based on a magnetostratigraphy framework (Heine et al., 2013). He et al. (2008) and Heine et al. (2013) are in preference of the timing proposed by Gee and Kent (2007), based on a review of seafloor spreading velocities globally, as an older M0r age would significantly increase spreading velocities prior to this time. Additional evidence is presented from a dike on the Falkland Islands, which, using Ar-Ar dating, was aged at 121.3±1.2 Ma by Stone et al. (2008), close to the age proposed by Gee and Kent (2007) for M0r. As the Gradstein et al. (2012) time scale has an unavoidable age-shift in the M sequence, the Gee and Kent (2007) time scale is considered more reliable and used henceforth (Table 2.1).

Table 2.1: Ages from Gee and Kent (2007) for the Moulin et al. (2010) isochrons As the LMA is the integration of M11 and M9, the formers' ages have been assigned. However, as these magnetic isochrons were also considered over-interpreted, there is some level of uncertainty with this age assignment.

Isochron	Age
LMAo (or M11o)	132.47
LMAy (or M9y)	128.34
M7n	127.23 - 127.49
M4n	125.67 - 126.57
M2n	123.55 - 124.05
M0r	120.60 - 121.00

The magnetic data imply the direction of opening from South to North. The presence of M7 on the conjugate margins suggests ocean crust was in production by 127.49 Ma, at least towards the south. The magnetic data are limited by the Cretaceous Magnetic Quiet Zone (Fig. 2.11), the latter being a gap in magnetic reversals between M0 and C34 (aged at 120.6 Ma and 83 Ma respectively).

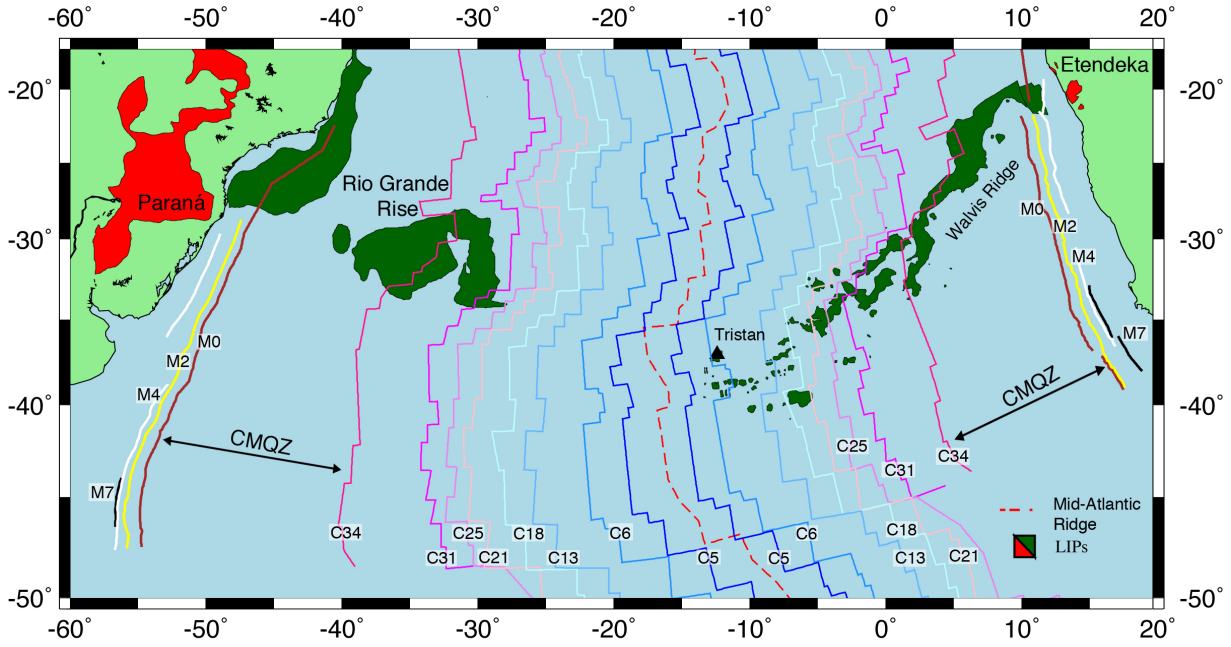


Figure 2.11: Location of chrons M7 to M0 from Moulin et al. (2010), and chrons C34 to C5 from Seton et al. (2012). The gap between M0 (aged 120.6 Ma by Gee and Kent (2007)) and C34 (aged 83 Ma by Gee and Kent (2007)) is known as the Cretaceous Magnetic Quiet Zone (CMQZ), where no magnetic reversals occurred. LIPs are from Coffin and Eldholm (1994).

Heine et al. (2013) summarised sea floor spreading rates through the South Atlantic break-up from 140 Ma to 100 Ma according to basins, calculated from age-coded flowlines (Fig. 2.12). At the time of magnetic isochron M4 (126.57 Ma), the spreading rates ranged from 10 to 18 mm yr^{-1}, increasing towards the south. For the period 126.57–120.6 Ma, following the Salado Basin, the rates increase up to 35 mm yr^{-1}, and subsequently increased to 58 mm yr^{-1} (Fig. 2.12; Heine et al., 2013). Moulin et al. (2010) has similar rates for these times and for the same area, at 38 mm yr^{-1} and 50 mm yr^{-1} respectively, but does not suggest a rate prior to M4. As Heine et al. (2013) also uses the Gee and Kent (2007) time scale (Table 2.1), these spreading rates are used henceforth for consistency.

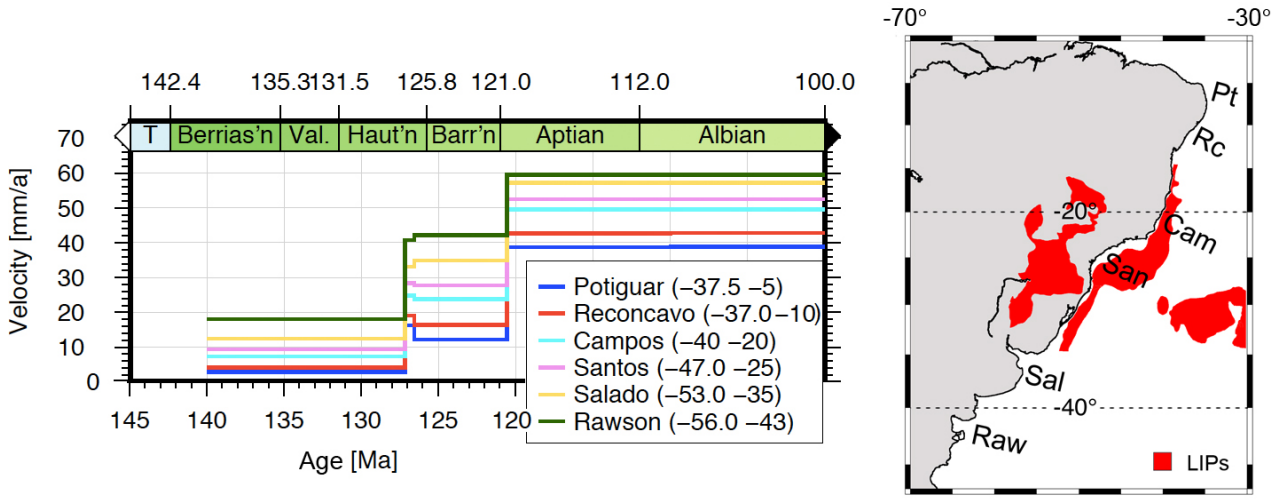


Figure 2.12: Spreading rates for the South Atlantic, adapted from Heine et al. (2013). Rates are summarised by basin from 140 Ma to 100 Ma, with locations found in map. Basins are Raw = Rawson, Sal = Salado, San = Santos, Cam = Campos, Rc = Reconcavo, Pt = Potiguar.

2.7 Segmentation

Like most continental margins, the southern South Atlantic has clear segmentation present along-strike. Areas of structural weakness in the pre-rift continents (e.g. mobile belts) on the South American and African continents are inferred to have influenced continental break-up and initial seafloor spreading (Rosendahl, 1987; Clemson et al., 1997, 1999; Jungslager, 1999; Franke et al., 2007). These are visible through fracture zones present throughout the South Atlantic oceanic lithosphere. To map the lithospheric segment boundaries, the segment boundaries identified by Franke et al. (2007) on the South American margin and Koopmann et al. (2014b) on the African margin were used as a starting point, both being largely defined by continental structural variations. The locations of the major fracture zones were then independently picked from the satellite gravity and magnetic data sets (Sandwell et al., 2013; Maus et al., 2009) and tested for conjugate symmetry using GPlates, making small refinements to the boundary locations. This work was done in conjunction with another PhD student (Carl McDermott) within the group and a UROP student (Noemi Gyori).

Within the study area, the Moulin et al. (2010) model has five sub-plates forming part of the South American continent (São Francisco, Santos, Rio de la Plata, Argentina, and Salado blocks, Fig. 2.13), with a single sub-plate forming the southern part of Africa (Austral block). The sub-plate boundaries on the South American margins are used to define the 'first-order segments', numbered 1 - 4. These sub-plates boundaries also coincide with major fracture zones (defined as having a minimum offset of 50 km at the modern ridge axis), craton locations (Gubanov and Mooney, 2009), and other onshore zones of weakness (Moulin et al., 2010; Heine et al., 2013). In addition, 'second-order segments' were recognised, where clear fracture zone traces on conjugate sides were present (numbered alphabetically, e.g. Segments 3b & 3a).

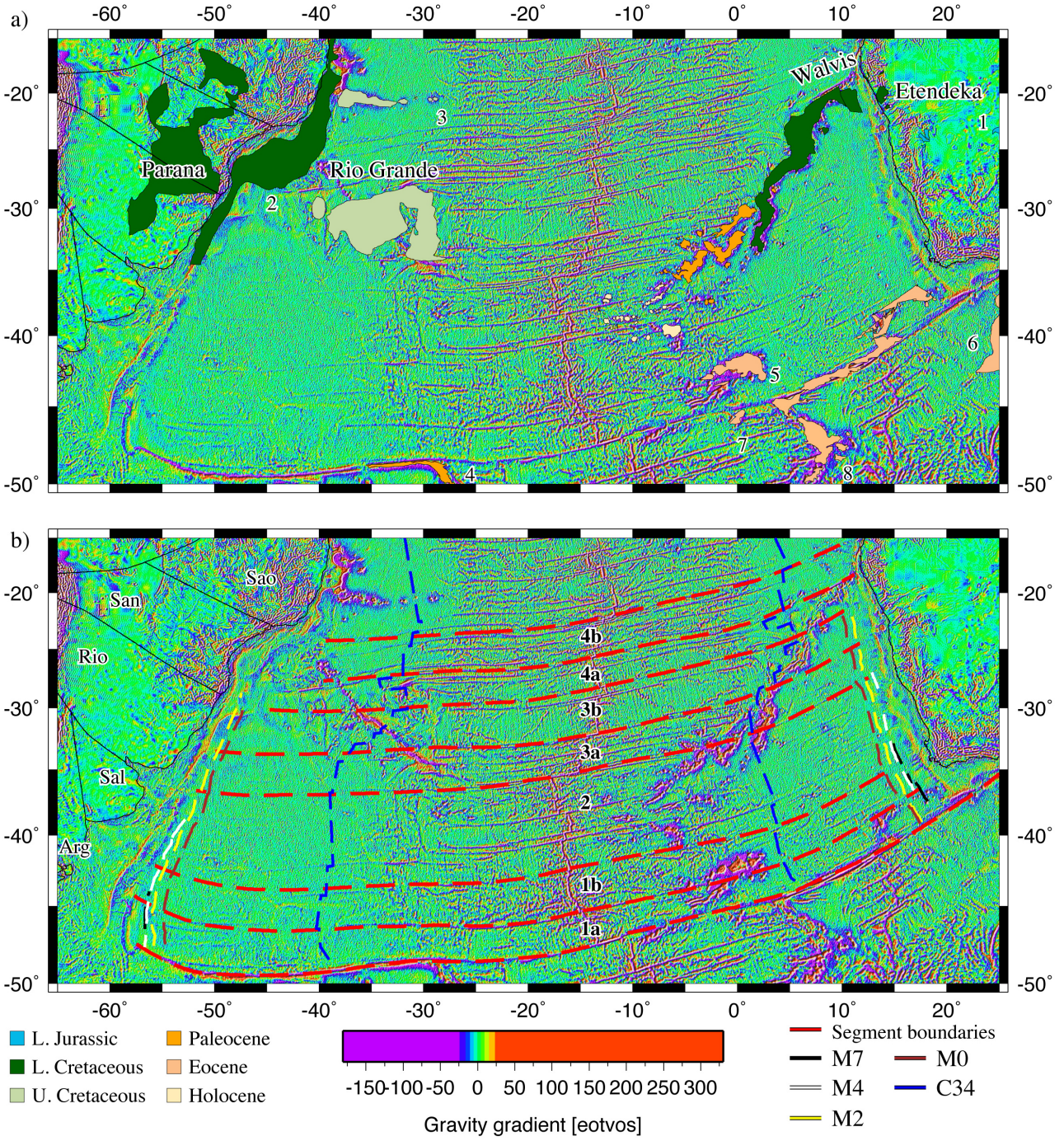


Figure 2.13: Map of the gravity gradient from Sandwell et al. (2013) for the study area. Part (a) shows the main tectonic features with age progressive LIPs (Coffin and Eldholm, 1994): 1 = Karoo, 2 = Sao Paolo, 3 = Vitoria-Trinidade, 4 = Falkland 5 = Discovery, 6 = Agulhas Plateau, 7 = Hardman volcano, and 8 = Meteor Ridge. Also shown are the sub-plate boundaries (thin black lines) from Moulin et al. (2010). Part (b) shows interpreted location of the major segment boundaries. Four major segments are identified (numbered 1 - 4) consistent with the sub-plate boundaries of South America from Moulin et al. (2010). Second-order segments were also identified, from clear fracture zone traces on conjugate sides (numbered alphabetically, e.g. Segments 1b & 1a). Also shown are sea floor spreading magnetic anomalies M7, M4, M2 & M0 from Moulin et al. (2010), C34 from Seton et al. (2012). Sub-plates: Arg = Argentina, Sal = Salado, Rio = Rio de la Plata, San = Santos, Sao = São Francisco.

2.8 Rio Grande Rise and Walvis Ridge

Two of the dominant features created post-rift are the Rio Grande Rise and Walvis Ridge. They are assumed to represent the Tristan Plume volcanic trail through a series of volcanic islands and seamounts. The Rio Grande Rise does not extend to the Mid-Atlantic ridge, suggested to have occurred from a plume drift ∼80 Ma (O'Connor and Duncan, 1990), stopping the production of the Rio Grande Rise on the South American side (White and McKenzie, 1989; O'Connor and Duncan, 1990). There is also some debate about the Rio Grande Rise being a fragment of continental crust due to the dredging of granite boulders in its vicinity (Than, 2013). South of the Rio Grande Rise, a gravity signal found in the Vema Channel suggests there is an abandoned mid-ocean ridge segment, proposed by Pérez-Díaz and Eagles (2014) to be a ridge jump dated ∼93 Ma. Despite uncertainties for the evolution of the Rio Grande Rise, for the Walvis Ridge, studies using ^{40}Ar-^{39}Ar dating on dredge samples and DSDP core samples (Sites 516, 525 & 528; locations Fig. 2.14) shows a clear younging age progression from ∼120 Ma to present day (Rohde et al., 2013; O'Connor and Jokat, 2015).

2.9 DSDP expeditions

In addition to seismic, gravity and magnetic data, there are a total of 55 Deep Sea Drilling Project (DSDP) drill holes in the vicinity of the study area (locations Fig. 2.14; more details in **Appendix B**). Due to the variation of DSDP expeditions, of these a total of 19 drill holes reached basement and 6 reached pre/syn-rift sediments (Fig. 2.14). Among the first to reach basement was DSDP Leg 3 (Maxwell et al., 1970), with a mission to help understand the concept of plate tectonics, still a relatively new idea at the time. They identified the age of sediments and basalts to increase away from the ridge axis, which, at the time, was a validation of sea-floor spreading within the South Atlantic.

Leg 40 was centred around the Walvis Ridge with the aim of obtaining a complete sedimentary sequence from a continental slope (Bolli et al., 1978). Of the six sites, Sites 361, 363 and 364 all reached sediment ageing back to the Aptian/early Cretaceous. Site 361, the furthest South, had a well-preserved nanofossil suggesting sediments dating from the Valanginian to lower Aptian (139.4-112.5Ma) (Bolli et al., 1978). Site 363, found just North of the Walvis Ridge, had nanofossils indicating age of sediments possibly of Hautevarian age (132.9-129.4Ma), but definitely of Upper Aptian age (125-112.5 Ma) (Bolli et al., 1978). Finally, Site 364, the most northern of the sites, had indication of Upper Aptian (125-112.5Ma) to Upper Albian (112.5-100.5Ma) biostratigraphy (Bolli et al., 1978). The ages found in the drillsites indicated a younging of sediments moving in a north direction, suggesting the opening of the South Atlantic from a south to north direction. Although a few drillholes reached basement, special care had to be taken to filter out samples that were too altered (more details **Appendix B**) in order to consider them for further use. Major element oxides compositions from these samples along with Mid-Atlantic dredge samples will be used in the context of the numerical model of continental rifting (more details in **Chapter 6**).

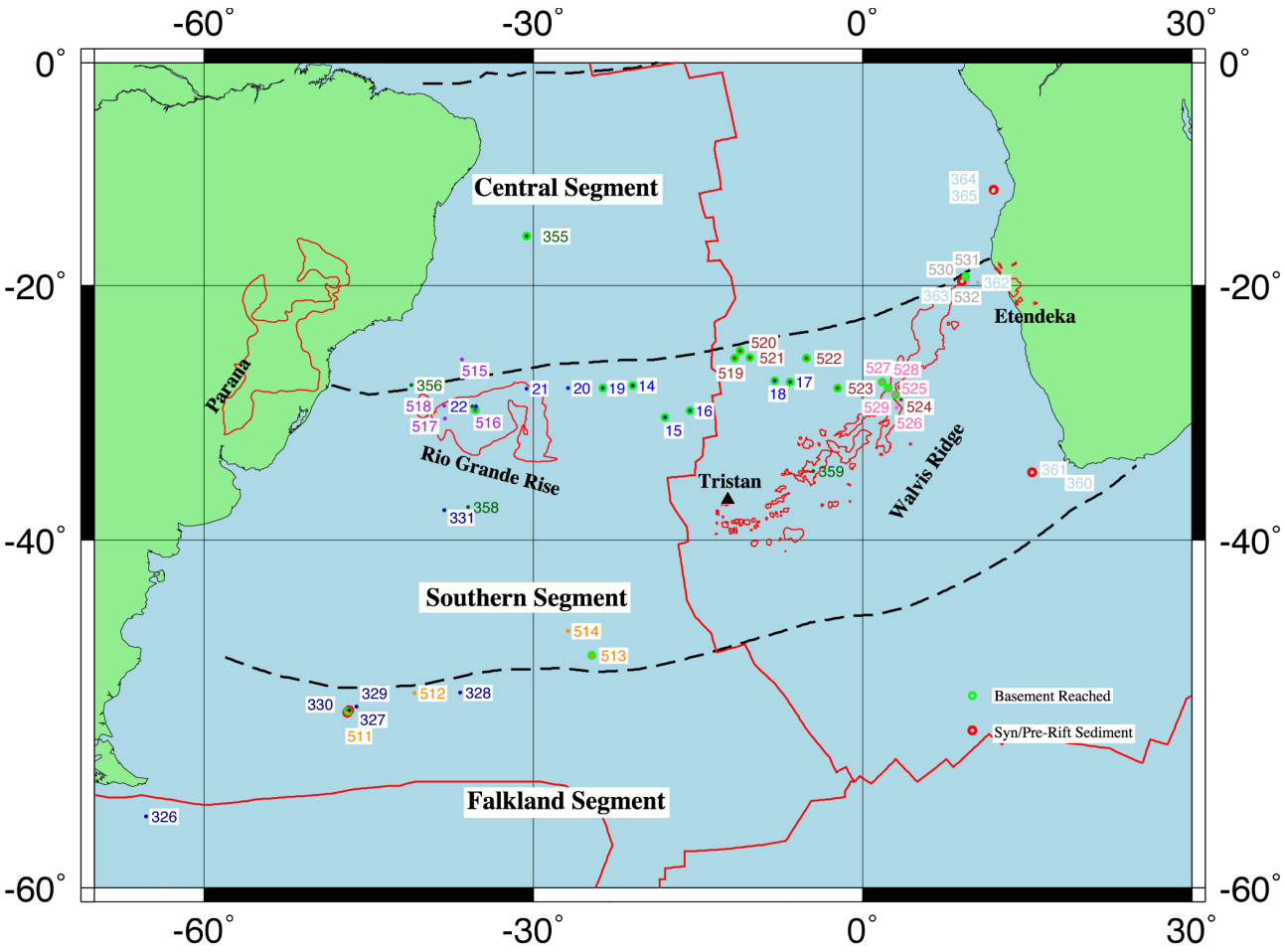


Figure 2.14: Map of DSDP drill hole locations in region. DSDP locations marked by green circles indicate basement has been reached, and locations marked with red circles indicate that pre and/or syn-rift sediments have been reached.

2.10 Departures from *Mantle Plume - VPM Theory* within the South Atlantic

The elevated MgO values in dyke swarms (Fig. 2.7), the eruption of the Paraná-Etendeka traps and the presence of volcanic passive margins (validated by SDRs and HVLC bodies) suggest an elevated mantle temperature at time of break-up. Although historically the break-up in the South Atlantic is attributed to the arrival of the Tristan Plume, there are several departures from the *Mantle Plume - VPM Theory*, with notable asymmetries in the east-west and north-south direction. In the east-west direction, there is a large discrepancy between the volumes of continental flood basalts, where the Paraná traps are significantly larger than the Etendeka traps, with areas of 1.5 million km^2 (Courtillot et al., 1999; Peate, 1997) and 80,000 km^2 (Erlank et al., 1984) respectively. For the asymmetry in the north-south direction, the conjugate margins found south of the Rio Grande Rise and Walvis Ridge are volcanic with an abundance of SDRs. North of the aseismic ridges however, the conjugate margins are magma-poor and lack SDRs (Contrucci et al., 2004; Aslanian et al., 2009; Reston, 2010), with the exception of several localised areas (e.g., Fraser and Clark, 2016; Marzoli et al., 1999; Quirk

et al., 2013). There is also an extremely rapid transition from volcanic to non-volcanic at the Walvis Ridge (Fig. 1.8; Fromm et al., 2015).

These asymmetries do not match the classic "mushroom" head model, where the plume head would flatten with an axisymmetric geometry (Fig. 1.5; Section 1.5) and the presence of volcanism would be expected both north and south of the Rio Grande Rise and Walvis Ridge. There should additionally be systematic decreasing volumes of magmatism away from the plume axis, which was not observed for SDRs by Franke et al. (2007) and Koopmann et al. (2014a). Due to these discrepancies, other mechanisms have been suggested for the formation of volcanic passive margins in the Southern Segment, such as active upwelling and segmentation (Section 1.8).

In order to measure the magnitude of magmatism within the South Atlantic, seismic profiles showing the full margin structure from continental to oceanic crust inclusive of the Moho are used. These provide the evolution of the margin through time. Observations taken from these seismic profiles can primarily be used to understand the variation of magmatism along-strike, and further used to compare to results from numerical modelling of continental rifting. This will bring us one step closer to understanding the initial break-up conditions for the southern South Atlantic.

Chapter 3

Observational Constraints

3.1 Introduction

In this project, numerical modelling of magmatism is presented for the conjugate volcanic passive margins of the southern South Atlantic. Observational constraints form the basis for comparison against numerical model results. In order to quantify the degree of magmatism along the margins, three measurements are compiled from active-source seismic data: (1) initial oceanic crustal thickness, (2) syn-rift melt areas and (3) syn-rift seismic velocity trends. Although numerous seismic surveys have been carried out on the South Atlantic margins (Fig. 2.8), limited surveys reaching the Moho and showing the full margin structure have been carried out. The best seismic data to study melt volumes and seismic velocity trends are wide-angle lines. The wide-angle seismic data set for this region (Fig. 3.1 & 3.17) is relatively sparse. As a result, multichannel seismic profiles (MCS) will provide important consolidation to any trends in magmatism seen along the continental margin, and will help to better understand the break-up of the South Atlantic.

In 1995, sets of MCS and wide-angle data were collected by BGR, AWI and GFZ [1] on the African margin in the Walvis Basin area (Bauer et al., 2000). These surveys represented a first in this area, penetrating through the crustal structure of the margin to reach the Moho (Bauer et al., 2000). Other wide-angle surveys showing the full crustal structure of the margin include joint wide-angle surveys from GFZ, BGR & South Africa's Council for Geoscience, with a line published in the masters thesis from Schinkel (2006), the latter published in Schulze et al. (2007), and another line in Hirsch et al. (2009) (wide-angle locations in Fig. 3.1). The most recent published wide-angle lines found along the margin are from Fromm et al. (2015), showing several profiles crossing the Walvis Ridge. There are more MCS profiles found along the African margin, such as those carried out by CGG Veritas between 1996-2003 in the Orange basin (de Vera et al., 2010), and 12,200 km of MCS lines from BGR shot between 1991-2003, some of which are published by Koopmann et al. (2014b). The MCS lines

[1] BGR = Bundesanstalt fr Geowissenschaften und Rohstoffe (BGR) in Hannover, AWI = Alfred Wegener Institute, GFZ = GeoForschungsZentrum

did not however image the full crustal structure of the margins.

For the South American margin, the first wide-angle profile published imaging a full crustal structure was from Schnabel et al. (2008), with a coincident MCS line. There are two more recent wide-angle profiles from from Becker et al. (2014), also with coincident MCS lines (wide-angle locations in Fig. 3.17). In addition to these three published wide-angle profiles, there are several MCS lines published from the BGR data set of ∼25,000 km regional MCS lines (e.g., Hinz et al., 1999; Franke et al., 2007, 2010; locations Fig. 3.30). Collected from 1978 to 2004, they cover the outermost shelf, slope and rise of southern South American continental margin. They have relatively good seismic resolutions at shallow depths (Blaich et al., 2009), and, unlike the MCS lines found on the African margin, these include some that image down to the Moho.

In addition to published MCS profiles, there is currently ∼24,000 km of high-resolution, deep-penetrating 2D seismic lines from ION Geophysical in the Southern Segment, as part of the ION BasinSPAN programme (titled PelotasSPAN, UruguaySPAN, ArgentinaSPAN and NamibiaSPAN; ION Geophysical, 2013a,b,c,d). As yet, only a few sections have been successfully published from a similar data set covering the Central Segment (e.g. Clerc et al., 2015, Unternehr et al., 2010, Cowie et al., 2016 and Péron-Pinvidic et al., 2015). However, some of the data from the PelotasSPAN, UruguaySPAN and ArgentinaSPAN are used for this study, limited to the identification and production of initial ocean crust.

In order to use the seismic data accurately, precise locations and velocity profiles (if a wide-angle line) have to be obtained. This is achieved by extracting locations and velocity profiles from the digitization of maps and profiles. Additionally, an age-grid from the location of magnetic isochrons is created in order to age-assign points on the seismic profiles according to their coordinates. A seismic line will only be used if it penetrates the full structure of the continental margin, including the Moho. A total of 5 wide-angle profiles from the African margin (Section 3.3; locations Fig. 3.1) and 3 from the South American margin are used in this study (Section 3.4; locations Fig. 3.17). There is also an additional 30 MCS lines used on the South American margin, including some from unpublished data sets (Section 3.6; locations Fig. 3.30).

3.2 Identification of Magmatism

In this project, a differentiation between syn-rift magmatism and post-rift magmatism is made. The post-rift magmatism pertains to the oceanic crustal thickness at the landward limit of ocean crust (**Chapter 5**). The syn-rift magmatism is measured from the area of HVLC bodies and SDRs, along with seismic velocity trends (**Chapter 6**). Post-rift and syn-rift magmatism observations are classified following a set of criteria for each profile. Following these criteria, and although they may already exist in published works, the interpretations for the locations and quantification of post and syn-rift magmatism have been done/redone for each seismic profile specifically within this project using the available data sets: this allows for consistency across all the observational constraints. The observations are then used as the basis for the comparison against numerical

modelling results.

3.2.1 Landward Limit of Oceanic Crust

In order to obtain a consistent indication of melt production along-strike, the thickness of the first formed oceanic crust is measured on each profile using a location criterion known as Landward Limit of Oceanic Crust, shortened to the LaLOC (used in **Chapter 5**). The LaLOC has been defined by Heine et al. (2013) as the 'boundary which delimits relatively homogeneous oceanic crust ocean-ward from either extended continental crust or exhumed continental lithospheric mantle landward or Seaward Dipping Reflectors (SDRs), where an interpretation of the Moho and/or the extent of continental crust is not possible'. In this project, the process of identification is altered slightly, and a combination of magnetic and seismic characteristics are used to locate the LaLOC. The interpretation of the location of the LaLOC and the thickness of the first formed oceanic crust was done/redone for all of the seismic profiles used within this project using the following criteria:

Process for identifying the LaLOC

- **Magnetic Isochron locations**: in the study area, magnetic isochrons M2 and M0 (Fig. 2.10) are generally recognised as sea floor-spreading being under way (Moulin et al., 2010), so the first oceanic crust must be landward of these.
- **SDRs**: the SDRs, which are relatively well-imaged on the seismic lines, are normally located landward of the oldest oceanic crust. However, their formation is still not fully understood, and it is possible that SDRs may overlay oceanic crust, therefore this must be coupled with other criteria.
- **HVLC bodies**: on wide-angle profiles, high P-wave velocity bodies in the lower crust, typically with values $>7.0\,\mathrm{km\,s^{-1}}$ (Becker et al., 2014; Trumbull et al., 2015), are recognised within this project to indicate the presence of highly intruded stretched continental or transitional crust. It must be noted that no HVLC bodies have been drilled or found exhumed, so their exact method of formation is unclear. However, within this project, based on HVLC bodies being intrusions within continental crust, the LaLOC is understood to be seaward of all these high velocity bodies observed on wide-angle seismic profiles.
- **Depth-V_p profiles**: depth-V_p profiles are extracted from the wide-angle models and tested for the presence of oceanic, stretched transitional or continental crust. The V_p limits from White et al. (1992) are used to define mature oceanic crust. Using this extra criterion, the LaLOC can coincide with overlying SDRs when supported by evidence. This criterion however is limited to wide-angle data, as seismic velocity information is necessary.
- **Reflectivity character**: the reflectivity character is considered, with true ocean crust typically being devoid of internal reflectivity. Additionally, a recognisable 'bumpy surface' indicates the presence of pillow lavas, which can be seen on MCS profiles. This criterion is limited to MCS data only, where this seismic characteristic can be identified.

3.2.2 Syn-rift magmatism

The identification of syn-rift magmatism is key to understanding the relationship between the mantle temperature, degree of active upwelling and melt generation (used in **Chapter 6**). In order to identify the location of syn-rift magmatism within the transitional crust, a strict process is applied for each seismic profile. As the use of seismic velocity is required, the identification can only be done for wide-angle seismic lines, and hence the location and quantification of syn-rift magmatism was done/redone for all the profiles of this type within this project using the following criteria:

Process for identifying syn-rift magmatism

- **Top basement**: determined by the first velocities found higher than those of typical oceanic sediments, around 4.5 - 4.8 $\mathrm{km\,s^{-1}}$.
- **SDRs**: the SDR locations were primarily author defined. However, for each profile, the distribution of SDRs was cross-correlated with the closest MCS line. The thickness of SDRs was then identified using a velocity range of 4.8 - 5.5 $\mathrm{km\,s^{-1}}$ (Bauer et al., 2000), a typical basalt seismic velocity. As SDRs are by nature basalt flows with interbedded sediments, a percentage was applied when calculating SDR areas. Ocean Drilling Program sites (Sites 642, 917 and 918) indicated SDRs could be up to 80% basalt (Planke, 1994), but previous authors have estimated a 50 - 50 basalt to sediment ratio, as shown by magnetic susceptibility values used (e.g., Bauer et al., 2000; Collier et al., 2008; Koopmann et al., 2014b). A compromise value of 65% was therefore used to calculate SDR areas.
- **HVLC bodies**: found within the transitional crust, they were located using seismic $V_p \geq 7.0$ - 7.2 $\mathrm{km\,s^{-1}}$ (Bauer et al., 2000; Schinkel, 2006; Schnabel et al., 2008; Hirsch et al., 2009; Becker et al., 2014).
- **Moho**: velocities were defined as ≥ 8.0 $\mathrm{km\,s^{-1}}$.

3.3 Wide-Angle Profiles: African Margin

In this section, wide-angle profiles found on the African margin are presented. These include (going from north to south) one profile published in Fromm et al. (2015) found on the Walvis Ridge, two profiles published in Bauer et al. (2000) found off the coast of Namibia, one profile originally from Schinkel (2006) found offshore South Africa, published in Schulze et al. (2007), and a final profile published in Hirsch et al. (2009), also offshore South Africa. The location of the landward limit of ocean crust will be investigated, along with the identification of syn-rift magmatism.

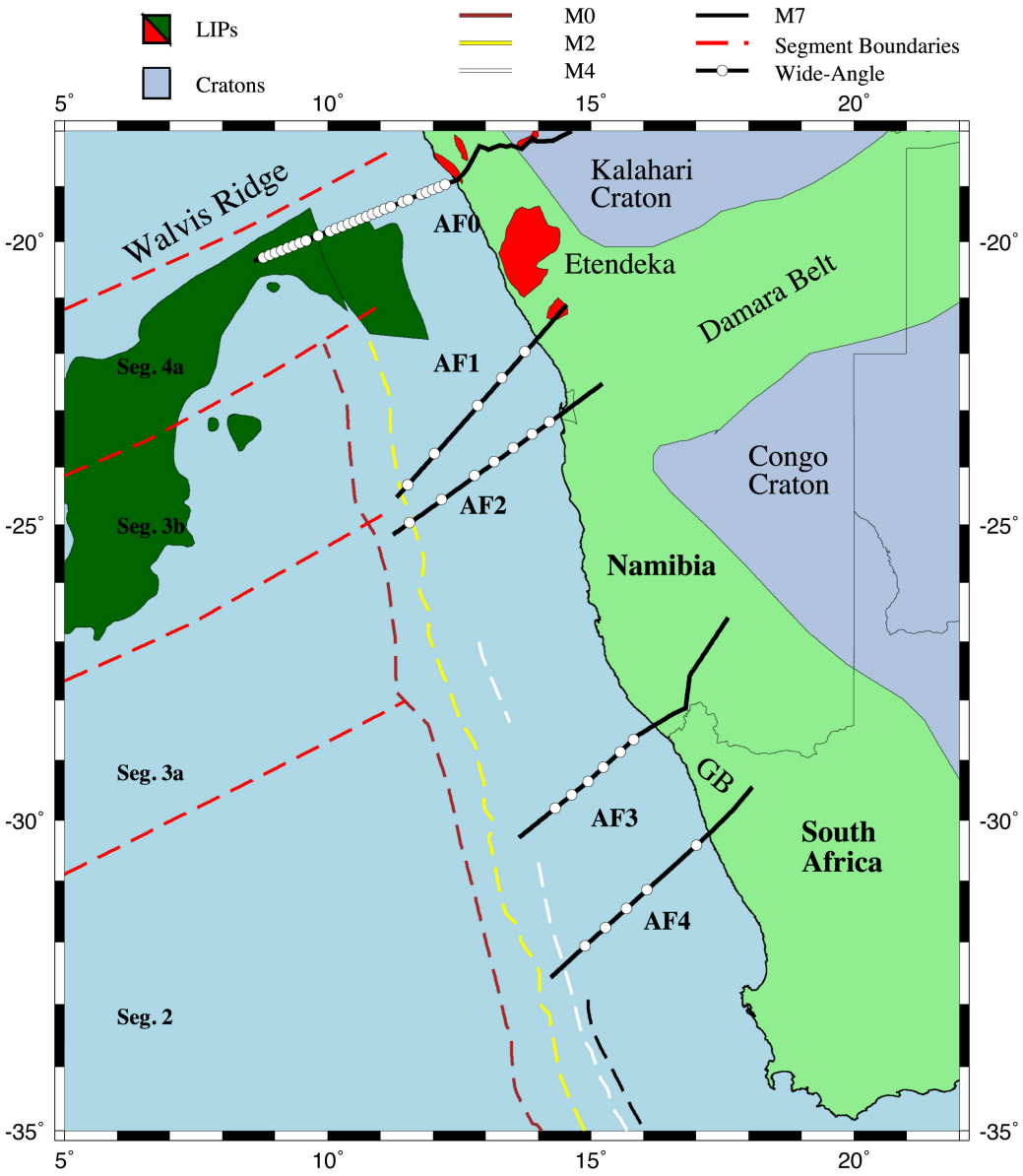


Figure 3.1: Location of African wide-angle seismic profiles with major geological features. Cratons positions (blue shapes) are from Gubanov and Mooney (2009), the location of the Etendeka flood basalts and Walvis Ridge (red and green shapes) from Coffin and Eldholm (1994). Damara Belt and Gariep Belt (GB) represent part of the network of early Paleozoic orogenic belts. Locations of Profiles AF0 - AF4 (black lines with dots representing OBHs) from Fromm et al. (2015); Bauer et al. (2000); Schinkel (2006); Hirsch et al. (2009). Segment boundaries (red dashed lines) have been previously identified in Section 2.7.

3.3.1 Profile from Fromm et al., 2015: Profile AF0

3.3.1.1 Original data

The most northern profile and newest line, line P100, was published in Fromm et al. (2015). Line P100, here referred to as Profile AF0, was found along the Walvis Ridge offshore from the Etendeka Igneous Province (Fig. 3.1), bordering the Koako Belt. This formed part of the SAMPLE (South Atlantic Margin Processes and Links with onshore Evolution), a series of on and offshore seismic experiments focusing on the African passive margin (Ryberg et al., 2016). Its main aim was to study the sub-Moho upper mantle seismic velocity. In addition to ocean bottom seismometers, there were 200 receivers onshore.

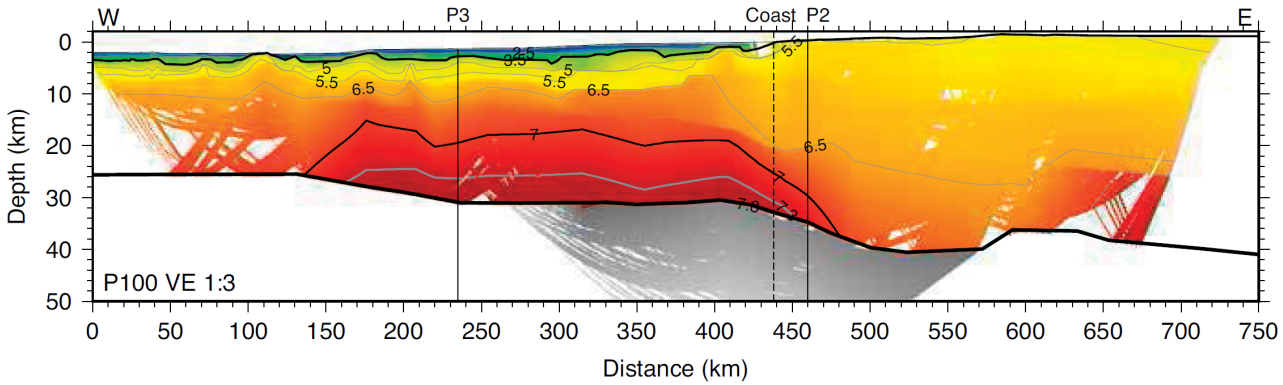


Figure 3.2: Profile AF0 (P100), adapted from Fromm et al. (2015), location in Fig. 3.1. The figure has both the seismic velocity and ray coverage.

A total of 27 Ocean Bottom Hydrophones (OBHs) were deployed along the line, with approximately 13 km between them, leading to a high level of ray trace coverage (Fig. 3.2). The location of the line was extracted from Fromm et al. (2015), and the velocity profile (Fig. 3.3) digitized from Fig. 3.2.

3.3.1.2 Identification of syn-rift magmatism

Profile AF0 (Fromm et al., 2015), located along the Walvis Ridge (Fig. 3.1), is considered as the volcanic trail of the Tristan plume. As a result, the oceanic crust for this profile is not expected to fit the typical characteristics used to identify ocean crust, and hence it will not be measured for this profile (Fig. 3.3). Instead, only syn-rift magmatism is identified (Fig. 3.3b). Profile AF0 features a HVLC body reaching seismic velocities of 7.5 - 7.6 $km\,s^{-1}$ and an igneous crustal thickness greater than 20 km. The HVLC body was found to taper out ~300 km offshore (Fig. 3.3b), however it extends ~50 km into the continental interior (Fromm et al., 2015). The total area of igneous crust was found to be 6610 km^2.

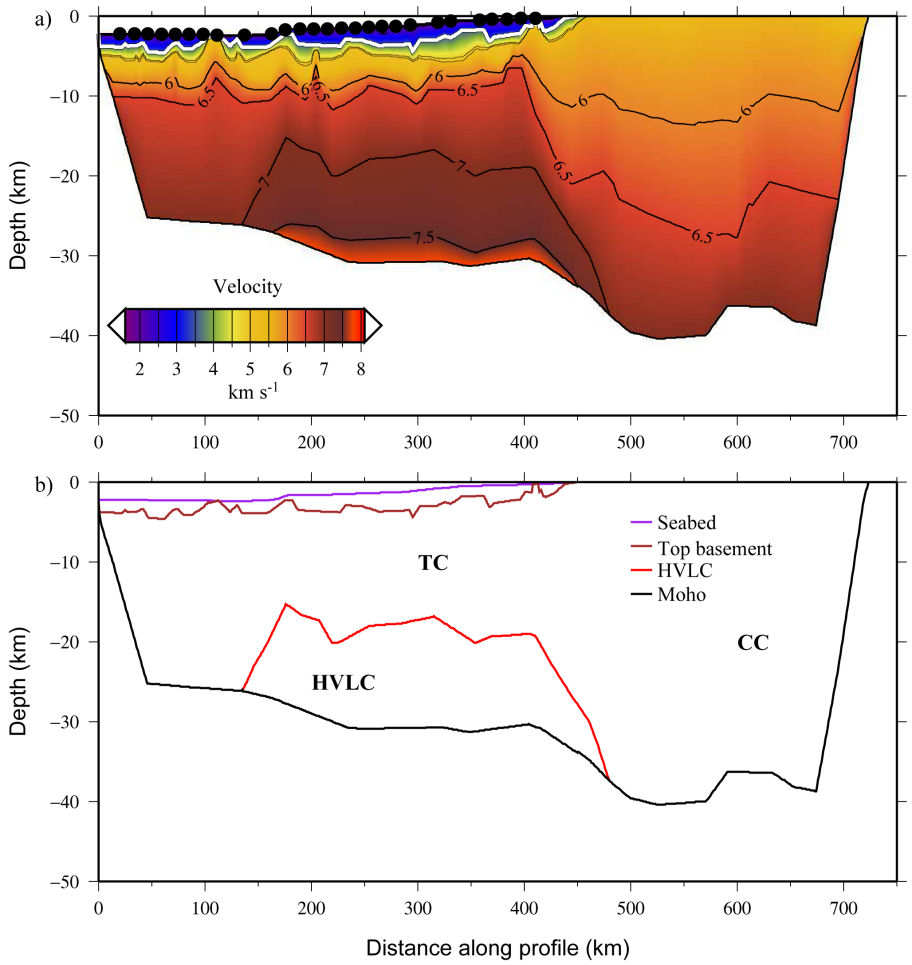


Figure 3.3: Location of syn-rift magmatism for Profile AF0. Part (a) is digitized from the velocity profile found in Fromm et al. (2015) (Fig. 3.2). Part (b) represents the identified syn-rift magmatism as a HVLC body, where TC = Transitional Crust and CC = Continental Crust.

3.3.2 Profiles from Bauer et al., 2000: Profiles AF1 & AF2

3.3.2.1 Original data

In 1995, MCS data from BGR were collected synchronously with data from OBHs operated by AWI, along with onshore seismometers operated by GFZ: this was published as wide-angle data in Bauer et al. (2000). The seismic velocity of the models was calculated using both the refraction/wide-angle data and MCS data, increasing the reliability of the P velocity models (Bauer et al., 2000).

Transects 1 and 2 from Bauer et al. (2000), here referred to as Profiles AF1 and AF2, encounter highly eroded Pre-Cambrian Damara Orogen rocks and both have SDRs and HVLC bodies present. Profile AF1 (Fig. 3.4) is found south to the Etendeka Traps (Fig. 3.1) and the area would have been highly affected by the Cretaceous volcanism (e.g. Cretaceous intrusive complexes, Cape Cross and Messum; Bauer et al., 2000). Profile AF2 is presented coupled with observed & calculated two-dimensional magnetics (Fig. 3.5). It lies ∼150 km south from Profile AF1, and, whilst still encountering the Damara basin (Fig. 3.1), the area has a higher degree of erosion

and was less affected by the volcanism (Bauer et al., 2000).

Both profiles have some areas with a lack of ray tracing coverage due to the distribution of OBHs (red boxes in Fig. 3.4c & 3.5c). Hence, for these areas, there is a lack of constraint for seismic velocities, and there will be some uncertainty for measurements taken from this region. Start and end locations for Profiles AF1 and AF2 were provided directly from Bauer et al., 2000 (Fig. A.1; further details on location found in Appendix A.2), as well as the velocity profiles (Fig. 3.6a & 3.7a).

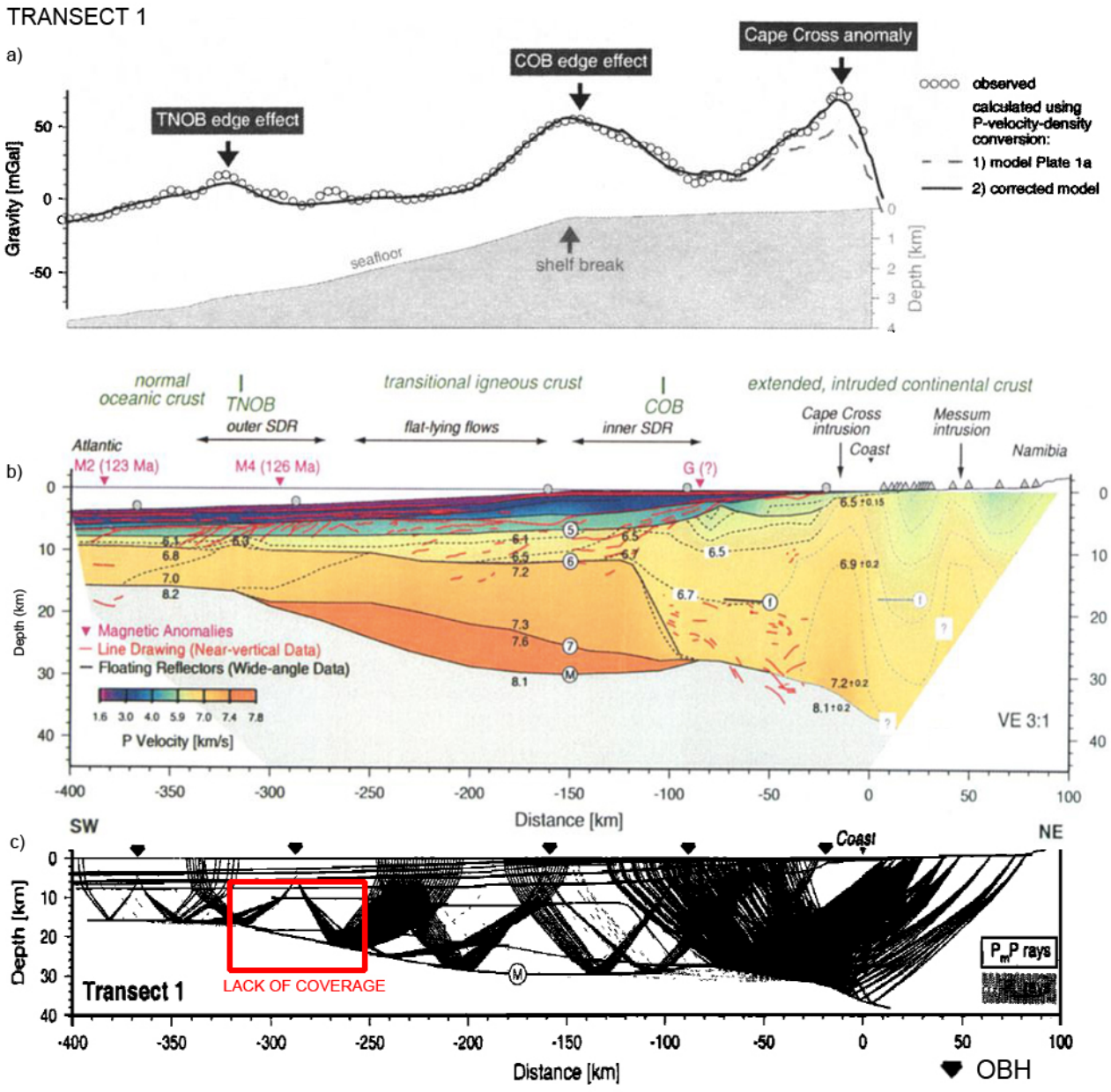


Figure 3.4: Profile AF1 (Transect 1), adapted from Bauer et al. (2000), location in Fig. 3.1. Part (a) represents calculated and observed free-air gravity anomalies. Part (b) represents interpreted crustal depth sections. Part (c) represents ray trace diagram showing coverage of data: the red box highlights an area where there is a lack of coverage.

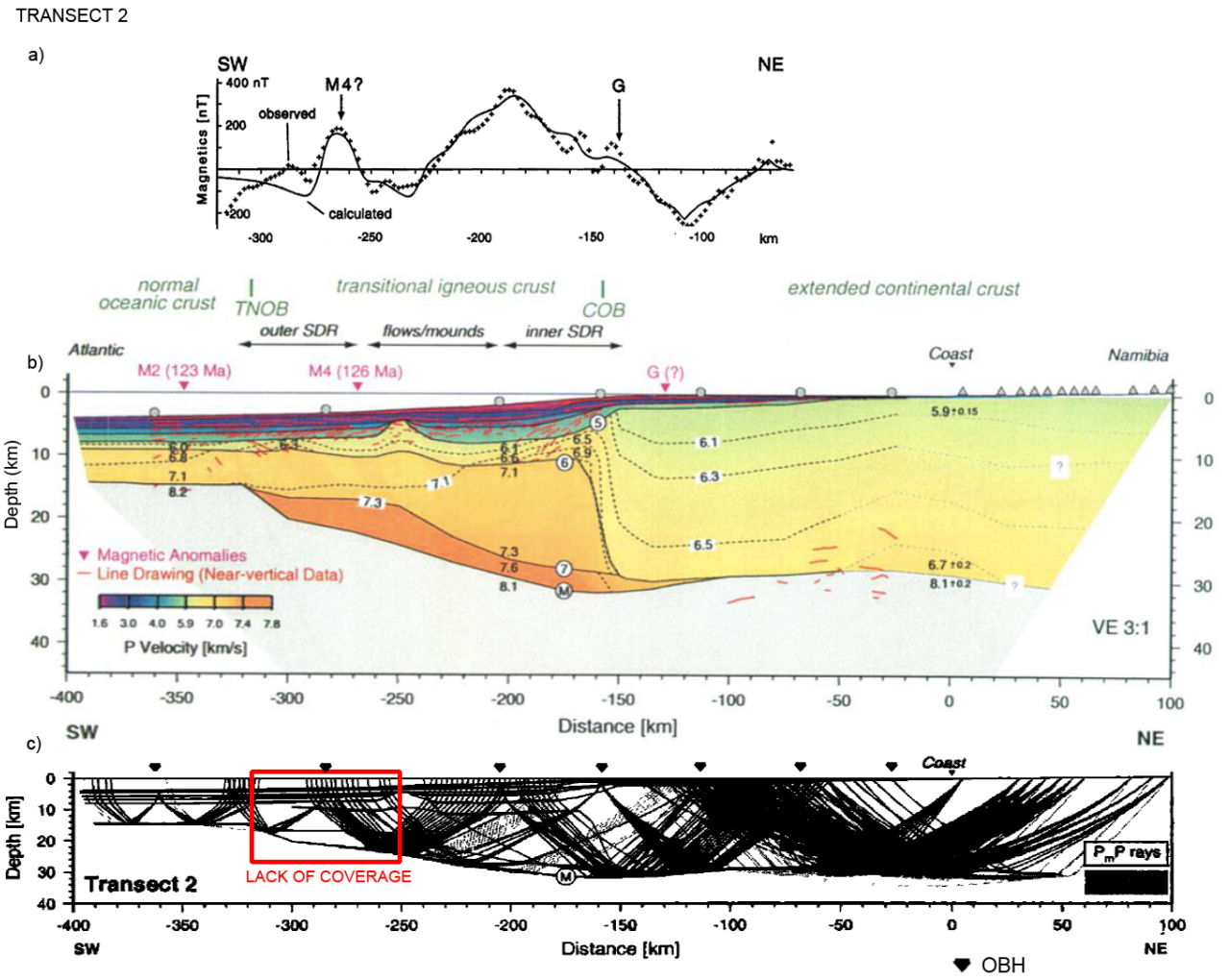


Figure 3.5: Profile AF2 (Transect 2), adapted from Bauer et al. (2000), location in Fig. 3.1. Part (a) represents two-dimensional magnetic model calculation. Part (b) represents interpreted crustal depth sections. Part (c) represents ray trace diagram showing coverage of data: the red box highlights an area where there is a lack of coverage.

3.3.2.2 Identification of LaLOC and syn-rift magmatism

The transitional crust of Profiles AF1 and AF2 can be characterised by the presence of SDRs and a HVLC body (Fig. 3.6). Prior to the study by Bauer et al. (2000), Gladczenko et al. (1998) published a transect based on depth converted MCS data and 2D gravity modelling, using crustal velocities projected from the nearby BGR refraction profiles, and found a HVLC body was necessary for the model. The profiles from Bauer et al. (2000) confirmed the existence of these bodies below SDRs in this region.

Two main wedges of SDRs are found on both Profiles AF1 and AF2, at -100 to -150 km and -300 km offshore (Fig. 3.6b and 3.7b), and are characterised by velocities of 5 - 5.5 km s^{-1}. The SDR wedges are found to be in conjunction with the HVLC bodies, between -300 to -100 km on Profile AF1 and -300 to -150 km on Profile AF2. SDRs can also be seen on a migrated MCS line from NAMCOR, studied by Koopmann et al. (2014b), found ~100 km north of Profile AF1 (Fig. 3.10). The commencement of the HVLC bodies and the landward

SDR wedges also correspond to a gravity high ("G" in Fig. 2.9), previously interpreted as a contrast between continental and oceanic crust (Rabinowitz and LaBrecque, 1979).

Using an upper boundary of 7.1 km s^{-1}, Profiles AF1 and AF2 show HVLC bodies >21 km thick, with a V_p reaching 7.5 - 7.6 km s^{-1} (Fig. 3.6 & 3.7). The HVLC bodies reach ~30 km in depth, with larger crustal thickness towards the landward edge of the transition zones (Fig. 3.6c & 3.7c). The HVLC body in AF1 has a maximum thickness of 18.2 km and an area of ~3660 km^2. Although Profile AF2 has a thicker HVLC body at a maximum thickness of 21.1 km, its area is lesser at ~2820 km^2. When considering additional SDR areas, the area of total melt increased up to a maximum of ~3780 km^2 and ~2940.1 km^2 for Profiles AF1 and AF2 respectively. Crustal velocities decreased rapidly landward of the HVLC, and were attributed to the end of the transition zone and presence of continental crust.

It must be noted that Profile AF1 can be considered slightly oblique to the margin rather than perpendicular (Fig. 3.1). As noted by Becker et al. (2014), the volumes of magmatism may, as a result, be overestimated. Whilst rotating Profile AF1 was tested, it only reduced the HVLC volume by ~100 km^2. As there is no information about the 3D shape of the HVLC body, it could not be corrected for in a constrained manner and was not pursued.

For Profiles AF1 and AF2 three possible LaLOC locations are chosen (Fig. 3.6a & 3.7a). The locations take into account the poor ray coverage found on the seismic profile (Fig. 3.4c & 3.5c), and the location of the HVLC bodies (Fig. 3.6c & 3.7c). These points are seaward of the M4 isochron (Fig. 3.9) and near the termination of SDRs. They are also found landward of the M2 isochron, which can be recognized as the first true ocean crust magnetic reversal in this area.

The depth-V_p for Profiles AF1's measurement points (Fig. 3.8a) have a generally good fit until an 8 km depth. The most seaward point is determined as the LaLOC location, with the best fit and a thickness of 11.7 km. The depth-V_p for Profiles AF2's landward point (Fig. 3.8b) is discarded relative to the others. Whilst the seaward point clearly represents oceanic crust, the mid point is selected as the first point of oceanic crust with a thickness of 8.2 km. Despite their relative spatial closeness between Profiles AF1 and AF2, the 3.2 km difference in initial ocean crust thickness is similar to the degree of reduction seen for HVLC and SDR areas.

In order to validate the LaLOC location, coincident MCS data were checked. The closest MCS lines were found from Koopmann et al. (2014b) some 100 km north (Fig. 3.10). Similarly to Profiles AF1 and AF2, the commencement of ocean crust (distinguished by the rough top basement surface) is spatially close to the final seaward SDR wedge, making the LaLOC of wide-angle data coherent with MCS data.

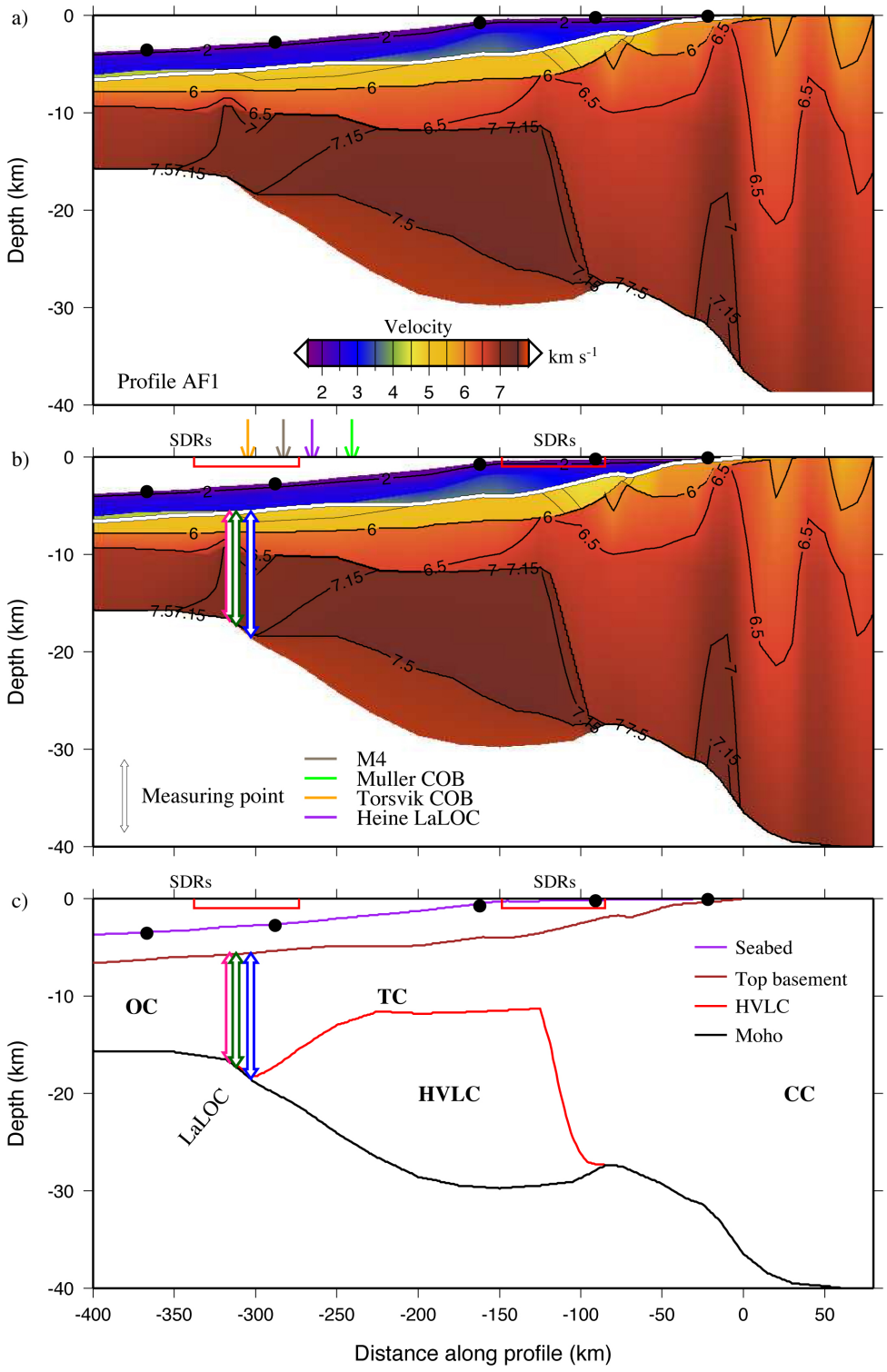


Figure 3.6: Location of syn-rift magmatism and possible LaLOC locations for Profile AF1. Part (a) is the velocity profile provided by the author Bauer et al. (2000). Part (b) has the SDR locations (red boxes, locations originate from Bauer et al. (2000) interpretation), previous continent-ocean boundaries (bright green arrow COB from Müller et al., 2008, orange arrow COB from Torsvik et al., 2009, purple arrow LaLOC from Heine et al., 2013) and location of magnetic isochron M4 (grey arrow) from Moulin et al. (2010). The three white arrows represent the first three estimations for the location of the LaLOC, where the seaward arrow is pink, the mid arrow is green and the landward arrow is blue. These are linked to the depth-V_p profiles found in Fig. 3.8a and locations in Fig. 3.9. Part (c) represents the identified syn-rift magmatism as a HVLC body, where OC = Oceanic Crust, TC = Transitional Crust and CC = Continental Crust.

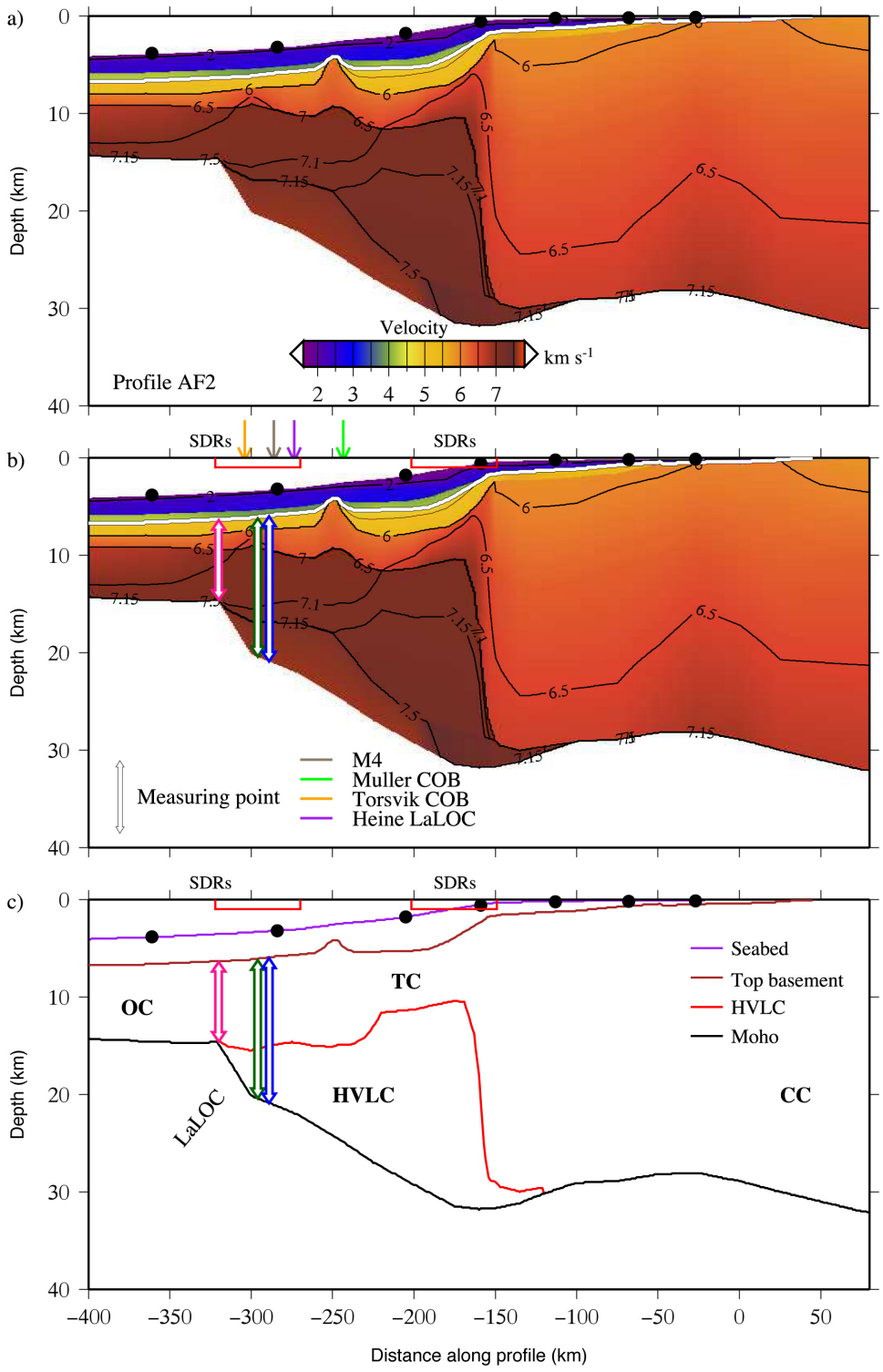


Figure 3.7: Location of syn-rift magmatism and possible LaLOC locations for Profile AF2. Part (a) is the velocity profile provided by the author Bauer et al. (2000). Part (b) has the SDR locations (red boxes, locations originate from Bauer et al. (2000) interpretation), previous continent-ocean boundaries (bright green arrow COB from Müller et al., 2008, orange arrow COB from Torsvik et al., 2009, purple arrow LaLOC from Heine et al., 2013) and location of magnetic isochron M4 (grey arrow) from Moulin et al. (2010). The three white arrows represent the first three estimations for the location of the LaLOC, where the seaward arrow is pink, the mid arrow is green and the landward arrow is blue. These are linked to the depth-V_p profiles found in Fig. 3.8b and locations in Fig. 3.9. Part (c) represents the identified syn-rift magmatism as a HVLC body, where OC = Oceanic Crust, TC = Transitional Crust and CC = Continental Crust.

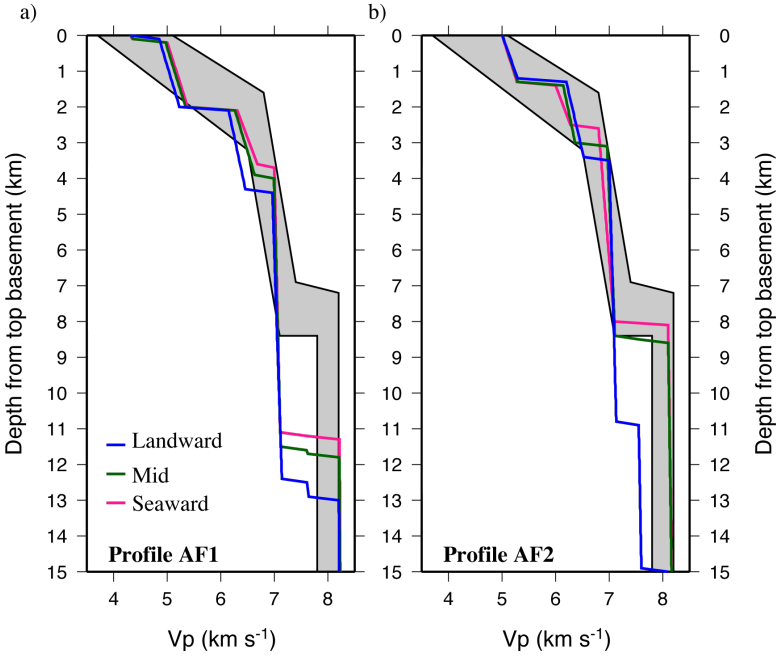


Figure 3.8: Depth-V_p profiles for the three potential LaLOC locations (Fig. 3.6b & 3.7b) for Profiles AF1 (part a) and AF2 (part b). Grey shaded area is the seismic velocity limits for mature oceanic crust from White (1992), and the y-axis represents depth from top basement.

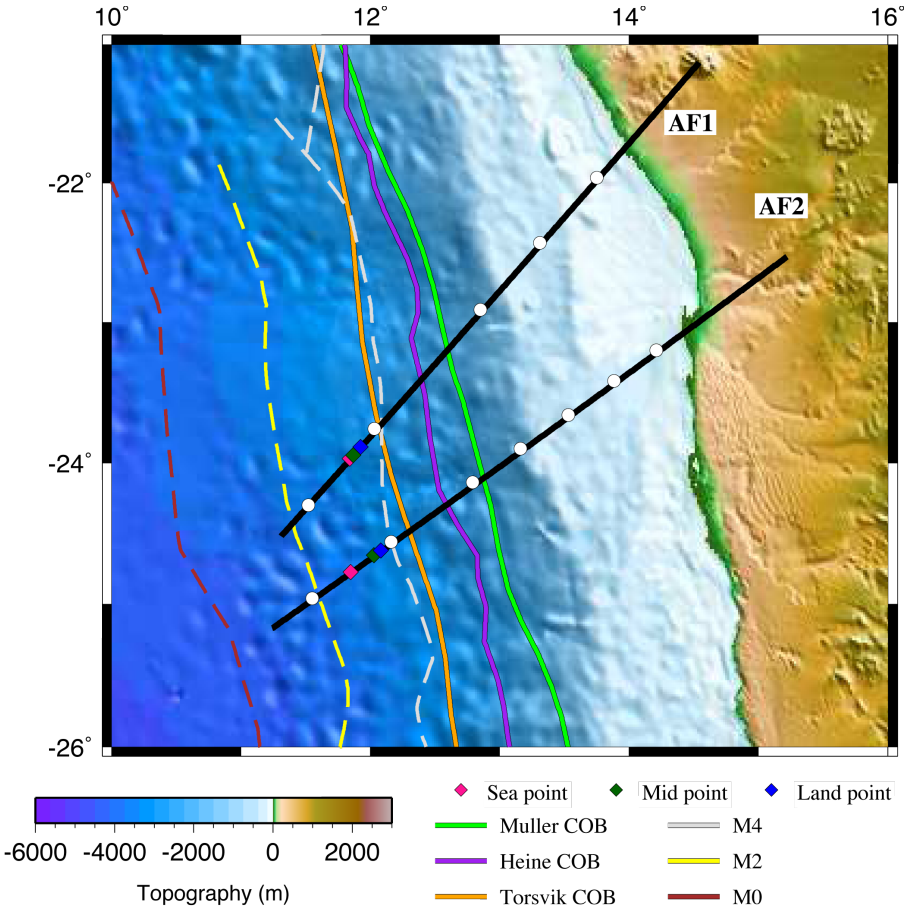


Figure 3.9: Map of possible LaLOC locations for Profiles AF1 and AF2. Seismic profiles are the black lines, with white dots representative of OBH locations. Previous continent-ocean boundaries are the COB from Müller et al. (2008) - bright green line, COB from Torsvik et al. (2009) - orange line, LaLOC from Heine et al. (2013)) - purple line, and location of magnetic isochrons M4 (grey dashed line), M2 (yellow line) and M0 (brown line) from Moulin et al. (2010). Three possible LaLOC locations are in pink (most seaward point), dark green (mid point) and blue (landward point).

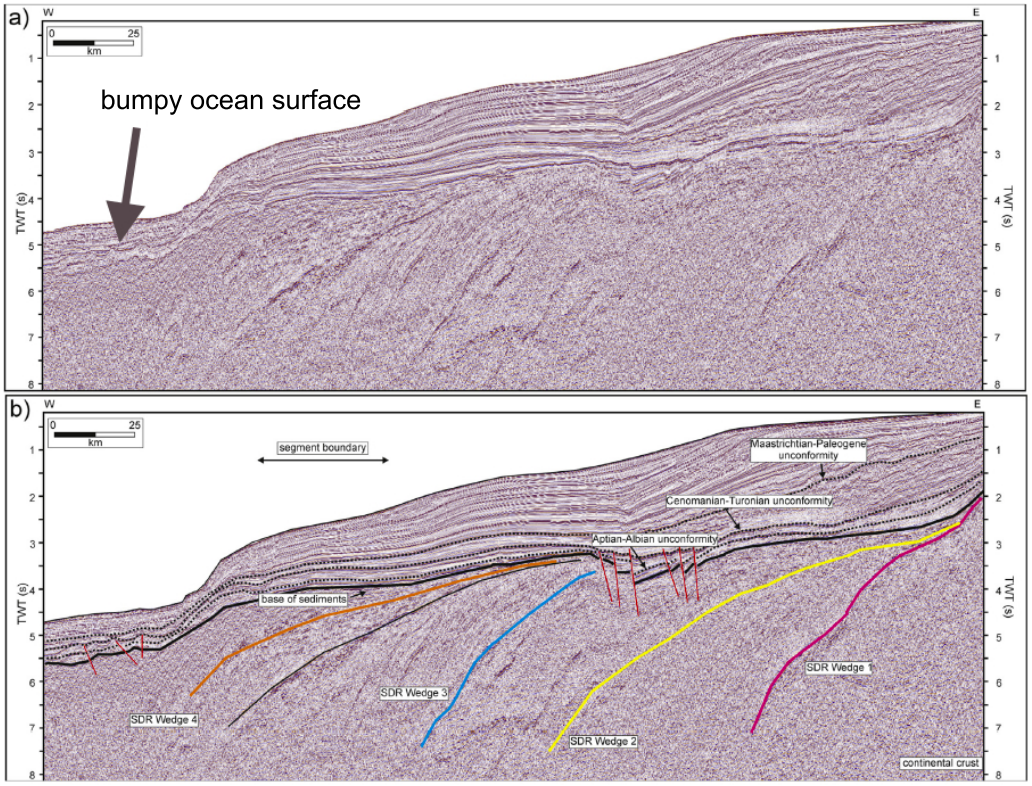


Figure 3.10: Proximal MCS profile to Profiles AF1 and AF2 from Koopmann et al. (2014b). Grey arrow signifies potential commencement of oceanic crust from a distinctively bumpy surface.

3.3.3 Profiles from Schinkel, 2006 and Hirsch et al., 2009: Profiles AF3 & AF4

3.3.3.1 Original data

There are two lines found south of the Bauer et al. (2000) transects, the Orange and Springbok profiles, here referred to as Profiles AF3 and AF4 respectively (Fig. 3.1). Profile AF3 (the Orange Profile) was carried out in 1995 by BGR, AWI and GFZ, as part of the same experiment as Profiles AF1 and AF2 (more details in Table A.1). Profile AF4 (Springbok profile) was carried out in early 2003 by BGR, GFZ & the Council for Geoscience (R.S.A) to study the crustal structure of the western margin of South Africa. Profile AF3 was found near the Orange river, and Profile AF4 found between the Orange and Olifants rivers. The profiles were found perpendicular to the Gariep belt, and the region is the western-most area of the Kalahari shield. The Gariep belt was formed during the construction of Gondwana, part of a network of early Paleozoic orogenic belts (Kaoko, Damara, and Gariep Mobile Belts; Section 2.2).

Schinkel (2006) presented the Orange profile (Fig. 3.11), and the seismic data set was collected using 6 OBHs and 20 onshore seismometers. With velocity contours not as clear as in other profiles, this is the lowest quality velocity profile. From the distribution of OBHs towards the seaward edge of the profile, although not shown, it can be assumed the ray coverage was sparse for this region. A certain amount of uncertainty is expected for this region.

The location of Profile AF3 was obtained from a digitized map in Schulze et al. (2007) (Fig. A.2). Due to its low quality, the location was consolidated using a map from Becker et al. (2014) (further checks to the location of the profiles can be found in Appendix A.2). The velocity profile was digitized from Fig. 3.11, with the velocity profile originating from Schinkel (2006) and published in Schulze et al. (2007).

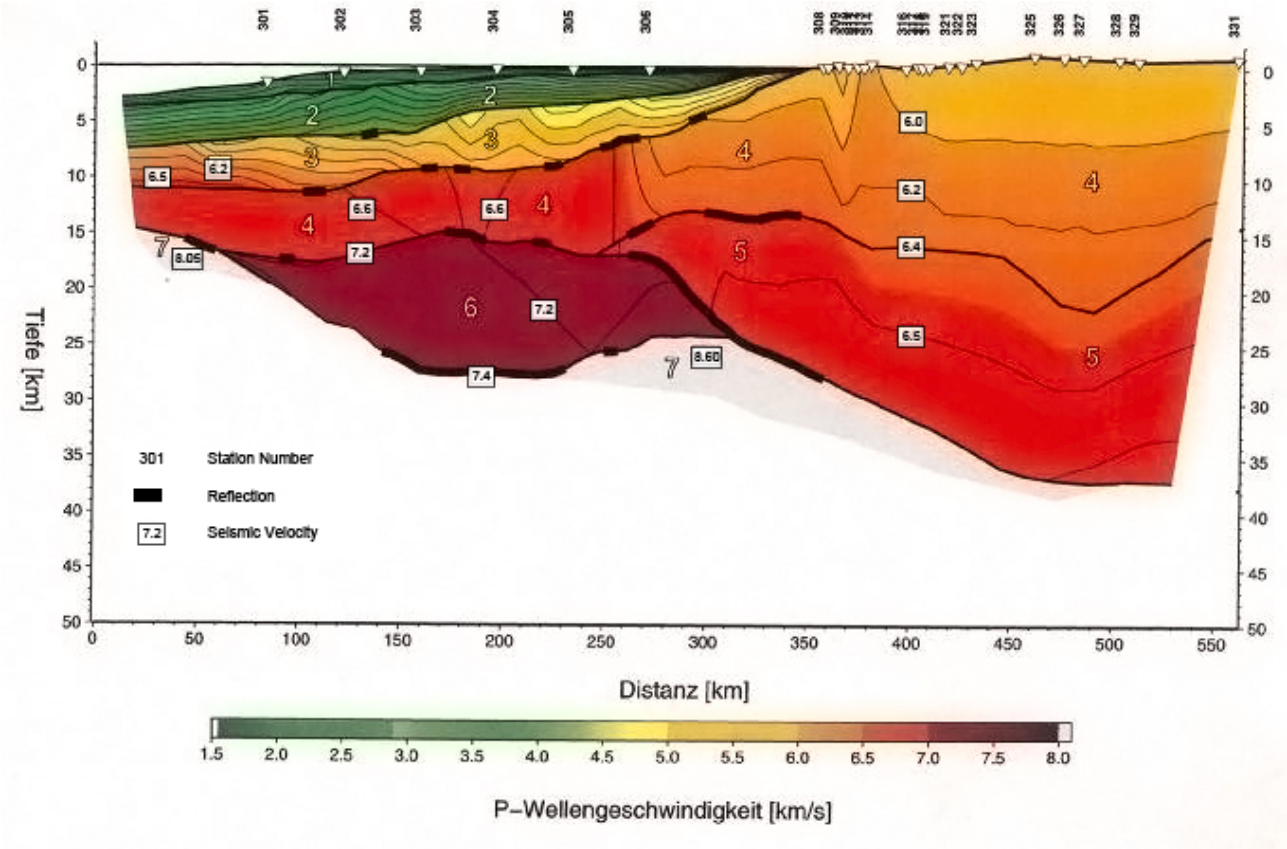


Figure 3.11: Profile AF3 (Orange line), adapted from Schulze et al. (2007), originating from Schinkel (2006). The only figure available, it represents the seismic velocity of the profile. Location from Fig. A.2.

Hirsch et al. (2009) published the Springbok line (Profile AF4; Fig. 3.12) found in the Orange Basin. Both reflection and refraction offshore seismic data were collected, using 5 OBHs, 40 seismometers and MCS data. The velocity model across the Springbok profile was calculated using forward and inverse modelling, coupled with a free-air gravity anomaly model (Fig. 3.12a) and an isostasy model, with a depth converted seismic section (Fig. 3.12b).

The location of the Springbok line was digitized from Hirsch et al. (2009) (inset Fig. A.3). The location was confirmed by matching depth of the OBH and bathymetry (Fig. A.3, Table A.4). The velocity profile was digitized from Fig. 3.12 (Hirsch et al., 2009), through the use of the P wave velocities.

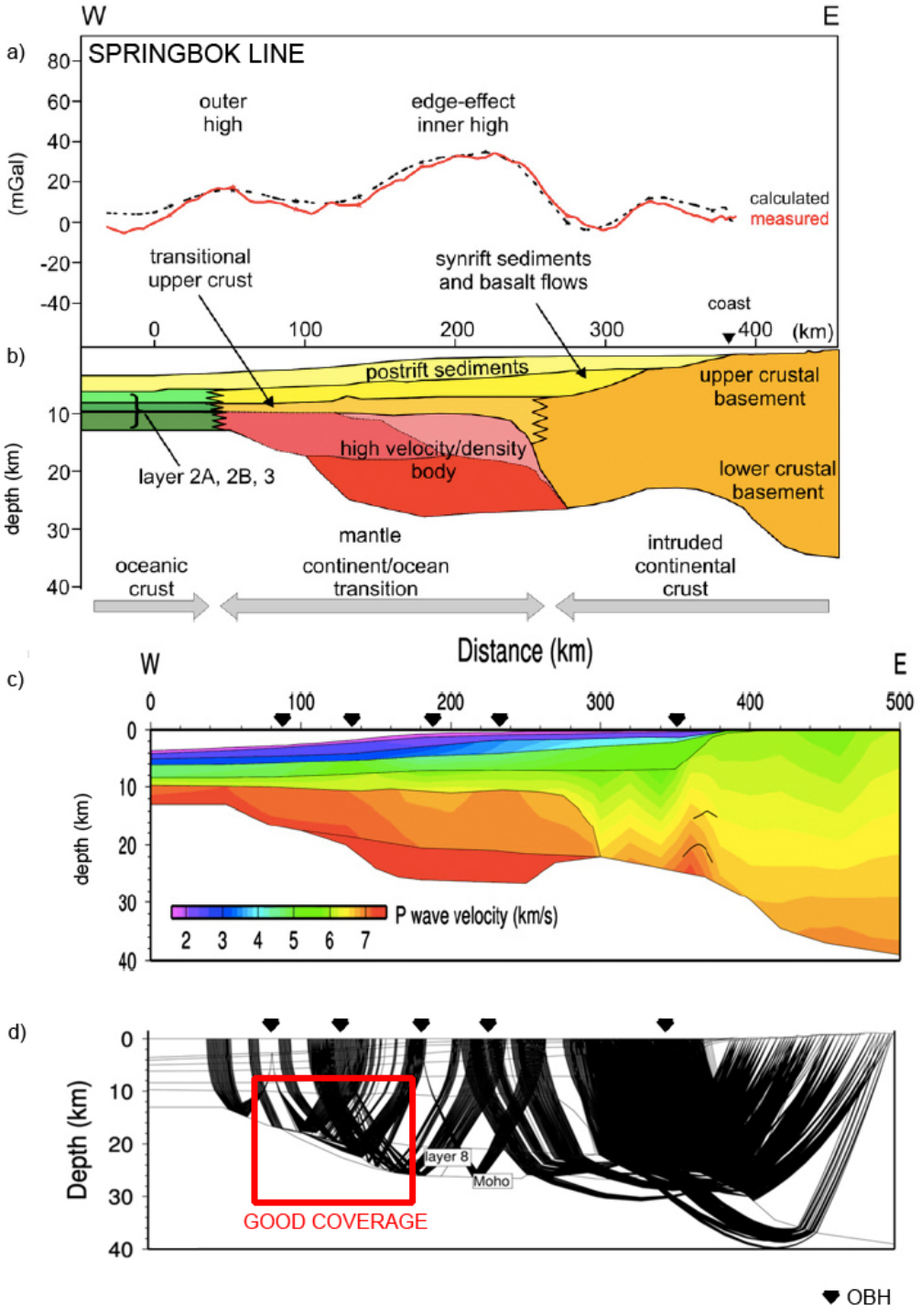


Figure 3.12: Profile AF4 (Springbok line), adapted from Hirsch et al. (2009), location in Fig. 3.1. (a) and (b) adapted from Hirsch et al. (2009). Part (a) represents calculated and observed gravity free air anomaly. Part (b) represents interpretation of Springbok line. Part (c) represents the seismic velocity of the profile. Part (d) represents ray trace diagram showing coverage of data: the red box highlights an area where there is good coverage, at the crucial area of interpretation of termination of underplating and commencement of oceanic crust.

3.3.3.2 Identification of LaLOC and syn-rift magmatism

Profile AF3 has oceanic crust between ~0 - 40 km and the transitional zone is found between ~40 - 325 km, characterised by a HVLC body, reaching a seismic velocity of 7.4 km s^{-1} (Fig. 3.13). The HVLC body has a maximum thickness of 12.4 km and an area of 2595 km^2. This is complimented by SDRs, also seen in a composite section of migrated MCS lines from Forest Oil studied by Koopmann et al. (2014b), ~50 km south of Profile AF3. With the addition of SDR areas, total melt increases to ~2700 km^2.

Towards the south, Profile AF4's ocean crust is found from ~0 - 50 km along the profile and the transitional crust is found between ~50 - 250 km, characterised by the presence of SDRs and a HVLC body with velocities reaching 7.4 km s^{-1} (Fig. 3.14). With an upper boundary limit of 7.1 km s^{-1}, the HVLC body for this profile only has a maximum thickness of 6.3 km, and an area of 2590 km^2. The HVLC body is also complimented by SDR packages, also seen in BGR migrated MCS line BGR03-16A from Koopmann et al. (2014b), ~85 km south. Including SDR areas increases the total melt area to ~2860 km^2. For both Profiles AF3 and AF4, continental crust is characterised by decreasing seismic velocities ranging from 5.9 - 6.1 km s^{-1} at the surface. The HVLC bodies for Profiles AF3 and AF4 also correspond to the same gravity high as for Profiles AF1 and AF2 ("G" in Fig. 2.9). Farther offshore however, there is a second positive anomaly (Fig. 2.9) first seen by Bauer et al. (2000). The "outer gravity high" is most prominent between 27 °S and 33 °S (Fig. 2.9, Hirsch et al., 2009), and can be associated with the change from transitional crust to oceanic crust.

Similar to Profiles AF1 and AF2, three possible LaLOC locations are chosen for Profiles AF3 and AF4 (Fig. 3.13a & 3.14a). The points are landward of the M4 isochron (Fig. 3.16), and in this case near the Heine et al. (2013) LaLOC location. For Profile AF3, all three locations have an overall good depth-V_p fit (Fig. 3.15a), and the most landward point is selected as the LaLOC location with a thickness of 7.2 km. The most landward point in Profile AF4 falls outside the mature oceanic boundaries (Fig. 3.15b), and hence the mid point is selected as the LaLOC location with a thickness of 7.0 km. Although Profiles AF3 & AF4 have initial oceanic crustal thicknesses close the global average (~7 km; White et al., 1992), the presence of HVLC bodies and SDRs validates their classification as a region of volcanic passive margins.

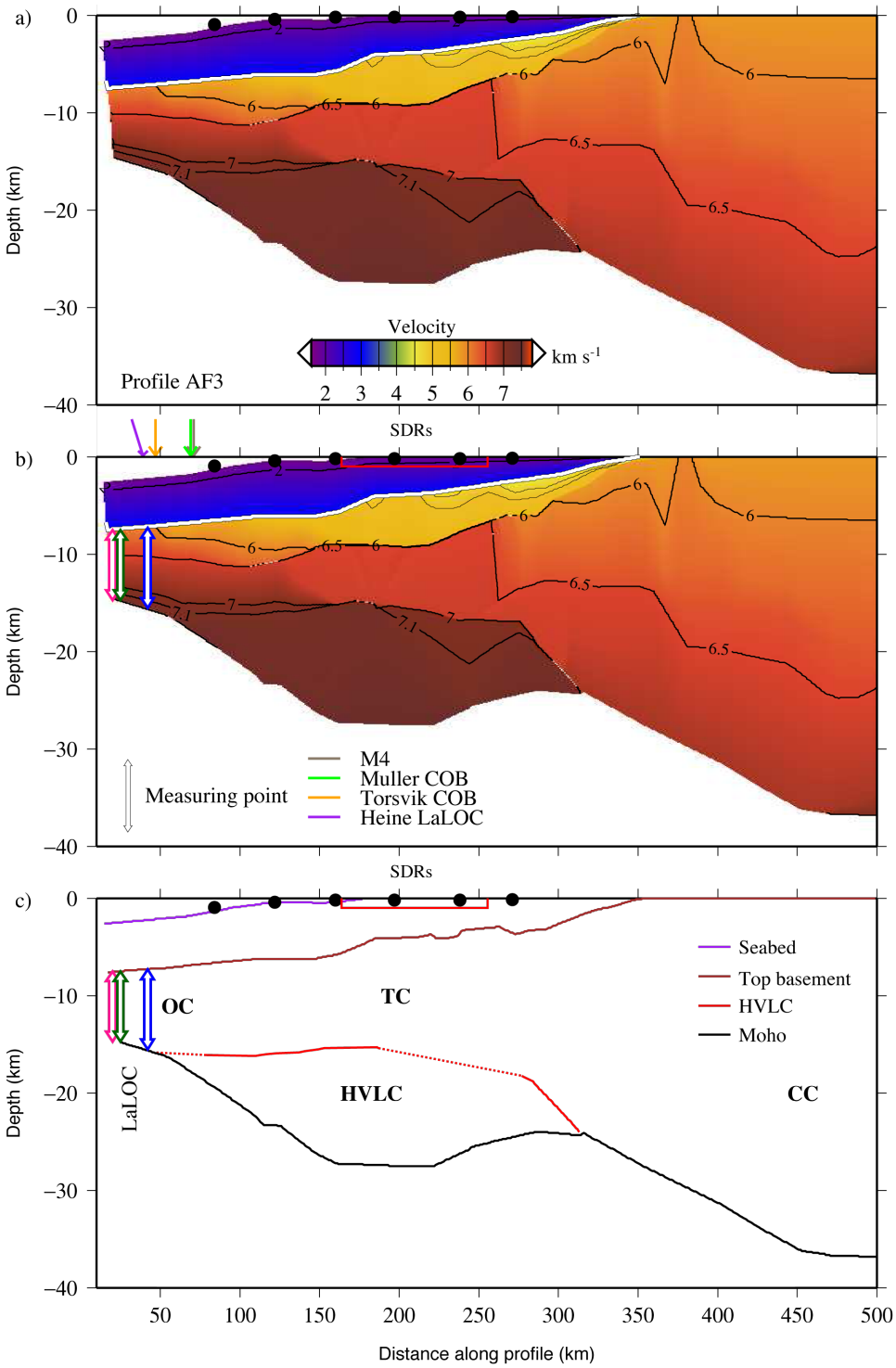


Figure 3.13: Location of syn-rift magmatism and possible LaLOC locations for Profile AF3. Part (a) is the velocity profile, digitized from the velocity profile found in Schulze et al. (2007) (Fig. 3.11). Part (b) has the SDR locations (red boxes, locations originate from Becker et al. (2014) interpretation), previous continent-ocean boundaries (bright green arrow COB from Müller et al., 2008, orange arrow COB from Torsvik et al., 2009, purple arrow LaLOC from Heine et al., 2013) and location of magnetic isochron M4 (grey arrow) from Moulin et al. (2010). The three white arrows represent the first three estimations for the location of the LaLOC, where the seaward arrow is pink, the mid arrow is green and the landward arrow is blue. These are linked to the depth-V_p profiles found in Fig. 3.15a and locations in Fig. 3.16. Part (c) represents the identified syn-rift magmatism as a HVLC body, where OC = Oceanic Crust, TC = Transitional Crust and CC = Continental Crust.

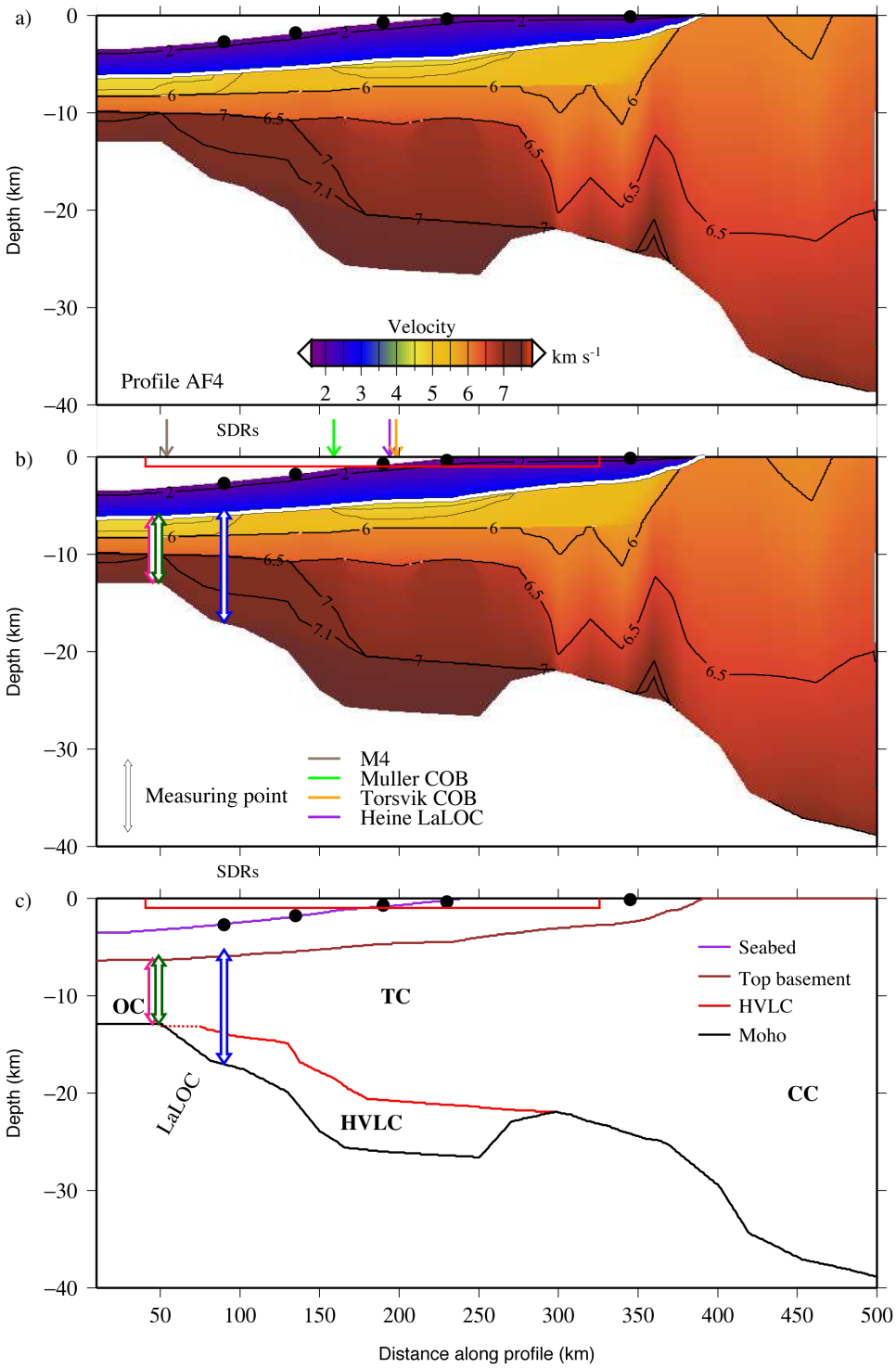


Figure 3.14: Location of syn-rift magmatism and possible LaLOC locations for Profile AF4. Part (a) is the velocity profile, digitized from the velocity profile found in Hirsch et al. (2009) (Fig. 3.12). Part (b) has the SDR locations (red boxes, locations originate from Hirsch et al. (2009) interpretation), previous continent-ocean boundaries (bright green arrow COB from Müller et al., 2008, orange arrow COB from Torsvik et al., 2009, purple arrow LaLOC from Heine et al., 2013) and location of magnetic isochron M4 (grey arrow) from Moulin et al. (2010). The three white arrows represent the first three estimations for the location of the LaLOC, where the seaward arrow is pink, the mid arrow is green and the landward arrow is blue. These are linked to the depth-V_p profiles found in Fig. 3.15b and locations in Fig. 3.16. Part (c) represents the identified syn-rift magmatism as a HVLC body, where OC = Oceanic Crust, TC = Transitional Crust and CC = Continental Crust.

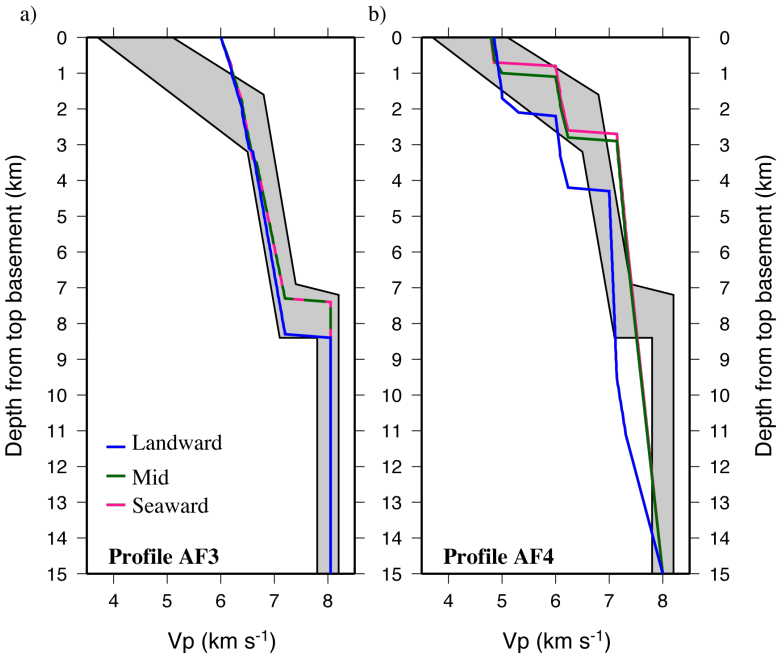


Figure 3.15: Depth-V_p profiles for the three potential LaLOC locations (Fig. 3.13b & 3.14b) for Profiles AF3 (part a) and AF4 (part b). Grey shaded area is the seismic velocity limits for mature oceanic crust from White (1992), and the y-axis represents depth from top basement.

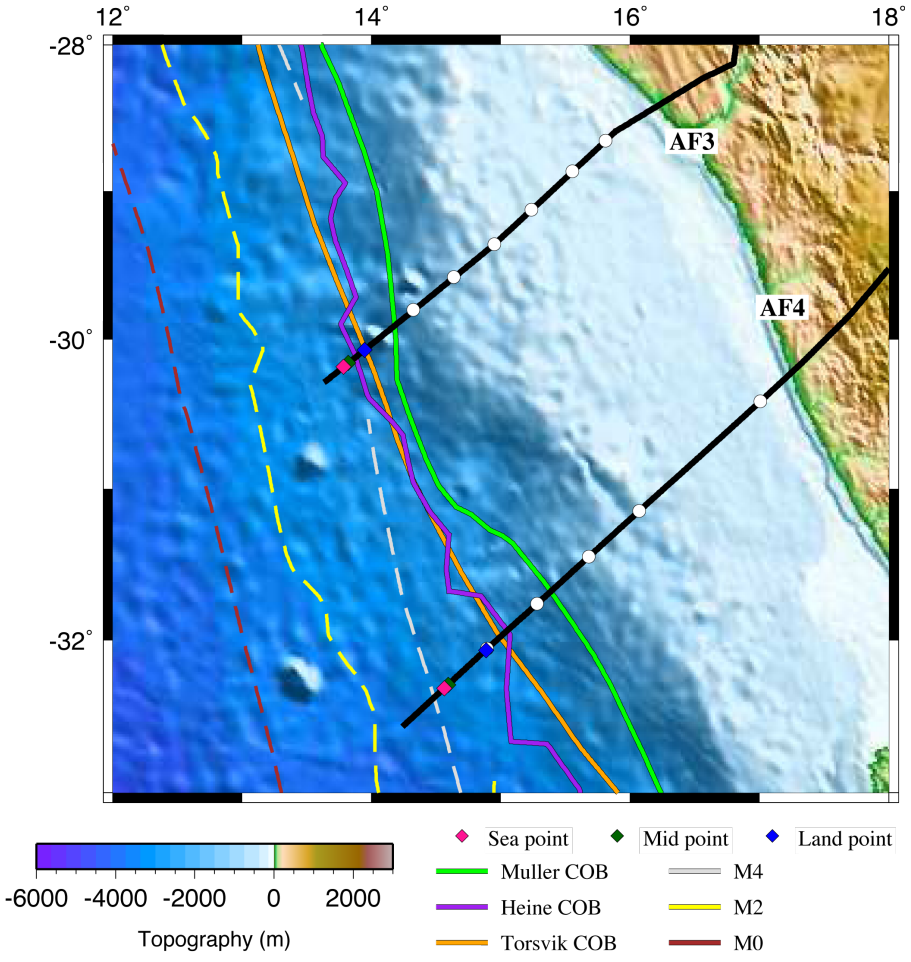


Figure 3.16: Map of possible LaLOC locations for Profiles AF3 and AF4. Seismic profiles are the black lines, with white dots representative of OBH locations. Previous continent-ocean boundaries are the COB from Müller et al. (2008) - bright green line, COB from Torsvik et al. (2009) - orange line, LaLOC from Heine et al. (2013)) - purple line, and location of magnetic isochrons M4 (grey dashed line), M2 (yellow line) and M0 (brown line) from Moulin et al. (2010). Three possible LaLOC locations are in pink (most seaward point), dark green (mid point) and blue (landward point).

3.4 Wide-Angle Profiles: South American Margin

In this section, wide-angle profiles found on the South American margin are presented. These include (going from north to south) one profile published in Becker et al. (2014) found offshore Uruguay, one profile published in Schnabel et al. (2008) found offshore Argentina, and a second profile published in Becker et al. (2014), also found offshore Argentina. The profiles from Becker et al. (2014) will be explored together, and the location of the landward limit of ocean crust for all profiles will be investigated, along with the identification of syn-rift magmatism.

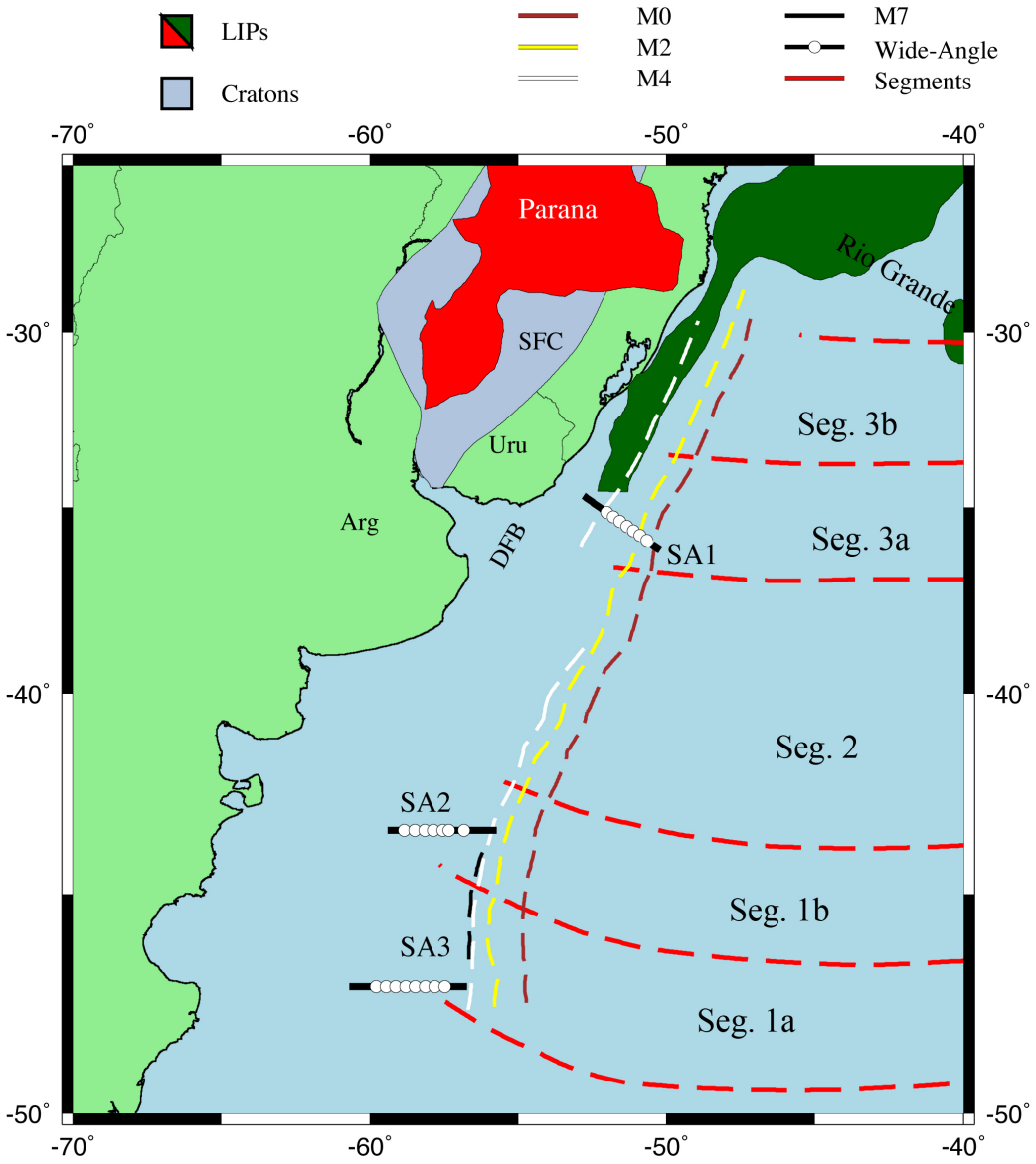


Figure 3.17: Location of South American wide-angle seismic profiles with major geological features. Cratons position for the San Francisco Craton (SFC, blue shape) is from Gubanov and Mooney (2009), the location of the Paraná flood basalts and Rio Grande Rise (red and green shapes) from Coffin and Eldholm (1994). Locations of SA1 - SA3 from Schnabel et al. (2008) and Becker et al. (2014). Sao Francisco Craton (SFC) location is from Gubanov and Mooney (2009). The mobile belt separates the Sao Francisco Craton from the coast in the Dom Feliciano Belt (DFB). Segment boundaries (red dashed lines) have been previously identified in Section 2.7.

3.4.1 Profiles from Becker et al., 2014: Profiles SA1 & SA3

3.4.1.1 Original data

Becker et al. (2014) presents wide-angle seismic data and gravity data, collected by BGR and GFZ (locations Fig. 3.17). BGR04-01, here referred to as Profile SA1, (Fig. 3.18) is ∼287 km long and had 7 OBHs (location Fig. 3.17). It was shot in the vicinity of the Salado basin at 35-36°S and passes through Neoproterozoic arc terrane on the Uruguay margin. BGR04-02, here referred to as Profile SA3, found on the broad Argentine continental shelf (Fig. 3.19), was published as wide-angle data by Becker et al. (2014) as part of the same seismic experiment as Profile SA1 (more details in Table A.1). Both profiles were complimented by 2D free-air gravity anomaly modelling.

The locations for both of these lines, along with OBH locations, were obtained directly from Becker et al. (2014), hence considered to be reliable and correct (more details in Appendix A.2). The velocity profiles were digitized from Fig. 3.18 and 3.19 (Becker et al., 2014), through the use of the P wave velocities contours. The sediment found on the landward edge of Profile SA3 was not digitized, as there was no lower crustal information in this region (Fig. 3.19a).

Both of the seismic wide-angle profiles have a comprehensive gravity model showing the transition from oceanic to continental crust. However, the continental crust is not seen on the seismic sections, despite there being OBHs located in this crucial transition zone. This will affect the measurements of syn-rift magmatism found within the transitional zone. The absence of data here is most likely due to the strong Western boundary current found in the ocean along the South American margin (Peterson, 1992), which often leads to complications with sensitive equipment, therefore affecting the measurements from OBHs.

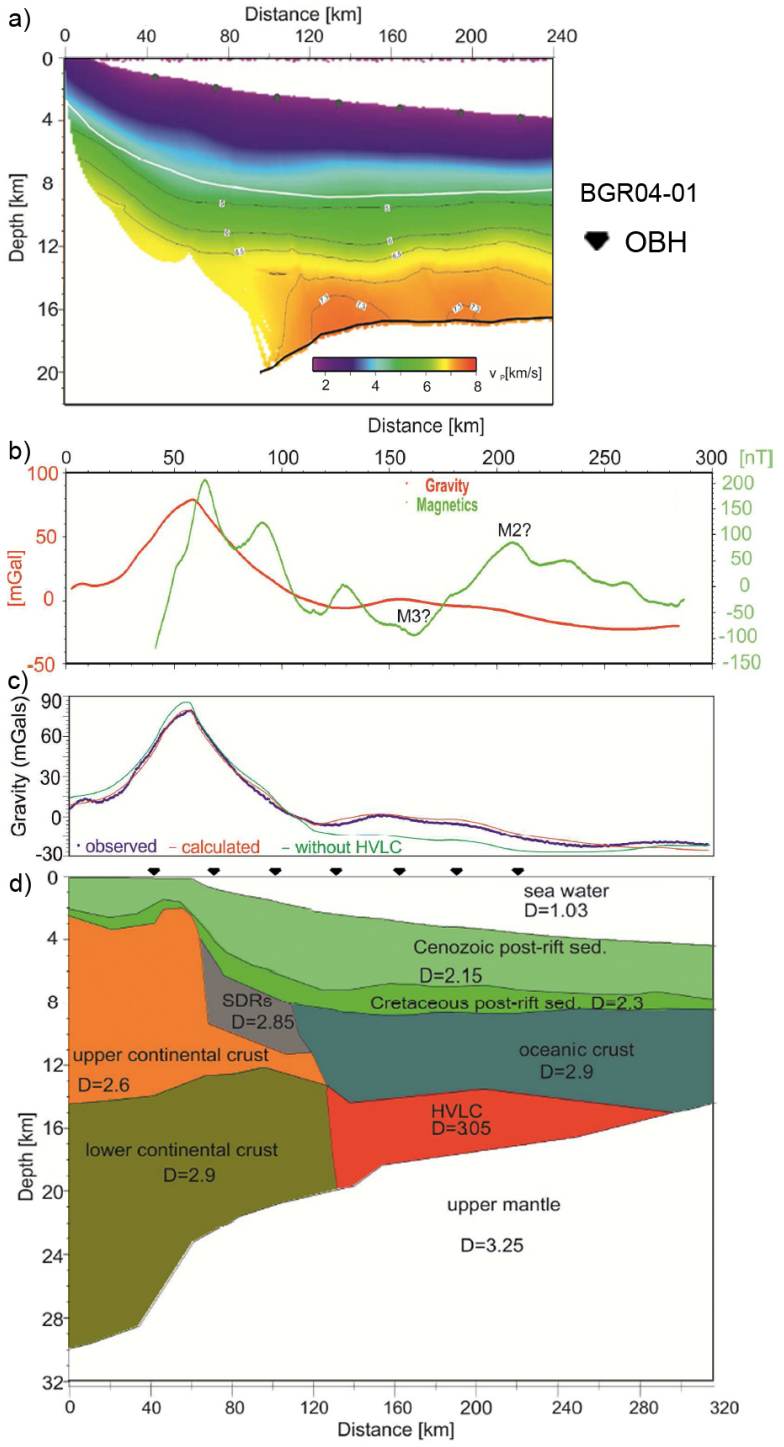


Figure 3.18: Profile SA1 (BGR04-01) adapted from Becker et al. (2014). Part (a) represents velocity-depth model derived from refraction seismic traveltime modelling, with the figure also showing the ray coverage. Part (b) represents the free-air gravity and magnetic profile. Part (c) represents the results of free-air gravity modelling. Part (d) represents the resulting line drawing for the section.

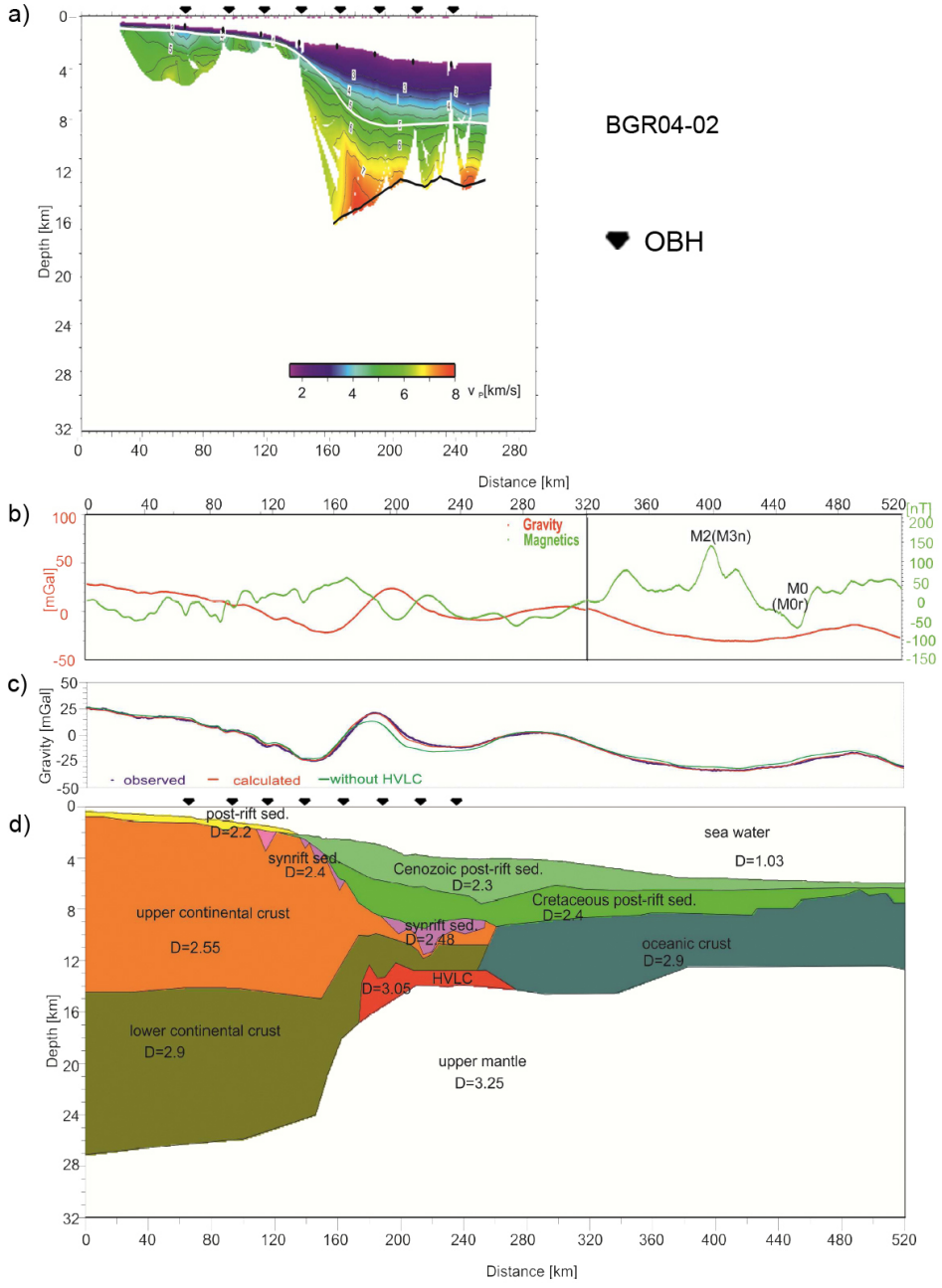


Figure 3.19: Profile SA3 (BGR04-02) adapted from Becker et al. (2014). Part (a) represents velocity-depth model derived from refraction seismic traveltime modelling, with the figure also showing the ray coverage. Part (b) represents the free-air gravity and magnetic profile. Part (c) represents the results of free-air gravity modelling. Part (d) represents the resulting line drawing for the section.

3.4.1.2 Identification of LaLOC and syn-rift magmatism

A HVLC body is shown for both profiles in the line drawings (Fig. 3.18d & 3.19d) underneath oceanic crust. It is possible these HVLC bodies have been wrongly identified, and they are a part of the initial oceanic crust formation. The definition used in this project is that an 'underplated' HVLC body is an intrusion into thinned transitional crust and it cannot be found under oceanic crust. The definition used by Becker et al. (2014) is that all zones with velocities $\geq 7\,\mathrm{km\,s^{-1}}$ form the HVLC body, representing P wave velocities and densities greater than typically found in lower oceanic crust. Whilst velocities are high ($\geq 7\,\mathrm{km\,s^{-1}}$), such velocities do exist in oceanic crust at these depths (White et al., 1992). Additionally, the poor data quality may have led to this misinterpretation, and the HVLC body most likely extends into the continental crust, not imaged on these profiles. Apart from SDRs seen from the coincident MCS line to Profile SA1 (Fig. 3.21b), there is no clear syn-rift magmatism found along Profiles SA1 and SA3.

Two points were considered as the LaLOC for Profile SA1 (Fig. 3.20 & 3.24) with accompanying depth-V_p profiles (Fig. 3.23a). Although the seaward point has a slightly better fit in the depth-V_p, the MCS data coincident to Profile SA1 (Fig. 3.21) supports the landward point as the commencement of oceanic crust. Oceanic crust is recognized from the appearance of fractured basalts at this point, and it is also found seaward of the SDRs. The identified LaLOC point has a thickness of 8.2 km, the same thickness as observed for Profile AF2, found ∼380 km north on the conjugate margin. Finally, there were two LaLOC location choices for Profile SA3 (Fig. 3.27a & 3.25), with the landward point having the best depth-V_p profile (Fig. 3.23b). This point had a thickness of 6.9 km, close to the global average for ocean crust thickness (∼7 km; White et al., 1992). Although Becker et al. (2014) suggests the presence of a HVLC body through gravity modelling (Fig. 3.19c), the presence of a volcanic passive margin in this region cannot be confirmed through observations alone.

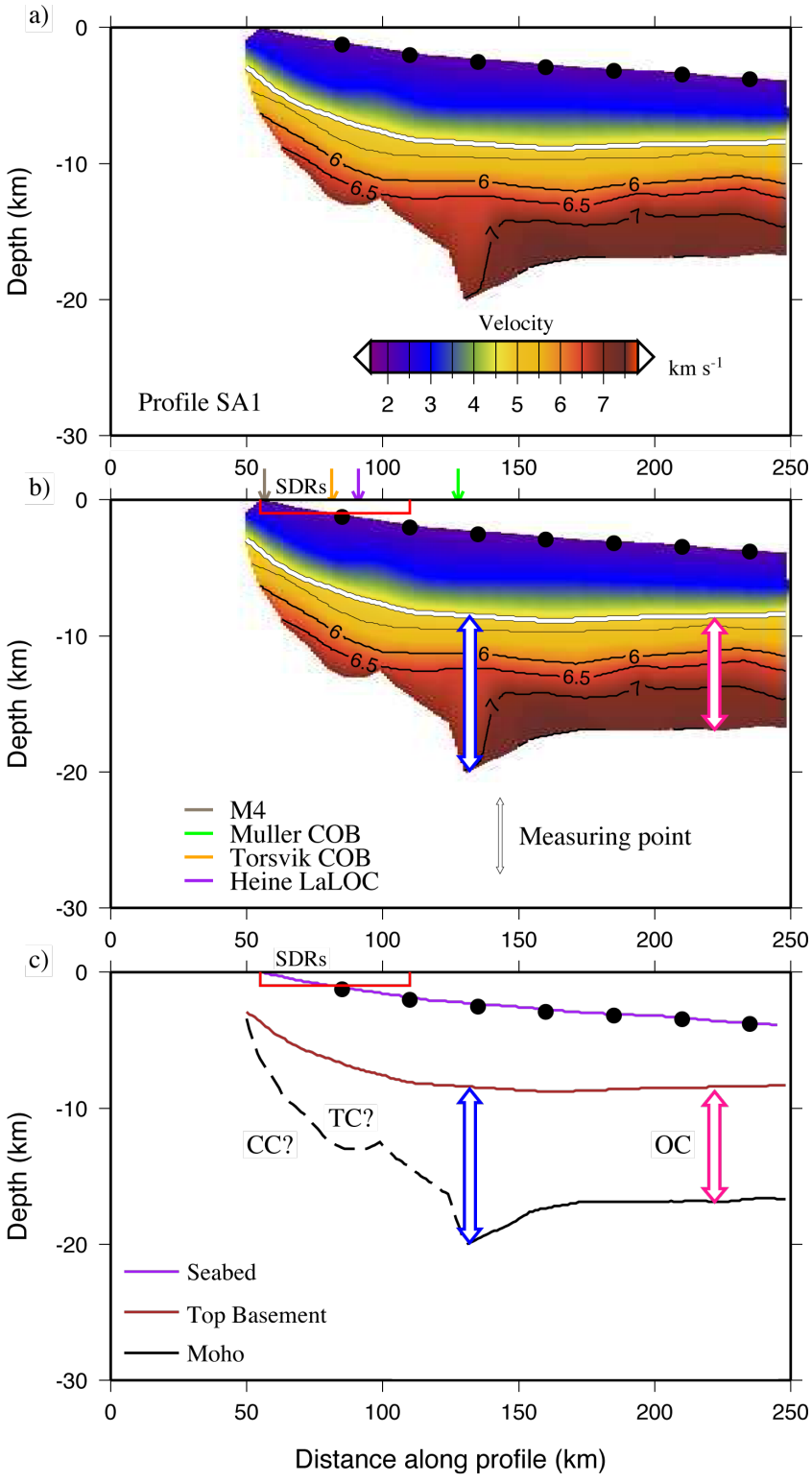


Figure 3.20: Location of syn-rift magmatism and possible LaLOC locations for Profile SA1. Part (a) is the velocity profile, digitized from the velocity profile found in Becker et al. (2014) (Fig. 3.18). Part (b) has the SDR locations (red boxes, locations originate from Becker et al. (2014) interpretation), previous continent-ocean boundaries (bright green arrow COB from Müller et al., 2008, orange arrow COB from Torsvik et al., 2009, purple arrow LaLOC from Heine et al., 2013) and location of magnetic isochron M4 (grey arrow) from Moulin et al. (2010). The two white arrows represent the first two estimations for the location of the LaLOC, where the seaward arrow is pink and the landward arrow is blue. These are linked to the depth-V_p profiles found in Fig. 3.23a and locations in Fig. 3.24. Part (c) represents the interpreted crustal structure, where OC = Oceanic Crust, TC = Transitional Crust and CC = Continental Crust. Due to the strong currents most likely resulting in issues with instruments recording, the location of transitional and oceanic crusts is in question.

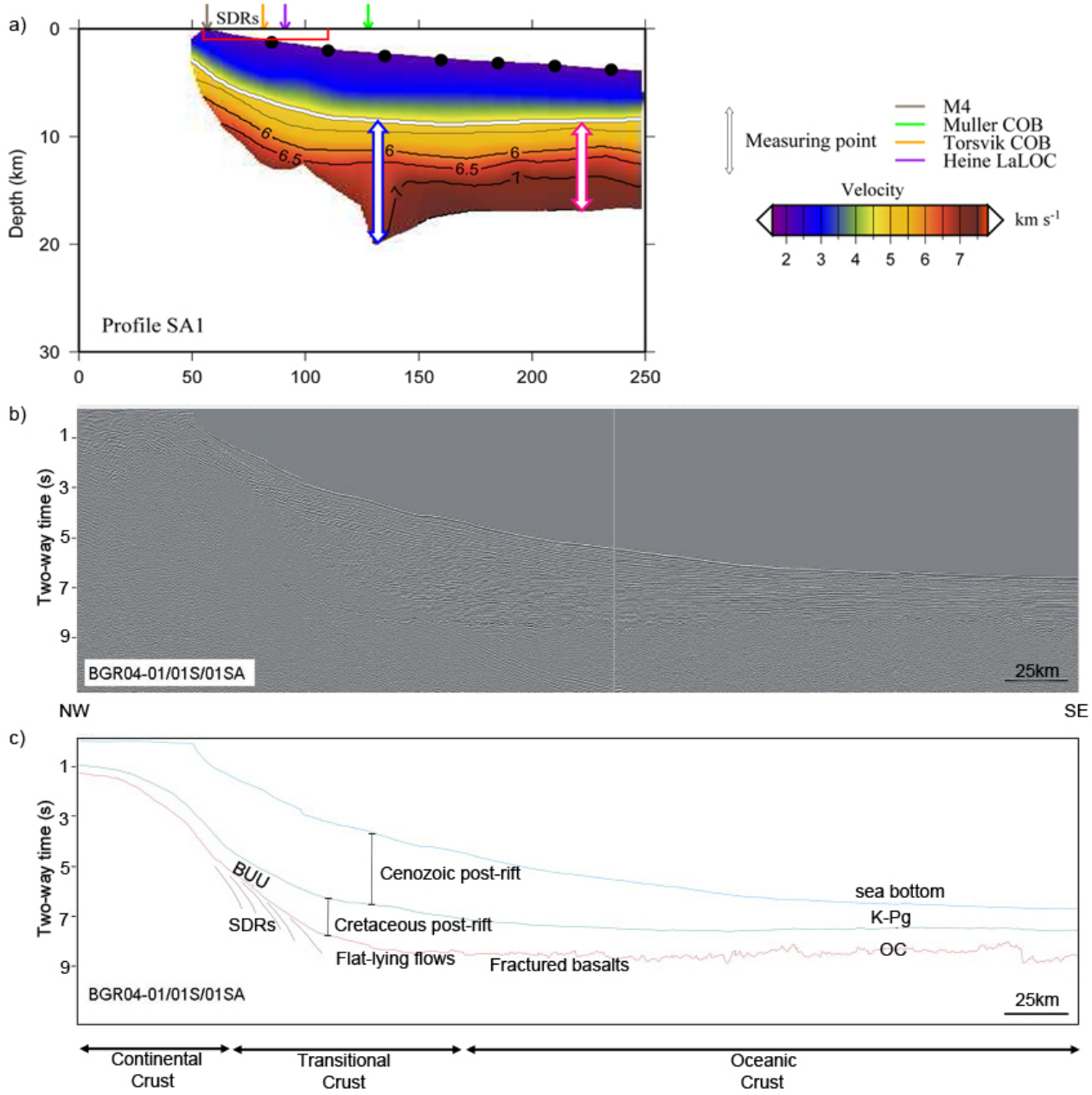


Figure 3.21: Part (a) is the velocity profile, digitized from the velocity profile found in Becker et al. (2014) (Fig. 3.18), with SDR locations (red boxes, locations originate from Becker et al. (2014) interpretation), previous continent-ocean boundaries (bright green arrow COB from Müller et al., 2008, orange arrow COB from Torsvik et al., 2009, purple arrow LaLOC from Heine et al., 2013) and location of magnetic isochron M4 (grey arrow) from Moulin et al. (2010). The two white arrows represent the first two estimations for the location of the LaLOC. Part (b) and (c) is the coincidental MCS data and line drawing, adapted from Soto et al. (2011).

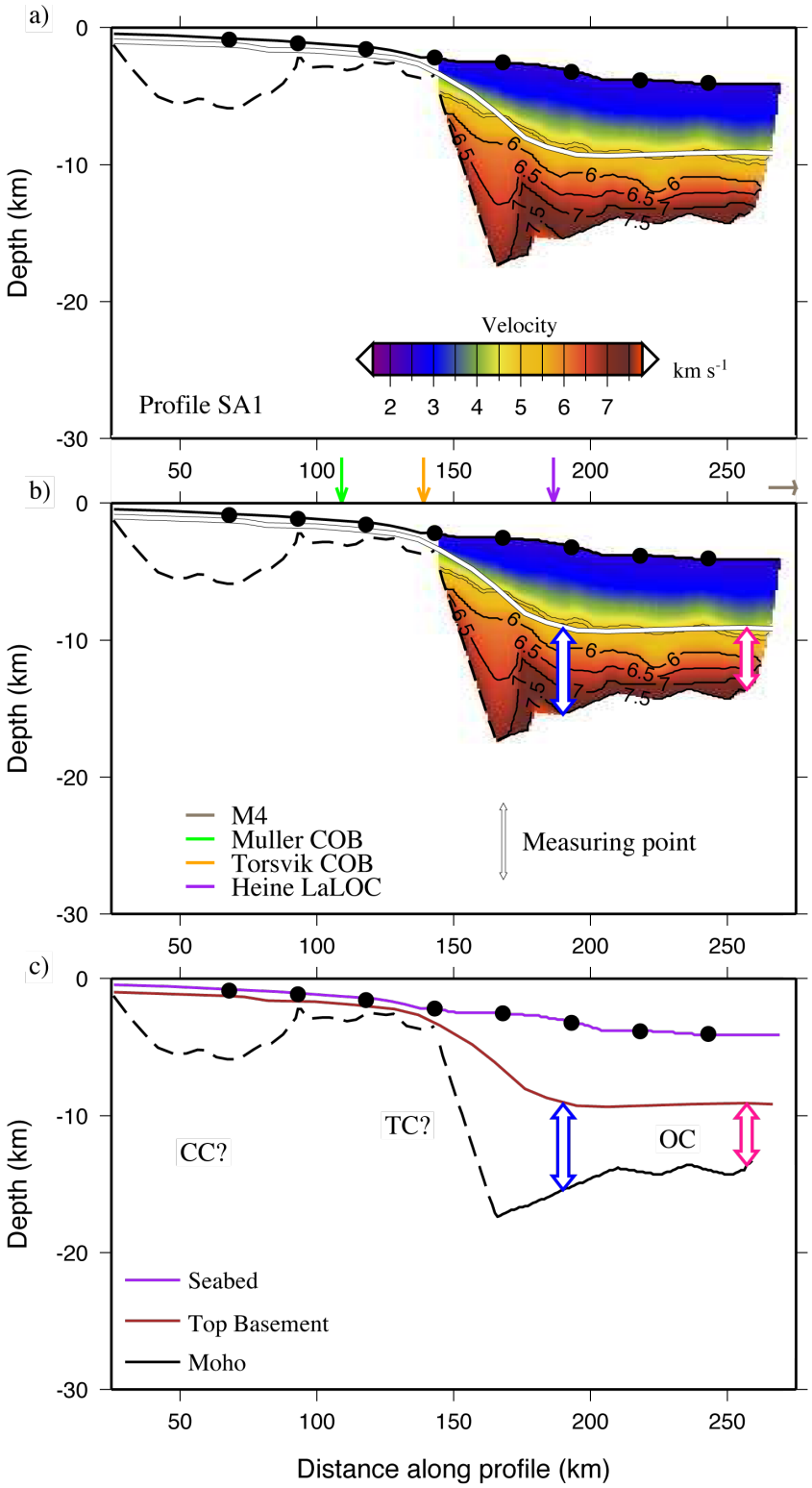


Figure 3.22: Location of syn-rift magmatism and possible LaLOC locations for Profile SA3. Part (a) is the velocity profile, digitized from the velocity profile found in Becker et al. (2014) (Fig. 3.19). Part (b) has the SDR locations (red boxes, locations originate from Becker et al. (2014) interpretation), previous continent-ocean boundaries (bright green arrow COB from Müller et al., 2008, orange arrow COB from Torsvik et al., 2009, purple arrow LaLOC from Heine et al., 2013) and location of magnetic isochron M4 (grey arrow) from Moulin et al. (2010). The two white arrows represent the first two estimations for the location of the LaLOC, where the seaward arrow is pink and the landward arrow is blue. These are linked to the depth-V_p profiles found in Fig. 3.23b and locations in Fig. 3.25. Part (c) represents the interpreted crustal structure, where OC = Oceanic Crust, TC = Transitional Crust and CC = Continental Crust. Due to the strong currents most likely resulting with issues of instrument recording, the location of transitional and oceanic crusts is in question.

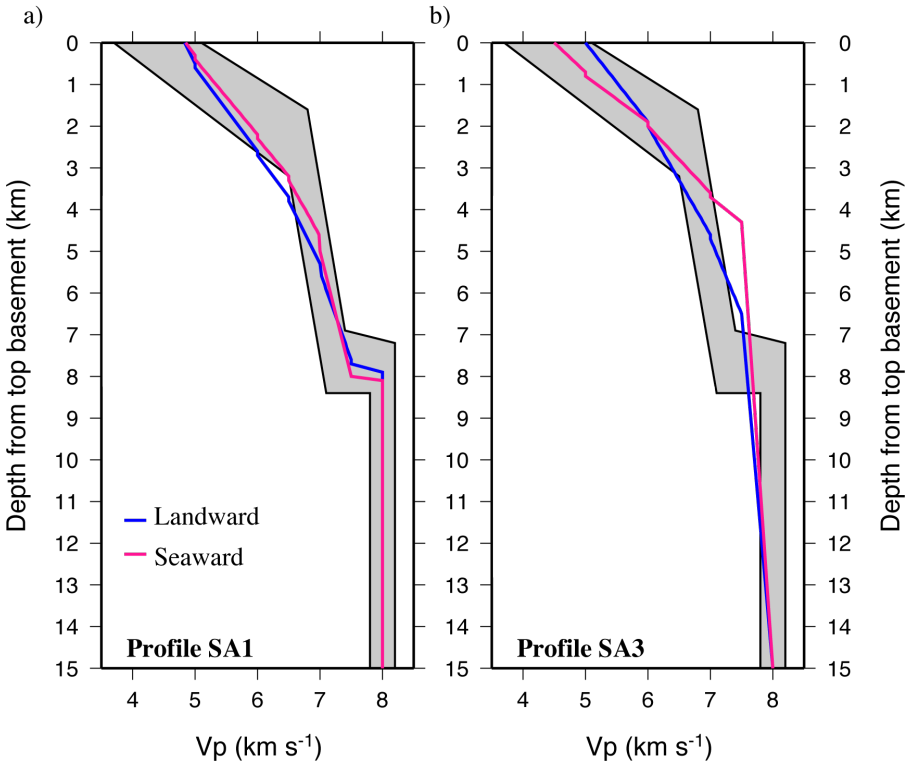


Figure 3.23: Depth-V_p profiles for the two potential LaLOC locations (Fig. 3.20b & 3.22b) for Profiles SA1 (part a) and SA3 (part b). Grey shaded area is the seismic velocity limits for mature oceanic crust from White (1992), and the y-axis represents depth from top basement.

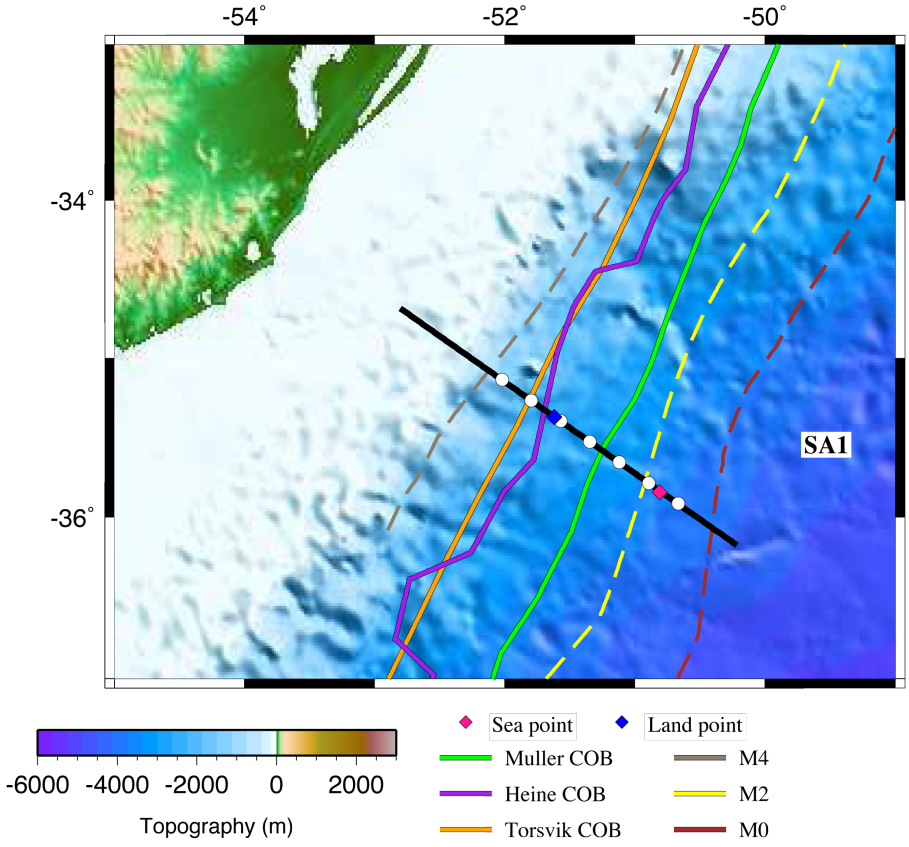


Figure 3.24: Map of possible LaLOC locations for Profile SA1. Seismic profiles is the black lines, with white dots representative of OBH locations. Previous continent-ocean boundaries are the COB from Müller et al. (2008) - bright green line, COB from Torsvik et al. (2009) - orange line, LaLOC from Heine et al. (2013)) - purple line, and location of magnetic isochrons M4 (grey dashed line), M2 (yellow dashed line) and M0 (brown dashed line) from Moulin et al. (2010). Possible LaLOC locations are in pink (most seaward point), and blue (landward point).

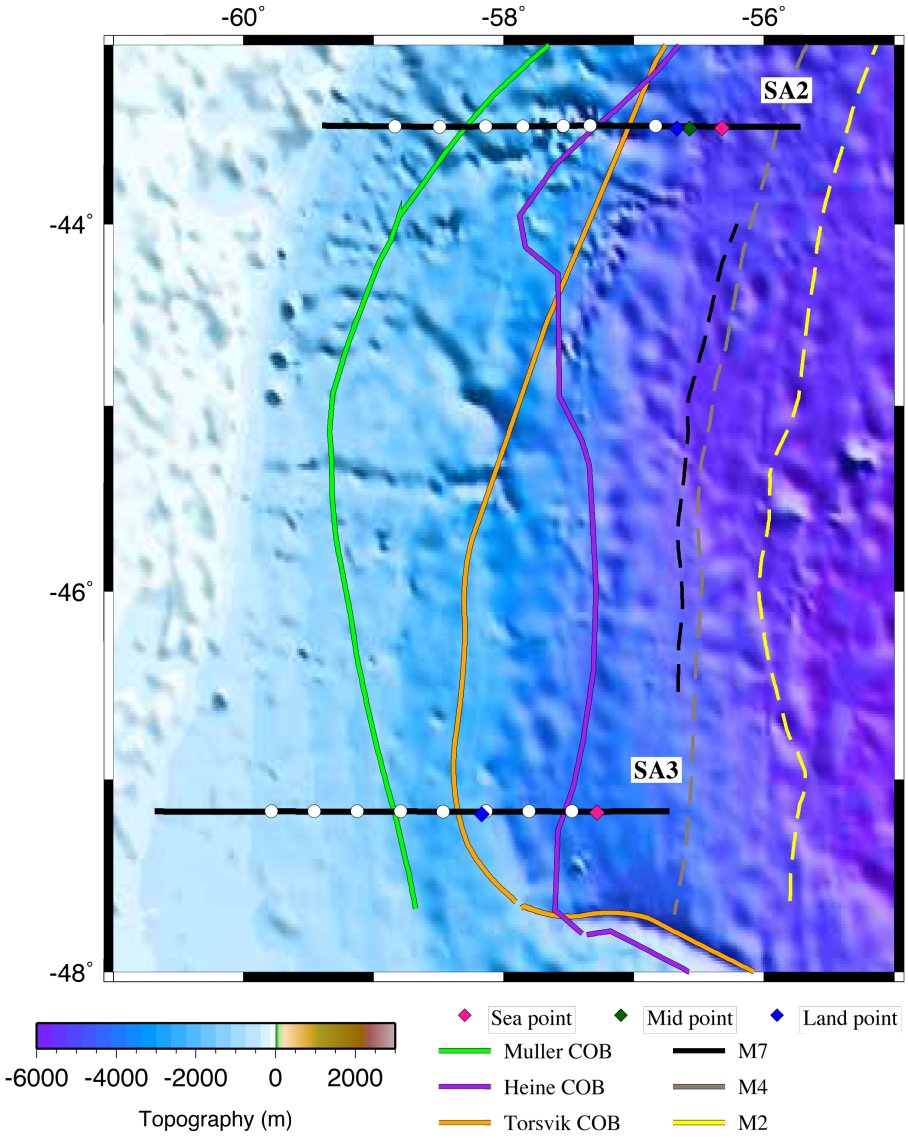


Figure 3.25: Map of possible LaLOC locations for Profiles SA2 and SA3. Seismic profiles are the black lines, with white dots representative of OBH locations. Previous continent-ocean boundaries are the COB from Müller et al. (2008) - bright green line, COB from Torsvik et al. (2009) - orange line, LaLOC from Heine et al. (2013)) - purple line, and location of magnetic isochrons M7 (black dashed line), M4 (grey dashed line) and M2 (yellow dashed line) from Moulin et al. (2010). Possible LaLOC locations are in pink (most seaward point), dark green (mid point) and blue (landward point).

3.4.2 Profile from Schnabel et al., 2008: Profile SA2

3.4.2.1 Original data

Line BGR98-REFR2, here referred to as Profile SA2, was the first wide-angle seismic survey along the Argentine margin (Schnabel et al., 2008). It lies between Profiles SA1 and SA3 (location Fig. 3.17), and has coincident gravity data. Prior to this, there had been no concrete evidence for HVLC bodies to compliment the well known structures of SDRs in this region. There are two seismic transects presented here, running along the same track, with SO85-005 being a multi-channel line and BGR98-REFR2 a refraction seismic line (location Fig. 3.17). From the extensive ray coverage (Fig. 3.26), it is clear the OBH measurements were more successful than for Profiles SA1 and SA3.

The location for this seismic line was digitized from Schnabel et al. (2008) (inset in Fig. A.4) and confirmed from the bathymetry (Fig. A.4, Table A.6). Therefore, the location of this seismic line is considered to be accurate. The velocity profiles were digitized from Fig. 3.26 (Schnabel et al., 2008), through the use of the P wave velocities contours.

3.4.2.2 Identification of LaLOC and syn-rift magmatism

Profile SA2 features two smaller HVLC bodies reaching seismic velocities of 7.3 - 7.5 $\mathrm{km\,s^{-1}}$ with thicknesses of 5 km. The HVLC bodies were found between ∼125 - 225 km along the profile, with coincident SDRs. The total area of the HVLC bodies were 560 $\mathrm{km^2}$.

For Profile SA2, there were three possible LaLOC locations (Fig. 3.27a & 3.25). The mid point was chosen as it not only had a reasonable depth-V_p profile (Fig. 3.28), but it also matched the first oceanic crust located from the coincident MCS profile (Fig. 3.29). The mid point had a thickness of 7.8 km.

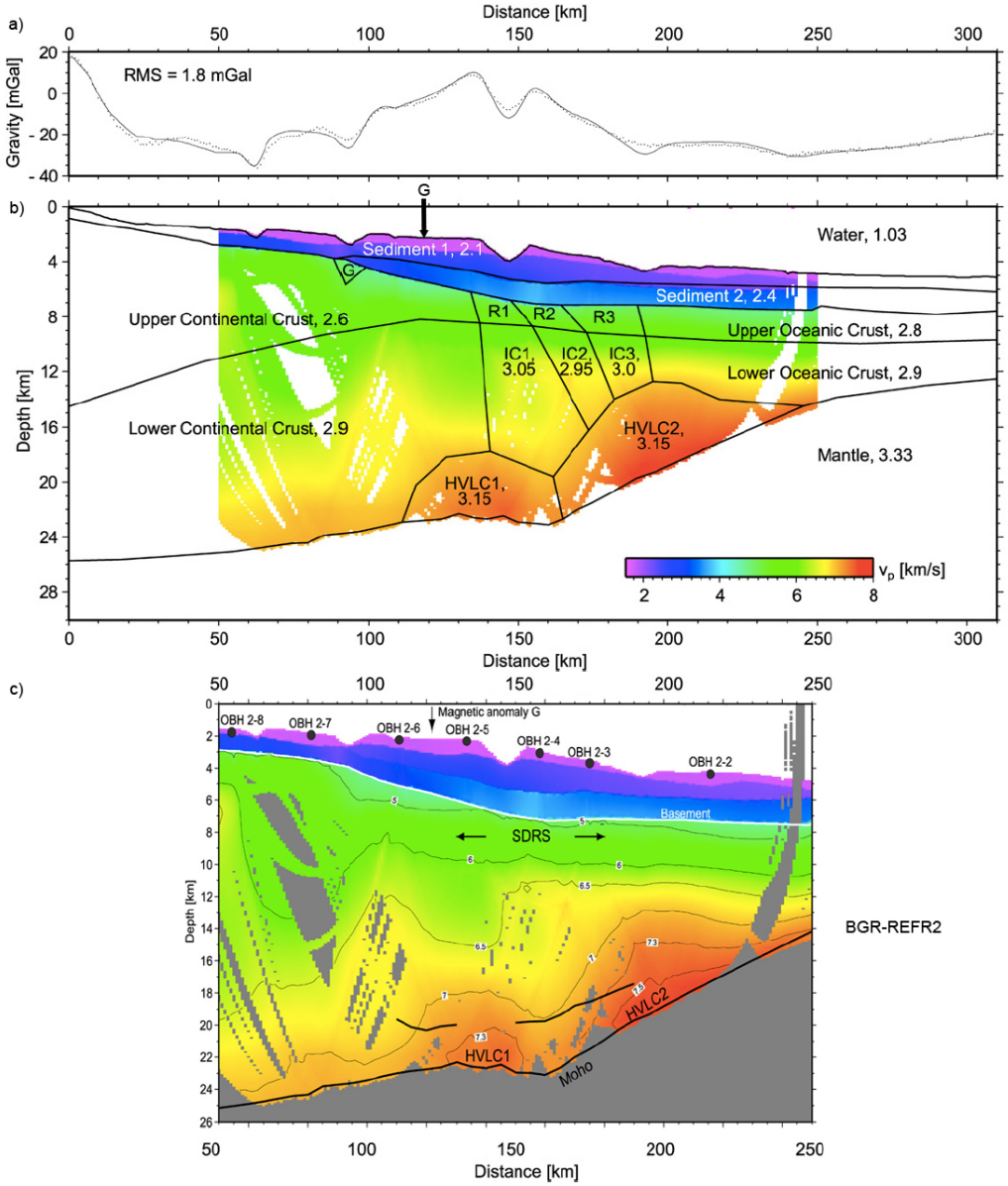


Figure 3.26: Profile SA2 (BGR98-REFR2) adapted from Schnabel et al. (2008). Part (a) represents free-air gravity anomaly modelling, taking into account a denser upper crust within the transition zone. Part (b) represents the result of gravity modelling, with different blocks and their respective densities. G = half graben, R1, 2 & 3 = SDRs, IC = intruded crust, HVLC = high-velocity lower-crustal bodies. Part (c) represents the resulting velocity-depth distribution for wide-angle profile BGR98-REFR2.

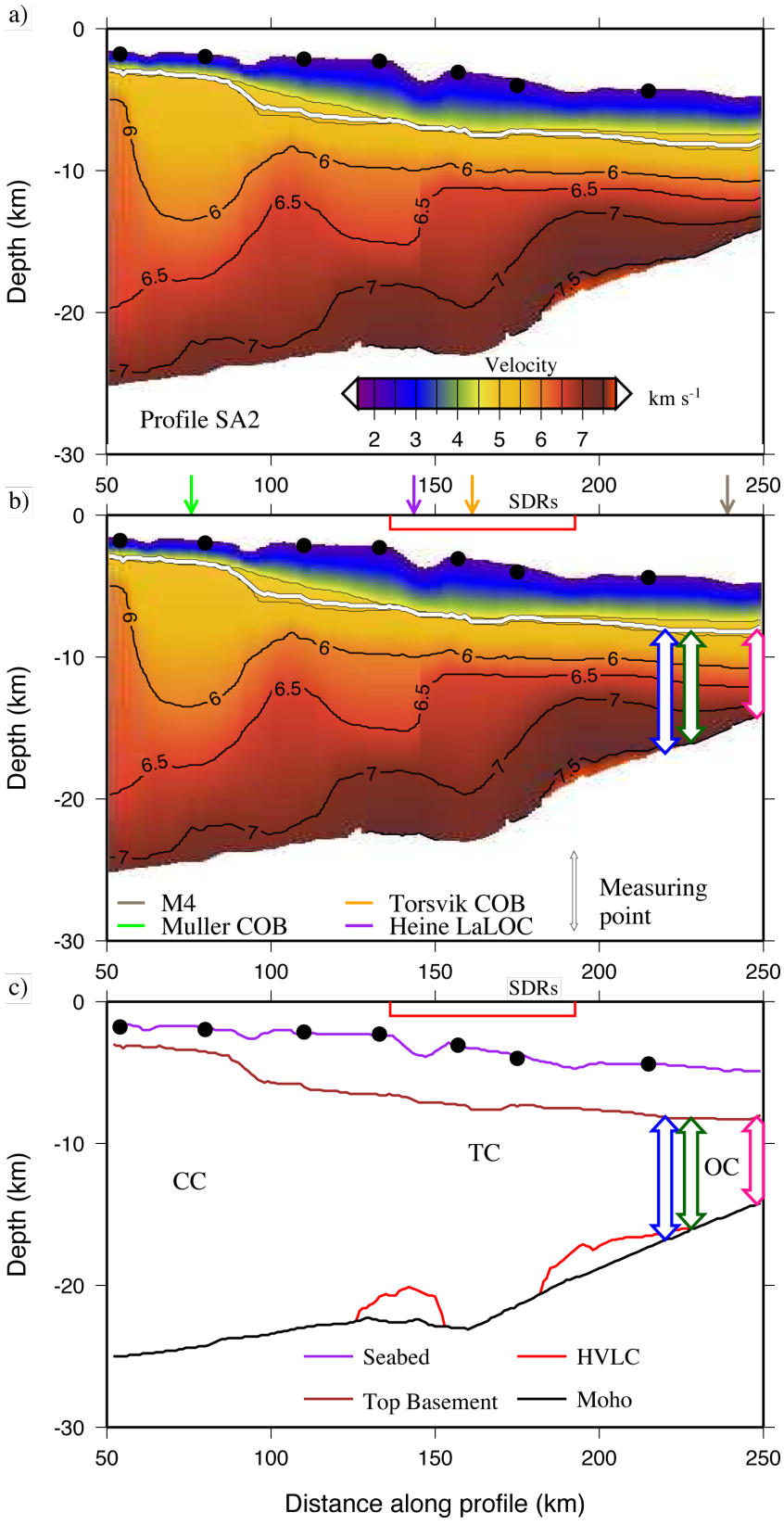


Figure 3.27: Location of syn-rift magmatism and possible LaLOC locations for Profile SA2. Part (a) is the velocity profile, digitized from the velocity profile found in Schnabel et al. (2008) (Fig. 3.26). Part (b) has the SDR locations (red boxes, locations originate from Schnabel et al., 2008 interpretation), previous continent-ocean boundaries (bright green arrow COB from Müller et al., 2008, orange arrow COB from Torsvik et al., 2009, purple arrow LaLOC from Heine et al., 2013) and location of magnetic isochron M4 (grey arrow) from Moulin et al. (2010). The three white arrows represent the first three estimations for the location of the LaLOC, where the seaward arrow is pink, the mid arrow is green and the landward arrow is blue. These are linked to the depth-V_p profiles found in Fig. 3.28 and locations in Fig. 3.25. Part (c) represents the interpreted crustal structure, where OC = Oceanic Crust, TC = Transitional Crust and CC = Continental Crust.

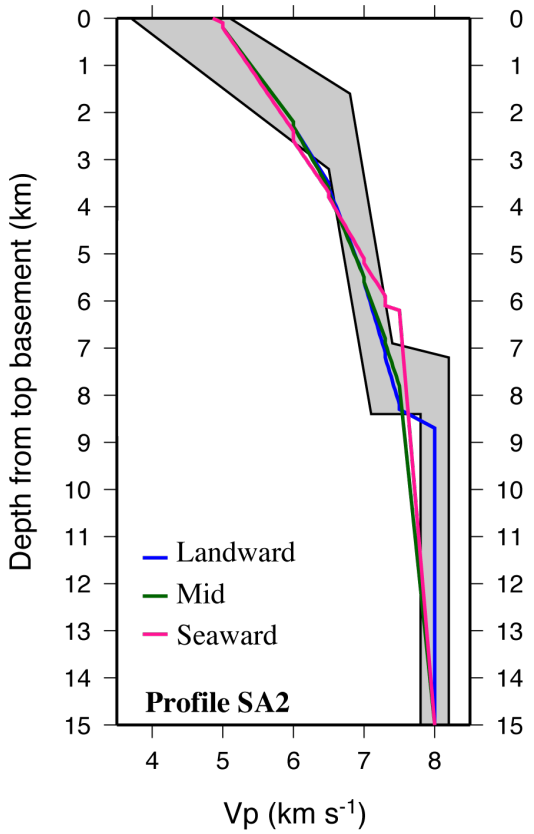


Figure 3.28: Depth-V_p profiles for the three potential LaLOC locations (Fig. 3.27) for Profile SA2. Grey shaded area is the seismic velocity limits for mature oceanic crust from White (1992), and the y-axis represents depth from top basement.

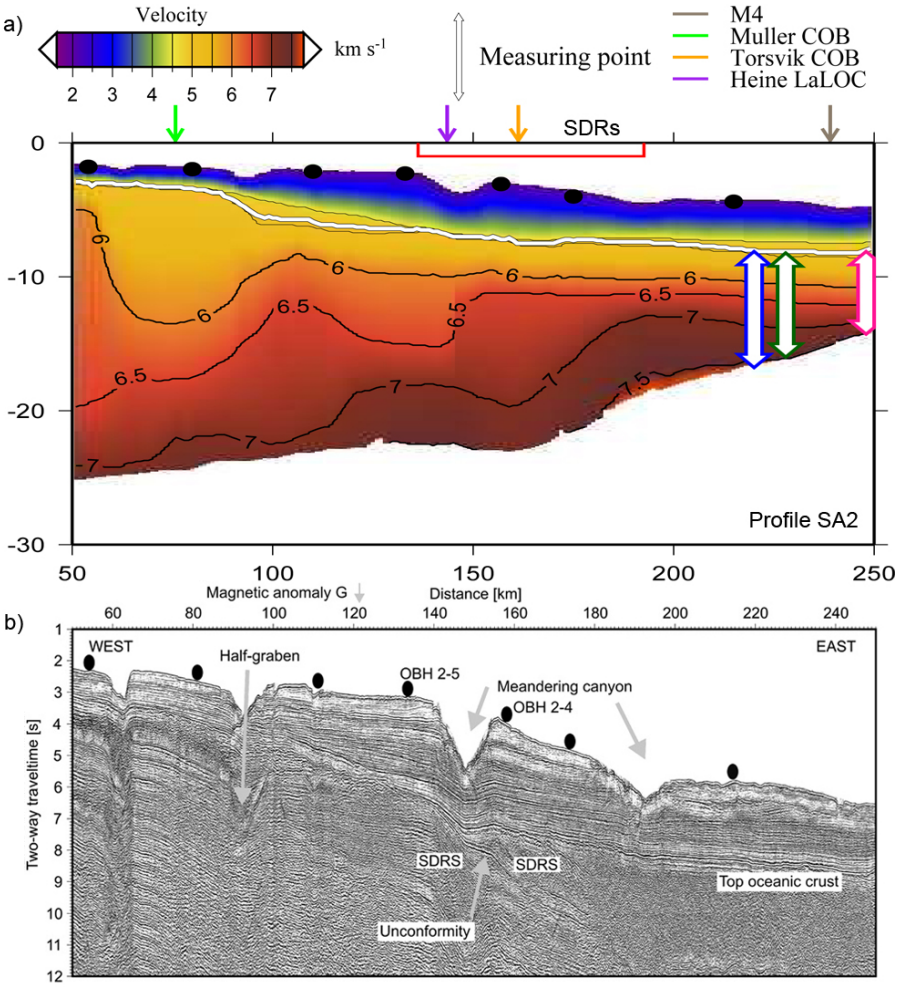


Figure 3.29: Coincidental MCS line with Profile SA2, originating from Schnabel et al. (2008).

3.5 Summary of Wide-Angle Profiles

A total of 8 appropriate published wide-angle profiles are found on the conjugate margins of the southern South Atlantic, originating from various sources (more details in Table A.1). There are clear decreasing trends for initial oceanic crustal thicknesses from 11.7 km thick crust observed on Profile AF1, reducing to 8.2 km for Profile AF2, and trending to the average thickness of oceanic crust at 6.9 km thick crust observed on Profile SA3 at a distance of 2300 km along-strike (Table 3.2). This decrease in thickness is explored in more detail in **Chapter 5**, and will be coupled with measurement from MCS profiles, representing more evenly spread observational constraints along-strike. There is also a clear reduction in HVLC and SDR areas on the African margin, from an area of 6610 km^2 observed on Profile AF0 to 2590 km^2 observed on Profile AF4 (Table 3.1; explored in more detail in **Chapter 6**). Although there is little evidence of HVLC bodies on the South American margin at present from current publications, the probability of the existence of HVLC bodies is strengthened with the distribution of SDRs and thickened oceanic crust. The presence of HVLC bodies in this region will most likely become evident as higher quality data sets are published.

Table 3.1: Summary of seismic data results for syn-rift magmatism for Profiles AF0 - AF4 (Fig. 3.3, 3.6, 3.7, 3.13, 3.14) and SA2 (Fig. 3.27). Profiles SA1 and SA3 are not included, as they did not show any concrete results for syn-rift magmatism (Fig. 3.20 and 3.22).

Profile	Lat.	Thickness at LaLOC (km)	Maximum HVLC thickness (km)	Melt Area (km^2)	Melt Area with SDRs (km^2)	Maximum V_p ($km\,s^1$)
AF0	-19.0	N/A	24.0	6610	N/A	7.6
AF1	-21.1	11.7	18.3	3660	3780	7.6
AF2	-22.5	8.2	21.1	2820	2940	7.6
AF3	-28.2	7.2	12.4	2595	2700	7.4
AF4	-30.4	7.0	6.3	2590	2860	7.4
SA2	-43.5	7.8	6.8	560	660	7.5

3.6 Multi-Channel Seismic Data

3.6.1 Original data

MCS lines were vital in order to consolidate any variations observed in magmatism from wide-angle data. The MCS lines were limited to the South American margin, as it was required that the seismic lines imaged both the top basement and the Moho to measure the thickness of the ocean crust. In order to ensure consistency between oceanic crust thickness measurements at the landward limit of ocean crust made from wide-angle and MCS profiles, all measurements were performed on time sections for MCS data and converted to distance. The two way travel time was converted to distance using a mean seismic velocity value for oceanic crust of $6.7\,\mathrm{km\,s^{-1}}$ (White et al., 1992). White et al. (1992) found 90 % of the ocean crust velocity estimates fall within a range of $6.4 - 7.0\,\mathrm{km\,s^{-1}}$, representing a ± 0.45 km error for a crustal thickness of 10 km.

Ten MCS published sections are used from Hinz et al. (1999) and Franke et al. (2007, 2010) (green diamonds in Fig. 3.30). The MCS lines from Hinz et al. (1999), Franke et al. (2007) and Franke et al. (2010) originate from different cruises from BGR between 1987 - 2004, with a total track length of 25,677 km (Franke et al., 2007). The seismic data focused on the outermost shelf, and streamers ranged from 3000 - 4500 m in length. In addition to seismic data, magnetic and gravity data were acquired coincidentally. Six additional MCS profiles (orange diamonds in Fig. 3.30) are from Winterbourne et al. (2014), which originate from a mixture of unpublished seismic industry. Finally, fourteen unpublished, industry, high quality seismic reflection survey lines from the BasinSPAN acquisition project of ION Geophysical were used. These formed part of a seismic survey with >18,000 km of 2D MCS data, with a 12 km long streamer. They often reached depths of 40 km in depth migrated images, and are considered very high quality. The locations of the lines used ranged from near the Rio Grande Rise to 42.5 °S (pink dots in Fig. 3.30).

3.6.2 Identification of LaLOC

The MCS lines in the area are more reliant on the seismic characteristics in order to locate the LaLOC, compared to the wide-angle profiles that had the benefit of depth-V_p profiles. The reflectivity character was considered, with true ocean crust typically being devoid of internal reflectivity, and a recognisable 'bumpy surface' indicating the presence of pillow lavas. The location of magnetic isochrons was also considered. These criteria were followed for the MCS lines from Hinz et al. (1999), Franke et al. (2007) and Franke et al. (2010) (Fig. 3.31 - 3.36), as well as the ION seismic reflection lines (not shown in this study due to copyright). Measurements had already been carried out by Winterbourne et al. (2014) for the latter's profiles (Fig. 3.37). Even before the conversion to distance, the TWTT values of initial oceanic crustal thickness show a clear reduction along-strike (Table 3.2).

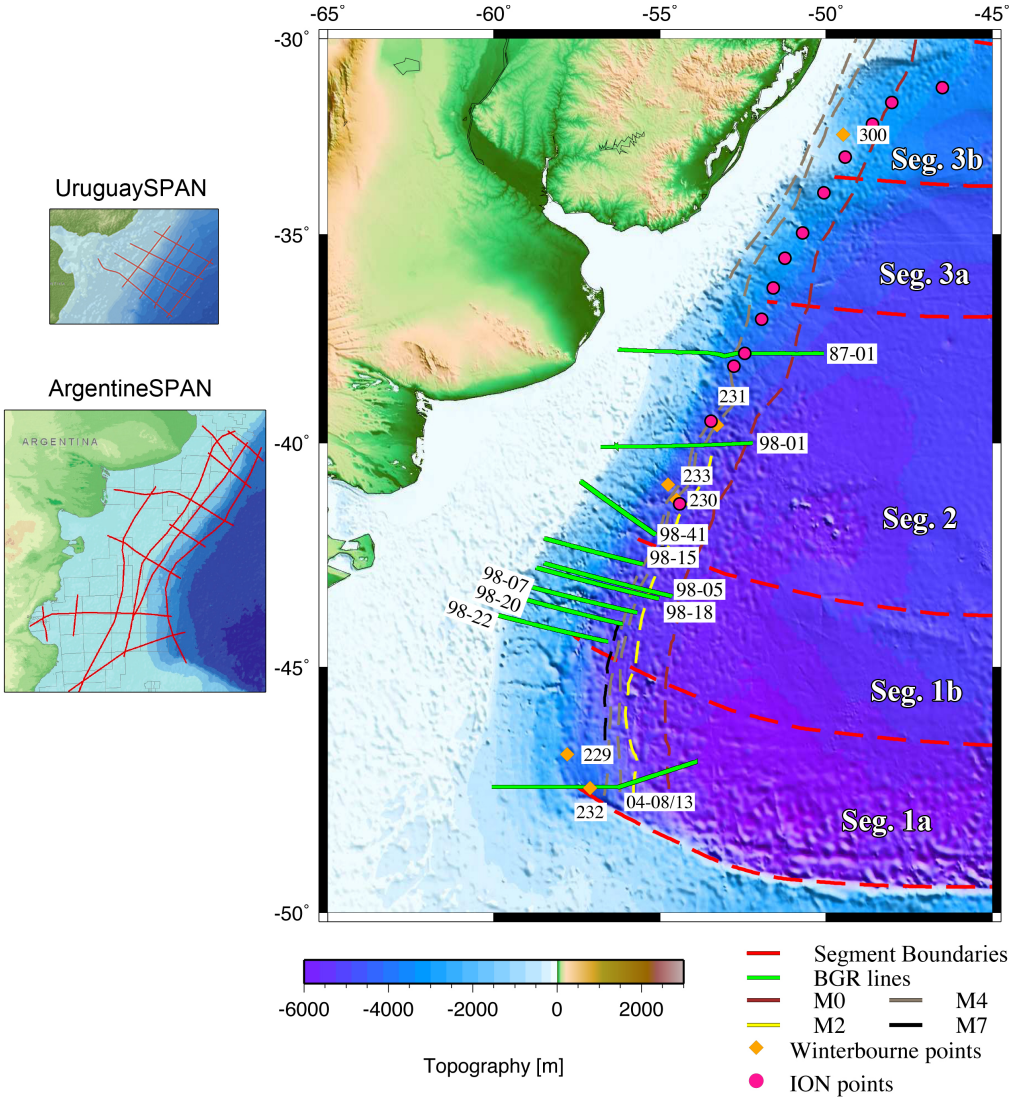


Figure 3.30: Map of the BGR MCS line locations (green lines) for Fig. 3.31 - 3.36, published points (orange diamonds) from Winterbourne et al. (2014) for Fig. 3.37 and location of ION Geophysical lines (pink circles). The approximate locations of the ION Geophysical lines are shown in the maps to the left. Topography and bathymetry is from ETOP01 (Armante, 2009). The sea floor spreading magnetic anomalies (M0, M2, M4 and M7) are from Moulin et al. (2010). Segment boundaries (red dashed lines) have been previously identified in Section 2.7.

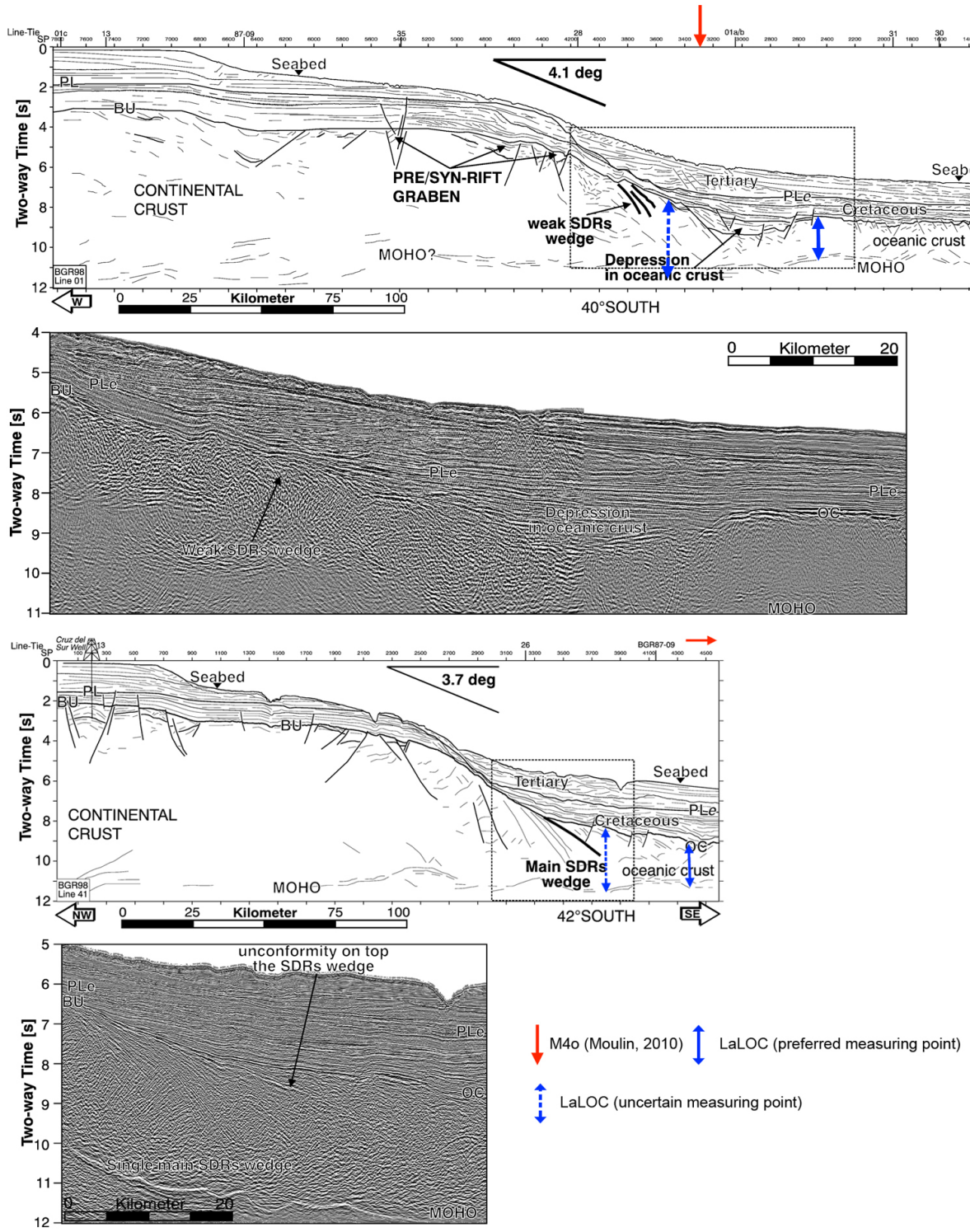


Figure 3.31: Seismic profiles BGR98-01 and 41, showing the line interpretations and MCS profiles from Franke et al. (2007). Locations of magnetic isochrons from Moulin et al. (2010). Blue arrow represents LaLOC location, where the latter has been identified using the criteria specified in this project.

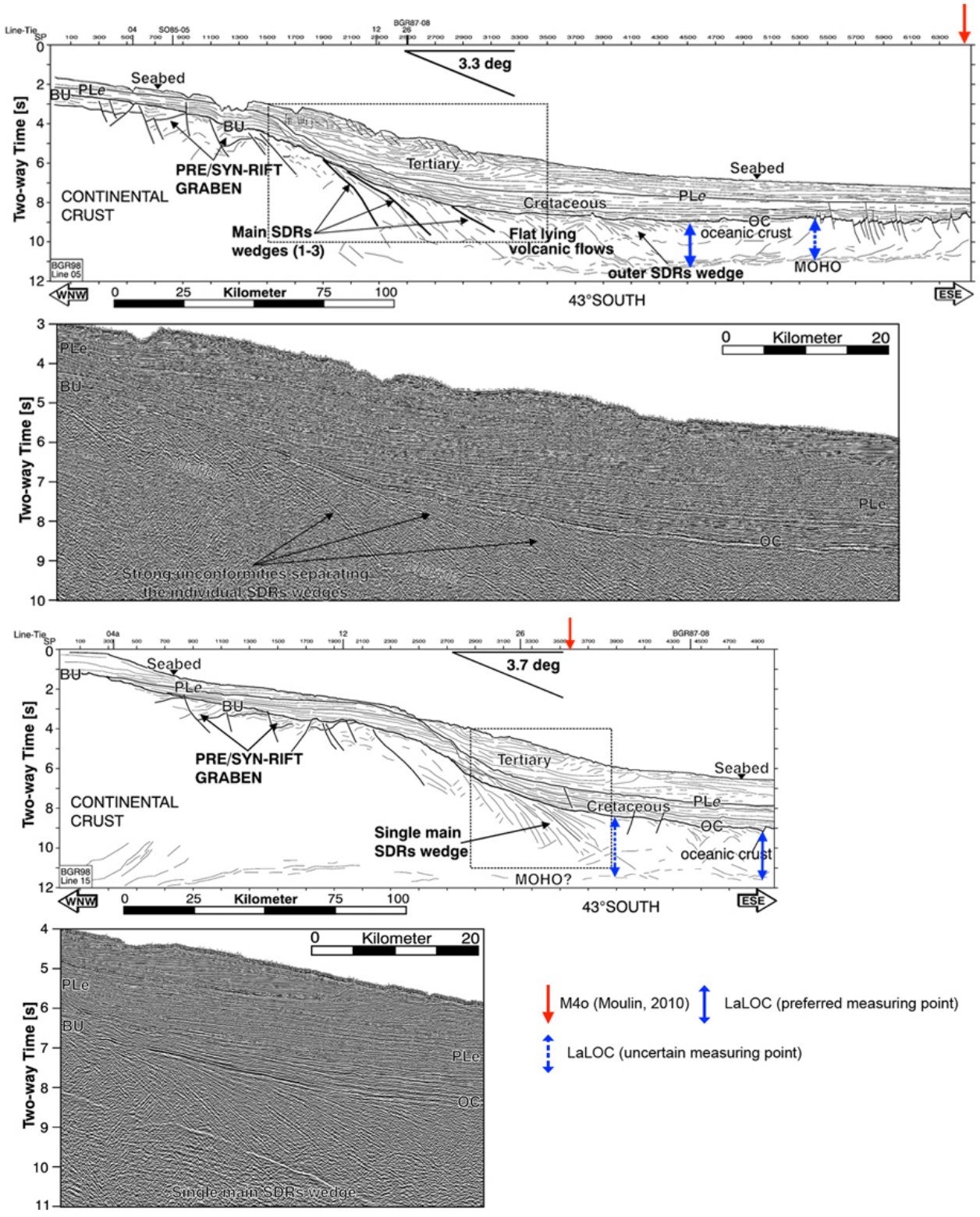


Figure 3.32: Seismic profiles BGR98-05 and 15, showing the line interpretations and MCS profiles from Franke et al. (2007). Locations of magnetic isochrons from Moulin et al. (2010). Blue arrow represents LaLOC location, where the latter has been identified using the criteria specified in this project.

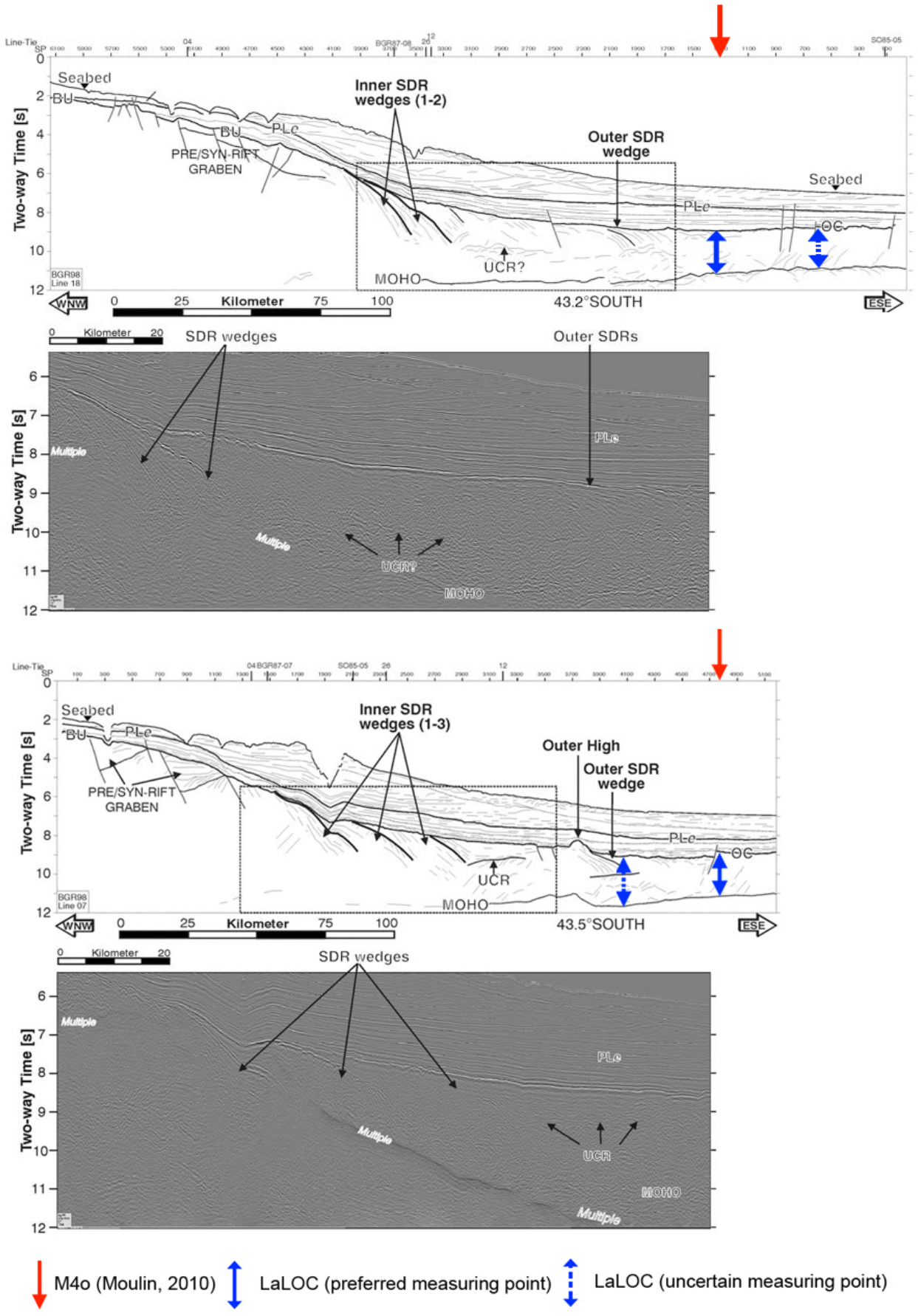


Figure 3.33: Seismic profiles BGR98-18 and 07, showing the line interpretations and MCS profiles from Franke et al. (2010). Locations of magnetic isochrons from Moulin et al. (2010). Blue arrow represents LaLOC location, where the latter has been identified using the criteria specified in this project.

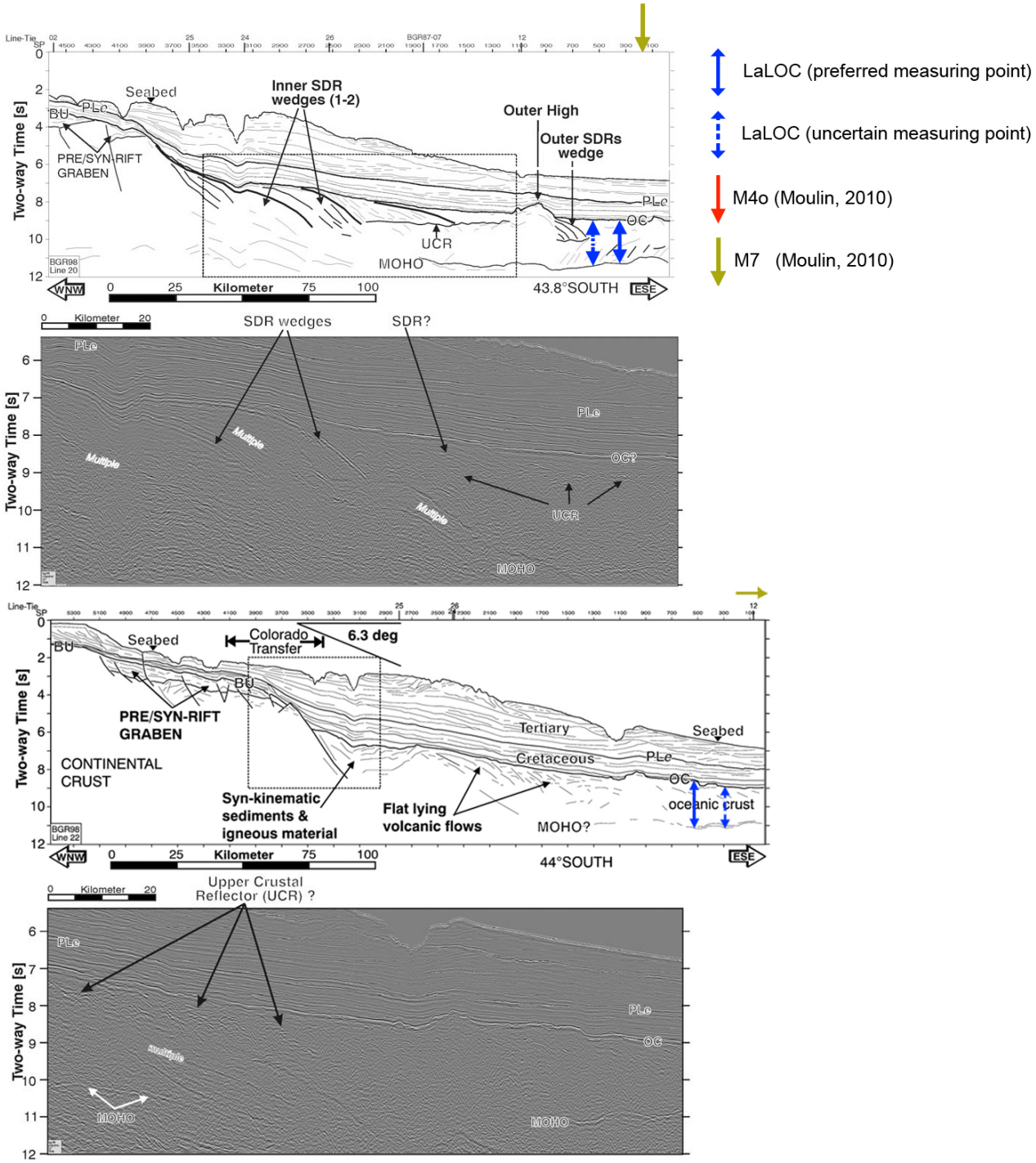


Figure 3.34: Seismic profiles BGR98-20 and 22, showing the line interpretations and MCS profiles from Franke et al. (2010). Locations of magnetic isochrons from Moulin et al. (2010). Blue arrow represents LaLOC location, where the latter has been identified using the criteria specified in this project.

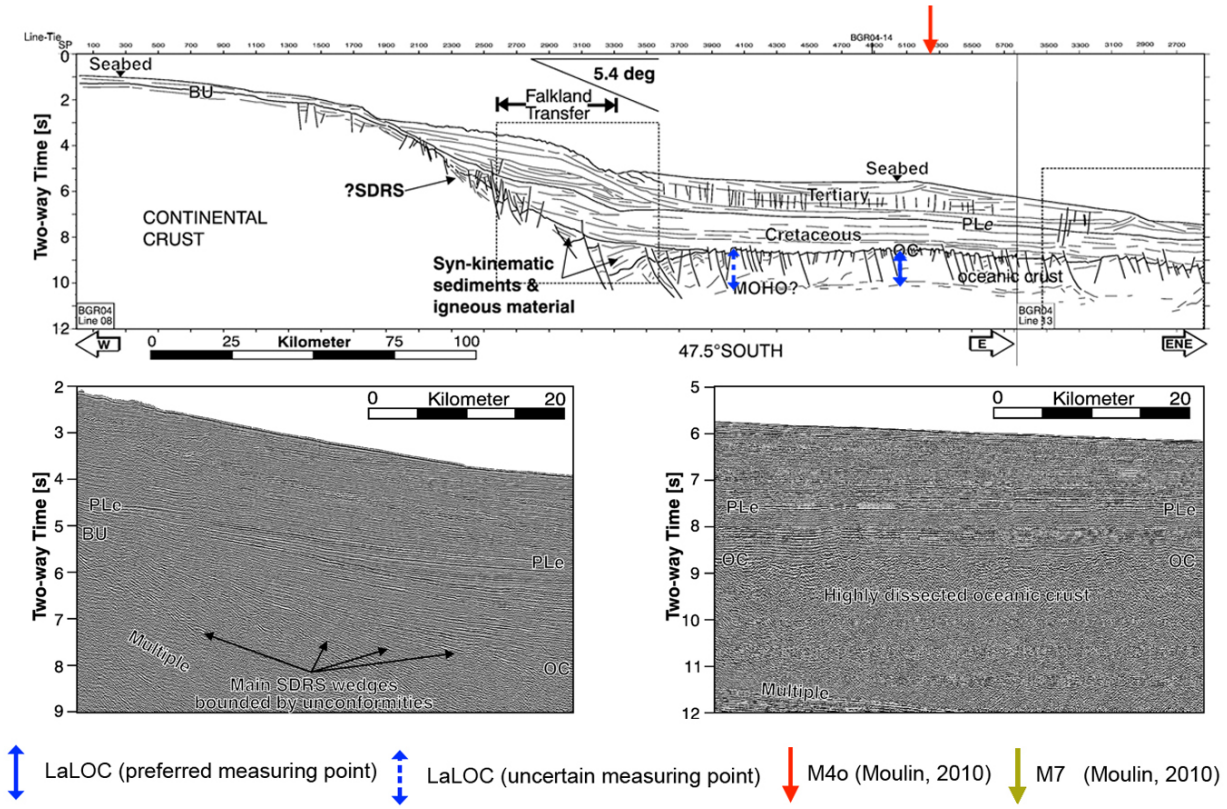


Figure 3.35: Seismic profile BGR04-08/13, showing the line interpretations and MCS profiles from Franke et al. (2007). Locations of magnetic isochrons from Moulin et al. (2010). Blue arrow represents LaLOC location, where the latter has been identified using the criteria specified in this project.

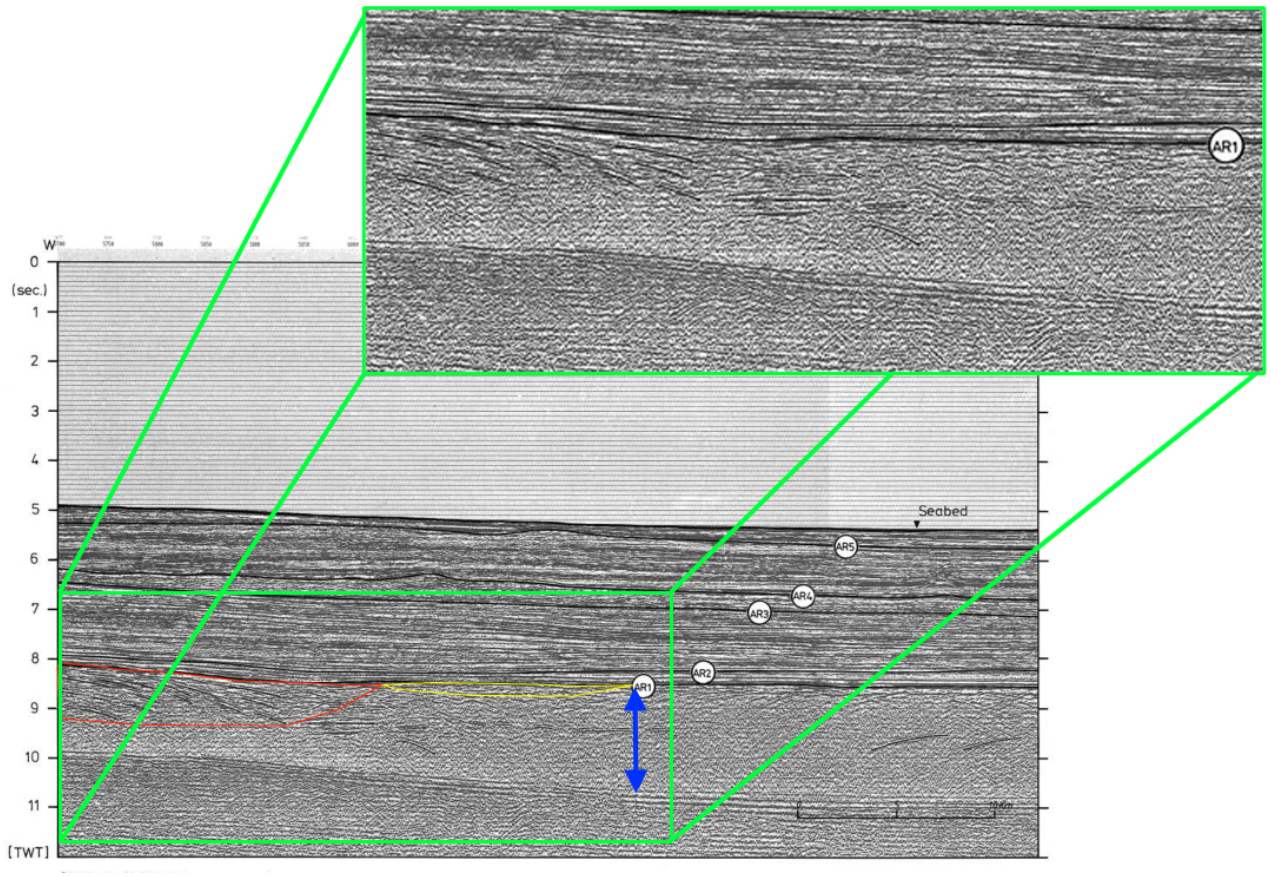


Figure 3.36: Seismic profile BGR87-01B, from Hinz et al. (1999). Red and yellow shapes represent the termination of SDR wedges, with a zoomed in perspective in the green box area. Blue arrow represents LaLOC location, where the latter has been identified using the criteria specified in this project.

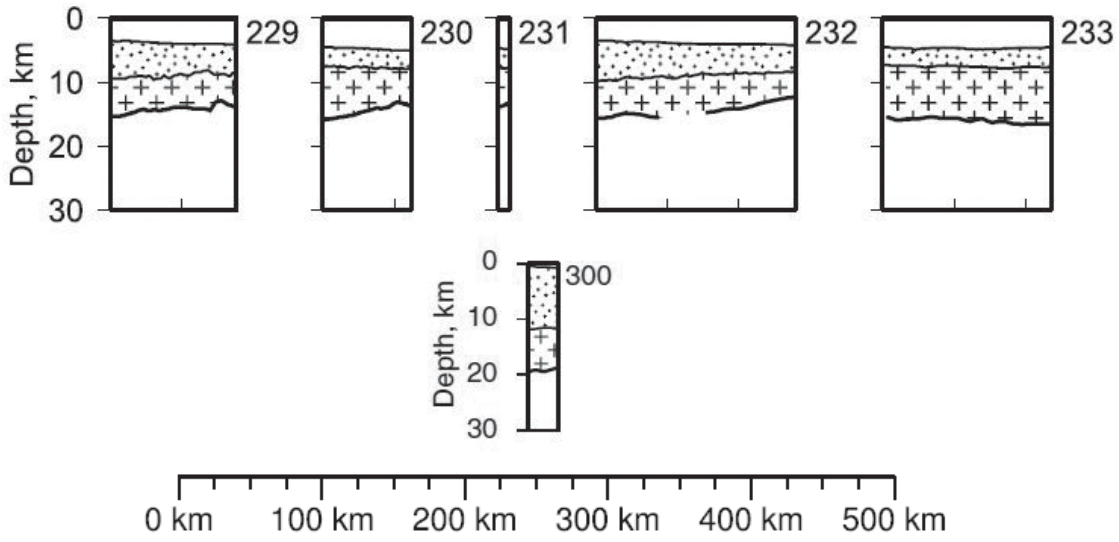


Figure 3.37: Schematic interpretations of MCS profiles from industry used from Winterbourne et al. (2014) data. Ocean crust depicted by '+', and sediment by dots.

3.7 Age Constraints

In order to understand the timings of the South Atlantic continental break-up, a reliable time scale assigning ages to the magnetic isochrons was selected (Section 2.6). Unlike the Gradstein et al. (2012) time scale, the Gee and Kent (2007) time scale was selected as it does not contain the large age-shift at the Barremian-Aptian boundary. Also preferred by Heine et al. (2013) and He et al. (2008), as it is based on a review of seafloor spreading velocities globally, it will be the time scale used throughout this project.

Following the selection of the time scale, the magnetic isochrons from Moulin et al. (2010) were age assigned (Table 2.1) and an age-grid was created for both Africa and South America (Fig. 3.38). Magnetic isochron C34 (Seton et al., 2012) was added in order to complete the grid, with the age of 83 - 120.6 Ma (Gee and Kent, 2007). The creation of the age-grid allows the age-assignment of any known coordinate point. Profiles AF0–AF4 and SA1–SA3 were all age-assigned according to their location using this age-grid.

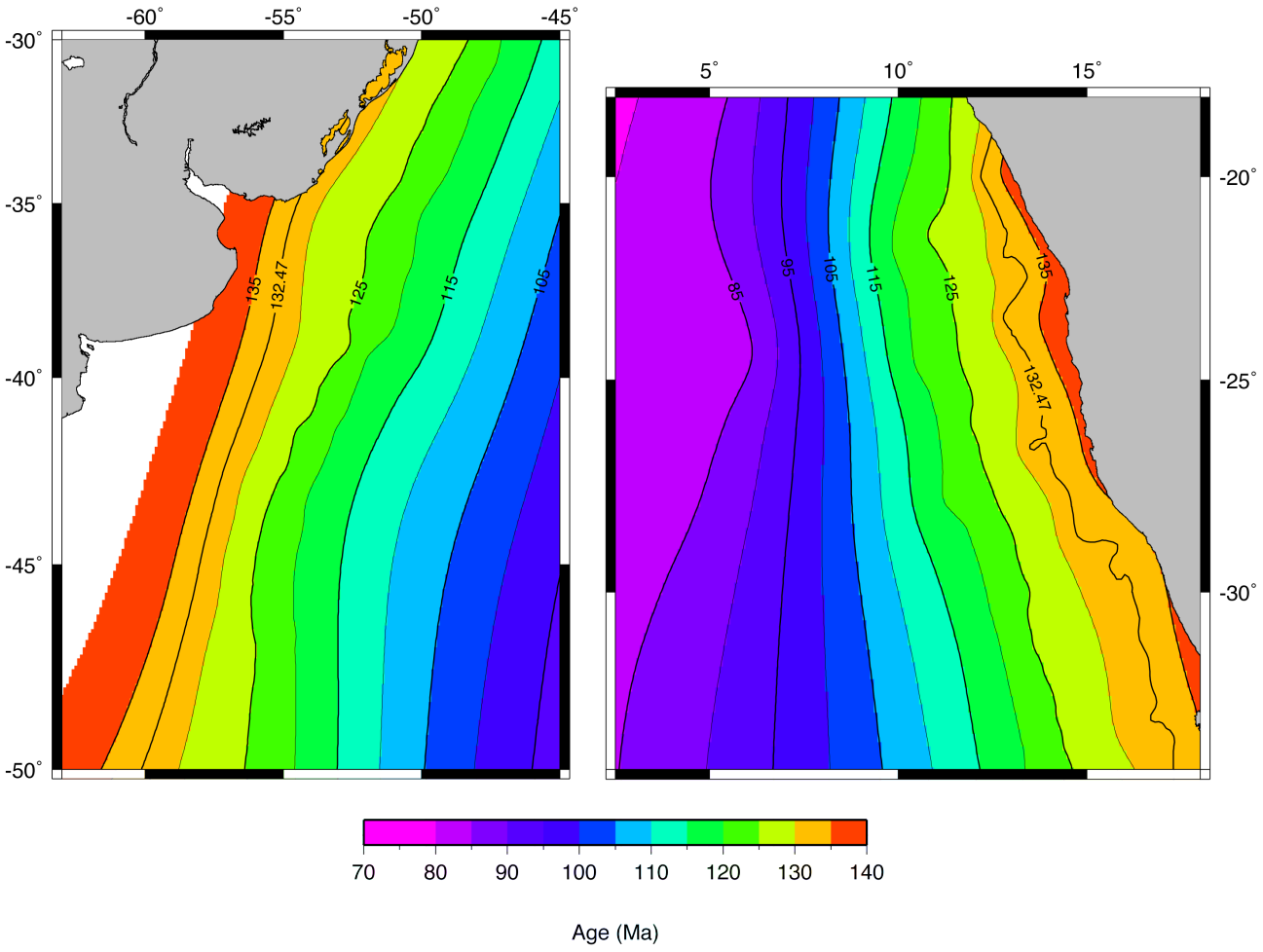


Figure 3.38: Moulin-Gee age grid for South America and Africa. Based on the magnetic isochron locations from Moulin et al. (2010) for M7, M4, M2, M0 and Seton et al. (2012) for C34, and time scale from Gee and Kent (2007).

3.8 Summary

The observational constraints form the basis for the comparison against numerical modelling results and to the understanding of the break-up of the South Atlantic. The interpretation for the location of the landward limit of oceanic crustal has been identified for 31 wide-angle and MCS profiles within this project, with an additional 6 pre-measured data points. The thicknesses observed (summary Table 3.2) are shown in graphical form in **Chapter 5**. In addition to this, areas of syn-rift melt have been extracted using the criteria within this project for the wide-angle profiles, and are further explored, along with seismic velocity trends, in **Chapter 6**. For both **Chapters 5 & 6**, the observations extracted from the seismic data, coupled with their age-assignment from the Moulin-Gee age grid, can be matched to the numerical modelling results of magmatism, used to gain insight on the thermal structure of the southern South Atlantic at break-up.

Table 3.2: Crustal thickness measurements at the LaLOC for all seismic sections used in this study, also shown on a reconstructed map in Fig. 3.39.(Fig. 3.6, 3.7, 3.13, 3.14, 3.20, 3.27, 3.22, 3.31 - 3.37). Distance is measured from the Rio Grande Rise and Walvis Ridge commencements points (marked '+' in Fig. 2.6). Uncertainties in the measured oceanic crustal thickness are also shown. Bauer00 = Bauer et al. (2000), Schinkel06 = Schinkel (2006), Hirsch09 = Hirsch et al. (2009), Becker14 = Becker et al. (2014), Hinz99 = Hinz et al. (1999), Franke10 = Franke et al. (2010), Franke07 = Franke et al. (2007), WB14 = Winterbourne et al. (2014), ION = lines originating from ION Geophysical.

Profile Name	Reference	Long.	Lat.	Distance along-strike (km)	Thickness (TWTT s)	Thickness (km)	Thickness max. (km)	Thickness min. (km)
AF1	Bauer00	11.9	-23.8	450	n/a	11.7	12.9	11.2
AF2	Bauer00	12.1	-24.6	538	n/a	8.2	10.9	8.0
AF3	Schinkel06	13.8	-30.1	1174	n/a	7.2	8.2	6.2
AF4	Hirsch09	14.6	-32.3	1422	n/a	7.0	11.7	6.7
SA1	Becker14	-51.6	-35.4	922	n/a	8.2	8.2	7.9
SA2	Schnabel08	-56.6	-43.5	1895	n/a	7.8	8.7	6.2
SA3	Becker14	-58.1	-47.2	2288	n/a	6.9	6.9	3.8
BGR87-01	Hinz99	-52.6	-37.9	1165	2.26	7.6	7.9	7.3
BGR98-18	Franke10	-55.8	-43.4	1850	2.23	7.4	7.7	7.1
BGR98-07	Franke10	-55.9	-43.8	1894	2.30	7.7	8.0	7.4
BGR98-20	Franke10	-56.5	-44	1925	2.27	7.6	7.9	7.3
BGR98-01	Franke07	-53.6	-40	1464	2.16	7.2	7.5	6.9
BGR98-41	Franke07	-55.2	-42.1	1681	2.12	7.1	7.4	6.8
BGR98-05	Franke07	-55.7	-43.3	1790	2.32	7.8	7.2	6.6
BGR98-15	Franke07	-55.6	-42.7	1804	2.06	6.9	8.1	7.5
BGR98-22	Franke07	-56.8	-44.4	1981	2.05	6.9	7.2	6.6
BGR04-08/13	Franke07	-56.7	-47.5	2258	1.8	6.0	6.3	5.7
Profile 300	WB14	-49.6	-32.6	593	n/a	7.7	8.0	7.4
Profile 231	WB14	-53.3	-39.6	1380	n/a	5.9	6.2	5.6
Profile 233	WB14	-54.8	-41	1578	n/a	8.4	8.8	8.0
Profile 230	WB14	-54.5	-41.3	1595	n/a	6.8	7.1	6.5
Profile 229	WB14	-57.2	-46.7	2210	n/a	5.1	5.3	4.9
Profile 232	WB14	-57.3	-47.3	2261	n/a	5.1	5.3	4.9
PS1-0090	ION	-46.5	-31.3	262	2.94	9.9	10.3	9.5
PS1-0070	ION	-48.2	-31.5	405	2.87	9.6	10.0	9.2
PS1-0060	ION	-48.8	-32	488	3.35	11.2	11.7	10.7
PS1-0040	ION	-49.7	-32.9	609	3.24	10.9	11.4	10.4
PS1-0030	ION	-49.9	-34.6	695	2.17	7.3	7.6	7.0
PS1-0010	ION	-50.7	-35	828	2.55	8.5	8.9	8.1
UY1-4700	ION	-51.2	-35.6	911	2.18	7.3	7.6	7.0
UY1-4500	ION	-51.6	-36.3	992	2.39	8.0	8.4	7.6
UY1-4300	ION	-51.9	-37.1	1076	2.36	7.9	8.3	7.5
UY1-4000	ION	-52.4	-37.9	1176	2.25	7.5	7.8	7.2
AR1-3800	ION	-52.8	-38.2	1220	2.54	8.5	8.9	8.1
AR1-3500	ION	-53.5	-39.5	1369	2.73	9.1	9.5	8.7
AR1-3000	ION	-54.4	-41.4	1583	1.93	6.4	6.7	6.1
AR1-2600	ION	-55.9	-42.5	1760	2.89	9.7	10.1	9.3

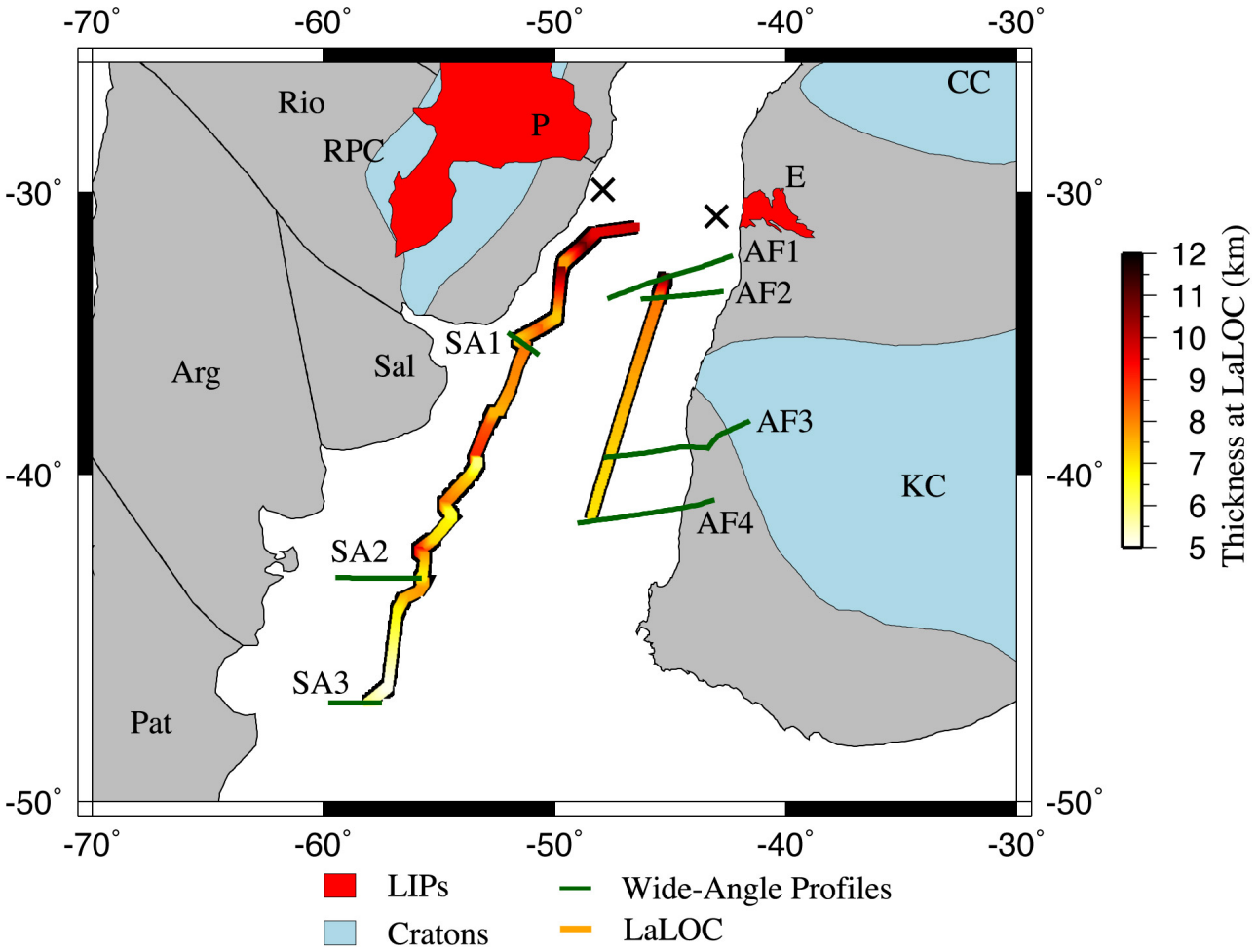


Figure 3.39: Reconstructions using GPlates, shown at 121 Ma using rotation poles of Moulin et al. (2010). Also shown are the sub-plates of South America (thin black lines) and major geological features. The positions of cratons (blue shapes) are from Gubanov and Mooney (2009), the location of the Etendeka-Paraná flood basalts (red shapes) is from Coffin and Eldholm (1994). The '+' mark the reconstructed landfall of the Rio Grande Rise and Walvis Ridge. Sub-plates: Pat = Patagonia, Arg = Argentina, Sal = Salado, Rio = Rio de la Plata. Cratons: RPC = Rio de la Plata Craton, CC = Congo Craton, KC = Kalahari Craton. LIPS: P = Parana, E = Etendeka. Wide-angle profiles shown are Profiles AF1–AF4 & SA1–SA3 (green lines). The thick yellow-red gradient line represents the location of the LaLOC and the measured oceanic thickness at this point from Table 3.2.

Chapter 4

Numerical modelling of Continental Rifting

4.1 Introduction

Although numerous analogue models have been designed to study continental rifting, numerical models have a significant advantage as they have the capability of reproducing rock properties in terms of temperature and stress dependent viscosity, composite rheology, heat conduction and radiogenic heating. Some of the first numerical models of rifting were from Turcotte and Oxburgh (1967) and McKenzie (1967). Turcotte and Oxburgh (1967) had a basic spreading model with no mechanical layer and with large scale convection directly at the sea-floor. McKenzie (1967) on the other hand, had a mechanical layer representing the lithosphere. These were the beginnings of our understanding of the relationship between rifting and magmatism. White and McKenzie (1989) was to be a highly influential 1D model, proposing that temperature was the driving force for the volume of magmatism during break-up, and the *Mantle Plume - VPM Theory* owes a large part of its basis from their initial observation and numerical modelling results.

There have been many numerical models of lithospheric stretching, both kinematic and dynamic, developed to study the formation of rifted continental margins since Turcotte and Oxburgh (1967), McKenzie (1967) and White and McKenzie (1989). Kinematic models were amongst the first models of continental rifting (e.g., Mutter et al., 1988; White and McKenzie, 1989; Scott, 1992; Bown and White, 1994), using an isoviscous mantle that was forced to convect, and continue to be developed (e.g., Dean et al., 2009; Ranero and Pérez-Gussinyé, 2010). Whilst the large majority of kinematic and dynamic models agree on the basic equations of fluid flow, they differ on the choice of rheology and boundary conditions, with fluid dynamic models created using kinematic boundary conditions.

Three main types of models with varying amounts of complexity have emerged with different methods of break-up: (1) simple 2D models that impose break-up within a Cartesian box by applying a velocity to the upper boundary (e.g., Nielsen and Hopper, 2004; Fig 4.1a), (2) the lithosphere moving in opposing directions, where there is a uniform flow of material into the rifting region from the sides (e.g., Huismans and Beaumont, 2011; Fig 4.1b) and (3) the assumption of a uniform horizontal flow away from the centre of rifting, where the rifting zone is replenished with a uniform vertical flow (Phipps Morgan et al., 2015).

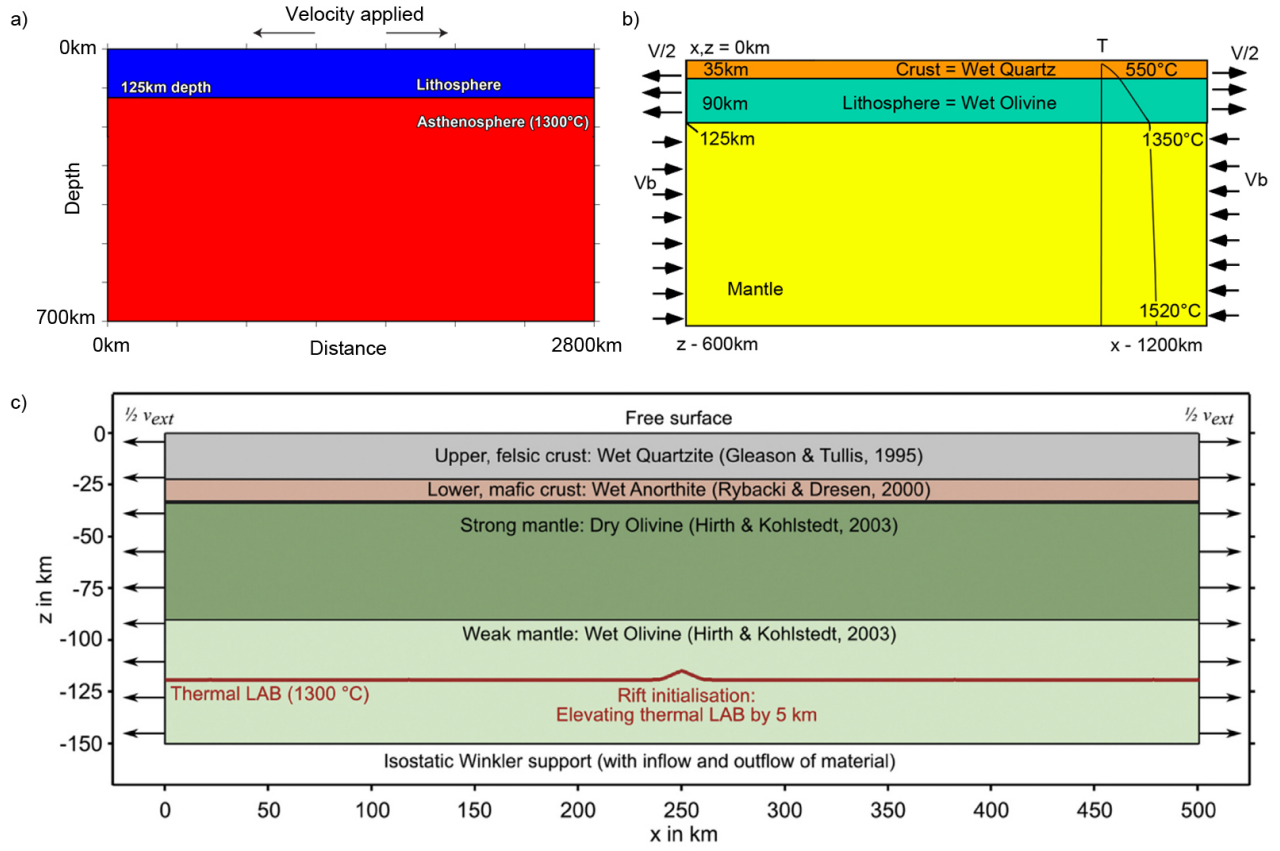


Figure 4.1: Examples of different types of numerical models of rifting, with different lithospheric stretching and depth dependent viscosities. Part (a) represents a uniform stretching model with viscous deformation, and a velocity applied to the upper boundary to simulate rifting. Part (b) is adapted from Huismans and Beaumont (2011), and demonstrates a depth-dependent extension model with a visco-plastic rheology. Rifting is initiated with the lithosphere moving in opposing direction, with material moving into the rifting region from the sides. Part (c) is adapted from Brune et al. (2016) and also shows a depth-dependent visco-plastic extension model, but with a differentiation between strong and weak mantle.

There is also a distinction between models that have a simpler uniform extension of the lithosphere considering only viscous deformation (e.g., Nielsen and Hopper, 2004; Armitage et al., 2011; Fig 4.1a), and those that have a lithosphere with different layers and a depth-dependent extension (e.g., Pérez-Gussinyé et al., 2006; Huismans and Beaumont, 2003, 2011; Fig 4.1b & c). Models that solve for margin structure often consider a visco-plastic rheology (e.g., Pérez-Gussinyé et al., 2006; Huismans and Beaumont, 2014) or even a visco-elastic-plastic rheology (e.g., Petersen et al., 2015), believed to be a more accurate representation of the crust and lithosphere (Brune et al., 2016). These models have the capability of brittle failure in the upper crust and ductile flow in the lower crust and mantle lithosphere. Additionally, as computing power has increased, there is now the capability of building viable 3D models with increasing resolution (e.g., Popov and Sobolev,

2008; Koopmann et al., 2014a). An elastic rheology is necessary in order to recreate flexural deformation of lithospheric plates (Popov and Sobolev, 2008), as demonstrated by Koptev et al. (2015) using a 3D model. With relatively simple initial conditions, Koptev et al. (2015) was capable of reproducing observations from the Central East African Rift, a complex system with both magmatic and amagmatic rift systems.

In this project, a 2D viscous model of the upper mantle to simulate continental break-up is used, with uniform extension and an applied velocity to the upper boundary. It has previously been used to test observations in Southeast Greenland and the Indian Ocean (Nielsen and Hopper, 2004; Armitage et al., 2010, 2011). The numerical model, based on CitCom (California Institute of Technology Convection in the Mantle; Moresi et al., 1996), is a finite element code designed to solve incompressible thermochemical convection problems relevant to the Earth's mantle. It is a fluid dynamic model capable of handling large viscosity contrasts where Stokes equations are solved in a fixed Cartesian domain (Moresi et al., 1996). The model was modified by Nielsen and Hopper (2004) to explore how melt induced changes of the mantle's physical properties due to decompression melting affect the flow of the solid mantle. It was further modified by Armitage (2008) to include major element oxide composition. Equations are solved in 2D, using the Boussinesq approximation where (1) density variations are assumed sufficiently small that they only affect gravitational forces and (2) effect on mantle density due to mass transfer during melting is small (Cordery and Morgan, 1993). Additionally, dislocation creep is used to recreate deformation by dislocation within the lattice or grains, with the latter occurring at high stresses and/or with large grain sizes (Karato and Wu, 1993). As the relationship between stress and strain becomes non-linear, the fluid movement can be described as non-Newtonian (Turcotte and Schubert, 2002). Therefore the model is set up to have a non-Newtonian dislocation creep (Karato and Wu, 1993; Turcotte and Schubert, 2002).

CitCom's modular approach allows for the creation of a modified model by altering its modules, which was also done within this project. The code is based on the White and McKenzie (1989) model, with mantle temperature being the primary factor on melt generation. The model also uses certain aspects from Scott (1992), Boutilier and Keen (1999), Ito et al. (1999). The Scott (1992) model is capable of predicting oceanic crustal thickness similar to those seen in White (1992), but not melt volumes during rifting. It uses large-scale passive flow, with an imposed velocity on the upper boundary. Similar fluid mechanical equations are used for a rheology dependent on temperature and pressure (Armitage, 2008).

The Boutilier and Keen (1999) model found that the formation of volcanic passive margins could be from small-scale convection, not excess temperature. Using a non-Newtonian rheology, small-scale convection was generated with specific density and viscosity conditions, resulting in thickened oceanic crust, albeit with no consistency. Dehydration in the upper 80 km was introduced, stabilising the flow and producing a more uniform oceanic crustal thickness.

Ito et al. (1999) introduced a model capable of explaining observational constraints for the Iceland plume. This was done by incorporating dehydration in the rheological law:

$$\eta = \chi_{H_2O}\, A \exp\left[\frac{E + pV}{RT}\right] \tag{4.1}$$

where η is viscosity, where χ_{H_2O} is the viscosity increase due to dehydration, A is the rheological parameter, E is the activation energy, p is pressure, V is activation volume, R is the gas constant and T is temperature (more details in Table 4.1). The value of χ_{H_2O} increases linearly from 1 to 10 with melt progression. When 2% melt has occurred, the value of χ_{H_2O} is increased to 100 to recreate the dehydration of mantle rocks (Hirth and Kohlstedt, 1996). By introducing a 'dehydrated layer', the model can have a high-temperature and a narrow plume source consistent with geochemical data and the crustal structure.

The fluid dynamical model code used in this project was modified by Nielsen and Hopper (2004). Improving on the small-convection model from Boutilier and Keen (1999) and by implementing the dehydration strengthening by Ito et al. (1999), the rheological law was:

$$\eta = \chi_{H_2O}\, \chi_m\, A\, \dot{\epsilon}^{(\frac{1-n}{n})} \exp\left(\frac{E + pV}{RT}\right) \tag{4.2}$$

where χ_m is the viscosity decrease factor due to interstitial melt, $\dot{\epsilon}$ is the strain rate and n is the stress exponent (Table 4.1). Following the inclusion of dehydration, the resulting viscosity increase suppresses any buoyant upwelling above the dry solidus, eliminating the break-up instability. With the addition of a thermal anomaly layer, the model was capable of matching igneous crustal thickness observations from the Southeast Greenland volcanic rifted margin (Nielsen and Hopper, 2004).

The fluid dynamical model was subsequently modified and used by Armitage et al. (2008), Armitage et al. (2009), Armitage et al. (2010) & Armitage et al. (2011). Armitage et al. (2008) successfully integrated the major and rare-earth primary melt composition parametrisations; this was done through a combination of the Stokes and energy equations, developed by Moresi et al. (1996) and Nielsen and Hopper (2004), to give the modular finite element solver. The code was also made to run stable solutions, following criteria taken from Moresi et al. (1996). The model variables include initial mantle temperature, spreading rate and choice of mantle composition parametrisation (Armitage et al., 2008). It has the capability to explore and examine the evolution of volcanic margins, the thermal and chemical nature under margins, in addition to seeing the effect of initial temperature structure and early spreading rates (Armitage et al., 2008).

Due to the model only considering a viscous rheology, it does not have the capability of studying margin structure and asymmetry between conjugate margins, unlike models with a visco-elastic rheology or visco-elastic-plastic rheology (e.g., Pérez-Gussinyé et al., 2006; Popov and Sobolev, 2008; Brune et al., 2016). However, due to its many attributes and flexibility at adaptation, the fluid dynamic model used here is an excellent tool to study continental break-up along volcanic margins through melt volumes and melt compositions. The model, having already been used for the North Atlantic and Indian Oceans, is now being used to test how the thermal

structure of the mantle varies along strike in the southern South Atlantic.

Table 4.1: Variables used for 2D-modelling, as used in previous iterations of the model (Nielsen and Hopper, 2004; Armitage, 2008; Armitage et al., 2008, 2009, 2010, 2011).

Variable	Definition	Value
A	rheological parameter	
c_p	specific heat capacity, $\mathrm{J\,kg^{-1}\,K^{-1}}$	1200
C_l	weight percent melt/liquid composition, %	
C_s	weight percent solid residue composition, %	
D	composition partition coefficient	
d	reference length, km	700
g	acceleration of gravity, $\mathrm{m\,s^{-2}}$	9.8
E	activation energy, $\mathrm{J\,mol^{-1}}$	$530\,\mathrm{x}\,10^3$
F	melt fraction	
h_c	crustal thickness, km	
L	latent heat upon melting, $\mathrm{J\,mol^{-1}}$	
$\dot{m}$	dimensionless melt production rate	
n	stress exponent	3
p	pressure, Pa	
R	gas constant, $\mathrm{J\,K^{-1}\,mol^{-1}}$	8.314
Ra	Rayleigh number	$4.877\,\mathrm{x}\,10^5$
T	mantle temperature, K	
T_d	super-adiabatic temperature drop, K	
T_m	mantle reference temperature, K	
T_s	wet or dry solidus temperature, K	
T_{s0}	dry solidus surface temperature, K	
u	mantle creep, $\mathrm{m\,s^{-1}}$	
V	activation volume, $\mathrm{J\,mol^{-1}}$	$5\,\mathrm{x}\,10^{-6}$
X	concentration of perfectly compatible trace element	
x	displacement, km	
z	depth, km	
α	coefficient of thermal expansion, $\mathrm{K^{-1}}$	$3.3\,\mathrm{x}\,10^{-5}$
$\dot{\epsilon}$	strain rate, $\mathrm{s^{-1}}$	
η	viscosity, Pa s	
η_0	reference viscosity, Pa s	10^{20}
κ	thermal diffusivity, $\mathrm{m^2\,s^{-1}}$	10^{-6}
λ_i	unit vector in vertical direction	
ϕ	retained melt (porosity)	
$\Delta\rho$	density change due to temperature and melt generation, $\mathrm{kg\,m^{-3}}$	
ρ_m	mantle reference density, $\mathrm{kg\,m^{-3}}$	3340
ρ_l	melt density, $\mathrm{kg\,m^{-3}}$	2800
τ_{ij}	deviatoric stress, Pa	
χ_{H_2O}	viscosity increase due to dehydration	
χ_m	viscosity decrease factor due to interstitial melt	

4.2 Equations of Conservation

The dynamics of the system are solved by equations of thermal convection. They are expressed in tensor notation with the understanding that repeat indices are summed. The conservation of mass, momentum and energy are calculated by:

$$\frac{\partial u_i}{\partial x_i} = 0 \tag{4.3}$$

$$-\frac{\partial \tau_{ij}}{\partial x_j} + \frac{\partial p}{\partial x_i} = \Delta\rho g \lambda_i \tag{4.4}$$

$$\frac{\partial T}{\partial t} = -u_i \frac{\partial T}{\partial x_i} + \kappa \frac{\partial^2 T}{\partial x_j^2} - \frac{L\dot{m}}{c_p} \tag{4.5}$$

where u is the solid mantle creep, x is the displacement in the horizontal and vertical directions, τ_{ij} is the deviatoric stress tensor, p is the pressure, $\Delta\rho$ is the density change due to temperature and melt generation, g is the gravity, λ_i is the unit vector in the vertical direction, T is the mantle temperature, t is time, κ is the coefficient of thermal diffusion, L is the latent heat of melting, $\dot{m}$ is the melt production rate and c_p is the specific heat capacity (nomenclature found in Table 4.1).

4.3 Decompression Melting

The effect of decompression melting is included within the model, and it considers the effect of mantle depletion and dehydration. In order to track the melt production, a perfectly compatible trace element X is introduced (Scott, 1992). The element is advected with the solid mantle, and is enriched as melt production increases. X is given as:

$$\frac{\partial X}{\partial t} + u_i \frac{\partial X}{\partial x_i} = \frac{X}{1-\phi}\,\dot{m} \tag{4.6}$$

where ϕ is melt volume and $\dot{m}$ is melt production rate. When no melting has occurred, the concentration of $X = 1$. The value of X is always positive throughout melting. By assuming batch melting for each time step, the value of X can be associated to the degree of depletion due to F, the melt fraction, calculated following Scott (1992) by using

$$X\,(1-F) = 1\ . \tag{4.7}$$

The conservation of energy (Eq. 4.5) and the continuity of the concentration of X (Eq. 4.6) are linked by the melt production rate $\dot{m}$, in turn dependent on the definition of the dry solidus temperature, T_s. The latter is calculated by finding the position of the wet and dry solidus (Fig. 4.2) for each timestep (Nielsen and Hopper,

2004). Whilst the solidus is usually a function of depth (as per Scott, 1992 and Phipps Morgan, 2001), in this case it is considered as a function of depth and depletion, tracked by the perfectly compatible element X.

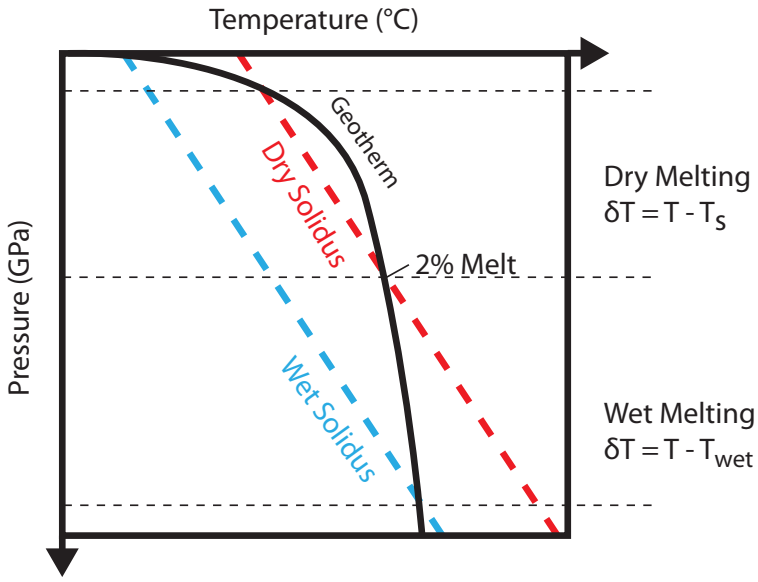


Figure 4.2: Schematic demonstrating the difference between wet (blue dashed line) and dry (red dashed line) solidus melting regimes. The geotherm (thick black line) is compartmentalised between regions of wet and dry melting. Depending on the melting regime, the calculation of δT is different within the equation for melt production (Eq. 4.12). Adapted from Armitage (2008).

The dry solidus is calculated by

$$T_s^{real} = T_{s0} + z\left(\frac{\partial T_s}{\partial z}\right)_X + \left(\frac{\partial T_s}{\partial X}\right)_z (X-1) \tag{4.8}$$

where T_s^{real} is the temperature of the solidus, T_{s0} is the dry solidus surface temperature, T_s is the dry solidus defined by depth only, and z is the depth. As the solidus is defined not only by depth but also depletion, the solidus-depth gradient has to be adjusted to include the adiabatic gradient. This is calculated by

$$\left(\frac{\partial T}{\partial z}\right)_s = \frac{g\alpha T}{c_p} \ , \tag{4.9}$$

where α is the coefficient of thermal expansion. The solidus can now be defined as:

$$T_s = T_{s0} + z\left(\left(\frac{\partial T_s}{\partial z}\right)_X - \left(\frac{\partial T}{\partial z}\right)_s\right) + \left(\frac{\partial T_S}{\partial X}\right)_z (X-1) \ . \tag{4.10}$$

Mantle volatiles will preferentially partition into the melt as decompression melting occurs. Wet melting is considered to occur until 2% of melt is produced, where $\Delta X = X - 1 < 1.02$ (Fig. 4.2; Hirth and Kohlstedt, 1996). Once 2% melt has been achieved, the depleted residue is considered to no longer hold any volatiles and melting is dry (Hirth and Kohlstedt, 1996). Following Braun et al. (2000), the wet solidus is calculated by

$$T_{wet} = T_s - 200\,\frac{1.02 - X}{\Delta X} \quad . \tag{4.11}$$

If the potential temperature exceeds the solidus, melting will occur (Fig. 4.2). The amount of melting is calculated for each timestep, following Scott (1992)

$$\delta m = \frac{\delta T}{\frac{L}{c_p} + \frac{\partial T_s}{\partial \phi}} \tag{4.12}$$

where T_s is the temperature of the dry solidus, ϕ is the retained melt, and $\delta T = T - T_s$ or $\delta T = T - T_{wet}$ depending if it is in the dry or wet melting regime respectively. Additionally, the calculation of the differential $\partial T_s/\partial \phi$ is different for the wet and dry melting regime (from Braun et al., 2000). It is calculated for the dry regime by

$$\frac{\partial T_s}{\partial \phi} = 440\,\frac{X}{1 - \phi} \tag{4.13}$$

and for the wet regime by

$$\frac{\partial T_s}{\partial \phi} = 1440\,\frac{X}{1 - \phi} \quad . \tag{4.14}$$

After the establishment of the melting regime, the melt production rate can be calculated by

$$\dot{m} = \frac{\delta m}{\delta t} \quad , \tag{4.15}$$

where δt represents the advection time step. Following Ito et al. (1996), the crustal thickness h_c can be calculated by

$$h_c = \frac{2}{u_z}\left(\frac{\rho_m}{\rho_l}\right)\int\int_{melt} \dot{m}\,dx\,dz \tag{4.16}$$

where u_z is the velocity of the movement of mantle material in the vertical direction, ρ_m is the density of the lithospheric mantle, ρ_l is the melt density. For each timestep, there is the assumption that all melt generated erupts at the centre of extension and is removed.

4.4 Calculation of Major Element Oxide Composition

In addition to calculating crustal thickness, the numerical model has the capability of calculating major element oxides during break-up through to a steady-state system. The major element compositions of accumulated melt is a function of temperature, pressure and melt fraction. To estimate the melt composition, two empirical parametrisations are compared: Watson and McKenzie (1991), or WM91, and Niu (1997), or N97. Their methods of calculation are different, and hence their major element oxide compositional results will also be different.

WM91 calculates melt composition related only to total melting. It relates the instantaneous melt composition of aluminium, iron, magnesium, calcium, sodium, potassium, titanium and 'the rest' to the degree of melt, where 'the rest' include all other elements bar silicon. Silicon content is found as the difference between the total and summation of all others. Watson and McKenzie (1991) based their parametrisation on the same model as McKenzie and Bickle (1988), where the major element oxides were calculated through fitting polynomial functions to batch melting experiments, essentially 'back calculating' from a bulk silicate earth state. Although WM91 uses the same bulk silicate earth composition from McKenzie and Bickle (1988) (Table C3), it was modified to maintain consistency with the olivine/liquid partition coefficient for iron and magnesium oxides. Using an empirical formula, the instantaneous melt composition (C_l) can be calculated:

$$C_l = a + b(1 - F)^{\frac{1-D}{D}} \quad , \tag{4.17}$$

where a range of experimental data was used to estimate a, b and D (Appendix C in Watson and McKenzie, 1991), and F is the fraction of melt generated, which can be associated to perfectly compatible trace element X using Eq. 4.7. The WM91 parametrisation has some limitations: calcium oxide tends to be overestimated at low fractions of melting, and the bulk composition of sodium oxide may also be overestimated (Langmuir et al., 1992). Despite this, it is a robust, relatively easy to use quantitative parametrisation (Armitage et al., 2008).

N97 uses solid residue and determines the ratio of a particular oxide within solid and liquid phases by calculating partition coefficient D in order to calculate major element oxides (Niu, 1997):

$$D = \frac{C_s}{C_l} \quad , \tag{4.18}$$

where C_s is the weight percent solid composition and C_l is the liquid composition. By using a range of experimental data (Jacques and Green, 1980; Falloon et al., 1988; Hirose and Kushiro, 1993), the apparent partition coefficient D is found for the major element oxides as a function of temperature and degree of melting. The coefficient partition, calculated at each time step for each major element oxide, is then used to construct

a mass balance.

Unlike WM91, the bulk earth composition can be changed in the N97 parametrisation and different types of mantle can be tested for. MORB pyrolite and a peridotite are compared. Pyrolite, a theoretical rock and a model for composition of the upper mantle, where values from Falloon and Green (1987) were used, is referred to as N97-FG87. Peridotite, a coarse grained ultra-basic rock, believed to be the main constituent of the Earth's upper mantle, where values from Hirose and Kushiro (1993) were used, is referred as N97-HK93. A bulk earth composition based on peridodite is considered the better choice as it was shown to be more accurate when calculating predictions in composition (Behn and Grove, 2015; Robinson et al., 1998; Hirschmann et al., 1998).

In order to incorporate WM91 and N97 into the model, pressure and degree of depletion is extracted at every node. Pressure is determined by the known depth and density of above material, whilst degree of melt depletion is tracked by a compatible trace element X (Eq. 4.6 & 4.7), known at every node point. For WM91, if melt is present, the composition is then calculated using a relatively simple look-up table (Armitage, 2008). For N97, the partition coefficients are calculated for each major element oxide based on a range of experimental data.

Previous iterations of this model calculated mean melt composition following Watson and McKenzie (1991), where integrals are found over the melt region, and the weighted mean composition (C) is found for each element oxide i. To do this, composition is weighted by melt fraction F (Watson and McKenzie, 1991):

$$\overline{C}_i = \frac{\int\int_{melt} FC_i \, dxdz}{\int\int_{melt} F \, dxdz} \tag{4.19}$$

where all melt is removed instantaneously from up to 100 km in depth. There is some debate if this can be justified (e.g., Armitage et al., 2009). Behn and Grove (2015) however suggested using melt production rate (Eq. 4.15) to calculate the mean composition:

$$\overline{C}_i = \frac{\int\int_{melt} \dot{m} C_i \, dxdz}{\int\int_{melt} \dot{m} \, dxdz} \ . \tag{4.20}$$

Scaling relations within the asthenosphere show the domination of melt buoyancy over mantle pressure gradients on melt migration (e.g., Spiegelman and McKenzie, 1987; Morgan, 1987; Montesi et al., 2011), and the assumption of vertical melt migration, and thus the use of melt production, can be justified (Behn and Grove, 2015). This method was implemented for the model within this project, by editing the module relating to calculation of major element oxides.

In order to choose the most appropriate composition parametrisation, a comparison will be made within this project between normalised values of Mid-Atlantic Ridge (MAR) dredge samples and basement-reaching

DSDP samples (**Appendix B**) to major oxides element compositions from model results (**Chapter 6**).

4.4.1 Calculation of seismic velocity from major element oxides

An empirical formula using major element oxides was used to calculate seismic velocity. A relationship between seismic velocity and major element composition was derived by Kelemen and Holbrook (1995), using published laboratory experiments. They looked at seismic velocity of igneous and meta-igneous rocks, using pressures similar to that of the lower crust, to derive a multiple linear regression using SiO_2 and MgO with an accuracy of $\pm\,0.19 km\,s^{-1}$. This was further explored by Behn and Kelemen (2003), who constructed a linear relationship between seismic velocity and composition using P-wave velocities calculated from synthetic data. Valid for all igneous compositions, they found multiple linear regression results linking seismic velocity to SiO_2, MgO and CaO (Eq. 4.21). Additional major element oxides were found to not improve the fit significantly. This function was found to have an accuracy of ± 0.13 km s^{-1} and was valid for a depth range of 5 - 50 km. This formula (Eq. 4.21) was used for future calculations of seismic velocity:

$$V_p = 6.90 - 0.011\,wt\%\,SiO_2 + 0.037\,wt\%\,MgO + 0.045\,wt\%\,CaO \tag{4.21}$$

4.5 Model Set-Up

4.5.1 Dimensions

The main equations of flow (Eqs. 4.3, 4.4 and 4.5) are made non-dimensional by the following,

$$x = dx',\ t = \frac{d^2}{\kappa}t',\ T = T_d T',\ \eta = \eta_0 \eta' \tag{4.22}$$

where d is the depth of the model space and T_d is the steep temperature drop (classified as super adiabatic) from the surface of the model to depth d.

The Rayleigh number is defined as,

$$Ra = \frac{\alpha g \rho T_d d^3}{\kappa \eta_0} \tag{4.23}$$

where α is the coefficient of thermal expansion and g is the acceleration due to gravity. The Rayleigh number is set to 4.877×10^6, using a scaling viscosity (η_0) of 1×10^{20} Pa s (Armitage et al., 2013, 2015). The viscosity has been previously defined in Eq. 4.2, where Nielsen and Hopper (2004) incorporated elements from Boutilier and Keen (1999) and Ito et al. (1999) (Section 4.1).

4.5.2 Model space

The model space has a domain 2,800 km wide, 700 km deep with a grid dimension of 256 x 256 elements, or a resolution of 10.94 km x 5.47 km. A hot layer is used to recreate the presence of a mantle plume (Fig. 4.3). Temperature and melting residue (defined by perfectly compatible element X) are prescribed for each node. The initial lithosphere is assumed to be melt depleted and is therefore compositionally buoyant relative to the asthenosphere (Fig. 4.5a; Armitage et al., 2010). By having a surface velocity boundary condition at a fixed spreading rate, extension is imposed, driving the lithosphere apart laterally (Fig. 4.5b & 4.4b). As the lithosphere extends and thins, material moves upwards leading to decompression melting (Fig. 4.5c & 4.4c). The number of timesteps is user defined, and the model is run in an iterative manner until the n^{th} timestep is reached (Fig. 4.6). A timestep is completed when the model solves the Stokes Equations of creeping flow (Eq. 4.3, 4.4 & 4.5) and meets the stability conditions for Petrov-Galerkin solver (Armitage, 2008).

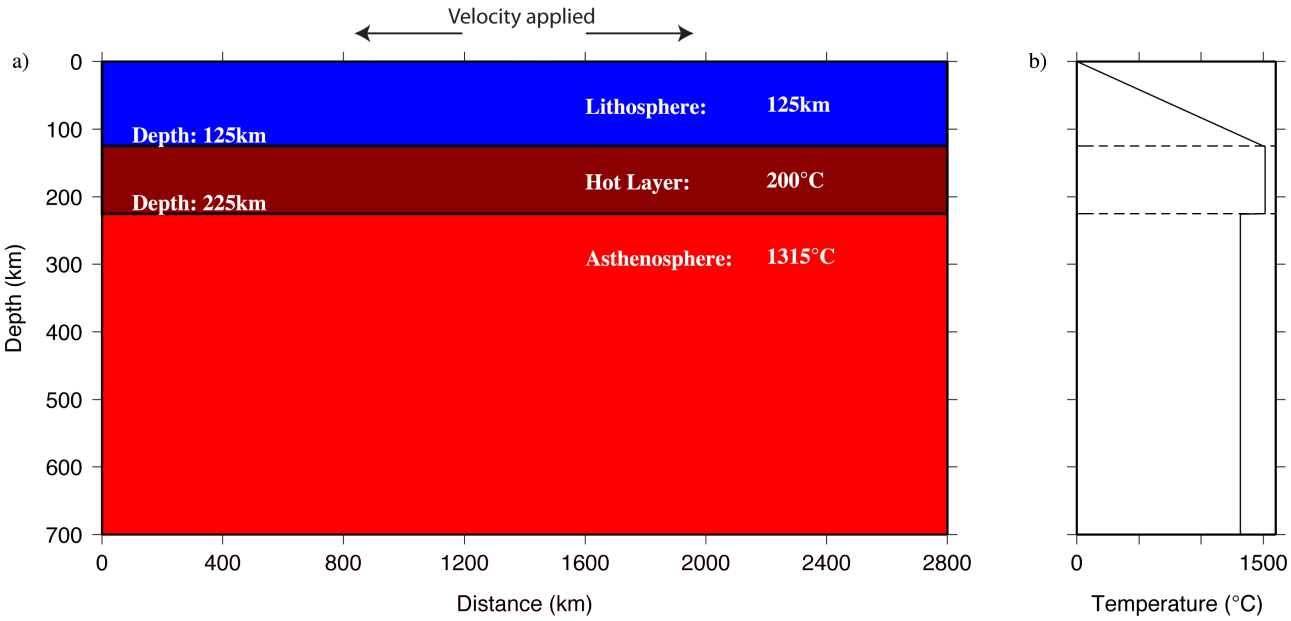


Figure 4.3: Example of the initial conditions for the numerical model. Part (a) is the model domain for the 2D simulation. Extension is driven by a divergent velocity boundary condition on the upper surface. The initial lithosphere thickness is within the range of 95 and 140 km, and the hot layer is assumed to have a thickness of 100 km and a temperature of 50 to 200 °C in excess of the model asthenosphere temperature. (b) An example of an initial temperature profile with depth, where in this case the model asthenosphere temperature is 1315 °C and the hot layer has an excess temperature of 200 °C.

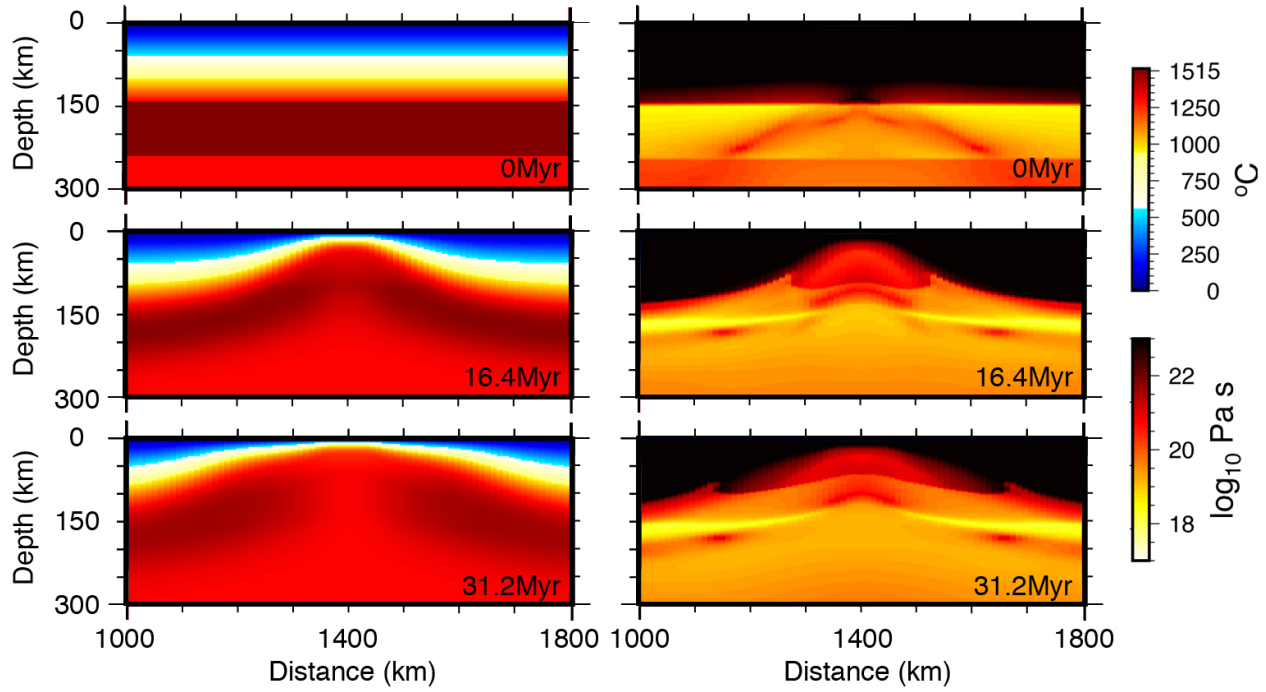


Figure 4.4: A comparison of the model at different timesteps in terms of evolving temperature and viscosity. Same as Fig. 4.5, but zoomed to the centre of extension, between a depth of 0 to 300 km and a distance of 1000 to 1800 km.

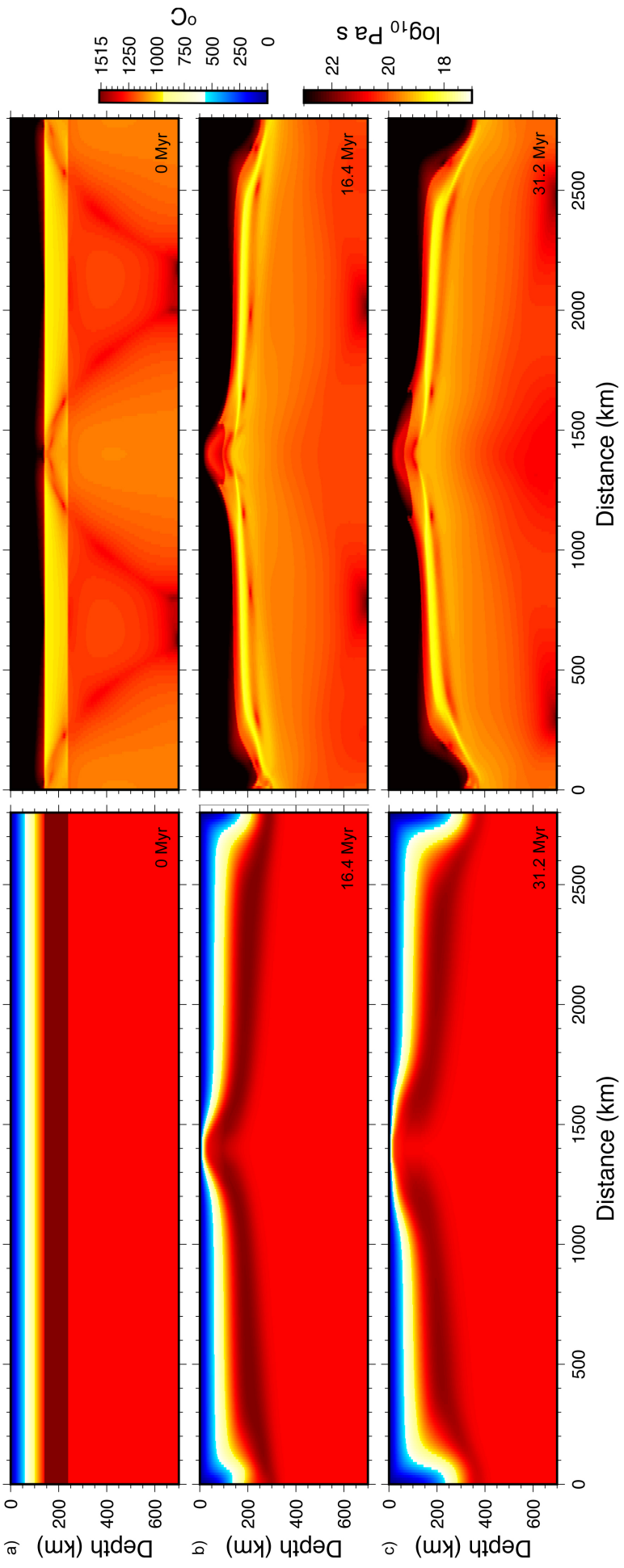


Figure 4.5: A comparison of the model at different timesteps in terms of evolving temperature and viscosity. There is a 200 °C hot layer, with a lithosphere thickness of 140 km and spreading rate of 12 mm yr^{-1}. Part (a) represents the model at 0 Myr, similar to Fig. 4.3. Part (b) represents the model at 16.4 Myr approximately matching peak melt thickness during the syn-rift phase (Fig. 4.9), and part (c) represents the model at 31.2 Myr, in the post-rift phase. In parts (b) and (c) the zone of partial melting is observed at the centre top of the model. The reflective boundaries can be seen in (b) and (c), and are considered far enough not to affect melt thickness production. Centre of extension showed in focus in Fig. 4.4.

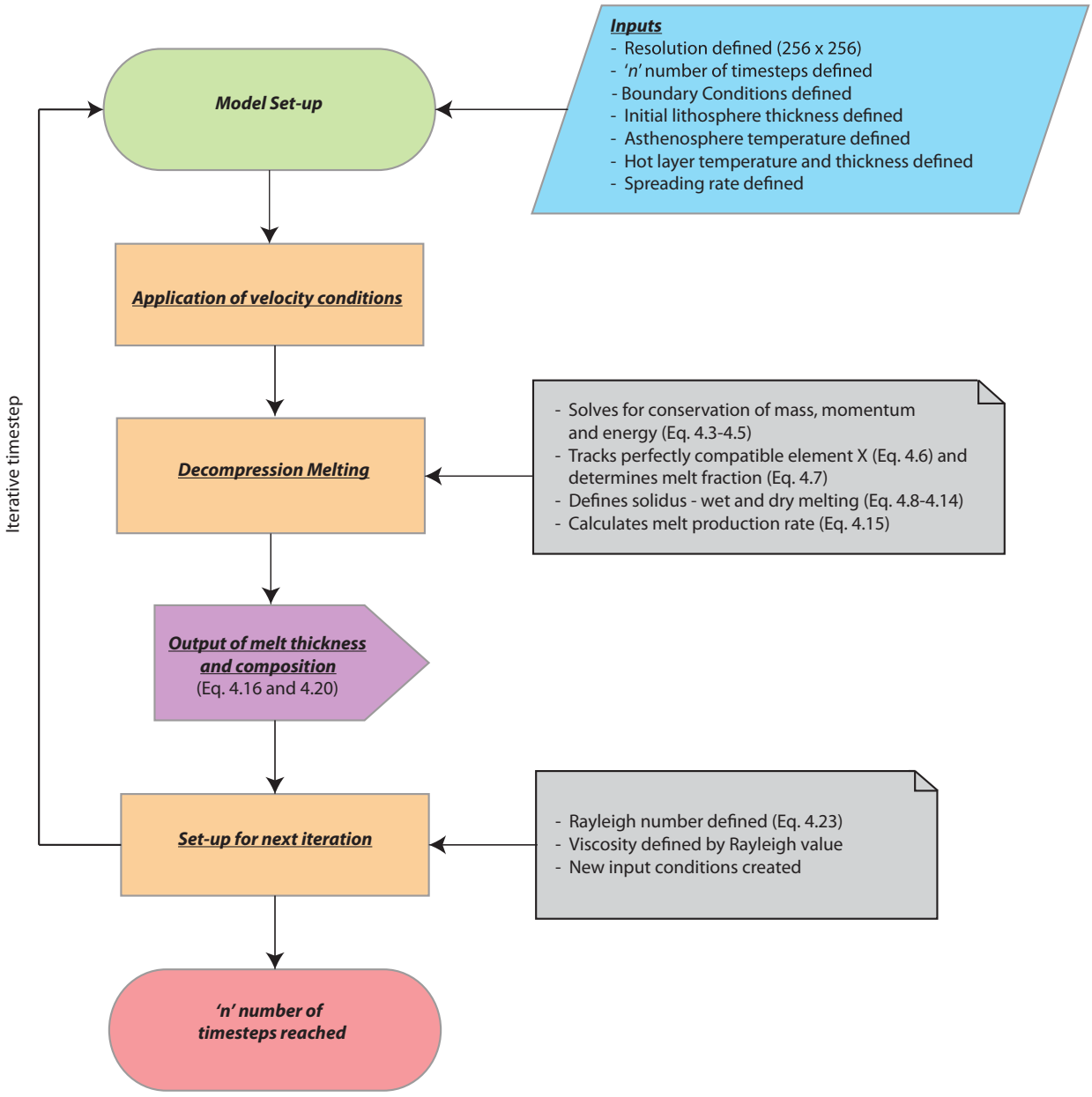


Figure 4.6: Basic flowchart for the CitCom model. The green box represents the start of the model, blue box represents inputs, light orange boxes represent processes, grey boxes represent notes, the purple box represents the output and the light red box represents the end of the model.

4.6 Model Sensitivities: the Choice of Parameters

To understand the sensitivities of the model, a simple simulation with a model asthenosphere temperature of 1300 °C, spreading velocity of 12 mm yr^{-1}, and an initial lithosphere thickness of 125 km was run as a base model. The model has previously been extensively tested by Nielsen and Hopper (2004) and Armitage (2008). For this project, different parameters were tested: (1) a higher resolution, (2) an increase in model asthenosphere temperature, (3) the introduction of a hot layer, (4) different spreading velocities, (5) changes in initial lithosphere thickness and (6) choice of composition parametrisation.

4.6.1 Resolution

The difference between a 256 x 256 and 512 x 512 resolution was tested for this project by running models with the different resolutions but same initial conditions (Fig. 4.7). The difference in predicted crustal thickness was found to be on average of 0.65% (Fig. 4.7), and thus the less computationally expensive resolution (256 x 256) was used.

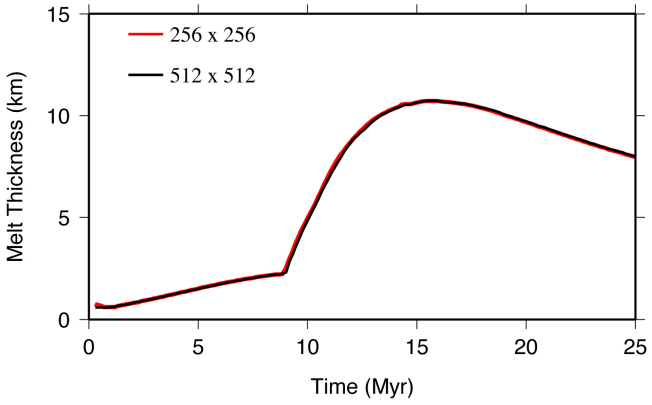


Figure 4.7: Two models run with different resolutions: 256 x 256 (thicker red line) and 512 x 512 (thinner black line). Both models have a 1315 °C mantle asthenosphere temperature, an initial lithosphere thickness of 125 km, a spreading rate of 12 mm yr^{-1} and a hot layer an excess temperature of 200 °C. There is an average of 0.65% difference of crustal thickness between the two resolutions.

4.6.2 Temperature, spreading rate and lithosphere thickness

In this section, four main parameters are tested: mantle asthenosphere temperature, hot layer temperature, spreading rate and initial lithosphere thickness. First, a model with no hot layer was run with varying mantle asthenosphere temperatures (Fig. 4.8). The choice of the model asthenosphere temperature range is crucial, with a change in temperature of 12.5 °C accounting for melt thickness changes by up to 1 km (McKenzie et al., 2005). A similar range is seen for this numerical model, with a change in temperature of 10 °C accounting for melt thickness changes by up to 1 km (Fig. 4.8).

Secondly, a model with no hot layer, a hot layer of 100 °C and 200 °C were run. Three main stages of melt production based on the quantity of magmatism can be seen for the model as the lithosphere thins and is finally broken (Fig. 4.9): pre-rift, syn-rift and post-rift. The pre-rift stage is where there is little magmatism

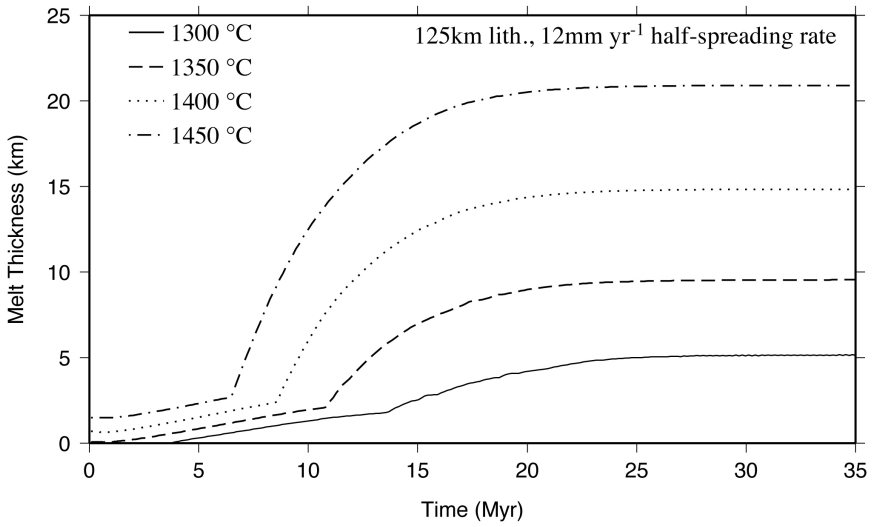


Figure 4.8: Varying model asthenosphere temperatures, with initial lithosphere thickness of 125 km and spreading rate of 12 mm yr^{-1}.

and syn-rift is where there is a magmatism peak. There is a clear increase in output magmatism as the hot layer temperature increases, with ∼3 times as much for the 200 °C hot layer relative to no hot layer (Fig. 4.9). Following the peak magmatism in the syn-rift phase, the post-rift phase represents a shift towards steady-state sea floor spreading (Fig. 4.9). The hottest model, with a thermal anomaly 200 °C hotter than the model

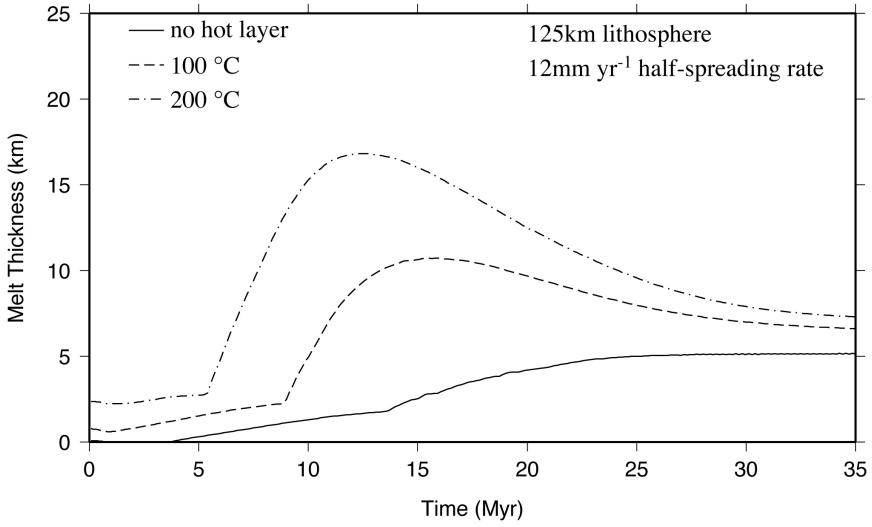


Figure 4.9: Varying hot layer temperatures, with a 1300 °C model asthenosphere temperature. Model has an initial lithosphere thickness of 125 km and spreading rate of 12 mm yr^{-1}.

asthenosphere temperature, displayed peak melt production ∼3 Myr earlier than the equivalent model with a 100 °C hot thermal anomaly (Fig. 4.9). For model runs without a hot layer present, there is no peak in magmatism for any of the models.

Next, models with varying spreading rates were run, with rates of 5, 10 and 20 mm yr^{-1} (Fig. 4.10). A varying spreading rate will affect the timing of peak melting, where doubling the rate of extension will reduce the time needed to reach steady state by at least half. When a hot layer is present, the model with the faster spreading rate has a larger pulse of decompression melting, as the faster rate causes a greater amount of material to be fluxed through the zone of partial melting (Fig. 4.5b and c). A slower spreading rate will significantly increase the duration of rifting and the time taken by the model to ultimately reach steady state. Although a model with a 20 mm yr^{-1} rate reaches peak melt thickness first, the total melt area over 35 Myr is ∼319 km^2,

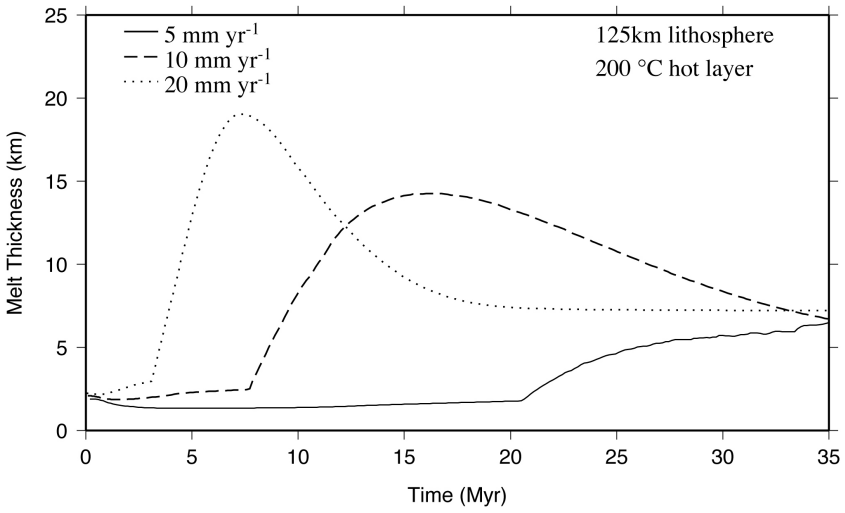


Figure 4.10: Differing spreading rates with a 1300 °C model asthenosphere temperature, a 200 °C hot layer and an initial lithosphere thickness of 125 km.

similar to that of a model with a 10 mm yr^{-1} rate, with a melt area of ∼305 km^2 in the same timespan. The lower spreading rate of 5 mm yr^{-1} takes ∼70 Myr years to achieve a similar melt area, due to the hot layer being exhausted with a slower spreading rate.

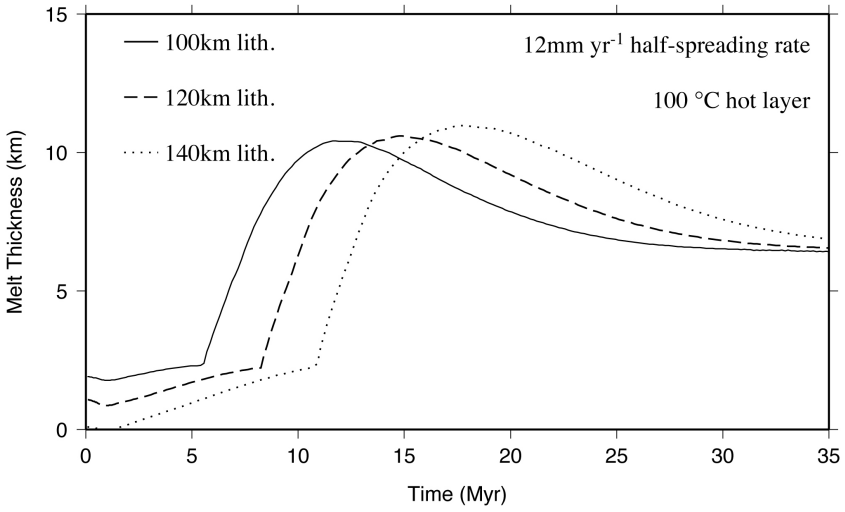


Figure 4.11: Differing initial lithosphere thickness, with a 1300 °C model asthenosphere temperature and 100 °C hot layer.

Finally, from varying the initial lithosphere thickness and hot layer temperature, the time of maximum melt production is found to be a function of both of these (Fig.. 4.11). A thinner lithosphere (100 km) is found to reach peak melt first, as it will extend and thin allowing for faster decompression melting, whilst a thicker lithosphere (140 km) can take up to an additional ∼8 Myr to reach this point.

4.6.3 Composition parametrisation and major element oxides

In addition to the calculation of crustal thickness, the model is capable of calculating major element oxide compositions. There are two methods with which to calculate compositions (melt depletion and melt production), and two composition parametrisations to choose from (WM91 and N97). The difference in composition results using melt depletion (Eq. 4.19) and melt production (Eq. 4.15) was tested for WM91 and N97-FG87 (Fig. 4.12 & 4.13), revealing similar trends for all major element oxides. As Behn and Grove (2015) considered calculating composition using melt production was a more realistic method, with the domination of melt buoyancy over mantle pressure gradients on melt migration, and the assumption of vertical melt migration, melt production (Eq. 4.15) was used henceforth to calculate composition.

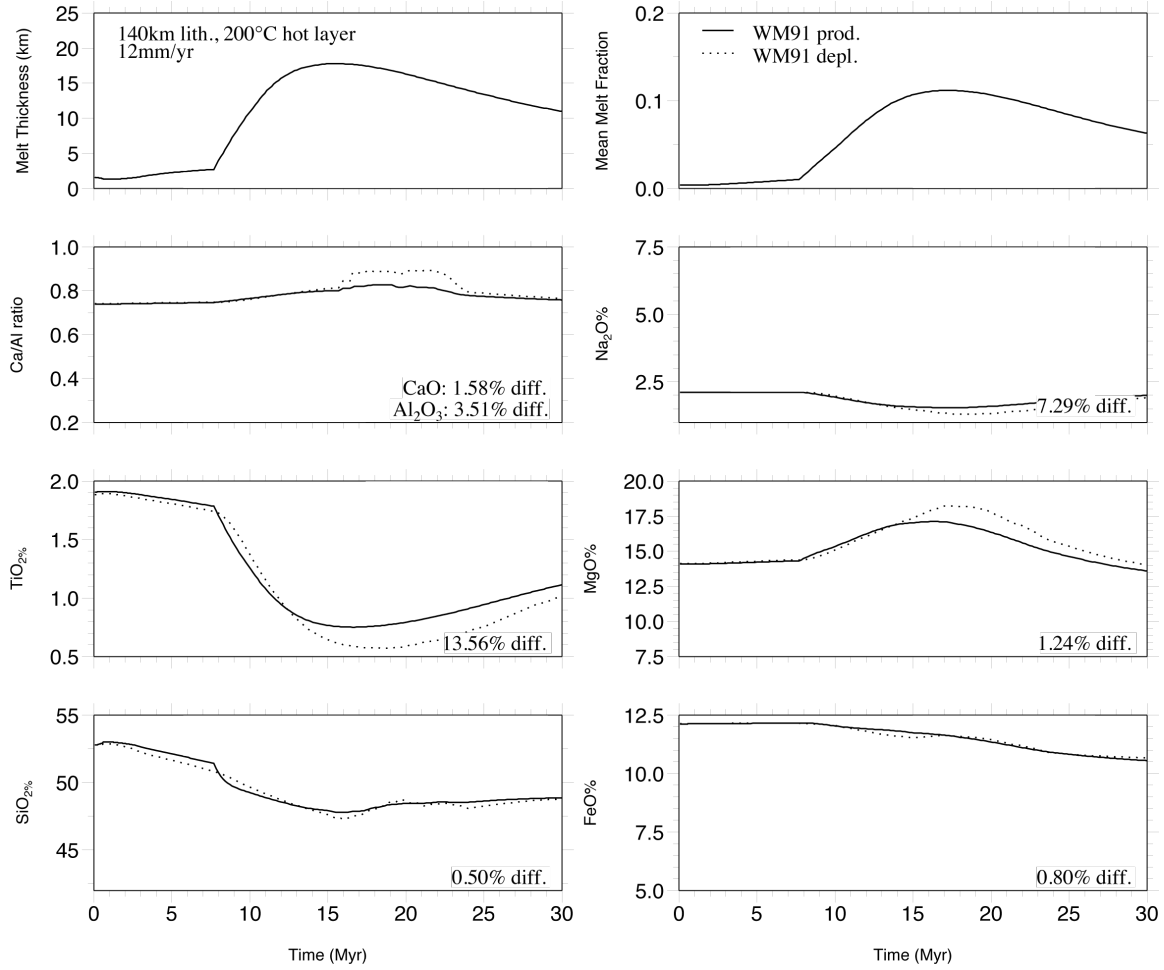


Figure 4.12: Melt production vs Melt depletion for WM91 for major element oxides. Models have a mantle asthenosphere temperature of 1315 °C, an initial lithosphere thickness of 140 km, a hot layer of 200 °C and a spreading rate of 12 mm yr^{-1}. Two models are run here using the WM91 composition parametrisation, using melt production (new method developed by Behn and Grove (2015) and implemented within this project) and melt depletion (original method). Melt fraction was predicted through the use of perfectly compatible trace element X (Eq. 4.6 & 4.7). The percentage differences in the bottom left corner of each major element oxide output represents the mean percentage difference between melt production and depletion.

To demonstrate the difference between the composition parametrisations, models using the melt production calculation were run with an initial lithosphere thickness of 140 km, a hot layer of 200 °C and differing composi-

tion parametrisations (Fig. 4.14). Several similar trends for WM91, N97-FG87 and N97-HK93 were identified. At low melt fraction values, NaO and TiO_2 are incompatible and partition early on (Fig. 4.14). As melting continues and increases, there is an increase in more compatible elements, such as MgO, SiO_2 and FeO, as seen for both N97 models. By using the Ca/Al ratio, the ratio for clinopyroxene and plagioclase can be studied. With increasing melt fractions, the exhaustion of clinopyroxene (Hirose and Kawamura, 1994; Hirschmann et al., 1998) is seen by a peak in the ratio of Ca/Al in the N97 models but not for WM91.

In order to choose the most appropriate composition parametrisation, a comparison will be made to normalised values of Mid-Atlantic Ridge (MAR) dredge samples and basement-reaching DSDP samples (**Appendix B**; Fig. B.1; Tables B.1 and B.2) to model results (**Chapter 6**).

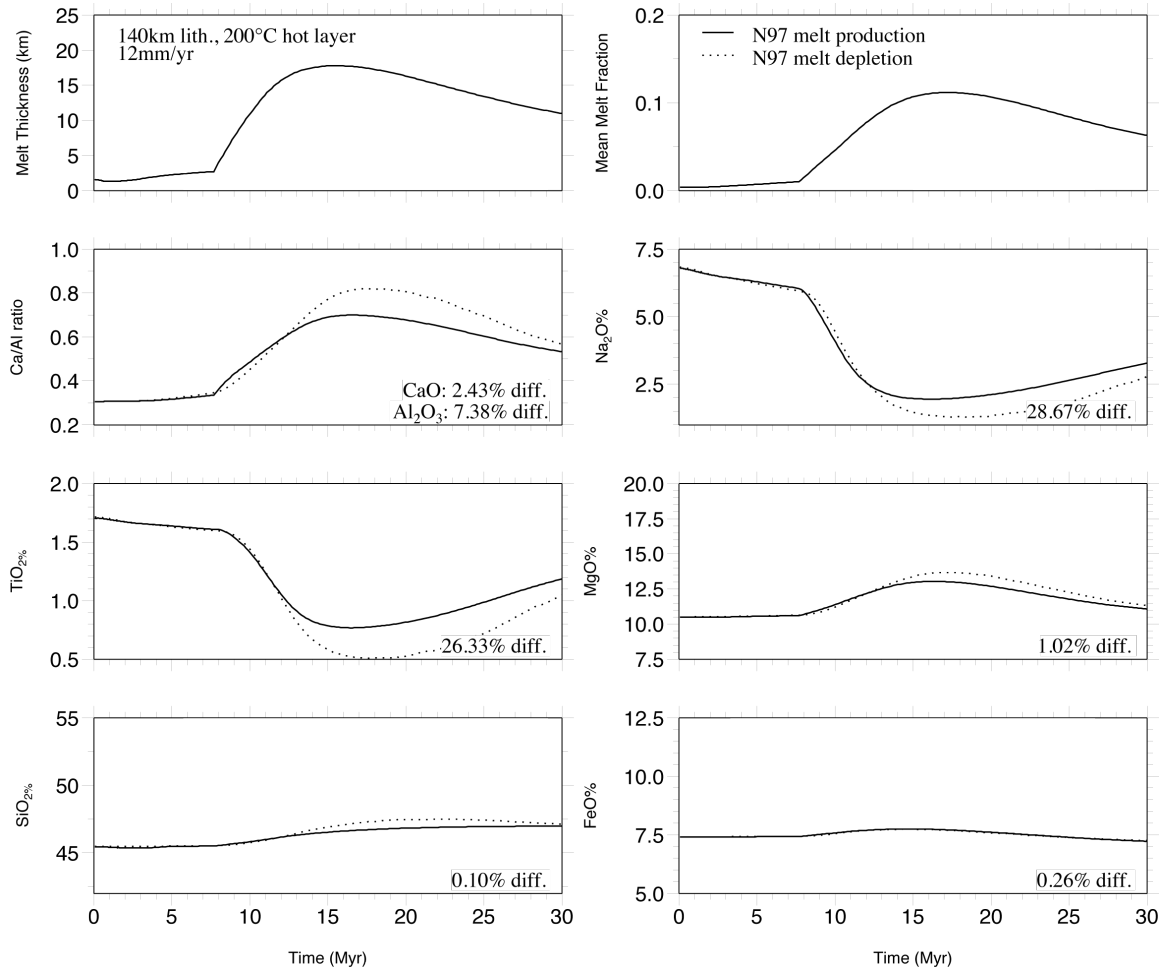


Figure 4.13: As Fig. 4.12, but for composition parametrisation N97.

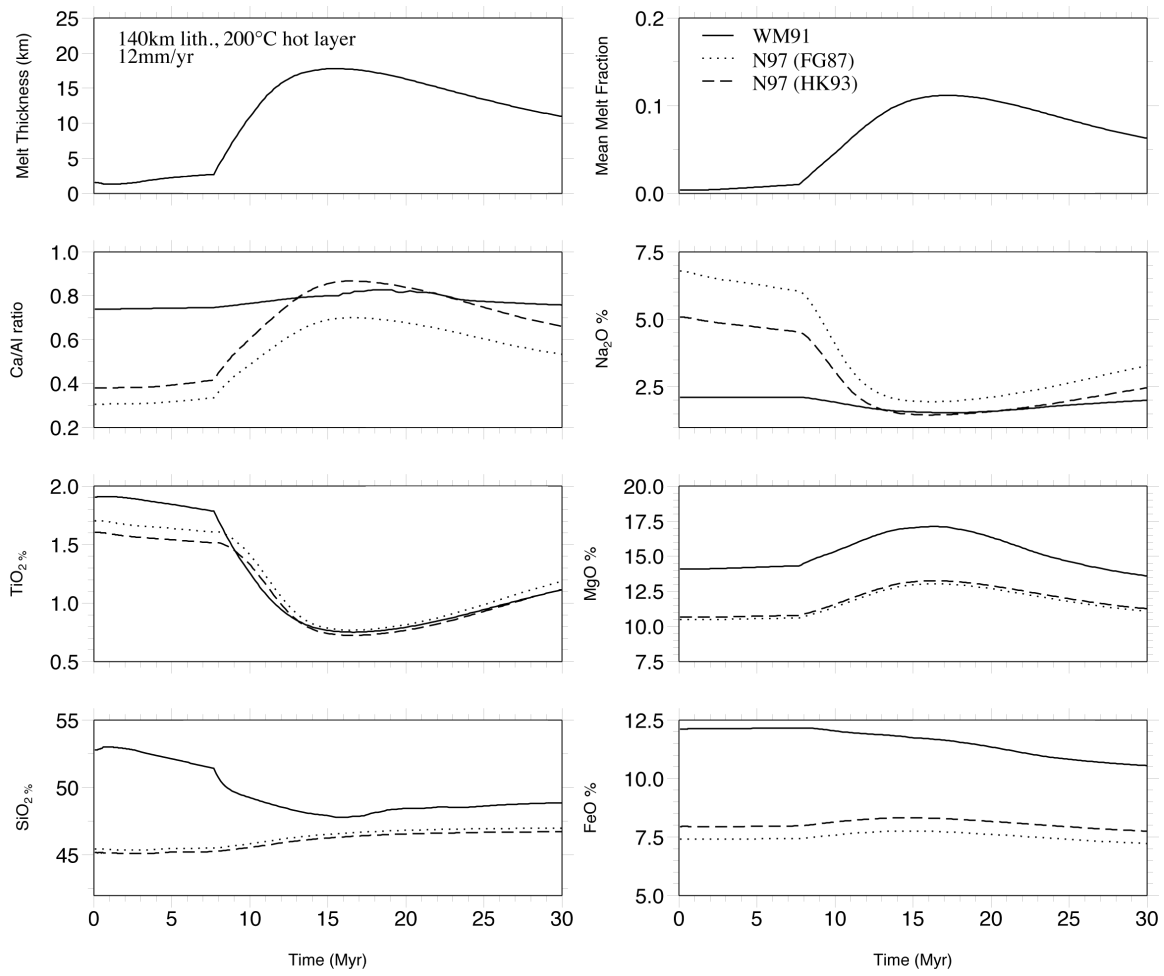


Figure 4.14: Models have a mantle asthenosphere temperature of 1315 °C, an initial lithosphere thickness of 140 km, a hot layer of 200 °C and a spreading rate of 12 mm yr^{-1}. Three models are run here, with composition parametrisation WM91, N97-FG87 and N97-HK93. Melt fraction was predicted through the use of perfectly compatible trace element X (Eq. 4.6 & 4.7).

4.7 Summary

With the implementation of the small-scale convection model from Boutilier and Keen (1999) and the introduction of dehydration strengthening from Ito et al. (1999), Nielsen and Hopper (2004) developed a stable model capable of recreating igneous crustal observations from Southeast Greenland with the inclusion of a hot layer. Armitage et al. (2008) incorporated the calculation of major element oxide compositions, capable of recreating relatively close major element oxide compositions compared to primary melts also in the Southeast Greenland margin. In this chapter, the model sensitivities were explored with the use of changes in crustal thickness through time (Eq. 4.16) for model asthenosphere temperature, hot layer temperature, spreading rate and initial lithosphere thickness (Fig. 4.8-4.11).

Additionally, there is a choice of two different composition parametrisations to be made: (1) Watson and McKenzie, 1991 (WM91) and (2) Niu, 1997 (N97). WM91 relates instantaneous melt composition of Al_2O_3, FeO, MgO, CaO, Na_2O, K_2O and TiO_2 and 'the rest' to the degree of melt depletion, and SiO_2 comprises of

the difference between the total and summation of others. This composition parametrisation fits polynomial functions to batch melting experiments, and its bulk earth composition cannot be changed. N97 uses residue and determines the ratio of a particular oxide within the solid and liquid phases by calculating partition coefficient D (Eq. 4.18). This parametrisation has the capability of changing its bulk earth composition, and peridotite and pyrolite were compared. The final choice of composition parametrisation will be aided by the use of geochemical data from the Mid-Atlantic Ridge and DSDP samples in **Chapter 6**. Additionally, the use of melt production (Eq. 4.20) over melt depletion (Eq. 4.19) was considered more realistic with the assumption of vertical melt migration (Behn and Grove, 2015), and used henceforth.

The model results can be used to match observations from observational constraints from seismic data in the southern South Atlantic (**Chapter 3**). Before the models can be matched to initial ocean crust thicknesses, the initial lithosphere thickness, spreading rates and mantle asthenosphere temperature need to be determined (**Chapter 5**). The calculated crustal thickness (h_c) will be used to first match thickness observed at the landward limits of ocean crust and beyond for the wide-angle and high quality MCS data set (**Chapter 5**). Following this, areas of syn-rift magmatism from the African margin can be matched to melt areas results from the model (**Chapter 6**). Once the choice of composition parametrisation using the geochemical data is finalised (Section 6.3.1), seismic velocity can be calculated using an empirical formula derived from laboratory experiments. As a result, the model also has the capability of matching seismic velocity trends observed from wide-angle data. With a wide spread of observations derived from seismic data (up to $\sim$2300 km south of the Rio Grande Rise and Walvis Ridge), the numerical modelling results can aid in understanding the distribution and cause of along-strike variation of magmatism in the southern South Atlantic.

Chapter 5

Asthenosphere and lithosphere structure controls on early onset oceanic crust production in the southern South Atlantic

The following chapter is adapted from Taposeea et al. (2016): Asthenosphere and lithosphere structure controls on early onset oceanic crust production in the southern South Atlantic, Tectonophysics, http://dx.doi.org/10.1016/j.tecto.2016.06.026

5.1 Introduction

Rifting and magmatism are fundamental geological processes that shape the surface of our planet. A relationship between the two is acknowledged, but its precise nature is still not fully understood. White and McKenzie (1989) were among the first to observe a variability in the volume of volcanism during continental break-up world-wide. From a simple 1-D model of lithosphere extension, they concluded that initial lithosphere thickness had little influence on this variability. As a result, mantle temperature was considered as the most influential control on volcanism and the source of increased temperature was suggested to be mantle plumes (White and McKenzie, 1989; White and McKenzie, 1995; Storey, 1995). According to this model, a starting mantle plume impinges the rheological barrier of the lithosphere-asthenosphere boundary, causing its head to flatten and spread into a disk with a diameter of 2000-2500 km (Griffiths and Campbell, 1990, 1991). It is assumed that the highest temperatures are found at the plume axis, with the hot conduit of material supplying this central area, and

there is a reduction in temperature towards the fringes of the plume head (Campbell, 2007). In the North Atlantic, the spread of the mantle plume head is represented by the volcanic passive margins, seen north and south of the Greenland-Iceland-Faeroe aseismic ridges (White and McKenzie, 1989), with a systematic reduction in volcanism along-strike (Holbrook et al., 2001; Collier et al., 2009). Later workers proposed more complicated shapes than the classic "mushroom head" geometry (Houseman, 1990), and that sublithospheric bathymetry, forming an 'upside-down drainage pattern', can have a profound effect on the lateral flow of plume material (Sleep, 1996, 2006).

The validity of temperature as the main control over the degree of volcanism has been questioned by many authors. This work suggests that volcanism during break-up can be strongly influenced by other factors. Previous rift history, initial lithosphere thickness, and possibly even sedimentation, can alter the melting characteristics during margin formation (e.g., Hopper et al., 1992; Lizarralde et al., 2007; Bialas and Buck, 2009; Minshull et al., 2008; Armitage et al., 2010; Buiter and Torsvik, 2014; Fromm et al., 2015). Two contrasting examples are found in the North Atlantic and north-west Indian Ocean pertaining to previous rift history and initial lithosphere thickness. In the North Atlantic, extension before rifting caused a focused upwelling, enhancing melt generation. If this previous extension had not occurred, the thermal anomaly would have been held beneath a 125 km thick lithosphere and not produced ocean crust 17 km thick (Armitage et al., 2010). In opposition to this, in the Indian Ocean, a previous extension event had the opposite effect, causing the mantle thermal anomaly to exhaust with reduced melt generation represented by ocean crust only 5.2 km thick (Armitage et al., 2010). As an alternative to the "mantle plume-volcanic margin" association, lithospheric structure can therefore be considered a major factor.

In the South Atlantic, the association between mantle plumes and volcanic margins has also been challenged. Unlike in the North Atlantic, no systematic increase towards the starting plume was observed within the extent and volumes of seaward dipping reflectors (SDRs) (Franke et al., 2007). Instead, it was suggested that the lithospheric segment boundaries act as rift-propagation barriers to convecting asthenospheric mantle material, resulting in enhancing and focusing volcanic activity south of these zones (Koopmann et al., 2014a). The increased melting resulted in increased SDR thicknesses and volumes (Franke et al., 2007; Koopmann et al., 2014a,b). In numerical models, a lateral pressure gradient between sequentially opening segments causes a rift-parallel flow, with consequent elevation in temperature at segment boundaries. The modelling results showed increased decompression melting relative to the interior of the segments (Koopmann et al., 2014a). Thus, segmentation is suggested to be an influential control of volcanism in this region.

Here, the primary cause of along-strike variation of volcanism in the South Atlantic is investigated by compiling measurements of initial oceanic crustal thickness and testing the influence of temperature and segmentation. Initial oceanic crust provides an independent test of melt volumes previously inferred from syn-rift magmatism, consisting of SDRs and high-velocity lower-crustal intrusions (underplating). The ocean crust thickness represents a 'snapshot' of the asthenosphere conditions immediately post break-up, and can hence be used as a proxy for temperature. To test the primary cause of along-strike variation, the thickness of early onset oceanic

crust is first mapped, and then these observations are matched to numerical model predictions of volcanism to explore the controls on magmatism within this region.

5.2 Methodology

5.2.1 Tectonic framework: along-strike variability

The spatial variation of the thickness of initial oceanic crust was analysed for the study area. In order to compare the data from conjugate margins, the current plate reconstruction models were assessed. The models of Torsvik et al. (2009), Moulin et al. (2010) and Heine et al. (2013) were investigated in detail. Using the GPlates software package, these reconstructions were combined with the most-recent satellite gravity and magnetic data sets (Sandwell et al., 2013; Maus et al., 2009). From the reconstructed gravity and magnetic data sets, it was concluded that within the southern South Atlantic the magnetic isochrons correlated best with the Moulin et al. (2010) plate reconstruction (Section 2.3; Fig. 2.5). Using this framework, the distance along-strike is measured relative to the reconstructed locations for the Rio Grande Rise and Walvis Ridge respectively (shown by the two '+' symbols in Fig. 2.6).

The lithospheric segment boundaries have been previously identified in Section 2.7 (Fig. 2.13). They are based on major fracture zones identified from satellite gravity and magnetic data sets (Sandwell et al., 2013; Maus et al., 2009) and tested for conjugate symmetry using GPlates (Fig. 2.5b). Sub-plate boundaries from the Moulin et al. (2010) reconstruction model define first-order segments, numbered 1 - 4. There are additional 'second-order segments' showing clear fracture zone traces on conjugate sides, numbered alphabetically (e.g. Segments 3b & 3a).

5.2.2 Initial oceanic crustal thickness

To explore the thermal structure of the study area immediately post break-up, the thickness of the first oceanic crust generated was used as a proxy for melt production. To measure this thickness, a compilation was done of wide-angle and multichannel seismic reflection (MCS) profile data within the study area. In total, 37 profiles were sourced, consisting of 7 wide-angle profiles and 30 MCS profiles (details of each line in **Chapter 3**. NB: Profile AF0 is not included as its oceanic crust will not fit any of the selection criteria). The wide-angle profiles are distributed across both the conjugate margins and along-strike, with 4 on the African side (Profiles AF1 - 4; locations Fig. 3.1; Bauer et al., 2000; Schinkel, 2006; Hirsch et al., 2009) and 3 on the South American side (Profiles SA1 - 3; location in Fig. 3.17; Becker et al., 2014; Schnabel et al., 2008). The MCS data set was limited to the South American margin, as the seismic lines were required to image both the top basement and the Moho. Ten MCS published sections were used from Hinz et al. (1999) and Franke et al. (2007, 2010) (locations

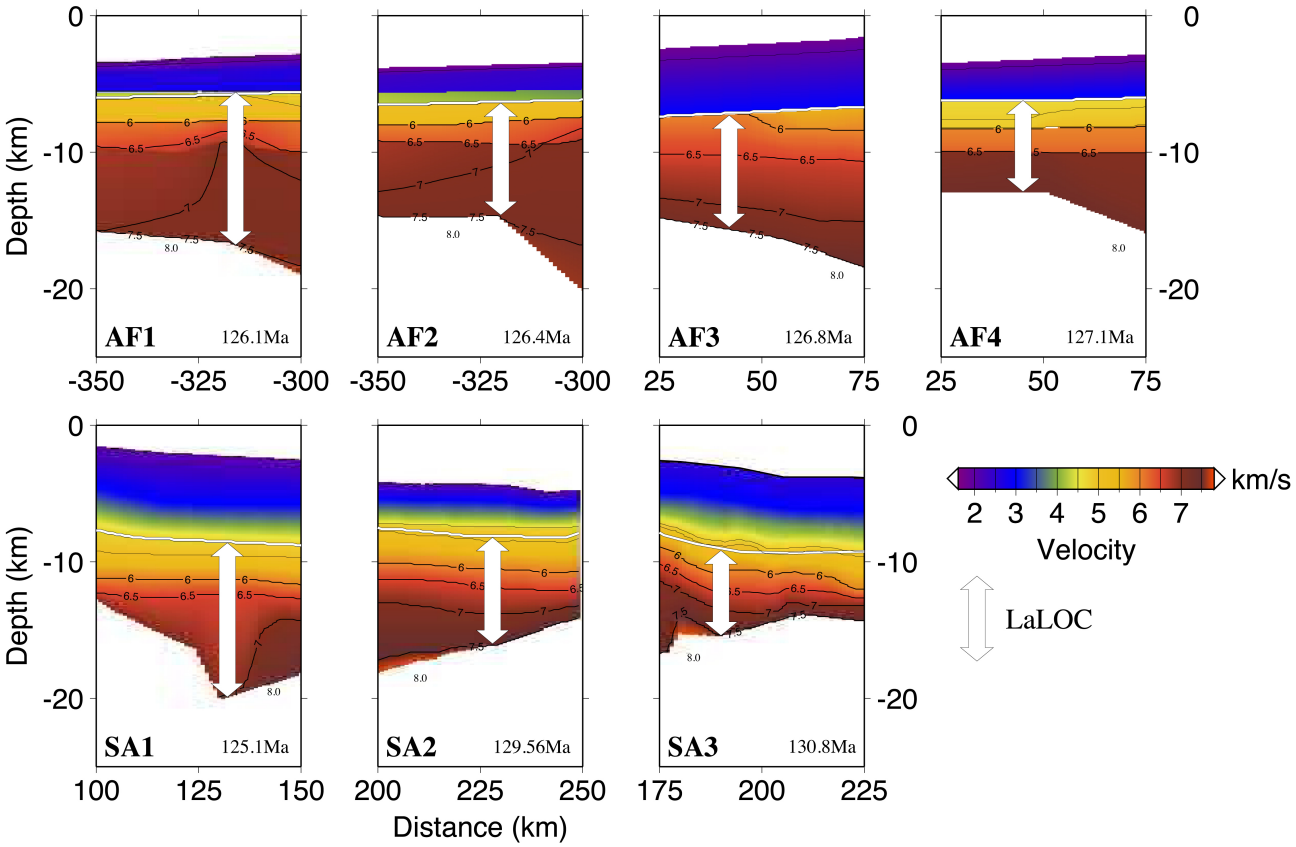


Figure 5.1: Ocean crust measurement points at the preferred LaLOC for wide-angle seismic profiles, based on the depth-V_p profiles in **Chapter 3**. AF1 & 2, 3 and 4 from Bauer et al. (2000), Schinkel (2006) and Hirsch et al. (2009) respectively, SA1 & 2 and SA3 from Becker et al. (2014) and Schnabel et al. (2008) respectively. Ages are determined from an age grid using the Gee and Kent (2007) time scale and Moulin et al. (2010) magnetic isochrons.

in Fig. 3.30; profiles Fig. 3.31 - 3.36). Six additional MCS profiles (locations Fig. 3.30; profiles 3.37) were from Winterbourne et al. (2014), which originate from a mixture of unpublished seismic industry data and published seismic data. Finally, fourteen lines of unpublished, industry, high quality seismic reflection survey lines were used from the BasinSPAN acquisition project of ION Geophysical (locations Fig. 3.30). Due to copyright agreements, only the results from these profiles are shown within this project.

In order to obtain a consistent indication of melt production along-strike, the thickness of oceanic crust was measured on each profile using a criterion known as Landward Limit of Oceanic Crust (LaLOC). The LaLOC is defined as the 'boundary which delimits relatively homogeneous oceanic crust ocean-ward from either extended continental crust or exhumed continental lithospheric mantle landward or Seaward Dipping Reflectors (SDRs), where an interpretation of the Moho and/or the extent of continental crust is not possible' (Heine et al., 2013).

A combination of magnetic and seismic characteristics was used to locate the LaLOC (more details found in Section 3.2). Firstly, in the study area, magnetic isochrons M2 and M0 (Section 2.6; Fig. 2.13) are generally recognised as sea floor-spreading being underway (Moulin et al., 2010). Secondly, the SDRs, which are relatively well-imaged on all lines, are normally located landward of the oldest oceanic crust. On wide-angle profiles, high P-wave velocity bodies in the lower crust (underplating), typically with values >7.0 km s^{-1} (Becker et al., 2014;

Trumbull et al., 2015), are taken to indicate the presence of highly intruded stretched continental or transitional crust. Hence, the LaLOC must be seaward of all underplating observed on wide-angle seismic profiles. As an additional check, depth-V_p profiles were extracted from the wide-angle models and tested for the presence of oceanic, stretched transitional or continental crust. The V_p limits from White et al. (1992) were used to define mature oceanic crust. Using this extra criterion, the LaLOC can coincide with overlying SDRs when supported by evidence. Finally, the reflectivity character was considered, with true ocean crust typically being devoid of internal reflectivity and showing a recognisable 'bumpy surface', as an indication of the presence of pillow lavas. This identification was done for all (summary Table 5.1) of the wide-angles (Fig. 5.1) and MCS profiles (Fig. 3.31 - 3.36; more details in Chapter 3).

Table 5.1: Crustal thickness measurements, with maximum and minimum ranges at the LaLOC for all seismic sections used in this study. These ranges provide the error bars shown in Fig. 5.6. The sections themselves are reproduced for wide-angles in Fig. 5.1 and for MCS profiles in Fig. 3.31 - 3.37. The measurements reported in Winterbourne et al. (2014) are from proprietary data. Distance along-strike refers to the location of the LaLOC relative to the commencement of the Rio Grande Rise and Walvis Ridge, marked with '+' in Fig. 2.6.

Profile Name	Reference	Distance along-strike (km)	Thickness (km)	Thickness max. (km)	Thickness min. (km)
AF1	Bauer et al., 2000	450	11.7	12.9	11.2
AF2	Bauer et al., 2000	538	8.2	10.9	8.0
AF3	Schinkel et al., 2006	1174	7.2	8.2	6.2
AF4	Hirsch et al., 2009	1422	7.0	11.7	6.7
SA1	Becker et al., 2014	922	8.2	8.2	7.9
SA2	Schnabel et al., 2008	1895	7.8	8.7	6.2
SA3	Becker et al., 2014	2288	6.9	6.9	3.8
BGR87-01B	Hinz et al., 1999	1165	7.6	7.9	7.3
BGR98-18	Franke et al., 2010	1850	7.4	7.7	7.1
BGR98-07	Franke et al., 2010	1894	7.7	8.0	7.4
BGR98-20	Franke et al., 2010	1925	7.6	7.9	7.3
BGR98-41	Franke et al., 2007	1681	7.1	7.4	6.8
BGR98-05	Franke et al., 2007	1790	7.8	8.1	7.5
BGR98-15	Franke et al., 2007	1804	6.9	7.2	6.6
BGR98-22	Franke et al., 2007	1981	6.9	7.2	6.6
BGR04-08/13	Franke et al., 2007	2258	6.0	6.3	5.7
Profile 300	Winterbourne et al., 2014	593	7.7	8.0	7.4
Profile 231	Winterbourne et al., 2014	1380	5.9	6.2	5.6
Profile 233	Winterbourne et al., 2014	1578	8.4	8.8	8.0
Profile 230	Winterbourne et al., 2014	1595	6.8	7.1	6.5
Profile 229	Winterbourne et al., 2014	2210	5.1	5.3	4.9
Profile 232	Winterbourne et al., 2014	2261	5.1	5.3	4.9
PS1-0090	ION Geophysical	262	9.9	10.3	9.5
PS1-0070	ION Geophysical	405	9.6	10.0	9.2
PS1-0060	ION Geophysical	488	11.2	11.7	10.7
PS1-0040	ION Geophysical	609	10.9	11.4	10.4
PS1-0030	ION Geophysical	695	7.3	7.6	7.0
PS1-0010	ION Geophysical	828	8.5	8.9	8.1
UY1-4700	ION Geophysical	911	7.3	7.6	7.0
UY1-4500	ION Geophysical	992	8.0	8.4	7.6
UY1-4300	ION Geophysical	1076	7.9	8.3	7.5
UY1-4000	ION Geophysical	1176	7.5	7.8	7.2
AR1-3800	ION Geophysical	1220	8.5	8.9	8.1
AR1-3500	ION Geophysical	1369	9.1	9.5	8.7
AR1-3000	ION Geophysical	1583	6.4	6.7	6.1
AR1-2600	ION Geophysical	1760	9.7	10.1	9.3

In order to ensure consistency between oceanic crust thickness measurements at the LaLOC made from MCS profiles, all measurements were performed on time sections (Fig. 3.30). These were then converted to distance using a mean V_p value for oceanic crust of $6.7\,\mathrm{km\,s^{-1}}$ (White et al., 1992). White et al. (1992) found 90 % of the ocean crust velocity estimates fall within a range of $6.4 - 7.0\,\mathrm{km\,s^{-1}}$, representing a $\pm 0.45\,\mathrm{km}$ error for a

crustal thickness of 10 km.

The majority of the available seismic profiles stop soon after the LaLOC as they were collected to study the continent-ocean transition. The ION Geophysical lines however extend up to $\sim$ 660 km into oceanic crust (Fig. 5.7). This allowed for the measurement of the age trend of oceanic crustal production in the north of the study area. To map the oceanic crust thickness to sea floor age, the Gee and Kent (2007) time scale (reasoning in Appendix 3.7) and Moulin et al. (2010) magnetic isochrons were used for the study area. This allowed for distance along the profile to be converted to age, and subsequently the thickness was averaged into 1.5 Myr bins ranging from 127 Ma to 95 Ma.

5.2.3 Numerical modelling

To better the understanding of the study area's initial break-up conditions, a 2D viscous model of the upper mantle to simulate continental break-up is used (Chapter 4). The numerical model, based on CitCom (Moresi et al., 1996), is a finite element code designed to solve incompressible thermochemical convection problems relevant to the Earth's mantle. It is a fluid dynamic model capable of handling large viscosity contrasts where Stokes equations are solved in a fixed Cartesian domain (Moresi et al., 1996). This model was modified by Nielsen and Hopper (2004) to include melt production due to decompression melting. Equations are solved in 2D (Sections 4.2 & 4.3), using the Boussinesq approximation with the understanding that (1) density variations are sufficiently small that they only affect gravitational forces and (2) effect on mantle density due to mass transfer during melting is small (Cordery and Morgan, 1993). The model is set up with a non-Newtonian dislocation creep as described in Section 4.5.

The model space (more detail in Section 4.5.2) is represented by a domain 2,800 km wide, 700 km deep, with 256x256 elements (Fig. 4.3). The initial lithosphere is assumed to be melt depleted and therefore compositionally buoyant relative to the asthenosphere. A hot layer is introduced, simulating the presence of an impacted plume head at the lithosphere/asthenosphere boundary (Fig. 4.3). Extension is imposed by a surface velocity boundary condition at a fixed spreading rate, driving the lithosphere apart laterally (see for example Nielsen and Hopper, 2004; Armitage et al., 2010). As the lithosphere extends and thins, material moves upwards leading to decompression melting. Crustal thickness (h_c) is calculated with the assumption that all melt is focused and accreted at the ridge axis using Eq. 4.16 (further details in Section 4.3). The sides of the model domain are reflective boundaries, with no lateral flow of heat or material across them (Fig. 4.5). This is assumed not to affect melt thickness results, as the reflective boundaries (example Fig. 4.5) are considered to be far enough from the centre of extension (Nielsen and Hopper, 2004).

5.2.3.1 Understanding model sensitivity

The sensitivities of the model have previously been tested in Chapter 4 (Section 4.6). To test the effect of the presence of a hot layer, a simple simulation with a model asthenosphere temperature of 1300 °C, spreading

velocity of 12 mm yr^{-1}, and an initial lithosphere thickness of 125 km was run. In some of the models, a 100 km thick hot layer was introduced as the impacted plume head at the lithosphere/asthenosphere boundary. Three model runs are first demonstrated with no hot layer, a 100 °C hot layer, and a 200 °C hot layer in excess of the model asthenosphere temperature (Fig. 5.2). Three main stages of melt production can be seen for the model as the lithosphere thins and is finally broken (Fig. 5.2): pre-rift, syn-rift and post-rift. The pre-rift stage is where there is little magmatism and syn-rift is where there is a magmatism peak. There is a clear increase in output magmatism as the hot layer temperature increases, with ∼3 times as much for the 200 °C hot layer relative to no hot layer (Fig. 5.2). Following the peak magmatism in the syn-rift phase, the post-rift phase represents a shift towards steady-state sea floor spreading (Fig. 5.2). The first instance of ocean crust will occur along this decreasing trend, and can be matched to observations of the seismic data.

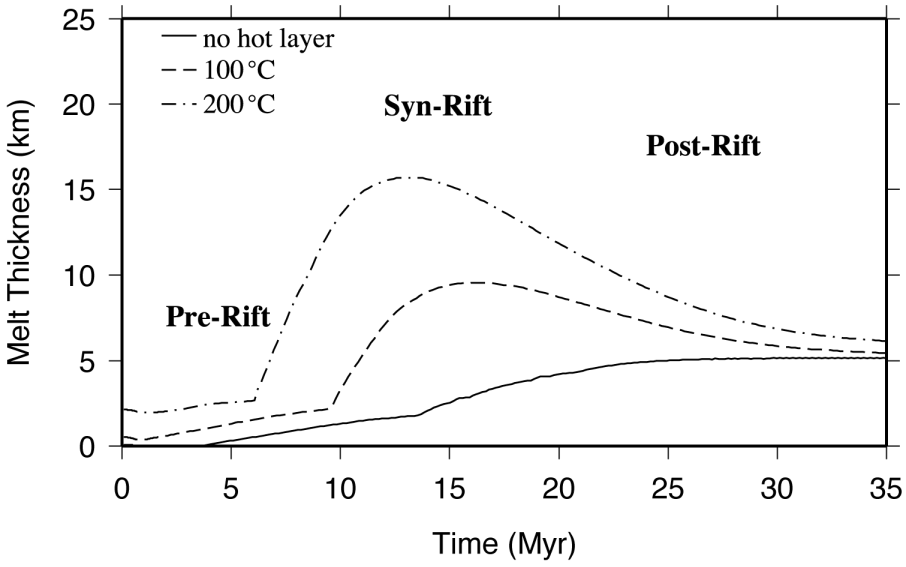


Figure 5.2: Varying hot layer temperatures, with a 1300 °C model asthenosphere temperature. The interpreted location of the pre, syn and post-rift phases are shown. Models have an initial lithosphere thickness of 125 km and spreading rate of 12 mm yr^{-1} unless otherwise specified.

The evolution of the numerical model from pre-rift to post-rift is a function of the hot layer temperature (Fig. 5.2). The hottest model, with a thermal anomaly 200 °C hotter than the model asthenosphere temperature, displays peak melt production ∼3 Myr earlier than the equivalent model that has a 100 °C hot thermal anomaly (Fig. 5.2). For model runs without a hot layer present, there is no syn-rift peak in magmatism. Increasing the model asthenosphere temperature reduces the model duration for the pre-rift phase, and increases the steady-state oceanic crustal thickness (Fig. 4.8). Varying the spreading rate likewise affects the duration of pre and syn-rift phases, and ultimately when the post-rift phase is achieved (Fig. 4.10). Doubling the rate of extension reduces the pre-rift duration by at least half. A faster spreading rate creates a larger pulse of decompression melting during the syn-rift phase when a hot layer is present, and a slower spreading rate will significantly increase the duration of the pre-rift phase (Fig. 4.10). This is because a faster rate of extension causes a greater amount of material to be fluxed through the zone of partial melting (Fig. 4.8 & 4.10).

To explore how the model that includes a thermal anomaly (e.g. Fig. 5.2) evolves for a range of hot layer temperatures (50 to 200 °C) and initial lithosphere thicknesses (100 to 140 km), the melt thickness was plotted at three model times, 10, 15 and 20 Myr (Fig. 5.3). If the hot layer temperature is 50 °C, then the melt thickness is always less than 10 km. Increasing this temperature increases the volume of melt, but the time of maximum

melt production is a function of the hot layer temperature (Fig. 5.2) and also of the initial lithosphere thickness (Fig. 5.3). For models with an initial lithosphere thickness of 140 km and hot layer temperatures ≥100 °C, at 10 Myr melting is reduced. However, if the initial lithosphere thickness is 100 km, then by 20 Myr the thermal anomaly is exhausted (Fig. 5.3). This demonstrates the importance of understanding the timing of initial oceanic crustal thickness, and to constrain the initial lithosphere thickness from the available geophysical evidence.

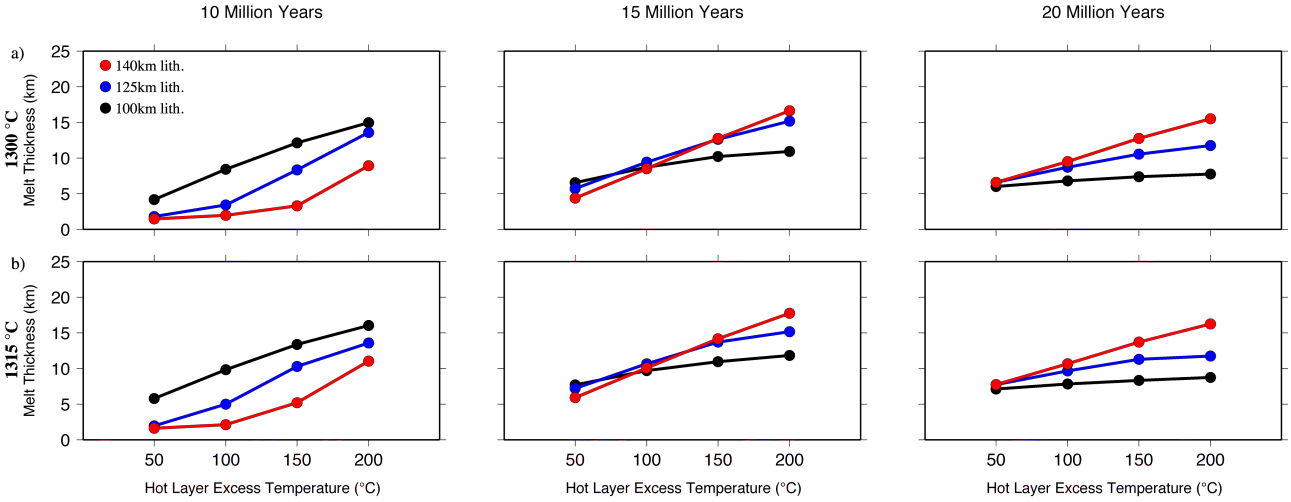


Figure 5.3: Evolution plots for differing initial lithosphere thickness and excess hot layer temperature. Melt thickness at 10, 15 and 20 Myr after the initiation of extension for an asthenosphere temperature of 1300 °C (a) and 1315 °C (b). In all cases, there is a spreading rate of 12 mm yr^{-1}. Note how varying initial lithosphere thickness results in the peak magmatism occurring at different times.

5.2.3.2 Initial lithosphere thickness and rate of extension

To reduce the number of unknowns, it was assumed that the initial lithospheric thickness and extension rate could be estimated from geophysical observations. The initial lithosphere thickness is estimated from the point at which the available seismic imaging suggests un-stretched continental crust to be present. To estimate the lithosphere thickness at this point, the tomographic model of Priestley and McKenzie (2006) was used for the South American side, and Fishwick and Bastow (2011) was used for the African side (Table 5.2). The Fishwick and Bastow (2011) model was used for the African side for several reasons. The increased number and distribution of seismic station allows more ray coverage in this region, with Fishwick and Bastow (2011) having a specific focus on Southern Africa (Fishwick, 2010). Although it uses the empirical parameterisations from the Priestley and McKenzie (2006) model, the latter has an automated code and the former employs a semi-automated code, using a manual comparison of multiple inversions for each path (Fishwick, 2010). Through the use of a model based on petrology, mineral physics, gravity anomaly and heat flow, Fernandez et al. (2010) gave an estimate of lithosphere thickness in the Namibia region. Given the different methods and different resolution, the lithosphere thickness model agrees better with the model from Fishwick and Bastow (2011), and the latter is considered more reliable in this area (Fig. 5.4). In order to address the observational uncertainties and differences seen in the two models (Fig. 5.4), simulations with varying initial lithosphere thicknesses were included (Table 5.2) to ensure the robustness of the excess model asthenosphere temperature predictions.

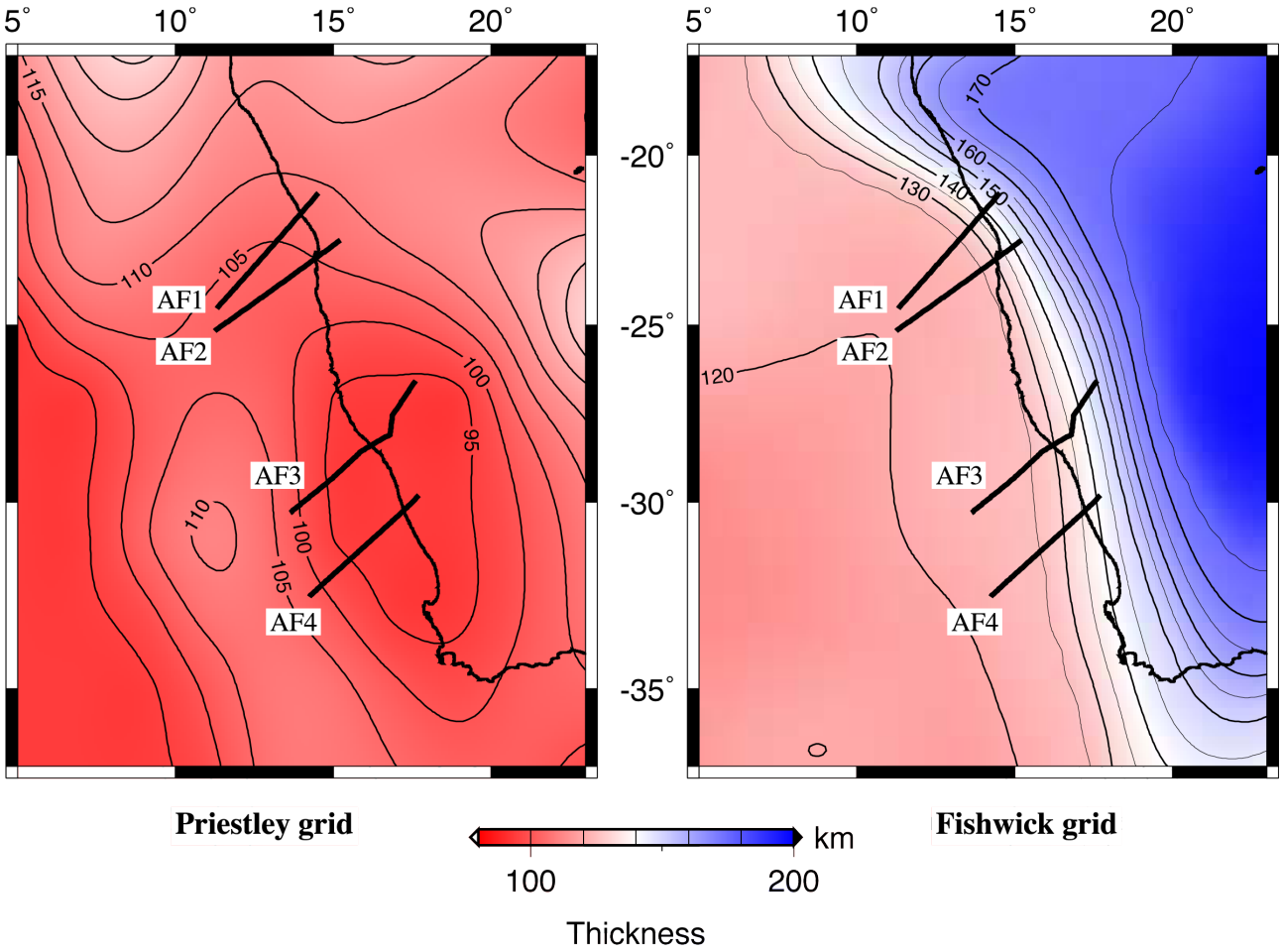


Figure 5.4: Comparison of two seismic tomography models of lithospheric thickness of South West Africa used in the study from Priestley and McKenzie (2006) and Fishwick and Bastow (2011). Labelled lines show the location of the wide-angle profiles used.

The reliability of using present day estimates of lithosphere thickness as a proxy for pre-break-up lithosphere thickness was explored by McKenzie et al. (2015). They presented a map of lithospheric thickness for Pangea, using a reconstruction of continental plates within the Permian, assuming the lithosphere moves with overlying continents. They found a continuity of thicker and thinner lithosphere, for example at the Pan-African orogenic zones and cratons. If lithosphere deformation had occurred since the Permian, there should be no reason for them to fit within a reconstruction of Pangea. This was tested using the rotation poles from Moulin et al. (2010) with the lithospheric grid from Priestley and McKenzie (2006), the latter covering both sides, and likewise found that there was a good correlation between the conjugate sides in terms of lithospheric thickness (Fig. 5.5). Hence, it was assumed present day values could be used as a parameter for initial lithosphere thickness within the model.

Heine et al. (2013) summarised sea floor spreading rates through the South Atlantic break-up from 126.57 Ma (magnetic isochron M4) to 100 Ma. These range from 10 to 18 mm yr^{-1}, increasing in speed towards the south (Table 5.2). In the modelling, it was assumed the pre-break-up extension rates matched those seen during early sea floor spreading. The primary value used was 12 mm yr^{-1}, as this applied to Segments 3b, 3a and 2

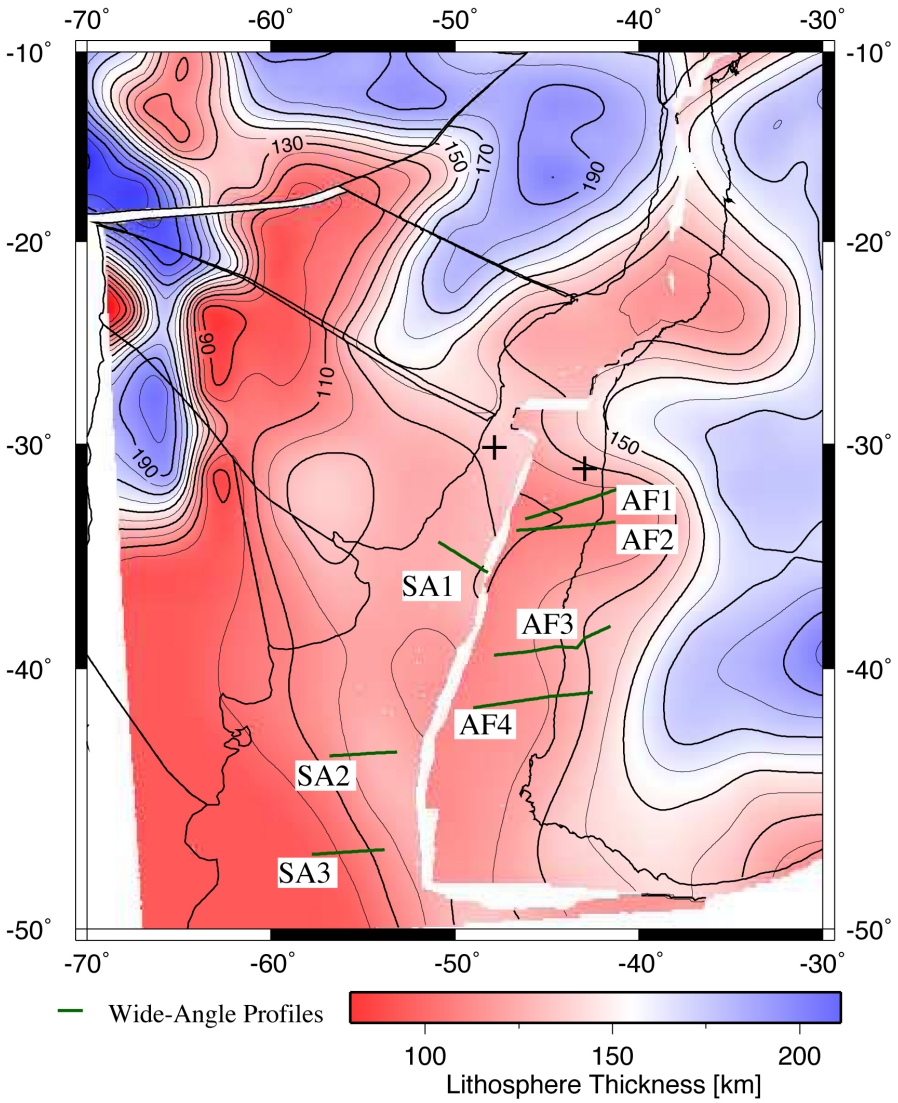


Figure 5.5: Reconstructions using GPlates shown at 121 Ma using rotation poles of Moulin et al. (2010) with the sub-plates of South America (thin black lines). Reconstruction of lithosphere thickness using the data set of Priestley and McKenzie (2006), the latter covering the whole area. The seven wide angle seismic profiles used in this study are labelled AF1 to AF4 and SA1 to SA3. The '+' marks the reconstructed landfall of the Rio Grande Rise and Walvis Ridge.

until 126.57 Ma (M4). Following this, the rate increased to 35 mm yr^{-1} for the period 126.57-120.6 Ma, and subsequently increased to 58 mm yr^{-1} (Heine et al., 2013). Moulin et al. (2010) has similar rates for these times, at 38 mm yr^{-1} and 50 mm yr^{-1} respectively, but does not suggest a rate prior to M4. Heine et al. (2013) found the spreading rate of 18 mm yr^{-1} in the extreme south of the study area, covering Segments 1b and 1a.

Table 5.2: Assigned model parameters: lithosphere thickness and spreading rates per segment. Opening ages are assumed by sub-plate from Moulin et al. (2010). M7, M4, M2 and M0 are dated 127.23 Ma, 126.57 Ma, 124.05 Ma and 120.6 Ma respectively (Gee and Kent, 2007). Seismic tomography models from Fishwick and Bastow (2011) and Priestley and McKenzie (2006) grids (Fig. 5.4). Spreading rates are from Heine et al. (2013).

	Opening Ages	Lithosphere thickness (km)			Spreading Rates
Segment		African margin (Fishwick)	African margin (Priestley)	S. American margin (Priestley)	(mm yr^{-1})
3b	M2-M0	135-140	105-110	125	12
3a	M2-M0	125-130	100-105	125	12
2	M4-M2	130-135	95-100	100-110	12
1b	pre-M7	130-135	95-100	110-115	18
1a	pre-M7	135-140	95-105	95-100	18

5.2.3.3 Model asthenosphere temperature structure

The choice of the model asthenosphere temperature range is crucial, with a change in temperature of 12.5 °C accounting for melt thickness changes by up to 1 km (McKenzie et al., 2005). Herzberg et al. (2007) found that mid-ocean ridge basalts (MORBs) with a 10-13 % MgO content would have potential temperature range of 1280-1400 °C. This should cover the feasible range for model asthenosphere temperature in the South Atlantic. To refine this range of temperatures, the long-offset ION Geophysical lines found in the north-west region of the study area were used (locations in Fig.5.7). These profiles record the reduction in oceanic crustal thickness away from the passive margin and towards steady-state. Therefore, the crustal thickness farthest from the margin was compared with that generated by the model at a steady-state.

A hot layer with a temperature in excess of the model asthenosphere temperature was added to recreate the distal regions of the mantle plume or thermal anomaly (Fig. 4.3; Armitage et al., 2010). The hot layer can vary in temperature where, classically, temperature is considered the main driver of crustal thickness (White and McKenzie, 1989). In all models, it was assumed the hot layer was present below the lithosphere before the onset of extension. The excess temperature of the hot layer closest to the centre of the province can be estimated from the thickness of the basaltic crust from the Rio Grande Rise and Walvis Ridge. The Walvis Ridge thickness is observed between $\sim$26-28 km from seismic sections (Fromm et al., 2015). When the McKenzie and Bickle (1988) melting model is used, a 200 °C excess temperature is required to match this thickness (Campbell, 2007). Hence, a 200 °C excess temperature for the hot layer was assumed with proximity to the Rio Grande Rise and Walvis Ridge, varying it along-strike. Decompression melting was solved for at various hot layer temperatures and compared to the results to the along-strike variation in ocean crust thicknesses measured at the LaLOC for the wide-angle profiles (Fig. 5.1). Relative ages of the oceanic crust were used at the LaLOC location, known from location of magnetic isochrons, to discriminate between results from models with different hot layer temperatures.

5.3 Results

5.3.1 Observed variation in ocean crustal thicknesses

When all the initial oceanic crustal thickness measurements were considered (Table 5.1), there was a clear negative trend when comparing oceanic crust thinning with increasing distance along-strike from the Rio Grande Rise and Walvis Ridge (Fig. 5.6a). The trend has a gradient of -2×10^{-3} and a correlation coefficient of 0.7. This translates to a reduction in oceanic crustal thickness of 0.16 km per 100 km in a southern direction from the aseismic ridges. On the African margin, a thicker ocean crust was observed towards the Walvis Ridge. The wide-angle seismic Profile AF1 has an initial oceanic crustal thickness measuring 11.7 km at an along-strike distance of ∼450 km (Fig. 5.1), which reduces to a thickness of 7.0 km at Profile AF4 in the south at an along-strike distance of ∼1420 km (Fig. 5.1). This trend is very similar on the South American margin, with a maximum thickness of 10.0 km from the most northern ION Geophysical profile ∼260 km away, to only 6.0 km in the southern edge of measurements ∼2300 km away.

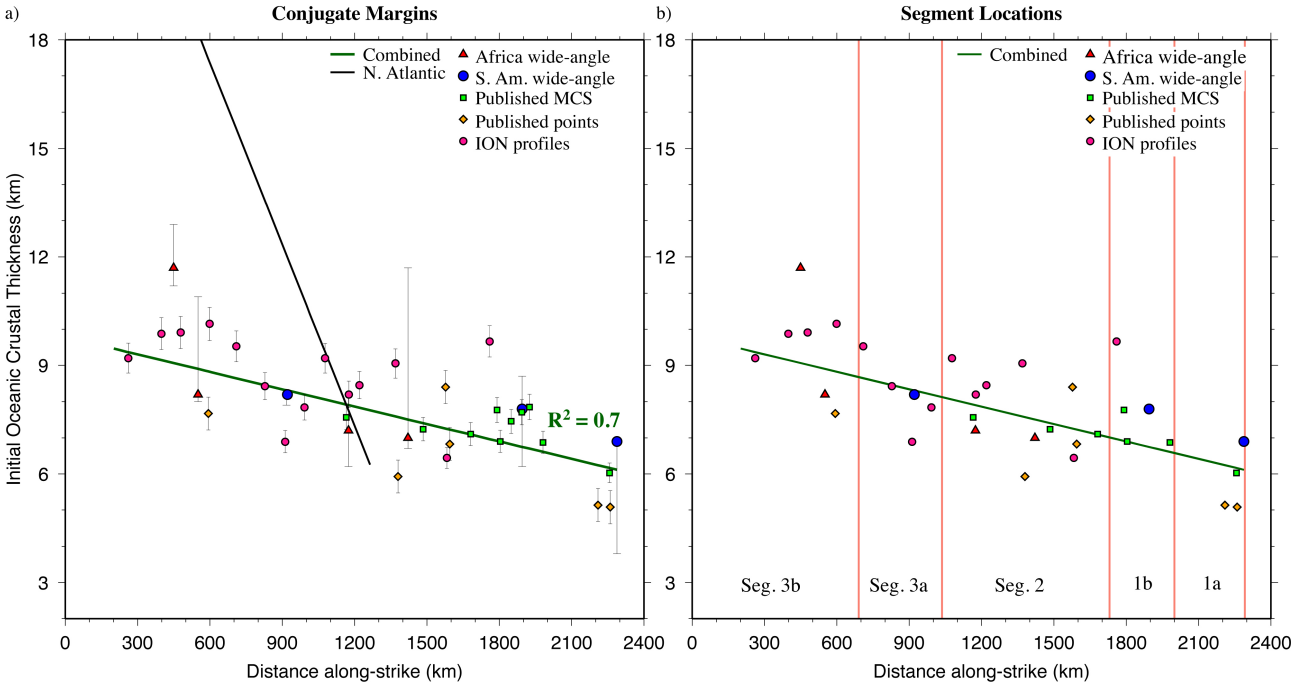


Figure 5.6: Initial oceanic crustal thickness plotted against distance along-strike. Data sources are given in Table 3.2. (a) Initial oceanic crustal thickness versus distance along-strike for all measured locations. The error bars on individual measurement points come from the uncertainty in locating LaLOC on individual profiles (Table 5.1). Regression analysis shows a reasonable linear relationship (green line with a regression coefficient, $R^2 = 0.7$). For comparison, the trend found for the initial oceanic crustal thickness in the North Atlantic is shown by the black line (from Collier et al., 2009). (b) Initial oceanic crustal thickness shown relative to segment boundaries (red lines).

When the oceanic crustal thickness measurements at the LaLOC location were compared to the segment boundaries (Fig. 5.6), no obvious thickening south of the segment boundaries was found. By using the ION Geophysical long-profiles that extend to a distance of 660 km offshore, covering an age range of approximately

15 Myr (Fig. 5.7), a signal in the oceanic crustal thickness as the profiles cross segment boundaries was checked for (Fig. 5.7 and 5.8). The long-profiles have an overlying trend of a decrease in oceanic crustal thickness with distance from the passive margin and no clear indication of increased decompression melting at the segment boundaries (Fig. 5.8). From the seismic sections, clear oceanic crust could be seen, devoid of internal structure with a bumpy surface, representative of pillow lavas.

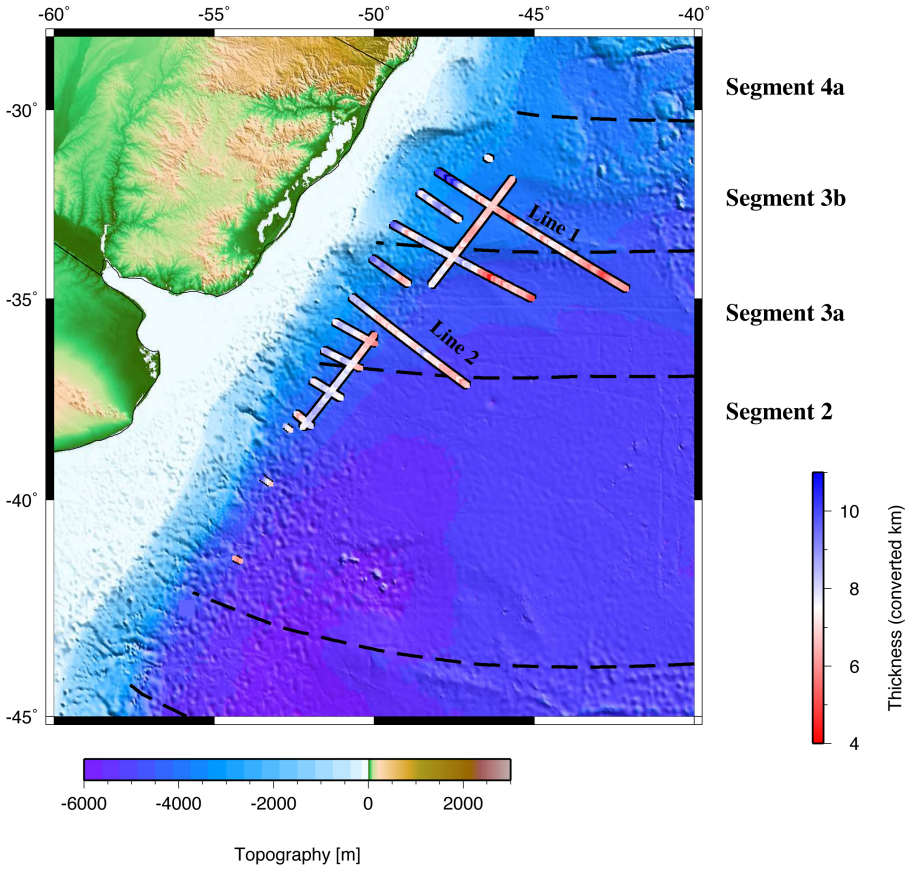


Figure 5.7: Ocean crustal thickness from the ION Geophysical long-offset data, which was measured in TWTT and converted to kilometres assuming a mean V_p value for oceanic crust of 6.7 km s^{-1} (White et al., 1992). Line 1 and 2 are show in detail in Fig. 5.8.

Lines 1 and 2 were further investigated, both transgressing segment boundaries (Fig. 5.8). The ocean crust thickness for both of the lines show local thickness variations with an amplitude of 1 km. Oceanic crustal thickness decreases from 10.2 to 6.3 km along Line 1 (Fig. 5.8a), and 8.5 to 6.5 km for Line 2 (Fig. 5.8b). A sharp change in melt production was not observed, as had been described by Franke et al. (2007) and Koopmann et al. (2014b), but there is an overall decreasing trend with age.

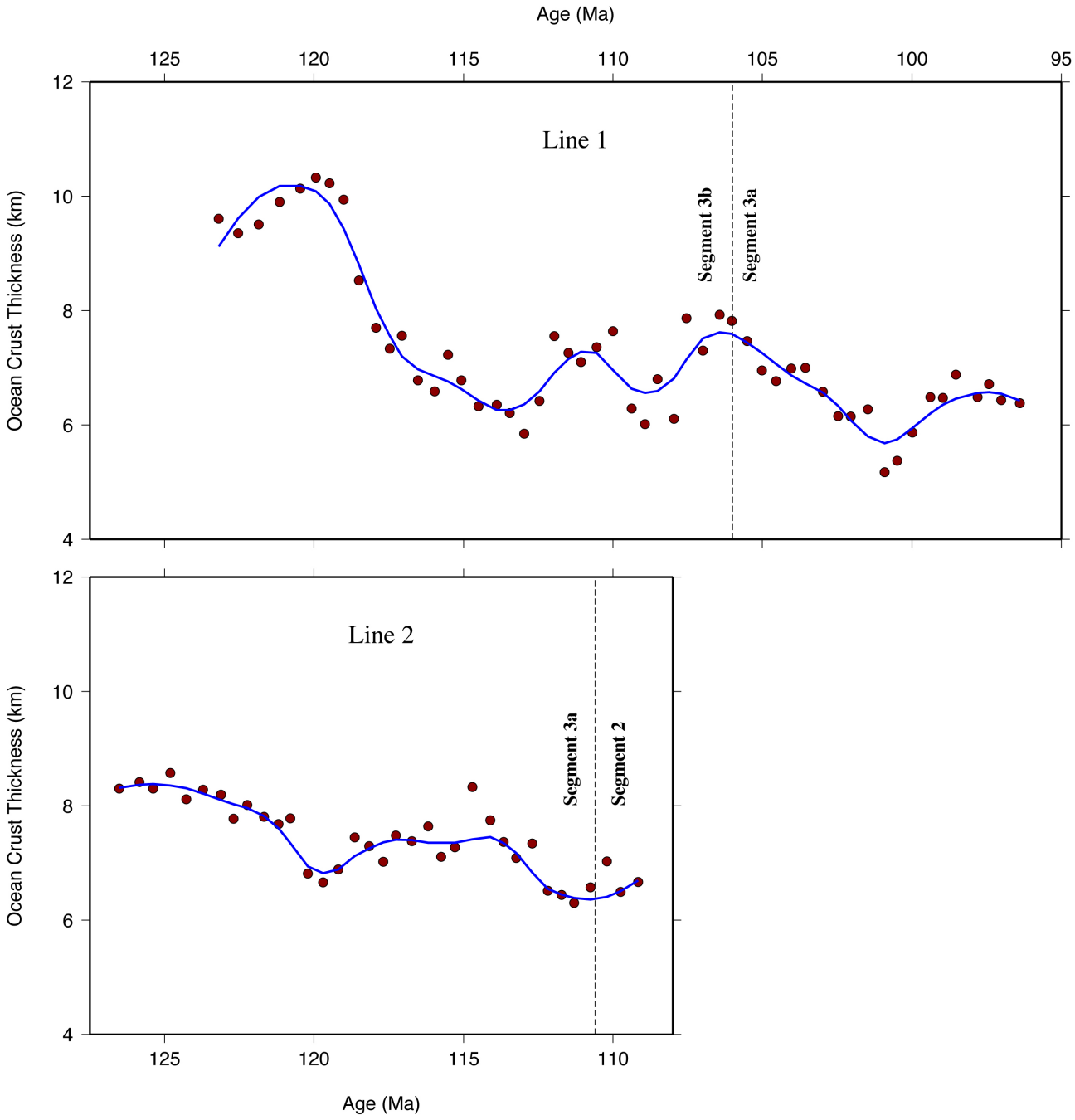


Figure 5.8: Ocean crustal thickness from two of the ION Geophysical long-offset data plotted against age. Locations of Lines 1 and 2 are found in Fig. 5.7. Ages assigned in accordance to the Gee and Kent (2007) time scale and Moulin et al. (2010) magnetic isochrons. Thickness averaged over 1.5 Myr bins ranging from 127 Ma to 95 Ma (maroon dots), and smoothed with a Gaussian filer (blue lines).

5.3.2 Results from numerical model

5.3.2.1 Establishing model asthenosphere temperature

The long offset ION Geophysical data demonstrate decreasing oceanic crustal thickness with distance from the passive margin (Fig. 5.8). Having age-assigned the lines according to location, it was found for Segments 3b, 3a and 2 that the oceanic crustal thickness trends to 7.2, 6.7, and 6.6 km respectively (Fig. 5.9). This suggests that towards the end of these profiles steady-state oceanic crustal production has been achieved.

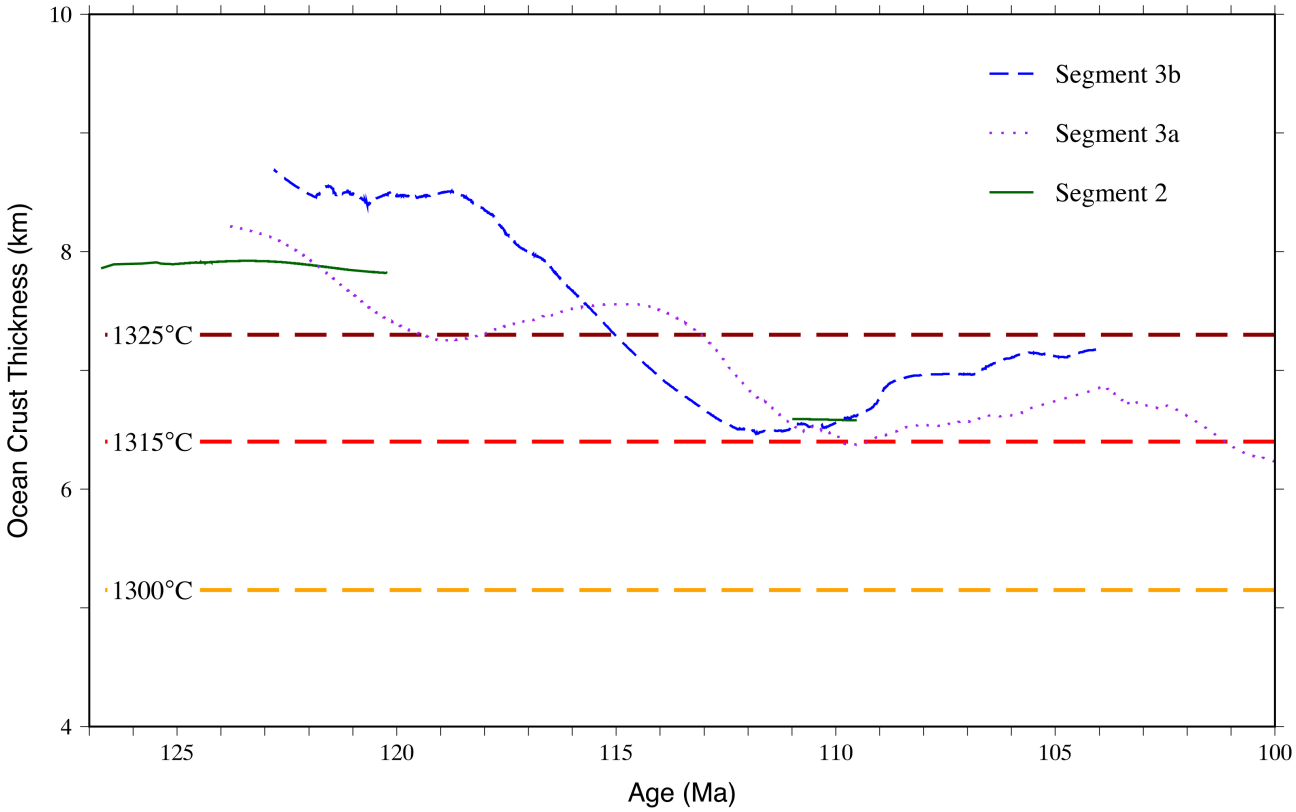


Figure 5.9: Determining the model asthenosphere temperature using ocean crust thicknesses from the long-offset ION Geophysical lines. All oceanic crustal thickness measurements within a given segment were averaged into 1.5 Myr bins ranging from 127 Ma to 95 Ma, and a smoothing Gaussian filter was applied. Several model asthenosphere temperatures were tested, in this case 1300, 1315 and 1325 °C, electing to use 1315 °C as the model asthenosphere temperature in all of the subsequent models.

Comparing these trends to the model predictions without any thermal hot layer allowed for the conclusion that the model asthenosphere temperature was in the range of 1315-1325 °C (Fig. 5.9). A higher thickness for Segment 3b was seen, attributed to local thickening of the ocean crust over Line 1 and possibly due to a seamount (Fig. 5.8a), causing an overall increased thickness. However, before this, the thickness was also tending to 1315 °C. Therefore, 1315 °C was used as the model asthenosphere temperature in all the models.

5.3.2.2 Establishing hot layer temperatures

Having established a model asthenosphere temperature of 1315 °C, the excess temperature of the hot layer was solved for. For all models, it was assumed the hot layer was present below the lithosphere prior to the onset of extension (as demonstrated in Fig. 5.2). The temperature of the hot layer was estimated by comparing variations in ocean crustal thicknesses for the wide-angle profiles at the LaLOC location (Fig. 5.10).

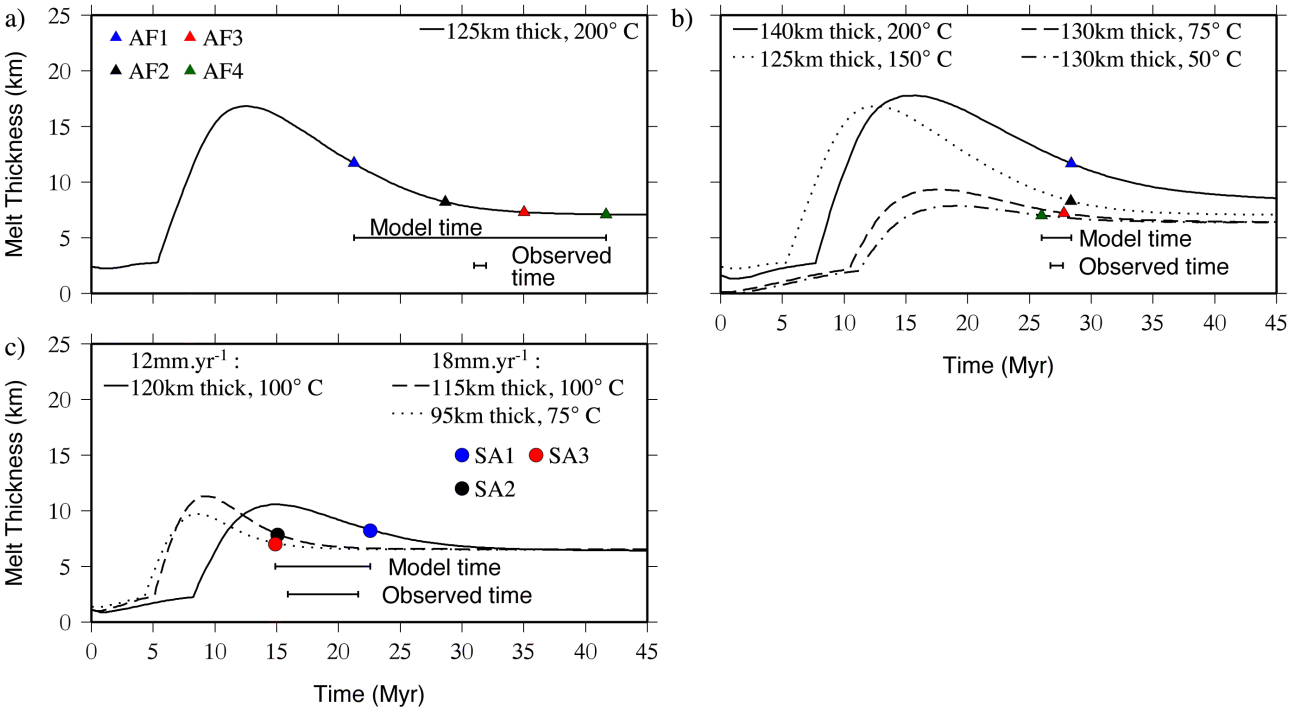


Figure 5.10: Models results for wide-angle profiles. Model asthenosphere temperature of 1315 °C, and spreading rate of 12 mm yr^{-1} unless specified otherwise. The ages between profiles have been calculated according to the LaLOC location (Fig. 5.1). Panel (a) has a hot layer of 200 °C and an initial lithosphere thickness of 125 km, capable of matching values of AF1 - 4 over a 20 Myr period. For panels (b) and (c) each wide-angle profile has been tested for different hot layer models and corresponding initial lithosphere thickness (Table 5.2). On the African margin, panel (b) shows matches of first ocean crust thicknesses over 2.5 Myr, much closer to the observed range of 1.0 Myr (maximum and minimum errors found in Fig. 5.11). For the South American margin, the models in panel (c) have a range of spreading velocities, where Segment 3a (for SA1) has a rate of 12 mm yr^{-1}, and Segment 1 (for SA2 and 3) has a rate of 18 mm yr^{-1}. Here the models match over a time of 7.7 Myr, relatively close to the observed time of 5.7 Myr.

It was assumed that the present day continental lithosphere thickness at the margin is representative of the initial configuration (Fig. 5.5) and the temperature of the hot layer was varied within the range of 50 to 200 °C. Using a model asthenosphere temperature of 1315 °C and spreading rates of 12 and 18 mm yr^{-1} covering Segments 1 - 3, several scenarios were tested. To demonstrate the effect of initial lithosphere thickness and the importance of timing, a model was run with an initial lithosphere thickness of 125 km (Fig. 5.10a). The model was capable of matching all values for the initial oceanic crust in the post-rift stage (ie. Fig. 5.2) from wide-angle seismic profiles AF1 to AF4 on the African side of the South Atlantic, but this match required a 20 Myr difference in age along the margin (Fig. 5.10a). With magnetic isochron data from Moulin et al. (2010) and using the Gee and Kent (2007) time scale, the range in age along the margin was estimated for the initial

oceanic crust produced. A range of ages of 1.0 Myr was found for the African profiles and 5.7 Myr for the South American profiles. As there was no method to 'fix' the start age of the model and a certain degree of uncertainty remains with the time scale, the models were matched to the observations by finding the closest model age range to that of the observed age range.

If the temperature of the hot layer was allowed to vary along-strike, it was found that the model with an excess temperature of 200 °C matched the observations for wide-angle seismic Profile AF1 (Fig. 5.10b) in its post-rift stage. Moving southward along the African margin, models with a reduced excess temperature of 150, 75 and 50 °C and varying initial lithosphere thicknesses were in line with the observed thickness, fitting the first oceanic crustal thickness for Profiles AF2, AF3 and AF4 respectively (Fig. 5.10b). Therefore, by taking the observed continental lithosphere thickness and changing the hot layer temperature, the thickness of the first oceanic crust could be matched within a consecutive time range of 2.5 Myr, much closer to the observed range of 1.0 Myr. If the assumption of a constant extension rate is correct, then these models also imply that the total duration of rifting in the South Atlantic was of the order of 25 to 30 Myr.

Rates of early sea floor spreading along the South American margin vary from 12 mm yr^{-1} for Profile SA1 in Segment 3a to 18 mm yr^{-1} for Profiles SA2 and SA3 in Segment 1a and 1b (Table 5.2). To capture this, two extension rates were modelled along with varying the temperature of the hot layer. Accounting for this difference, a set of models were found that could match the distribution of initial oceanic crustal thickness in the post-rift stage close to the 5.7 Myr age window of the three measurement points (Fig. 5.10c). A model with an excess temperature of 100 °C is concurrent with observations for SA1, and moving south, this reduced to 75 °C for SA3 (Fig. 5.10c). These fits imply a reduced duration of extension for the most southerly part of the South American margin relative to the more northerly conjugate margins in South America and on the African side. A rift duration of 15 Myr is predicted, due to the faster rate of extension for Profiles SA2 and SA3, compared to 25 to 30 Myr for Profiles AF1 - 4 and SA1.

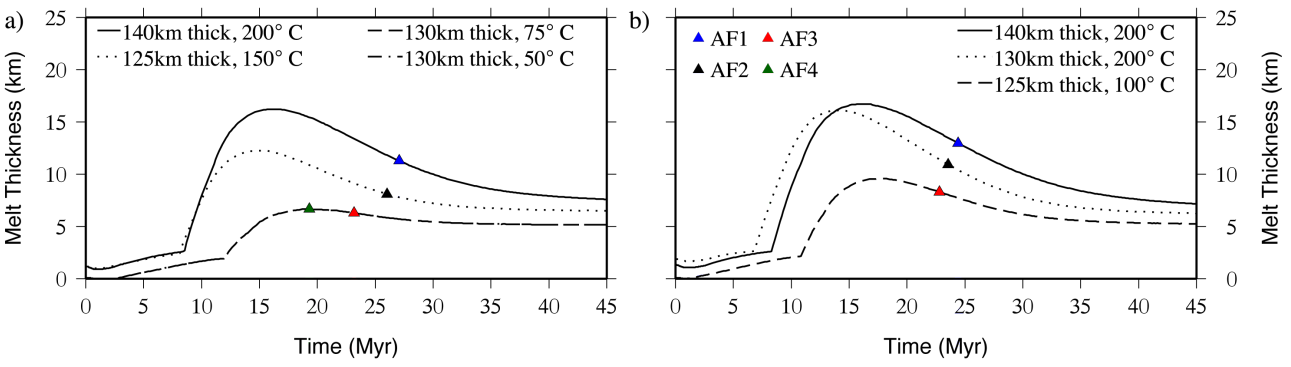


Figure 5.11: Models run with asthenosphere temperature of 1315 °C and spreading rate of 12 mm yr^{-1} for maximum and minimum ranges of the African wide-angle profiles. Panel (a) uses the minimum error range of initial ocean crustal thicknesses, however this results in the same hot layer temperature matches as in Fig. 5.10a. Panel (b) uses the maximum error range of initial ocean crustal thickness. AF4 is not included here due to its larger error range. Although hotter layers are required for AF2 and AF3, a decrease in temperature along-strike is still seen.

5.3.2.3 Results for segment-age trends

To compliment the results from wide-angle profiles, the segment-age trend observations from the long offset ION Geophysical profiles were used (Fig. 5.9). The oceanic crustal thickness was plotted for each segment binned into 1.5 Myr intervals ranging from 127 Ma to 95 Ma (Fig. 5.12). Since these data are from Segments 3b, 3a and 2, a model spreading rate of 12 mm yr^{-1} was assumed (Table 5.2). Although this rate of extension is valid until 126.57 Ma (Heine et al., 2013), once at steady-state, changing the spreading rate produces oceanic crustal

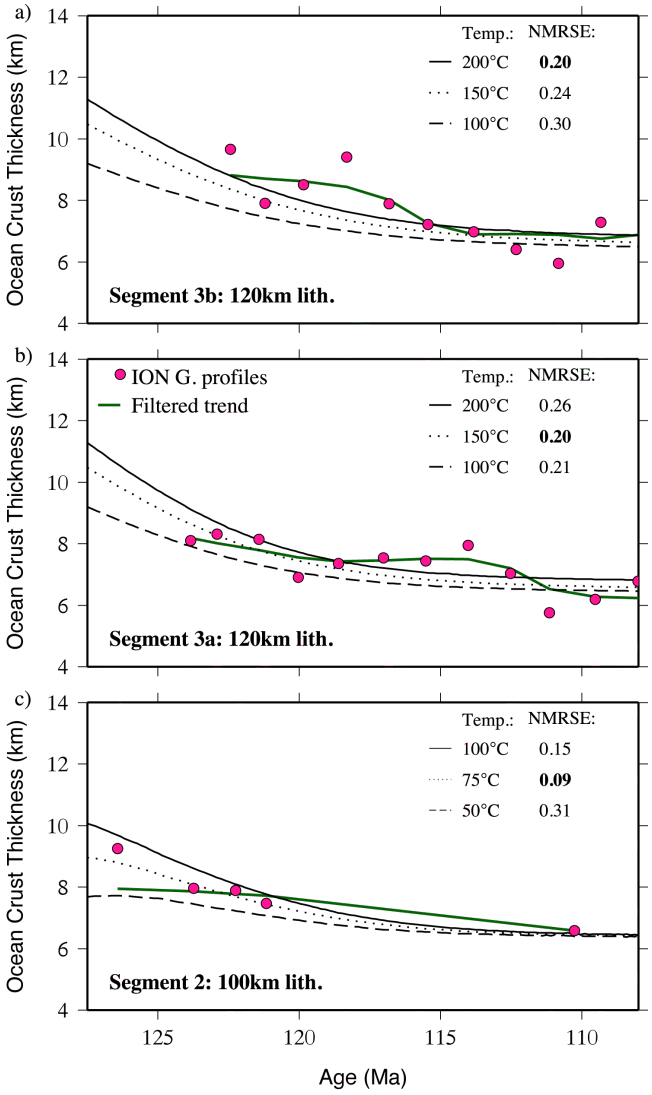


Figure 5.12: Model results per segment on the South American margin. Model asthenosphere temperature of 1315 °C, and spreading rate of 12 mm yr^{-1}. Each segment is tested for different hot layer models. The best match model trend was found by calculating a normal root mean square error (NRMSE) for each of the 1.5 Myr binned observation points (pink dots) with the preferred result in bold. Results for Segments 3b (a), 3a (b) and 2 (c) have hot layers with temperatures of 200 °C, 150 °C and 75 °C respectively.

thickness within the same range of values (Fig. 4.10c). Therefore, for simplicity the spreading rate was kept at 12 mm yr^{-1}. As before, the models have a model asthenosphere temperature of 1315 °C, with varying hot layers and initial lithosphere thickness per segment. The preferred model was determined by calculating a normalised root mean square error (NRMSE), calculated using the equation:

$$RMSE = \sqrt{\frac{(y_{mod} - y_{obs})^2}{n}} \quad , \quad \therefore NMRSE = \frac{RMSE}{y_{max} - y_{min}} \quad , \tag{5.1}$$

where y_{mod} is the value produced by the model, y_{obs} is the value observed, n is the number of data points, and $y_{max} - y_{min}$ represents the range of data.

The post-rift stage of the models with hot layers of 50 to 200 °C were compared against the trend of reducing oceanic crustal thickness with age for each segment (Fig. 5.12). For Segment 3b, it was found that a model with a hot layer of 200 °C provided the best fit to the observations (Fig. 5.12a). This model implied that extension initiated at 147 Ma. For Segment 3a, the best fit model had a hot layer of 150 °C where extension was also initiated at 147 Ma (Fig. 5.12b). Segment 2 was best matched by a model with a hot layer of excess temperature 75 °C, suggesting extension initiated at 141 Ma. As for the comparison to the wide-angle data (Fig. 5.10), these models suggest a similar Late Jurassic age for the initiation of extension in the southern South Atlantic.

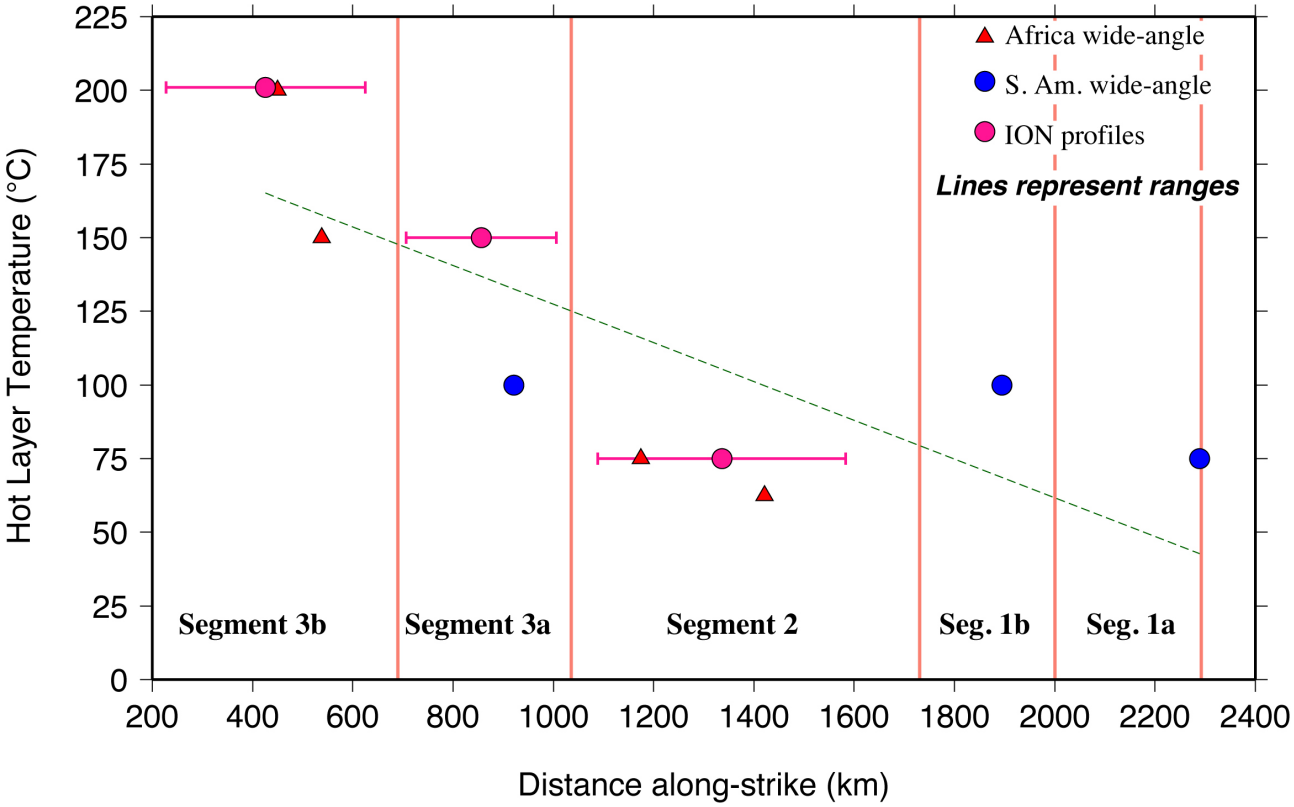


Figure 5.13: Hot layer temperature vs. distance along-strike. Results for the wide-angle profiles shown in Fig. 5.10 are given as symbols. Results for the long MCS profiles shown in Fig. 5.12 are marked as pink circles with horizontal bars marking distribution of the profiles. There is an overall reduction of ∼40 °C per 500km.

The modelling matches to the oceanic crustal thickness from the wide-angle seismic lines (Fig. 5.10) and the long offset ION Geophysical profiles (Fig. 5.12) allow for the change in hot layer temperature to be plotted against distance along-strike for both margins (Fig. 5.13). A general temperature decrease trend was observed from a thermal anomaly of 200 °C in the north to 75 °C in the south (Fig. 5.13). A linear fit to all the data points would suggest a reduction of ∼40 °C per 500 km distance along-strike. Within this general trend, evidence was

found, for example within both Segments 3b and 3a, for a drop of temperature of ∼50 °C over roughly 100 km distance. While there is a large degree of uncertainty on these model predictions, these drops in temperature occur within the segments and not at their edges, contrary to what the segmentation model suggests. This may suggest that segment boundaries play only a minor role in the volcanic nature of continental break-up, with a larger number of wide-angle profiles spread along-strike necessary to confirm this.

5.4 Discussion

Franke et al. (2007) and Koopmann et al. (2014b) have suggested lithospheric segmentation as a highly influential factor affecting volcanism in the South Atlantic. They established this from increasing widths and volumes of SDRs towards segment boundaries, and did not take initial oceanic crustal thicknesses into account. The precise measurement and mapping of SDRs is difficult due to the high-scatter of seismic waves within them, and the mechanism for their formation is still not fully understood. Only with full high-quality 3D seismic data sets will their variations be understood. This study differs from these previous publications on continental break-up in the southern South Atlantic, as it concentrates on post-rift volcanism, where initial production of ocean crust is located, rather than syn-rift volcanism, where SDRs are found (Franke et al., 2007; Koopmann et al., 2014b,a). From the results, it is suggested that oceanic crustal thickness is primarily controlled by temperature and initial lithosphere thickness. With a measurement point on average every 55 km along-strike, there is no clear systematic trend for increased magmatism relative to segments boundaries from ocean crust thickness observations and consequent modelling (Figs. 5.6b, 5.8, and 5.13).

In the North Atlantic (Fig. 5.6a), Collier et al. (2009) presented ocean crust measurements both south and north of the Greenland-Iceland-Faeroe Ridges. The trend for this area was a reduction of 1.67 km per 100 km increased distance from the aseismic ridges, a stark difference to the trend seen in the South Atlantic, with a reduction of 0.16 km per 100 km (Fig. 5.6a). In the past, continental break-up in the North and South Atlantic have been regarded similar, with mantle temperature being deduced as the primary factor (e.g., White and McKenzie, 1989). The North Atlantic is considered in line with the classic 'mushroom head' plume model, with an axisymmetric geometry inferred from volcanic margins both north and south of the Greenland-Iceland-Faeroe Ridges. This is not seen in the South Atlantic, where volcanic passive margins are found on conjugate margins south of the Rio Grande Rise and Walvis Ridge, but magma-poor passive margins are found to the north (Contrucci et al., 2004; Aslanian et al., 2009; Reston, 2010; Fromm et al., 2015). Additionally, the North Atlantic underwent a pre-thinning extension event prior to break-up, causing enhanced melt generation through focused upwelling (Armitage et al., 2010). This is not seen in the study area, and given the effect of temperature and lithosphere thickness on break-up volcanism modelled here (e.g. Fig. 5.8), it is suggested that the varying trends seen between the North and South Atlantic indicate differing initial break-up conditions, in both initial lithosphere structure and mantle temperature.

Through the simulations, it is shown that a simple 2D model can match initial ocean crust thickness,

and is sensitive to changes in initial lithosphere thickness, mantle asthenosphere temperatures and hot layer temperatures (Fig. 5.3 and 5.13). These results indicate the presence of a reduction of temperature, both in direction parallel to the margin along-strike and in time. The along-strike decrease can be linked to a reduction in temperature, moving from a mantle plume axis to its fringes (e.g., Campbell, 2007). From modelling the thickness of oceanic crust generated by decompression melting, it is estimated that there is a reduction in temperature from 1515 °C near the Rio Grande Rise and Walvis Ridge (Profile AF1 with a distance of 450 km) to 1365 - 1390 °C at the edge of the segments in the south (Profile SA3 at a distance of 2300 km). This suggests the presence of a mantle plume, or at the very least a thermal anomaly, reaching temperatures of 200 °C above the model asthenosphere temperature of 1315 °C.

Putirka (2005) calculated the temperature for the Hawaii and Iceland plumes, finding them to be 250 ± 50 °C and 165 ± 60 °C hotter than asthenosphere temperature, which is within range of the maximum excess temperature of 200 °C. Coupled with a model asthenosphere temperature of 1315 °C, the maximum temperature of 1515 °C falls in the limits of the maximum potential temperature for the Rio Grande Rise and Walvis Ridge in the northern region of the study area, estimated at 1450 - 1540 °C (Gallagher and Hawkesworth, 1994). Furthermore, these results agree with thermobarometry results from Trumbull (2014), where, from a compilation of onshore basalts, a north to south decrease in temperatures of 140 °C from 1520 °C in the north to 1380 °C in the south is seen.

With the models, the duration of rifting can also be estimated. A rift duration in the order of 23.5 to 30 Myr is predicted for Segments 2 and 3, reduced to 15 Myr for Segment 1. Given that the first magnetic isochrons are roughly 126 Ma, this places the onset of extension for the study area to be within the Late Jurassic at 156 Ma for the African wide-angle profiles, 147 Ma for ION Geophysical profiles in Segment 3, and 141 Ma for the South American wide-angle profiles and ION Geophysical profiles in Segment 2. Despite the simplifications of the geodynamic model, such an age for the onset of extension is quite reasonable. Several studies have found evidence for the commencement of rifting in the Late Jurassic (e.g., Maslanyj et al., 1992; Light et al., 1993; Clemson et al., 1997, 1999; Gallagher and Brown, 1999; Aizawa et al., 2000), and syn-rift sediments within the Namibian passive margin are dated to be between 130 and 150 Ma (Clemson et al., 1997; Guillocheau et al., 2012).

5.5 Summary

The LaLOC location was identified and initial oceanic crustal thickness was measured for 37 seismic profiles along conjugate margins in the southern South Atlantic. The along-strike distance was measured from the commencement of the Rio Grande Rise and Walvis Ridges for all of these points and the spatial variability of ocean crust thickness was studied. A trend of reduction in initial oceanic crustal thickness of 0.16 km per 100 km south from the Rio Grande Rise and Walvis Ridge was found (Fig. 5.6a), with thickness ranging from 11.7 km adjacent to the ridges, decreasing to 6.1 km at the most southerly point. No strong correlation between

segment boundaries and oceanic crustal thickness was found (Fig. 5.6b and 5.8).

The relatively simple numerical model of continental break-up used here has previously demonstrated the importance of lithosphere thickness on break-up volcanism (Armitage et al., 2010). Present-day lithosphere values were used with the assumption of little change since break-up (McKenzie et al., 2015). By also assuming the sea floor spreading rates are indicative of the rate of extension during break-up, the mantle potential and hot layer temperatures were varied in an attempt to fit the observed age and thickness of the first oceanic crust produced.

From the long-offset ION Geophysical lines, the model asthenosphere temperature was first determined to be 1315 °C using the observed reduction in oceanic crustal thickness with time and distance from the passive margin (Fig. 5.9). To match the initial oceanic crustal thicknesses from the seismic data, it was found there must have been an increased temperature relative to the model asthenosphere temperature. From an initial value of 1515 °C with proximity to the Rio Grande Rise and Walvis Ridge, representing an excess temperature of 200 °C, there was a reduction of ∼40 °C per 500 km, matching the initial oceanic crustal thickness estimated from the seismic data (Fig. 5.13). This supports the evidence of the presence of a mantle plume or thermal anomaly as the origin for excessive melt production in the study area. In addition, the rifting duration range from 15 - 30 Myr, suggesting rifting had started in the Late Jurassic, in agreement with evidence from sedimentary accumulations (e.g., Clemson et al., 1997; Guillocheau et al., 2012). Therefore, while other factors, such as segmentation or sediment loading (e.g., Bialas and Buck, 2009; Koopmann et al., 2014b), can influence rift architecture, the volcanic nature of a rifted margin is fundamentally controlled by the structure of the lithosphere and asthenosphere.

Chapter 6

Testing models of syn-rift melt generation in the southern South Atlantic

6.1 Introduction

This chapter's main objective is to test the possible influence of active mantle upwelling on magmatism and the validity of the *Mantle Plume - VPM Theory* using observational constraints from syn-rift magmatism. Observational constraints are from Profiles AF0–AF4 on the African margin, representing consistent along-strike measurements of syn-rift magmatism. Due to the lack of wide-angle profiles with syn-rift magmatism on the South American margin, the latter was not considered. In order to quantify syn-rift magmatism, estimations of SDR and HVLC body areas were made from the wide-angle profiles. The location and areas of HVLC bodies & SDR locations were previously identified for Profiles AF0 - AF4 in **Chapter 3** following criteria largely based on seismic velocity (summary in Table 3.1). Overall from north to south, there was a general decrease in (1) maximum HVLC thickness, (2) melt areas (with and without SDRs) and (3) maximum seismic velocity. Using these observations, the presence of active mantle upwelling and validity of the *Mantle Plume - VPM Theory* will be tested for. As segmentation was already tested for in **Chapter 5** with a higher quantity of data points and dismissed, it will not be considered within this chapter.

6.1.1 Active Mantle Upwelling

As an alternative to the *Mantle Plume - VPM Theory*, the first part of this chapter will test the presence of active mantle upwelling by adopting the H_c-V_p method. Active mantle upwelling was proposed as an alternative mechanism for the formation of the volcanic passive margin found on the East Coast of the U.S. (Kelemen and Holbrook, 1995). As it has no linked flood basalt, no hotspot trail and erupted over a 38 Myr period (Morgan, 1983; De Boer et al., 1988; Klitgord et al., 1988; Manspeizer and Cousminer, 1988), it does not comply with the *Mantle Plume - VPM Theory* and an alternate method of formation was necessary. The H_c-V_p method is an approach for understanding the relationship between mantle temperature, degree of active upwelling, and melt generation, using data extracted from syn-rift magmatism. From the trends in crustal thickness versus seismic velocity, the effect of upwelling and mantle temperature on melt production can be separated.

In a pure passive upwelling model, when a plume is present, a thicker crust is created due to a higher temperature, where the elevated temperature increases the depth range of melting (Kelemen and Holbrook, 1995). Increased temperature in the zone of partial melting increases the magnesium content and reduces the silicon content within the melt, increasing the overall seismic velocity (Kelemen and Holbrook, 1995; Hopper et al., 2003). However, for an active upwelling scenario, there is an increase in material flux, without an alteration in the depth of melting. Hence, there is no rise in magnesium content or consequently in seismic velocity (Kelemen and Holbrook, 1995). By plotting igneous crustal thickness, H_c, versus average bulk crustal velocity, V_p, the cause of melting could be separated. Holbrook et al. (2001) used this method with the SIGMA profiles in Southeast Greenland (locations inset map Fig. 1.6), and found evidence for active mantle upwelling during the break-up of the North Atlantic with the presence of the Iceland Plume. Using observational constraints from Profiles AF0–AF4, the presence of active mantle upwelling can be tested for the southern South Atlantic.

6.1.2 Numerical model of continental rifting and the *Mantle Plume - VPM Theory*

In the second part of this chapter, the numerical model of continental rifting is used to test the validity of the *Mantle Plume - VPM Theory* for the African margin. The results from the numerical model of continental rifting will be used in an attempt to match observational constraints from syn-rift magmatism, in terms of melt areas and seismic velocity trends. The numerical model is used with the same parameters and initial conditions as in **Chapter 5**, with a hot layer recreating the presence of a mantle plume and the lithosphere driven apart by a divergent velocity boundary condition on the upper surface (Fig. 4.3). In addition to calculating melt volumes, the numerical model has the capability of calculating the composition of major element oxides during break-up, with two different composition parametrisations available (previously explored in Section 4.4). The composition parametrisation choice for the South Atlantic mantle will be aided by geochemistry from DSDP sites and the Mid-Atlantic Ridge dredge samples (Appendix B). Following this, the calculated major element

oxide percentages are used to calculate average seismic velocity through time, using an empirical formula from Behn and Kelemen (2003). The resulting seismic velocity trends and melt areas from model results are then compared to seismic data observations in order to explore the controls on magmatism within this region.

6.2 Testing for the presence of Active Mantle Upwelling: H_c-V_p method

Prior to comparing crustal thickness to seismic velocity, alterations to the rock from burial, alteration and porosity have to be accounted for. Velocities obtained from the seismic data need to be corrected from the *in situ* temperature and pressure to a reference state (Breivik et al., 2012). For example, normal oceanic crust has an average velocity ranging from 6.8 - 7.0 $km\,s^{-1}$, but volcanic rocks, having undergone burial and alteration, have a velocity range of 5.0 - 6.0 $km\,s^{-1}$ (White et al., 1992; Kelemen and Holbrook, 1995). Here, two corrections for *in situ* velocities from different approaches of the H_c-V_p method to account for changes in seismic velocity from burial, alteration and porosity were explored: the Holbrook et al. (2001) approach (Fig. 6.2) and the Parkin and White (2008) approach (Fig. 6.3). Both were based on an empirical function developed from Kelemen and Holbrook (1995) using data from Kinzler and Grove (1992) for the relationship between seismic velocity, pressure of melting and melt fraction. As the two approaches to account for changes in *in situ* seismic velocities differ, it means that the resulting mean seismic velocities cannot be compared, and the individual reference models must be used. Additionally, the two approaches will differ in crustal thickness and seismic velocities used, with Holbrook et al. (2001) considering full igneous crustal thickness and Parkin and White (2008) only considering lower crust (orange and purple lines in Fig. 6.1). Changes in terms of thickness and seismic velocity should be reflected when only considering HVLC bodies. However, in order to compare results to the reference models of the two approaches, the original definitions of igneous crustal thickness and lower crustal velocity will be kept.

6.2.1 Holbrook et al. (2001) approach

In this approach, igneous crust was first defined by a lower limit of seismic velocity of 6.5 $km\,s^{-1}$, and seismic velocity was then corrected to account for burial alteration and porosity (orange line in Fig. 6.1b). Holbrook et al. (2001) assumed all seismic velocities lower than 6.85 $km\,s^{-1}$ were affected by alteration or porosity and not representative of the bulk composition, and were replaced with this value. This value corresponds to the velocity of a zero-porosity tholeiitic basalt and to ODP sampled SDR compositions (Kelemen and Holbrook, 1995). Corrections following the initial replacement of values 6.85 $km\,s^{-1}$ and under were then applied for pressure and temperature with respect to depth. These were $2.2 \times 10^{-4}\,km\,s^{-1}\,MPa^{-1}$ and $-5.0 \times 10^{-4}\,km\,s^{-1}\,°C^{-1}$, with a linear temperature gradient from 10 °C at the seafloor to 750 °C at 40 km depth, as well as a 600 MPa pressure correction (Christensen, 1979). Pressure was estimated by first calculating density from velocity using an empirical calculation from Ludwig et al. (1970). Following the corrections, a bulk average seismic velocity

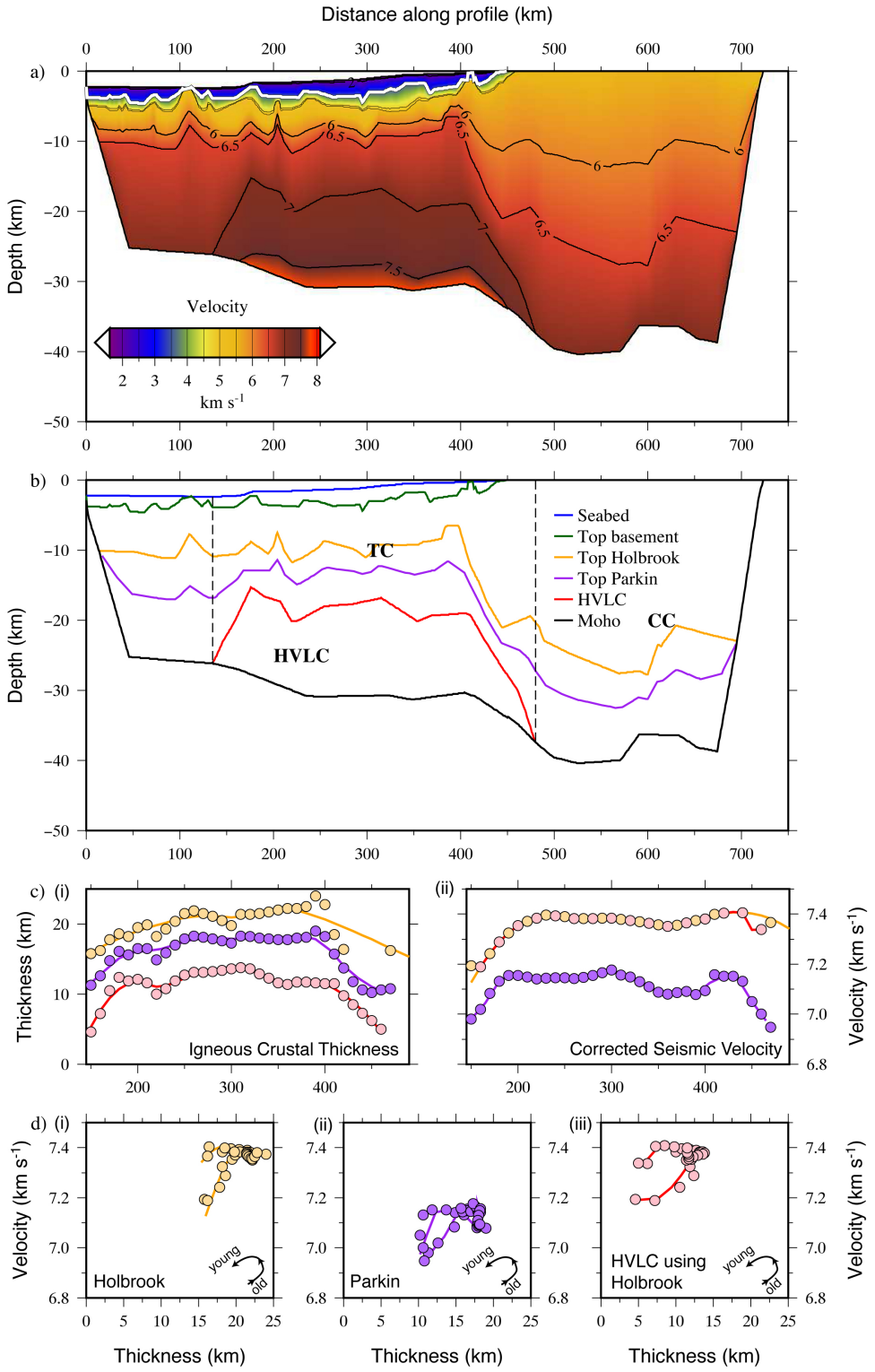


Figure 6.1: Profile AF0: velocity model and line drawing. Part (a) shows the seismic velocity section from Fromm et al. (2015). Part (b) shows the line drawing of major features. Locations are shown for the ocean crust (OC), transitional crust (TC), high-velocity lower-crustal (HVLC) body and continental crust (CC). Also shown are the top igneous crust contour (orange line - defined as $6.5\,\mathrm{km\,s^{-1}}$ by Holbrook et al., 2001) and top lower crust contour (purple line - defined as $6.7\,\mathrm{km\,s^{-1}}$ by Parkin and White, 2008). Part (c) shows the extracted igneous crustal thickness (part i) and extracted correction seismic velocity (part ii) following the Holbrook et al. (2001) approach (orange line/yellow dots) and the Parkin and White (2008) approach (purple line/purple dots), as well as for the HVLC body only following the Holbrook et al. (2001) approach (red line/pink dots). The seismic data points are similar for the Holbrook et al. (2001) and HVLC body due to the $6.85\,\mathrm{km\,s^{-1}}$ threshold. Part (d) shows the H_c-V_p curves from the Holbrook et al. (2001) approach (part i), the Parkin and White (2008) approach (part ii) and for the HVLC body only following the Holbrook et al. (2001) approach (part iii). The arrows in the bottom left show the direction of the data, representing the transition from near to continental crust (old) to oceanic crust (young).

could be obtained.

Holbrook et al. (2001) assumed all melt was produced in the mantle below the evolving rift, with the assumption that the resulting mean crustal composition was representative of the original melt. In order to categorise between passive upwelling and different active upwelling rates, melting models were used as a reference frame (Fig. 6.2). Seismic velocity was calculated from the empirical formula using melt pressure and fractionation from Kelemen and Holbrook (1995). With this approach, the McKenzie and Bickle (1988) and Langmuir et al. (1992) melting models were used to differentiate between passive and active upwelling, with both showing an increase in melt thickness and seismic velocity with increasing mantle temperature. The McKenzie and Bickle (1988) model was additionally used to compare different ratios of active mantle upwelling, with ratios (X) of 2, 4 and 8. With these increasing ratios, thicker crust was produced with only a slight increase in mean seismic velocity (Fig. 6.2), allowing the differentiation between increase in temperature and active mantle upwelling.

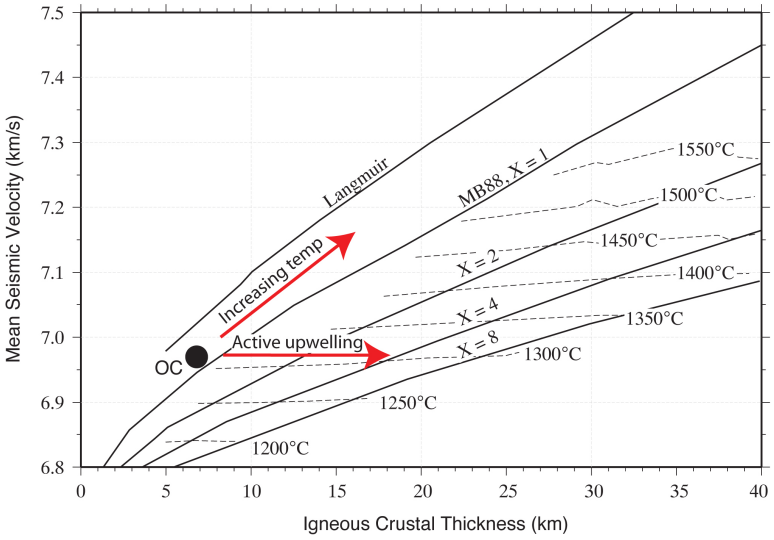


Figure 6.2: H_c-V_p reference models, adapted from Holbrook et al. (2001). There is a comparison of melt properties generated by passive upwelling (lines labelled Langmuir and MB88, X = 1) and active upwelling (lines with X = 2, 4 & 8). The two melting models are from Langmuir et al. (1977) (upper most line, labelled) and McKenzie and Bickle (1988) (remaining lines, with differing active upwelling ratios of X from 1 to 8). Top angled red arrow represents effect of increased temperature, causing an increase in both crustal thickness and seismic velocity. Bottom flat red arrow represents increased active upwelling where there is an increased crustal thickness with no significant change in mean crustal velocity (Holbrook et al., 2001). Reference ocean crust (OC) is the large black circle.

6.2.2 Parkin and White (2008) approach

Parkin and White (2008) had a slightly different approach (Fig. 6.3), using only lower crustal data with a lower limit of 6.7 $\mathrm{km\,s^{-1}}$ (purple line in Fig. 6.1b). As lower crust is suggested to contain the first fractionates from primary melt, it is argued to be representative of the upper boundary on bulk velocity (Korenaga et al., 2002). Using the identified lower crust, seismic velocity was corrected for temperature and pressure to 150 °C and 230MPa, and the applied corrections were slightly different, with $-4.0\,\mathrm{x}\,10^{-4}\,\mathrm{km\,s^{-1}\,{}^{\circ}C^{-1}}$ for temperature and $2.0\,\mathrm{x}\,10^{-4}\,\mathrm{km\,s^{-1}\,MPa^{-1}}$ for pressure. Likewise to Holbrook et al. (2001), Parkin and White (2008) use different melting models as a reference frame. The theoretical H_c-V_p curves for melt generation from a normal pyrolitic mantle are from White and McKenzie (1989); Kelemen and Holbrook (1995); Korenaga et al. (2002); Sallarès

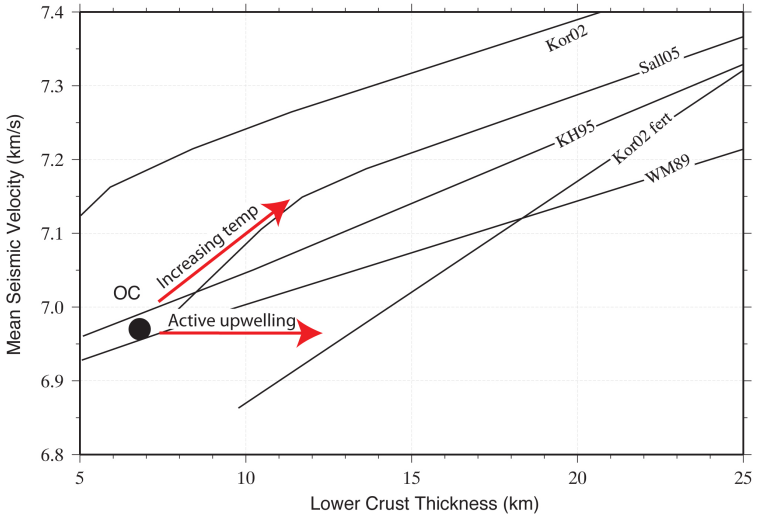


Figure 6.3: H_c-V_p reference models, adapted from Parkin and White (2008). There is a comparison of melt properties generated for melt generation from a normal pyrolitic mantle (White and McKenzie, 1989; Kelemen and Holbrook, 1995; Korenaga et al., 2002; Sallarès et al., 2005) and from a fertile mantle (Korenaga et al., 2002). Average normal oceanic crust is represented by the circle (White et al., 1992), with arrows showing what the resulting changes in H_c-V_p represent in terms of upwelling and mantle temperature (Parkin and White, 2008). Reference ocean crust (OC) is the large black circle.

et al. (2005) and for a fertile mantle from Korenaga et al. (2002). The curves are all plotted with the same average temperature of 150 °C and reference pressure of 230 MPa, considered in this case representative of only lower-crust information.

6.2.3 H_c - V_p curves for Profiles AF0–AF4

To establish a reference point for the H_c - V_p interpretations, an ocean crust thickness and a starting velocity were needed. For ocean crust thickness, an average of steady-state oceanic crust production was used from Segments 3a, 3b and 2 (Fig. 5.7) on the South American margin, determined in **Chapter 5** at 6.8 km (Fig. 5.9). The oceanic crustal velocity was averaged from the reference points from the Holbrook et al. (2001) and Parkin and White (2008) approaches. Holbrook et al. (2001) obtained the reference velocity from 1 Myr old ocean crust in the East Pacific Rise, whilst Parkin and White (2008) used an average of lower-crustal velocity from White (1992). However, the seismic velocities are quite similar at 6.96 $km\,s^{-1}$ and 6.98 $km\,s^{-1}$ respectively, and an average of 6.97 $km\,s^{-1}$ was used.

The presence of active mantle upwelling was tested using both the approaches from Holbrook et al. (2001) and Parkin and White (2008) (Fig. 6.4 and 6.5 respectively) and also tested using information from only HVLC bodies (Fig. 6.6). Only the portions with identified syn-rift magmatism are used, due to possible continental contamination on the landward side, and the curves expected to trend towards average oceanic crustal values on the seaward side (see limits for Profile AF0 in Fig. 6.1b). Profile AF0 is used as a case study to understand the impacts the different approaches have on igneous crustal thickness and corrected seismic velocity (Fig. 6.1c & d), showing the results for the Holbrook et al. (2001) approach, Parkin and White (2008) approach, and for the HVLC body only using the Holbrook et al. (2001) approach. Igneous crustal thicknesses differ due to the different criteria imposed on each approach (Fig. 6.1c(i)). The seismic velocity correction for the Holbrook et al. (2001) approach and HVLC body are the same due to the 6.85 $km\,s^{-1}$ threshold (Fig. 6.1c(ii)). Finally, the H_c - V_p curves for the different approaches may all progress in the same direction (arrows in the left bottom

corners of Fig. 6.1d), but due to the varying approaches differing they have to be compared separately. This process was done for the remaining profiles (Fig. 6.4-6.6).

Following the Holbrook et al. (2001) approach and correction of seismic velocity (Fig. 6.2), the H_c - V_p curves for Profiles AF0 - 4 are all found to be in the area of above-normal mantle temperature, decreasing towards the south. With the increase in both H_c and V_p (similar to the upwards arrow in Fig. 6.2), all of the profiles began with an increasing mantle temperature. For Profiles AF0, AF1, AF2 and AF3 there was a reduction in both average seismic velocity and crustal thickness, and the curves were overall close to the reference models for passive upwelling. In the first half of the curves for Profiles AF1-AF3 (bottom section of data points, left to right), the curves intersect in a relatively perpendicular manner to the reference curves for active mantle upwelling. Only Profile AF4 indicates the possible presence of active mantle upwelling, with the oldest data points being relatively parallel to the active mantle upwelling curves. Overall however, the second half of the curves from Profiles AF2-AF4 (top section of data points, right to left) match closely to the Langmuir et al. (1992) melting model for passive upwelling. The inflection points are inferred to be representative of the exhaustion of the thermal anomaly with age and additionally Profiles AF1–AF4 all tend towards the reference point for ocean crust. Overall, a thermal anomaly is present during break-up over a distance of at least 1420 km south of the Walvis Ridge, with little suggestion for active mantle upwelling.

Thickness of lower crust and corrections to seismic velocity following the Parkin and White (2008) approach are also presented (Fig. 6.5). For the Parkin and White (2008) approach, the seismic profiles showed similar increases and decreases in both average seismic velocity and crustal thickness through time, with comparable inflection points. The most dissimilar H_c - V_p curve was for AF3, with significantly faster than average seismic velocities at an older age. As previously noted however, this wide-angle profile is considered the least reliable (Section 3.3.3). Overall, both increasing and decreasing average seismic velocities and crustal thicknesses through time could still be observed, with all the curves from Profiles AF0–AF4 lying on a similar trend. Therefore, using the Parkin and White (2008) approach, and compliant with results using the Holbrook et al. (2001) approach, it can be suggested that mantle temperature and not active mantle upwelling is responsible for magmatism observed within the study area, as there are positive correlations between increasing igneous crustal thickness and seismic velocities.

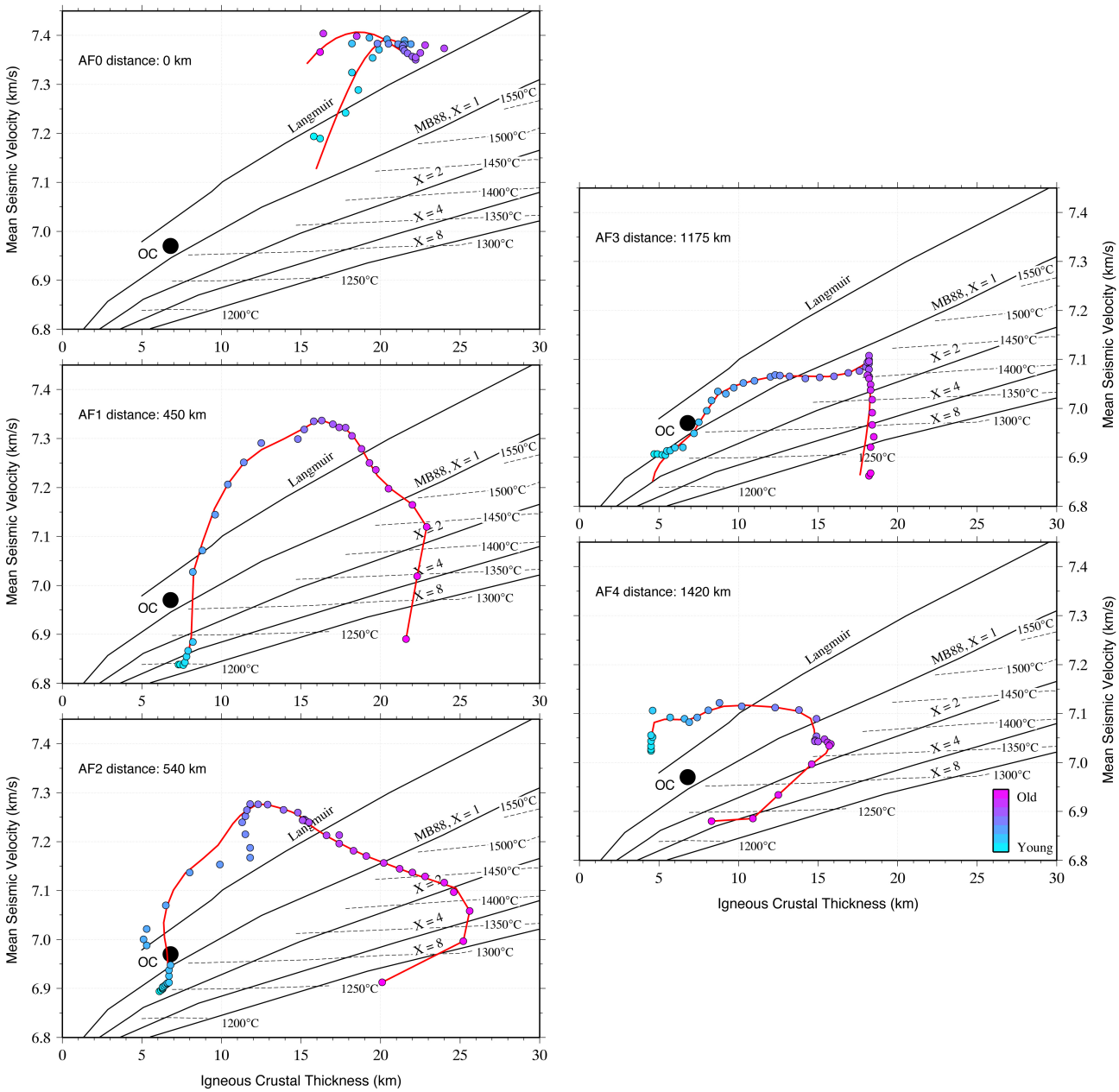


Figure 6.4: H_c-V_p for African profiles, using the Holbrook et al. (2001) approach for identification of igneous crust and correction of *in situ* seismic velocities. Curve interpretations are drawn using Fig. 6.2. Distances represent distance south of the Walvis Ridge.

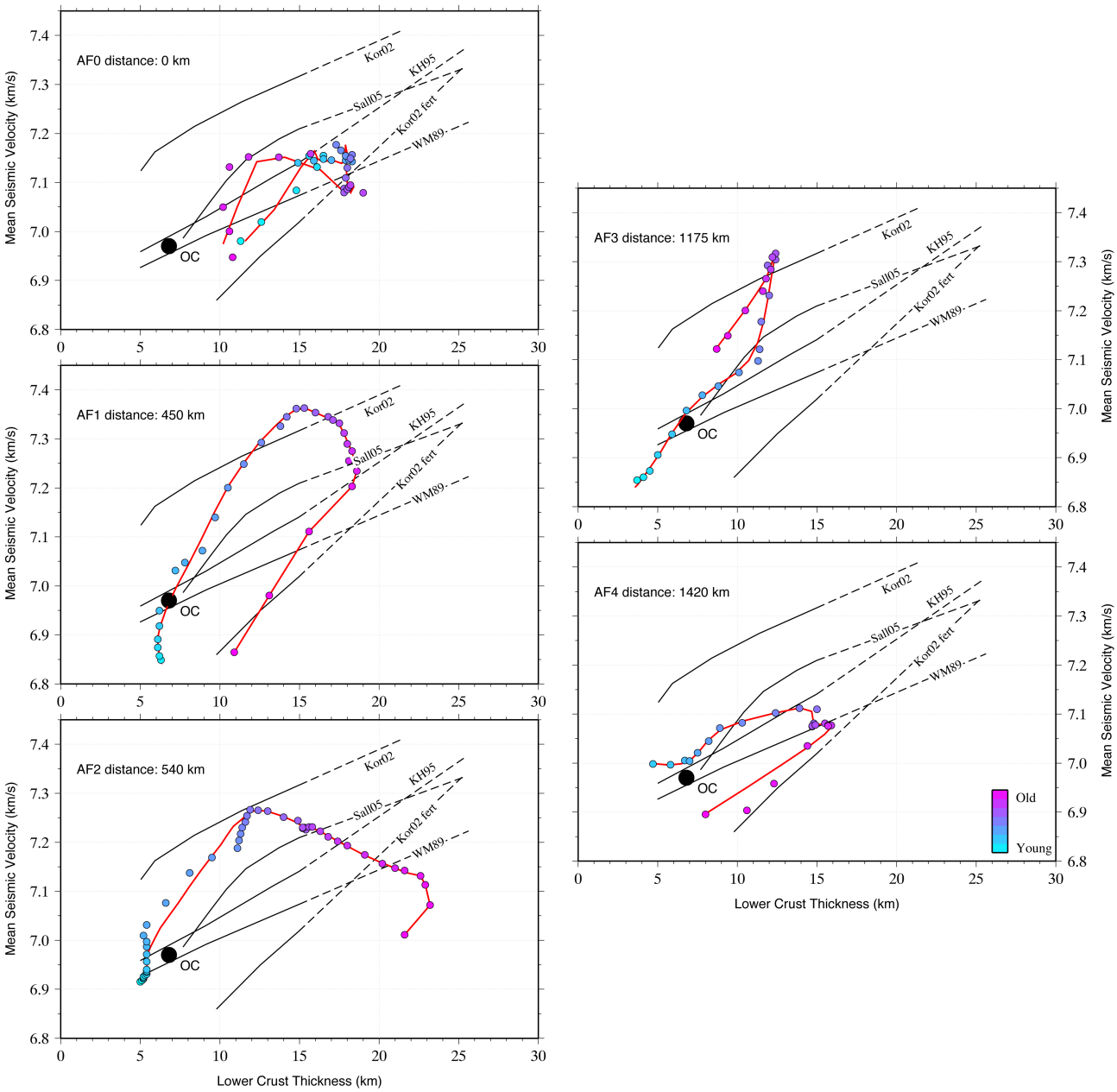


Figure 6.5: H_c-V_p for African profiles, using the Parkin and White (2008) approach for identification of igneous crust and correction of *in situ* seismic velocities. Curve interpretations are drawn using Fig. 6.3. Note that the thickness values are different to that of the Holbrook et al. (2001) correction (Fig. 6.4) due to the use of only lower crust for this approach. Distances represent distance south of the Walvis Ridge.

The presence of active mantle upwelling was also tested using information solely from the HVLC bodies based on the shape of the curves, with the understanding that they would not be compliant with any of the reference models from the two approaches due to their different definitions of thickness (Fig. 6.6). The curves had similar trends to those seen previously, lying in the direction of mantle temperature influence (slanted red arrow in Fig. 6.2), with reduced thicknesses and elevated mean seismic velocities. However, there was still little to no evidence of active mantle upwelling. The validity of mantle temperature influencing magmatism was further tested using the numerical modelling of continental rifting.

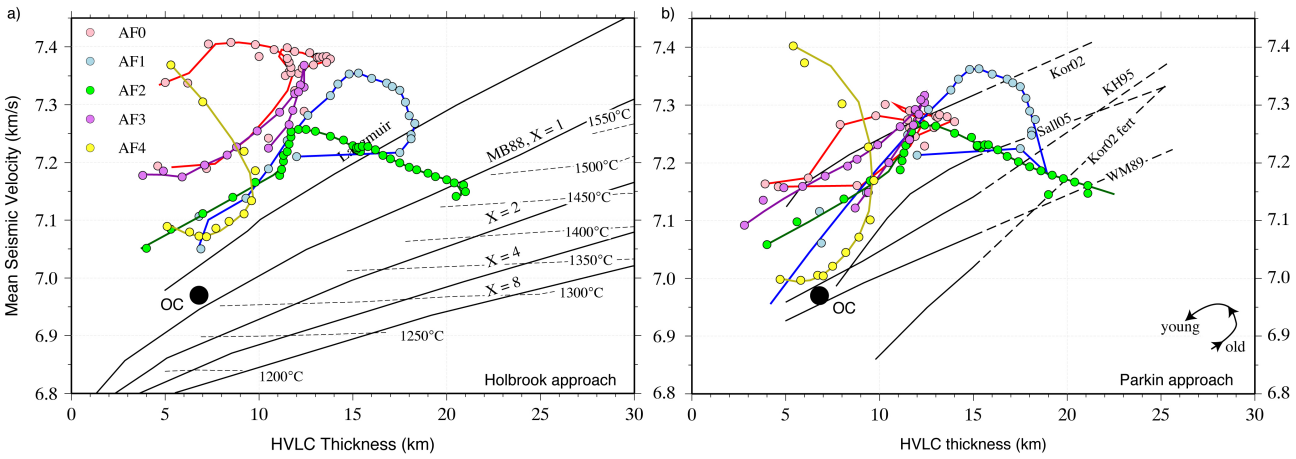


Figure 6.6: H_c-V_p for African profiles using information solely from the HVLC bodies. Part (a) uses the Holbrook et al. (2001) approach for the correction of *in situ* seismic velocities and part (b) uses the Parkin and White (2008) approach. Reference models are the same as Fig. 6.2 & 6.3.

6.3 Assessing the *Mantle Plume - VPM Theory* for Syn-Rift Magmatism: Numerical Modelling of Continental Rifting

The model space is the same as used previously, with a domain 2,800 km wide, 700 km deep and 256 x 256 elements, and a hot layer used to recreate the presence of a mantle plume (Fig. 4.3). Through the use of geophysical observations, the lithosphere thickness and extension rates had previously been estimated for the study area and specific to each profile (Section 5.2.3.2). The initial lithosphere thickness was estimated at the most seaward location of un-stretched continental crust using the tomographic model from Fishwick and Bastow, 2011 (Fig. 5.4b; Table 6.1) and the spreading rates summarised by Heine et al. (2013) (Fig. 2.12), assigned for each segment. For Segments 3b, 3a and 2 (Profiles AF1–AF4), the primary spreading rate was 12 mm yr^{-1}, and for Segment 4a (Profile AF0), the primary spreading rate was 10 mm yr^{-1} (Table 6.1).

Prior to varying the hot layer temperature, the choice of composition parametrisation must be determined. With the inclusion of major element oxide compositions through time, the model is capable of being compared to melt areas and seismic velocity trends for observational constraints. Although there is a general agreement that a HVLC body comprises of mafic to ultra mafic intrusions into stretched continental crust, this may happen in a more complex and random temporal-spatial pattern. The model however assumes all melt is focused and accreted into the rift axis in a vertical columnar fashion, which may not be representative. As the igneous crustal thickness (h_c) is estimated for each time step from the melt focused at the rift axis (Eq. 4.16), using a melt area could reduce some uncertainty regarding the formation of a HVLC body. Whilst igneous crustal thicknesses should still be somewhat representative of changes in the mantle thermal structure through time, this change will be better reflected through averaged seismic velocity, and hence seismic velocity trends are used.

Melt areas from model results are calculated from the integration of melt thickness results (e.g. Fig. 4.9). In order to compare model results to observational constraints where melt areas are in square kilometres, the age output for the model was converted to distance, using the spreading rate specific to the seismic profile (10 - 12 mm yr^{-1}, Table 6.1). In addition, to compare the melt area to syn-rift magmatism, the oceanic crustal thickness at the LaLOC location was used as a limit on model curves. Seismic velocity trends from model results are compared to averaged seismic velocities from the wide-angle profiles, using NRMSE values to quantify the best match (Eq. 5.1).

Table 6.1: Assigned model parameters: lithosphere thickness and spreading rates per segment. Opening ages are assumed by sub-plate from Moulin et al. (2010). M4, M2 and M0 are dated 127.23 Ma, 126.57 Ma, 124.05 Ma and 120.6 Ma respectively (Gee and Kent, 2007). Seismic tomography models from Fishwick and Bastow (2011) (Fig. 5.4). Spreading rates are from Heine et al. (2013).

Segment	Opening Age	Profile	Lithosphere thickness (km)	Spreading Rate (mm yr^{-1})
4a	M2-M0	AF0	140-150	10
3b	M2-M0	AF1	135-140	12
3a	M2-M0	AF2	125-130	12
2	M4-M2	AF3 & AF4	130-135	12

6.3.1 Composition parametrisation for the calculation of major element oxides

The numerical model has the capability of calculating major element oxides during break-up through to a steady-state system. By implementing this, seismic velocity can be calculated. The major element compositions of accumulated melt is a function of temperature, pressure and melt fraction (Eq. 4.20). To estimate the melt composition, two empirical parametrisations are compared: Watson and McKenzie (1991), or WM91, and Niu (1997), or N97. In addition, the N97 parametrisation has the capability of changing the bulk earth composition, and a pyrolite (N97-FG87; Falloon and Green, 1987) and a peridotite (N97-HK93; Hirose and Kushiro, 1993) are compared.

The methods of calculation for WM91 and N97 are different (more details in Section 4.4), and hence the compositional results and in turn the seismic velocity trends will also differ (Fig. 4.14). WM91 calculates major element oxides through fitting polynomial functions to batch melting experiments, essentially back calculating from a bulk silicate earth state. N97 however uses residue and determines the ratio of a particular oxide within solid and liquid phases by calculating partition coefficient D in order to calculate major element oxides (Eq. 4.18).

In order to determine the most suitable parametrisation to calculate composition, normalised values of basement-reaching DSDP samples and Mid-Atlantic Ridge (MAR) dredge samples (Appendix B) were compared to model results (Fig. 6.7 and 6.8). DSDP samples originated from 10 different drillholes (Table B.1) and the dredge samples were obtained from PetDB (http://www.earthchem.org/petdb), using a total of 85 samples over the Southern Segment MAR (Table B.2). Both the DSDP and dredge samples were filtered for values of magnesium less than 4%, as these are considered to be too altered, and following this, the remaining samples

had the volatile-free values of magnesium calculated (Trumbull, pers. comm., 11 Jan, 2016). The two data sets had similar averages and ranges for magnesium oxide, with an average 8.05% & range of 5.24-11.08% for DSDP samples, and an average of 7.94% and a range of 5.14-10.20% for dredge samples. The rest of the major element oxides also had similar average values (Table B.1 & B.2).

The models used to test the different composition parametrisations had no hot layer, a mantle potential temperature ranging from 1300 - 1325 °C and a lithosphere thickness of 125 km. Models were run with three possible parametrisations: WM91, N97-FG87 (a pyrolite based bulk earth composition) and N97-HK93 (a peridotite based bulk earth composition). The comparison was made when the model reached steady state. Melt generated at steady-state in a mid-ocean ridge is assumed to accumulate at the ridge axis, where it would undergo crystallisation. Mid-Atlantic Ridge crystallisation pressures are ∼200 Mpa (Herzberg, 2004), and these needed to be applied to model results in order to compare to real-world geochemistry data sets. This was done using MELTs, a program capable of predicting MORB compositions produced when assuming a crystallisation pressure (Ghiorso and Sack, 1995; Asimow and Ghiorso, 1998). Assuming a crystallisation pressure of 200 Mpa, melt water composition of 0.2% and a fayalite-magnetite-quartz redox reaction to calculate the ratio of FeO to Fe_3O_2, the liquid lines of descent were tracked until the MgO value was 8%. This value was chosen as it was close to the average magnesium content for both DSDP values at 8.05% and MAR values at 7.94% (Tables B.1 and B.2).

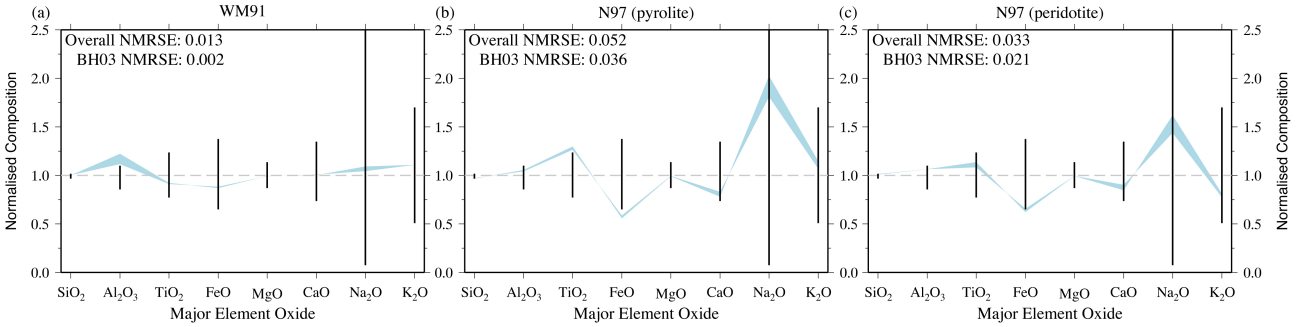


Figure 6.7: Comparison of model composition at steady-state to normalised DSDP values. The range of major element compositions are shown by the black lines (normalised from Table B.1). The range of model predictions are shown by the blue lines. Part (a) is for WM91, part (b) is for N97-FG87 with a pyrolite based bulk earth composition, and part (c) is for N97-HK93 with a peridotite based bulk earth composition. Models have a mantle potential temperature ranging 1300 - 1325 °C, a spreading rate of 12 mm yr $^{-1}$ and a lithosphere thickness of 125 km. Two NRMSEs (Eq. 5.1) relative to the normalised composition are calculated: one using all of the elements (overall) and the other one only using SiO_2, MgO and CaO from the formula of seismic velocity (BH03, Behn and Kelemen, 2003).

Two normalised root mean squares errors were calculated (Fig. 6.7 and 6.8). The first root mean square was an overall value considering all major element oxides, whilst the second was done for just SiO_2, MgO and CaO, being the major element oxides used in the calculation of seismic velocity from Behn and Kelemen, 2003 (Eq. 4.21). Comparing the results for the different composition parametrisations (Fig. 6.7 and 6.8), the NRMSE values were relatively low. However, the N97 parametrisations have a more realistic Ca/Al ratio, representative of the exhaustion of clinopyroxene with increased melt fraction (further discussed in Section 4.6.3; Fig. 4.14). Unlike WM91, the N97 parametrisation can be adjusted to use peridodite as bulk earth composition. A bulk

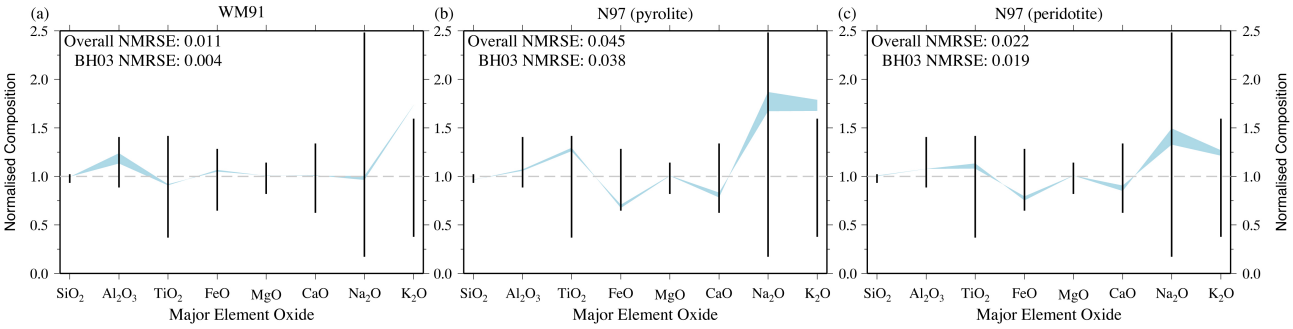


Figure 6.8: Same as Fig. 6.7, but compared to normalised MAR values (taken from Table B.2).

earth composition based on peridodite is considered the better choice as it was shown to be more accurate when calculating predictions in composition (Behn and Grove, 2015; Robinson et al., 1998; Hirschmann et al., 1998). As the NRMSE values were still low when using the N97-HK93 peridodite parametrisation at 0.021 (Fig. 6.7) and 0.019 (Fig. 6.8), this parametrisation was used hereafter.

6.3.2 Model asthenosphere temperature structure

In addition to lithosphere thickness and spreading rate, the model asthenosphere temperature had previously been determined in **Chapter 5**. Section 5.2.3.3 summarised how ION Geophysical lines were used to establish a model asthenosphere temperature of 1315 °C (Fig. 5.9). This value was assigned as the model asthenosphere temperature and used henceforth. With the pre-assignment of the initial lithosphere thickness, spreading rate and model asthenosphere temperature, and following the choice of composition parametrisation for major element oxides, the next step was to solve for the excess temperature of the hot layer.

Magnetostratigraphy studies for the Etendeka suggest the eruption had started by at least magnetic isochron M15n at 135.96 Ma (Dodd et al., 2015). With wide-spread seafloor spreading not occurring until M7 at 127.23 Ma (Fig. 2.10), the assumption of a hot layer present before break-up is valid. The temperature of the hot layer can be estimated following the McKenzie and Bickle (1988) melting model. Campbell (2007) found a minimum of 200 °C excess temperature was required to match the thickness observed at the Walvis Ridge, however this was for an estimated thickness of 26 km. Recent wide-angle surveys published in Fromm et al. (2015) suggest a thicker igneous crust of up to 30 km (Fig. 1.8). This was closer to the thickness observed in the vicinity of the Iceland Plume, for which Campbell (2007) suggested a 250 °C excess temperature. As a result, hot layers were tested starting from 250 °C for Profile AF0 and reducing towards the south.

6.3.3 Results from numerical model of continental rifting

6.3.3.1 Matching of model melt areas to observed melt areas

In order to match the model to the observations, total area of melt was used from seismic profiles and model results. Profile AF2 was used as a case study to demonstrate this process. It was found in **Chapter 3** that AF2 has a melt area of 2820 km^2 (Table 3.1). By using the oceanic crustal thickness at the LaLOC point (8.2 km, Table 3.2) as a limiting point, the total melt produced by the model was calculated (Fig. 6.9). The area for a model with a 175 °C hot layer was found to be 3140 km^2, reducing to 2700 km^2 for a model with a 150 °C hot layer (Fig. 6.9). Hence, the model closest to matching the observed area from Profile AF2 must be within this range. The range was further narrowed down to a hot layer ranging from 155 - 160 °C, with volumes of 2785 km^2 and 2870 km^2 respectively. The same process was applied for the melt area including SDR measurements (Table 6.3). For AF2, the total melt area with SDR area increased to 2940 km^2, and the hot layer range increased by 5 °C to 160 - 165 °C (Table 6.3).

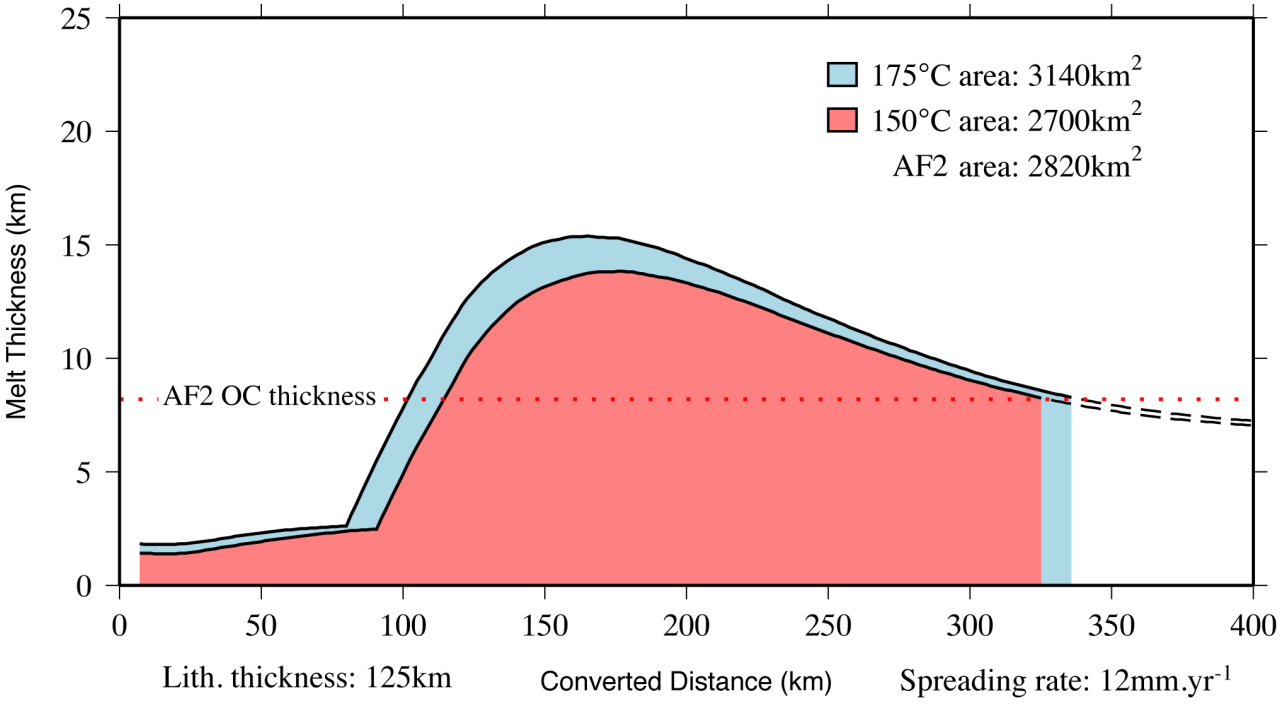


Figure 6.9: Comparison of model melt areas to areas from Profile AF2. Two models with different hot layers (150 and 175 °C) are presented here, with an initial lithosphere thickness of 125 km and spreading rate of 12 mm yr^{-1}. Areas are limited by the initial oceanic crustal thickness for AF2 (dashed red line). The model with a hot layer of 175 °C (blue shaded area) predictably has an area 15% greater than for a model with a hot layer of 150 °C (red shaded area).

This process, including melt areas with and without SDR areas, was repeated for Profiles AF0, AF1, AF3 and AF4 (Table 6.2 & 6.3). They models were all run with the profile's corresponding initial lithosphere thicknesses and with a 12 mm yr^{-1} spreading rate except for Profile AF0, run with a rate of 10 mm yr^{-1}. The closest matches were selected using an iterative script, with models with hot layers ranging from 95 °C, increasing every 5 °C, to 260 °C run. Using the initial oceanic crustal thickness as a limit, it was found that models

with excess temperature ranging from 250 - 255 °C matched the observations for Profile AF0. This lessened to 195 - 205 °C for Profile AF1 and to 155 - 165 °C for AF2. This decreasing trend continued southward for Profiles AF3 and AF4, with hot layer temperatures ranging from 110 - 120 °C and 100 - 120 °C respectively. The SDR areas increased the hot layer necessary to match area measurements by 5 °C, except in the case of Profile AF4 where it raised by 10 °C. The overlying trend seen here is a decrease in hot layer temperature with increasing distance from Walvis Ridge along the margin (Fig. 6.14a).

Table 6.2: Model results in comparison to crustal areas without additional SDR areas. Bold numbers represent the crustal areas from seismic data, with closest upper and lower hot layer possibilities above and below respectively. The results are also shown in Fig. 6.10. These results show a decreasing trend from north to south in hot layer temperature (Fig. 6.14).

Profile/ Model	Melt Area (km^2)	Hot Layer Temp. (°C)	Lith. Thickness (km)
Model 1	6660	255	150
AF0	**6610**		
Model 2	6340	250	150
Model 1	3730	200	140
AF1	**3660**		
Model 2	3585	195	140
Model 1	2870	160	125
AF2	**2820**		
Model 2	2785	155	125
Model 1	2630	115	130
AF3	**2595**		
Model 2	2520	110	130
Model 1	2725	105	130
AF4	**2590**		
Model 2	2440	100	130

Table 6.3: Same as Table 6.2, but using additional SDR areas and variations in initial lithosphere thickness, with results also shown in Fig. 6.10. These results still show a decreasing trend from north to south in hot layer temperature (Fig. 6.14).

Profile/ Model	Melt Area (km^2)	Hot Layer Temp. (°C)	Lith. Thickness (km)
Model 1	3885	205	140
AF1	**3780**		
Model 2	3730	200	140
Model 1	2970	165	125
AF2	**2940**		
Model 2	2870	160	125
Model 1	2745	120	130
AF3	**2700**		
Model 2	2630	115	130
Model 1	2880	120	130
AF4	**2860**		
Model 2	2770	115	130

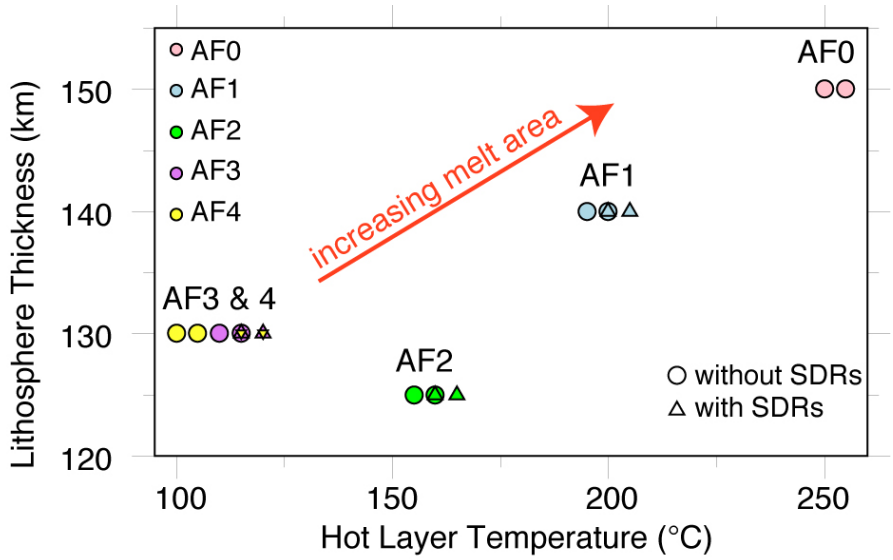


Figure 6.10: Results from matching model results to melt areas from Profiles AF0-AF4, presented as hot layer temperature against lithosphere thickness. Results from Table 6.2 with no SDR areas considered are shown as dots, and results considering SDR area from Table 6.3 are shown as triangle and inverted triangles (done to avoid overlap at similar data points). The red arrow shows the direction of increasing melt area.

6.3.3.2 Matching of model seismic velocity trends to observed seismic velocity trends

In order to match the seismic velocity model values to the observations, the variation in seismic velocity through time was used. Unlike melt, where the total area was compared, here the average seismic velocity was considered for each point for both the model and seismic data. This was done with the understanding that the intrusions forming a HVLC body may occur in a more complex and random temporal-spatial pattern, where an averaged seismic velocity will be more representative of the mantle thermal structure through time than the igneous crustal thickness. Therefore, the area of melt does not need to be calculated, and average seismic velocity is simply plotted against time. The N97-HK03 composition parametrisation was used to calculate major element oxides. Additionally, an empirical formula was used to calculate seismic velocity from major element oxides (Eq. 4.21). As the model does not correct for pressure, and can therefore not differentiate between upper and lower crust, the seismic velocity data for Profiles AF0–AF4 were corrected using the Holbrook et al. (2001) approach. The seismic velocity trends were limited by the commencement of ocean crust.

As a first step to match the model trends to the observations, the seismic data starting point was adjusted to achieve the 'best-fit' relative to different models. However, these were kept at the same scale and in-line with real ages, extracted from the age grid created from the Moulin et al. (2010) magnetic isochron and Gee and Kent (2007) time scale (Fig. 3.38). Note that this grid assumes that the ages of syn-rift magmatism are an extension of the magnetic anomaly dated oceanic crust that follows. This assumption was used in earlier applications of this numerical model rifting in different global localities (e.g., Armitage et al., 2011). A normalised root mean square error (NRMSE) was calculated in order to quantify the best fit (Eq. 5.1). With the range of values present, a NRMSE below 0.350 was considered a moderate fit, and anything below 0.200 a good fit.

Using a model asthenosphere temperature of 1315 °C and a spreading rate of 10 - 12 mm yr^{-1} (Table 6.4), the model was capable of matching the seismic velocity of Profiles AF0 - AF2 with hot layers ranging from 150 - 250 °C with NRMSE values below 0.350. For Profile AF0, a model with a hot layer of 250 °C was capable

of matching the data with a moderate fit (Fig. 6.11, Table 6.4). Two models were run, with spreading rates of 10 and 12 mm yr^{-1} and with NRMSEs of 0.350 and 0.385 respectively, with the former having a better match (Fig. 6.10) and agreeing with hot layer temperatures from melt area results. The initial lithosphere was not changed for Profile AF0, as it was clear from seismic tomography that it was 150 km thick in this region.

This agreement continued with Profiles AF1 and AF2. A model with a 200 °C hot layer matched the seismic velocity of Profile AF1 with a moderate fit (Fig. 6.12a), however the model could not match the sharp increase in seismic velocity seen with Profile AF1. This may be a result of uncertainty from the Moulin-Gee age grid (Fig. 3.38), and there could be a wider range of ages. If so, the initial trend would be less abrupt, closer to the one seen on Profile AF2 (Fig. 6.12b). Models with hot layers ranging between a 150-175 °C matched the seismic velocity of Profile AF2 with a good fit (Fig. 6.12b, Table 6.4).

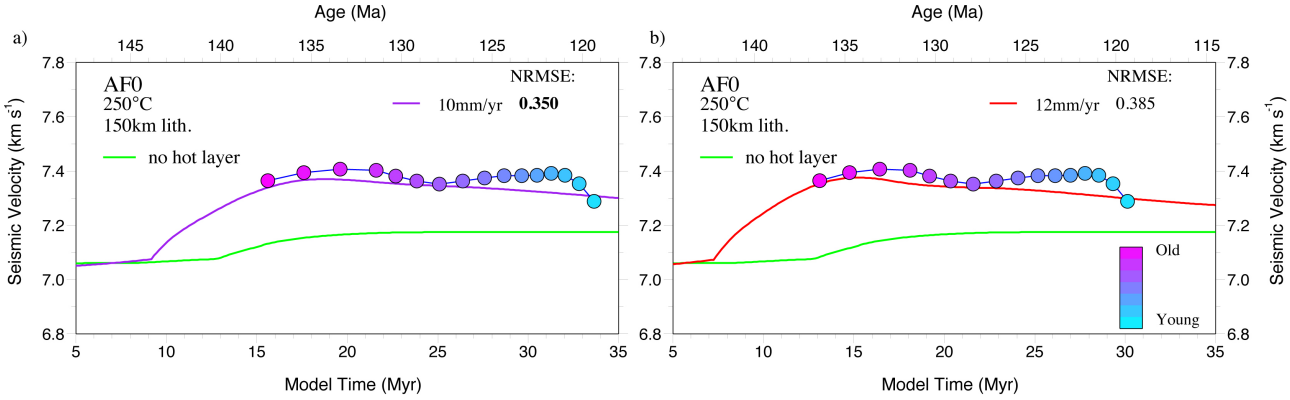


Figure 6.11: Models results for Profile AF0. Model asthenosphere temperature of 1315 °C, and spreading rate of 12 mm yr^{-1} unless specified otherwise. The ages between start and end of the data points from seismic profiles have been calculated according to their location on the Muller-Gee age grid (Fig. 3.38). The green line represents a model with no hot layer, used to show seismic velocity changes with the addition of hot layers. Panels (a) and (b) have hot layers at 250 °C and spreading rates at 10 and 12 mm yr^{-1} respectively, capable of matching the data from Profile AF0 both in seismic velocity and time range.

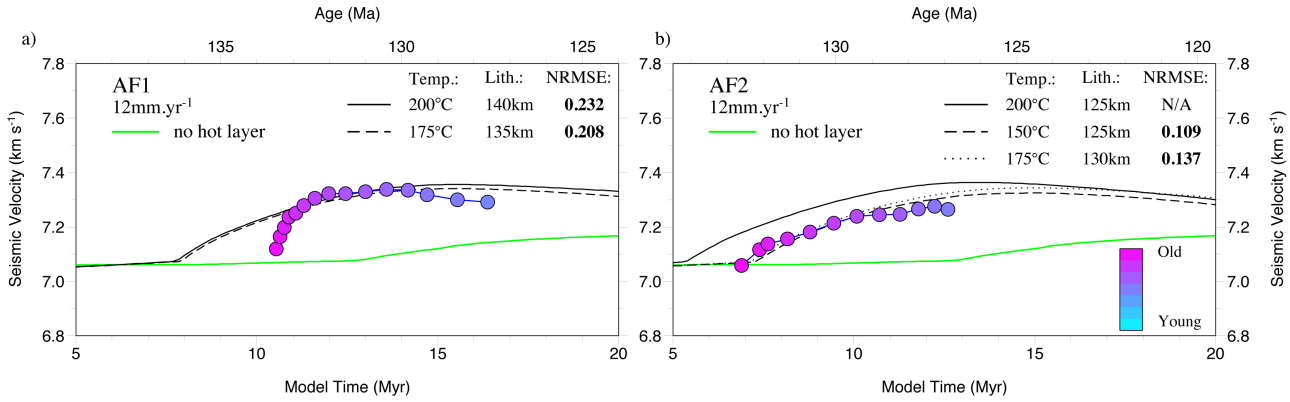


Figure 6.12: Same as Fig. 6.11, but for Profiles AF1 - AF2. Panel (a) has a hot layer of 200 °C capable of matching the data from Profile AF1 over a similar time range. Panel (b) has two possibilities of hot layers, ranging from 150 - 175 °C capable of matching the data from Profile AF2 in both seismic velocity and time.

Compared to Profiles AF0 - AF2, Profiles AF3 and AF4 had less favourable results for a model asthenosphere temperature of 1315 °C (Fig. 6.13a & b). Due to the lower seismic velocity values for these profiles, models with a lower model asthenosphere temperature were tested. However, the reduction did little to improve the fit. As

the mantle asthenosphere temperature was previously well established (Section 5.3.2.1; Fig. 5.9) and

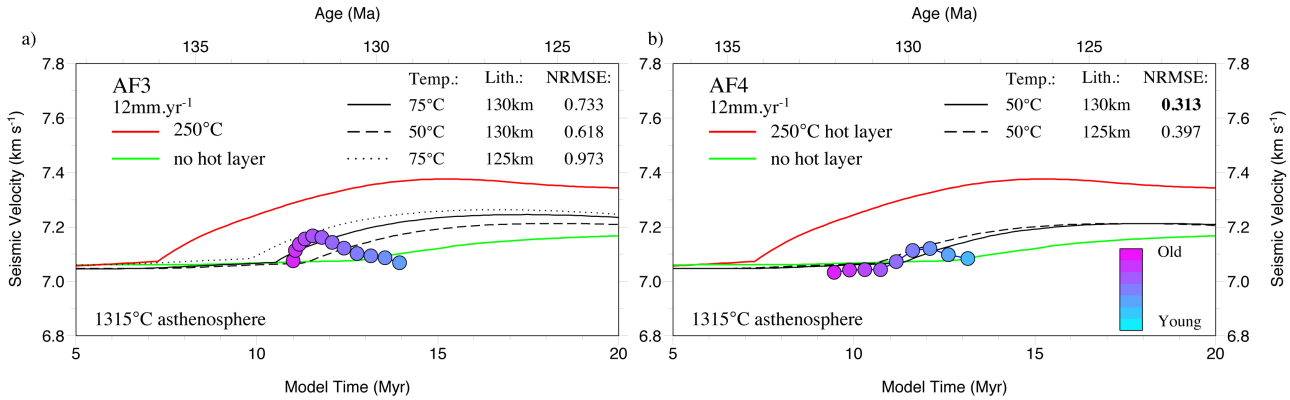


Figure 6.13: Same as Fig. 6.11 & 6.12, but for Profiles AF3 - AF4. The red line represents a model with a hot layer of 250 °C, used to show seismic velocity changes with the addition of hot layers. Panel (a), representing the results for Profile AF3, does not have a hot layer match under the 0.350 NRMSE threshold. For Profile AF4 however, represented in panel (b), there is a moderate fit for a hot layer of 50 °C.

Table 6.4: Summary of model matches to observational constraints from seismic velocity trends. All models have a model asthenosphere temperature of 1315 °C. These results show a decreasing trend from north to south in hot layer temperature (Fig. 6.14).

	Model			
Profile	Lith. Thickness (km)	Hot Layer Temp. (°C)	Spreading Rate ($mm\,yr^{-1}$)	NRMSE
AF0	150	250	12	0.385
	150	250	10	0.350
AF1	140	200	12	0.232
	135	175	12	0.208
AF2	125	150	12	0.109
	130	175	12	0.137
AF3	130	75	12	0.618
AF4	130	50	12	0.313

considering the ramifications to previous melt areas and initial oceanic crustal thickness matches, this was not pursued. The model's long syn-rift phase did not match the fast drop in seismic velocity seen for Profile AF3, but this profile is recognized as being the lowest quality seismic velocity model (Section 3.3.3). The best matches found for Profiles AF3 and AF4 were with hot layers of 75 and 50 °C respectively with a model asthenosphere temperature of 1315 °C (Table 6.4).

6.4 Summary

The syn-rift magmatism was identified for five wide-angle profiles on the African margin. Four of these profiles (AF1 - AF4) had already been considered in **Chapter 5**, and wide-angle Profile AF0 was used for the first time. Melt areas and seismic velocity trends had previously been extracted using a set of criteria in **Chapter 3**. A general decrease in maximum HVLC body thickness, melt area (with and without SDRs) and maximum seismic velocity was observed with increasing distance along-strike from the Walvis Ridge, all in compliance with what

is expected from the *Mantle Plume - VPM Theory*.

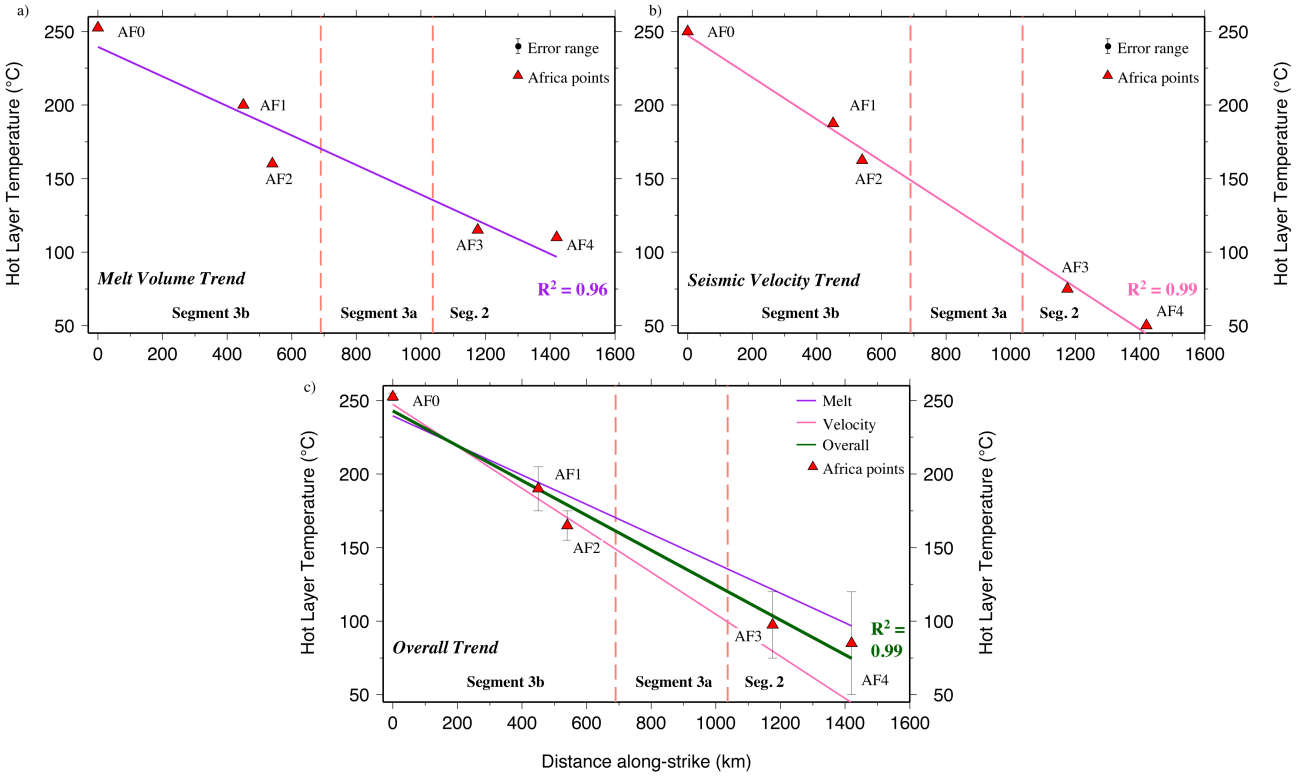


Figure 6.14: Hot layer temperature vs. distance along-strike for syn-rift magmatism. Results for the seismic profiles are shown by the red triangles. Panel (a) shows the results using purely melt areas (Fig. 6.10) and panel (b) shows the results using purely seismic velocity trends (Fig. 6.11, 6.12 & 6.13 and Table 6.4). The purple and pink lines show the linear trends for melt area results and seismic velocity trends respectively. Panel (c) shows the combined results for model areas and seismic velocities, where the range represents the disparities between melt area results and seismic velocity trend results. The linear trend is shown by the dark green line. There is an overall reduction of 60 °C per 500 km.

In order to test for the influence of active mantle upwelling on the volcanic passive margins, the H_c-V_p method was used, using approaches from both Holbrook et al. (2001) and Parkin and White (2008). The two were tested due to their slightly different approach to the method, chiefly with Parkin and White (2008) only using lower crustal information. The H_c - V_p curves for Profiles AF0–AF4 were all found to be in the area of above-normal mantle temperature with an inflection point suggesting the exhaustion of the thermal anomaly as rifting proceeded (Fig. 6.4 & 6.5). Overall, a mantle thermal anomaly is suggested to be present during break-up over a distance of at least 1420 km south of the Walvis Ridge was seen, with little evidence for active mantle upwelling.

The same 2D viscous model of upper mantle as in **Chapter 5** was used here to test the validity of the *Mantle Plume - VPM Theory* using observational constraints from syn-rift magmatism. In addition to melt output, the model had the capability of calculating composition of major element oxides. This added a choice of composition parametrisation as a variable to the numerical model (Fig. 4.14). N97-HK93 was ultimately chosen due to its low NRMSE values compared to MAR and DSDP geochemical data and its peridotite-based bulk earth composition (Fig. 6.7 & 6.8). Following this, hot layer temperatures were varied in an attempt to fit melt areas and seismic velocity trends from seismic profiles.

A change in hot layer temperature was plotted against along-strike distance for the African margin, based on melt areas, seismic velocity trends and a combination of both these results (Fig. 6.14). For all three scenarios, using a mantle asthenosphere temperature of 1315 °C, it was found that a temperature of ∼1565 °C, representing an excess temperature of 250 °C, was needed to fit observations from Profile AF0. This dropped to 50 - 110 °C for Profile AF4 in the south. There was a decreasing linear trends of 50 °C per 500 km for melt areas (Fig. 6.14a) and one of 70 °C per 500 km for seismic velocity trends (Fig. 6.14b). Profile AF1 and AF3 had sharp trends that could not be well matched, but this may have stemmed from the uncertainty of ageing the profiles. However, the seismic velocity trends fit relatively well for a simple numerical model with no inversion needed. Using results from melt area and seismic trends, the mean overall trend is 60 °C per 500 km (Fig. 6.14c). These trends strongly support the results found in **Chapter 5**, reinforcing the *Mantle Plume - VPM Theory* where a mantle plume, or at very least a hot layer, was present at the time of break-up in the South Atlantic.

Chapter 7

Discussion: the evidence for a plume in the South Atlantic

7.1 Introduction

The main aim of this PhD was to investigate the cause of magmatism and any resulting variations observed along-strike for the conjugate margins of the southern South Atlantic. The observational constraints from seismic data (**Chapter 3**) along with the numerical model of continental rifting (**Chapter 4**) provide important information about the development of the continental margins. The first part of this chapter will evaluate alternative mechanisms suggested to be a possible cause of magmatism in the southern South Atlantic (mentioned in **Chapter 1**). This will be done using results from this project's observational constraints and numerical modelling results. In the following part of this chapter, there is a critical evaluation of the validity of the *Mantle Plume - VPM Theory* within the study area. The presence of a mantle plume is discussed using the main results from post-rift and syn-rift magmatism (**Chapters 5 and 6**). This includes the departures from the *Mantle Plume - VPM Theory* and a comparison to other global localities.

7.2 Critical evaluation of Alternative Models

One modification and three main alternatives to *Mantle Plume - VPM Theory* were proposed in this project to explain the observed magmatism during break-up. Rift history, considered to be a modification to the *Mantle Plume - VPM Theory*, was disregarded as a factor in continental break-up. This is due to the lack of evidence of continental thinning within the southern South Atlantic prior to the eruption of the Paraná-Etendeka Traps compared to what was observed in the Hatton Bank and the Gop Rift (Section 1.7). Small-scale convection and

edge-driven convection as a result of sublithospheric topography was dismissed as an alternative in **Chapter 1** (Section 1.8.1), as several numerical models found it was not a viable method to recreate volumes of magmatism observed on volcanic passive margins (e.g., Nielsen et al., 2002; Nielsen and Hopper, 2004; Sleep, 2007; Simon et al., 2009).

Active mantle upwelling however was not discounted as a possible mechanism. Along with segmentation, these two final alternatives to the *Mantle Plume - VPM Theory* (Sections 1.8.3 & 1.8.2) were tested using this project's observational constraints and numerical model of continental rifting. The influence of segmentation on magmatism was tested through the variation of initial oceanic crustal thickness along-strike in **Chapter 5**, and the presence of active mantle upwelling was assessed by using the H_c-V_p method for Profiles AF0–AF4 on the African margin in **Chapter 6**.

7.2.1 Evidence for segmentation

Segmentation was proposed as having an effect on magmatism along-strike within the study area (Section 1.8.3). Observations from Franke et al. (2007), Franke et al. (2010), and Koopmann et al. (2014b) concluded there was no systematic increase of SDR areas towards the Rio Grande Rise and Walvis Ridge, a direct contradiction to what is expected with the *Mantle Plume - VPM Theory* (Section 1.5). It was suggested that the lithospheric segment boundaries acted as rift-propagation barriers to convecting asthenospheric mantle material, resulting in enhancing and focusing volcanic activity south of these zones (Fig. 1.14). This method was subsequently tested with a numerical model by Koopmann et al. (2014a) with favourable results (Fig. 1.15).

In this project, segmentation was tested by identifying the landward limit of oceanic crust (Section 3.2) and measuring ocean crustal thickness at this location for 37 profiles from the conjugate margins (Table 5.1). The seismic profiles were distributed throughout five segments and sub-segments over a distance of ∼2300 km (Fig. 3.1, 3.17 & 3.30). Segments were redefined using sub-plate boundaries from Moulin et al. (2010) and major fracture zones (Section 2.7; Fig. 2.13). With respect to segment boundaries, a different result to what Franke et al. (2007), Franke et al. (2010), and Koopmann et al. (2014b) noted for SDR volumes and distributions was observed using initial ocean crust thicknesses (Fig. 5.6b), suggesting segmentation had little influence over oceanic crustal production. In the proximity to the Rio Grande Rise and Walvis Ridge, initial oceanic crustal thicknesses were found to be thicker than the global average at 11.7 km for Profile AF1, with a clear decreasing trend of ∼0.16 km per 100 km towards the south (Fig. 5.6a). There was no signal relating to segmentation (Fig. 5.6b). Additionally, the numerical modelling results for the post-rift magmatism using observational constraints from wide-angle and ION profiles (Fig. 5.13) showed no overlying trend relating to segmentation, with a systematic decrease in mantle temperature along-strike. Finally, HVLC body areas were calculated for Profiles AF0–AF4 (Section 3.3), and a clear decrease in HVLC body areas towards the south was observed (Table 3.1). From the observational constraints and numerical results presented in this project, there was no dominant signal resulting from segmentation on the conjugate margins of the southern South Atlantic.

7.2.2 Active mantle upwelling

A difference in resulting major element oxide compositions can be made for melting due to active mantle upwelling or increased mantle temperature by using the H_c-V_p method (Section 6.2; Fig. 6.2; Kelemen and Holbrook, 1995; Holbrook et al., 2001; Parkin and White, 2008). Active mantle upwelling, with a shallower depth of melting, will produce melt with a lower MgO content and higher SiO_2 content, and thus a lower overall seismic velocity. An increased mantle temperature will deepen the solidus, and the opposite will be true with higher MgO and lower SiO_2 content, and thus a higher overall seismic velocity.

In Southeast Greenland there is evidence of active upwelling recorded in the surveys despite the widespread recognition for the Iceland Plume being the main influential factor on magmatism. Holbrook et al. (2001) suggested the presence of active mantle upwelling by using the H_c-V_p method for profiles SIGMA-1 and SIGMA-2 (Fig. 7.1b). They postulated this contributed to the thick igneous crust in the North Atlantic. Further south of the Greenland-Iceland Ridge, the curves for SIGMA-3 and SIGMA-4 were found to be close to the passive upwelling curve where $X = 1$ (Fig. 7.1b). To the north of the Greenland-Iceland Ridge, using a profile at a similar distance to SIGMA-2, Breivik et al. (2012) found some indication of possible active mantle upwelling, with a positive trend for Profile 7-00 ranging between an upwelling ratio of $X = 1$ to $X = 2$. Farther afield though, similar to what Holbrook et al. (2001) observed for SIGMA-3 and SIGMA-4, Parkin and White (2008) found little evidence of active mantle upwelling. Parkin and White (2008) presented the H_c-V_p for profiles on the Faroe and Hatton banks, found on the conjugate margin to SIGMA-3. As expected with crust produced from same spreading centre, similar positive trends indicative of passive decompression melting were observed for the Faroes and Hatton profiles studied. Overall, Holbrook et al. (2001), Parkin and White (2008) and Breivik et al. (2012) all found a margin-wide mantle thermal anomaly present at break-up.

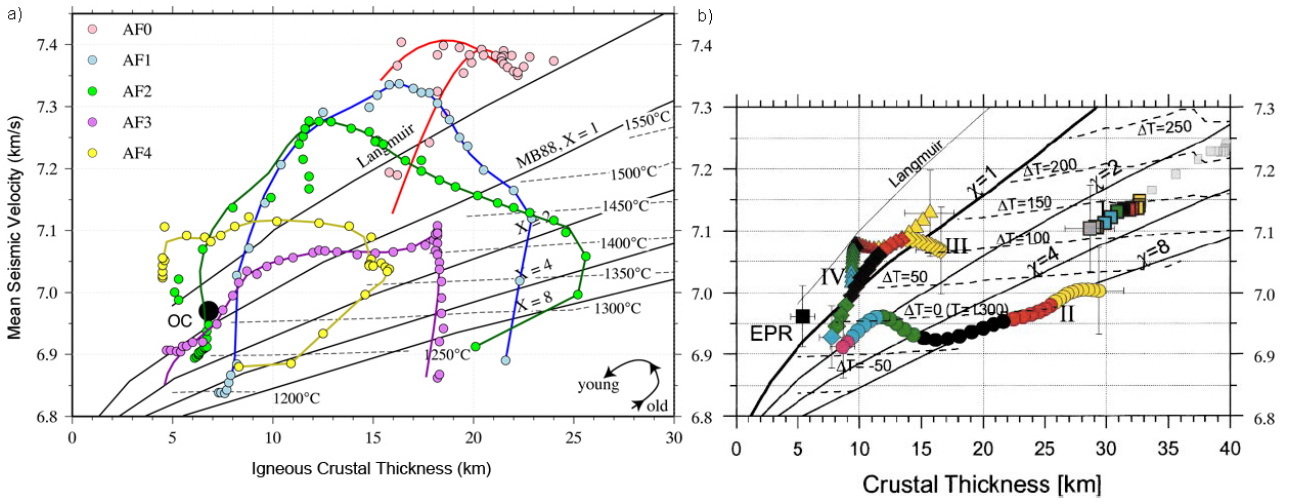


Figure 7.1: H_c-V_p curves for the African margin of the southern South Atlantic and the Southeast Greenland margin, using the Holbrook et al. (2001) correction. Part (a) shows the curves from Profiles AF0–AF4, with the arrow in bottom right corner showing direction of ageing (more details for individual profiles in Fig. 6.4). Part (b) shows the curves from SIGMA-1 to SIGMA-4 (locations in Fig. 1.6), decreasing in age from yellow to pink.

The presence of active mantle upwelling in this project was tested for the African margin in **Chapter 6**. Seismic velocity trends were extracted from syn-rift magmatism, and corrected to account for burial and alteration from the *in situ* temperature and pressure to a reference state using the approaches from Holbrook et al. (2001) and Parkin and White (2008). The H_c-V_p curves extracted from the wide-angle profiles using the two approaches consistently show a decrease in both crustal thickness and seismic velocity along-strike (summarised in Fig. 7.1a). By using the H_c-V_p method, the results clearly indicate an increased mantle temperature at the start of break-up, and a point of inflection possibly indicating the exhaustion of the hot layer (Fig. 7.1a). Unlike what was observed for the SIGMA profiles offshore Southeast Greenland (Fig. 7.1b), there is no clear evidence for the presence of active mantle upwelling on the African margin during break-up from the observational constraints used within this project.

7.3 Critical evaluation of the *Mantle Plume - VPM Theory*

The presence of a mantle plume and its subsequent influence on continental rifting can be identified through several characteristics. Flood basalts are often considered the first sign of a mantle plume, occurring shortly prior to continental break-up. There is still some debate as to whether flood basalts erupt exclusively before break-up, or erupt coevally to rifting (Buiter and Torsvik, 2014). The duration of rifting can be estimated using magnetostratigraphy data from the flood basalts, seafloor spreading reversals and the time expansed in matching numerical model results. Additionally, the lateral distribution of the plume head and decreasing mantle temperatures (Fig. 1.5a) should be reflected by the extent of the associated volcanic passive margin. The latter can be determined by observational constraints and the requirement of a hot layer in numerical models. This project presents clear evidence of (1) the presence of an increased mantle temperature through H_c-V_p curves, (2) decreasing initial oceanic crustal thickness, (3) decreasing maximum seismic velocities and (4) decreasing syn-rift magmatism along-strike through the use of observational constraints. In addition to this, results from a numerical model of continental rifting demonstrates a hot layer reducing in temperature along-strike, matching characteristics expected from the *Mantle Plume - VPM Theory*.

7.3.1 Duration of rifting

With respect to observational constraints from initial oceanic crustal thickness, the numerical model is capable of giving an indication of rift duration. The estimation of the rift duration can be aided using information from flood basalts, the commencement of ocean crust production and basin development. The Etendeka traps erupted over a period of at least 5 Myr between magnetic isochrons M15n and M11n (age 135.96 Ma and 130.84 Ma respectively; Dodd et al., 2015). The reinterpretation of M11 as the Large Magnetic Anomaly by Moulin et al., 2010, found in SDR packages along the African margin, suggests rifting was possibly under way at this point (Fig. 2.10). However, magnetic isochron M7 (age 127.23 Ma) is generally considered as the first true seafloor spreading anomaly within the region, suggested the Etendeka traps had erupted prior to the production

of ocean crust. As Buiter and Torsvik (2014) proposed, it is more likely the eruption of the flood basalts were coeval to break-up, and they suggested rifting commenced as early as 160 Myr in the South Atlantic. Several other studies have also suggested the start of rifting in the region to be in the Late Jurassic (e.g., Maslanyj et al., 1992; Light et al., 1993; Clemson et al., 1997, 1999; Gallagher and Brown, 1999; Aizawa et al., 2000), in agreement with syn-rift sediments dated between 130 and 150 Ma found in the Namibian passive margin (Clemson et al., 1997; Guillocheau et al., 2012).

The numerical model results that matched to observational constraints from post-rift magmatism in **Chapter 5** imply that the duration of rifting was ∼20–30 Myr for Segments 3a & 3b and ∼15 Myr for Segment 2. Assuming ocean crust production was underway by ∼126 Ma (magnetic isochron M4), this time scale is in favour of rifting commencing in the Late Jurassic. Additionally, rifting durations increase towards the Rio Grande and Walvis Ridges (Fig. 5.10 & 5.12), as is expected with reducing spreading velocities between Segments 2 & 3 (rates at $18\,\mathrm{mm\,yr^{-1}}$ and $12\,\mathrm{mm\,yr^{-1}}$ respectively). With a rifting duration range of ∼15-30Myr, rifting commencing in the Late Jurassic is in agreement with evidence from sedimentary accumulations within the Namibian passive margin and the initial rifting age proposed by Buiter and Torsvik (2014) and several other workers.

7.3.2 Extent of volcanic passive margins in the Southern Segment

A volcanic passive margin is defined as having (1) HVLC bodies, (2) SDRs and (3) thickened initial ocean crust. The expanse of volcanic passive margins should be reflected by a plume head's suggested area of influence, estimated to be 2000-2500 km by Griffiths and Campbell (1990, 1991), and can be inferred by the numerical model results requiring the presence of a hot layer. Using the aforementioned criteria, the results within this project suggest that the extent of volcanic passive margins within the southern South Atlantic stretch to at least ∼1800 km and up to ∼2300 km south of the Rio Grande Rise and Walvis Ridge (Fig. 5.6). On the South American margin, oceanic crust with above average thickness (>7 km) is observed for Profile SA2 (7.8 km; distance 1895 km), which additionally has SDRs present and a HVLC body with elevated velocities reaching $7.5\,\mathrm{km\,s^{-1}}$ (Fig. 3.26). Profile AR1-2600, at a distance of 1760 km, was also found to have above average initial oceanic crustal thickness of 9.7 km (Table 5.1). Furthermore, MCS profiles BGR98-18, BGR98-07 and BGR98-20 all had SDRs present and an initial oceanic crustal thickness >7 km (yellow stars in Fig. 7.2). This suggests the volcanic margins may stretch to a distance ∼1900 km south of the Rio Grande Rise. A hot layer was also required within the numerical model to match the post-rift observational constraint from Profile SA3 (Fig. 5.10c; location Fig. 7.2). This profile is 2300 km from the Walvis Ridge, suggesting the area of influence, and as a result, that the volcanic passive margins may stretch even further.

A similar distance for the extent of volcanic passive margins was observed on the African margin. Although Profile AF4 does not demonstrate thickened oceanic crust (7 km; distance 1420 km south of the Walvis Ridge; location Fig. 7.2), it does have both a HVLC body with velocities reaching up to $7.4\,\mathrm{km\,s^{-1}}$ and the presence of

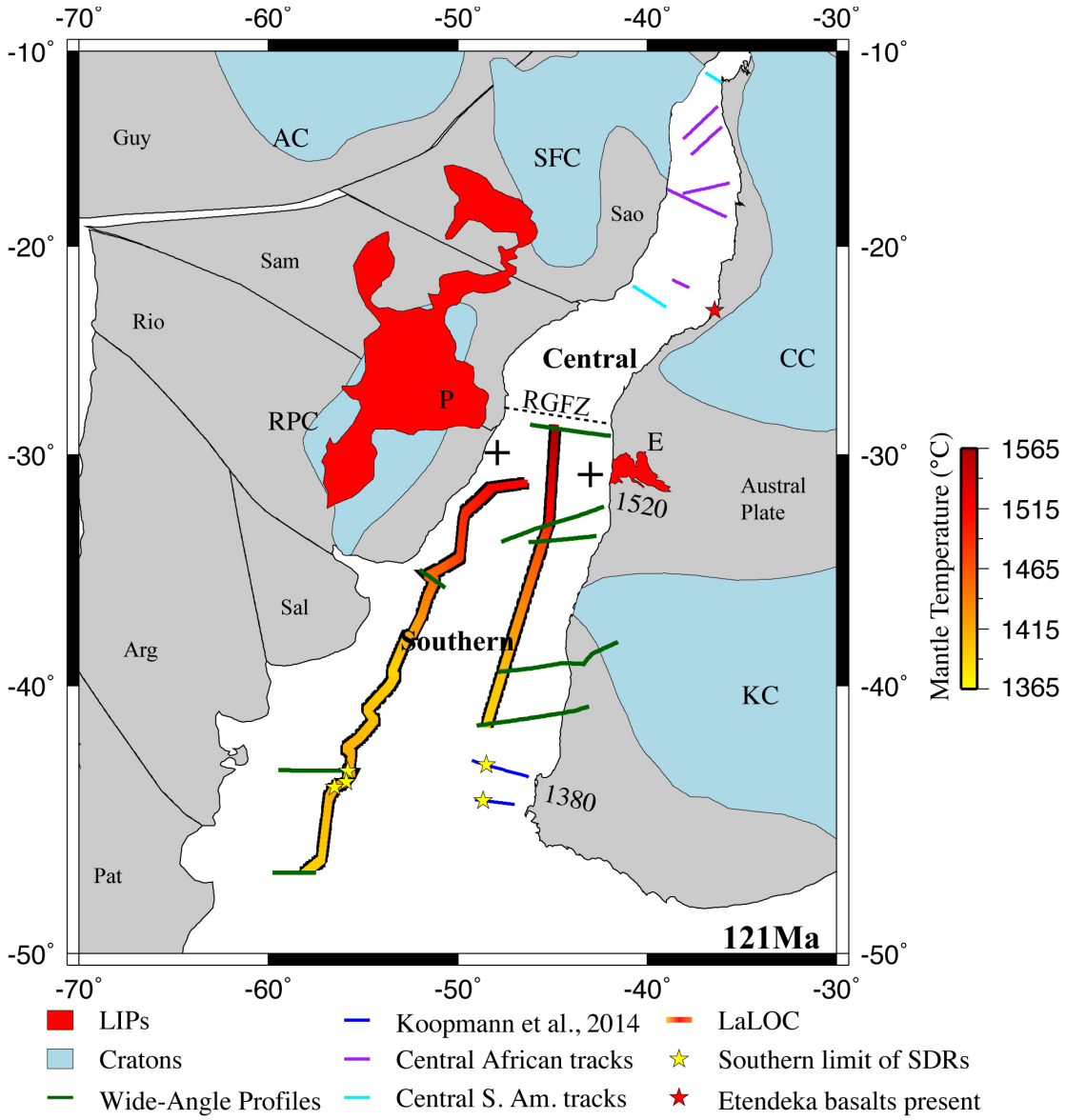


Figure 7.2: Reconstructions using GPlates, shown at 121 Ma using rotation poles of Moulin et al. (2010). Also shown are the sub-plates of South America (thin black lines) and major geological features. The positions of cratons (blue shapes) are from Gubanov and Mooney (2009), the location of the Etendeka-Paraná flood basalts (red shapes) is from Coffin and Eldholm (1994). The '+' mark the reconstructed landfall of the Rio Grande Rise and Walvis Ridge. Sub-plates: Pat = Patagonia, Arg = Argentina, Sal = Salado, Rio = Rio de la Plata, San = Santos, Sao = São Francisco, Guy = Guyana. Cratons: AC = Amazonian Craton, SFC = Sao Fransisco Craton, RPC = Rio de la Plata Craton, CC = Congo Craton, KC = Kalahari Craton. LIPS: P = Parana, E = Etendeka. The Southern and Central Segments are separated by the Rio Grande Fracture Zone (RGFZ - dotted line). In the Central Segment, the profiles on the South American margin are from Mohriak et al., 1995 and Quirk et al., 2013 and on the African margin from Dupre et al., 2011, Contrucci et al., 2004 and Quirk et al., 2013 (more details in Fig. 7.7). Also shown is the location of the northernmost outcrop of Etendeka basalts, identified by Marzoli et al., 1999 (more details in Fig. 7.7). In the Southern Segment, wide-angle profiles are Profiles AF0–AF4 & SA1–SA3 (green lines) and tracklines from Koopmann et al., 2014b are MCS profiles BGR03-16A and BGR03-12 (dark blue lines). Southern limits of SDR locations are shown with the yellow stars. The thick yellow-red gradient line represents the location of the LaLOC from Table 3.2 (N.B. Extended to Profile AF0 on African side) and the mantle temperature as per the numerical modelling results (Fig. 7.4). The mantle temperature is based on the mantle asthenosphere temperature (1315 °C) and the corresponding averaged hot layer temperature for each profile. Additionally, the values onshore Africa (1520 °C & 1380 °C) represent thermobarometry results based on MgO values from a compilation of onshore basalts (Trumbull, 2014).

SDRs. Likewise to Profile SA3, a hot layer was required to match the post and syn-rift observational constraints from Profile AF4 (Fig. 5.10b & 6.13; Table 6.3). Additionally, SDRs were seen some ∼85 km south of Profile AF4 in BGR migrated MCS line BGR03-16A (located with yellow star in Fig. 7.2; Koopmann et al., 2014b). MCS line BGR03-12 from Koopmann et al. (2014b) at a distance of ∼1780 km south of the Walvis Ridge also demonstrates the presence of SDRs (yellow star in Fig. 7.2). The expanse of volcanic passive margins and the presence of a hot layer is also supported by the existence of Cretaceous dykes onshore (Fig. 2.7). Thermobarometry results based on the geochemistry of the dykes (onshore values in Fig. 7.2) suggest an elevated mantle temperature coincident to the southern limit of SDRs, at a distance of ∼1780 km south of the Walvis Ridge.

Overall, the length of the volcanic passive margin for both the South American and African margins is suggested to be between ∼1780–2300 km. Although the distribution of the volcanic passive margins in the southern South Atlantic is slightly shorter compared to others (2300–2900 km for the North Atlantic and East Coast of U.S; Bradley, 2008), they are still within the same order of magnitude. More importantly, following the *Mantle Plume - VPM Theory*, the extent of the volcanic passive margins are in line with the expected region affected by an impacting plume head.

7.3.3 Reduction in magmatism along-strike from observational constraints

Observational constraints of magmatism show a clear consistent decrease along-strike in the Southern Segment. As previously mentioned, there was no clear evidence for segmentation influencing the variation of magmatism along strike (Fig. 5.6b). Additionally, the H_c–V_p graphs for Profiles AF0–AF4 did not show any sign of active upwelling, but suggested the presence of an increased mantle temperature (Fig. 7.1). In agreement with the *Mantle Plume - VPM Theory*, a reduction in magmatism should be observed along-strike away from the plume-axis (White and McKenzie, 1989; Kelemen and Holbrook, 1995). Results from **Chapter 5** show a clear decrease from above average initial oceanic crustal thickness on the conjugate sides, at a rate of ∼0.16 km per 100 km, towards the south (Fig. 5.6a). Results from **Chapter 6** also showed a clear decrease in HVLC volumes and seismic velocities along-strike on the African margin (Table 3.1).

In addition to the reduction of magmatism along-strike, a reduction of magmatic productivity rates and varying igneous crustal thickness are observed through time. Calculated using the HVLC bodies for Profiles AF0–AF4, there is a clear reduction seen in magmatic productivity rates and igneous crustal thickness in both distance and time. In the proximal zone of the plume axis, there was an initial magmatic productivity rate of $1635 \pm 40\,km^3$ /km /Ma, reducing to $435 \pm 55\,km^3$/km/Ma over a ∼7 Myr period. At the distal zone, this initial rate was $695 \pm 20\,km^3$/km/Ma, reducing to $175 \pm 5\,km^3$/km/Ma over a ∼6 Myr period. The initial rates for the proximal and distal zones were similar to those seen by Holbrook et al. (2001) on the Greenland-Iceland Ridge using the SIGMA profiles (locations inset map of Fig. 1.6), at $\sim 1800 \pm 300\,km^3$/km/Ma and $700 \pm 200\,km^3$/km/Ma respectively. A similar magmatic productivity rate was observed by Mjelde et al. (2008) for the Greenland-Iceland-Faroe ridge at time of break up, at $\sim 1710\,km^3$/km/Ma in the proximal zone and

reducing to ∼400 km^3/km/Ma in the distal zone at the Lofoten margin offshore Norway.

Igneous crustal thickness can also be observed along-strike and in time (Fig. 7.3). Although the peak production for Profile AF0 does not begin until ∼130 Myr, it still has the largest area of igneous crust (∼2500 km^2 greater than Profile AF1; Table 3.1). Similarly, Profile AF2 consistently has a thicker igneous crust than Profile AF1, but it was found to have an overall lesser area (∼840 km^2 less; Table 3.1). Despite this, there is a clear reduction of igneous crustal thickness along-strike and through time. From observational constraints alone, it can therefore be suggested that a hot layer, possibly in the form of a mantle plume, is responsible for the variations in magmatism seen in the southern South Atlantic.

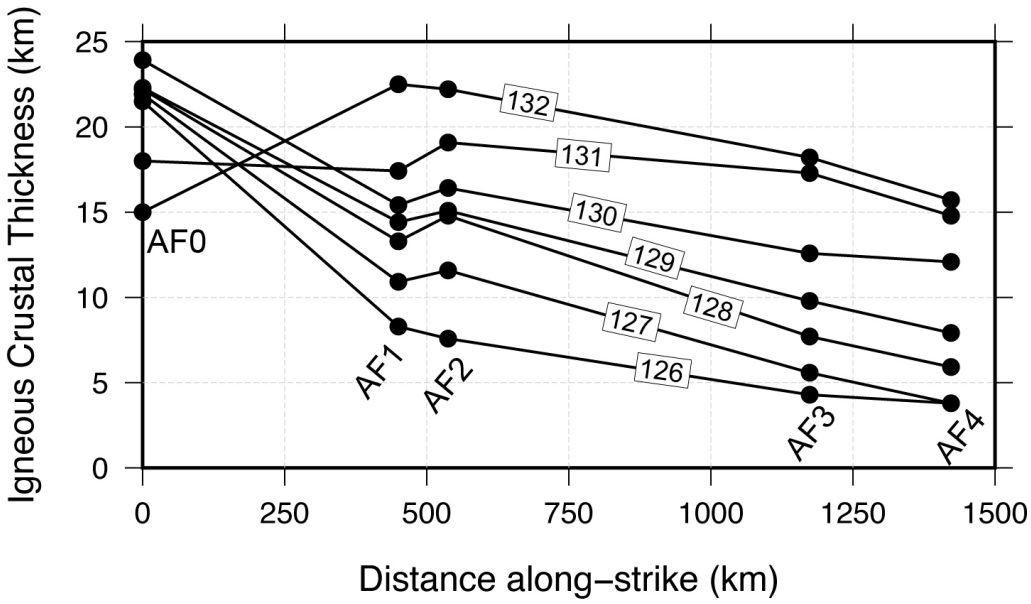


Figure 7.3: Igneous Crustal Thickness for Profiles AF0–AF4 (locations Fig. 3.1) as a function of distance along-strike and age. Number labels represent the variation of igneous thickness for the profiles at different ages (132–126 Ma).

7.3.4 Evidence from results of the numerical model of continental rifting

The presence of a hot layer or mantle plume is further exemplified from numerical modelling results. In order to match observations from post-rift magmatism (i.e. initial ocean crust thickness; **Chapter 5**) and syn-rift magmatism (i.e. HVLC bodies and SDRs; **Chapter 6**), a model asthenosphere temperature was first established. The long offset ION Geophysical data demonstrated decreasing oceanic crustal thickness with distance from the passive margins (Fig. 5.7). The trends of ocean crust thickness for Segments 3b, 3a & 2 ultimately matched with results from a model with an asthenosphere temperature of 1315 °C, and were used for all consequent models (Section 5.3.2.1; Fig. 5.9). Present day continental lithosphere thickness and spreading rates specific to the individual profiles were used for the initial model space (Fig. 4.5.2). A hot layer was assumed present prior to the start of rifting, as suggested by the ages of the Etendeka Traps (Dodd et al., 2015), and its temperature was varied between 50 to 250 °C.

From post-rift observational constraints from wide-angle profiles (**Chapter 5**; Section 5.3.2.2), the temperature of the hot layer was estimated by comparing variations in ocean crustal thicknesses for the wide-angle profiles at the LaLOC location (Fig. 5.10). The importance of varying lithosphere thickness according to the location was tested, and whilst a model with a fixed lithosphere thickness could match all of the observations from Profiles AF1–AF4 (Fig. 5.10a), this was over a 20 Myr spread, quite a few orders of magnitude greater than age range observed. By varying the initial lithosphere thickness according to the location of the individual profiles, the numerical model was capable of matching first ocean crust thicknesses over 2.5 Myr and 7.7 Myr for the African and South American margins respectively (Fig. 5.10b & c), closer in magnitude to the observed age range at 1.0 Myr and 5.7 Myr respectively.

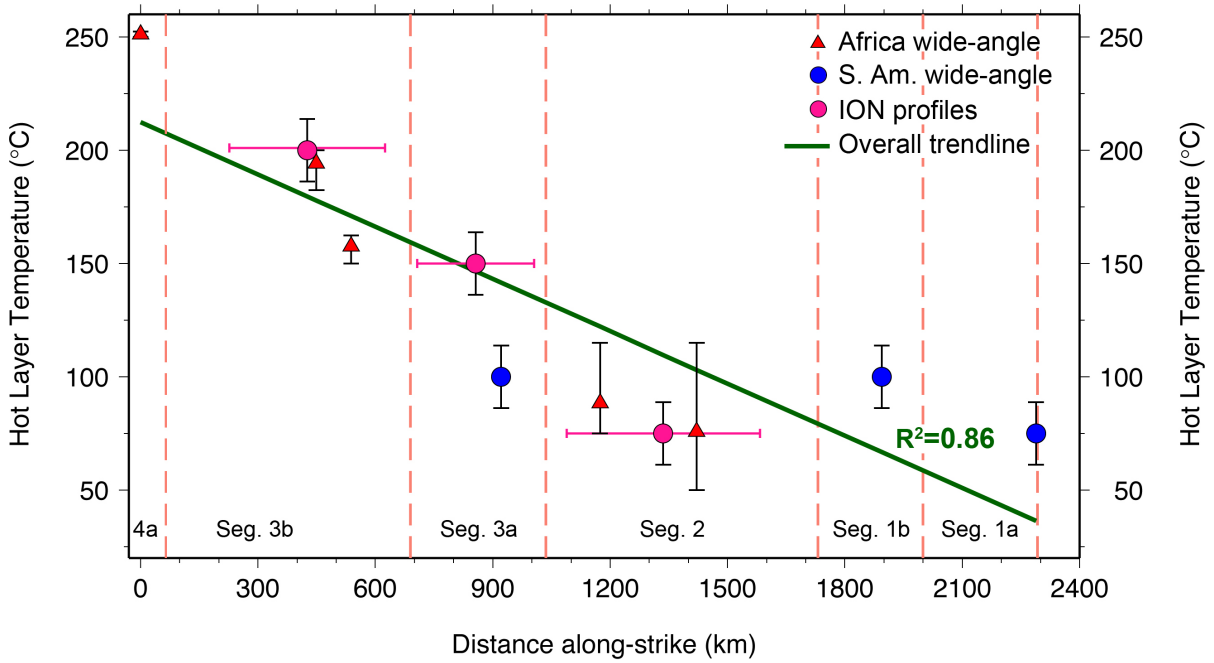


Figure 7.4: Overall trend for hot layer temperature vs. distance along-strike using model results matched to observational constraints from both post and syn-rift magmatism. Post-rift results from wide-angle profiles (Profiles AF1–AF4 and SA1–SA3; Fig. 5.10) and from ION profiles (averaged per segment, with horizontal bars marking distribution of the profiles; Fig. 5.12). Syn-rift results from African wide angle profiles for melt areas (Fig. 6.10) and seismic velocity trends (Fig. 6.11, 6.12 & 6.13 and Table 6.4). The linear trend is shown by the dark green line, with an overall reduction of ∼40 °C per 500 km.

From syn-rift observational constraints from Profiles AF0–AF4 (**Chapter 6**), the temperature of the hot layer was estimated by comparing variations HVLC & SDR areas and seismic velocity trends. HVLC body areas instead of thickness were used to account for the most likely complex and random temporal and spatial formation of the mafic intrusions. Additionally, by using an empirical formula for major element oxide compositions (Eq. 4.21), the model is also capable of producing seismic velocity trends through time. Prior to doing this, there was a choice of two composition parametrisations: WM91 or N97 (Watson and McKenzie, 1991 & Niu, 1997 respectively). For this project, major element oxides samples from DSDP expeditions and the Mid-Atlantic Ridge were used to aid the choice of composition parametrisation (Fig. 6.7 & 6.8). The N97-HK93 parametrisation with a peridotite based bulk earth composition from Hirose and Kushiro (1993) was ultimately chosen due to (1) its peak in Ca/Al ratio, representative of the exhaustion of clinopyroxene with increased melt fraction (Fig. 4.14), (2) the use of peridotite as a bulk earth composition, considered the better choice as it was

shown to be more accurate when calculating predictions in composition and (3) relatively low NMRSE values when comparing the model composition at steady-state to normalised DSDP and MAR values (Fig. 6.7 & 6.8). The model was capable of matching observational constraints from syn-rift magmatism for a large majority of the profiles.

With findings from the numerical model based on both post and syn-rift magmatism, the hot layer temperatures ranged from 250 °C at the Walvis Ridge for Profile AF0, to 50–75 °C in the proximal margins for Profiles SA3 and AF4. The results from conjugate margins for Profiles AF1 and the ION Geophysical profiles from Segment 3b both required a hot layer temperature of ∼200 °C to match observations from both post and syn-rift magmatism. Farther south on the African margin, hot layer temperatures within Segment 2 ranged from 75-120 °C for Profile AF3 and 50-120 °C for Profile AF4. Numerical model results using initial oceanic crustal thickness and seismic velocity trends as constraints for Profiles AF3 and AF4 had overall lower hot layer temperatures compared to those based on HVLC melt areas, but the ION Geophysical profiles in Segment 2 on the conjugate margin were found to be in a similar temperature range. The southernmost data point was Profile SA3 at a distance of ∼2300 km, where a hot layer of 75 °C was necessary to match observations.

Overall, considering findings from initial ocean crustal thickness, HVLC & SDR areas and seismic velocity trends, there is a clear reduction in hot layer temperature along-strike, moving south away from the Rio Grande Rise and Walvis Ridge. The overall combined average reduction is ∼40 °C per 500 km (Fig. 7.4). Results from numerical models matched to observational constraints from seismic data in the southern South Atlantic margins are in line with the *Mantle Plume - VPM Theory*, suggesting a reduction in temperature along-strike from the plume axis to the distal margins (Fig. 7.4).

7.3.5 Comparison to the North Atlantic and Indian Ocean

Several localities have been previously tested with regards to the *Mantle Plume - VPM Theory*. The North Atlantic margins in proximity to the Greenland-Iceland-Faroe Ridges have been recognized by numerous workers to be influenced by the Iceland Plume (e.g., White and McKenzie, 1989; Holbrook et al., 2001). The rate of decrease in mantle temperature based on observational constraints from post-rift magmatism was similar to those observed by White (1997) in the North Atlantic. Using ocean crust ∼50 Myr and older, the ocean crust thickness was calculated from residual height of the basement for 24 profiles north and south of the Greenland-Iceland-Faeroe Ridges (White, 1997). From the ocean crust thickness, the mantle temperature was calculated assuming isentropic decompression melting, using values from Bown and White (1994). There was an overall reduction of ∼45 °C per 500 km in the mantle potential temperature observed in the North Atlantic, similar to what is seen in the southern South Atlantic with an average of ∼40 °C per 500 km.

The observational constraints from the SIGMA profiles, among others, have been the focus of numerous numerical models of continental rifting (e.g., Nielsen and Hopper, 2004). In addition to this, there are some numerical models of continental rifting using observational constraints from the Indian Ocean (Collier et al.,

2009; Armitage et al., 2010, 2011). In order to compare results from other regions, profiles from the North Atlantic and Indian Ocean were measured in terms of distance along-strike and analysed against numerical model results from this project (Fig. 7.5).

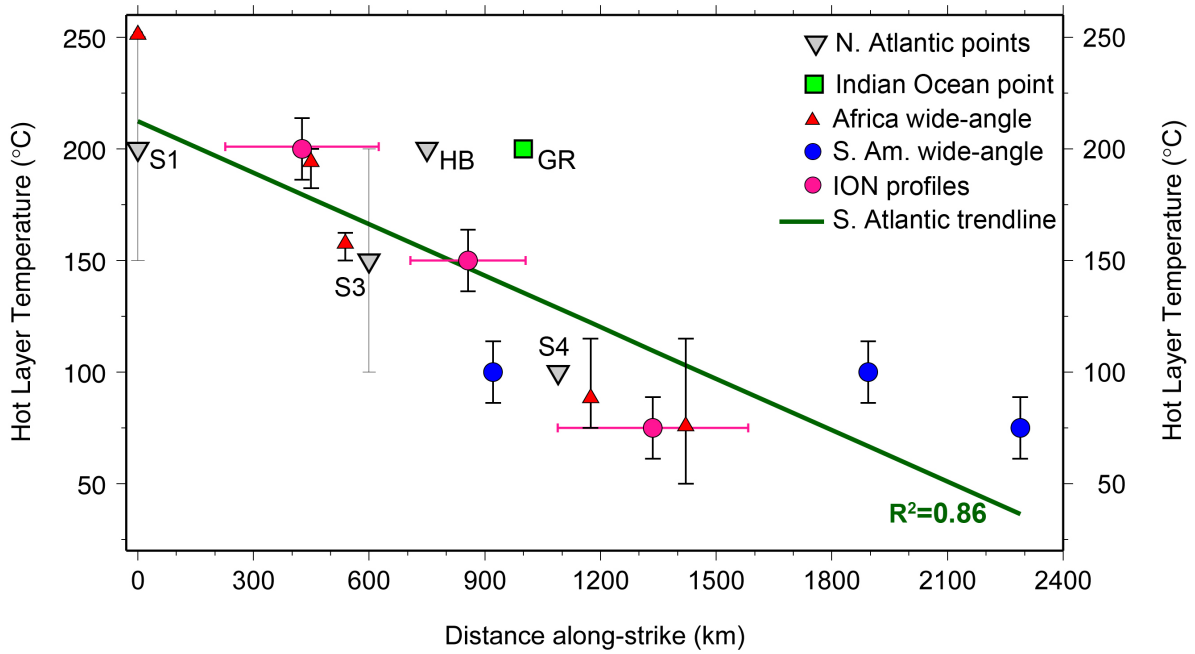


Figure 7.5: Numerical model results for hot layer temperature for this project in the southern South Atlantic compared to results from the North Atlantic and Indian Ocean. Post-rift and syn-rift results from wide-angle profiles in this project (AF0–AF4, SA1–SA3 and results from ION profiles) are the same as in Fig. 7.4. The linear trend for the southern South Atlantic is shown by the dark green line. Four profiles from the North Atlantic (inverted grey triangles) and one result from the Indian Ocean (green square) are shown. The numerical modelling results for the North Atlantic correspond to observational constraints from SIGMA-1 (S1; Holbrook et al., 2001), SIGMA-3 (S3; Holbrook et al., 2001; Nielsen and Hopper, 2004; Armitage et al., 2008), the Hatton Bank (HB; location in Fig. 1.7a; Armitage et al., 2009) and SIGMA-4 (S4; location of SIGMA profiles in Fig. 1.6; Holbrook et al., 2001). The observational constraint for the numerical modelling result within the Indian Ocean is from Gop Rift (GR; location in Fig. 1.9).

With an earlier iteration of the same numerical model of continental rifting used in this project, Nielsen and Hopper (2004) and Armitage et al. (2008) presented results for SIGMA-3, using igneous crustal thickness and major element oxides compositions from ODP sites 917 and 990. A hot layer between 100-200 °C was found necessary to match observations. The average hot layer temperature for SIGMA-3 is in close agreement to the hot layer matched with Profile AF2 (Fig. 7.5). The closest conjugate profile for SIGMA-3 is found on the Hatton Bank (location in Fig. 1.7a), where a 200 °C was predicted by Armitage et al. (2009) to match observational constraints, relatively high compared to numerical results from the southern South Atlantic margin. Additionally, using the same numerical model, a hot layer of 200 °C was suggested to match observational constraints from the Gop Rift at a distance of ∼1000 km from the plume axis in the Indian Ocean (location in Fig. 1.9). This was significantly hotter than the trends for both the North and South Atlantic (Armitage et al., 2010, 2011).

Furthermore, using a different method, Holbrook et al. (2001) suggested hot layer temperatures for SIGMA-1 and SIGMA-4. For SIGMA-1, a hot layer temperature of 200 ± 50 °C was necessary to recreate the igneous

crustal thickness observed, which is within the range of the temperature required to match the observation from Profile AF0 (Fig. 7.5). A hot layer of 100 °C was suggested for SIGMA-4, relatively close to results for Profiles SA1 and SA3. This is also the distance at which initial oceanic crustal thicknesses tend to the same value for both North and South Atlantic margins (Fig. 5.6a), suggesting a similar thermal structure at this distance.

When taking the upper limit of numerical modelling results for SIGMA-3 coupled with the results for the Hatton Bank, it can be suggested that the North Atlantic appears hotter overall (Fig. 7.5). However, Holbrook et al. (2001) suggested active mantle upwelling may have played a significant impact on melting in the North Atlantic. They calculated the magmatic productivity rates in the North Atlantic halving over a 13 Myr. A similar reduction was observed for Profiles AF0–AF1, but over a much quicker time of 6–7 Myr. The inclusion of active mantle upwelling, concluded not to affect magmatism in the study area in **Chapter 6**, could also explain the elevated magmatic productivity rates and thicker initial oceanic crust observed in the North Atlantic. Additionally, both the Hatton Bank and Gop Rift were affected by a pre-thinning event prior break-up, for which there is little evidence of in the southern South Atlantic.

7.4 Departures from the *Mantle Plume - VPM Theory*

Despite the evidence presented in this project from both observational constraints and numerical model results for the presence of a mantle plume in the southern South Atlantic, there remains some departures from the *Mantle Plume - VPM Theory*. This includes the apparent asymmetry present between the conjugate margins in the Southern Segment, and the stark contrast between volcanic and non-volcanic margins with an abrupt transition (Fig. 1.8) between the Southern and Central Segments respectively.

7.4.1 Asymmetry in magmatism between the conjugate margins

Becker et al. (2014) suggested an asymmetry within the South Atlantic margins, with HVLC bodies on the African margin up to 4 times bigger than those on the South American margin. A similar difference in area was calculated for Profiles AF4 and SA2 (southernmost wide-angle profiles in Fig. 7.6), the conjugate profiles with a ~475 km distance between them, with areas of 2590 km^2 and 560 km^2 respectively. However, in this project, a HVLC body was considered not imaged on Profile SA1 (Fig. 7.6) due to apparent instrumental problems with the OBHs (Section 3.4.1.2). It is likely that HVLC bodies have most likely not yet been imaged and/or published. The likelihood of a more even distribution for HVLC bodies is strengthened by the fact

that Koopmann et al. (2014b) observed relatively symmetrical SDR distributions within the conjugate margins. Additionally, in this project, the initial oceanic crustal thickness trend observed from all the collective profiles (Fig. 5.6) had no indication of asymmetry between the conjugate margins.

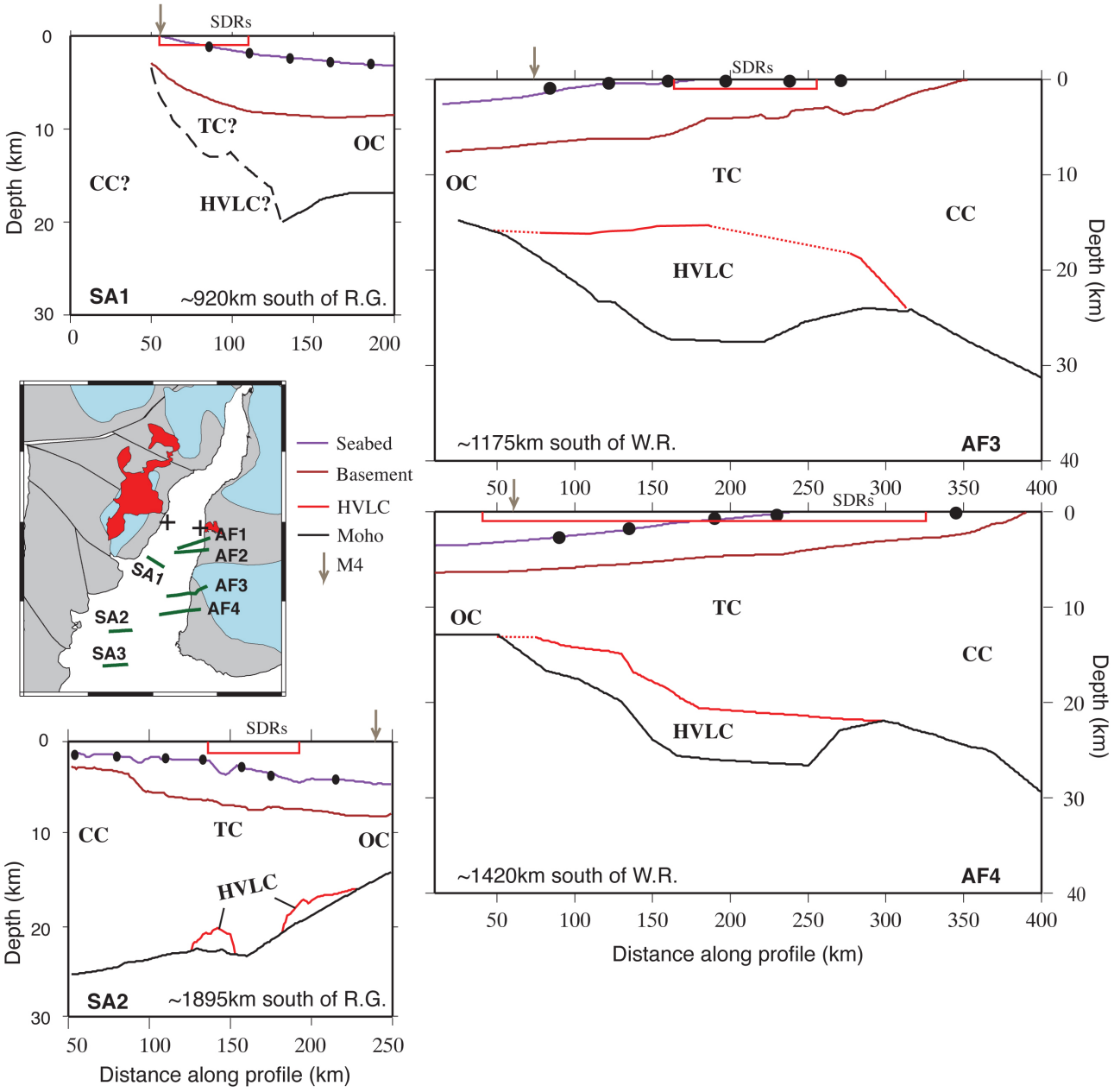


Figure 7.6: Line drawings of Profiles SA1 and SA3 on the South American margin and the closest conjugates Profiles AF3 and AF4 on the African margin, with map of locations. Distance south of Rio Grande Rise (R.G.) and Walvis Ridge (W.R.) are marked for each profile. Also shown is the location of magnetic isochron M4 (grey arrow), continental crust (CC), transitional crust (TC) and ocean crust (OC).

7.4.2 Magmatism in the Central Segment

The margins north of the Rio Grande and Walvis Ridge in the Central Segment have been classified as non-volcanic (e.g., Contrucci et al., 2004), compared to the volcanic margins in the Southern Segment (Section 2.5). Although Fromm et al. (2015) demonstrated a stark contrast immediately north of the Walvis Ridge (Fig. 1.8), there remains some evidence for magmatic activity in the Central Segment. On the South American margin, SDRs have been imaged offshore Brazil, extending to at least 500 km north of the Rio Grande Rise (Mohriak et al., 1990; Chang et al., 1992). SDR bodies have also been imaged further north, but they are relatively thin at 3 km (from Mohriak et al., 1995; location in Fig. 7.7). Additionally, Quirk et al. (2013) suggests the presence of mafic underplating from gravity modelling and seismic data offshore Brazil (locations in Fig. 7.7).

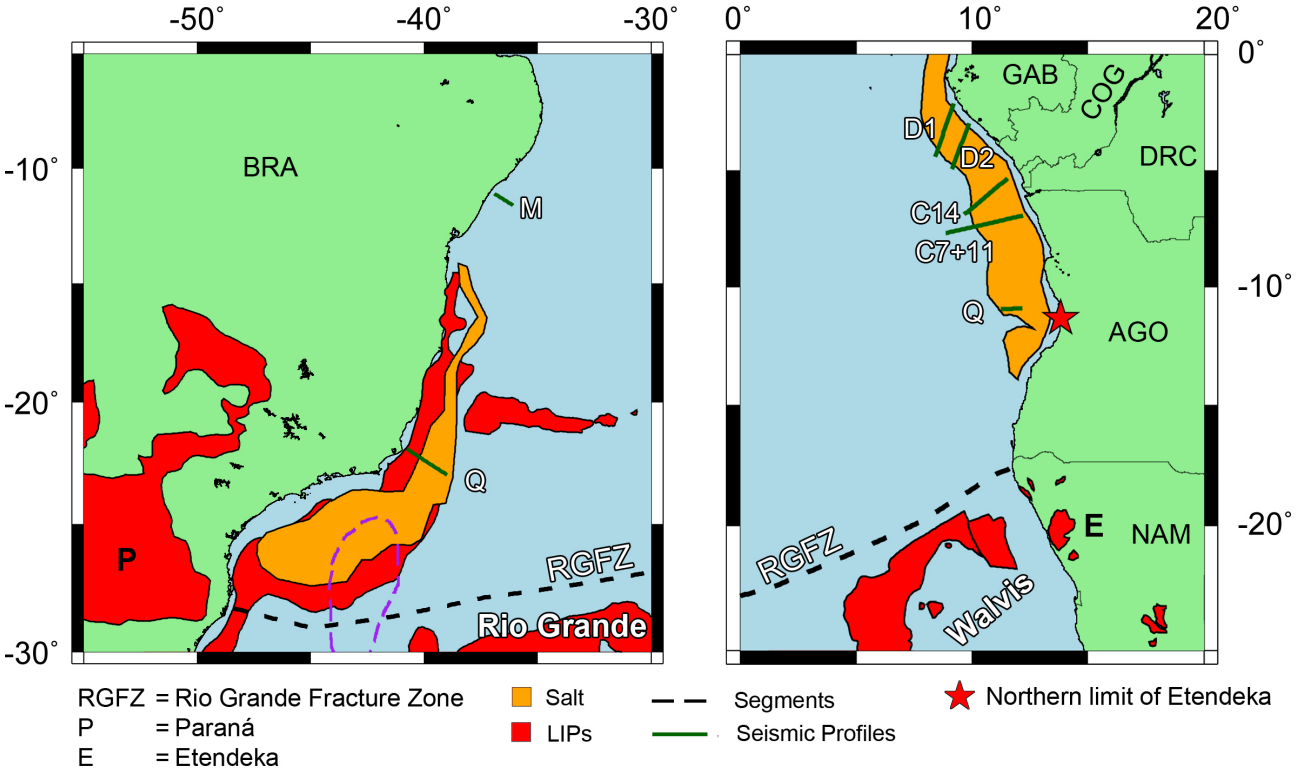


Figure 7.7: Map of the Central Segment with seismic tracklines. Tracklines from Quirk et al. (2013) and Mohriak et al. (1995) (marked Q and M respectively) are on the South American side. The purple dashed area is the interpreted location of magmatic underplating from gravity modelling (Quirk et al., 2013). On the African side there are tracklines from Dupre et al. (2011) (marked D1 & D2 for Lines 1 & 2 respectively), Contrucci et al. (2004) (marked C14 & C7+11 for Profiles 14 & 7+11 respectively) and Quirk et al. (2013) (marked Q). There is additionally the northernmost location of the Etendeka flood basalts from Marzoli et al. (1999) (location marked by red star). NB: Profile locations from Quirk et al. (2013) are only approximate due to sensitivity issues.

On the African margin, Contrucci et al. (2004) and Dupre et al. (2011) debated if the presence of high-velocity lower-crustal bodies observed on the Angolan and Gabon margins represented serpentinized mantle, high grade metamorphic rock or intrusions mafic in origin. Contrucci et al. (2004) dismissed the latter as an option, as MCS profiles from Moulin (2003) found offshore the Angolan margin did not image any SDRs. Additionally, Contrucci et al. (2004) found oceanic crustal thickness close to the global average at ~6–7 km with a distance

of ∼1380–1490 km north of the Walvis Ridge, using refraction profiles '7+11' and '14' (locations in Fig. 7.7). However, a more recent study from Quirk et al. (2013) has revealed the presence of SDRs offshore Angola (location in Fig. 7.7). The offshore SDR location also coincides with the onshore most northern outcrop of the Etendeka volcanics, identified by Marzoli et al. (1999). This was identified through similarities in petrographical, major element, trace element and Sr-isotopic compositions (location as red star in Fig. 7.7). Dupre et al. (2011), in contrast, did not fully dismiss the possibility of mafic intrusions offshore Gabon, and additionally proposed ocean crust with a thickness of 10 km for 'Line 1', ∼1660 km north of the Walvis Ridge (location in Fig. 7.7). This thickness reduced to 7 km at a distance of 1800 km north of the Walvis Ridge for 'Line 2' (location Fig. 7.7), closer to the values seen offshore Angola. Although the volumes of magmatism are not close in magnitude to those seen south of the Rio Grande Rise and Walvis Ridge, the definition of 'weakly magmatic' by Blaich et al. (2008, 2011) is perhaps more adept.

There is currently ∼24,000 km of high-resolution, deep-penetrating 2D seismic lines from ION Geophysical covering the Central and Southern Segments, as part of the ION BasinSPAN programme (titled PelotasSPAN, ArgentinaSPAN, UruguaySPAN and NamibiaSPAN; ION Geophysical, 2013a,b,c,d). As yet, only a few sections have been successfully published (e.g. Clerc et al., 2015, Unternehr et al., 2010, Cowie et al., 2016 and Péron-Pinvidic et al., 2015), however these do not coincide with the lines within this project. As more lines are published, our understanding of the distribution of magmatism on the margins in the Central and Southern Segments of the South Atlantic will be more complete.

7.5 Tristan Plume: a configuration

There have been several suggestions for the origin of contrasting margin types seen in the Central and Southern Segments of the South Atlantic. The sharp transition from the thick Walvis Ridge to thin ocean crust in Angola (Fig. 1.8) is similar to the contrast seen on the Southwest Greenland margin (Section 1.6.1). In the Southwest Greenland margin, the role of lithosphere thickness and resulting sublithospheric topography was considered to influence magmatism in the region. Sleep (1996) suggested the sublithospheric bathymetry has a profound effect on the mantle plume near a ridge axis, forming an 'upside-down drainage pattern'. Through numerical models, it was found that only a relatively thin layer of plume material would spread up slope to a ridge axis, and that normal lithosphere surrounding a plume material would in some capacity form a levée. The location of Greenland Craton was suggested to impede the spread of the plume head in the Labrador Sea, creating the stark contrast observed in magmatism (Nielsen et al., 2002). For the South Atlantic, the positioning of the Congo Craton may have similarly affected the spread of the plume head towards the north.

Taking a north-south transect of reconstructed lithosphere thickness at time of break-up, the location of the Congo Craton causes a significant increase in lithosphere thickness to the north of the approximate location of the plume axis (Fig. 7.8). This is coupled with slowed spreading rates in this region, ranging from $4-8\,\mathrm{mm\,yr^{-1}}$ (Fig. 2.12; Heine et al., 2013) as rifting moves northward. Cores in the Etendeka volcanic province, dated at

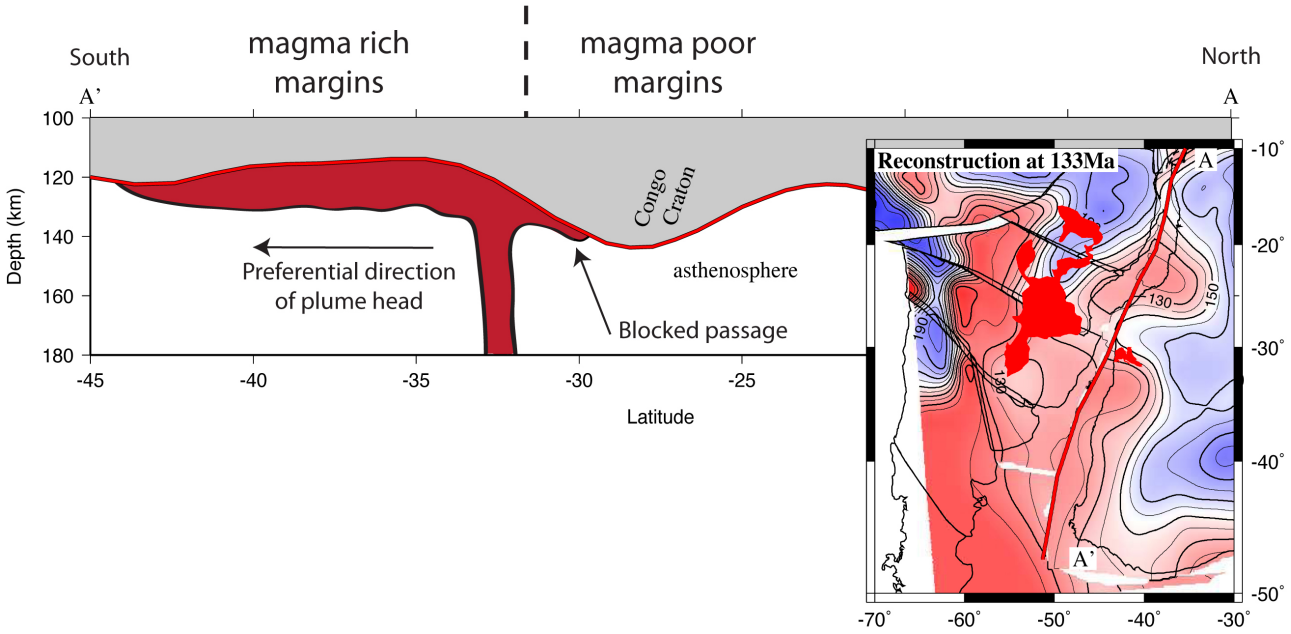


Figure 7.8: Schematic of a possible explanation for the magma-rich and magma-poor passive margins in the South Atlantic. Lithosphere thickness (from Priestley and McKenzie, 2006) at 133 Ma, with the latter covering the whole area. The transect is shown on map, and approximate locations of major features are marked.

magnetic isochron 15n (Dodd et al., 2015) and with an age of 135.96 Ma (Gee and Kent, 2007), confirm the presence of the plume, or at least a hot layer, before break-up. It can be suggested that in the southern South Atlantic, as the plume impinged the base of the lithosphere, it would have ponded towards the thinner lithosphere and spread preferentially towards the South where extension had already commenced. As a result, it would have caused the asymmetry observed with respect to volcanism along the passive margins south and north of the Rio Grande Rise and Walvis Ridge.

7.5.1 Additional observational constraints for the Tristan Plume

In addition to the evidence presented in this project favouring the *Mantle Plume - VPM Theory*, Courtillot et al. (2003) had criteria used to determine the presence of a deep-seated plume. Including already recognized (1) long-lived tracks and (2) the eruption of traps around time of impact, a deep-seated plume was also defined to have (3) a buoyancy flux $>10^3\,\mathrm{kg\,s^{-1}}$, (4) high $^4He/^3He$ or $^{21}Ne/^{22}Ne$ ratios and (5) the presence of anomalously low shear velocity zone. The Tristan plume had previously garnered a score of 3/5, with long lived tracks (Rio Grande Rise and Walvis Ridge), the eruption of traps (Paraná-Etendeka traps) and a buoyancy flux of $1.7\,\mathrm{x}\,10^3\,\mathrm{kg\,s^{-1}}$ (Courtillot et al., 2003). Negative results were from a low $^4He/^3He$ found on Tristan da Cunha and Gough Island (Kurz et al., 1982; Farley and Neroda, 1998), and at the time no low shear velocity was found below Tristan da Cunha.

French and Romanowicz (2015) recently presented work using a global, radially anisotropic, whole-mantle shear-wave velocity model. They were able to image the presence of several broad, dome-like, possibly ther-

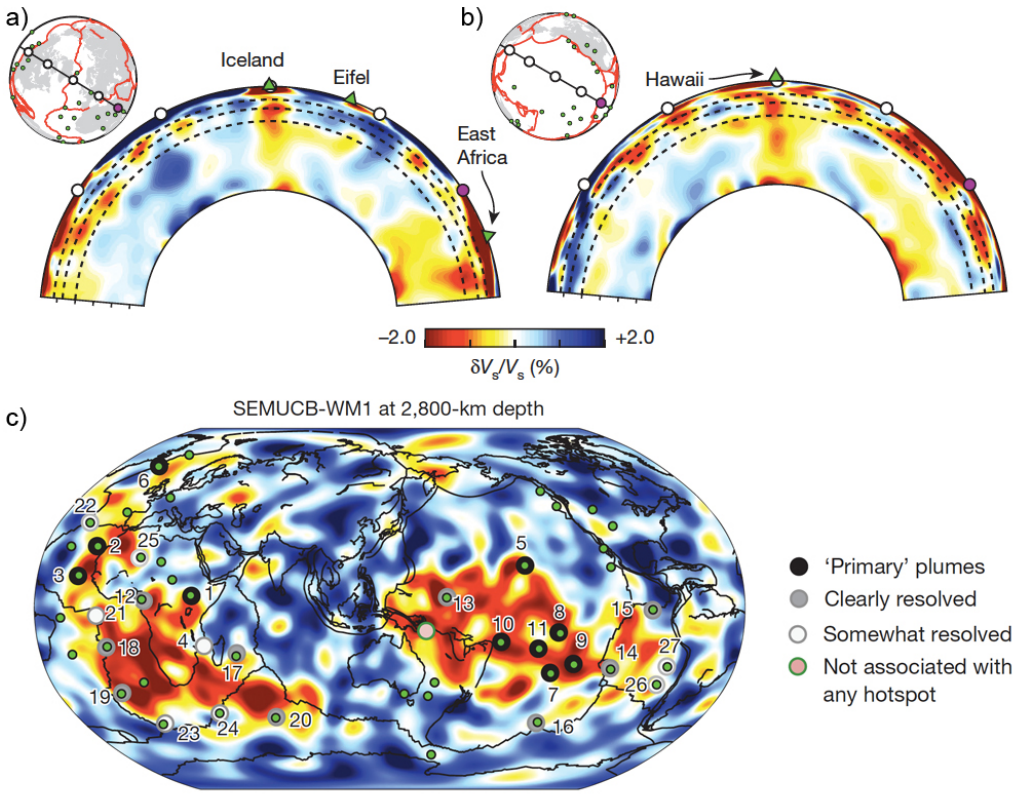


Figure 7.9: Evidence of plumes within the mantle using a global, radially anisotropic, whole-mantle shear-wave velocity model. Figures adapted from French and Romanowicz (2015). Parts (a) and (b) show the distinct vertical areas of reduced shear-wave velocity of 1.5–2 % under Iceland and Hawaii respectively. Part (c) shows the results of the shear-wave velocity model against global hotspot locations (defined by Steinberger, 2000). There is a total of 11 matching distinct plumes (black dots), 9 clearly resolved plumes (grey dots) and 7 somewhat resolved plums (white dots). The Tristan Plume is defined as clearly resolved (location no. 18). There is additionally one area in Indonesia that is not associated with any of the global hotspot locations (pink and green dot).

mochemical, plumes, including under Iceland (Fig. 7.9a) and Hawaii (Fig. 7.9b). They were distinguished with a reduction in shear velocity of 1.5–2 %. Although some deep-rooted plumes became pinched between 500–1000 km above the core-mantle boundary, the majority of reduced shear-wave velocity zones identified were relatively broad (French and Romanowicz, 2015). Distinct vertical areas of reduced shear-wave velocity with a δ V_s/V_s less than -1.5% for most of the depth interval 1,000–2,800 km constituting the lower mantle were found beneath numerous plume-related volcanoes, with 11 distinct plumes, 9 clearly resolved plumes and 7 somewhat resolved plumes (Fig. 7.9c). The Tristan Plume was recognised as a clearly resolved plume by French and Romanowicz (2015). This low velocity shear zone was previously not recognized by Courtillot et al. (2003), hence increasing the Tristan plume's 'score' for the presence of a deep-seated plume from 3/5 to 4/5. Whilst there are inconsistencies in the variation of magmatism (e.g. weakly magmatic Central Segment, asymmetry between Paraná-Etendeka areas), it can be concluded that for the southern South Atlantic, the Tristan plume is the primary influence on magmatism observed.

Chapter 8

Conclusions

The conjugate margins of the southern South Atlantic are of high interest, among others, to the petroleum industry. In order to understand the petroleum play for this region, comprehending the conditions of break-up, including the initial thermal structure, will aid the exploration effort. The arrival of the Tristan Plume has often been considered the cause of break-up in the South Atlantic (e.g., White and McKenzie, 1989), with several characteristics in line with the *Mantle Plume - VPM Theory*. These include flood basalts formed around break-up represented by the Paranà-Etendeka Traps, long-lived volcanic seamount/volcano trails in the form of the Rio Grande Rise and Walvis Ridge and associated volcanic passive margins observed on the conjugate margins of the southern South Atlantic. The volcanic passive margins are identified by the presence of high-velocity lower-crust bodies, seaward dipping reflectors and thickened initial oceanic crustal thickness, all of which, following the *Mantle Plume - VPM Theory*, are expected to decrease in magnitude away from the plume axis.

However, within the South Atlantic, several important departures from the *Mantle Plume - VPM Theory* are observed. Previous studies have shown (1) SDR volumes seemingly affected by segmentation and with no systematic increase towards the Rio Grande Rise and Walvis Ridge, (2) a four-fold asymmetry of syn-rift magmatism volumes between the conjugate margins, and (3) a stark contrast between non-volcanic and volcanic passive margins in the Central and Southern Segments respectively. As a result, different mechanisms for the formation of the volcanic passive margins and subsequent influence on magmatism were proposed. Small-scale convection resulting from sub-lithospheric topography was not considered as an alternate mechanism, with several numerical models not capable of recreating the results needed to match observational constraints (e.g., Nielsen and Hopper, 2004; Sleep, 2007). The influence of pre-thinning events prior to the eruption of flood basalts was also not explored, as there was little evidence for this happening within the South Atlantic. The two alternate mechanisms explored in this project were the influence of segmentation and active mantle upwelling on magmatism within the study area. Their potential influence was tested, along with the validity of the *Mantle Plume - VPM Theory*, through the use of observational constraints of post and syn-rift magmatism

and a numerical model of continental rifting.

Observational constraints for post and syn-rift magmatism originated from 38 seismic profiles from published and unpublished sources over an along-strike distance of 2,800 km (**Chapter 3**). Profiles were selected if they showed the full margin crustal structure, inclusive of the Moho. Published data originated from eight wide-angle surveys and ten MCS profiles, with six additional cropped MCS profiles from previously unpublished industry data. A newer set of unpublished data were also used in this project, originating from fourteen high quality seismic reflection survey lines from the BasinSPAN acquisition project of ION Geophysical. Following a strict set of criteria, the Landward Limit of Ocean Crust was found for all of the profiles. In order to compare thicknesses to the wide-angle depth sections, MCS lines were converted to distance using the mean seismic velocity value for oceanic crust of $6.7 \pm 0.3\,\mathrm{km\,s^{-1}}$. Inclusive to the measurement of initial oceanic crustal thickness, the syn-rift magmatism on wide-angle profiles was quantified in terms of melt areas and average seismic velocity trends, using a set of criteria largely based on seismic velocity. Syn-rift magmatism was observed on the conjugate margins, with the imaging of both HVLC bodies and SDRs.

Using the post and syn-rift magmatism information extracted from seismic data in terms of initial oceanic crustal thickness, melt areas and seismic velocity trends, these observational constraints were then matched to results from a numerical model of continental rifting. A 2D viscous model of the upper mantle was used in this project (**Chapter 4**). The model has been previously used within the North Atlantic and Indian Ocean, and is capable of predicting melt thickness and major element oxide composition through time. The variables of the model included mantle asthenosphere temperature, initial lithosphere thickness, spreading velocity, composition parametrisation and hot layer temperatures. Mantle asthenosphere temperature was set at 1315 °C, determined by using the observed reduction in oceanic crustal thickness with time and distance with respect to the the passive margin from the long-offset ION Geophysical lines. Initial lithosphere thicknesses were determined for each profile using present day lithosphere thickness values from seismic tomography models and a spreading velocity was assigned using values from Heine et al. (2013) specific to the profile locations. The model is capable of predicting major element oxide compositions through the use of two composition parametrisations, WM91 and N97 (Watson and McKenzie, 1991 & Niu, 1997). Due to their differing methods of calculation, the resulting major element oxide compositions also differ. In order to aid the composition parametrisation choice, major element oxide compositions from DSDP drillholes and Mid-Atlantic Ridge dredge samples were compared to results from steady-state models. N97-HK93 was ultimately chosen due to its low normalised root mean square error values compared to the geochemical data and its peridotite-based bulk earth composition. Finally, the hot layer temperatures were varied from 50–250 °C in order to match observational constraints from post and syn-rift magmatism.

Due to the high number of measurements for initial oceanic crustal thickness, using 37 out of the possible 38 profiles, post-rift magmatism was used to test the influence of segmentation against the *Mantle Plume - VPM Theory* in **Chapter 5**. The influence of segmentation on magmatism had only previously been tested using SDR areas (Franke et al., 2007; Koopmann et al., 2014a,b). As measurements from the conjugate margins were being

used, segments were redefined to ensure conjugate symmetry, using sub-plate boundaries and fracture zones. When plotted against distance along-strike from the Rio Grande Rise and Walvis Ridge, the overlying trend observed from initial oceanic crustal thickness values was that of decreasing thickness from north to south at a rate of ∼0.16 km per 100 km. Apart from an earlier synthesis using similar data plotted in Collier et al. (2009), this is the first time such a comprehensive trend of initial oceanic crustal thicknesses plotted along-strike has been carried out for the southern South Atlantic. No strong correlation between segment boundaries and oceanic crustal thickness was found. The influence of segmentation was further tested by using the numerical model of continental rifting. To match the initial oceanic crustal thicknesses from the seismic data, it was found there must have been a hot layer present. From an overall mantle temperature of 1515 °C with proximity to the Rio Grande Rise and Walvis Ridge, representing an excess temperature of 200 °C, there was a reduction of ∼40 °C per 500 km necessary in order to match initial oceanic crustal thickness from the observational constraints on the conjugate margins. This supports the evidence of the presence of a mantle plume or thermal anomaly as the origin for excessive melt production, reinforcing the validity of the *Mantle Plume - VPM Theory* for this region.

Active mantle upwelling was suggested as a mechanism for the formation of the volcanic passive margin on the East Coast of the U.S. and as additionally having an influence on magmatism within the North Atlantic (Kelemen and Holbrook, 1995; Holbrook et al., 2001). Through the relationship between igneous crustal thickness and average seismic velocity (the H_c-V_p method), the presence of active mantle upwelling or a thermal anomaly was tested. Using observational constraints from syn-rift magmatism, five wide-angle profiles on the African margin were used to measure igneous crustal thickness and average seismic velocity, through which the presence of active mantle upwelling was tested for the first time within the southern South Atlantic (**Chapter 6**). The H_c-V_p curves for all the profiles showed the presence of above-normal mantle temperature, consistently decreasing along-strike, as per the *Mantle Plume - VPM Theory.* There is little evidence for the presence of active mantle upwelling. The variation of the mantle temperature was tested with the numerical model of continental rifting using observational constraints from melt area and seismic velocity trends from syn-rift magmatism on the African margin. Results matched to observational constraints from Profile AF0, located on the Walvis Ridge, suggested an overall mantle temperature of 1565 °C, representing a hot layer with an excess temperature of 250 °C. This reduced towards the south at a rate of ∼60 °C per 500 km, reaching a temperature of 1365 °C, or a hot layer with an excess temperature of 50 °C for Profile AF4. Combining numerical modelling results matched to both observational constraints from post and syn-rift magmatism, there is a clear trend of decreasing mantle temperature from north to south at a rate of ∼40 °C per 500 km.

Other observations that were in agreement with the *Mantle Plume - VPM Theory* within the study area included the extent of volcanic passive margins, variations in magmatic productivity rates, and igneous crustal thickness along-strike and through time. Additionally, the South Atlantic is often compared with observations from the Iceland Plume system in the North Atlantic. Within the Southern Segment, the volcanic passive margins were found to have a length of ∼1780–2300 km. Even though this length may be on the shorter end of the global spectrum, with distributions ranging from 2300 km to 2900 km for the North Atlantic and East Coast

of U.S (Bradley, 2008), they are still in the same order of magnitude as other global localities and are in line with the expected diameter of an arriving plume head. Early magmatic productivity rates based on syn-rift magmatism on the African margin decreased along-strike, from $1635 \pm 40\,km^3$ /km /Ma to $695 \pm 20\,km^3$/km/Ma, similar to the values seen for the SIGMA profiles in the North Atlantic. The rates in the South Atlantic reduced by approximately four times over a 6–7 Myr year period, twice as fast as observed in the North Atlantic. The overall igneous crustal thicknesses on the African margin also decreased along-strike and through time. However, Profile AF0, with the thickest igneous crust of ∼25 km, and Profile AF1, with the thickest initial oceanic crust of 11.7 km, fell short of the maximum thickness observed in the North Atlantic. Furthermore, numerical results of continental rifting for the North Atlantic suggested an overall hotter mantle in comparison to the study area. As Holbrook et al. (2001) suggested, active mantle upwelling may have contributed to magmatism in the North Atlantic. However, the lack of active mantle upwelling within the study area could be a possible suggestion for the differences observed within the North and South Atlantic for both post and syn-rift magmatism.

Despite the dismissal of segmentation and active mantle upwelling, there were still some unexplained departures from the *Mantle Plume - VPM Theory* in the region. An asymmetry was noted between syn-rift magmatism melt areas between the South American and African margins of the study area. This apparent asymmetry may however be due to a lack of currently published data. As SDR volumes had been found relatively symmetrical on the conjugate margins, it is likely that as more data are published on the South American margin, the degree of this apparent asymmetry will reduce. From the extent of volcanic passive margins north and south of the Greenland-Iceland-Faroe Ridges in the North Atlantic, the stark difference observed between non-volcanic and volcanic passive margins in the Central and Southern Segments is not anticipated by the *Mantle Plume - VPM Theory*. However, by reconstructing the lithosphere thickness at break-up, it was suggested within this project that the sublithospheric topography had a strong influence on magmatism throughout the South Atlantic, including on the asymmetry in magmatism along the margins. The magma-poor area north of the Rio Grande Rise and Walvis Ridge is adjacent to the Congo Craton, and the lateral flow of the potential mantle plume could have been hindered by this continental root. To the south of the Congo Craton, the magmatism observed due to break-up was found to be a result of a more subtle interplay between lithosphere thickness and mantle temperature. Additional evidence for a deep-seated plume was presented from a reduced shear wave velocity zone located beneath Tristan da Cunha Island. Whilst departures from the model are still present, the Tristan Plume can be concluded as being the primary influence of magmatism for the continental margins of the southern South Atlantic.

Finally, there are several areas of additional work that would be beneficial to this project, furthering its results and consolidating its conclusions. In terms of data availability, a significant amount of additional seismic lines will soon be available for academic use from ION Geophysical, including the full margin crustal structure offshore South America and lines located offshore West Africa. From these, there will be the opportunity for more observations and measurements of initial oceanic crustal thickness and syn-rift magmatism, resulting in a greater insight into the variation of both ocean crust and the distribution of HVLC bodies along strike. Additionally, the ION Geophysical lines benefit from long streamer lengths, allowing velocity data to be distinguished within SDR

bodies. This will allow for a more complete measurement of SDR thicknesses and volumes to be compared with respect to segment boundaries. Regarding the numerical modelling, and in order for a better insight into the thermal structure, the use of a 3D model with visco-plastic rheology would be appropriate to match the increase of observational constraints from the ION Geophysical data. Additional modelling would also be beneficial to model the impacting plume head and how it is influenced by the sublithospheric topography. Whilst there is already certainty that the Tristan Plume is the primary influencer of magmatism in the area, further work is necessary to truly understand the evolution of the thermal structure of the southern South Atlantic preceding break-up to present day.

Bibliography

Aizawa, M., Bluck, B., Cartwright, J., Milner, S., Swart, R., and Ward, J. (2000). Constraints on the geomorphological evolution of Namibia from the offshore stratigraphic record. *Communications of the Geological Survey of Namibia*, 12:337–346.

Anderson, D. L. (1994). The sublithospheric mantle as the source of continental flood basalts; the case against the continental lithosphere and plume head reservoirs. *Earth and Planetary Science Letters*, 123(1):269–280.

Armante, C.; Eakins, B. (2009). ETOPO1 1 Arc-Minute Global Relief Model: Procedures, Data Sources and Analysis. *Memorandum NESDIS NGDC-24*, page 19.

Armitage, J., Jaupart, C., Fourel, L., and Allen, P. (2013). The instability of continental passive margins and its effect on continental topography and heat flow. *Journal of Geophysical Research: Solid Earth*, 118(4):1817–1836.

Armitage, J. J. (2008). *Modelling the Controls on Melt Generation During Continental Extension and Breakup*. PhD thesis, University of Southampton.

Armitage, J. J., Collier, J. S., and Minshull, T. A. (2010). The importance of rift history for volcanic margin formation. *Nature*, 465(7300):913–917.

Armitage, J. J., Collier, J. S., Minshull, T. A., and Henstock, T. J. (2011). Thin oceanic crust and flood basalts: India-Seychelles breakup. *Geochemistry Geophysics Geosystems*, 12. Q0AB07.

Armitage, J. J., Ferguson, D. J., Goes, S., Hammond, J. O., Calais, E., Rychert, C. A., and Harmon, N. (2015). Upper mantle temperature and the onset of extension and break-up in Afar, Africa. *Earth and Planetary Science Letters*, 418:78–90.

Armitage, J. J., Henstock, T. J., Minshull, T. A., and Hopper, J. R. (2008). Modelling the composition of melts formed during continental breakup of the Southeast Greenland margin. *Earth and Planetary Science Letters*, 269(1-2):248–258.

Armitage, J. J., Henstock, T. J., Minshull, T. A., and Hopper, J. R. (2009). Lithospheric controls on melt production during continental breakup at slow rates of extension: Application to the North Atlantic. *Geochemistry Geophysics Geosystems*, 10. Q06018.

Asimow, P. D. and Ghiorso, M. S. (1998). Algorithmic modifications extending MELTS to calculate subsolidus phase relations. *American Mineralogist*, 83(9-10):1127–1132.

Aslanian, D., Moulin, M., Olivet, J. L., Unternehr, P., Matias, L., Bache, F., Rabineau, M., Nouze, H., Klingelheofer, F., Contrucci, I., and Labails, C. (2009). Brazilian and African passive margins of the Central Segment of the South Atlantic Ocean: Kinematic constraints. *Tectonophysics*, 468(1-4):98–112.

Attoh, K., Brown, L., Guo, J., and Heanlein, J. (2004). Seismic stratigraphic record of transpression and uplift on the Romanche transform margin, offshore Ghana. *Tectonophysics*, 378(1-2):1–16. 765NV.

Austin, J. A. and Uchupi, E. (1982). Continental-Oceanic Crustal Transition Off Southwest Africa. *AAPG Bulletin*, 66(9):1328–1347.

Barker, P. F., Johnson, D. A., Carlson, R. L., Cepek, P., Coulbourn, W. T., Gamboa, L. A., Hamilton, N., de Melo, U., Pujol, C., Shor, A. N., Suzyumov, A. E., Tjalsma, L. R. C., and Walton, W. H. (1983). Initial reports of the Deep Sea Drilling Project covering Leg 72 of the cruises of the drilling vessel Glomar Challenger, Santos, Brazil to Santos, Brazil. *Texas A & M University*.

Barton, A. and White, R. (1997). Crustal structure of Edoras Bank continental margin and mantle thermal anomalies beneath the North Atlantic. *Journal of Geophysical Research: Solid Earth*, 102(B2):3109–3129.

Bauer, K., Neben, S., Schreckenberger, B., Emmermann, R., Hinz, K., Fechner, N., Gohl, K., Schulze, A., Trumbull, R. B., and Weber, K. (2000). Deep structure of the Namibia continental margin as derived from integrated geophysical studies. *Journal of Geophysical Research: Solid Earth*, 105(B11):25829–25853.

Becker, K., Franke, D., Trumbull, R., Schnabel, M., Heyde, I., Schreckenberger, B., Koopmann, H., Bauer, K., Jokat, W., and Krawczyk, C. (2014). Asymmetry of high-velocity lower crust on the South Atlantic rifted margins and implications for the interplay of magmatism and tectonics in continental breakup. *Solid Earth*, 5(2):1011.

Behn, M. D. and Grove, T. L. (2015). Melting systematics in mid-ocean ridge basalts: Application of a plagioclase-spinel melting model to global variations in major element chemistry and crustal thickness. *Journal of Geophysical Research: Solid Earth*, 120(7):4863–4886.

Behn, M. D. and Kelemen, P. B. (2003). Relationship between seismic P-wave velocity and the composition of anhydrous igneous and meta-igneous rocks. *Geochemistry Geophysics Geosystems*, 4(5). 1041.

Bellieni, G., Brotzu, P., Comin-Chiaramonti, P., Ernesto, M., Melfi, A., Pacca, I., Piccirilo, E., and Stolfa, D. (1983). Petrological and paleomagnetic data on the plateau basalts to rhyolite sequences of the Southern Paraná Basin (Brazil). *Anais da Academia Brasileira de Ciências*, 55(4):355–383.

Berndt, C., Planke, S., Alvestad, E., Tsikalas, F., and Rasmussen, T. (2001). Seismic volcanostratigraphy of the Norwegian Margin: constraints on tectonomagmatic break-up processes. *Journal of the Geological Society*, 158(3):413–426.

Bialas, R. W. and Buck, W. R. (2009). How sediment promotes narrow rifting: Application to the Gulf of California. *Tectonics*, 28(4).

Blaich, O. A., Faleide, J. I., and Tsikalas, F. (2011). Crustal breakup and continent-ocean transition at South Atlantic conjugate margins. *Journal of Geophysical Research: Solid Earth*, 116(B1).

Blaich, O. A., Faleide, J. I., Tsikalas, F., Franke, D., and Leon, E. (2009). Crustal-scale architecture and segmentation of the Argentine margin and its conjugate off South Africa. *Geophysical Journal International*, 178(1):85–105.

Blaich, O. A., Tsikalas, F., and Faleide, J. I. (2008). Northeastern Brazilian margin: Regional tectonic evolution based on integrated analysis of seismic reflection and potential field data and modelling. *Tectonophysics*, 458(1-4):51–67.

Bolli, H. M., Ryan, W. B., McKnight, B. K., Kagami, H., Melguen, M., Siesser, W. G., Natland, J. H., Longoria, J. F., Decima, F. P., Foresman, J. B., and Hottman, W. E. (1978). Initial reports of the Deep Sea Drilling Project covering Leg 40 of the cruises of the drilling vessel Glomar Challenger; Cape Town, South Africa to Abidjan, Ivory Coast. *Texas A & M University*.

Borissova, I., Totterdell, J., Southby, C., Owen, K., and Bernardel, G. (2015). Characteristics of the Frontier Northern Houtman Sub-Basin Formed on a Magma-Rich Segment of the Western Australian Margin. In *AAPG/SEG International Conference & Exhibition, Melbourne, Australia*.

Boutilier, R. and Keen, C. (1999). Small-scale convection and divergent plate boundaries. *Journal of Geophysical Research: Solid Earth*, 104(B4):7389–7403.

Bown, J. and White, R. (1994). Variation with spreading rate of oceanic crustal thickness and geochemistry. *Earth and Planetary Science Letters*, 121(3):435–449.

Bradley, D. C. (2008). Passive margins through earth history. *Earth-Science Reviews*, 91(1):1–26.

Braun, M. G., Hirth, G., and Parmentier, E. (2000). The effects of deep damp melting on mantle flow and melt generation beneath mid-ocean ridges. *Earth and Planetary Science Letters*, 176(3):339–356.

Breivik, A. J., Mjelde, R., Faleide, J. I., and Murai, Y. (2012). The eastern Jan Mayen microcontinent volcanic margin. *Geophysical Journal International*, 188(3):798–818.

Brune, S., Heine, C., Clift, P. D., and Pérez-Gussinyé, M. (2016). Rifted margin architecture and crustal rheology: Reviewing Iberia-Newfoundland, Central South Atlantic, and South China Sea. *Marine and Petroleum Geology*.

Bryan, S. E. and Ferrari, L. (2013). Large igneous provinces and silicic large igneous provinces: Progress in our understanding over the last 25 years. *Geological Society of America Bulletin*, 125(7-8):1053–1078.

Buiter, S. J. and Torsvik, T. H. (2014). A review of Wilson Cycle plate margins: A role for mantle plumes in continental break-up along sutures? *Gondwana Research*, 26(2):627–653.

Campbell, I. H. (2007). Testing the plume theory. *Chemical Geology*, 241(3-4):153–176.

Canales, J. P., Detrick, R. S., Bazin, S., Harding, A. J., and Orcutt, J. A. (1998). Off-Axis Crustal Thickness Across and Along the East Pacific Rise Within the MELT Area. *Science*, 280(5367):1218–1221.

Chalapathi Rao, N., Burgess, R., Lehmann, B., Mainkar, D., Pande, S., Hari, K., and Bodhankar, N. (2011). $^{40}Ar/^{39}Ar$ ages of mafic dykes from the Mesoproterozoic Chhattisgarh basin, Bastar craton, central India: Implication for the origin and spatial extent of the Deccan Large Igneous Province. *Lithos*, 125(3):994–1005.

Chalapathi Rao, N. and Lehmann, B. (2011). Kimberlites, flood basalts and mantle plumes: New insights from the Deccan Large Igneous Province. *Earth-Science Reviews*, 107(3):315–324.

Chalmers, J. A. and Laursen, K. H. (1995). Labrador Sea: the extent of continental and oceanic crust and the timing of the onset of seafloor spreading. *Marine and Petroleum Geology*, 12(2):205–217.

Chang, H. K., Kowsmann, R. O., Figueiredo, A. M. F., and Bender, A. (1992). Tectonics and stratigraphy of the East Brazil Rift system: an overview. *Tectonophysics*, 213(1):97–138.

Chian, D., Louden, K., and Reid, I. (1995). Crustal structure of the Labrador Sea conjugate margin and implications for the formation of nonvolcanic continental margins. *Journal of Geophysical Research: Solid Earth*, 100(B12):24239–24253.

Chian, D. and Louden, K. E. (1994). The continent-ocean crustal transition across the southwest Greenland margin. *Journal of Geophysical Research: Solid Earth*, 99(B5):9117–9135.

Christensen, N. I. (1979). Compressional wave velocities in rocks at high temperatures and pressures, critical thermal gradients, and crustal low-velocity zones. *Journal of Geophysical Research: Solid Earth*, 84(B12):6849–6857.

Clemson, J., Cartwright, J., and Booth, J. (1997). Structural segmentation and the influence of basement structure on the Namibian passive margin. *Journal of the Geological Society*, 154(3):477–482.

Clemson, J., Cartwright, J., and Swart, R. (1999). The Namib Rift: a rift system of possible Karoo age, offshore Namibia. *Geological Society, London, Special Publications*, 153(1):381–402.

Clerc, C., Jolivet, L., and Ringenbach, J. (2015). Ductile extensional shear zones in the lower crust of a passive margin. *Earth and Planetary Science Letters*, 431:1–7.

Coffin, M. F., Duncan, R. A., Eldholm, O., Fitton, J. G., Frey, F. A., Larsen, H. C., Mahoney, J. J., Saunders, A. D., Schlich, R., and Wallace, P. J. (2006). Large igneous provinces and scientific ocean drilling: status quo and a look ahead. *Oceanography*, 19(4):150–160.

Coffin, M. F. and Eldholm, O. (1994). Large igneous provinces: Crustal structure, dimensions, and external consequences. *Reviews of Geophysics*, 32(1):1–36.

Collier, J., Sansom, V., Ishizuka, O., Taylor, R., Minshull, T., and Whitmarsh, R. (2008). Age of Seychelles–India break-up. *Earth and Planetary Science Letters*, 272(1):264–277.

Collier, J. S., Minshull, T. A., Hammond, J. O. S., Whitmarsh, R. B., Kendall, J. M., Sansom, V., Lane, C. I., and Rumpker, G. (2009). Factors influencing magmatism during continental breakup: New insights from a wide-angle seismic experiment across the conjugate Seychelles-Indian margins. *Journal of Geophysical Research: Solid Earth*, 114(B3).

Contrucci, I., Matias, L., Moulin, M., Geli, L., Klingelhofer, F., Nouze, H., Aslanian, D., Olivet, J. L., Rehault, J. P., and Sibuet, J. C. (2004). Deep structure of the West African continental margin (Congo, Zaïre, Angola), between 5°S and 8°S, from reflection/refraction seismics and gravity data. *Geophysical Journal International*, 158(2):529–553.

Cook, P. J. and McElhinny, M. (1979). A reevaluation of the spatial and temporal distribution of sedimentary phosphate deposits in the light of plate tectonics. *Economic Geology*, 74(2):315–330.

Cordery, M. J. and Morgan, J. P. (1993). Convection and melting at mid-ocean ridges. *Journal of Geophysical Research: Solid Earth*, 98(B11):19477–19503.

Courtillot, V. (1994). Mass extinctions in the last 300 million years: one impact and seven flood basalts. *Israel Journal of Earth Sciences*, 43(255):66.

Courtillot, V., Davaille, A., Besse, J., and Stock, J. (2003). Three distinct types of hotspots in the Earths mantle. *Earth and Planetary Science Letters*, 205(3):295–308.

Courtillot, V., Jaupart, C., Manighetti, I., Tapponnier, P., and Besse, J. (1999). On causal links between flood basalts and continental breakup. *Earth and Planetary Science Letters*, 166(3-4):177–195.

Courtillot, V. E. and Renne, P. R. (2003). On the ages of flood basalt events. *Comptes Rendus Geoscience*, 335(1):113–140.

Cowie, L., Angelo, R., Kusznir, N., Manatschal, G., and Horn, B. (2016). The palaeo-bathymetry of base Aptian salt deposition on the northern Angolan rifted margin: constraints from flexural back-stripping and reverse post-break-up thermal subsidence modelling. *Petroleum Geoscience*, 22(1):59–70.

Dannberg, J. and Sobolev, S. V. (2015). Low-buoyancy thermochemical plumes resolve controversy of classical mantle plume concept. *Nature communications*, 6. http://dx.doi.org/10.10.1038/ncomms7970.

De Boer, J., McHone, J., Puffer, J., Ragland, P., and Whittington, D. (1988). Mesozoic and Cenozoic magmatism. *The Geology of North America*, 2:217–241.

de Vera, J., Granado, P., and McClay, K. (2010). Structural evolution of the Orange Basin gravity-driven system, offshore Namibia. *Marine and Petroleum Geology*, 27(1):223–237.

Dean, S., Murton, B., Minshull, T., Henstock, T., and White, R. (2009). An integrated kinematic and geochemical model to determine lithospheric extension and mantle temperature from syn-rift volcanic compositions. *Earth and Planetary Science Letters*, 278(1):26–39.

Diebold, J. B., Stoffa, P. L., Group, L. S., et al. (1988). A large aperture seismic experiment in the Baltimore Canyon Trough. *The Geology of North America*, 1:2.

Dobretsov, N. (2008). Geological implications of the thermochemical plume model. *Russian Geology and Geophysics*, 49(7):441–454.

Dobretsov, N., Kirdyashkin, A., and Kirdyashkin, A. (2003). Physicochemical conditions at the core-mantle boundary and formation of thermochemical plumes. In *Doklady earth sciences*, volume 393, pages 1319–1322.

Dodd, S. C., Mac Niocaill, C., and Muxworthy, A. R. (2015). Long duration (> 4 Ma) and steady-state volcanic activity in the early Cretaceous Paraná–Etendeka Large Igneous Province: New palaeomagnetic data from Namibia. *Earth and Planetary Science Letters*, 414:16–29.

Dragoi-Stavar, D. and Hall, S. (2009). Gravity modeling of the ocean-continent transition along the South Atlantic margins. *Journal of Geophysical Research: Solid Earth*, 114.

Duncan, R. A., Hooper, P., Rehacek, J., Marsh, J., and Duncan, A. (1997). The timing and duration of the Karoo igneous event, southern Gondwana. *Journal of Geophysical Research: Solid Earth*, 102(B8):18,127–18,138.

Dupre, S., Cloetingh, S., and Bertotti, G. (2011). Structure of the Gabon Margin from integrated seismic reflection and gravity data. *Tectonophysics*, 506(1-4):31–45.

Eldholm, O., Sundvor, E., and Myhre, A. (1979). Continental margin off Lofoten-Vesterålen northern Norway. *Marine Geophysical Researches*, 4(1):3–35.

Erlank, A., Marsh, J., Duncan, A., Miller, R. M., Hawkesworth, C., Betton, P., and Rex, D. (1984). Geochemistry and petrogenesis of the Etendeka volcanic rocks from SWA/Namibia. *Special Publication Geological Society of South Africa*, 13:195–245.

Evain, M., Afilhado, A., Rigoti, C., Loureiro, A., Alves, D., Klingelhoefer, F., Schnurle, P., Feld, A., Fuck, R., Soares, J., et al. (2015). Deep structure of the Santos Basin-São Paulo Plateau System, SE Brazil. *Journal of Geophysical Research: Solid Earth*, 120(8):5401–5431.

Falloon, T. and Green, D. (1987). Anhydrous partial melting of MORB pyrolite and other peridotite compositions at 10 kbar: Implications for the origin of primitive MORB glasses. *Mineralogy and Petrology*, 37(3-4):181–219.

Falloon, T. J., Green, D. H., Hatton, C., and Harris, K. (1988). Anhydrous Partial Melting of a Fertile and Depleted Peridotite from 2 to 30 kb and Application to Basalt Petrogenesis. *Journal of Petrology*, 29(6):1257–1282.

Farley, K. and Neroda, E. (1998). Noble gases in the Earth's mantle. *Annual Review of Earth and Planetary Sciences*, 26(1):189–218.

Fernandez, M., Afonso, J. C., and Ranalli, G. (2010). The deep lithospheric structure of the Namibian volcanic margin. *Tectonophysics*, 481(1-4):68–81.

Fishwick, S. (2010). Surface wave tomography: Imaging of the lithosphere–asthenosphere boundary beneath central and southern Africa? *Lithos*, 120(1):63–73.

Fishwick, S. and Bastow, I. D. (2011). Towards a better understanding of African topography: a review of passive-source seismic studies of the African crust and upper mantle. *Geological Society, Special Publications*, 357(1):343–371.

Foster, D. A., Goscombe, B. D., and Gray, D. R. (2009). Rapid exhumation of deep crust in an obliquely convergent orogen: The Kaoko Belt of the Damara Orogen. *Tectonics*, 28(4).

Foulger, G. and Natland, J. (2003). Is" hotspot" volcanism a consequence of plate tectonics? *Science*, 300(5621):921–922.

Fowler, S., White, R., Spence, G., and Westbrook, G. (1989). The Hatton Bank continental margin–II. Deep structure from two-ship expanding spread seismic profiles. *Geophysical Journal International*, 96(2):295–309.

Franke, D. (2013). Rifting, lithosphere breakup and volcanism: Comparison of magma-poor and volcanic rifted margins. *Marine and Petroleum Geology*.

Franke, D., Ladage, S., Schnabel, M., Schreckenberger, B., Reichert, C., Hinz, K., Paterlini, M., de Abelleyra, J., and Siciliano, M. (2010). Birth of a volcanic margin off Argentina, South Atlantic. *Geochemistry Geophysics Geosystems*, 11(2). Q0AB04.

Franke, D., Neben, S., Ladage, S., Schreckenberger, B., and Hinz, K. (2007). Margin segmentation and volcano-tectonic architecture along the volcanic margin off Argentina/Uruguay, South Atlantic. *Marine Geology*, 244(1-4):46–67.

Franke, D., Neben, S., Schreckenberger, B., Schulze, A., Stiller, M., and Krawczyk, C. M. (2006). Crustal structure across the Colorado Basin, offshore Argentina. *Geophysical Journal International*, 165(3):850–864.

Fraser, S. and Clark, I. (2016). Continent-Ocean Transitions, How Do They Form? An Example From Sergipe Alagoas, Brazil. In *AAPG/SEG International Conference & Exhibition*.

French, S. W. and Romanowicz, B. (2015). Broad plumes rooted at the base of the Earth's mantle beneath major hotspots. *Nature*, 525(7567):95–99.

Frimmel, H., Basei, M., and Gaucher, C. (2011). Neoproterozoic geodynamic evolution of SW-Gondwana: a southern African perspective. *International Journal of Earth Sciences*, 100(2-3):323–354.

Fromm, T., Planert, L., Jokat, W., Ryberg, T., Behrmann, J., Weber, M., and Haberland, C. (2015). South Atlantic opening: A plume-induced breakup? *Geology*, 43(10):931–934.

Furlong, K. P. and Fountain, D. M. (1986). Continental crustal underplating: Thermal considerations and seismic-petrologic consequences. *Journal of Geophysical Research: Solid Earth*, 91(B8):8285–8294.

Gallagher, K. and Brown, R. (1999). Denudation and uplift at passive margins: the record on the Atlantic Margin of southern Africa. *Philosophical Transactions of the Royal Society of London A: Mathematical, Physical and Engineering Sciences*, 357(1753):835–859.

Gallagher, K. and Hawkesworth, C. (1994). Mantle plumes, continental magmatism and asymmetry in the South Atlantic. *Earth and Planetary Science Letters*, 123(13):105–117.

Gee, J. S. and Kent, D. V. (2007). Source of oceanic magnetic anomalies and the geomagnetic polarity timescale. *Treatise on Geophysics, Vol. 5: Geomagnetism*, pages 455–507.

Geoffroy, L. (2005). Volcanic passive margins. *Comptes Rendus Geoscience*, 337(16):1395–1408.

Geoffroy, L., Burov, E., and Werner, P. (2015). Volcanic passive margins: another way to break up continents. *Scientific reports*, 5.

Gerrard, I. and Smith, G. (1982). Post-Paleozoic Succession and Structure of the Southwestern African Continental Margin: Rifted Margins: Field Investigations of Margin Structure and Stratigraphy. *AAPG Special Volumes*.

Ghiorso, M. S. and Sack, R. O. (1995). Chemical mass transfer in magmatic processes IV. A revised and internally consistent thermodynamic model for the interpolation and extrapolation of liquid-solid equilibria in magmatic systems at elevated temperatures and pressures. *Contributions to Mineralogy and Petrology*, 119(2-3):197–212.

Gladczenko, T., Hinz, K., Eldholm, O., Meyer, H., Neben, S., and Skogseid, J. (1997). South Atlantic volcanic margins. *Journal of the Geological Society*, 154(3):465–470.

Gladczenko, T. P., Skogseid, J., and Eldhom, O. (1998). Namibia volcanic margin. *Marine Geology*, 20(4):313–341.

Goldschmidt-Rokita, A., Hansch, K. J., Hirschleber, H. B., Iwasaki, T., Kanazawa, T., Shimamura, H., and Sellevoll, M. A. (1994). The ocean/continent transition along a profile through the Lofoten Basin, Northern Norway. *Marine geophysical researches*, 16(3):201–224.

Gradstein, F. M., Ogg, J. G., Schmitz, M., and Ogg, G. (2012). On The Geologic Time Scale. *Newsletters on Stratigraphy*, 45/2:171–188.

Gradstein, F. M., Ogg, J. G., Smith, A. G., Bleeker, W., and Lourens, L. J. (2004). A new Geologic Time Scale, with special reference to Precambrian and Neogene. *Episodes*, 27(2):83–100.

Green, A. (2014). S Africa oil: time to look offshore? https://www.ft.com/content/32a0eaa3-a85a-3dcd-ba9f-2b33c13aa378. [Online; accessed 26-Dec-2016].

Griffiths, R. and Campbell, I. (1991). Interaction of mantle plume heads with the Earth's surface and onset of small-scale convection. *Journal of Geophysical Research: Solid Earth*, 96(B11):18295–18310.

Griffiths, R. W. and Campbell, I. H. (1990). Stirring and structure in mantle starting plumes. *Earth and Planetary Science Letters*, 99(1):66–78.

Grill, H. (1996). *The Permo-Carboniferous glacial to marine Karoo record in southern Namibia: sedimentary facies and sequence stratigraphy*. PhD thesis, Freunde d. Würzburger Geowissenschaften e. V.

Gubanov, A. and Mooney, W. (2009). New global geological maps of crustal basement age. In *AGU Fall Meeting Abstracts*.

Guillocheau, F., Rouby, D., Robin, C., Helm, C., Rolland, N., Le Carlier de Veslud, C., and Braun, J. (2012). Quantification and causes of the terrigeneous sediment budget at the scale of a continental margin: a new method applied to the Namibia–South Africa margin. *Basin Research*, 24(1):3–30.

Gurnis, M. (1988). Large-scale mantle convection and the aggregation and dispersal of supercontinents. *Nature*, 332(6166):695–699.

Hawkesworth, C., Gallagher, K., Kelley, S., Mantovani, M., Peate, D., Regelous, M., and Rogers, N. (1992). Paraná magmatism and the opening of the South Atlantic. *Geological Society, Special Publications*, 68(1):221–240.

Hay, W. W., Sibuet, J.-C., Barron, E. J., Brassell, S., Dean, W. E., Hue, A. Y., Keating, B. H., McNulty, C. L., Meyers, P. A., Nohara, M., Schallreuter, R. E., Steinmetz, J. C., Stow, D., and Stradner, H. (1984). Initial reports of the Deep Sea Drilling Project covering Leg 75 of the cruises of the drilling vessel Glomar Challenger, Walvis Bay, South Africa, to Recife, Brazil. *Texas A & M University*.

He, H., Pan, Y., Tauxe, L., Qin, H., and Zhu, R. (2008). Toward age determination of the M0r (Barremian–Aptian boundary) of the Early Cretaceous. *Physics of the Earth and Planetary Interiors*, 169(1):41–48.

Heine, C., Zoethout, J., and Müller, R. D. (2013). Kinematics of the South Atlantic rift. *Solid Earth*, 4(2):215–253.

Herzberg, C. (2004). Partial Crystallization of Mid-Ocean Ridge Basalts in the Crust and Mantle. *Journal of Petrology*, 45(12):2389–2405.

Herzberg, C., Asimow, P. D., Arndt, N., Niu, Y., Lesher, C. M., Fitton, J. G., Cheadle, M. J., and Saunders, A. D. (2007). Temperatures in ambient mantle and plumes: Constraints from basalts, picrites, and komatiites. *Geochemistry, Geophysics, Geosystems*, 8(2). Q02006.

Herzberg, C., Fyfe, W., and Carr, M. (1983). Density constraints on the formation of the continental Moho and crust. *Contributions to Mineralogy and Petrology*, 84(1):1–5.

Herzberg, C. and Ohara, M. (2002). Plume-Associated Ultramafic Magmas of Phanerozoic Age. *Journal of Petrology*, 43(10):1857–1883.

Hinz, K. (1981). A hypothesis on terrestrial catastrophes: Wedges of very thick oceanward dipping layers beneath passive continental margins; their origin and paleoenvironmental significance. *Geologisches Jahrbuch, Reihe E: Geophysics*, pages 3–28.

Hinz, K. (1990). The Argentine eastern continental margin; structure and geological development. *AAPG Bulletin*, 74(5):675–676.

Hinz, K., Neben, S., Schreckenberger, B., Roeser, H., Block, M., Souza, K., and Meyer, H. (1999). The Argentine continental margin north of 48°S: sedimentary successions, volcanic activity during breakup. *Marine and Petroleum Geology*, 16(1):1–25.

Hinz, K. and Weber, J. (1976). Zum geologischen aufbau des Norwegischen Kontinentalrandes und der Barents-See nach reflexionsseismischen Messungen. *Compendium*, 75(76):3–29.

Hirose, K. and Kawamura, K. (1994). A new experimental approach for incremental batch melting of peridotite at 1.5 GPa. *Geophysical research letters*, 21(19):2139–2142.

Hirose, K. and Kushiro, I. (1993). Partial melting of dry peridotites at high pressures: Determination of compositions of melts segregated from peridotite using aggregates of diamond. *Earth and Planetary Science Letters*, 114(4):477–489.

Hirsch, K. K., Bauer, K., and Scheck-Wenderoth, M. (2009). Deep structure of the western South African passive margin - Results of a combined approach of seismic, gravity and isostatic investigations. *Tectonophysics*, 470(1-2):57–70.

Hirschmann, M., Ghiorso, M., Wasylenki, L., Asimow, P., and Stolper, E. (1998). Calculation of Peridotite Partial Melting from Thermodynamic Models of Minerals and Melts. I. Review of Methods and Comparison with Experiments. *Journal of Petrology*, 39(6):1091–1115.

Hirth, G. and Kohlstedt, D. L. (1996). Water in the oceanic upper mantle: implications for rheology, melt extraction and the evolution of the lithosphere. *Earth and Planetary Science Letters*, 144(1):93–108.

Holbrook, W. and Kelemen, P. (1993). Large igneous province on the US Atlantic margin and implications for magmatism during continental breakup. *Nature*, 364(6436):433–436.

Holbrook, W. S., Larsen, H., Korenaga, J., Dahl-Jensen, T., Reid, I. D., Kelemen, P., Hopper, J., Kent, G., Lizarralde, D., Bernstein, S., et al. (2001). Mantle thermal structure and active upwelling during continental breakup in the North Atlantic. *Earth and Planetary Science Letters*, 190(3):251–266.

Holbrook, W. S., Purdy, G. M., Sheridan, R. E., III, L. G., Talwani, M., Ewing, J., and Hutchinson, D. (1994a). Seismic structure of the U.S. Mid-Atlantic continental margin. *Journal of Geophysical Research: Solid Earth*, 99(B9):17871–17891.

Holbrook, W. S., Reiter, E., Purdy, G., Sawyer, D., Stoffa, P., Austin, J., Oh, J., and Makris, J. (1994b). Deep structure of the U.S. Atlantic continental margin, offshore South Carolina, from coincident ocean bottom and multichannel seismic data. *Journal of Geophysical Research: Solid Earth*, 99(B5):9155–9178.

Hopper, J. R., Dahl-Jensen, T., Holbrook, W. S., Larsen, H. C., Lizarralde, D., Korenaga, J., Kent, G. M., and Kelemen, P. B. (2003). Structure of the SE Greenland margin from seismic reflection and refraction data: Implications for nascent spreading center subsidence and asymmetric crustal accretion during North Atlantic opening. *Journal of Geophysical Research: Solid Earth*, 108(B5).

Hopper, J. R., Mutter, J. C., Larson, R. L., and Mutter, C. Z. (1992). Magmatism and rift margin evolution: Evidence from northwest Australia. *Geology*, 20(9):853–857.

Houseman, G. (1990). The thermal structure of mantle plumes: axisymmetric or triple-junction? *Geophysical Journal International*, 102(1):15–24.

Hsü, K. J., LaBrecque, J. L., Max F. Carman, J., Andrew M. Gombos, J., Karpoff, A.-M., McKenzie, J. A., Stephen F. Percival, J., Petersen, N. P., Pisciotto, K. A., Poore, R. Z., Schreiber, E., Tauxe, L., Tucker, P., and Weissert, H. J. (1984). Initial reports of the Deep Sea Drilling Project covering Leg 73 of the cruises of the drilling vessel Glomar Challenger, Santos, Brazil to Cape Town, South Africa. *Texas A & M University*.

Huismans, R. and Beaumont, C. (2011). Depth-dependent extension, two-stage breakup and cratonic underplating at rifted margins. *Nature*, 473(7345):74–78.

Huismans, R. S. and Beaumont, C. (2003). Symmetric and asymmetric lithospheric extension: Relative effects of frictional-plastic and viscous strain softening. *Journal of Geophysical Research: Solid Earth*, 108(B10).

Huismans, R. S. and Beaumont, C. (2014). Rifted continental margins: The case for depth-dependent extension. *Earth and Planetary Science Letters*, 407:148–162.

Humphris, S. E., Thompson, G., Schilling, J.-G., and Kingsley, R. H. (1985). Petrological and geochemical variations along the Mid-Atlantic Ridge between 46°S and 32°S: Influence of the Tristan da Cunha mantle plume. *Geochimica et Cosmochimica Acta*, 49(6):1445–1464.

ION Geophysical (2013a). ArgentineSPAN. http://www.iongeo.com/Data_Library/South_America/Argentina/. [Online; accessed 26-Dec-2016].

ION Geophysical (2013b). NamibiaSPAN. http://www.iongeo.com/Data_Library/Africa/NamibiaSPAN/. [Online; accessed 26-Dec-2016].

ION Geophysical (2013c). PelotasSPAN. http://www.iongeo.com/Data_Library/South_America/Brazil/PelotasSPAN/. [Online; accessed 26-Dec-2016].

ION Geophysical (2013d). UruguaySPAN. http://www.iongeo.com/Data_Library/South_America/Uruguay/. [Online; accessed 26-Dec-2016].

Ito, G., Lin, J., and Gable, C. W. (1996). Dynamics of mantle flow and melting at a ridge-centered hotspot: Iceland and the Mid-Atlantic Ridge. *Earth and Planetary Science Letters*, 144(12):53 – 74.

Ito, G., Shen, Y., Hirth, G., and Wolfe, C. J. (1999). Mantle flow, melting, and dehydration of the Iceland mantle plume. *Earth and Planetary Science Letters*, 165(1):81–96.

Jacques, A. and Green, D. (1980). Anhydrous melting of peridotite at 0–15 kb pressure and the genesis of tholeiitic basalts. *Contributions to Mineralogy and Petrology*, 73(3):287–310.

Jay, A. E. and Widdowson, M. (2008). Stratigraphy, structure and volcanology of the SE Deccan continental flood basalt province: implications for eruptive extent and volumes. *Journal of the Geological Society*, 165(1):177–188.

Jungslager, E. H. (1999). Petroleum habitats of the Atlantic margin of South Africa. *Geological Society, London, Special Publications*, 153(1):153–168.

Karato, S. and Wu, P. (1993). Rheology of the Upper Mantle: A Synthesis. *Science*, 260(5109):771–778.

Keen, C. and Boutilier, R. (2000). Interaction of rifting and hot horizontal plume sheets at volcanic margins. *Journal of Geophysical Research: Solid Earth*, 105(B6):13375–13387.

Kelemen, P. B. and Holbrook, W. S. (1995). Origin of thick, high-velocity igneous crust along the US East Coast Margin. *Journal of Geophysical Research: Solid Earth*, 100(B6):10077–10094.

King, S. D. and Anderson, D. L. (1995). An alternative mechanism of flood basalt formation. *Earth and Planetary Science Letters*, 136(3):269–279.

King, S. D. and Anderson, D. L. (1998). Edge-driven convection. *Earth and Planetary Science Letters*, 160(3):289–296.

King, S. D. and Ritsema, J. (2000). African Hot Spot Volcanism: Small-Scale Convection in the Upper Mantle Beneath Cratons. *Science*, 290(5494):1137–1140.

Kinzler, R. J. and Grove, T. L. (1992). Primary magmas of mid-ocean ridge basalts 1. Experiments and methods. *Journal of Geophysical Research: Solid Earth*, 97(B5):6885–6906.

Klingelhoefer, F., Labails, C., Cosquer, E., Rouzo, S., Geli, L., Aslanian, D., Olivet, J.-L., Sahabi, M., Nouze, H., and Unternehr, P. (2009). Crustal structure of the SW-Moroccan margin from wide-angle and reflection seismic data (the DAKHLA experiment) Part A: Wide-angle seismic models. *Tectonophysics*, 468(1):63–82.

Klitgord, K. D., Hutchinson, D. R., and Schouten, H. (1988). US Atlantic continental margin; structural and tectonic framework. *The Geology of North America*, 2:19–55.

Koopmann, H., Brune, S., Franke, D., and Breuer, S. (2014a). Linking rift propagation barriers to excess magmatism at volcanic rifted margins. *Geology*, 42(12):1071–1074.

Koopmann, H., Franke, D., Schreckenberger, B., Schulz, H., Hartwig, A., Stollhofen, H., and di Primio, R. (2014b). Segmentation and volcano-tectonic characteristics along the SW African continental margin, South Atlantic, as derived from multichannel seismic and potential field data. *Marine and Petroleum Geology*, 50:22–39.

Koptev, A., Calais, E., Burov, E., Leroy, S., and Gerya, T. (2015). Dual continental rift systems generated by plume-lithosphere interaction. *Nature Geoscience*, 8(5):388–392.

Korenaga, J., Kelemen, P. B., and Holbrook, W. S. (2002). Methods for resolving the origin of large igneous provinces from crustal seismology. *Journal of Geophysical Research: Solid Earth*, 107(B9):ECV–1.

Kröner, A. and Stern, R. (2004). Africa: Pan-African orogeny. *Encyclopedia of Geology. Elsevier*, pages 1–12.

Kurz, M. D., Jenkins, W. J., and Hart, S. R. (1982). Helium isotopic systematics of oceanic islands and mantle heterogeneity. *Nature*, 297(5861):43–47.

Langmuir, C. H., Bender, J., Bence, A., Hanson, G., and Taylor, S. (1977). Petrogenesis of basalts from the FAMOUS area: Mid-Atlantic Ridge. *Earth and Planetary Science Letters*, 36(1):133–156.

Langmuir, C. H., Klein, E. M., and Plank, T. (1992). Petrological systematics of Mid-Ocean Ridge Basalts: Constraints on Melt Generation Beneath Ocean Ridges. *Geophysical Monograph - American Geophysical Union*, 71:183–280.

LASE Study Group et al. (1986). Deep structure of the US East Coast passive margin from large aperture seismic experiments (LASE). *Marine and Petroleum Geology*, 3(3):234–242.

Lavier, L. L. and Manatschal, G. (2006). A mechanism to thin the continental lithosphere at magma-poor margins. *Nature*, 440(7082):324–328.

Lawver, L. A. and Müller, R. D. (1994). Iceland hotspot track. *Geology*, 22(4):311–314.

Leach, D. L., Bradley, D., Lewchuk, M. T., Symons, D. T., de Marsily, G., and Brannon, J. (2001). Mississippi Valley-type lead–zinc deposits through geological time: implications from recent age-dating research. *Mineralium Deposita*, 36(8):711–740.

Leyden, R., Ludwig, W. J., and Ewing, M. (1971). Structure of Continental Margin off Punta del Este, Uruguay, and Rio de Janeiro, Brazil. *AAPG Bulletin*, 55(12):2161–2173.

Light, M., Maslanyj, M., and Banks, N. (1992). New geophysical evidence for extensional tectonics on the divergent margin offshore Namibia. *Geological Society, Special Publications*, 68(1):257–270.

Light, M., Maslanyj, M., Greenwood, R., and Banks, N. (1993). Seismic sequence stratigraphy and tectonics offshore Namibia. *Geological Society, London, Special Publications*, 71(1):163–191.

Lizarralde, D., Axen, G. J., Brown, H. E., Fletcher, J. M., González-Fernández, A., Harding, A. J., Holbrook, W. S., Kent, G. M., Paramo, P., Sutherland, F., et al. (2007). Variation in styles of rifting in the Gulf of California. *Nature*, 448(7152):466–469.

Lizarralde, D., Holbrook, W. S., and Oh, J. (1994). Crustal structure across the Brunswick magnetic anomaly, offshore Georgia, from coincident ocean bottom and multi-channel seismic data. *Journal of Geophysical Research: Solid Earth*, 99(B11):21741–21757.

Lowman, J. P. and Jarvis, G. T. (1995). Mantle convection models of continental collision and breakup incorporating finite thickness plates. *Physics of the Earth and Planetary Interiors*, 88(1):53–68.

Lowman, J. P. and Jarvis, G. T. (1996). Continental collisions in wide aspect ratio and high Rayleigh number two-dimensional mantle convection models. *Journal of Geophysical Research: Solid Earth*, 101(B11):25485–25497.

Ludwig, W. J., Nafe, J. E., and Drake, C. L. (1970). Seismic refraction. *The Sea*, 4:53–84.

Mann, P., Gahagan, L., and Gordon, M. B. (2003). Tectonic Setting of the World's Giant Oil and Gas Fields. *AAPG Special Volumes*, 78:15–105.

Manspeizer, W. and Cousminer, H. L. (1988). Late Triassic-Early Jurassic synrift basins of the US Atlantic margin. *The Geology of North America*, 2:197–216.

Marzoli, A., Melluso, L., Morra, V., Renne, P. R., Sgrosso, I., D'Antonio, M., Morais, L. D., Morai, E. A. A., and Ricci, G. (1999). Geochronology and petrology of Cretaceous basaltic magmatism in the Kwanza basin (western Angola), and relationships with the Paraná-Etendeka continental flood basalt province. *Journal of Geodynamics*, 28(4-5):341–356.

Maslanyj, M. P., Light, M. P. R., Greenwood, R. J., and Banks, N. L. (1992). Extension tectonics offshore Namibia and evidence for passive rifting in the South Atlantic. *Marine and Petroleum Geology*, 9(6):590–601.

Maus, S., Barckhausen, U., Berkenbosch, H., Bournas, N., Brozena, J., Childers, V., Dostaler, F., Fairhead, J., Finn, C., Von Frese, R., et al. (2009). EMAG2: A 2–arc min resolution Earth Magnetic Anomaly Grid compiled from satellite, airborne, and marine magnetic measurements. *Geochemistry, Geophysics, Geosystems*, 10(8). Q08005.

Maxwell, A. E., Herzon, R. P. V., Andrews, J. E., Boyce, R. E., Milow, E. D., Hsu, K. J., Percival, S. F., and Saito, T. (1970). Initial Reports of the Deep Sea Drilling Project; covering Leg 3 of the cruises of the drilling vessel Glomar Challenger, Dakar, Senegal to Rio de Janeiro, Brazil. *Texas A & M University*.

McKenzie, D. and Bickle, M. (1988). The Volume and Composition of Melt Generated by Extension of the Lithosphere. *Journal of Petrology*, 29(3):625–679.

McKenzie, D., Daly, M. C., and Priestley, K. (2015). The lithospheric structure of Pangea. *Geology*, 43(9):783–786.

McKenzie, D., Jackson, J., and Priestley, K. (2005). Thermal structure of oceanic and continental lithosphere. *Earth and Planetary Science Letters*, 233(3):337–349.

McKenzie, D. P. (1967). Some remarks on heat flow and gravity anomalies. *Journal of Geophysical Research*, 72(24):6261–6273.

Michael, P. (1995). Regionally distinctive sources of depleted MORB: evidence from trace elements and H_2O. *Earth and Planetary Science Letters*, 131(3):301–320.

Michael, P. J., Forsyth, D. W., Blackman, D. K., Fox, P. J., Hanan, B. B., Harding, A. J., Macdonald, K. C., Neumann, G. A., Orcutt, J. A., Tolstoy, M., and Weiland, C. M. (1994). Mantle control of a dynamically evolving spreading center: Mid-Atlantic Ridge 31–345°S. *Earth and Planetary Science Letters*, 121(3):451–468.

Mihut, D. and Müller, R. D. (1998). Volcanic margin formation and Mesozoic rift propagators in the Cuvier Abyssal Plain off Western Australia. *Journal of Geophysical Research: Solid Earth*, 103(B11):27135–27149.

Miller, R. M. (1983). The Pan-African Damara Orogen of South West Africa/Namibia. *Geological Society of South Africa Special Publication*, 11:431–515.

Minshull, T. A., Lane, C. I., Collier, J. S., and Whitmarsh, R. B. (2008). The relationship between rifting and magmatism in the northeastern Arabian Sea. *Nature Geoscience*, 1(7):463–467.

Mjelde, R., Breivik, A., Raum, T., Mittelstaedt, E., Ito, G., and Faleide, J. (2008). Magmatic and tectonic evolution of the North Atlantic. *Journal of the Geological Society*, 165(1):31–42.

Mjelde, R., Sellevoll, M., Shimamura, H., Iwasaki, T., and Kanazawa, T. (1992). A crustal study off Lofoten, N. Norway, by use of 3-component Ocean Bottom Seismographs. *Tectonophysics*, 212(3-4):269–288.

Mohriak, W., Hobbs, R., and Dewey, J. (1990). Basin-forming processes and the deep structure of the Campos Basin, offshore Brazil. *Marine and Petroleum Geology*, 7(2):94–122.

Mohriak, W. U., Bassetto, M., and Vieira, I. S. (1998). Crustal architecture and tectonic evolution of the Sergipe-Alagoas and Jacuípe basins, offshore northeastern Brazil. *Tectonophysics*, 288(1-4):199–220.

Mohriak, W. U., Nobrega, M., Odegard, M. E., Gomes, B. S., and Dickson, W. G. (2010). Geological and geophysical interpretation of the Rio Grande Rise, south-eastern Brazilian margin: extensional tectonics and rifting of continental and oceanic crusts. *Petroleum Geoscience*, 16(3):231–245.

Mohriak, W. U., Rabelo, J. L., De Matos, R. D., and De Barros, M. C. (1995). Deep seismic reflection profiling of sedimentary basins offshore Brazil: Geological objectives and preliminary results in the Sergipe Basin. *Journal of Geodynamics*, 20(4):515–539.

Montelli, R., Nolet, G., Dahlen, F., Masters, G., Engdahl, E. R., and Hung, S.-H. (2004). Finite-frequency tomography reveals a variety of plumes in the mantle. *Science*, 303(5656):338–343.

Montesi, L. G., Behn, M. D., Hebert, L. B., Lin, J., and Barry, J. L. (2011). Controls on melt migration and extraction at the ultraslow Southwest Indian Ridge 10°–16°E. *Journal of Geophysical Research: Solid Earth*, 116(B10).

Moore, T. C., Rabinowitz, P. D., Boersma, A., Borella, P. E., Chave, A. D., Duée, G., Ftterer, D. K., Jiang, M.-J., Kleinert, K., Lever, A., Manivit, H., O'Connell, S., Richardson, S. H., and Shackleton, N. J. (1984). Initial reports of the Deep Sea Drilling Project covering Leg 74 of the cruises of the drilling vessel Glomar Challenger; Cape Town, South Africa, to Walvis Bay, South Africa. *Texas A & M University*.

Moresi, L., Zhong, S., and Gurnis, M. (1996). The accuracy of finite element solutions of Stokes's flow with strongly varying viscosity. *Physics of the Earth and Planetary Interiors*, 97(1):83–94.

Morgan, J. P. (1987). Melt migration beneath mid-ocean spreading centers. *Geophysical Research Letters*, 14(12):1238–1241.

Morgan, W. J. (1971). Convection Plumes in the Lower Mantle. *Nature*, 230:42–43.

Morgan, W. J. (1983). Hotspot tracks and the early rifting of the Atlantic. *Tectonophysics*, 94(1-4):123–139.

Moulin, M. (2003). *Etude géologique et géophysique des marges continentales passives: exemple du Zaïre et de l'Angola*. PhD thesis, Université de Bretagne Occidentale.

Moulin, M., Aslanian, D., Olivet, J. L., Contrucci, I., Matias, L., Geli, L., Klingelhoefer, F., Nouze, H., Rehault, J. P., and Unternehr, P. (2005). Geological constraints on the evolution of the Angolan margin based on reflection and refraction seismic data (ZaïAngo project). *Geophysical Journal International*, 162(3):793–810.

Moulin, M., Aslanian, D., and Unternehr, P. (2010). A new starting point for the South and Equatorial Atlantic Ocean. *Earth-Science Reviews*, 98(1):1–37.

Müller, R. D., Sdrolias, M., Gaina, C., and Roest, W. R. (2008). Age, spreading rates, and spreading asymmetry of the world's ocean crust. *Geochemistry Geophysics Geosystems*, 9(4). Q04006.

Müntener, O., Manatschal, G., Desmurs, L., and Pettke, T. (1993). Plagioclase Peridotites in Ocean–Continent Transitions: Refertilized Mantle Domains Generated by Melt Stagnation in the Shallow Mantle Lithosphere. *Journal of Petrology*, 51(1–2):255–294.

Mutter, J. C. (1985). Seaward dipping reflectors and the continent-ocean boundary at passive continental margins. *Tectonophysics*, 114(1):117–131.

Mutter, J. C., Buck, W. R., and Zehnder, C. M. (1988). Convective partial melting: 1. A model for the formation of thick basaltic sequences during the initiation of spreading. *Journal of Geophysical Research: Solid Earth*, 93(B2):1031–1048.

Mutter, J. C. and Larson, R. L. (1989). Extension of the Exmouth Plateau, offshore northwestern Australia: Deep seismic reflection/refraction evidence for simple and pure shear mechanisms. *Geology*, 17(1):15–18.

Mutter, J. C., Talwani, M., and Stoffa, P. L. (1982). Origin of seaward-dipping reflectors in oceanic crust off the Norwegian margin by "subaerial sea-floor spreading". *Geology*, 10(7):353–357.

Nielsen, T. K. and Hopper, J. R. (2004). From rift to drift: Mantle melting during continental breakup. *Geochemistry, Geophysics, Geosystems*, 5(7). Q07003.

Nielsen, T. K., Larsen, H. C., and Hopper, J. R. (2002). Contrasting rifted margin styles south of Greenland: implications for mantle plume dynamics. *Earth and Planetary Science Letters*, 200(3):271–286.

Niu, Y. L. (1997). Mantle Melting and Melt Extraction Processes beneath Ocean Ridges: Evidence from Abyssal Peridotites. *Journal of Petrology*, 38(8):1047–1074.

Njini, F. (2014). Namibia Expects Explorers to Drill Up to 5 Oil Wells in 2016. http://www.bloomberg.com/news/articles/2014-11-10/namibia-expects-explorers-to-drill-up-to-five-oil-wells-in-2016. [Online; accessed 26-Dec-2016].

O'Connor, J. M. and Duncan, R. A. (1990). Evolution of the Walvis Ridge-Rio Grande Rise Hot Spot System: Implications for African and South American Plate motions over plumes. *Journal of Geophysical Research: Solid Earth*, 95(B11):17475–17502.

O'Connor, J. M. and Jokat, W. (2015). Tracking the Tristan-Gough mantle plume using discrete chains of intraplate volcanic centers buried in the Walvis Ridge. *Geology*, 43(8):715–718.

Olafsson, I., Sundvor, E., Eldholm, O., and Grue, K. (1992). Møre Margin: Crustal structure from analysis of Expanded Spread Profiles. *Marine Geophysical Researches*, 14(2):137–162.

Parkin, C. and White, R. (2008). Influence of the Iceland mantle plume on oceanic crust generation in the North Atlantic. *Geophysical Journal International*, 173(1):168–188.

Peate, D. W. (1997). The Paraná-Etendeka Province. *Large igneous provinces: Continental, oceanic, and planetary flood volcanism*, pages 217–245.

Pérez-Díaz, L. and Eagles, G. (2014). Constraining South Atlantic growth with seafloor spreading data. *Tectonics*, 33(9):1848–1873.

Pérez-Gussinyé, M., Morgan, J. P., Reston, T. J., and Ranero, C. R. (2006). The rift to drift transition at non-volcanic margins: Insights from numerical modelling. *Earth and Planetary Science Letters*, 244(1):458–473.

Péron-Pinvidic, G., Manatschal, G., Masini, E., Sutra, E., Flament, J. M., Haupert, I., and Unternehr, P. (2015). Unravelling the along-strike variability of the Angola–Gabon rifted margin: a mapping approach. *Geological Society, London, Special Publications*, 438:SP438–1.

Petersen, K., Armitage, J., Nielsen, S., and Thybo, H. (2015). Mantle temperature as a control on the time scale of thermal evolution of extensional basins. *Earth and Planetary Science Letters*, 409:61–70.

Peterson, R. G. (1992). The boundary currents in the western Argentine Basin. *Deep Sea Research Part A. Oceanographic Research Papers*, 39(3):623–644.

Phipps Morgan, J. (2001). Thermodynamics of pressure release melting of a veined plum pudding mantle. *Geochemistry, Geophysics, Geosystems*, 2(4).

Phipps Morgan, J., de Monserrat, A., Hall, R., Taramon, J. M., and Perez-Gussinye, M. (2015). The Effects of Far-Field Boundary Conditions on 2D Numerical Solutions for Continental Rifting: Tests and Recipes for Improved Treatment of Asthenosphere Flow and Melting. In *2015 AGU Fall Meeting*.

Planke, S. (1994). Geophysical response of flood basalts from analysis of wire line logs: Ocean Drilling Program Site 642, Vøring volcanic margin. *Journal of Geophysical Research: Solid Earth*, 99(B5):9279–9296.

Planke, S., Rasmussen, T., Rey, S., and Myklebust, R. (2005). Seismic characteristics and distribution of volcanic intrusions and hydrothermal vent complexes in the Vøring and Møre basins. In *Geological Society, London, Petroleum Geology Conference series*, volume 6, pages 833–844. Geological Society of London.

Planke, S., Symonds, P. A., Alvestad, E., and Skogseid, J. (2000). Seismic volcanostratigraphy of large-volume basaltic extrusive complexes on rifted margins. *Journal of Geophysical Research: Solid Earth*, 105(B8):19335–19351.

Popoff, M. (1988). Du Gondwana à l'Atlantique sud: les connexions du fossé de la Bénoué avec les bassins du Nord-Est brésilien jusqu'à l'ouverture du golfe de Guinée au Crétacé inférieur. *Journal of African Earth Sciences (and the Middle East)*, 7(2):409–431.

Popov, A. and Sobolev, S. (2008). SLIM3D: A tool for three-dimensional thermomechanical modeling of lithospheric deformation with elasto-visco-plastic rheology. *Physics of the Earth and Planetary Interiors*, 171(1):55–75.

Porada, H. (1979). The Damara-Ribeira Orogen of the Pan-African Brasiliano cycle in Namibia (Southwest Africa) and Brazil as interpreted in terms of continental collision. *Tectonophysics*, 57(2):237–265.

Priestley, K. and McKenzie, D. (2006). The thermal structure of the lithosphere from shear wave velocities. *Earth and Planetary Science Letters*, 244(1):285–301.

Putirka, K. D. (2005). Mantle potential temperatures at Hawaii, Iceland, and the mid-ocean ridge system, as inferred from olivine phenocrysts: Evidence for thermally driven mantle plumes. *Geochemistry Geophysics Geosystems*, 6(5). Q05L08.

Quirk, D. G., Hertle, M., Jeppesen, J. W., Raven, M., Mohriak, W. U., Kann, D. J., Nørgaard, M., Howe, M. J., Hsu, D., Coffey, B., et al. (2013). Rifting, subsidence and continental break-up above a mantle plume in the central South Atlantic. *Geological Society, London, Special Publications*, 369(1):185–214.

Rabinowitz, P. D. and LaBrecque, J. (1979). The Mesozoic South Atlantic Ocean and evolution of its continental margins. *Journal of Geophysical Research: Solid Earth*, 84(B11):5973–6002.

Ranero, C. R. and Pérez-Gussinyé, M. (2010). Sequential faulting explains the asymmetry and extension discrepancy of conjugate margins. *Nature*, 468(7321):294–299.

Ratcliffe, V. (2014). Namibia: Africa's next big oil frontier? https://www.ft.com/content/be5693d9-8b33-33a1-870e-166596a79527. [Online; accessed 26-Dec-2016].

Reichow, M. K., Pringle, M., Al'Mukhamedov, A., Allen, M., Andreichev, V., Buslov, M., Davies, C., Fedoseev, G., Fitton, J., Inger, S., Medvedev, A., Mitchell, C., Puchkov, V., Safonova, IY, S. R., and Saunders, A. (2009). The timing and extent of the eruption of the Siberian Traps large igneous province: Implications for the end-Permian environmental crisis. *Earth and Planetary Science Letters*, 277(1):9–20.

Renne, P. R., Ernesto, M., Pacca, I. G., Coe, R. S., Glen, J., Prévot, M., Perrin, M., et al. (1992). The Age of Paraná Flood Volcanism, Rifting of Gondwanaland, and the Jurassic-Cretaceous Boundary. *Science*, 258(5084):975–979.

Reston, T. J. (2007). The formation of non-volcanic rifted margins by the progressive extension of the lithosphere: the example of the West Iberian margin. *Geological Society, Special Publications*, 282(1):77–110.

Reston, T. J. (2010). The opening of the central segment of the South Atlantic: symmetry and the extension discrepancy. *Petroleum Geoscience*, 16(3):199–206.

Rey, S. S., Planke, S., Symonds, P. A., and Faleide, J. I. (2008). Seismic volcanostratigraphy of the Gascoyne margin, Western Australia. *Journal of Volcanology and Geothermal Research*, 172(1):112–131.

Roberts, D., Backman, J., Morton, A., Murray, J., and Keene, J. (1984). Evolution of Volcanic Rifted Margins - Synthesis of Leg 81 Results on the West margin of Rockall Plateau. *Initial Reports of the Deep Sea Drilling Project*, pages 883–911.

Robinson, J., Wood, B., and Blundy, J. (1998). The beginning of melting of fertile and depleted peridotite at 1.5 GPa. *Earth and Planetary Science Letters*, 155(1):97–111.

Rohde, J. K., van den Bogaard, P., Hoernle, K., Hauff, F., and Werner, R. (2013). Evidence for an age progression along the Tristan-Gough volcanic track from new ^{40}Ar-^{39}Ar ages on phenocryst phases. *Tectonophysics*, 604:60–71.

Rosendahl, B. R. (1987). Architecture of continental rifts with special reference to East Africa. *Annual Review of Earth and Planetary Sciences*, 15:445.

Rupke, N. (1970). Continental drift before 1900. *Nature*, 227:349–350.

Ryberg, T., Braeuer, B., and Weber, M. (2016). Upper mantle structure at Walvis Ridge from P_n tomography. *Tectonophysics*. http://dx.doi.org/10.1016/j.tecto.2016.08.009.

Sallarès, V., Charvis, P., Flueh, E. R., Bialas, J., et al. (2005). Seismic structure of the Carnegie ridge and the nature of the Galápagos hotspot. *Geophysical Journal International*, 161(3):763–788.

Sandwell, D., Garcia, E., Soofi, K., Wessel, P., Chandler, M., and Smith, W. H. (2013). Toward 1-mGal accuracy in global marine gravity from CryoSat-2, Envisat, and Jason-1. *The Leading Edge*, 32(8):892–899.

Saunders, A. D., Storey, M., Kent, R., and Norry, M. (1992). Consequences of plume-lithosphere interactions. *Geological Society, Special Publications*, 68(1):41–60.

Schinkel, J. (2006). *Tiefenstruktur der Kontinent-Ozean-Grenze vor dem Orange Fluss, Namibia*, Masters Thesis, Friedrich-Schiller-Universitaet Jena.

Schnabel, M., Franke, D., Engels, M., Hinz, K., Neben, S., Damm, V., Grassmann, S., Pelliza, H., and Dos Santos, P. R. (2008). The structure of the lower crust at the Argentine continental margin, South Atlantic at 44°S. *Tectonophysics*, 454(1-4):14–22.

Schulze, A., Bauer, K., Ryberg, T., Stankiewicz, J., Hirsch, K., Weber, M., Lindeque, A., Gohl, K., Schinkel, J., and Neben, S. (2007). Seismic Investigations in Namibia and RSA (1995-2007). In *10th SAGA Biennial Technical Meeting and Exhibition*.

Scott, D. R. (1992). *Small-Scale Convection and Mantle Melting Beneath Mid-Ocean Ridges*. American Geophysical Union.

Seton, M., Müller, R., Zahirovic, S., Gaina, C., Torsvik, T., Shephard, G., Talsma, A., Gurnis, M., Turner, M., Maus, S., and Chandler, M. (2012). Global continental and ocean basin reconstructions since 200Ma. *Earth-Science Reviews*, 113(3):212–270.

Simon, K., Huismans, R. S., and Beaumont, C. (2009). Dynamical modelling of lithospheric extension and small-scale convection: implications for magmatism during the formation of volcanic rifted margins. *Geophysical Journal International*, 176(1):327–350.

Sleep, N. H. (1996). Lateral flow of hot plume material ponded at sublithospheric depths. *Journal of Geological Research: Solid Earth*, 101(B12):28065–28083.

Sleep, N. H. (2006). Mantle plumes from top to bottom. *Earth-Science Reviews*, 77(4):231–271.

Sleep, N. H. (2007). Edge-modulated stagnant-lid convection and volcanic passive margins. *Geochemistry, Geophysics, Geosystems*, 8(12).

Smith, L., White, R., Kusznir, N., and iSIMM Team (2005). Structure of the Hatton Basin and adjacent continental margin. In *Geological Society, London, Petroleum Geology Conference series*, volume 6, pages 947–956. Geological Society of London.

Sobolev, S. V. and Babeyko, A. Y. (1994). Modeling of mineralogical composition, density and elastic wave velocities in anhydrous magmatic rocks. *Surveys in Geophysics*, 15(5):515–544.

Soto, M., Morales, E., Veroslavsky, G., de Santa Ana, H., Ucha, N., and Rodríguez, P. (2011). The continental margin of Uruguay: Crustal architecture and segmentation. *Marine and Petroleum Geology*, 28(9):1676–1689.

Spiegelman, M. and McKenzie, D. (1987). Simple 2-D models for melt extraction at mid-ocean ridges and island arcs. *Earth and Planetary Science Letters*, 83(1):137–152.

Steinberger, B. (2000). Plumes in a convecting mantle: Models and observations for individual hotspots. *Journal of Geophysical Research: Solid Earth*, 105(B5):11127–11152.

Stewart, J., Watts, A. B., and Bagguley, J. G. (2000). Three-dimensional subsidence analysis and gravity modelling of the continental margin offshore Namibia. *Geophysical Journal International*, 141(3):724–746.

Stica, J. M., Zalán, P. V., and Ferrari, A. L. (2014). The evolution of rifting on the volcanic margin of the Pelotas Basin and the contextualization of the Paraná–Etendeka LIP in the separation of Gondwana in the South Atlantic. *Marine and Petroleum Geology*, 50:1–21.

Stollhofen, H., Gerschütz, S., Stanistreet, I. G., and Lorenz, V. (1998). Tectonic and volcanic controls on Early Jurassic rift-valley lake deposition during emplacement of Karoo flood basalts, southern Namibia. *Palaeogeography, Palaeoclimatology, Palaeoecology*, 140(1):185–215.

Stone, P., Richards, P., Kimbell, G., Esser, R., and Reeves, D. (2008). Cretaceous dykes discovered in the Falkland Islands: implications for regional tectonics in the South Atlantic. *Journal of the Geological Society*, 165(1):1–4.

Storey, B. C. (1995). The role of mantle plumes in continental breakup: case histories from Gondwanaland. *Nature*, 377(6547):301–308.

Talwani, M., Ewing, J., Sheridan, R. E., Holbrook, W. S., and Glover III, L. (1995). The EDGE Experiment and the US East Coast Magnetic Anomaly. In *Rifted Ocean-Continent Boundaries*, pages 155–181. Springer.

Taposeea, C., Armitage, J., and Collier, J. (2016). Asthenosphere and lithosphere structure controls on early onset oceanic crust production in the southern South Atlantic. *Tectonophysics*. http://dx.doi.org/10.1016/j.tecto.2016.06.026.

Tegner, C., Duncan, R., Bernstein, S., Brooks, C., Bird, D., and Storey, M. (1998). $^{40}Ar/^{39}Ar$ geochronology of Tertiary mafic intrusions along the East Greenland rifted margin: Relation to flood basalts and the Iceland hotspot track. *Earth and Planetary Science Letters*, 156(1):75–88.

Than, K. (2013). Lost Lands Found by Scientists. http://news.nationalgeographic.com/news/2013/13/130509-brazilian-atlantis-lost-continents-geography-world/. [Online; accessed 26-Dec-2016].

Torsvik, T. H., Rousse, S., Labails, C., and Smethurst, M. A. (2009). A new scheme for the opening of the South Atlantic Ocean and the dissection of an Aptian salt basin. *Geophysical Journal International*, 177(3):1315–1333.

Trumbull, R., Sobolev, S., and Bauer, K. (2002). Petrophysical modeling of high seismic velocity crust at the Namibian volcanic margin. *Volcanic Rifted Margins - Geologic Society of America Special Paper*, 362:221.

Trumbull, R. B. (2014). Causes and consequences of continental breakup in the South Atlantic: lessons learned from the SAMPLE program. In *EGU General Assembly Conference Abstracts*, volume 16, page 1430.

Trumbull, R. B., Franke, D., Bauer, K., and Sobolev, S. V. (2015). Petrophysical models of high velocity lower crust on the South Atlantic rifted margins: whence the asymmetry? In *EGU General Assembly Conference Abstracts*, volume 17, page 10976.

Trumbull, R. B., Reid, D. L., De Beer, C., Van Acken, D., and Romer, R. L. (2007). Magmatism and continental breakup at the west margin of southern Africa: A geochemical comparison of dolerite dikes from northwestern Namibia and the Western Cape. *South African Journal of Geology*, 110(2-3):477–502.

Turcotte, D. and Oxburgh, E. (1967). Finite amplitude convective cells and continental drift. *Journal of Fluid Mechanics*, 28(01):29–42.

Turcotte, D. L. and Schubert, G. (2002). *Geodynamics*. Cambridge University Press.

Turner, J. P., Rosendahl, B. R., and Wilson, P. G. (2003). Structure and evolution of an obliquely sheared continental margin: Rio Muni, West Africa. *Tectonophysics*, 374(1-2):41–55.

Turner, S., Regelous, M., Kelley, S., Hawkesworth, C., and Mantovani, M. (1994). Magmatism and continental break-up in the South Atlantic: high precision ^{40}Ar-^{39}Ar geochronology. *Earth and Planetary Science Letters*, 121(3):333–348.

Unternehr, P., Péron-Pinvidic, G., Manatschal, G., and Sutra, E. (2010). Hyper-extended crust in the South Atlantic: in search of a model. *Petroleum Geoscience*, 16(3):207–215.

Urien, C. and Zambrano, J. (1973). The Geology of the Basins of the Argentine Continental Margin and Malvinas Plateau. In *The South Atlantic*, pages 135–169. Springer.

Vogt, U., Makris, J., O'Reilly, B. M., Hauser, F., Readman, P. W., Jacob, A., and Shannon, P. M. (1998). The Hatton Basin and continental margin: Crustal structure from wide-angle seismic and gravity data. *Journal of Geophysical Research: Solid Earth*, 103(B6):12545–12566.

Voss, M. and Jokat, W. (2007). Continent-ocean transition and voluminous magmatic underplating derived from *P*-wave velocity modelling of the East Greenland continental margin. *Geophysical Journal International*, 170(2):580–604.

Watson, S. and McKenzie, D. (1991). Melt Generation by Plumes: A Study of Hawaiian Volcanism. *Journal of Petrology*, 32(3):501–537.

Watts, A. and Fairhead, J. (1999). A process-oriented approach to modeling the gravity signature of continental margins. *The Leading Edge*, 18(2):258–263.

White, R. (1987). When Continents Rift. *Nature*, 327:191.

White, R. (1992). Magmatism during and after continental break-up. *Geological Society, Special Publications*, 68(1):1–16.

White, R. (1997). Rift–plume interaction in the North Atlantic. *Philosophical Transactions of the Royal Society of London A: Mathematical, Physical and Engineering Sciences*, 355(1723):319–339.

White, R. and McKenzie, D. (1989). Magmatism at Rift Zones - the Generation of Volcanic Continental Margins and Flood Basalts. *Journal of Geophysical Research: Solid Earth*, 94(B6):7685–7729.

White, R. and McKenzie, D. (1995). Mantle plumes and flood basalts. *Journal of Geophysical Research: Solid Earth*, 100(B9):17543–17585.

White, R., McKenzie, D., and O'Nions, R. (1992). Oceanic crustal thickness from seismic measurements and rare earth element inversions. *Journal of Geophysical Research: Solid Earth*, 97(B13):19683–19715.

White, R., Spence, G., Fowler, S. R., McKenzie, D., and Westbrook, G. (1987). Magmatism at rifted continental margins. *Nature*, 330:439–444.

Whitmarsh, R., Manatschal, G., and Minshull, T. (2001). Evolution of magma-poor continental margins from rifting to seafloor spreading. *Nature*, 413(6852):150–154.

Whitmarsh, R. and Miles, P. (1987). Seismic structure of a seaward-dipping reflector sequence southwest of Rockall Plateau. *Geophysical Journal International*, 90(3):731–739.

Whitmarsh, R., White, R., Horsefield, S., Sibuet, J., Recq, M., and Louvel, V. (1996). The ocean-continent boundary off the western continental margin of Iberia: Crustal structure west of Galicia Bank. *Journal of Geophysical Research: Solid Earth*, 101(B12):28291–28314.

Wilson, J. T. (1963). A possible origin of the Hawaiian Islands. *Canadian Journal of Physics*, 41(6):863–870.

Wilson, P. G., Turner, J. P., and Westbrook, G. K. (2003). Structural architecture of the ocean-continent boundary at an oblique transform margin through deep-imaging seismic interpretation and gravity modelling: Equatorial Guinea, West Africa. *Tectonophysics*, 374(1-2):19–40.

Winterbourne, J., White, N., and Crosby, A. (2014). Accurate measurements of residual topography from the oceanic realm. *Tectonics*, 33(6):982–1015.

Zambrano, J. and Urien, C. (1970). Geological outline of the basins in Southern Argentina and their continuation off the Atlantic shore. *Journal of Geophysical Research*, 75(8):1363–1396.

Zhou, D., Ru, K., and Chen, H.-z. (1995). Kinematics of Cenozoic extension on the South China Sea continental margin and its implications for the tectonic evolution of the region. *Tectonophysics*, 251(1):161–177.

Zhou, D. and Yao, B. (2009). Tectonics and sedimentary basins of the South China Sea: Challenges and progresses. *Journal of Earth Science*, 20:1–12.

Appendix A

Additional wide-angle seismic data information

In this section additional information on the wide-angle data set can be found. The details of the seismic surveys (Table A.1) are important to understand the data quality of the wide-angle profile. There is additional information on the OBH locations for Profiles AF1–AF4 and SA1–SA3 (Section A.2), used to consolidate the exact locations of the profiles.

A.1 Wide-Angle Seismic Surveys

Table A.1: Details of the wide-angle seismic surveys (locations in Fig. 3.1 & 3.17).

Name	Reference	Lines Used	Country	Year	Lat.	Agency	Type of Data	Streamer
AF0	Fromm et al. (2015)	P100	Namibia	2011	19°S	AWI, GFZ	MCS/OBS	Not specified
AF1	Bauer et al. (2000)	Transect 1	Namibia	1995	23°S	BGR, AWI, GFZ	MCS/OBS	3000m, 240 trace
AF2	Bauer et al. (2000)	Transect 2	Namibia	1995	23°S	BGR, AWI, GFZ	MCS/OBS	3000m, 240 trace
AF3	Schinkel (2006)	Orange Line	S. Africa	1995	29°S	BGR, AWI, GFZ	MCS/OBS	3000m, 240 trace
AF4	Hirsch et al. (2009)	Springbok Line	S. Africa	2003	31°S	GFZ, BGR, RSA	MCS/OBS	Not specified
SA1	Becker et al. (2014)	BGR04-01/Line 1	Uruguay	2004	35°S	BGR	MCS/OBS	8000m
SA2	Schnabel et al. (2008)	BGR98-REFR2	Argentina	1998	44°S	BGR	MCS/OBS	8000m
SA3	Becker et al. (2014)	BGR04-02/Line 3	Argentina	2004	47°S	BGR	MCS/OBS	8000m

A.2 Wide-Angle Data Location

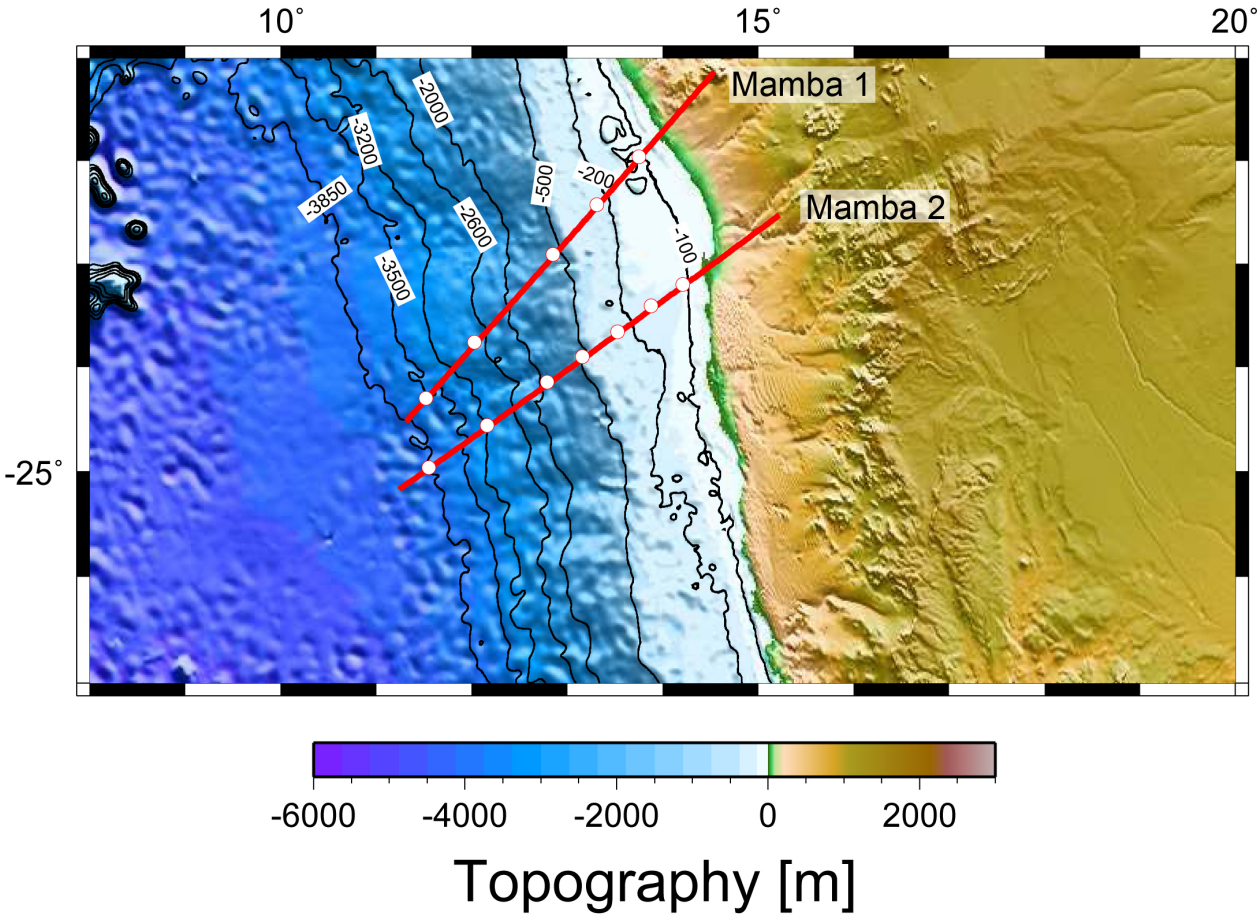


Figure A.1: Profile AF1 & AF2 trackline and OBH locations, with bathymetry. Seismic tracklines obtained from author, OBH (white circles) obtained from extrapolating latitude and longitude values along transect and digitized locations from section. OBH Depths summarized in Table A.2.

Table A.2: Profile AF1 & AF2 OBH coordinates (locations on map in Fig. A.1, locations on profiles in Fig. 3.4 & 3.5).

Profile AF1				Profile AF2			
OBH location (km)	Depth (m)	Longitude	Latitude	OBH location (km)	Depth (m)	Longitude	Latitude
-367	-3500	11.52	-24.30	-361	-3850	11.55	-24.96
-288	-2600	12.03	-23.76	-284	-3200	12.16	-24.56
-162	-500	12.85	-22.91	-205	-2000	12.79	-24.14
-91	-200	13.31	-22.43	-159	-500	13.16	-23.90
-22	-100	13.75	-21.96	-113	-250	13.88	-23.66
				-68	-150	14.21	-23.41
				-27	-100	14.21	-23.20

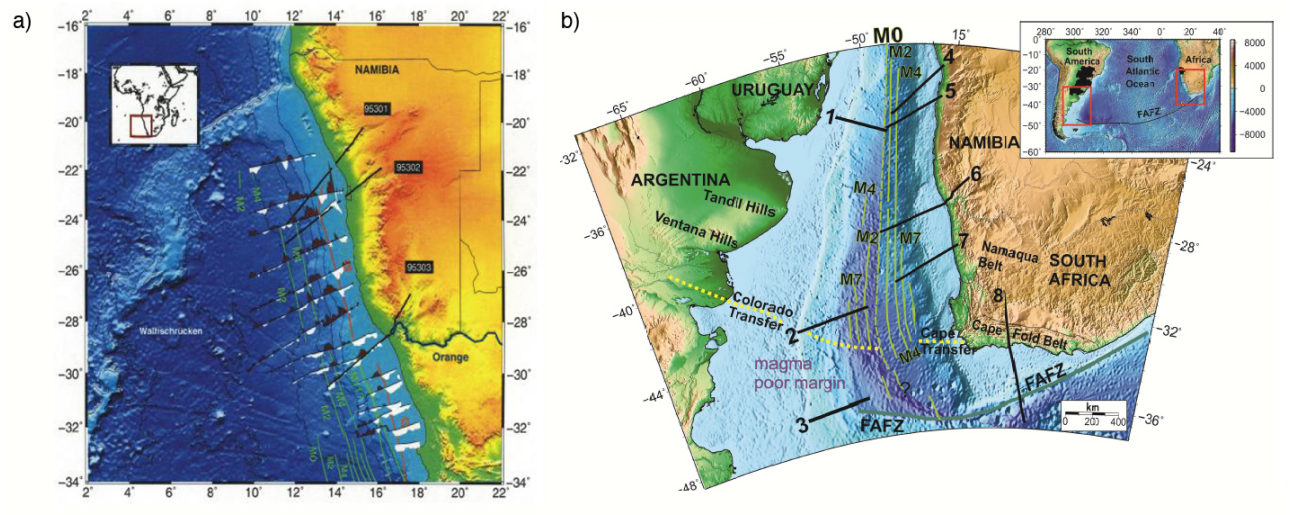


Figure A.2: Profile AF3 location from Schulze et al. (2007) and Becker et al. (2014). Part (a) from Schulze et al. (2007) where AF3 is Line 95303. Part (b) from Becker et al. (2014) where AF3 is line 6.

Table A.3: Profile AF3 OBH coordinates (locations on map in Fig. A.2, , locations on profile in Fig. 3.11).

Profile AF3		
OBH (km)	Longitude	Latitude
84	14.33	-29.80
122	14.64	-29.58
160	14.95	-29.36
197	15.24	-29.12
238	15.55	-28.86
271	15.81	-28.66

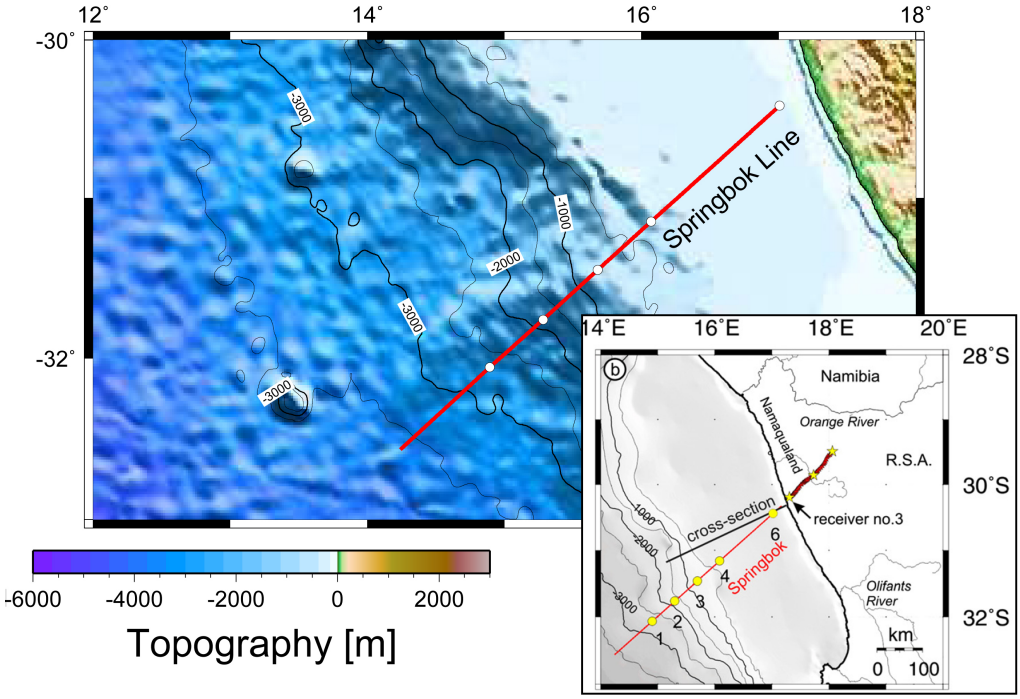


Figure A.3: Profile AF4 trackline and OBH locations, with bathymetry. Seismic trackline digitized from inset map, with OBH locations matched with respect to depth (inset, taken from Hirsch et al. (2009)). OBH locations summarised in Table A.4.

Table A.4: Profile AF4 OBH coordinates (locations on map in Fig. A.3, location on profile in Fig. 3.12).

Profile AF4			
OBH location (km)	Depth (m)	Longitude	Latitude
84	-2700	14.89	-32.06
136	-1800	15.28	-31.76
186	-700	15.68	-31.45
235	-350	16.07	-31.15
356	-150	17.01	-30.42

Table A.5: Profiles SA1 and SA3 OBH coordinates - provided by Becker et al. (2014) (locations on profiles in Fig. 3.18 & 3.19).

Profile SA1			Profile SA3		
OBH	Latitude	Longitude	OBH	Latitude	Longitude
1	-35.9158	-50.6678	1	-47.1665	-57.4758
2	-35.7874	-50.8932	2	-47.1665	-57.8055
3	-35.658	-51.1195	3	-47.1664	-58.1367
4	-35.5285	-51.3461	4	-47.1669	-58.4657
5	-35.3983	-51.5717	5	-47.1662	-58.7943
6	-35.269	-51.7966	6	-47.1666	-59.1261
7	-35.1396	-52.021	7	-47.1666	-59.4559
			8	-47.1663	-59.7859

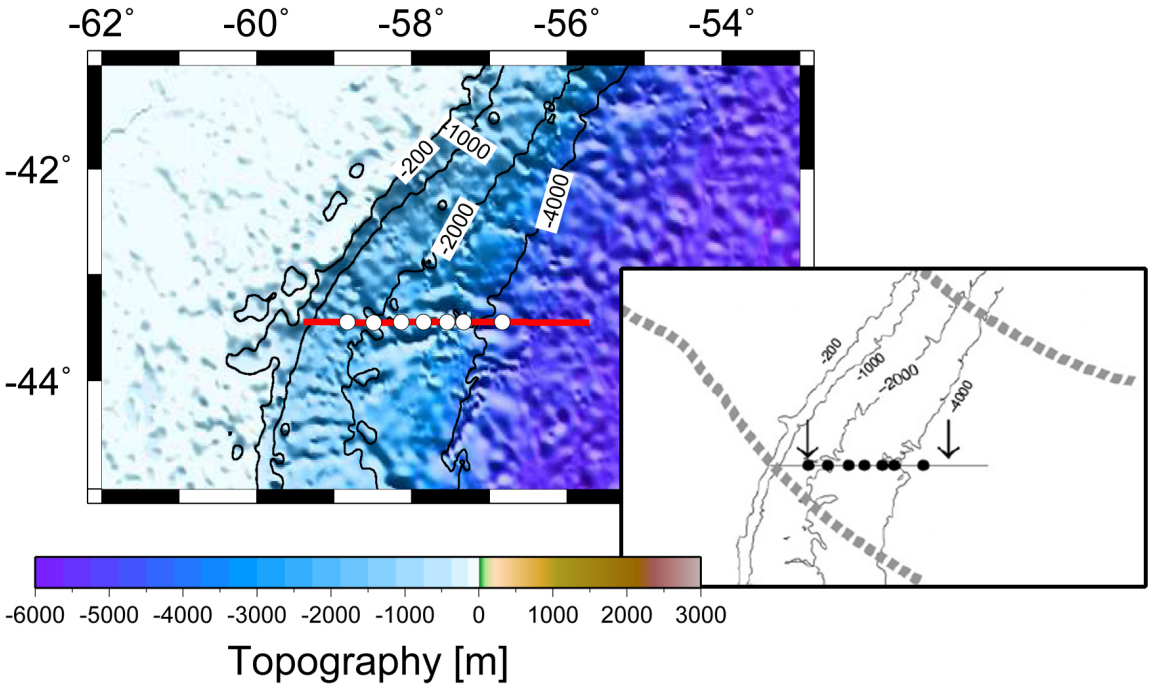


Figure A.4: Profile SA2 trackline and OBH locations, with bathymetry. Seismic tracklines digitized in both GPlates and Didger for correlation, location taken from Schnabel et al. (2008). OBH locations extracted from digitized seismic sections, locations summarised in Table A.6.

Table A.6: Profile SA2 OBH coordinates (locations on map in Fig. A.4, locations on profile in Fig. 3.26).

Profile SA2			
OBH	Depth (m)	Latitude	Longitude
1	-1770	-43.4558	-58.8367
2	-1950	-43.4594	-58.4925
3	-2160	-43.4565	-58.1395
4	-2295	-43.4568	-57.8527
5	-3055	-43.4539	-57.5438
6	-3990	-43.4508	-57.3364
7	-4390	-43.4545	-56.8334

Appendix B

Geochemistry Data

Geochemistry data (Fig. B.1) is important to have for several reasons. The major element oxide compositions from DSDP expeditions and Mid-Atlantic Ridge dredges are used in aiding the choice of composition parameterisation (Section 6.3.1). Additionally, the ages of syn-rift sediments can consolidate the direction of opening for break-up in the South Atlantic.

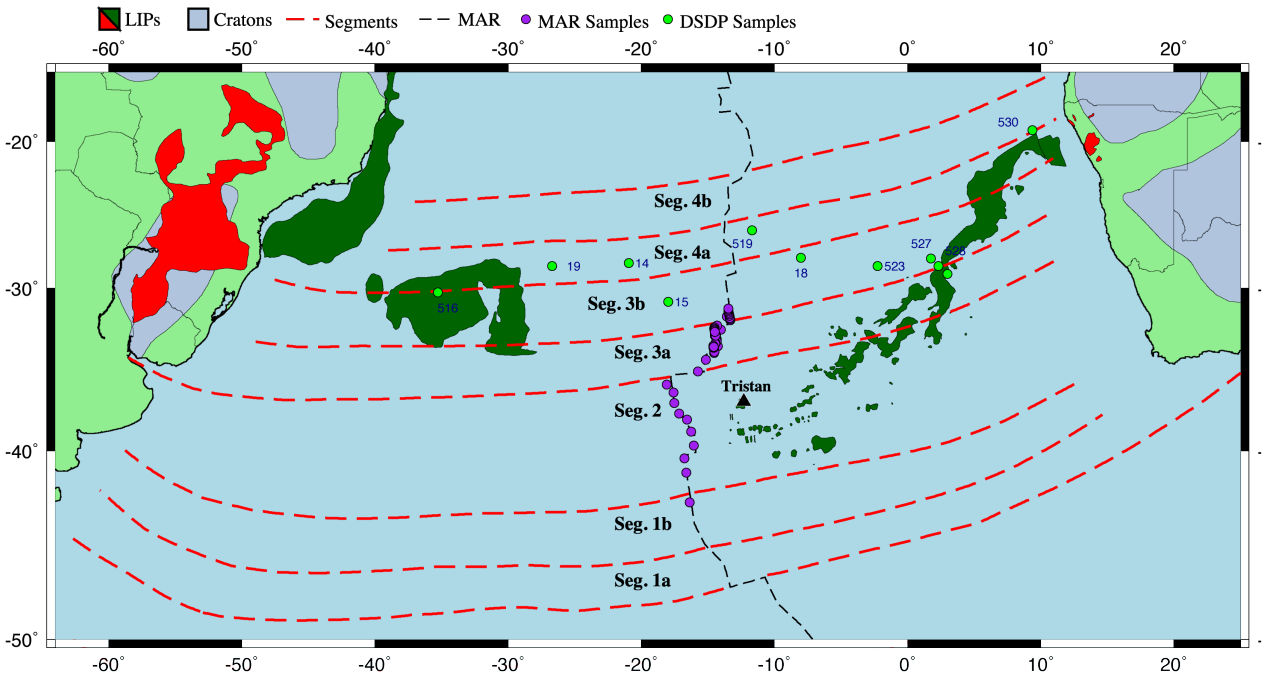


Figure B.1: Location of geochemistry data in the study area. Offshore values are dredge samples along the Mid-Atlantic Ridge from PetDB (http://www.earthchem.org/petdb) and DSDP samples (Tables B.2 and B.1).

B.1 DSDP Drill Holes

There are a total of 55 Deep Sea Drilling Project and Ocean Drilling Project drill holes in the study area (Fig. 2.14). Due to the variation of DSDP expeditions, not all the drillsites aimed to reach basement or pre/syn-rift sediments. Basement in this case is described as reaching igneous material (basalt). Basement is often based on site survey seismics, and can be represented by interbedded lava flows and sediment, or as part of the Rio Grande Rise and Walvis Ridge.

A total of 19 drill holes reached basement and 6 reached pre/syn-rift sediment. Following this initial screening, understanding the purpose of the drillsite and the quality of the core samples was vital to their potential further use, if at all. In addition, if a basalt had a magnesium content of less than 4 %, it was considered too altered and not used further (Trumbull, pers. comm., 11 Jan, 2016).

B.1.1 Drill holes reaching pre/syn-rift sediment

DSDP Leg 40

Leg 40 (locations in Fig. B.2) was centred around the Walvis Ridge and the primary objective was to 'complete a representative sedimentary sequence as possible from continental slope'. Of the six sites, Sites 361, 363 and 364 all reached sediment ageing back to the Aptian/early Cretaceous. Site 361, found offshore the South West of South Africa, presence of basalt was inferred by a few chips. However, as no published geochemical/petrological study of the basalt was found, Site 361 was not considered for basement.

Sites 361, 363 and 364 all have early Cretaceous sediments. Already known from sea-floor spreading anomalies, the unzipping of the South Atlantic occurred in a South-North direction. Site 361, the furthest South, had a well-preserved nanofossil suggesting sediments dating from the Valanginian to lower Aptian (139.4-112.5Ma) (Bolli et al., 1978). Site 363, found just North of the Walvis Ridge, had nanofossils indicating age of sediments possibly of Hautevarian age (132.9-129.4Ma), but definitely of Upper Aptian age (125-112.5 Ma) (Bolli et al., 1978). Finally, Site 364, the most northern of the sites, had indication of Upper Aptian (125-112.5Ma) to Upper Albian (112.5-100.5Ma) biostratigraphy (Bolli et al., 1978). This confirmed a younging of sediments moving in a north direction, and thus the opening of the South Atlantic from a South to North direction.

B.1.2 Drill holes reaching basement

A total of 10 DSDP sites were used reaching basement. Following the initial screening of all samples with MgO values less than 4%, the samples were selected based on their quality and degree of weathering, as described in the DSDP reports (Maxwell et al., 1970; Barker et al., 1983; Hsü et al., 1984; Moore et al., 1984; Hay et al.,

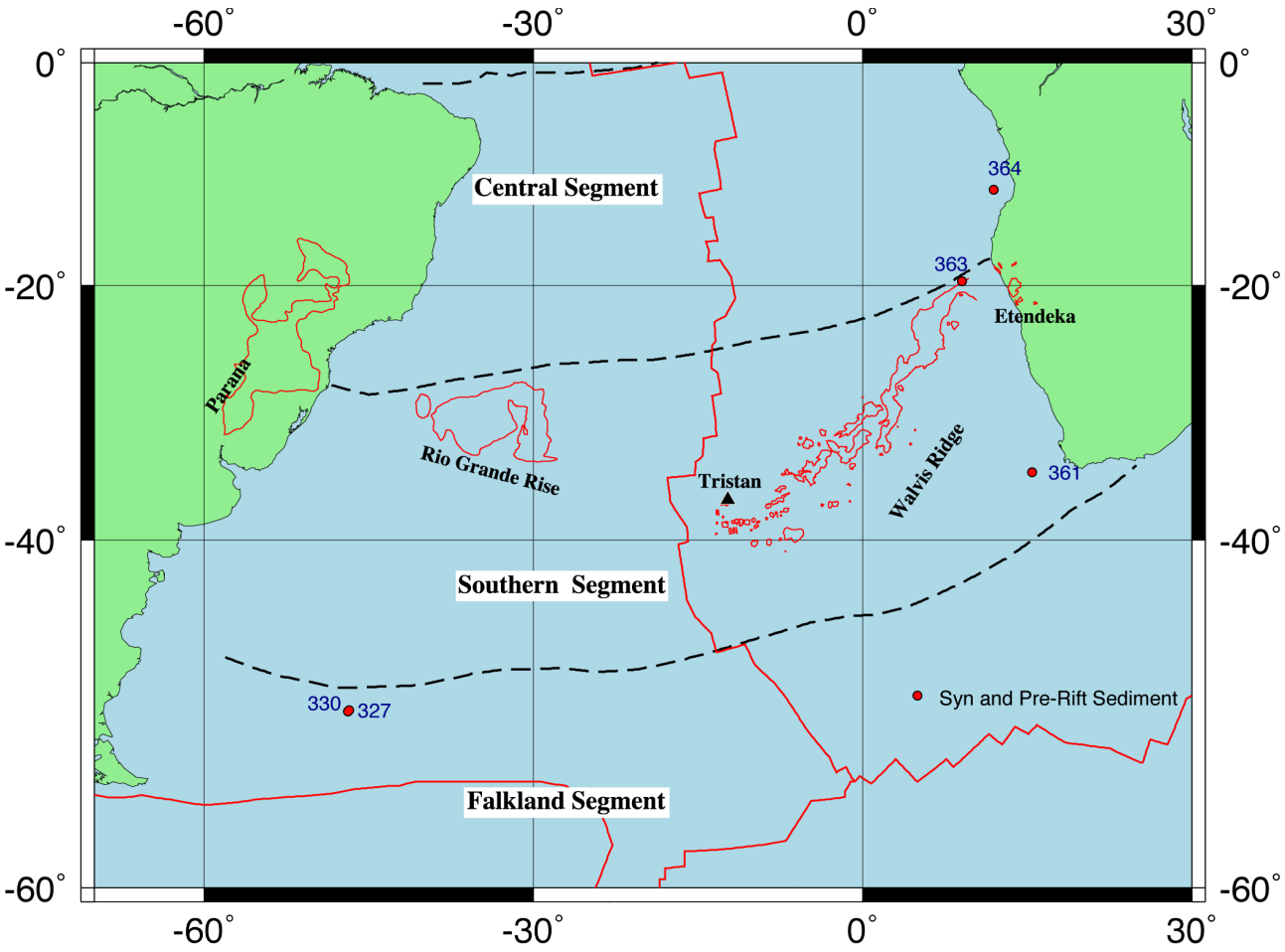


Figure B.2: Map of Location of DSDP drill holes reaching syn-rift sediment. There is a systematic decrease in age going northwards, concurrent with the direction of opening in the South Atlantic.

1984). The samples covered both sides of the Mid-Atlantic Ridge (locations in Fig. B.3) with MgO values ranging from 5.23–11.23% (Table B.1).

Table B.1: Major element oxides compositions from DSDP samples. All samples fulfil quality control and selected for further use (location Fig. B.3). MgO is recalculated on the basis of 100% volatile free, accounting for alteration from water and CO_2.

DSDP Site	Lat.	Long.	SiO_2	TiO_2	Al_2O_3	FeO	MgO	CaO	Na_2O	K_2O	P_2O_5	MgO*
3-14	-20.94	-28.33	50.00	0.79	17.40	8.22	9.81	12.90	2.28	0.02	N/A	9.67
3-15	-17.98	-30.89	51.00	2.20	13.50	11.30	6.68	10.90	3.30	0.11	N/A	6.75
3-18	-8.01	-27.98	50.35	0.76	16.85	7.98	10.04	13.05	1.81	0.02	N/A	9.95
3-19	-26.68	-28.53	51.00	1.00	15.58	9.20	8.49	12.02	2.33	0.08	N/A	8.52
72-516F	-35.26	-30.28	50.48	2.51	15.12	12.76	5.23	10.61	2.61	0.28	0.21	5.24
73-519	-11.67	-26.14	48.50	0.75	16.20	N/A	11.23	12.41	1.80	0.07	0.07	11.08
73-523	-2.25	-28.55	49.90	1.19	15.50	N/A	8.51	12.00	2.19	0.23	0.04	8.52
74-527	1.76	-28.04	50.10	1.83	15.33	12.06	6.40	10.38	2.67	0.59	0.25	6.43
74-528	2.32	-28.53	49.99	1.93	16.46	11.02	6.26	9.98	2.82	1.01	0.28	6.28
75-530A	9.39	-19.19	49.72	1.81	16.05	10.05	8.06	10.62	2.67	0.30	0.26	8.10
		Max.:	51.00	2.51	17.40	12.76	11.23	13.05	3.30	1.01	0.28	11.08
		Min.:	48.50	0.75	13.50	7.98	5.23	9.98	1.80	0.02	0.04	5.24
		Mean:	50.10	1.48	15.80	10.32	8.07	11.49	2.45	0.27	0.19	8.05

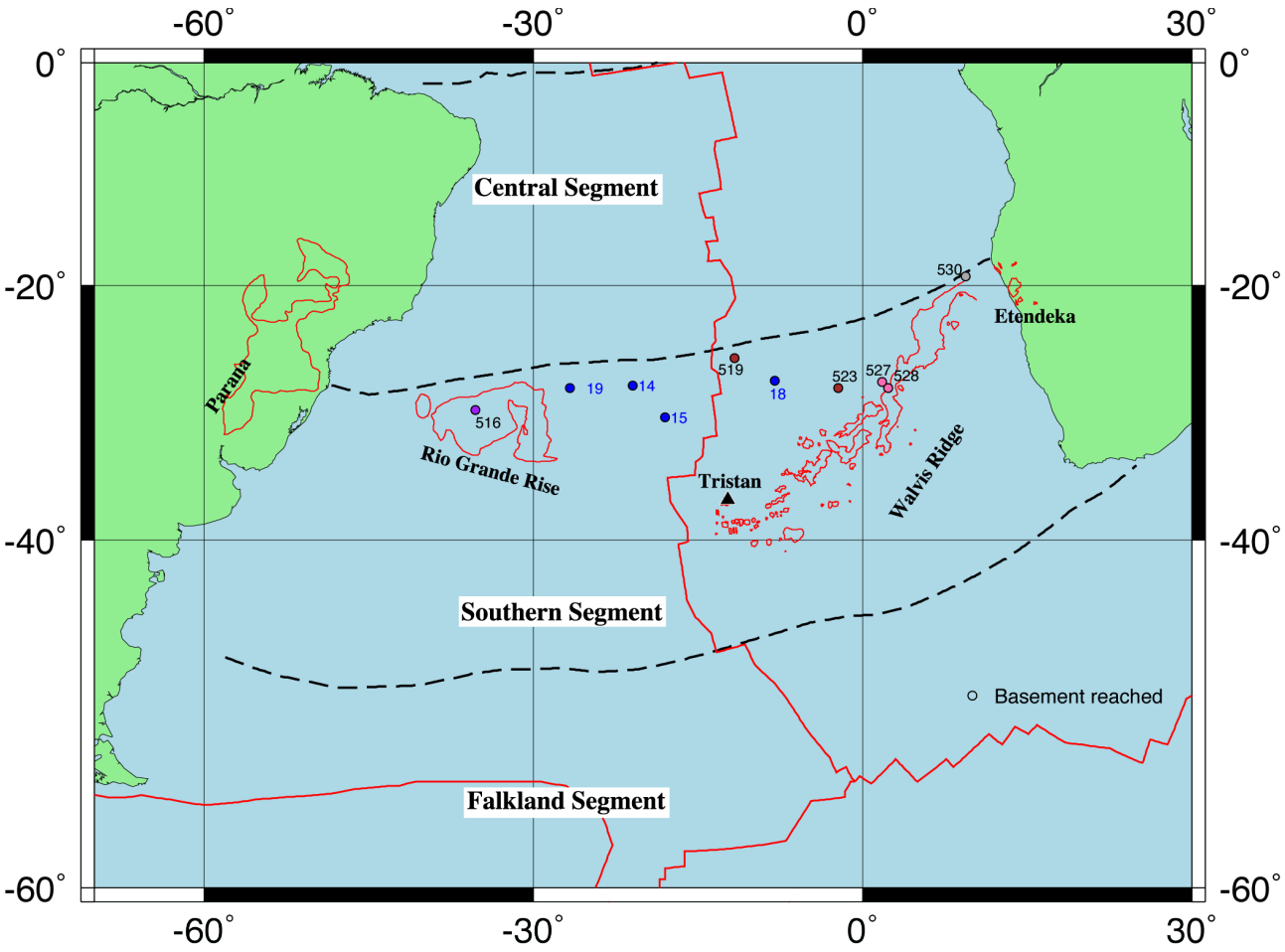


Figure B.3: Map of Location of DSDP drill holes reaching basement fulfilling quality control and selected for further use (Table B.1).

B.2 Mid-Atlantic Ridge Geochemistry

PetDB (http://www.earthchem.org/petdb) was used to find sources of basalt from the Southern Segment of the Mid-Atlantic Ridge (locations shown in Fig. B.1). To be selected, the dredge samples had to have results for all the major element oxides, and the MgO had to be over 4 % to eliminate samples that had undergone significant alteration (Trumbull, pers. comm., 11 Jan, 2016). A total of 73 samples were selected with results for major element oxides (Humphris et al., 1985; Michael et al., 1994; Michael, 1995). In addition, MgO was recalculated on the basis of 100% volatile free, accounting for alteration from water and CO_2 (Table B.2).

Table B.2: PetDB Mid-Atlantic Ridge dredge sample values from the Southern Segment (locations in Fig. B.1). MgO is recalculated on the basis of 100% volatile free, accounting for alteration from water and CO_2.

Sample Name	Lat.	Long.	SiO_2	TiO_2	Al_2O_3	FeO	MgO	CaO	Na_2O	K_2O	P_2O_5	MgO*
AII0107-7-004-009	-16.37	-42.92	50.21	1.47	15.40	7.30	8.18	11.75	2.84	0.14	0.15	8.39
AII0107-7-004-016	-16.37	-42.92	50.54	1.42	15.11	7.90	8.64	11.41	2.40	0.11	0.16	8.84
AII0107-7-006-004	-16.60	-41.25	50.14	1.34	15.83	7.61	8.40	11.70	2.38	0.10	0.15	8.60
AII0107-7-006-020	-16.60	-41.25	50.23	1.34	15.87	7.60	8.27	11.74	2.49	0.12	0.14	8.46
AII0107-7-007-003	-16.75	-40.44	50.40	1.36	15.19	8.00	8.96	11.43	2.30	0.09	0.14	9.16
AII0107-7-007-010	-16.75	-40.44	50.50	1.37	15.16	8.00	8.90	11.48	2.35	0.10	0.15	9.08
AII0107-7-007-098	-16.75	-40.44	49.98	1.29	14.93	7.89	9.95	11.10	2.15	0.10	0.17	10.20
AII0107-7-009-010	-16.05	-39.70	49.19	1.15	17.97	6.22	8.14	11.97	2.52	0.20	0.15	8.35
AII0107-7-009-039	-16.05	-39.70	49.88	1.41	18.37	5.04	7.14	11.06	3.23	0.13	0.14	7.41
AII0107-7-010-001	-16.24	-38.88	50.32	1.50	15.29	8.08	8.73	11.46	2.16	0.14	0.14	8.92
AII0107-7-011-002	-16.56	-38.18	48.83	1.69	15.99	6.80	7.89	11.72	2.60	0.09	0.18	8.24
AII0107-7-013-001	-17.14	-37.83	50.08	1.27	17.80	6.40	7.06	12.45	2.20	0.07	0.10	7.25
AII0107-7-013-002	-17.14	-37.83	50.67	1.40	17.51	5.13	6.26	12.70	2.51	0.26	0.09	6.49
AII0107-7-014-031	-17.52	-37.19	50.50	1.39	16.24	6.70	7.75	12.13	2.72	0.33	0.13	7.92
AII0107-7-014-040	-17.52	-37.19	51.44	1.45	15.18	6.80	7.53	11.99	2.62	0.29	0.12	7.73
AII0107-7-014-077	-17.52	-37.19	50.47	1.26	16.02	6.82	8.13	12.14	2.43	0.29	0.14	8.32
AII0107-7-015-002	-17.59	-36.56	50.85	1.68	15.52	7.59	7.36	11.24	2.49	0.28	0.17	7.57
AII0107-7-015-003	-17.59	-36.56	51.18	1.69	16.01	6.22	6.90	11.49	2.74	0.43	0.15	7.13
AII0107-7-015-035	-17.59	-36.56	51.22	1.62	15.87	6.92	7.51	11.04	2.69	0.38	0.18	7.71
AII0107-7-016-002	-18.08	-36.07	49.56	0.95	19.55	4.85	7.31	12.61	2.29	0.19	0.09	7.51
AII0107-7-017-026	-15.74	-35.28	50.86	1.63	15.80	6.62	7.56	11.06	2.82	0.36	0.19	7.80
AII0107-7-017-057	-15.74	-35.28	50.55	1.65	16.09	7.01	7.61	11.33	2.60	0.30	0.16	7.82
AII0107-7-017-071	-15.74	-35.28	50.86	1.61	15.73	6.89	7.59	11.07	2.71	0.29	0.19	7.83
AII0107-7-018-014	-15.15	-34.55	50.40	1.26	17.20	7.01	7.72	11.98	2.51	0.08	0.10	7.86
AII0107-7-018-028	-15.15	-34.55	50.14	1.25	17.28	7.11	7.69	11.91	2.47	0.07	0.11	7.84
AII0107-7-020-011	-14.25	-33.71	48.75	0.55	19.15	5.31	9.79	13.08	1.66	0.04	0.07	9.95
AII0107-7-023-002	-14.02	-32.68	46.96	0.65	22.28	3.16	4.75	12.06	2.17	0.07	0.24	5.14
AII0107-7-023-003	-14.02	-32.68	47.43	0.66	21.38	4.84	4.97	12.70	2.22	0.03	0.16	5.27
AII0107-7-025-001	-13.58	-31.83	51.16	1.64	16.14	6.31	7.10	12.14	2.73	0.40	0.14	7.26
AII0107-7-025-002	-13.58	-31.83	50.31	1.34	17.42	5.82	7.03	12.09	2.48	0.33	0.13	7.25
AII0107-7-025-013	-13.58	-31.83	50.39	1.60	15.97	6.22	7.11	12.17	2.78	0.35	0.15	7.35
WASPLUM-5-031-001	-14.30	-32.40	50.62	2.26	14.95	10.60	6.30	9.83	3.55	0.34	0.28	6.38
WASPLUM-5-032-001	-14.50	-32.53	50.98	2.02	14.60	10.86	6.58	10.16	2.87	0.33	0.22	6.67
WASPLUM-5-032-002	-14.50	-32.53	50.75	1.38	14.76	9.93	7.49	11.66	2.70	0.14	0.12	7.57
WASPLUM-5-033-001	-14.52	-32.60	50.52	1.92	15.18	10.32	7.12	10.47	2.88	0.32	0.22	7.20
WASPLUM-5-034-001	-14.49	-32.66	50.05	1.19	16.01	9.20	8.54	11.84	2.54	0.14	0.12	8.57
WASPLUM-5-034-002	-14.49	-32.66	51.07	1.71	14.47	10.40	7.00	11.15	2.83	0.21	0.17	7.07
WASPLUM-5-035-001	-14.50	-32.74	50.24	1.57	15.40	9.64	8.58	11.00	2.53	0.23	0.17	8.64
WASPLUM-5-036-001	-14.47	-32.88	49.98	1.11	15.90	9.87	8.55	11.49	2.39	0.10	0.10	8.59
WASPLUM-5-037-001	-14.46	-32.94	51.32	1.96	14.33	11.06	6.65	10.39	2.97	0.25	0.20	6.71
WASPLUM-5-038-001	-14.43	-33.00	50.68	1.43	16.02	9.19	7.88	11.11	2.60	0.32	0.15	7.93
WASPLUM-5-038-002	-14.43	-33.00	50.20	1.40	16.42	8.93	7.98	11.16	2.64	0.39	0.17	8.04
WASPLUM-5-039-001	-14.39	-33.00	51.10	1.40	14.68	10.07	7.49	11.75	2.87	0.12	0.12	7.52
WASPLUM-5-041-001	-14.41	-33.06	50.75	1.25	15.68	8.74	8.22	11.95	2.66	0.17	0.12	8.26
WASPLUM-5-042-001	-14.37	-33.14	48.39	1.44	17.04	9.10	8.93	11.11	2.49	0.31	0.16	9.02
WASPLUM-5-043-001	-14.36	-33.23	50.19	1.39	16.06	9.15	8.55	11.25	2.53	0.18	0.15	8.60
WASPLUM-5-044-001	-14.33	-33.27	51.02	1.26	14.93	9.17	8.15	12.31	2.60	0.12	0.12	8.18
WASPLUM-5-045-001	-14.33	-33.34	50.87	1.99	14.25	10.73	6.68	10.75	2.89	0.29	0.23	6.77
WASPLUM-5-046-001	-14.33	-33.40	50.40	1.48	15.51	9.83	7.99	11.07	2.67	0.17	0.14	8.05
WASPLUM-5-046-002	-14.33	-33.40	50.00	1.31	15.87	9.75	8.51	11.18	2.56	0.16	0.13	8.56
WASPLUM-5-047-001	-14.40	-33.51	50.87	1.81	14.80	10.57	7.71	10.39	2.89	0.17	0.19	7.76
WASPLUM-5-048-004	-14.45	-33.55	50.60	1.83	14.79	10.62	7.01	10.60	2.90	0.19	0.19	7.10
WASPLUM-5-050-001	-14.57	-33.70	50.35	1.45	15.73	9.17	8.35	11.29	2.73	0.12	0.15	8.41
WASPLUM-5-050-002	-14.57	-33.70	50.55	1.41	15.85	9.07	8.51	11.35	2.65	0.10	0.13	8.54
WASPLUM-5-051-001	-14.57	-33.77	50.32	1.32	15.38	9.30	9.03	11.29	2.58	0.08	0.12	9.08
WASPLUM-5-051-002	-14.57	-33.77	50.40	1.38	15.54	9.38	8.55	11.36	2.62	0.10	0.12	8.60
WASPLUM-5-052-001	-14.56	-33.85	50.50	1.31	15.38	8.88	8.20	11.76	2.77	0.08	0.12	8.28
WASPLUM-5-053-001	-14.52	-33.92	50.55	1.07	15.65	8.57	8.72	12.27	2.44	0.05	0.09	8.77
WASPLUM-5-053-002	-14.52	-33.92	50.64	1.57	15.25	9.50	7.72	11.52	2.87	0.08	0.13	7.78
WASPLUM-5-053-003	-14.52	-33.92	50.46	1.19	15.58	8.69	8.28	12.01	2.73	0.06	0.11	8.35
WASPLUM-5-054-001	-14.52	-33.97	50.38	1.32	15.63	9.03	8.40	11.70	2.66	0.07	0.11	8.46
WASPLUM-5-054-002	-14.52	-33.97	50.94	1.42	15.20	9.42	7.88	11.47	2.82	0.07	0.12	7.93
WASPLUM-5-055-001	-14.51	-34.06	50.30	1.77	14.75	10.70	7.29	11.00	3.00	0.10	0.16	7.36
WASPLUM-5-056-001	-14.52	-34.13	50.29	1.77	14.92	10.56	7.67	11.05	2.73	0.09	0.16	7.73
WASPLUM-5-056-006	-14.52	-34.13	50.34	1.38	15.63	9.38	8.22	11.62	2.79	0.08	0.13	8.26
WASPLUM-5-057-001	-14.51	-34.06	49.94	1.79	14.80	10.98	7.34	10.83	2.96	0.10	0.15	7.42
WASPLUM-5-058-001	-14.54	-33.81	50.50	1.54	15.65	9.41	8.36	10.94	2.77	0.11	0.16	8.41
WASPLUM-5-059-001	-14.56	-33.75	50.45	1.29	15.64	9.11	8.92	11.64	2.41	0.08	0.13	8.95
WASPLUM-5-059-005	-14.56	-33.75	50.44	1.05	15.76	8.60	9.53	11.87	2.28	0.06	0.10	9.56
WASPLUM-5-062-001	-13.30	-32.07	50.88	2.03	14.71	10.83	7.20	10.21	3.01	0.20	0.22	7.25
WASPLUM-5-063-001	-13.32	-31.99	50.53	1.79	15.13	10.02	7.37	10.72	2.89	0.19	0.20	7.46
WASPLUM-5-064-001	-13.33	-31.91	51.02	2.32	14.04	11.92	6.14	9.40	3.32	0.29	0.25	6.22
WASPLUM-5-066-001	-13.38	-31.79	50.50	0.99	15.53	8.24	9.00	12.25	2.38	0.10	0.10	9.08
WASPLUM-5-067-001	-13.39	-31.67	50.85	2.23	14.05	12.09	6.38	9.82	3.15	0.21	0.21	6.45
WASPLUM-5-068-001	-13.43	-31.58	50.23	1.19	16.36	8.37	8.68	11.65	2.64	0.10	0.12	8.74
WASPLUM-5-068-003	-13.43	-31.58	50.06	1.06	16.55	7.99	8.98	11.88	2.55	0.09	0.12	9.05
WASPLUM-5-069-001	-13.46	-31.50	50.69	1.55	15.06	9.69	7.74	11.46	2.59	0.18	0.16	7.81
WASPLUM-5-069-003	-13.46	-31.50	50.68	1.99	14.63	10.39	7.03	10.57	3.03	0.17	0.20	7.12
WASPLUM-5-070-001	-13.45	-31.40	50.60	1.67	15.01	9.63	7.48	11.30	2.95	0.14	0.16	7.56
WASPLUM-5-070-002	-13.45	-31.40	50.75	1.42	15.08	8.98	7.82	11.71	2.73	0.14	0.12	7.92
WASPLUM-5-070-004	-13.45	-31.40	50.64	1.25	15.70	8.59	8.28	11.71	2.70	0.12	0.13	8.35
WASPLUM-5-071-001	-13.44	-31.33	50.75	1.40	15.27	9.18	8.01	11.54	2.64	0.14	0.14	8.08
WASPLUM-5-R005	-14.48	-33.04	50.51	1.25	15.10	9.17	8.02	11.97	2.72	0.13	0.14	8.10
WASPLUM-5-R006	-14.42	-33.04	50.50	1.31	15.63	8.90	8.07	11.81	2.72	0.18	0.15	8.13
WASPLUM-5-R008	-14.46	-32.81	50.40	1.28	15.05	9.49	7.77	11.82	2.83	0.10	0.12	7.86
		Max.:	51.44	2.32	22.28	12.09	9.95	13.08	3.55	0.43	0.28	10.20
		Min.:	46.96	0.55	14.04	3.16	4.75	9.40	1.66	0.03	0.07	5.14
		Mean:	50.37	1.46	15.84	8.53	7.82	11.45	2.65	0.17	0.15	7.94

Appendix C

Permissions

JOHN WILEY AND SONS LICENSE TERMS AND CONDITIONS

Dec 01, 2016

This Agreement between Chandra Taposeea ("You") and John Wiley and Sons ("John Wiley and Sons") consists of your license details and the terms and conditions provided by John Wiley and Sons and Copyright Clearance Center.

License Number	4000310534013
License date	Dec 01, 2016
Licensed Content Publisher	John Wiley and Sons
Licensed Content Publication	Journal of Geophysical Research: Solid Earth
Licensed Content Title	Deep structure of the Namibia continental margin as derived from integrated geophysical studies
Licensed Content Author	
Licensed Content Date	Nov 10, 2000
Licensed Content Pages	25
Type of use	Dissertation/Thesis
Requestor type	University/Academic
Format	Electronic
Portion	Figure/table
Number of figures/tables	5
Original Wiley figure/table number(s)	Plate 1, Figure 6, Figure 9, Figure 14, Figure 15
Will you be translating?	No
Title of your thesis / dissertation	Numerical modelling of the continental break-up of the southern South Atlantic
Expected completion date	Jan 2017
Expected size (number of pages)	230

ELSEVIER LICENSE TERMS AND CONDITIONS

Dec 01, 2016

This Agreement between Chandra Taposeea ("You") and Elsevier ("Elsevier") consists of your license details and the terms and conditions provided by Elsevier and Copyright Clearance Center.

License Number	4000380536688
License date	Dec 01, 2016
Licensed Content Publisher	Elsevier
Licensed Content Publication	Marine and Petroleum Geology
Licensed Content Title	Rifted margin architecture and crustal rheology: Reviewing Iberia-Newfoundland, Central South Atlantic, and South China Sea
Licensed Content Author	Sascha Brune,Christian Heine,Peter D. Clift,Marta Pérez-Gussinyé
Licensed Content Date	January 2017
Licensed Content Volume Number	79
Licensed Content Issue Number	n/a
Licensed Content Pages	25
Start Page	257
End Page	281
Type of Use	reuse in a thesis/dissertation
Portion	figures/tables/illustrations
Number of figures/tables/illustrations	1
Format	both print and electronic
Are you the author of this Elsevier article?	No
Will you be translating?	No
Order reference number	
Original figure numbers	Fig. 2
Title of your thesis/dissertation	Numerical modelling of the continental break-up of the southern South Atlantic
Expected completion date	Jan 2017
Estimated size (number of pages)	230

JOHN WILEY AND SONS LICENSE TERMS AND CONDITIONS

Dec 01, 2016

This Agreement between Chandra Taposeea ("You") and John Wiley and Sons ("John Wiley and Sons") consists of your license details and the terms and conditions provided by John Wiley and Sons and Copyright Clearance Center.

License Number	4000380757841
License date	Dec 01, 2016
Licensed Content Publisher	John Wiley and Sons
Licensed Content Publication	Reviews of Geophysics
Licensed Content Title	Large igneous provinces: Crustal structure, dimensions, and external consequences
Licensed Content Author	Millard F. Coffin,Olav Eldholm
Licensed Content Date	Feb 1, 1994
Licensed Content Pages	36
Type of use	Dissertation/Thesis
Requestor type	University/Academic
Format	Print and electronic
Portion	Figure/table
Number of figures/tables	1
Original Wiley figure/table number(s)	Fig. 8
Will you be translating?	No
Title of your thesis / dissertation	Numerical modelling of the continental break-up of the southern South Atlantic
Expected completion date	Jan 2017
Expected size (number of pages)	230

JOHN WILEY AND SONS LICENSE TERMS AND CONDITIONS

Dec 01, 2016

This Agreement between Chandra Taposeea ("You") and John Wiley and Sons ("John Wiley and Sons") consists of your license details and the terms and conditions provided by John Wiley and Sons and Copyright Clearance Center.

License Number	4000381320303
License date	Dec 01, 2016
Licensed Content Publisher	John Wiley and Sons
Licensed Content Publication	Geochemistry, Geophysics, Geosystems
Licensed Content Title	Birth of a volcanic margin off Argentina, South Atlantic
Licensed Content Author	Dieter Franke,Stefan Ladage,Michael Schnabel,Bernd Schreckenberger,Christian Reichert,Karl Hinz,Marcelo Paterlini,Juan de Abelleyra,Miguel Siciliano
Licensed Content Date	Feb 12, 2010
Licensed Content Pages	1
Type of use	Dissertation/Thesis
Requestor type	University/Academic
Format	Print and electronic
Portion	Figure/table
Number of figures/tables	3
Original Wiley figure/table number(s)	Fig. 4, 5, 6
Will you be translating?	No
Title of your thesis / dissertation	Numerical modelling of the continental break-up of the southern South Atlantic
Expected completion date	Jan 2017
Expected size (number of pages)	230

ELSEVIER LICENSE TERMS AND CONDITIONS

Dec 01, 2016

This Agreement between Chandra Taposeea ("You") and Elsevier ("Elsevier") consists of your license details and the terms and conditions provided by Elsevier and Copyright Clearance Center.

License Number	4000381154979
License date	Dec 01, 2016
Licensed Content Publisher	Elsevier
Licensed Content Publication	Marine Geology
Licensed Content Title	Margin segmentation and volcano-tectonic architecture along the volcanic margin off Argentina/Uruguay, South Atlantic
Licensed Content Author	D. Franke,S. Neben,S. Ladage,B. Schreckenberger,K. Hinz
Licensed Content Date	8 October 2007
Licensed Content Volume Number	244
Licensed Content Issue Number	1-4
Licensed Content Pages	22
Start Page	46
End Page	67
Type of Use	reuse in a thesis/dissertation
Intended publisher of new work	other
Portion	figures/tables/illustrations
Number of figures/tables/illustrations	6
Format	both print and electronic
Are you the author of this Elsevier article?	No
Will you be translating?	No
Order reference number	
Original figure numbers	Fig. 3,4,5,6,7,8
Title of your thesis/dissertation	Numerical modelling of the continental break-up of the southern South Atlantic
Expected completion date	Jan 2017
Estimated size (number of pages)	230

ELSEVIER LICENSE TERMS AND CONDITIONS

Dec 01, 2016

This Agreement between Chandra Taposeea ("You") and Elsevier ("Elsevier") consists of your license details and the terms and conditions provided by Elsevier and Copyright Clearance Center.

License Number	4000390154988
License date	Dec 01, 2016
Licensed Content Publisher	Elsevier
Licensed Content Publication	Marine and Petroleum Geology
Licensed Content Title	Rifting, lithosphere breakup and volcanism: Comparison of magma-poor and volcanic rifted margins
Licensed Content Author	Dieter Franke
Licensed Content Date	May 2013
Licensed Content Volume Number	43
Licensed Content Issue Number	n/a
Licensed Content Pages	25
Start Page	63
End Page	87
Type of Use	reuse in a thesis/dissertation
Intended publisher of new work	other
Portion	figures/tables/illustrations
Number of figures/tables/illustrations	1
Format	both print and electronic
Are you the author of this Elsevier article?	No
Will you be translating?	No
Order reference number	
Original figure numbers	Fig. 1
Title of your thesis/dissertation	Numerical modelling of the continental break-up of the southern South Atlantic
Expected completion date	Jan 2017
Estimated size (number of pages)	230

This Agreement between Chandra Taposeea ("You") and Nature Publishing Group ("Nature Publishing Group") consists of your license details and the terms and conditions provided by Nature Publishing Group and Copyright Clearance Center.

Your confirmation email will contain your order number for future reference.

Printable details.

License Number	4010971154044
License date	Dec 16, 2016
Licensed Content Publisher	Nature Publishing Group
Licensed Content Publication	Nature
Licensed Content Title	Broad plumes rooted at the base of the Earth's mantle beneath major hotspots
Licensed Content Author	Scott W. French, Barbara Romanowicz
Licensed Content Date	Sep 2, 2015
Licensed Content Volume	525
Licensed Content Issue	7567
Type of Use	reuse in a dissertation / thesis
Requestor type	academic/educational
Format	electronic
Portion	figures/tables/illustrations
Number of figures/tables/illustrations	2
High-res required	no
Figures	Fig. 3 and 4
Author of this NPG article	no
Your reference number	
Title of your thesis / dissertation	Numerical modelling of the continental break-up of the southern South Atlantic
Expected completion date	Jan 2017
Estimated size (number of pages)	230

Geological Society of America LICENSE TERMS AND CONDITIONS

Dec 01, 201

This is a License Agreement between Chandra Taposeea ("You") and CCC Republication ("CCC Republication") provided by Copyright Clearance Center ("CCC"). The license consists of your order details, the terms and conditions provided by CCC Republication, and the payment terms and conditions.

All payments must be made in full to CCC. For payment instructions, please see information listed at the bottom of this form.

License Number	4000391412588
License date	Dec 01, 2016
Licensed content publisher	CCC Republication
Licensed content title	Geology
Licensed content date	Jan 1, 1973
Type of Use	Thesis/Dissertation
Requestor type	Academic institution
Format	Print, Electronic
Portion	chart/graph/table/figure
Number of charts/graphs/tables/figures	2
Title or numeric reference of the portion(s)	Figure 1 and 2
Title of the article or chapter the portion is from	South Atlantic opening: A plume-induced breakup?
Editor of portion(s)	N/A
Author of portion(s)	T. Fromm, L. Planert, W. Jokat, T. Ryberg, J. H. Behrmann, M.H. Weber and Christian Haberland
Volume of serial or monograph.	43
Page range of the portion	1 - 2
Publication date of portion	2015
Rights for	Main product
Duration of use	Life of current and all future editions

SPRINGER LICENSE TERMS AND CONDITIONS

Dec 01, 2016

This Agreement between Chandra Taposeea ("You") and Springer ("Springer") consists of your license details and the terms and conditions provided by Springer and Copyright Clearance Center.

License Number	4000390654297
License date	Dec 01, 2016
Licensed Content Publisher	Springer
Licensed Content Publication	International Journal of Earth Sciences
Licensed Content Title	Neoproterozoic geodynamic evolution of SW-Gondwana: a southern African perspective
Licensed Content Author	H. E. Frimmel
Licensed Content Date	Jan 1, 2010
Licensed Content Volume Number	100
Licensed Content Issue Number	2
Type of Use	Thesis/Dissertation
Portion	Figures/tables/illustrations
Number of figures/tables/illustrations	1
Author of this Springer article	No
Order reference number	
Original figure numbers	Fig. 1
Title of your thesis / dissertation	Numerical modelling of the continental break-up of the southern South Atlantic
Expected completion date	Jan 2017
Estimated size(pages)	230

E-theses letter template: request to reproduce an extract from a third party's published work

15th December 2016

Dear Sir/Madam,

I am completing my PhD thesis at Imperial College London entitled 'Numerical Modelling of the Continental Break-up of the southern South Atlantic'.

I seek your permission to reprint, in my thesis an extract from: Laurent Geoffroy (2005). *Volcanic Passive Margins*. C. R. Geoscience 337 (2005) 1395–1408. The extract to be reproduced is from Figure. 1 (found below).

I would like to include the extract in my thesis which will be added to Spiral, Imperial's institutional repository http://spiral.imperial.ac.uk/ and made available to the public under a Creative Commons Attribution-NonCommercial-NoDerivs licence.

If you are happy to grant me all the permissions requested, please return a signed copy of this letter. If you wish to grant only some of the permissions requested, please list these and then sign.

Yours sincerely,

Chandra S. Amber Taposeea

Issy-Les-Moulineaux, 7-Feb-2017

To the attention of Chandra Taposeea

-

Dear Madam,

As per your request below, we hereby grant you permission to reprint the material detailed in your request at no charge **in your thesis** subject to the following conditions:

1. If any part of the material to be used (for example, figures) has appeared in our publication with credit or acknowledgement to another source, permission must also be sought from that source. If such permissions are not obtained then that materials may not be included in your publication.
2. Any modification of the material is likely to harm the moral right of the authors and therefore should be first submitted and approved by the authors who are the sole owner of the moral right.
3. Suitable and visible acknowledgement to the source must be made, either as a footnote or in a reference list at the end of your publication, as follows:
   "Reproduced from *Authors name. Article title. Journal title year; volume number(issue number):first page-last page.* Copyright © *year [if applicable: name of learned society,* published by*]* Elsevier Masson SAS. All rights reserved."
4. Your thesis may be submitted to your institution in either print or electronic form.
5. Reproduction of this material is confined to the purpose for which permission is hereby given.
6. This permission is granted for non-exclusive world English rights only. For other languages please reapply separately for each one required. Permission excludes use in an electronic form other than submission. Should you have a specific electronic project in mind please reapply for permission.
7. Should your thesis be published commercially, please reapply for permission.

Yours sincerely,
Regina Lavanya Remigius
Senior Copyrights Coordinator, GR - Copyrights
ELSEVIER | Global Book Production

ELSEVIER LICENSE TERMS AND CONDITIONS

Dec 01, 2016

This Agreement between Chandra Taposeea ("You") and Elsevier ("Elsevier") consists of your license details and the terms and conditions provided by Elsevier and Copyright Clearance Center.

License Number	4000400287196
License date	Dec 01, 2016
Licensed Content Publisher	Elsevier
Licensed Content Publication	Marine and Petroleum Geology
Licensed Content Title	The Argentine continental margin north of 48°S: sedimentary successions, volcanic activity during breakup
Licensed Content Author	K. Hinz,S. Neben,B. Schreckenberger,H.A. Roeser,M. Block,K.Goncalves de Souza,H. Meyer
Licensed Content Date	15 February 1999
Licensed Content Volume Number	16
Licensed Content Issue Number	1
Licensed Content Pages	25
Start Page	1
End Page	25
Type of Use	reuse in a thesis/dissertation
Intended publisher of new work	other
Portion	figures/tables/illustrations
Number of figures/tables/illustrations	1
Format	both print and electronic
Are you the author of this Elsevier article?	No
Will you be translating?	No
Order reference number	
Original figure numbers	Fig. 8
Title of your thesis/dissertation	Numerical modelling of the continental break-up of the southern South Atlantic
Expected completion date	Jan 2017
Estimated size (number of pages)	230

ELSEVIER LICENSE TERMS AND CONDITIONS

Dec 01, 2016

This Agreement between Chandra Taposeea ("You") and Elsevier ("Elsevier") consists of your license details and the terms and conditions provided by Elsevier and Copyright Clearance Center.

License Number	4000400773154
License date	Dec 01, 2016
Licensed Content Publisher	Elsevier
Licensed Content Publication	Earth and Planetary Science Letters
Licensed Content Title	Mantle thermal structure and active upwelling during continental breakup in the North Atlantic
Licensed Content Author	W.Steven Holbrook,H.C. Larsen,J. Korenaga,T. Dahl-Jensen,I.D. Reid,P.B. Kelemen,J.R. Hopper,G.M. Kent,D. Lizarralde,S. Bernstein,R.S. Detrick
Licensed Content Date	15 August 2001
Licensed Content Volume Number	190
Licensed Content Issue Number	3-4
Licensed Content Pages	16
Start Page	251
End Page	266
Type of Use	reuse in a thesis/dissertation
Intended publisher of new work	other
Portion	figures/tables/illustrations
Number of figures/tables/illustrations	3
Format	both print and electronic
Are you the author of this Elsevier article?	No
Will you be translating?	No
Order reference number	
Original figure numbers	Fig. 1, 4, 6
Title of your thesis/dissertation	Numerical modelling of the continental break-up of the southern South Atlantic
Expected completion date	Jan 2017
Estimated size (number of pages)	230

ELSEVIER LICENSE TERMS AND CONDITIONS

Dec 01, 2016

This Agreement between Chandra Taposeea ("You") and Elsevier ("Elsevier") consists of your license details and the terms and conditions provided by Elsevier and Copyright Clearance Center.

License Number	4000400521466
License date	Dec 01, 2016
Licensed Content Publisher	Elsevier
Licensed Content Publication	Tectonophysics
Licensed Content Title	Deep structure of the western South African passive margin — Results of a combined approach of seismic, gravity and isostatic investigations
Licensed Content Author	Katja K. Hirsch,Klaus Bauer,Magdalena Scheck-Wenderoth
Licensed Content Date	17 May 2009
Licensed Content Volume Number	470
Licensed Content Issue Number	1-2
Licensed Content Pages	14
Start Page	57
End Page	70
Type of Use	reuse in a thesis/dissertation
Intended publisher of new work	other
Portion	figures/tables/illustrations
Number of figures/tables/illustrations	3
Format	both print and electronic
Are you the author of this Elsevier article?	No
Will you be translating?	No
Order reference number	
Original figure numbers	Fig. 5, 6, 12
Title of your thesis/dissertation	Numerical modelling of the continental break-up of the southern South Atlantic
Expected completion date	Jan 2017
Estimated size (number of pages)	230

NATURE PUBLISHING GROUP LICENSE TERMS AND CONDITIONS

Dec 24, 2016

This Agreement between Chandra Taposeea ("You") and Nature Publishing Group ("Nature Publishing Group") consists of your license details and the terms and conditions provided by Nature Publishing Group and Copyright Clearance Center.

License Number	4015210766559
License date	Dec 24, 2016
Licensed Content Publisher	Nature Publishing Group
Licensed Content Publication	Nature
Licensed Content Title	Depth-dependent extension, two-stage breakup and cratonic underplating at rifted margins
Licensed Content Author	Ritske Huismans and Christopher Beaumont
Licensed Content Date	May 4, 2011
Licensed Content Volume Number	473
Licensed Content Issue Number	7345
Type of Use	reuse in a dissertation / thesis
Requestor type	academic/educational
Format	print and electronic
Portion	figures/tables/illustrations
Number of figures/tables/illustrations	1
High-res required	no
Figures	Figure A6
Author of this NPG article	no
Your reference number	
Title of your thesis / dissertation	Numerical modelling of the continental break-up of the southern South Atlantic
Expected completion date	Jan 2017
Estimated size (number of pages)	230

JOHN WILEY AND SONS LICENSE TERMS AND CONDITIONS

Dec 01, 2016

This Agreement between Chandra Taposeea ("You") and John Wiley and Sons ("John Wiley and Sons") consists of your license details and the terms and conditions provided by John Wiley and Sons and Copyright Clearance Center.

License Number	4000401046778
License date	Dec 01, 2016
Licensed Content Publisher	John Wiley and Sons
Licensed Content Publication	Journal of Geophysical Research: Solid Earth
Licensed Content Title	Origin of thick, high-velocity igneous crust along the U.S. East Coast Margin
Licensed Content Author	Peter B. Kelemen,W. Steven Holbrook
Licensed Content Date	Jun 10, 1995
Licensed Content Pages	18
Type of use	Dissertation/Thesis
Requestor type	University/Academic
Format	Print and electronic
Portion	Figure/table
Number of figures/tables	1
Original Wiley figure/table number(s)	Fig. 1
Will you be translating?	No
Title of your thesis / dissertation	Numerical modelling of the continental break-up of the southern South Atlantic
Expected completion date	Jan 2017
Expected size (number of pages)	230

Geological Society of America LICENSE TERMS AND CONDITIONS

Dec 01, 2016

This is a License Agreement between Chandra Taposeea ("You") and Geological Society of America ("Geological Society of America") provided by Copyright Clearance Center ("CCC"). The license consists of your order details, the terms and conditions provided by Geological Society of America, and the payment terms and conditions.

All payments must be made in full to CCC. For payment instructions, please see information listed at the bottom of this form.

License Number	4000420455686
License date	Dec 01, 2016
Licensed content publisher	Geological Society of America
Licensed content title	Geology
Licensed content date	Jan 1, 1973
Type of Use	Thesis/Dissertation
Requestor type	Academic institution
Format	Print, Electronic
Portion	chart/graph/table/figure
Number of charts/graphs/tables/figures	2
Title or numeric reference of the portion(s)	Fig. 3 and 4
Title of the article or chapter the portion is from	Linking rift propagation barriers to excess magmatism at volcanic rifted margins
Editor of portion(s)	N/A
Author of portion(s)	H Koopmann, S Brune, D Franke, S Breuer
Volume of serial or monograph.	42
Page range of the portion	1071-1074
Publication date of portion	2014
Rights for	Main product
Duration of use	Life of current and all future editions

ELSEVIER LICENSE TERMS AND CONDITIONS

Dec 01, 2016

This Agreement between Chandra Taposeea ("You") and Elsevier ("Elsevier") consists of your license details and the terms and conditions provided by Elsevier and Copyright Clearance Center.

License Number	4000401183910
License date	Dec 01, 2016
Licensed Content Publisher	Elsevier
Licensed Content Publication	Earth and Planetary Science Letters
Licensed Content Title	An alternative mechanism of flood basalt formation
Licensed Content Author	Scott D. King,Don L. Anderson
Licensed Content Date	December 1995
Licensed Content Volume Number	136
Licensed Content Issue Number	3-4
Licensed Content Pages	11
Start Page	269
End Page	279
Type of Use	reuse in a thesis/dissertation
Intended publisher of new work	other
Portion	figures/tables/illustrations
Number of figures/tables/illustrations	1
Format	both print and electronic
Are you the author of this Elsevier article?	No
Will you be translating?	No
Order reference number	
Original figure numbers	Fig. 3
Title of your thesis/dissertation	Numerical modelling of the continental break-up of the southern South Atlantic
Expected completion date	Jan 2017
Estimated size (number of pages)	230

ELSEVIER LICENSE TERMS AND CONDITIONS

Dec 01, 2016

This Agreement between Chandra Taposeea ("You") and Elsevier ("Elsevier") consists of your license details and the terms and conditions provided by Elsevier and Copyright Clearance Center.

License Number	4000401276516
License date	Dec 01, 2016
Licensed Content Publisher	Elsevier
Licensed Content Publication	Earth and Planetary Science Letters
Licensed Content Title	Edge-driven convection
Licensed Content Author	Scott D King,Don L Anderson
Licensed Content Date	August 1998
Licensed Content Volume Number	160
Licensed Content Issue Number	3-4
Licensed Content Pages	8
Start Page	289
End Page	296
Type of Use	reuse in a thesis/dissertation
Intended publisher of new work	other
Portion	figures/tables/illustrations
Number of figures/tables/illustrations	1
Format	both print and electronic
Are you the author of this Elsevier article?	No
Will you be translating?	No
Order reference number	
Original figure numbers	Fig. 1
Title of your thesis/dissertation	Numerical modelling of the continental break-up of the southern South Atlantic
Expected completion date	Jan 2017
Estimated size (number of pages)	230

ELSEVIER LICENSE TERMS AND CONDITIONS

Dec 01, 2016

This Agreement between Chandra Taposeea ("You") and Elsevier ("Elsevier") consists of your license details and the terms and conditions provided by Elsevier and Copyright Clearance Center.

License Number	4000420196313
License date	Dec 01, 2016
Licensed Content Publisher	Elsevier
Licensed Content Publication	Marine and Petroleum Geology
Licensed Content Title	Segmentation and volcano-tectonic characteristics along the SW African continental margin, South Atlantic, as derived from multichannel seismic and potential field data
Licensed Content Author	Hannes Koopmann,Dieter Franke,Bernd Schreckenberger,Henning Schulz,Alexander Hartwig,Harald Stollhofen,Rolando di Primio
Licensed Content Date	February 2014
Licensed Content Volume Number	50
Licensed Content Issue Number	n/a
Licensed Content Pages	18
Start Page	22
End Page	39
Type of Use	reuse in a thesis/dissertation
Intended publisher of new work	other
Portion	figures/tables/illustrations
Number of figures/tables/illustrations	1
Format	both print and electronic
Are you the author of this Elsevier article?	No
Will you be translating?	No
Order reference number	
Original figure numbers	Fig. 12
Title of your thesis/dissertation	Numerical modelling of the continental break-up of the southern South Atlantic
Expected completion date	Jan 2017
Estimated size (number of pages)	230

Geological Society of America LICENSE TERMS AND CONDITIONS

Dec 01, 2016

This is a License Agreement between Chandra Taposeea ("You") and Geological Society of America ("Geological Society of America") provided by Copyright Clearance Center ("CCC"). The license consists of your order details, the terms and conditions provided by Geological Society of America, and the payment terms and conditions.

All payments must be made in full to CCC. For payment instructions, please see information listed at the bottom of this form.

License Number	4000410066435
License date	Dec 01, 2016
Licensed content publisher	Geological Society of America
Licensed content title	Geology
Licensed content date	Jan 1, 1973
Type of Use	Thesis/Dissertation
Requestor type	Academic institution
Format	Print, Electronic
Portion	chart/graph/table/figure
Number of charts/graphs/tables/figures	1
Title or numeric reference of the portion(s)	Fig. 2
Title of the article or chapter the portion is from	The lithospheric structure of Pangea
Editor of portion(s)	N/A
Author of portion(s)	Dan McKenzie, Michael C. Daly, and Keith Priestley
Volume of serial or monograph.	43
Page range of the portion	783-786
Publication date of portion	2015
Rights for	Main product
Duration of use	Life of current and all future editions

JOHN WILEY AND SONS LICENSE TERMS AND CONDITIONS

Dec 01, 2016

This Agreement between Chandra Taposeea ("You") and John Wiley and Sons ("John Wiley and Sons") consists of your license details and the terms and conditions provided by John Wiley and Sons and Copyright Clearance Center.

License Number	4000420618852
License date	Dec 01, 2016
Licensed Content Publisher	John Wiley and Sons
Licensed Content Publication	Tectonics
Licensed Content Title	Constraining South Atlantic growth with seafloor spreading data
Licensed Content Author	Lucía Pérez-Díaz,Graeme Eagles
Licensed Content Date	Sep 30, 2014
Licensed Content Pages	26
Type of use	Dissertation/Thesis
Requestor type	University/Academic
Format	Print and electronic
Portion	Figure/table
Number of figures/tables	1
Original Wiley figure/table number(s)	Fig. 1
Will you be translating?	No
Title of your thesis / dissertation	Numerical modelling of the continental break-up of the southern South Atlantic
Expected completion date	Jan 2017
Expected size (number of pages)	230

JOHN WILEY AND SONS LICENSE TERMS AND CONDITIONS

Dec 01, 2016

This Agreement between Chandra Taposeea ("You") and John Wiley and Sons ("John Wiley and Sons") consists of your license details and the terms and conditions provided by John Wiley and Sons and Copyright Clearance Center.

License Number	4000410231161
License date	Dec 01, 2016
Licensed Content Publisher	John Wiley and Sons
Licensed Content Publication	Journal of Geophysical Research: Solid Earth
Licensed Content Title	The Mesozoic South Atlantic Ocean and evolution of its continental margins
Licensed Content Author	Philip D. Rabinowitz,John LaBrecque
Licensed Content Date	Oct 10, 1979
Licensed Content Pages	30
Type of use	Dissertation/Thesis
Requestor type	University/Academic
Format	Print and electronic
Portion	Figure/table
Number of figures/tables	2
Original Wiley figure/table number(s)	Fig. 1, 2
Will you be translating?	No
Title of your thesis / dissertation	Numerical modelling of the continental break-up of the southern South Atlantic
Expected completion date	Jan 2017
Expected size (number of pages)	230

ELSEVIER LICENSE
TERMS AND CONDITIONS

Dec 01, 2016

This Agreement between Chandra Taposeea ("You") and Elsevier ("Elsevier") consists of your license details and the terms and conditions provided by Elsevier and Copyright Clearance Center.

License Number	4000410655574
License date	Dec 01, 2016
Licensed Content Publisher	Elsevier
Licensed Content Publication	Tectonophysics
Licensed Content Title	The structure of the lower crust at the Argentine continental margin, South Atlantic at 44°S
Licensed Content Author	Michael Schnabel,Dieter Franke,Martin Engels,Karl Hinz,Sönke Neben,Volkmar Damm,Stefan Grassmann,Hugo Pelliza,Paulo Ricardo Dos Santos
Licensed Content Date	27 June 2008
Licensed Content Volume Number	454
Licensed Content Issue Number	1-4
Licensed Content Pages	9
Start Page	14
End Page	22
Type of Use	reuse in a thesis/dissertation
Intended publisher of new work	other
Portion	figures/tables/illustrations
Number of figures/tables/illustrations	3
Format	both print and electronic
Are you the author of this Elsevier article?	No
Will you be translating?	No
Order reference number	
Original figure numbers	Fig. 2, 4, 5
Title of your thesis/dissertation	Numerical modelling of the continental break-up of the southern South Atlantic
Expected completion date	Jan 2017
Estimated size (number of pages)	230

JOHN WILEY AND SONS LICENSE
TERMS AND CONDITIONS

Dec 01, 2016

This Agreement between Chandra Taposeea ("You") and John Wiley and Sons ("John Wiley and Sons") consists of your license details and the terms and conditions provided by John Wiley and Sons and Copyright Clearance Center.

License Number	4000411286502
License date	Dec 01, 2016
Licensed Content Publisher	John Wiley and Sons
Licensed Content Publication	Journal of Geophysical Research: Solid Earth
Licensed Content Title	Magmatism at rift zones: The generation of volcanic continental margins and flood basalts
Licensed Content Author	Robert White,Dan McKenzie
Licensed Content Date	Jun 10, 1989
Licensed Content Pages	45
Type of use	Dissertation/Thesis
Requestor type	University/Academic
Format	Print and electronic
Portion	Figure/table
Number of figures/tables	1
Original Wiley figure/table number(s)	Fig. 8
Will you be translating?	No
Title of your thesis / dissertation	Numerical modelling of the continental break-up of the southern South Atlantic
Expected completion date	Jan 2017
Expected size (number of pages)	230

JOHN WILEY AND SONS LICENSE
TERMS AND CONDITIONS

Dec 01, 2016

This Agreement between Chandra Taposeea ("You") and John Wiley and Sons ("John Wiley and Sons") consists of your license details and the terms and conditions provided by John Wiley and Sons and Copyright Clearance Center.

License Number	4000411441941
License date	Dec 01, 2016
Licensed Content Publisher	John Wiley and Sons
Licensed Content Publication	Tectonics
Licensed Content Title	Accurate measurements of residual topography from the oceanic realm
Licensed Content Author	Jeffrey Winterbourne,Nicky White,Alistair Crosby
Licensed Content Date	Jun 10, 2014
Licensed Content Pages	34
Type of use	Dissertation/Thesis
Requestor type	University/Academic
Format	Print and electronic
Portion	Figure/table
Number of figures/tables	1
Original Wiley figure/table number(s)	Fig. A1
Will you be translating?	No
Title of your thesis / dissertation	Numerical modelling of the continental break-up of the southern South Atlantic
Expected completion date	Jan 2017
Expected size (number of pages)	230

Appendix D

The following pages are from

Taposeea et al. (2016): *Asthenosphere and lithosphere structure controls on early onset oceanic crust production in the southern South Atlantic*, Tectonophysics, http://dx.doi.org/10.1016/j.tecto.2016.06.026

Tectonophysics xxx (2016) xxx–xxx

Contents lists available at ScienceDirect

Tectonophysics

journal homepage: www.elsevier.com/locate/tecto

Asthenosphere and lithosphere structure controls on early onset oceanic crust production in the southern South Atlantic

Chandra A. Taposeea [a,*], John J. Armitage [b], Jenny S. Collier [a]

[a] Department of Earth Science and Engineering, Imperial College London, London, UK
[b] Dynamique des Fluides Géologiques, Institut de Physique du Globe de Paris, Paris, France

ARTICLE INFO

Article history:
Received 29 February 2016
Received in revised form 12 June 2016
Accepted 18 June 2016
Available online xxxx

Keywords:
South Atlantic volcanic margins
Rifting
Volcanic passive margin
Melt generation
2D viscous modelling

ABSTRACT

The southern South Atlantic has often been considered a classic example of continental break-up in the presence of a starting mantle plume. Evidence for a mantle plume includes the Paranà-Etendeka continental flood basalts, which are associated with the Rio Grande Rise and Walvis Ridge, and the wide-spread presence of seaward dipping reflectors and high-velocity lower-crustal bodies along the conjugate margins. Observations from seaward dipping reflector distributions suggested that lithospheric segmentation played a major role in the pattern of volcanism during break-up in this region, and consequent numerical modelling was used to test this. We tested this hypothesis ourselves by measuring the thickness of the earliest oceanic crust generated. This was done through the use of 37 measurements of initial oceanic crustal thickness from wide-angle and multichannel seismic profiles collected along the conjugate margins. These measurements show that at 450 km south of the Paranà-Etendeka flood basalts the oceanic crust is thicker than the global average at 11.7 km. Farther south the oceanic crust thins, reaching 6.1 km at a distance of 2300 km along-strike. Overall, the along-strike trend of oceanic crustal thickness is linear with a regression coefficient of 0.7 and little indication of segmentation. From numerical models representing extension of the lithosphere, we find that observed melt volumes are matched with the presence of a hot layer. If we assume this region of hot mantle has a thickness of 100 km, its excess temperature relative to the asthenosphere has to decrease from 200 to 50 °C, north to south. This decrease in temperature, also seen in published thermobarometry results, suggests that temperature was the primary control of volcanism during the opening of the southern South Atlantic.

© 2016 Published by Elsevier B.V.

1. Introduction

Rifting and magmatism are fundamental geological processes that shape the surface of our planet. A relationship between the two is acknowledged, but its precise nature is still not fully understood. White and McKenzie (1989) were among the first to observe a variability in the volume of volcanism during continental break-up world-wide. From a simple 1-D model of lithosphere extension, they concluded that initial lithosphere thickness had little influence on this variability. As a result, mantle temperature was considered as the most influential control on volcanism and the source of increased temperature was suggested to be mantle plumes (White and McKenzie, 1989; White and McKenzie, 1995; Storey, 1995). According to this model, a starting mantle plume impinges the rheological barrier of the lithosphere-asthenosphere boundary, causing its head to flatten and spread into a disk with a diameter of 2000–2500 km (Griffiths and Campbell, 1990, 1991). It is assumed that the highest temperatures are found at the plume axis, with the hot conduit of material supplying this central area, and a reduction in temperature towards the fringes of the plume head (Campbell, 2007). In the North Atlantic, the spread of the mantle plume head is represented by the volcanic passive margins, seen north and south of the Greenland-Iceland-Faeroe aseismic ridges (White and McKenzie, 1989), with a systematic reduction in volcanism along-strike (Holbrook et al., 2001; Collier et al., 2009). Later workers proposed more complicated shapes than the classic "mushroom head" geometry (Houseman, 1990), and that sublithospheric bathymetry, forming an 'upside-down drainage pattern', can have a profound effect on the lateral flow of plume material (Sleep, 1996, 2006).

The validity of temperature as the main control over the degree of volcanism has been questioned by many authors. This work suggests that volcanism during break-up can be strongly influenced by other factors. Previous rift history, initial lithosphere thickness, and possibly even sedimentation, can alter the melting characteristics during margin formation (e.g. Hopper et al., 1992; Lizarralde et al., 2007; Bialas and Buck, 2009; Minshull et al., 2008; Armitage et al., 2010; Buiter and Torsvik, 2014; Fromm et al., 2015). Two contrasting examples are found in the North Atlantic and north-west Indian Ocean pertaining to previous rift history and initial lithosphere thickness. In the North Atlantic, extension before rifting caused a focused upwelling, enhancing melt

* Corresponding author.
E-mail address: chandra.taposeea07@imperial.ac.uk (C.A. Taposeea).

http://dx.doi.org/10.1016/j.tecto.2016.06.026
0040-1951/© 2016 Published by Elsevier B.V.

Please cite this article as: Taposeea, C.A., et al., Asthenosphere and lithosphere structure controls on early onset oceanic crust production in the southern South Atlantic, Tectonophysics (2016), http://dx.doi.org/10.1016/j.tecto.2016.06.026

generation. If this previous extension had not occurred, the thermal anomaly would have been held beneath a 125 km thick lithosphere and not produced ocean crust 17 km thick (Armitage et al., 2010). In opposition to this, in the Indian Ocean, a previous extension event had the opposite effect, causing the mantle thermal anomaly to exhaust with reduced melt generation represented by ocean crust only 5.2 km thick (Armitage et al., 2010). As an alternative to the "mantle plume-volcanic margin" association, lithospheric structure can therefore be considered a major factor.

In the South Atlantic, the association between mantle plumes and volcanic margins has also been challenged. Unlike in the North Atlantic, no systematic increase towards the starting plume was observed within the extent and volumes of seaward dipping reflectors (SDRs) (Franke et al., 2007). Instead it was suggested that the lithospheric segment boundaries act as rift-propagation barriers to convecting asthenospheric mantle material, resulting in enhancing and focusing volcanic activity south of these zones (Koopmann et al., 2014a). The increased melting resulted in increased SDR thicknesses and volumes (Franke et al., 2007; Koopmann et al., 2014a,b, Fig. S1). In numerical models, a lateral pressure gradient between sequentially opening segments causes a rift-parallel flow, with consequent elevation in temperature at segment boundaries. The modelling results show increased decompression melting relative to the interior of the segments (Koopmann et al., 2014a). Thus, segmentation is suggested to be an influential control of volcanism in this region.

Here we investigate the primary cause of along-strike variation of volcanism in the South Atlantic by compiling measurements of initial oceanic crustal thickness and testing the influence of temperature and segmentation. Initial oceanic crust provides an independent test of melt volumes previously inferred from syn-rift magmatism, consisting of SDRs and high-velocity lower-crustal intrusions (underplating). The ocean crust thickness represents a 'snapshot' of the asthenosphere conditions immediately post break-up, and can hence be used as a proxy for temperature. To test the primary cause of along-strike variation, we first map the thickness of early onset oceanic crust, and then match these observations to numerical model predictions of volcanism to explore the controls on magmatism within this region.

2. Geological SETTING

The break-up of West Gondwana during the Cretaceous to form the South Atlantic (Fig. 1) is commonly associated with the arrival of the Tristan Plume (White and McKenzie, 1989; O'Connor and Duncan, 1990; Renne et al., 1992; Campbell, 2007). The region is often regarded as a classic example of the association between continental break-up with onshore flood basalt provinces, volcanic aseismic ridges and an active volcanic island. The modern-day volcanic island of Tristan da Cunha is spatially and temporally linked via the Rio Grande Rise and Walvis Ridge to the Paranà-Etendeka traps in Brazil and Namibia respectively (Figs. 1a and 2a). The continental margins also display voluminous SDRs and high-velocity lower-continental crustal bodies (Hinz, 1981; Hinz et al., 1988; Gladczenko et al., 1998; Bauer et al., 2000; Franke et al., 2007; Schnabel et al., 2008; Hirsch et al., 2009; Becker et al., 2014).

There are however several departures from the classic starting plume model. Among them is the asymmetry between the Rio Grande Rise and Walvis Ridge, which has been explained by plume drift from the mid-ocean ridge to the African plate around 80 Ma (e.g. O'Connor and Duncan, 1990). This stopped the 'feed' to the Rio Grande Rise, causing the aseismic ridge to terminate production on the South American plate (White and McKenzie, 1989; O'Connor and Duncan, 1990). The Walvis Ridge continued to form, and is traced to the volcano still active today on the Tristan da Cunha island (White and McKenzie, 1989;

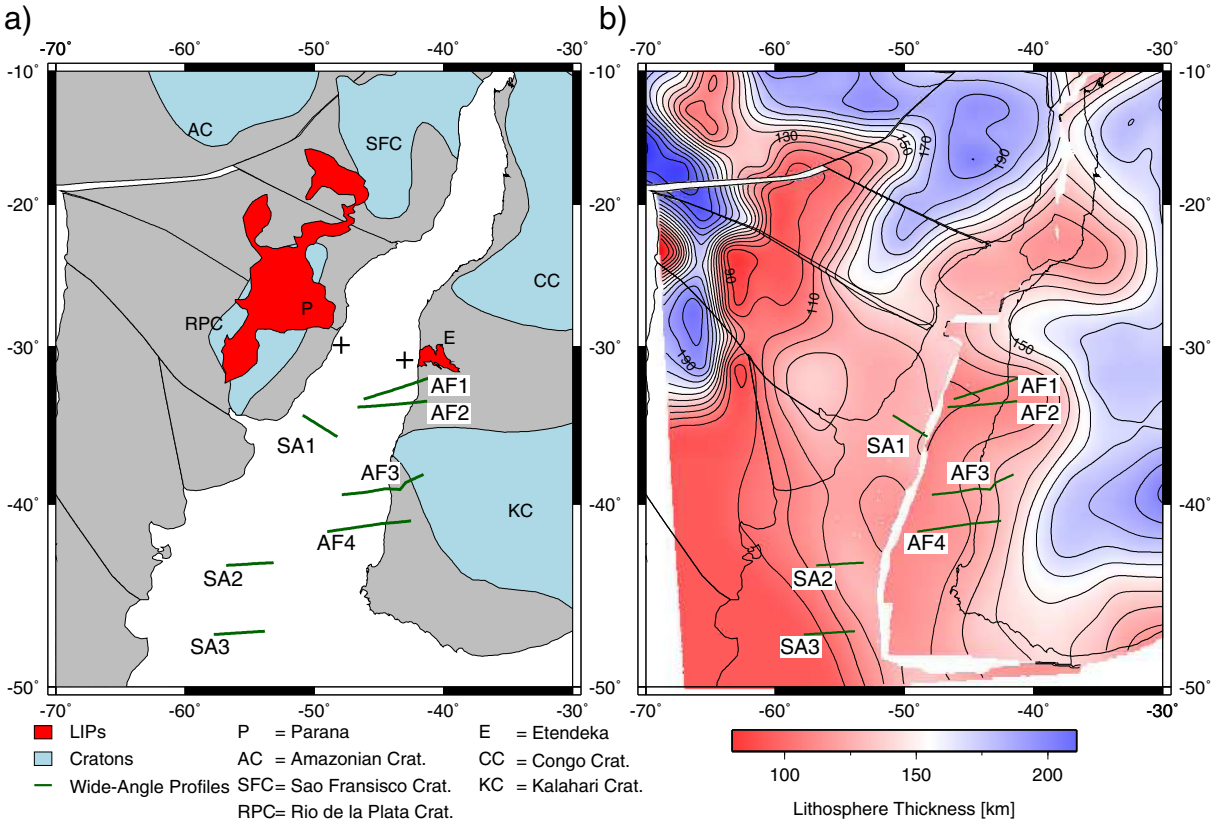


Fig. 1. Reconstructions using GPlates shown at 121 Ma using rotation poles of Moulin et al. (2010) with the sub-plates of South America (thin black lines). (a) Reconstruction showing the major geological features. The positions of cratons are from Gubanov and Mooney (2009), the location of the Etendeka-Paraná flood basalts is Coffin and Eldholm (1994). The seven wide angle seismic profiles used in this study are labelled AF1 to AF4 and SA1 to SA3. The '+' marks the reconstructed landfall of the Rio Grande Rise and Walvis Ridge. (b) Reconstruction of lithosphere thickness using the data set of Priestley and McKenzie (2006), the latter covering the whole area.

Please cite this article as: Taposeea, C.A., et al., Asthenosphere and lithosphere structure controls on early onset oceanic crust production in the southern South Atlantic, Tectonophysics (2016), http://dx.doi.org/10.1016/j.tecto.2016.06.026

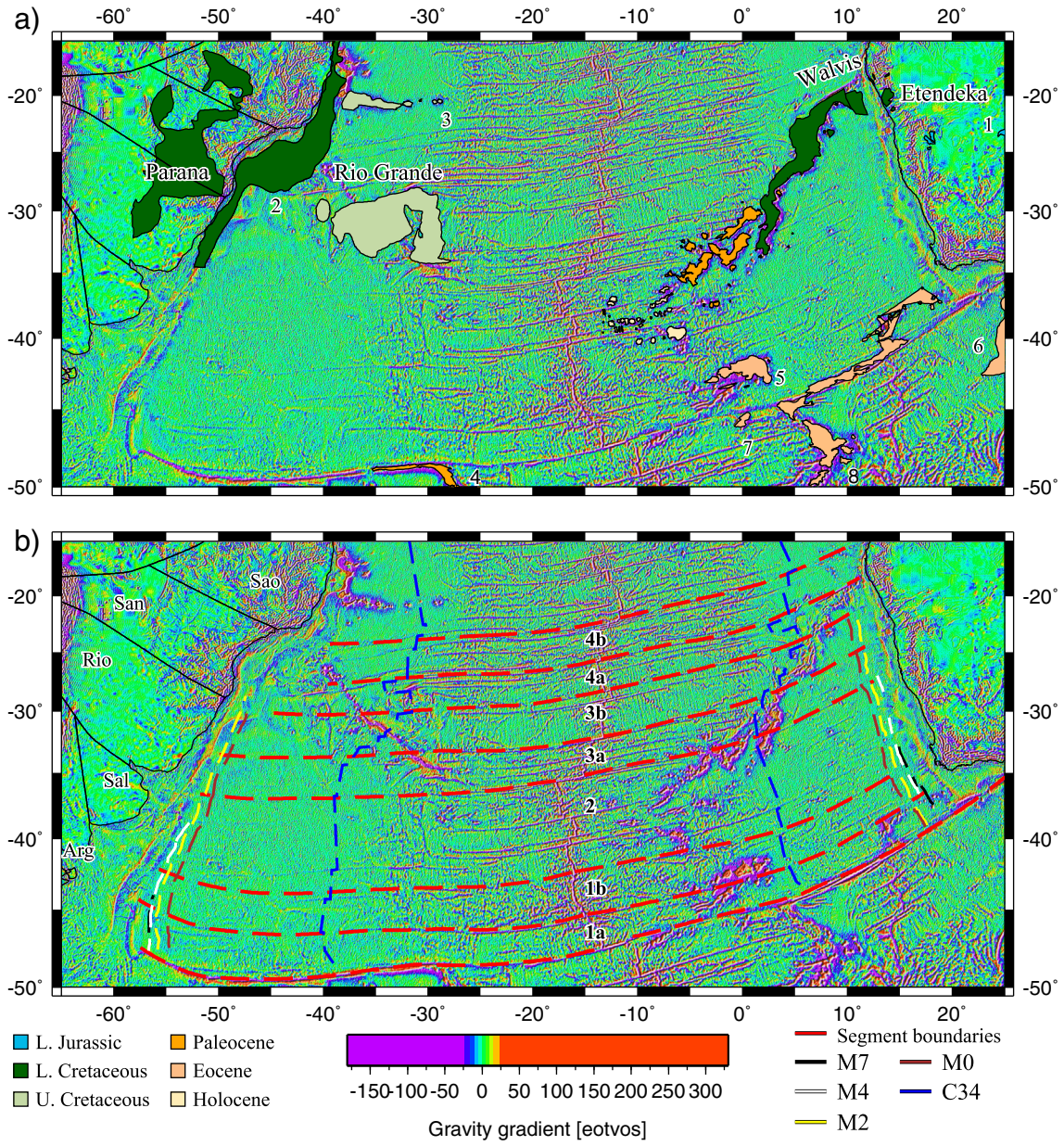


Fig. 2. Map of the gravity gradient from Sandwell et al. (2013) for our study area. (a) Main tectonic features with age progressive LIPs (Coffin and Eldholm, 1994): 1 = Karoo, 2 = Sao Paolo, 3 = Vitoria-Trinidade, 4 = Falkland 5 = Discovery, 6 = Agulhas Plateau, 7 = Hardman volcano, and 8 = Meteor Ridge. Also shown are the sub-plate boundaries (thin black lines) from Moulin et al. (2010). (b) Interpreted location of the major segment boundaries. We identify 4 major segments (numbered 1–4) consistent with the sub-plate boundaries of South America from Moulin et al. (2010). Also shown are sea floor spreading magnetic anomalies M7, M4, M2 & M0 from Moulin et al. (2010), C34 from Seton et al. (2012). Sub-plates: Arg = Argentina, Sal = Salado, Rio = Rio de la Plata, San = Santos, Sao = São Francisco. (For interpretation of the references to colour in this figure legend, the reader is referred to the web version of this article.)

O'Connor and Duncan, 1990; O'Connor et al., 2012). An additional observed asymmetry is between the volumes of continental flood basalts, where the Paraná traps are significantly larger than the Etendeka traps, with areas of 1.5 million km ^{2} (Courtillot et al., 1999; Peate, 1997) and 80,000 km ^{2} (Erlank et al., 1984) respectively. It has been suggested that the disparity between the Paraná-Etendeka traps could be the result of the topographical profile of the base of the lithosphere, causing an asymmetry in ponded plume material (Fromm et al., 2015; Sleep, 2006). The margin likewise has an asymmetric distribution in volcanism from north to south. South of the Rio Grande Rise and Walvis Ridge, the conjugate margins are volcanic with an abundance of SDRs. North of the Ridges, the conjugate margins are magma-poor and lack SDRs (Contrucci et al., 2004; Aslanian et al., 2009; Reston, 2010). This does not fit with the classic plume model, where the plume head would flatten with an axisymmetric geometry, and the presence of volcanism would be expected both north and south of the Rio Grande Rise and Walvis Ridge.

The duration of the continental flood basalts is debated. From 39Ar/40Ar dating and paleomagnetic results, Renne et al. (1992) concluded that the eruption of the Paranà occurred at 133 ± 1 Ma in a time frame of less than a million years, in agreement with Bellieni et al. (1983) and Hawkesworth et al. (1992). However, it is believed these previous samples did not represent the province as a whole (Peate et al., 1992). Turner et al. (1994) showed by using laser spot Ar-Ar analyses evidence of the eruption lasting for ~10 Myr, between 137 Ma and 127 Ma (Turner et al., 1994; Stewart et al., 1996). From recent magnetostratigraphy studies for the Etendeka portion of the large igneous province, the Tristan Plume

Please cite this article as: Taposeea, C.A., et al., Asthenosphere and lithosphere structure controls on early onset oceanic crust production in the southern South Atlantic, Tectonophysics (2016), http://dx.doi.org/10.1016/j.tecto.2016.06.026

is suggested to be already present by at least magnetic isochron M15n (Dodd et al., 2015), dated 135.96 Ma by Gee and Kent (2007).

The South Atlantic opened in a south to north unzipping fashion, with break-up happening in stages. Moulin et al. (2010) summarised the break-up by sub-plate, with five in our study area, the São Francisco, Santos, Rio de la Plata, Argentina, and Salado blocks, where the movement is fixed relative to the African plate. The sub-plates movements are timed according to sea floor magnetic isochrons M7, M4, M2 and M0 (127.23 Ma, 126.57 Ma, 124.05 Ma and 120.6 Ma respectively, locations in Fig. 2). Towards the south of our study area, there is evidence the Salado and Argentina sub-plates had started to move westward relative to the African plate prior to magnetic isochron M7. Between M7 and M4, the Rio de la Plata sub-plate moved westward, allowing the opening of the northern part of our study area. Following M2, the Rio de la Plata, Salado and Argentina sub-plates moved as one, and movement of the Santos plate also commenced. North of the Rio Grande Fracture Zone the timing of the Atlantic initiation is less well constrained as it occurred within the Cretaceous Magnetic Quiet Zone (CMQZ), ~121–83 Ma (Gee and Kent, 2007). Compared to the ages of the Paranà-Etendeka continental flood basalts, the timing of the first magnetic isochrons (M4 and M7) recognised on the conjugate margins in the south of our study area suggests the presence of an elevated mantle temperature prior to break-up.

Like most continental margins, the southern South Atlantic has clear segmentation present along-strike. The continents of South America and Africa contain areas of structural weakness, which are inferred to have influenced continental break-up and initial sea floor spreading (Rosendahl, 1987; Clemson et al., 1997, 1999; Jungslager, 1999; Franke et al., 2007). Franke et al. (2007) and Koopmann et al. (2014b) presented four major transfer zones in the South American and African margins respectively, linked to the Proterozoic mobile fold belts found on adjacent continents. Seen from observations of increasing volumes of SDRs towards segment boundaries (Fig. S1), they proposed that increased magmatism towards these zones is due to increased decompression melting. Franke et al. (2007) and Koopmann et al. (2014b) both suggested that segmentation has a high influence on magmatism in the South Atlantic region, seeing no systematic increase in SDR volumes towards the Rio Grande Rise and Walvis Ridge.

3. Methodology

3.1. Tectonic framework: along-strike variability

We analysed the spatial variation of the thickness of initial oceanic crust for our study area. In order to compare the data from conjugate margins, we assessed the current plate reconstruction models. We investigated in detail the models of Torsvik et al. (2009), Moulin et al. (2010) and Heine et al. (2013). Using the GPlates software package, we combined these reconstructions with the most-recent satellite gravity and magnetic data sets (Sandwell et al., 2013; Maus et al., 2007). From the reconstructed gravity and magnetic data, we concluded that within our study area the magnetic isochrons correlated best with the Moulin et al. (2010) plate reconstruction (Fig. 1). Using this framework, we then measured distance along-strike relative to the reconstructed locations for the Rio Grande Rise and Walvis Ridge respectively (shown by the two '+' symbols in Fig. 1).

To map the lithospheric segment boundaries, we started with those identified by Franke et al. (2007) on the South American margin and Koopmann et al. (2014b) on the African margin, both largely defined by continental structural variations (Fig. S1). We then independently picked the locations of the major fracture zones from the satellite gravity and magnetic data sets (Sandwell et al., 2013; Maus et al., 2009) and tested for conjugate symmetry using GPlates, making small refinements to the boundary locations. Within our study area, the Moulin et al. (2010) model has five sub-plates forming part of the South American continent (São Francisco, Santos, Rio de la Plata, Argentina, and Salado blocks, Fig. 2), with a single sub-plate forming part of Africa (Austral block). The sub-plate boundaries on the South American margins are used to define our 'first-order segments', numbered 1–4. These sub-plates boundaries also coincide with major fracture zones (defined as having a minimum offset of 50 km at the modern ridge axis), craton locations (Gubanov and Mooney, 2009), and other onshore zones of weakness (Moulin et al., 2010; Heine et al., 2013). In addition, we recognised 'second-order segments' that show clear fracture zone traces on conjugate sides, numbered alphabetically (e.g. Segments 3b & 3a).

3.2. Initial oceanic crustal thickness

To explore the thermal structure of our study area immediately post break-up, the thickness of the first oceanic crust generated was used as a proxy for melt production. To measure this thickness, we compiled wide-angle and multichannel seismic reflection (MCS) profile data within our study area. In total we sourced 37 profiles, consisting of 7 wide-angle profiles and 30 MCS profiles. The wide-angle profiles are distributed across both the conjugate margins and along-strike, with 4 on the African side (AF1–4) and 3 on the South American side (SA1–3; Bauer et al., 2000; Schinkel, 2006; Hirsch et al., 2009; Becker et al., 2014; Schnabel et al., 2008; see Table 1). The MCS data was limited to the South American margin, as we required that these seismic lines imaged both the top basement and the Moho. We used ten MCS published sections from Hinz et al. (1999) and Franke et al. (2007, 2010) (Fig. 4). Six additional MCS profiles (Fig. 4 and S7) were from Winterbourne et al. (2014), which originate from a mixture of unpublished seismic industry data and published seismic data. Finally, we used fourteen lines of unpublished, industry, high quality seismic reflection survey lines from the BasinSPAN acquisition project of ION Geophysical.

In order to obtain a consistent indication of melt production along-strike, we measured the thickness of oceanic crust on each profile using a criterion known as Landward Limit of Oceanic Crust (LaLOC). The LaLOC is defined as the 'boundary which delimits relatively homogeneous oceanic crust ocean-ward from either extended continental crust or exhumed continental lithospheric mantle landward or Seaward Dipping Reflectors (SDRs), where an interpretation of the Moho and/or the extent of continental crust is not possible' (Heine et al., 2013).

A combination of magnetic and seismic characteristics was used to locate the LaLOC. Firstly, in our study area, magnetic isochrons M2 and M0 (Fig. 2) are generally recognised as sea floor-spreading being underway (Moulin et al., 2010). Secondly, the SDRs, which are relatively well-imaged on all lines, are normally located landward of the oldest oceanic crust. On wide-angle profiles, high P-wave velocity bodies in the lower crust (underplating), typically with values >7.0 km s^{-1} (Becker et al., 2014; Trumbull et al., 2015), are taken to indicate the presence of highly intruded stretched continental or transitional crust. Hence, the LaLOC must be seaward of all underplating observed on wide-angle seismic profiles. As an additional check, we extracted depth-V_p profiles from the wide-angle models and tested for the presence of oceanic, stretched transitional or continental crust. We used the V_p limits from White et al. (1992) to define mature oceanic crust. Using this extra criterion, the LaLOC can coincide with overlying SDRs when supported by evidence. Finally, we considered the reflectivity character, with true ocean crust typically being devoid of internal reflectivity and showing a recognisable 'bumpy surface', as an indication of the presence of pillow lavas (Fig. S3–S6).

An example of our identification of the LaLOC location is given for wide-angle profile AF2 in Fig. 3. Underplating for this profile is characterised with a V_p >7.15 km s^{-1}, and we present 3 possible LaLOC locations seaward of this velocity body, representing a degree of uncertainty for initial oceanic crustal thicknesses (Fig. 3a). They are found near magnetic isochron M4 (Moulin et al., 2010), and as this coincides with SDRs, we tested the depth-V_p profiles for the seismic velocity boundaries of mature oceanic crust (White et al., 1992). This allowed us to locate the initial production point for oceanic crust (Fig. 3b) and

Please cite this article as: Taposeea, C.A., et al., Asthenosphere and lithosphere structure controls on early onset oceanic crust production in the southern South Atlantic, Tectonophysics (2016), http://dx.doi.org/10.1016/j.tecto.2016.06.026

Table 1
Crustal thickness measurements at the LaLOC for all seismic sections used in this study. The sections themselves are reproduced in the supplement (Fig. S2–S7). Distance along-strike refers to the location of the LaLOC relative to the commencement of the Rio Grande Rise and Walvis Ridge, marked with '+' in Fig. 1. Uncertainties in the measured oceanic crustal thickness are found in Table S1.

Profile Name	Reference	Long.	Lat.	Distance along- strike (km)	Thickness (TWTT s)	Thickness (km)
AF1	Bauer et al., 2000	11.9	−23.8	450	n/a	11.7
AF2	Bauer et al., 2000	12.1	−24.6	538	n/a	8.2
AF3	Schinkel, 2006	13.8	−30.1	1174	n/a	7.2
AF4	Hirsch et al., 2009	14.6	−32.3	1422	n/a	7
SA1	Becker et al., 2014	−51.6	−35.4	922	n/a	8.2
SA2	Schnabel et al., 2008	−56.6	−43.5	1895	n/a	7.8
SA3	Becker et al., 2014	−58.1	−47.2	2288	n/a	6.9
BGR87–01	Hinz et al., 1999	−52.6	−37.9	1197	2.26	7.6
BGR98–18	Franke et al., 2010	−55.8	−43.4	1844	2.23	7.4
BGR98–07	Franke et al., 2010	−55.9	−43.8	1884	2.30	7.7
BGR98–20	Franke et al., 2010	−56.5	−44.0	1931	2.27	7.6
BGR98–01	Franke et al., 2007	−53.6	−40.0	1439	2.16	7.2
BGR98–41	Franke et al., 2007	−55.2	−42.1	1697	2.12	7.1
BGR98–15	Franke et al., 2007	−55.6	−42.7	1774	2.06	6.9
BGR98–05	Franke et al., 2007	−55.7	−43.3	1829	2.32	7.8
BGR98–22	Franke et al., 2007	−56.8	−44.4	1982	2.05	6.9
BGR04–08/13	Franke et al., 2007	−56.7	−47.5	2263	1.80	6.0
Profile 300	Winterbourne et al., 2014	−49.6	−32.6	593	n/a	7.7
Profile 231	Winterbourne et al., 2014	−53.3	−39.6	1380	n/a	5.9
Profile 233	Winterbourne et al., 2014	−54.8	−41.0	1578	n/a	8.4
Profile 230	Winterbourne et al., 2014	−54.5	−41.3	1595	n/a	6.8
Profile 229	Winterbourne et al., 2014	−57.2	−46.7	2210	n/a	5.1
Profile 232	Winterbourne et al., 2014	−57.3	−47.3	2261	n/a	5.1
PS1–0090	ION Geophysical	−46.5	−31.3	262	2.94	9.9
PS1–0070	ION Geophysical	−48.2	−31.5	405	2.87	9.6
PS1–0060	ION Geophysical	−48.8	−32.0	488	3.35	11.2
PS1–0040	ION Geophysical	−49.7	−32.9	609	3.24	10.9
PS1–0030	ION Geophysical	−48.9	−34.6	695	2.17	7.3
PS1–0010	ION Geophysical	−50.7	−35.0	828	2.55	8.5
UY1–4700	ION Geophysical	−51.2	−35.6	911	2.18	7.3
UY1–4500	ION Geophysical	−51.6	−36.3	992	2.39	8.0
UY1–4300	ION Geophysical	−51.9	−37.1	1076	2.36	7.9
UY1–4000	ION Geophysical	−52.4	−37.9	1176	2.25	7.5
AR1–3800	ION Geophysical	−52.8	−38.2	1220	2.54	8.5
AR1–3500	ION Geophysical	−53.5	−39.5	1369	2.73	9.1
AR1–3000	ION Geophysical	−54.4	−41.4	1583	1.93	6.4
AR1–2600	ION Geophysical	−55.9	−42.5	1760	2.89	9.7

verify we are not in transitional crust. This process was followed for all of the wide-angle profile (Fig. S2).

In order to ensure consistency between oceanic crust thickness measurements at the LaLOC made from MCS profiles, all measurements were performed on time sections (Fig. 4). These were then converted to distance using a mean V_p value for oceanic crust of 6.7 km s^{-1} (White et al., 1992). White et al. (1992) found 90% of the ocean crust velocity estimates fall within a range of 6.4–7.0 km s^{-1}, representing a ±0.45 km error for a crustal thickness of 10 km.

The majority of the available seismic profiles stop soon after the LaLOC as they were collected to study the continent-ocean transition. The ION Geophysical lines however extend up to ~660 km into oceanic crust. This allowed us to measure the age trend of oceanic crustal production in the north of our study area (Fig. 2). To map the oceanic crust thickness to sea floor age, we used the Gee and Kent (2007) time scale and Moulin et al. (2010) magnetic isochrons for our study area. This allowed for distance along the profile to be converted to age, and subsequently we averaged the thickness into 1.5 Myr bins.

3.3. Numerical modelling

To better our understanding of our study area's initial break-up conditions, we use a 2D viscous model of the upper mantle to simulate continental break-up. The numerical model, based on CitCom (Moresi et al., 1996), is a finite element code designed to solve incompressible thermochemical convection problems relevant to the Earth's mantle. It is a fluid dynamic model capable of handling large viscosity contrasts where Stokes equations are solved in a fixed Cartesian domain (Moresi et al., 1996). This model was modified by Nielsen and Hopper (2004) to include melt production due to decompression melting. Equations are solved in 2D, using the Boussinesq approximation with the understanding that (1) density variations are sufficiently small that they only affect gravitational forces and (2) effect on mantle density due to mass transfer during melting is small (Cordery and Morgan, 1993). The model is set up with a non-Newtonian dislocation creep as described in Appendix A.

The model space is represented by a domain 2800 km wide, 700 km deep, with 256 × 256 elements (Fig. 5). An increased resolution of 512 × 512 elements was tested by Nielsen and Hopper (2004), however the differences in predicted crustal thicknesses were in the order of a few percent, so the less computationally expensive resolution was used. The initial lithosphere is assumed to be melt depleted and therefore compositionally buoyant relative to the asthenosphere. A hot layer is introduced, simulating the presence of an impacted plume head at the lithosphere/asthenosphere boundary (Fig. 5). Extension is imposed by a surface velocity boundary condition at a fixed spreading rate, driving the lithosphere apart laterally (see for example Nielsen and Hopper, 2004; Armitage et al., 2010). As the lithosphere extends and thins, material moves upwards leading to decompression melting.Crustal thickness (h_c) is calculated with the assumption that all melt is focused and accreted at the ridge axis using

$$h_c = \frac{2}{u_z}\left(\frac{\rho_m}{\rho_l}\right)\iint_{melt} \dot{m}\,\mathrm{dx}\,\mathrm{dz} \quad (1)$$

where u_z is the mantle flow in the vertical direction, ρ_m is the density of the lithospheric mantle, ρ_l the melt density and $\dot{m}$ is the melt production rate (Ito et al., 1996; Nielsen and Hopper, 2004). Further details of the

Please cite this article as: Taposeea, C.A., et al., Asthenosphere and lithosphere structure controls on early onset oceanic crust production in the southern South Atlantic, Tectonophysics (2016), http://dx.doi.org/10.1016/j.tecto.2016.06.026

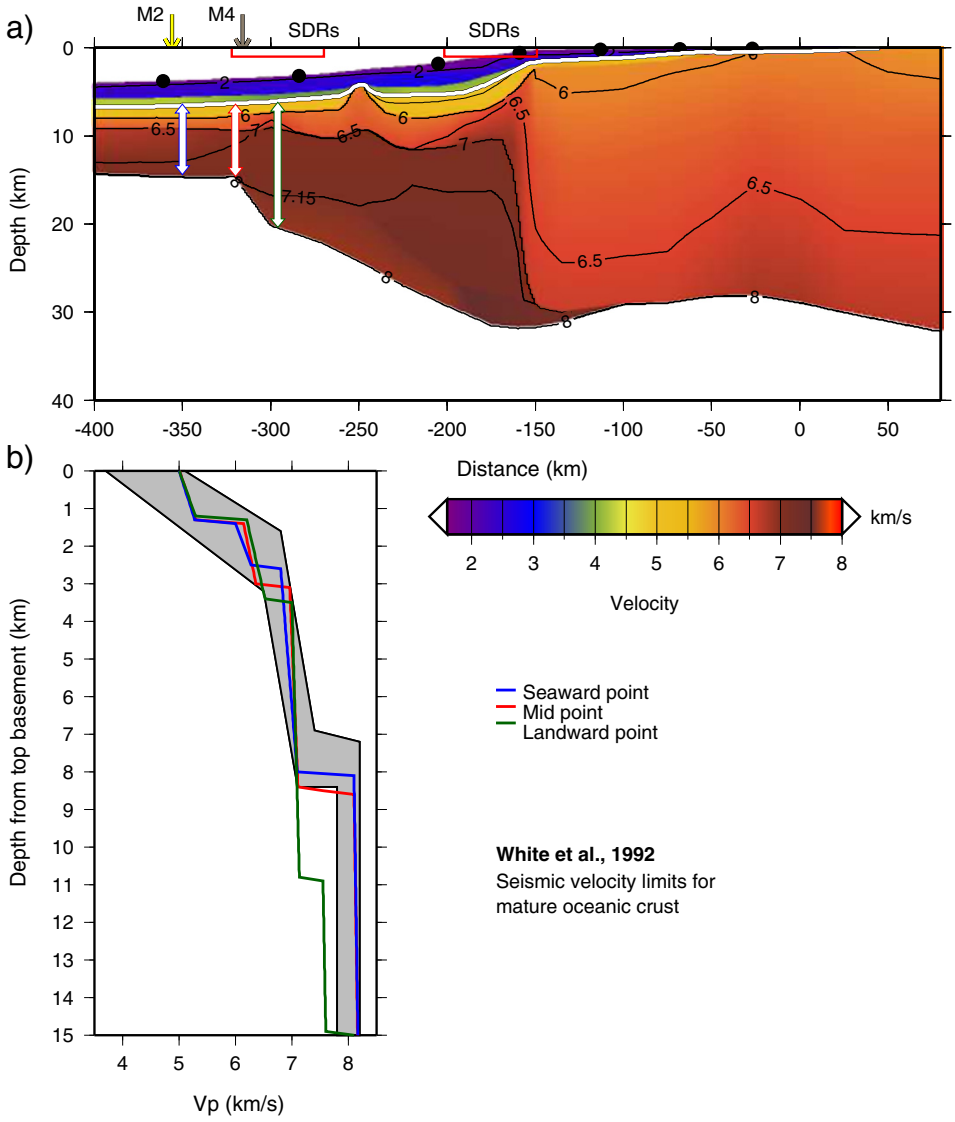


Fig. 3. Example of oceanic crustal thickness measurement at the Landward Limit of Oceanic Crust (LaLOC), using the AF2 seismic velocity profile (Bauer et al., 2000). (a) Depth-V_p profile showing positions of SDRs (red boxes) and OBS locations (black circles) from Bauer et al. (2000), and magnetic anomaly M4 (grey arrow) from Moulin et al. (2010). White arrows are potential locations for LaLOC that are compared to the White et al. (1992) seismic velocity boundaries for mature oceanic crust in part b. (b) Depth-V_p plot for the three test locations for the LaLOC (white arrows) and the seismic velocity limits for mature oceanic crust (grey shading) from White et al. (1992). The mid and seaward points are within the seismic velocity boundaries and can be considered as oceanic. As the LaLOC location is the first instance of ocean crust, the mid point is therefore the LaLOC for AF2. (For interpretation of the references to colour in this figure legend, the reader is referred to the web version of this article.)

model can be found in Appendix A. The sides of the model domain are reflective boundaries, with no lateral flow of heat or material across them (Fig. S9). This is assumed not to affect melt thickness results, as the reflective boundaries (example Fig. S9) are considered to be far enough from the centre of extension (Nielsen and Hopper, 2004).

3.3.1. Understanding model sensitivity

To understand the sensitivities of the model, we started with a simple simulation with a model asthenosphere temperature of 1300 °C, spreading velocity of 12 mm yr^{-1}, and an initial lithosphere thickness of 125 km. In some of the models, we introduced a 100 km thick hot layer as the impacted plume head at the lithosphere/asthenosphere boundary. Three model runs are first demonstrated with no hot layer, a 100 °C hot layer, and a 200 °C hot layer in excess of the model asthenosphere temperature (Fig. 6a). Three main stages of melt production can be seen for the model as the lithosphere thins and is finally broken (Fig. 6a): pre-rift, syn-rift and post-rift. The pre-rift stage is where there is little magmatism and syn-rift is where there is a magmatism peak. There is a clear increase in output magmatism as the hot layer temperature increases, with ~3 times as much for the 200 °C hot layer relative to no hot layer (Fig. 6a). Following the peak magmatism in the syn-rift phase, the post-rift phase represents a shift towards steady-state sea floor spreading (Fig. 6a). The first instance of ocean crust will occur along this decreasing trend, and can be matched to observations of the seismic data.

The evolution of the numerical model from pre-rift to post-rift is a function of the hot layer temperature (Fig. 6a). The hottest model, with a thermal anomaly 200 °C hotter than the model asthenosphere temperature, displays peak melt production ~3 Myr earlier than the equivalent model that has a 100 °C hot thermal anomaly (Fig. 6a). For model runs without a hot layer present, there is no syn-rift peak in magmatism for any of the models. Increasing the model asthenosphere temperature reduces the model duration for the pre-rift phase, and increases the steady-state oceanic crustal thickness (Fig. 6b). Varying the spreading rate likewise affects the duration of pre and syn-rift phases, and ultimately when the post-rift phase is achieved (Fig. 6c). Doubling the rate of extension reduces the pre-rift duration by at least half. A faster spreading rate creates a larger pulse of decompression

Please cite this article as: Taposeea, C.A., et al., Asthenosphere and lithosphere structure controls on early onset oceanic crust production in the southern South Atlantic, Tectonophysics (2016), http://dx.doi.org/10.1016/j.tecto.2016.06.026

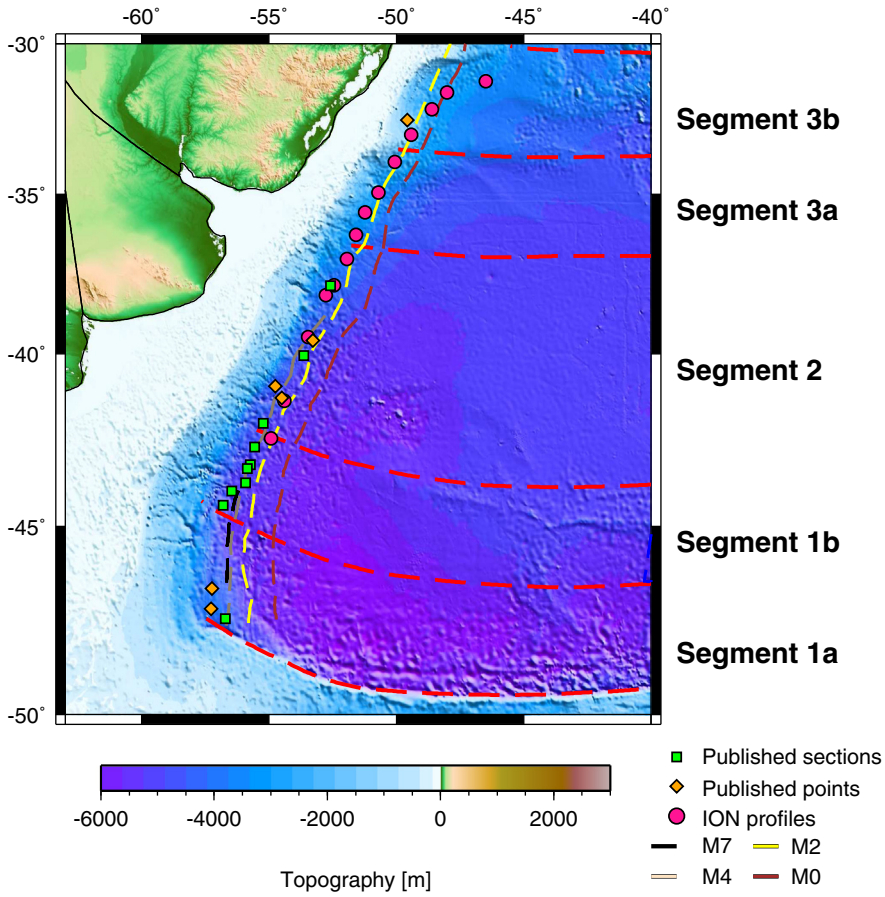


Fig. 4. Map of the Landward Limit of Oceanic Crust (LaLOC) locations for all MCS profiles used in this study (Table 1). Topography and bathymetry is from ETOP01 Armante (2009). The sea floor spreading magnetic anomalies (M0, M2, M4 and M7) and plate boundaries (thin black lines) are from Moulin et al. (2010). The data is divided into three types: (1) published sections from Franke et al. (2007), Franke et al. (2010) and Hinz et al. (1999) (Fig. S3–S6), (2) published points from Winterbourne et al. (2014) (Fig. S7), and (3) ION Geophysical MCS data. (For interpretation of the references to colour in this figure legend, the reader is referred to the web version of this article.)

melting during the syn-rift phase when a hot layer is present, and a slower spreading rate will significantly increase the duration of the pre-rift phase (Fig. 6c). This is because a faster rate of extension causes a greater amount of material to be fluxed through the zone of partial melting (Fig. S9b and c).

To explore how the model that includes a thermal anomaly (e.g. Fig. 6a) evolves for a range of hot layer temperatures (50 to 200 °C) and initial lithosphere thicknesses (100 to 140 km), we plotted the melt thickness at three model times, 10, 15 and 20 Myr (Fig. 7). If the hot layer temperature is 50 °C, then the melt thickness is always

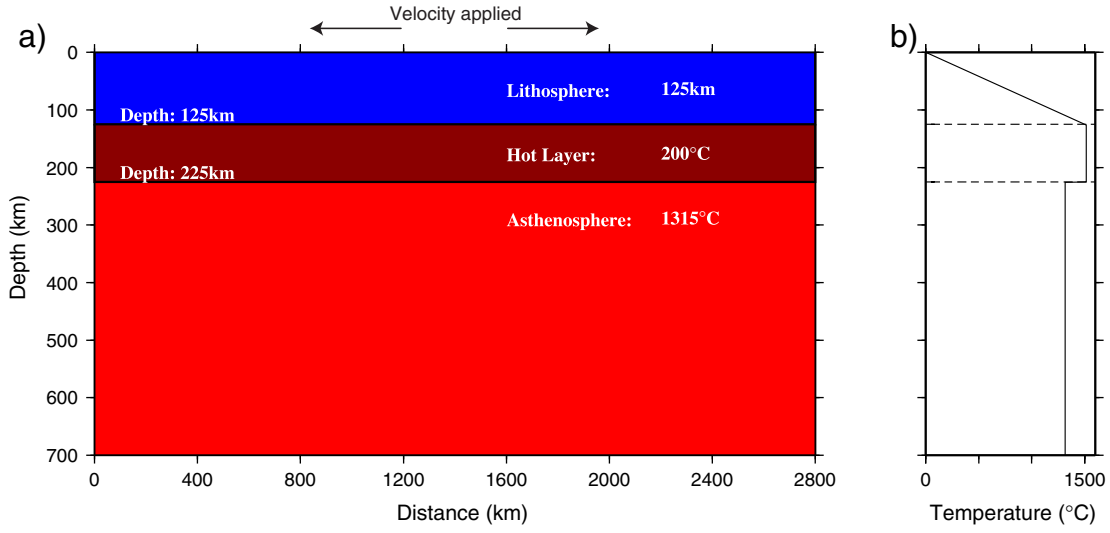


Fig. 5. Example of the initial conditions for the numerical model. (a) Model domain for the 2D simulation. Extension is driven by a divergent velocity boundary condition on the upper surface. The initial lithosphere thickness is within the range of 95 and 140 km, and the hot layer is assumed to have a thickness of 100 km and a temperature of 50 to 200 °C in excess of the model asthenosphere temperature. (b) An example of an initial temperature profile with depth, where in this case the model asthenosphere temperature is 1315 °C and the hot layer has an excess temperature of 200 °C.

Please cite this article as: Taposeea, C.A., et al., Asthenosphere and lithosphere structure controls on early onset oceanic crust production in the southern South Atlantic, Tectonophysics (2016), http://dx.doi.org/10.1016/j.tecto.2016.06.026

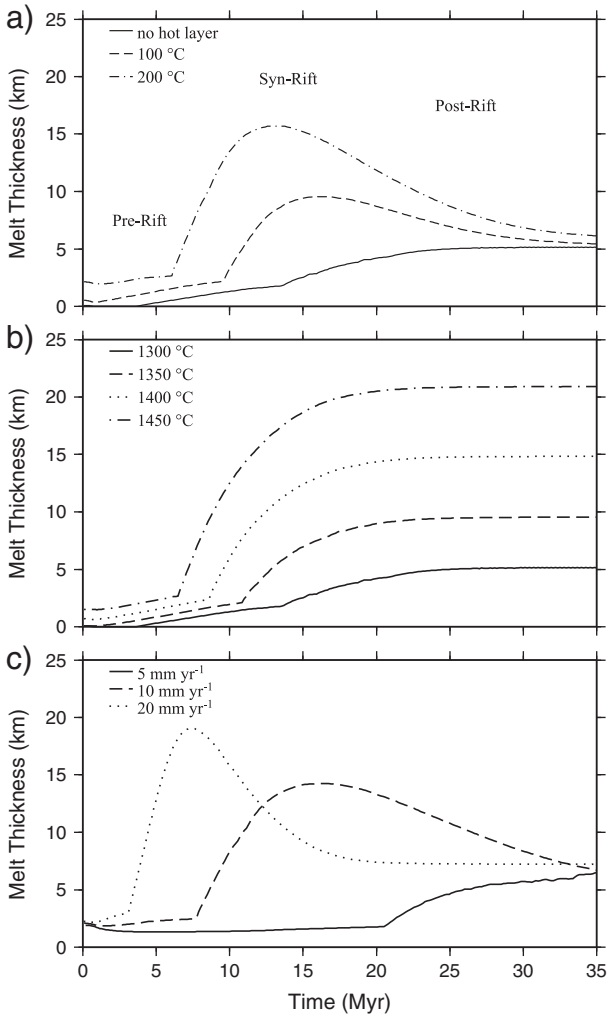


Fig. 6. Base model runs to demonstrate dependence of melt production on initial model parameters. All models have an initial lithosphere thickness of 125 km and spreading rate of 12 mm yr^{-1} unless otherwise specified. (a) Varying hot layer temperatures, with a 1300 °C model asthenosphere temperature. The interpreted location of the pre, syn and post-rift phases are shown. (b) Varying model asthenosphere temperatures. (c) Differing spreading rates with a 1300 °C model asthenosphere temperature and a 200 °C hot layer.

<10 km. Increasing this temperature increases the volume of melt, but the time of maximum melt production is a function of the hot layer temperature (Fig. 6a) and also of the initial lithosphere thickness (Fig. 7). For models with an initial lithosphere thickness of 140 km and hot layer temperatures ≥100 °C, at 10 Myr melting is reduced. However, if the initial lithosphere thickness is 100 km, then by 20 Myr the thermal anomaly is exhausted (Fig. 7). This demonstrates the importance for understanding the timing of initial oceanic crustal thickness, and to constrain the initial lithosphere thickness from the available geophysical evidence.

3.3.2. Initial lithosphere thickness and rate of extension

To reduce the number of unknowns, we assumed that the initial lithospheric thickness and extension rate could be estimated from geophysical observations. The initial lithosphere thickness is estimated from the point at which the available seismic imaging suggests unstretched continental crust to be present. To estimate the lithosphere thickness at this point, we used the tomographic models of Priestley and McKenzie (2006) for the South American side, and Fishwick and Bastow (2011) for the African side (Table 2). We used the Fishwick and Bastow (2011) model for the African side for several reasons. The increased number and distribution of seismic station allows more ray coverage in this region, with Fishwick and Bastow (2011) having a specific focus on Southern Africa (Fishwick, 2010). Although it uses the empirical parameterisations from the Priestley and McKenzie (2006) model, the latter has an automated code and the former employs a semi-automated code, using a manual comparison of multiple inversions for each path (Fishwick, 2010). Through the use of a model based on petrology, mineral physics, gravity anomaly and heat flow, Fernandez et al. (2010) gave an estimate of lithosphere thickness in the Namibia region. Given the different methods and different resolution, the lithosphere thickness model agrees better with the model from Fishwick and Bastow (2011), and therefore consider the latter more reliable in this area (Fig. S10). In order to address the observational uncertainties and differences seen in the two models (Fig. S10), we included simulations with varying initial lithosphere thicknesses (Table 2) to ensure the robustness of our excess model asthenosphere temperature predictions.

The reliability of using present day estimates of lithosphere thickness as a proxy for pre-break-up lithosphere thickness was explored by McKenzie et al. (2015). They presented a map of lithospheric thickness for Pangea, using a reconstruction of continental plates within the Permian, assuming the lithosphere moves with overlying continents. They found a continuity of thicker and thinner lithosphere, for example at the Pan-African orogenic zones and cratons. If lithosphere deformation had occurred since the Permian, there should be no reason for them to fit within a reconstruction of Pangea. We tested this using the rotation poles from Moulin et al. (2010) with the lithospheric grid from Priestley and McKenzie (2006), the latter covering both sides, and likewise found that there was a good correlation between the conjugate sides in terms of lithospheric thickness (Fig. 1b). Hence, we assumed present day values could be used as a parameter for initial lithosphere thickness within the model.

Heine et al. (2013) summarised sea floor spreading rates through the South Atlantic break-up from 126.57 Ma (magnetic isochron M4) to 100 Ma. These range from 10 to 18mmyr^{-1}, increasing in speed towards the south (Table 2). In our modelling, we assumed the pre-break-up extension rates matched those seen during early sea floor spreading. The primary value we used is 12 mm yr^{-1}, as this applied to Segments 3b, 3a and 2 until 126.57 Ma (M4). Following this, the rate increased to 35 mm yr^{-1} for the period 126.57–120.6 Ma, and subsequently increased to 158 mm yr^{-1} (Heine et al., 2013). Moulin et al. (2010) has similar rates for these times, at 38 mm yr^{-1} and 50 mm yr^{-1} respectively, but does not suggest a rate prior to M4. Heine et al. (2013) found the spreading rate of 18 mm yr^{-1} in the extreme south of our study area, covering Segments 1b and 1a.

3.3.3. Model asthenosphere temperature structure

The choice of the model asthenosphere temperature range is crucial, with a change in temperature of 12.5 °C accounting for melt thickness changes by up to 1 km (McKenzie et al., 2005). Herzberg et al. (2007) found that mid-ocean ridge basalts (MORBs) with a 10–13% MgO content would have potential temperature range of 1280–1400 °C. This should cover the feasible range for model asthenosphere temperature in the South Atlantic. To refine this range of temperatures, we made use of the long-offset ION Geophysical lines found in the north-west region of our study area. These profiles record the reduction in oceanic crustal thickness away from the passive margin and towards steady-state. We can therefore compare this crustal thickness farthest from the margin with that generated by the model at a steady-state.

A hot layer with a temperature in excess of the model asthenosphere temperature was added to recreate the distal regions of the mantle plume or thermal anomaly (Fig. 5; Armitage et al., 2010). The hot layer can vary in temperature where, classically, temperature is considered the main driver of crustal thickness (White and McKenzie, 1989). In all models, we assumed the hot layer was present below the lithosphere before the onset of extension. The excess temperature of the

Please cite this article as: Taposeea, C.A., et al., Asthenosphere and lithosphere structure controls on early onset oceanic crust production in the southern South Atlantic, Tectonophysics (2016), http://dx.doi.org/10.1016/j.tecto.2016.06.026

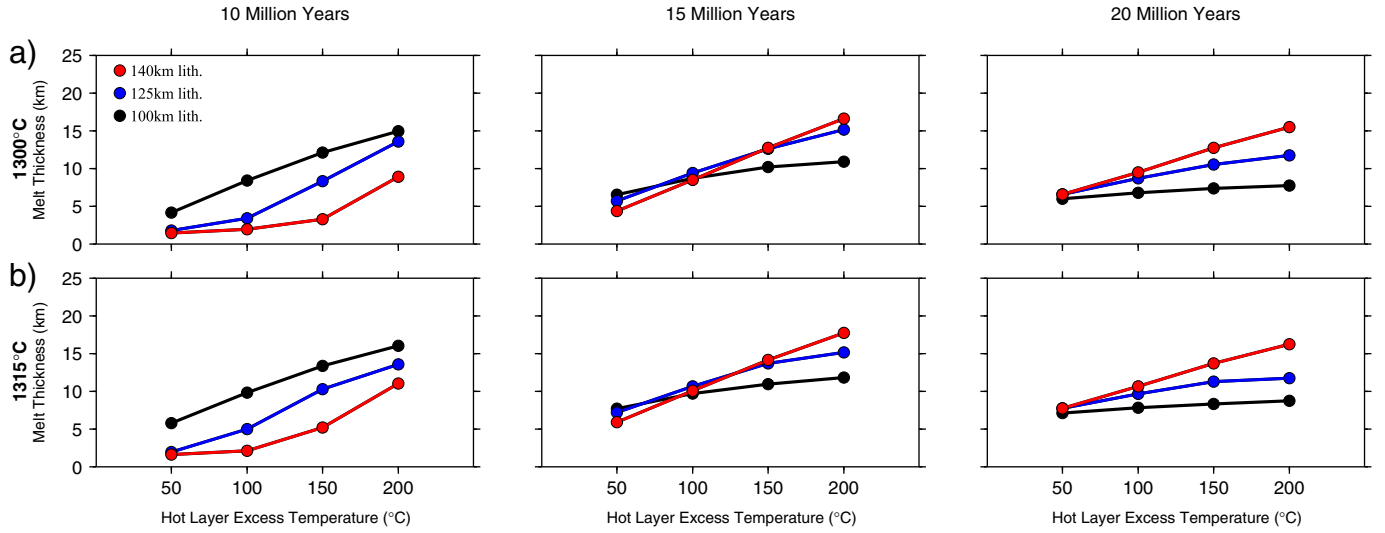


Fig. 7. Evolution plots for differing initial lithosphere thickness and excess hot layer temperature. Melt thickness at 10, 15 and 20 Myr after the initiation of extension for an asthenosphere temperature of 1300 °C (a) and 1315°C (b). In all cases, there is a spreading rate of 12 mm yr^{-1}. Note how varying initial lithosphere thickness results in the peak magmatism occurring at different times. (For interpretation of the references to colour in this figure legend, the reader is referred to the web version of this article.)

hot layer closest to the centre of the province can be estimated from the thickness of the basaltic crust from the Rio Grande Rise and Walvis Ridge. The Walvis Ridge thickness is observed between ~26–28 km from seismic sections (Fromm et al., 2015). When the McKenzie and Bickle (1988) melting model is used, a 200 °C excess temperature is required to match this thickness (Campbell, 2007). We assumed such an excess temperature for the hot layer with proximity to the Rio Grande Rise and Walvis Ridge and varied it along-strike. We solved for decompression melting at various hot layer temperatures and compared the results to the along-strike variation in ocean crust thicknesses measured at the LaLOC for the wide-angle profiles (Fig. S2). We used the relative ages of the oceanic crust at the LaLOC location, known from location of magnetic isochrons, to discriminate between results from models with different hot layer temperatures.

4. Results

4.1. Observed variation in ocean crustal thicknesses

When all the initial oceanic crustal thickness measurements were considered (Table 1), there was a clear negative trend with oceanic crust thinning with increasing distance along-strike from the Rio Grande Rise and Walvis Ridge (Fig. 8a). The trend has a gradient of -2×10^{-3} and a correlation coefficient of 0.7. This translates to a reduction in oceanic crustal thickness of 0.16 km per 100 km in a southern direction from the aseismic ridges. On the African margin, we observed a thicker ocean crust towards the Walvis Ridge. The wide-angle seismic profile AF1 has an initial oceanic crustal thickness measuring 11.7 km at an along-strike distance of ~450 km (Fig. S2), which reduces to a thickness of 7.0 km at profile AF4 in the south at an along-strike distance of ~1420 km (Fig. S2). This trend is very similar on the South American margin, with a maximum thickness of 10.0 km from the most northern ION Geophysical profile ~260 km away, to only 6.0 km in the southern edge of measurements ~2300 km away.

When the oceanic crustal thickness measurements at the LaLOC location were compared to the segment boundaries (Fig. 8), we did not find any obvious thickening south of the segment boundaries. By using the ION Geophysical long-profiles that extend to a distance of 660 km offshore, covering an age range of approximately 15 Myr (Fig. 9), we checked if there was a signal in the oceanic crustal thickness as the profiles cross segment boundaries (Figs. 9 and 10). The long-profiles have an overlying trend of a decrease in oceanic crustal thickness with distance from the passive margin and no clear indication of increased decompression melting at the segment boundaries (Fig. 10). From the seismic sections, we could see clear oceanic crust, devoid of internal structure with a bumpy surface, representative of pillow lavas.

We further investigated Lines 1 and 2, both transgressing segment boundaries (Fig. 10). The ocean crust thickness for both of the lines show local thickness variations with an amplitude of 1 km. Oceanic crustal thickness decreases from 10.2 to 6.3 km along Line 1 (Fig. 10a), and 8.5 to 6.5 km for Line 2 (Fig. 10b). We did not observe a sharp change in melt production as described by Franke et al. (2007) and Koopmann et al. (2014b), but there is an overall decreasing trend with age.

4.2. Results from numerical model

4.2.1. Establishing model asthenosphere temperature

The long offset ION Geophysical data demonstrates the decreasing oceanic crustal thickness with distance from the passive margin

Table 2
Assigned model parameters: lithosphere thickness and spreading rates per segment. Opening ages are assumed by sub-plate from Moulin et al. (2010). M7, M4, M2 and M0 are dated 127.23 Ma, 126.57 Ma, 124.05 Ma and 120.6 Ma respectively (Gee and Kent, 2007). Seismic tomography models from Fishwick and Bastow (2011) and Priestley and McKenzie (2006) grids (Fig. S10). Spreading rates are from Heine et al. (2013).

Segment	Opening ages	Lithosphere thickness (km)			Spreading rates ($mm\ yr^{-1}$)
		African margin (Fishwick)	African margin (Priestley)	S. American margin (Priestley)	
3b	M2-M0	135–140	105–110	125	12
3a	M2-M0	125–130	100–105	125	12
2	M4-M2	130–135	95–100	100–110	12
1b	Pre-M7	130–135	95–100	110–115	18
1a	Pre-M7	135–140	95–105	95–100	18

Please cite this article as: Taposeea, C.A., et al., Asthenosphere and lithosphere structure controls on early onset oceanic crust production in the southern South Atlantic, Tectonophysics (2016), http://dx.doi.org/10.1016/j.tecto.2016.06.026

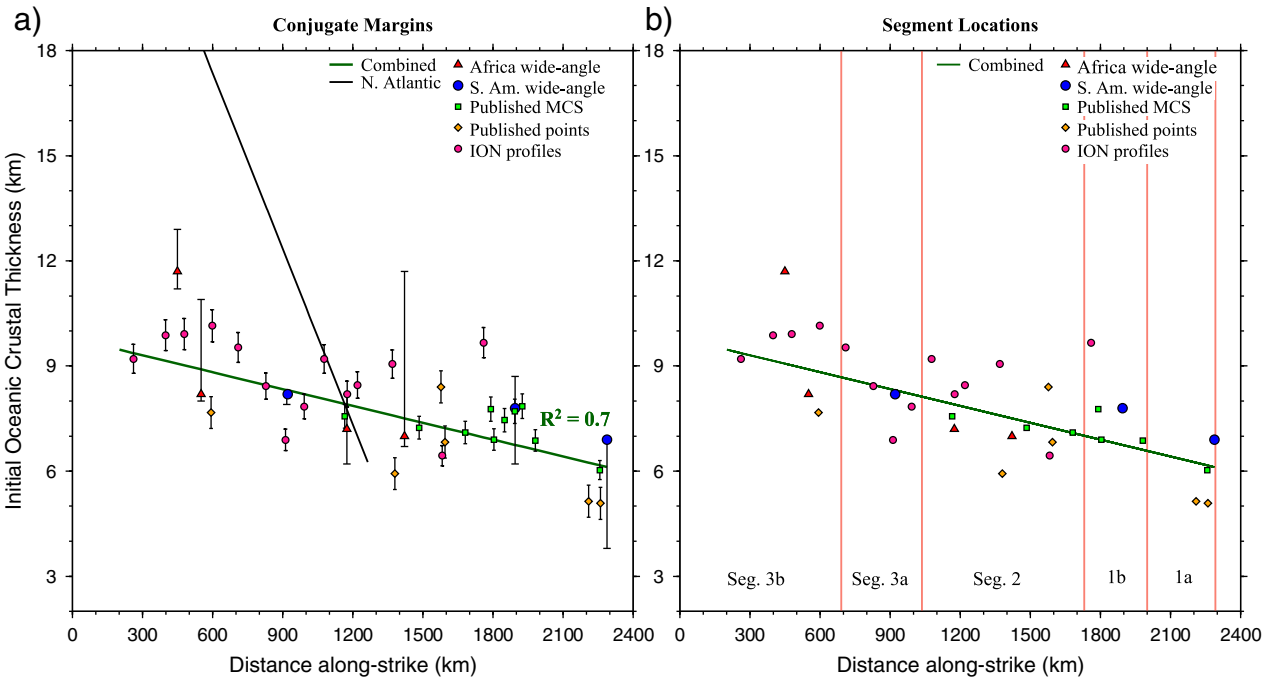


Fig. 8. Initial oceanic crustal thickness plotted against distance along-strike. Data sources are given in Table 1. (a) Initial oceanic crustal thickness versus distance along-strike for all measured locations. The error bars on individual measurement points come from the uncertainty in locating LaLOC on individual profiles (Table S1). Regression analysis shows a reasonable linear relationship (green line with a regression coefficient, $R^2 = 0.7$). For comparison, the trend found for the initial oceanic crustal thickness in the North Atlantic is shown by the black line (from Collier et al., 2009). (b) Initial oceanic crustal thickness shown relative to segment boundaries (red lines). (For interpretation of the references to colour in this figure legend, the reader is referred to the web version of this article.)

(Fig. 10). Having age-assigned the lines according to location, we found for Segments 3b, 3a and 2 that the oceanic crustal thickness trends to 7.2, 6.7, and 6.6 km respectively (Fig. 11). This suggests that towards the end of these profiles steady-state oceanic crustal production has been achieved.

Comparing these trends to our model predictions without any thermal hot layer allowed us to conclude that the model asthenosphere temperature was in the range of 1315–1325 °C (Fig. 11). We saw a higher thickness for Segment 3b due to local thickening of the ocean crust over Line 1 (Fig. 10a), causing an overall increased thickness. However, before this, the thickness was also tending to 1315 °C. Therefore, we used 1315 °C as our model asthenosphere temperature in all our models.

4.2.2. Establishing hot layer temperatures

Having established a model asthenosphere temperature of 1315 °C, we then solved for the excess temperature of the hot layer. For all models, we assumed the hot layer was present below the lithosphere prior to the onset of extension (as demonstrated in Fig. 6a). We estimated the temperature of the hot layer by comparing variations in ocean crustal thicknesses for our wide-angle profiles at the LaLOC location (Fig. 12).

We assumed that the present day continental lithosphere thickness at the margin is representative of the initial configuration (Fig. 1b) and we varied the temperature of the hot layer within the range of 50 to 200 °C Using a model asthenosphere temperature of 1315 and spreading rates of 12 and 18 mm yr^{-1} covering Segments 1–3, we tested several scenarios. To demonstrate the effect of initial lithosphere thickness and the importance of timing, we ran a model with an initial lithosphere thickness of 125 km (Fig. 12a). The model was capable of matching all values for the initial oceanic crust in the post-rift stage (ie. Fig. 6a) from wide-angle seismic profiles AF1 to AF4 on the African side of the South Atlantic, but this match required a 20 Myr difference in age along the margin (Fig. 12a). With magnetic isochron data from Moulin et al. (2010) and using the Gee and Kent (2007) timescale, we estimated the range in age along the margin for the initial oceanic crust produced. We found a range of ages of 1.0 Myr for the African profiles and 5.7 Myr for the South American profiles.

If we allowed the temperature of the hot layer to vary along-strike, we found that the model with an excess temperature of 200 °C matched the observations for wide-angle seismic profile AF1 (Fig. 12b) in its post-rift stage. Moving southward along the African margin, models with a reduced excess temperature of 150, 75 and 50 °C and varying initial lithosphere thicknesses were in line with the observed thickness, fitting the first oceanic crustal thickness for profiles AF2, AF3 and AF4 respectively (Fig. 12b). We therefore found that by taking the observed continental lithosphere thickness and changing the hot layer temperature, we could match the thickness of the first oceanic crust within a consecutive time range of 2.5 Myr, much closer to the observed range of 1.0 Myr. If our assumption of a constant extension rate is correct, then these models also imply that the total duration of rifting in the South Atlantic was of the order of 25 to 30 Myr.

Rates of early sea floor spreading along the South American margin vary from 12 mm yr^{-1} for profile SA1 in Segment 3a to 18 mm yr^{-1} for profiles SA2 and SA3 in Segment 1a and 1b (Table 2). To capture this, we modelled two extension rates along with varying the temperature of the hot layer. Accounting for this difference, we found a set of models that could match the distribution of initial oceanic crustal thickness in the post-rift stage close to the 5.7 Myr age window of the three measurement points (Fig. 12c). A model with an excess temperature of 100 °C is concurrent with observations for SA1, and moving south, this reduced to 75 °C for SA3 (Fig. 12c). These fits imply a reduced duration of extension for the most southerly part of the South American margin relative to the more northerly conjugate margins in South America and on the African side. We predict a rift duration of 15 Myr due to the faster rate of extension for profiles SA2 and SA3, compared to 25 to 30 Myr for profiles AF1–4 and SA1.

Please cite this article as: Taposeea, C.A., et al., Asthenosphere and lithosphere structure controls on early onset oceanic crust production in the southern South Atlantic, Tectonophysics (2016), http://dx.doi.org/10.1016/j.tecto.2016.06.026

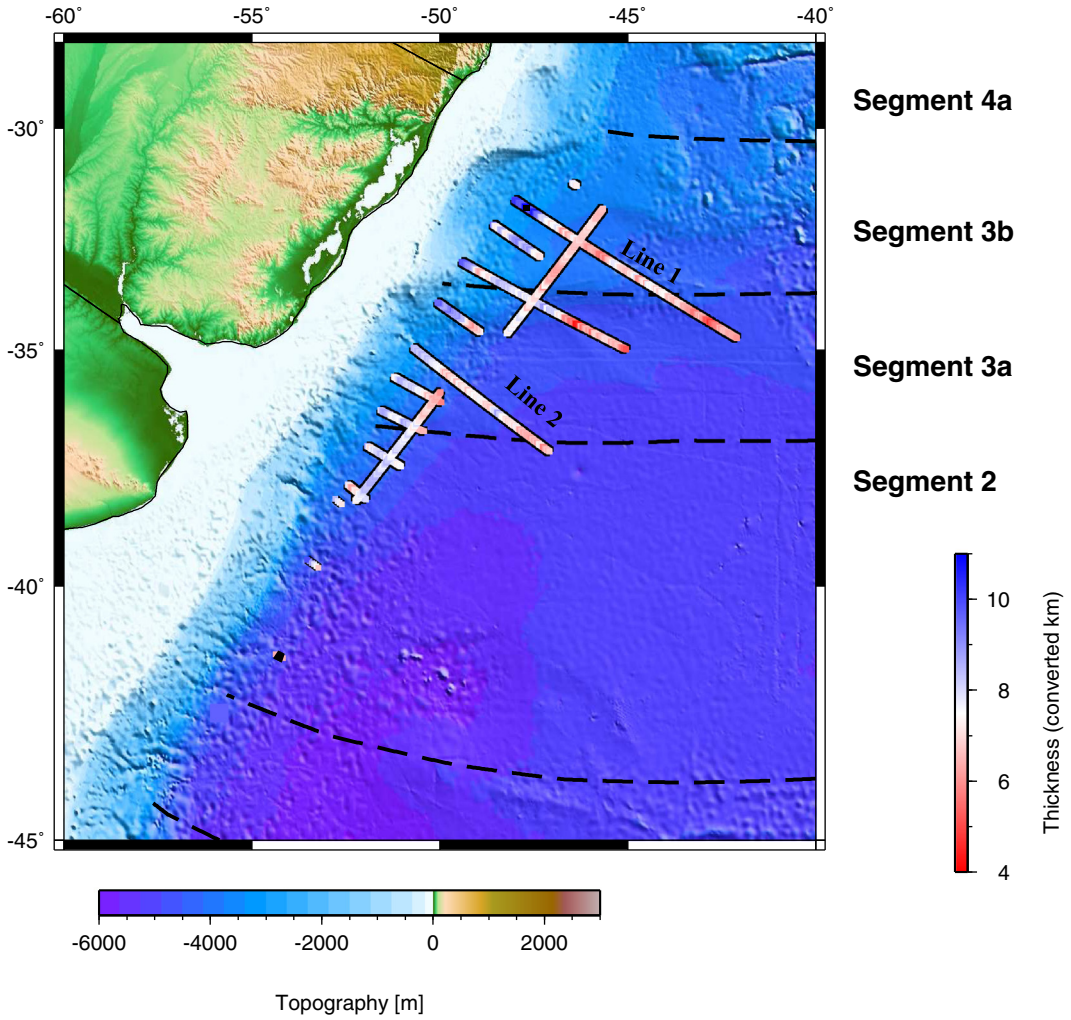


Fig. 9. Ocean Crustal Thickness from the ION Geophysical long-offset data, which was measured in TWTT and converted to kilometres assuming a mean V_p value for oceanic crust of 67 km s^{-1} (White et al., 1992). Line 1 and 2 are show in detail in Fig. 10. (For interpretation of the references to colour in this figure legend, the reader is referred to the web version of this article.)

4.2.3. Results for segment-age trends

To compliment our results from wide-angle profiles, we used our segment-age trend observations from the long offset ION Geophysical profiles (Fig. 11). The oceanic crustal thickness was plotted for each segment binned into 1.5 Myr intervals (Fig. 13). Since this data is from Segments 3b, 3a and 2, we assumed a model spreading rate of 12 mm yr^{-1} (Table 2). Although this rate of extension is valid until 126.57 Ma (Heine et al., 2013), once at steady-state, changing the spreading rate produces oceanic crustal thickness within the same range of values (Fig. 6c). Therefore, for simplicity the spreading rate was kept at 12 mm yr^{-1}. As before, the models have a model asthenosphere temperature of 1315 °C, with varying hot layers and initial lithosphere thickness per segment. The preferred model was determined by calculating a normalised root mean square error (NRMSE).

We compared the post-rift stage of the models with hot layers of 50 to 200 °C against the trend of reducing oceanic crustal thickness with age for each segment (Fig. 13). We found for Segment 3b that a model with a hot layer of 200 °C provided the best fit to the observations (Fig. 13a). This model implied that extension initiated at 147 Ma. For Segment 3a, the best fit model had a hot layer of 150 °C where extension was also initiated at 147 Ma (Fig. 13b). Segment 2 was best matched by a model with a hot layer of excess temperature 75 °C, suggesting extension initiated at 141 Ma. As for the comparison to the wide-angle data (Fig. 12), these models suggest a similar Late Jurassic age for the initiation of extension in the southern South Atlantic.

The modelling matches to the oceanic crustal thickness from the wide-angle seismic lines (Fig. 12) and the long offset ION Geophysical profiles (Fig. 13) allow for the change in hot layer temperature to be plotted against distance along-strike for both margins (Fig. 14). Here we observe a general temperature decrease trend from a thermal anomaly of 200 °C in the north to 75 °C in the south (Fig. 14). A linear fit to all the data points would suggest a reduction of ~40 °C per 500 km distance along-strike. Within this general trend, we found evidence, for example within both Segments 3b and 3a, for a drop of temperature of ~50 °C over roughly 100 km distance. While there is a large degree of uncertainty on these model predictions, these drops in temperature occur within the segments and not at their edges. This may suggest that segment boundaries play only a minor role in the volcanic nature of continental break-up.

5. Discussion: Evidence for a mantle plume?

Franke et al. (2007) and Koopmann et al. (2014b) have suggested lithospheric segmentation as a highly influential factor affecting volcanism in the South Atlantic. They established this from increasing widths and volumes of SDRs towards segment boundaries, and did not take initial oceanic crustal thicknesses into account (Fig. S1). Our study differs from these previous publications on continental break-up in the southern South Atlantic, as it concentrates on post-rift volcanism, where initial production of ocean crust is located, rather than syn-rift volcanism,

Please cite this article as: Taposeea, C.A., et al., Asthenosphere and lithosphere structure controls on early onset oceanic crust production in the southern South Atlantic, Tectonophysics (2016), http://dx.doi.org/10.1016/j.tecto.2016.06.026

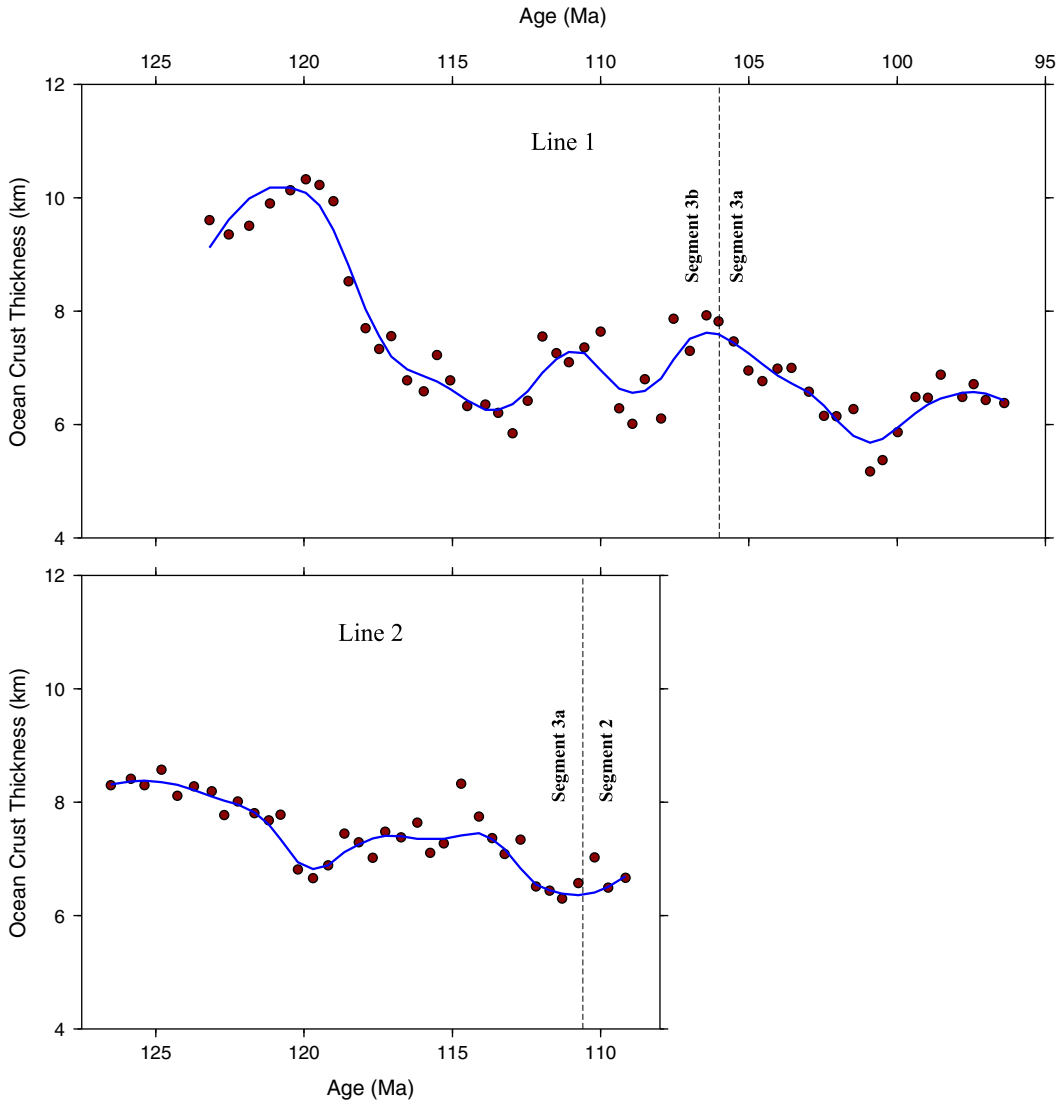


Fig. 10. Ocean crustal thickness from two of the ION Geophysical long-offset data plotted against age. Locations of Lines 1 and 2 are found in Fig. 9. Ages assigned in accordance to the Gee and Kent (2007) time scale and Moulin et al. (2010) magnetic isochrons. Thickness averaged over 1.5 Myr bins (maroon dots), and smoothed with a Gaussian filer (blue lines). (For interpretation of the references to colour in this figure legend, the reader is referred to the web version of this article.)

where SDRs are found (Franke et al., 2007; Koopmann et al., 2014a, b). From our results, we suggest that oceanic crustal thickness is primarily controlled by temperature and initial lithosphere thickness. There is no clear systematic trend for increased magmatism relative to segments boundaries from ocean crust thickness observations and consequent modelling (Figs. 8b, 10, and 14).

In the North Atlantic (Fig. 8a), Collier et al. (2009) presented ocean crust measurements both south and north of the Greenland-Iceland-Faeroe Ridges. The trend for this area was a reduction of 1.67 km per 100 km increased distance from the aseismic ridges, a stark difference to the trend seen in the South Atlantic, with a reduction of 0.16 km per 100 km (Fig. 8a). In the past, continental break-up in the North and South Atlantic have been regarded similar, with mantle temperature being deduced as the primary factor (e.g. White and McKenzie, 1989). The North Atlantic is considered in line with the classic 'mushroom head' plume model, with an axisymmetric geometry inferred from volcanic margins both north and south of the Greenland-Iceland-Faeroe Ridges. This is not seen in the South Atlantic, where volcanic passive margins are found on conjugate margins south of the Rio Grande Rise and Walvis Ridge, but magma-poor passive margins are found to the north (Contrucci et al., 2004; Aslanian et al., 2009; Reston, 2010; Fromm et al., 2015). Additionally, the North Atlantic underwent a pre-thinning extension event prior to break-up, causing enhanced melt generation through focused upwelling (Armitage et al., 2010). This is not seen in our study area, and given the effect of temperature and lithosphere thickness on break-up volcanism modelled here (e.g. Fig. 10), we suggest that the varying trends seen between the North and South Atlantic indicate differing initial break-up conditions, in both initial lithosphere structure and mantle temperature.

Through our simulations, we show a simple 2D model can match initial ocean crust thickness, and is sensitive to changes in initial lithosphere thickness, mantle asthenosphere temperatures and hot layer temperatures (Figs. 7 and 14). Our results indicate the presence of a reduction of temperature, both in direction parallel to the margin along-strike and in time. The along-strike decrease can be linked to a reduction in temperature as we move from a mantle plume axis to its fringes (e.g. Campbell, 2007). From modelling the thickness of oceanic crust generated by decompression melting, we estimate that there is a reduction in temperature from 1515°C near the Rio Grande Rise and Walvis Ridge (Profile AF1 with a distance of 450 km) to 1365–1390°C at the edge of the segments in the south (Profile SA3 at a distance of 2300 km). This suggests the presence of a mantle plume, or at the

Please cite this article as: Taposeea, C.A., et al., Asthenosphere and lithosphere structure controls on early onset oceanic crust production in the southern South Atlantic, Tectonophysics (2016), http://dx.doi.org/10.1016/j.tecto.2016.06.026

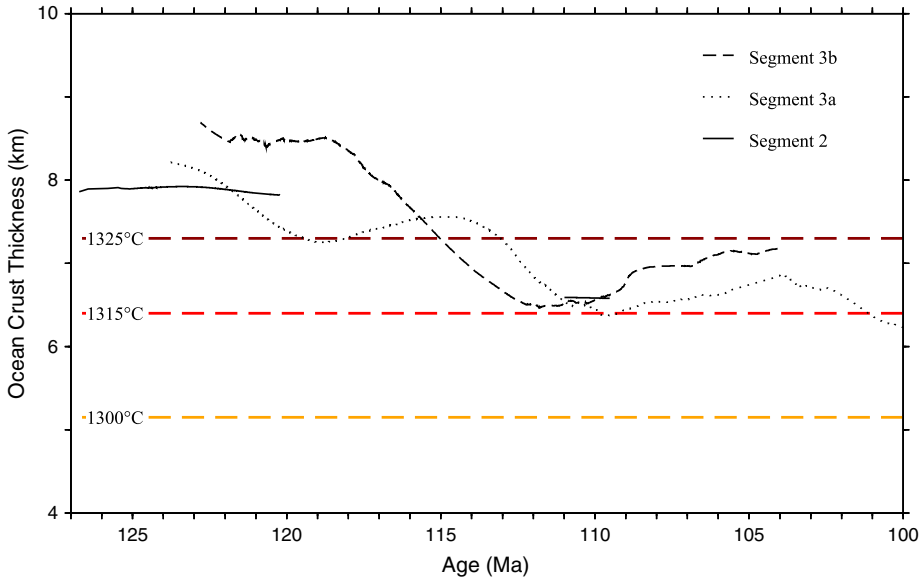


Fig. 11. Determining the model asthenosphere temperature using ocean crust thicknesses from the long-offset ION Geophysical lines. All oceanic crustal thickness measurements within a given segment were averaged into 1.5 Myr bins. We test for several model asthenosphere temperatures, in this case 1300, 1315 and 1325 °C, electing to use 1315 °C as our model asthenosphere temperature in all of our subsequent models.

very least a thermal anomaly, reaching temperatures of 200°C above the model asthenosphere temperature of 1315°C.

Putirka (2005) calculated the temperature for the Hawaii and Iceland plumes, finding them to be 250 ± 50 °C and 165 ± 60 °C hotter than asthenosphere temperature, which is within range of our maximum excess temperature of 200 °C. Coupled with a model asthenosphere temperature of 1315 °C, our maximum temperature of 1515 °C falls in the limits of the maximum potential temperature for the Rio Grande Rise and Walvis Ridge in the northern region of our study area, estimated at 1450–1540 °C (Gallagher and Hawkesworth, 1994). Furthermore, our results agree with thermobarometry results from Trumbull (2014), where from a compilation of onshore basalts, a north to south decrease in temperatures of 140 °C from 1520 °C in the north to 1380 °C in the south is seen.

With our models, we can also estimate the duration of rifting. We predict a rift duration in the order of 23.5 to 30 Myr for Segments 2 and 3,

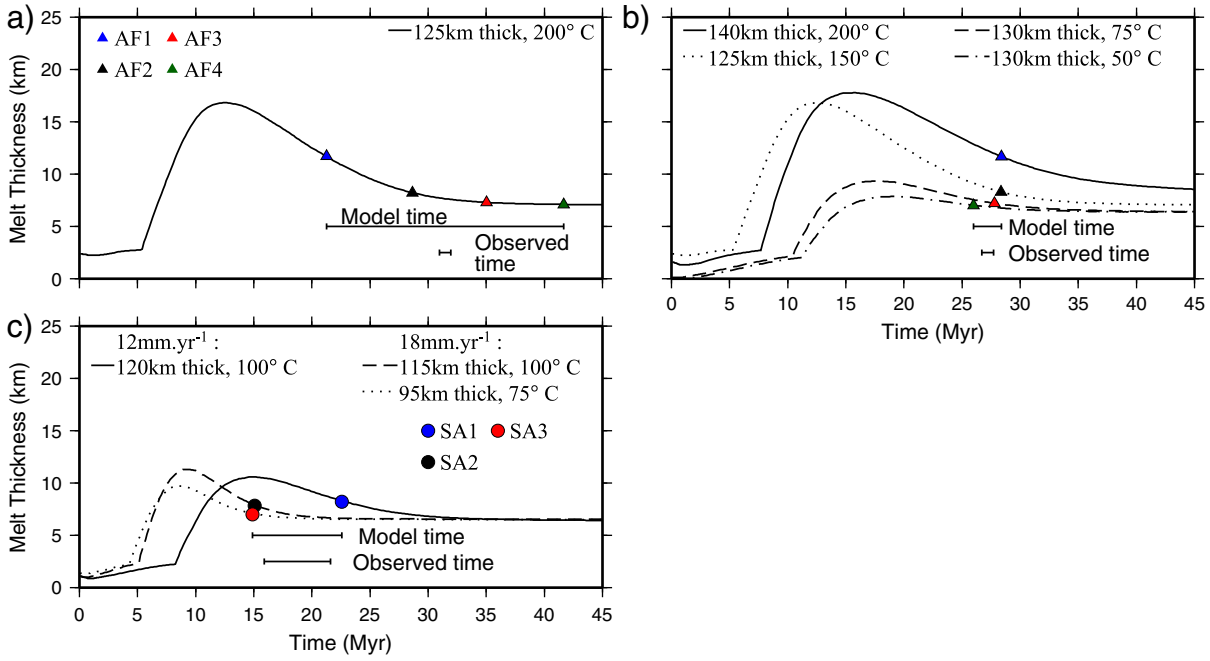


Fig. 12. Models results for wide-angle profiles. Model asthenosphere temperature of 1315 °C, and spreading rate of 12 mm yr^{-1} unless specified otherwise. The ages between profiles have been calculated according to the LaLOC location (Fig. S2). Panel (a) has a hot layer of 200 and an initial lithosphere thickness of 125 km, capable of matching values of AF1–4 over a 20 Myr period. For panels (b) and (c) each wide-angle profile has been tested for different hot layer models and corresponding initial lithosphere thickness (Table 2). On the African margin, panel (b) shows matches of first ocean crust thicknesses over 2.5 Myr, much closer to the observed range of 1.0 Myr. For the South American margin, the models in panel (c) have a range of spreading velocities, where Segment 3a (for SA1) has a rate of 12 mm yr^{-1}, and Segment 1 (for SA2 and 3) has a rate of 18 mm yr^{-1}. Here the models match over a time of 7.7 Myr, relatively close to the observed time of 5.7 Myr. (For interpretation of the references to colour in this figure legend, the reader is referred to the web version of this article.)

Please cite this article as: Taposeea, C.A., et al., Asthenosphere and lithosphere structure controls on early onset oceanic crust production in the southern South Atlantic, Tectonophysics (2016), http://dx.doi.org/10.1016/j.tecto.2016.06.026

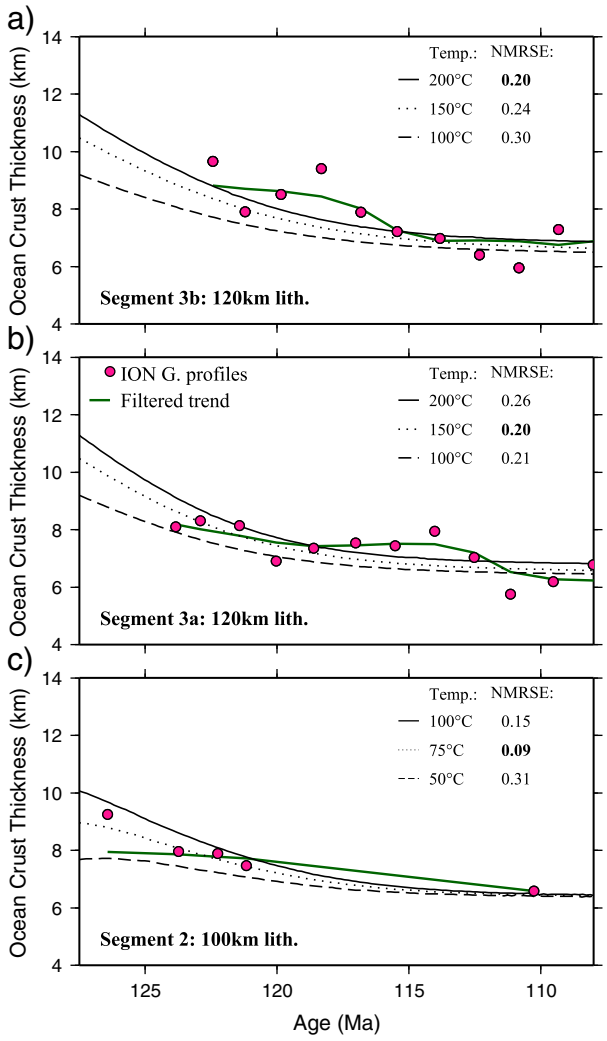


Fig. 13. Model results per segment on the South American margin. Model asthenosphere temperature of 1315 °C, and spreading rate of 12 mm yr^{-1}. Each segment is tested for different hot layer models. The best match model trend was found by calculating a normal root mean square error (NMRSE) for each of the 1.5 Myr binned observation points (pink dots) with the preferred result in bold. Results for Segments 3b (a), 3a (b) and 2 (c) have hot layers with temperatures of 200 °C, 150 °C and 75 °C respectively. (For interpretation of the references to colour in this figure legend, the reader is referred to the web version of this article.)

reduced to 15 Myr for Segment 1. Given that the first magnetic isochrons are roughly 126 Ma, this places the onset of extension for our study area to be within the Late Jurassic. Despite the simplifications of the geodynamic model, such an age for the onset of extension is quite reasonable. Several studies have found evidence for the commencement of rifting in the Late Jurassic (e.g. Maslanyj et al., 1992; Light et al., 1993; Clemson et al., 1997, 1999; Gallagher and Brown, 1999; Aizawa et al., 2000), and syn-rift sediments within the Namibian passive margin are dated to be between 130 and 150 Ma (Clemson et al., 1997; Guillocheau et al., 2012).

There have been several suggestions for the origin of magma-rich and magma-poor margins. A suggestion for the asymmetry seen is shift of the plume centre over the mid-ocean ridge at 93 Ma to the South American side (O'Connor and Jokat, 2015), forming the São Paulo Plateau (Fig. 2; Pérez-Díaz and Eagles, 2014). Therefore, this tectonic event could be the cause of the sharp transition from 26 to 28 km thick Walvis Ridge to the 6 km thin oceanic crust in Angola. Another possible explanation for the asymmetry in volcanism north and south of the Rio Grande Rise and Walvis Ridge is the role of lithosphere thickness. We have already established its importance for our numerical modelling. Taking a north-south transect of reconstructed lithosphere thickness at time of break-up (133 Ma, from Moulin et al., 2013), the location of the Congo craton causes a significant increase in lithosphere thickness to the north of the approximate location of the plume axis (Fig. 15). This is coupled with slowed spreading rates in this region, ranging from 4–8 mm yr^{-1} (Heine et al., 2013) as rifting moves northward. Sleep (1996) suggested the sublithospheric bathymetry has a profound effect on the mantle plume near a ridge axis, forming an 'upside-down drainage pattern'. Through numerical models, it was found only a relatively thin layer of plume material would spread up slope to a ridge axis, and that normal lithosphere surrounding a plume material would 'to some extent act as a levée' (e.g. Sleep, 1996; Nielsen et al., 2002). Cores in the Etendeka volcanic province, dated at magnetic isochron 15n (Dodd et al., 2015) and with an age of 135.96 Ma (Gee and Kent, 2007), confirm the presence of the plume, or at least a hot layer, before break-up of our study area. We suggest that in the southern South Atlantic, as the plume impinged the base of the lithosphere, it would have ponded towards the thinner lithosphere (Nielsen et al., 2002) and spread preferentially towards the South where extension had already commenced. As a result, it would have caused the asymmetry observed with respect to volcanism along the passive margins south and north of the Rio Grande Rise and Walvis Ridge.

6. Conclusions

We identified the LaLOC location and measured initial oceanic crustal thickness for 37 seismic profiles along conjugate margins in the southern South Atlantic. We measured the along-strike distance from the commencement of the Rio Grande Rise and Walvis Ridges for all of these points and studied the spatial variability of ocean crust thickness. We found a trend of reduction in initial oceanic crustal thickness of 0.16 km per 100 km south from the Rio Grande Rise and Walvis Ridge (Fig. 8a), with thickness ranging from 11.7 km adjacent to the ridges, decreasing to 6.1 km at the most southerly point. We found no strong correlation between segment boundaries and oceanic crustal thickness (Figs. 8b and 10).

The relatively simple numerical model of continental break-up used here has previously demonstrated the importance of lithosphere thickness on break-up volcanism (Armitage et al., 2010). We used the present-day lithosphere values with the assumption of little change since break-up (McKenzie et al., 2015). By also assuming the sea floor spreading rates are indicative of the rate of extension during break-up, we then varied mantle potential and hot layer temperatures in an attempt to fit the observed age and thickness of the first oceanic crust produced.

From the long-offset ION Geophysical lines, we first determined the model asthenosphere temperature to be 1315 using the observed reduction in oceanic crustal thickness with time and distance from the passive margin (Fig. 11). To match the initial oceanic crustal thicknesses from the seismic data, we found there must have been an increased temperature relative to the model asthenosphere temperature. From an initial value of 1515 °C with proximity to the Rio Grande Rise and Walvis Ridge, representing an excess temperature of 200 °C, there was a reduction of ~40 °C per 500 km, matching the initial oceanic crustal thickness estimated from the seismic data (Fig. 14). This supports the evidence of the presence of a mantle plume or thermal anomaly as the origin for excessive melt production in our study area. In addition, our rifting duration range from 15 to 30 Myr, suggesting rifting had started in the Late Jurassic, in agreement with evidence from sedimentary accumulations (e.g. Clemson et al., 1997; Guillocheau et al., 2012). Therefore, while other factors, such as segmentation or sediment loading (e.g. Bialas and Buck, 2009; Koopmann et al., 2014b), can influence rift architecture, the volcanic nature of a rifted margin is fundamentally controlled by the structure of the lithosphere and asthenosphere.

Please cite this article as: Taposeea, C.A., et al., Asthenosphere and lithosphere structure controls on early onset oceanic crust production in the southern South Atlantic, Tectonophysics (2016), http://dx.doi.org/10.1016/j.tecto.2016.06.026

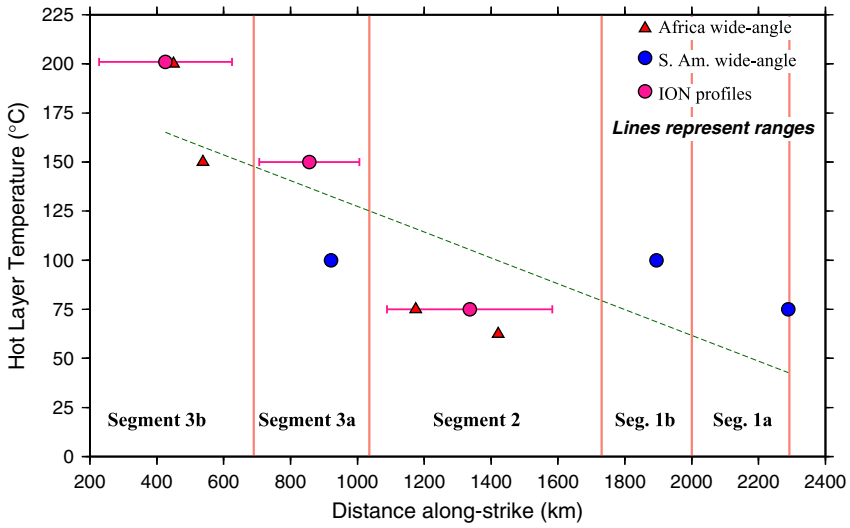


Fig. 14. Hot layer temperature vs. distance along-strike. Results for the wide-angle profiles shown in Fig. 12 are given as symbols. Results for the long MCS profiles shown in Fig. 13 are marked as pink circles with horizontal bars marking distribution of the profiles. There is an overall reduction of ~40 °C per 500 km. (For interpretation of the references to colour in this figure legend, the reader is referred to the web version of this article.)

By reconstructing the lithosphere thickness at break-up, we suggest the sublithospheric topography had a strong influence on volcanism throughout the South Atlantic, including the asymmetry in volcanism along the margins. The magma-poor area north of the Rio Grande Rise and Walvis Ridge is adjacent to the Congo Craton. As previously suggested by Sleep (1996), the lateral flow of the potential mantle plume could have been hindered by this continental root. To the south of the Congo Craton, the volcanism observed due to break-up is found to be a result of a more subtle interplay between lithosphere thickness and mantle temperature.

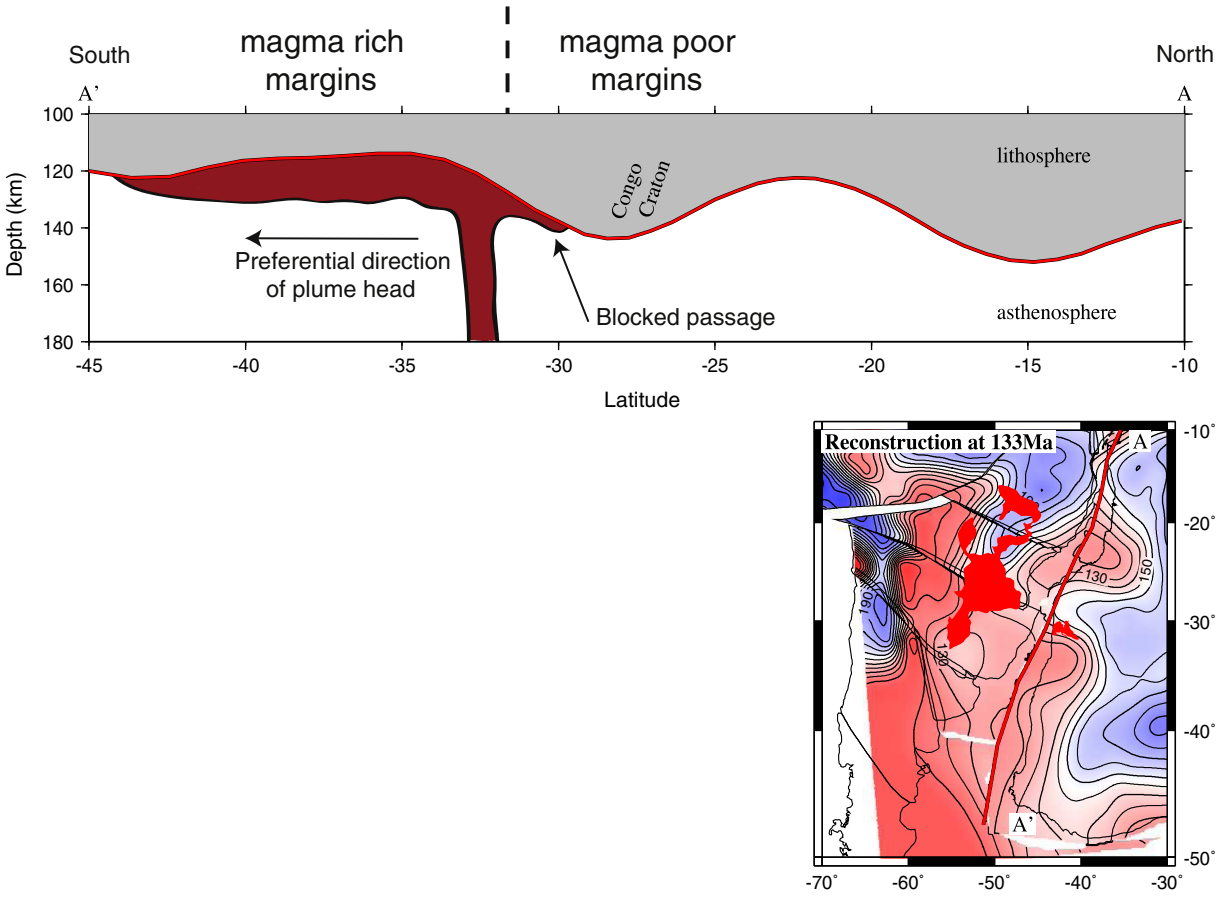


Fig. 15. Cartoon of a possible explanation for the magma-rich and magma-poor passive margins in the South Atlantic. Lithosphere thickness (from Priestley and McKenzie, 2006) at 133 Ma, with the latter covering the whole area. The transect is shown on map, and approximate locations of major features are marked.

Please cite this article as: Taposeea, C.A., et al., Asthenosphere and lithosphere structure controls on early onset oceanic crust production in the southern South Atlantic, Tectonophysics (2016), http://dx.doi.org/10.1016/j.tecto.2016.06.026

Acknowledgments

We would like to thank Carl McDermott and Noemi G. Gyori (Imperial College London) for their contribution to the location of segments and reconstruction work respectively. We would like to thank ION Geophysical for access to their seismic lines. We would like to thank Dr. Klaus Bauer for his wide-angle datasets, Dr. Maryline Moulin for providing us with isochron locations, and Dr. Stewart Fishwick for access to his lithospheric thickness grid. The GPlates and GMT programs have also been invaluable. This work was funded by a Royal Astronomical Society Fellowship and an ANR grant, InterRift, to John J. Armitage, and the John Archer Scholarship to Chandra A. Taposeea.

Appendix A. Supplementary data

Supplementary data to this article can be found online at http://dx.doi.org/10.1016/j.tecto.2016.06.026.

References

Aizawa, M., Bluck, B., Cartwright, J., Milner, S., Swart, R., Ward, J., 2000. Constraints on the geomorphological evolution of Namibia from the offshore stratigraphic record. Commun. Geol. Surv. Namibia 12, 337–346.
Armante, C., Eakins, B., 2009. ETOPO1 1 arc-minute global relief model: procedures, data sources and analysis. Memorandum NESDIS NGDC 24, 19.
Armitage, J.J., Collier, J.S., Minshull, T.A., 2010. The importance of rift history for volcanic margin formation. Nature 465 (7300), 913–917.
Aslanian, D., Moulin, M., Olivet, J.L., Unternehr, P., Matias, L., Bache, F., Rabineau, M., Nouze, H., Klingelheofer, F., Contrucci, I., Labails, C., 2009. Brazilian and African passive margins of the central segment of the South Atlantic Ocean: kinematic constraints. Tectonophysics 468 (1–4), 98–112.
Bauer, K., Neben, S., Schreckenberger, B., Emmermann, R., Hinz, K., Fechner, N., Gohl, K., Schulze, A., Trumbull, R.B., Weber, K., 2000. Deep structure of the Namibia continental margin as derived from integrated geophysical studies. J. Geophys. Res. Solid Earth 105 (B11), 25829–25853.
Becker, K., Franke, D., Trumbull, R., Schnabel, M., Heyde, I., Schreckenberger, B., Koopmann, H., Bauer, K., Jokat, W., Krawczyk, C., 2014. Asymmetry of high-velocity lower crust on the South Atlantic rifted margins and implications for the interplay of magmatism and tectonics in continental breakup. Solid Earth 5 (2), 1011.
Bellieni, G., Brotzu, P., Comin-Chiaramonti, P., Ernesto, M., Melfi, A., Pacca, I., Piccirilo, E., Stolfa, D., 1983. Petrological and paleomagnetic data on the plateau basalts to rhyolite sequencies of the Southern Paraná Basin (Brazil). An. Acad. Bras. Cienc. 55 (4), 355–383.
Bialas, R.W., Buck, W.R., 2009. How sediment promotes narrow rifting: application to the gulf of california. Tectonics 28 (4), TC4014.
Buiter, S.J., Torsvik, T.H., 2014. A review of Wilson cycle plate margins: a role for mantle plumes in continental break-up along sutures? Gondwana Res. 26 (2), 627–653.
Campbell, I.H., 2007. Testing the plume theory. Chem. Geol. 241 (3–4), 153–176.
Clemson, J., Cartwright, J., Booth, J., 1997. Structural segmentation and the influence of basement structure on the Namibian passive margin. J. Geol. Soc. 154 (3), 477–482.
Clemson, J., Cartwright, J., Swart, R., 1999. The Namib Rift: a rift system of possible Karoo age, offshore Namibia. Geol. Soc. Lond., Spec. Publ. 153 (1), 381–402.
Coffin, M.F., Eldholm, O., 1994. Large igneous provinces: crustal structure, dimensions, and external consequences. Rev. Geophys. 32 (1), 1–36.
Collier, J.S., Minshull, T.A., Hammond, J.O.S., Whitmarsh, R.B., Kendall, J.M., Sansom, V., Lane, C.I., Rumpker, G., 2009. Factors influencing magmatism during continental breakup: new insights from a wide-angle seismic experiment across the conjugate Seychelles-Indian margins. J. Geophys. Res. Solid Earth 114 (B3).
Contrucci, I., Matias, L., Moulin, M., Geli, L., Klingelhofer, F., Nouze, H., Aslanian, D., Olivet, J.L., Rehault, J.P., Sibuet, J.C., 2004. Deep structure of the West African continental margin (Congo, Zaire, Angola), between 5 degrees S and 8 degrees S, from reflection/refraction seismics and gravity data. Geophys. J. Int. 158 (2), 529–553.
Cordery, M.J., Morgan, J.P., 1993. Convection and melting at mid-ocean ridges. J. Geophys. Res. Solid Earth 98 (B11), 19477–19503.
Courtillot, V., Jaupart, C., Manighetti, I., Tapponnier, P., Besse, J., 1999. On causal links between flood basalts and continental breakup. Earth Planet. Sci. Lett. 166 (3–4), 177–195.
Dodd, S.C., Mac Niocaill, C., Muxworthy, A.R., 2015. Long duration (>4 Ma) and steady-state volcanic activity in the early Cretaceous Paraná–Etendeka large igneous province: new palaeomagnetic data from Namibia. Earth Planet. Sci. Lett. 414, 16–29.
Erlank, A., Marsh, J., Duncan, A., Miller, R.M., Hawkesworth, C., Betton, P., Rex, D., 1984. Geochemistry and petrogenesis of the etendeka volcanic rocks from SWA/Namibia. Spec. Pub. Geol. Soc. S. Afr. 13, 195–245.
Fernandez, M., Afonso, J.C., Ranalli, G., 2010. The deep lithospheric structure of the Namibian volcanic margin. Tectonophysics 481 (1–4), 68–81.
Fishwick, S., 2010. Surface wave tomography: imaging of the lithosphere–asthenosphere boundary beneath central and southern Africa? Lithos 120 (1), 63–73.
Fishwick, S., Bastow, I.D., 2011. Towards a better understanding of African topography: a review of passive-source seismic studies of the African crust and upper mantle. Geol. Soc. Spec. Publ. 357 (1), 343–371.
Franke, D., Neben, S., Ladage, S., Schreckenberger, B., Hinz, K., 2007. Margin segmentation and volcano-tectonic architecture along the volcanic margin off Argentina/Uruguay, South Atlantic. Mar. Geol. 244 (1–4), 46–67.
Franke, D., Ladage, S., Schnabel, M., Schreckenberger, B., Reichert, C., Hinz, K., Paterlini, M., de Abelleyra, J., Siciliano, M., 2010. Birth of a volcanic margin off Argentina, South Atlantic. Geochem. Geophys. Geosyst. 11 (2).
Fromm, T., Planert, L., Jokat, W., Ryberg, T., Behrmann, J., Weber, M., Haberland, C., 2015. South Atlantic opening: a plume-induced breakup? Geology 43 (10), 931–934.
Gallagher, K., Brown, R., 1999. Denudation and uplift at passive margins: the record on the Atlantic Margin of southern Africa. Philos. Trans. R. Soc. Lond. A 357, 835–859.
Gallagher, K., Hawkesworth, C., 1994. Mantle plumes, continental magmatism and asymmetry in the South Atlantic. Earth Planet. Sci. Lett. 123 (13), 105–117.
Gee, J.S., Kent, D.V., 2007. Source of oceanic magnetic anomalies and the geomagnetic polarity time scale. Treatise on geophysics. Geomagn. 5, 455–507.
Gladczenko, T.P., Skogseid, J., Eldhom, O., 1998. Namibia volcanic margin. Mar. Geol. 20 (4), 313–341.
Griffiths, R.W., Campbell, I.H., 1990. Stirring and structure in mantle starting plumes. Earth Planet. Sci. Lett. 99 (1), 66–78.
Griffiths, R., Campbell, I., 1991. Interaction of mantle plume heads with the Earth's surface and onset of small-scale convection. J. Geophys. Res. Solid Earth 96 (B11), 18295–18310.
Gubanov, A., Mooney, W., 2009. New global geological maps of crustal basement age. AGU Fall Meeting Abstracts vol. 1, p. 1583.
Guillocheau, F., Rouby, D., Robin, C., Helm, C., Rolland, N., Le Carlier de Veslud, C., Braun, J., 2012. Quantification and causes of the terrigeneous sediment budget at the scale of a continental margin: a new method applied to the Namibia–South Africa margin. Basin Res. 24 (1), 3–30.
Hawkesworth, C., Gallagher, K., Kelley, S., Mantovani, M., Peate, D., Regelous, M., Rogers, N., 1992. Paraná magmatism and the opening of the South Atlantic. Geol. Soc. Spec. Publ. 68 (1), 221–240.
Heine, C., Zoethout, J., Müller, R.D., 2013. Kinematics of the South Atlantic rift. Solid Earth 4 (2), 215–253.
Herzberg, C., Asimow, P.D., Arndt, N., Niu, Y., Lesher, C.M., Fitton, J.G., Cheadle, M.J., Saunders, A.D., 2007. Temperatures in ambient mantle and plumes: constraints from basalts, picrites, and komatiites. Geochem. Geophys. Geosyst. 8 (2), Q02006.
Hinz, K., 1981. A hypothesis on terrestrial catastrophes: wedges of very thick oceanward dipping layers beneath passive continental margins; their origin and paleoenvironmental significance. Geologisches Jahrbuch, Reihe E. Geophysics 3–28.
Hinz, K., Popovici, A., Ronda, C., Beisner, H., 1988. On a multichannel seismic reconnaissance survey of the Argentine eastern continental margin by RV Explora. Tech. Rep., Internal Report 102.371, Bundesantalt fur Geowissenschaften und Rohsthoffe, Hannover.
Hinz, K., Neben, S., Schreckenberger, B., Roeser, H., Block, M., Souza, K., Meyer, H., 1999. The Argentine continental margin north of 48 S: sedimentary successions, volcanic activity during breakup. Mar. Pet. Geol. 16 (1), 1–25.
Hirsch, K.K., Bauer, K., Scheck-Wenderoth, M., 2009. Deep structure of the western South African passive margin - results of a combined approach of seismic, gravity and isostatic investigations. Tectonophysics 470 (1–2), 57–70.
Holbrook, W.S., Larsen, H., Korenaga, J., Dahl-Jensen, T., Reid, I.D., Kelemen, P., Hopper, J., Kent, G., Lizarralde, D., Bernstein, S., et al., 2001. Mantle thermal structure and active upwelling during continental breakup in the North Atlantic. Earth Planet. Sci. Lett. 190 (3), 251–266.
Hopper, J.R., Mutter, J.C., Larson, R.L., Mutter, C.Z., 1992. Magmatism and rift margin evolution: evidence from northwest Australia. Geology 20 (9), 853–857.
Houseman, G., 1990. The thermal structure of mantle plumes: axisymmetric or triple-junction? Geophys. J. Int. 102 (1), 15–24.
Ito, G., Lin, J., Gable, C.W., 1996. Dynamics of mantle flow and melting at a ridge-centered hotspot: Iceland and the Mid-Atlantic Ridge. Earth Planet. Sci. Lett. 144 (12), 53–74.
Jungslager, E.H., 1999. Petroleum habitats of the Atlantic margin of South Africa. Geol. Soc. Lond., Spec. Publ. 153 (1), 153–168.
Koopmann, H., Brune, S., Franke, D., Breuer, S., 2014a. Linking rift propagation barriers to excess magmatism at volcanic rifted margins. Geology 42 (12), 1071–1074.
Koopmann, H., Franke, D., Schreckenberger, B., Schulz, H., Hartwig, A., Stollhofen, H., di Primio, R., 2014b. Segmentation and volcano-tectonic characteristics along the SW African continental margin, South Atlantic, as derived from multichannel seismic and potential field data. Mar. Pet. Geol. 50, 22–39.
Light, M., Maslanyj, M., Greenwood, R., Banks, N., 1993. Seismic sequence stratigraphy and tectonics offshore Namibia. Geol. Soc. Lond., Spec. Publ. 71 (1), 163–191.
Lizarralde, D., Axen, G.J., Brown, H.E., Fletcher, J.M., González-Fernández, A., Harding, A.J., Holbrook, W.S., Kent, G.M., Paramo, P., Sutherland, F., et al., 2007. Variation in styles of rifting in the Gulf of California. Nature 448 (7152), 466–469.
Maslanyj, M.P., Light, M.P.R., Greenwood, R.J., Banks, N.L., 1992. Extension tectonics offshore Namibia and evidence for passive rifting in the South-Atlantic. Mar. Pet. Geol. 9 (6), 590–601.
Maus, S., Sazonova, T., Hemant, K., Fairhead, J., Ravat, D., 2007. National geophysical data center candidate for the world digital magnetic anomaly map. Geochem. Geophys. Geosyst. 8 (6), Q06017.
Maus, S., Barckhausen, U., Berkenbosch, H., Bournas, N., Brozena, J., Childers, V., Dostaler, F., Fairhead, J., Finn, C., Von Frese, R., et al., 2009. EMAG2: A 2–arc min resolution Earth Magnetic Anomaly Grid compiled from satellite, airborne, and marine magnetic measurements. Geochem. Geophys. Geosyst. 10 (8), Q08005.
McKenzie, D., Bickle, M., 1988. The volume and composition of melt generated by extension of the lithosphere. J. Petrol. 29 (3), 625–679.
McKenzie, D., Jackson, J., Priestley, K., 2005. Thermal structure of oceanic and continental lithosphere. Earth Planet. Sci. Lett. 233 (3), 337–349.
McKenzie, D., Daly, M.C., Priestley, K., 2015. The lithospheric structure of Pangea. Geology 43 (9), 783–786.

Please cite this article as: Taposeea, C.A., et al., Asthenosphere and lithosphere structure controls on early onset oceanic crust production in the southern South Atlantic, Tectonophysics (2016), http://dx.doi.org/10.1016/j.tecto.2016.06.026

Minshull, T.A., Lane, C.I., Collier, J.S., Whitmarsh, R.B., 2008. The relationship between rifting and magmatism in the northeastern Arabian Sea. Nat. Geosci. 1 (7), 463–467.
Moresi, L., Zhong, S., Gurnis, M., 1996. The accuracy of finite element solutions of Stokes's flow with strongly varying viscosity. Phys. Earth Planet. Inter. 97 (1), 83–94.
Moulin, M., Aslanian, D., Unternehr, P., 2010. A new starting point for the South and Equatorial Atlantic Ocean. Earth Sci. Rev. 98 (1), 1–37.
Moulin, M., Aslanian, D., Rabineau, M., Patriat, M., Matias, L., 2013. Kinematic keys of the Santos–Namibe basins. Geol. Soc. Spec. Publ. 369 (1), 91–107.
Nielsen, T.K., Hopper, J.R., 2004. From rift to drift: mantle melting during continental breakup. Geochem. Geophys. Geosyst. 5 (7), Q07003.
Nielsen, T.K., Larsen, H.C., Hopper, J.R., 2002. Contrasting rifted margin styles south of Greenland: implications for mantle plume dynamics. Earth Planet. Sci. Lett. 200 (3), 271–286.
O'Connor, J.M., Duncan, R.A., 1990. Evolution of the Walvis Ridge-Rio Grande rise hot spot system: implications for African and South American Plate motions over plumes. J. Geophys. Res. Solid Earth 95 (B11), 17475–17502.
O'Connor, J.M., Jokat, W., 2015. Tracking the Tristan-Gough mantle plume using discrete chains of intraplate volcanic centers buried in the Walvis ridge. Geology 43 (8), 715–718.
O'Connor, J.M., Jokat, W., Le Roex, A.P., Class, C., Wijbrans, J.R., Keßling, S., Kuiper, K.F., Nebel, O., 2012. Hotspot trails in the South Atlantic controlled by plume and plate tectonic processes. Nat. Geosci. 5 (10), 735–738.
Peate, D.W., 1997. The Paraná-Etendeka province. Large Igneous Provinces: Continental, Oceanic, and Planetary Flood Volcanism, pp. 217–245.
Peate, D.W., Hawkesworth, C.J., Mantovani, M.S., 1992. Chemical stratigraphy of the Paraná lavas (South America): classification of magma types and their spatial distribution. Bull. Volcanol. 55 (1–2), 119–139.
Pérez-Díaz, L., Eagles, G., 2014. Constraining South Atlantic growth with seafloor spreading data. Tectonics 33 (9), 1848–1873.
Priestley, K., McKenzie, D., 2006. The thermal structure of the lithosphere from shear wave velocities. Earth Planet. Sci. Lett. 244 (1), 285–301.
Putirka, K.D., 2005. Mantle potential temperatures at Hawaii, Iceland, and the mid-ocean ridge system, as inferred from olivine phenocrysts: evidence for thermally driven mantle plumes. Geochem. Geophys. Geosyst. 6 (5), Q05L08.
Renne, P.R., Ernesto, M., Pacca, I.G., Coe, R.S., Glen, J., Prévot, M., Perrin, M., et al., 1992. The age of Paraná flood volcanism, rifting of Gondwanaland, and the Jurassic-Cretaceous boundary. Science 258 (5084), 975–979.
Reston, T.J., 2010. The Opening of the Central Segment of the South Atlantic: Symmetry and the Extension Discrepancy Vol. 16 (3) pp. 199–206.
Rosendahl, B.R., 1987. Architecture of continental rifts with special reference to East Africa. Annu. Rev. Earth Planet. Sci. 15, 445.
Sandwell, D., Garcia, E., Soofi, K., Wessel, P., Chandler, M., Smith, W.H., 2013. Toward 1-mGal accuracy in global marine gravity from CryoSat-2, Envisat, and Jason-1. Lead. Edge 32 (8), 892–899.
Schinkel, J., 2006. Tiefenstruktur der Kontinent-Ozean-Grenze vor dem Orange Fluss, Namibia. Master Thesis, Institut für Geowissenschaften der Friedrich-Schiller Universität, Jena, Jena.
Schnabel, M., Franke, D., Engels, M., Hinz, K., Neben, S., Damm, V., Grassmann, S., Pelliza, H., Dos Santos, P.R., 2008. The structure of the lower crust at the Argentine continental margin, South Atlantic at 44 ° S. Tectonophysics 454 (1–4), 14–22.
Seton, M., Müller, R., Zahirovic, S., Gaina, C., Torsvik, T., Shephard, G., Talsma, A., Gurnis, M., Turner, M., Maus, S., et al., 2012. Global continental and ocean basin reconstructions since 200 Ma. Earth Sci. Rev. 113 (3), 212–270.
Sleep, N.H., 1996. Lateral flow of hot plume material ponded at sublithospheric depths. J. Geophys. Res. 101 (B12), 28065–28083.
Sleep, N.H., 2006. Mantle plumes from top to bottom. Earth Sci. Rev. 77 (4), 231–271.
Stewart, K., Turner, S., Kelley, S., Hawkesworth, C., Kirstein, L., Mantovani, M., 1996. 3-D 40Ar-39Ar geochronology in the Paraná continental flood basalt province. Earth Planet. Sci. Lett. 143 (1), 95–109.
Storey, B.C., 1995. The role of mantle plumes in continental breakup: case histories from Gondwanaland. Nature 377 (6547), 301–308.
Torsvik, T.H., Rousse, S., Labails, C., Smethurst, M.A., 2009. A new scheme for the opening of the South Atlantic Ocean and the dissection of an Aptian salt basin. Geophys. J. Int. 177 (3), 1315–1333.
Trumbull, R.B., 2014. Causes and consequences of continental breakup in the South Atlantic: lessons learned from the SAMPLE program. EGU General Assembly Conference Abstracts vol. 16, p. 1430.
Trumbull, R.B., Franke, D., Bauer, K., Sobolev, S.V., 2015. Petrophysical models of high velocity lower crust on the South Atlantic rifted margins: whence the asymmetry? EGU General Assembly Conference Abstracts vol. 17, p. 10976
Turner, S., Regelous, M., Kelley, S., Hawkesworth, C., Mantovani, M., 1994. Magmatism and continental break-up in the South Atlantic: high precision 40Ar-39Ar geochronology. Earth Planet. Sci. Lett. 121 (3), 333–348.
White, R., McKenzie, D., 1989. Magmatism at rift zones - the generation of volcanic continental margins and flood basalts. J. Geophys. Res. Solid Earth 94 (B6), 7685–7729.
White, R., McKenzie, D., 1995. Mantle plumes and flood basalts. J. Geophys. Res. 100 (B9), 17543–17585.
White, R.S., McKenzie, D., O'Nions, R.K., 1992. Oceanic crustal thickness from seismic measurements and rare earth element inversions. J. Geophys. Res. Solid Earth 97 (B13), 19683–19715.
Winterbourne, J., White, N., Crosby, A., 2014. Accurate measurements of residual topography from the oceanic realm. Tectonics 33 (6), 982–1015.

Please cite this article as: Taposeea, C.A., et al., Asthenosphere and lithosphere structure controls on early onset oceanic crust production in the southern South Atlantic, Tectonophysics (2016), http://dx.doi.org/10.1016/j.tecto.2016.06.026